UNITED STATES AIR FORCE

SUMMER RESEARCH PROGRAM -- 1999

SUMMER RESEARCH EXTENSION PROGRAM FINAL REPORTS

VOLUME 4
WRIGHT LABORATORY

RESEARCH & DEVELOPMENT LABORATORIES

5800 Uplander Way

Culver City, CA 90230-6608

Program Director, RDL
Gary Moore

Program Manager, AFOSR
Colonel Jan Cerveny

Program Manager, RDL
Scott Licoscos

Program Administrator, RDL
Johnetta Thompson

Program Administrator, RDL
Rebecca Kelly-Clemmons

Submitted to:

AIR FORCE OFFICE OF SCIENTIFIC RESEARCH

Bolling Air Force Base

Washington, D.C.

December 1999

20010319 011

AQM01-06-1176

PREFACE

This volume is part of a four-volume set that summarizes the research of participants in the 1999 AFOSR Summer Research Extension Program (SREP). The current volume, Volume 1 of 4, presents the final reports of SREP participants at Armstrong Laboratory.

Reports presented in this volume are arranged alphabetically by author and are numbered consecutively -- e.g., 1-1, 1-2, 1-3; 2-1, 2-2, 2-3, with each series of reports preceded by a 35 page management summary. Reports in the four-volume set are organized as follows:

VOLUME	TITLE
1	Armstrong Research Laboratory
2	Phillips Research Laboratory
3	Rome Research Laboratory
4	Wright Research Laboratory

REPORT DOCUMENTATION PAGE

Public reporting burden for this collection of information is estimated to average 1 hour per response, including the time for reviewing instructions, the collection of information. Send comments regarding this burden estimate or any other aspect of this collection of information, including Operations and Reports, 1215 Jefferson Davis Highway, Suite 1204, Arlington, VA 22202-4302, and to the Office of Management and Budget, I

AFRL-SR-BL-TR-00-

0422

nd reviewing
r Information

1. AGENCY USE ONLY *(Leave blank)*	2. REPORT DATE	3. REI
	December, 1999	

4. TITLE AND SUBTITLE
1999 Summer Research Program (SRP), Summer Research Extension Program (SREP), Final Report, Volume 4, Wright Laboratory

5. FUNDING NUMBERS
F49620-93-C-0063

6. AUTHOR(S)
Gary Moore

7. PERFORMING ORGANIZATION NAME(S) AND ADDRESS(ES)
Research & Development Laboratories (RDL)
5800 Uplander Way
Culver City, CA 90230-6608

8. PERFORMING ORGANIZATION REPORT NUMBER

9. SPONSORING/MONITORING AGENCY NAME(S) AND ADDRESS(ES)
Air Force Office of Scientific Research (AFOSR)
801 N. Randolph St.
Arlington, VA 22203-1977

10. SPONSORING/MONITORING AGENCY REPORT NUMBER

11. SUPPLEMENTARY NOTES

12a. DISTRIBUTION AVAILABILITY STATEMENT
Approved for Public Release

12b. DISTRIBUTION CODE

13. ABSTRACT *(Maximum 200 words)*

The United States Air Force Summer Research Program (SRP) is designed to introduce university, college, and technical institute faculty members to Air Force research. This is accomplished by the faculty members, graduate students, and high school students being selected on a nationally advertised competitive basis during the summer intersession period to perform research at Air Force Research Laboratory (AFRL) Technical Directorates and Air Force Air Logistics Centers (ALC). AFOSR also offers its research associates (faculty only) an opportunity, under the Summer Research Extension Program (SREP), to continue their AFOSR-sponsored research at their home institutions through the award of research grants. This volume consists of a listing of the participants for the SREP and the technical report from each participant working at the AF Wright Laboratory.

14. SUBJECT TERMS
Air Force Research, Air Force, Engineering, Laboratories, Reports, Summer, Universities, Faculty, Graduate Student, High School Student

15. NUMBER OF PAGES

16. PRICE CODE

17. SECURITY CLASSIFICATION OF REPORT	18. SECURITY CLASSIFICATION OF THIS PAGE	19. SECURITY CLASSIFICATION OF ABSTRACT	20. LIMITATION OF ABSTRACT
Unclassified	Unclassified	Unclassified	UL

Standard Form 298 (Rev. 2-89) (EG)
Prescribed by ANSI Std. 239.18
Designed using Perform Pro, WHS/DIOR, Oct 94

1999 SREP Final Technical Report Table of Contents

Armstrong Research Laboratory

Volume 1

	Principle Investigator	Report Title University/Institution	Laboratory & Directorate
1	Dr. Kenneth Graetz	Conflict Resolution in Distributed Meetings:Using Collaboration Technology to Support Battle Staff University of Dayton	AFRL/HEN
2	Dr. Nadini Kannan	Altitude Decompression Sickness: Modeling and Prediction University of Texas at San Antonio	AFRL/HEPR
3	Ms.Vanessa Le	A Study on Stress-Induced Alterations In Blood-BrainBarrrier Permeability to Pyridostigmine University of Texas at Austin	AFRL/HEDB
4	Dr. Ramaswamy Ramesh	Modeling and Analysis of DMT Systems: Training Effectiveness, Costs, Resource Management and Acquisition Strategies Research Foundation of SUNY	AFRL/HEA

1999 SREP Final Technical Report Table of Contents

Phillips Research Laboratory

Volume 2

	Principle Investigator	Report Title University/Institution	Laboratory & Directorate
1	Dr. Gurnam Gill	Adaptive signal Processing and its Applications in Space Space based Radar Naval Postgraduate School	AFRL/VSSS
2	Dr. Robert Hinde	Dopant-Induced Infrafed Activity in Solid Hydrogen An AB Initio and Quantum Monte Carlo Study University of Tennessee	AFRL/PRSP
3	Dr. Brian Jeffs	Algebraic Methods for Improved Blind Restoration of Adaptive Optics Images of Space Objects Brigham Young University	AFRL/DEHP
4	Dr. Donald Leo	Self-Sensing acoustic Sources For Interior Noise Control in Payload Fairings University of Toledo	AFRL/VSDV
5	Dr. Arfin Lodhi	Investigation into Time-Dependent Power Loses from AMTEC Components Texas Tech University	AFRL/VSDV
6	Dr. John McHugh	Atmospheric Gravity Waves Near the Tropopause University of New Mexico	AFRL/ VSBC
7	Dr. Stanly Steinberg	Lie-Algebraic representations of Product Integrals of Variable Matrices University of New Mexico	AFRL/DEOB
8	Mr. Kenneth Stephens II	Simulation of a Magnetized Target Fusion Concept Using MACH 2 University of North Texas	AFRL/VSDV

1999 SREP Final Technical Report Table of Contents

Rome Research Laboratory

Volume 3

	Principle Investigator	Report Title University/Institution	Laboratory & Directorate
1	Dr. Ercument Arvas	Realization of Low Noise MMIC Amplifier as a Microwave –to Optics Link for Radar Syracuse University	AFRL/SNDR
2	Dr. Kaliappan Gopalan	Detection of Acoustic Correlates of Stress from Modulation Characteristics Purdue Research Foundation	AFRL/IFEC
3	Dr. Donald Hung	An Investigation on Accelerating the Ray-Tracing Computations Washington State University	AFRL/IFSA
4	Dr. Adam Lutoborski	Transform Methods for Watermarking Digital Images Syracuse University	AFRL/IFEC
5	Dr. Brajendra Panda	Implementation of Petri Nets Based Multi-source Attack Detection Model University of North Dakota	AFRL/IFGB
6	Dr. Jerry Potter	Algorithms for Data Intensive Knowledge Discovery Kent State University	AFRL/IFGA
7	Dr. Shambhu Upadhyaya	A Distributed concurrent Intrusion Detection and Recovery Scheme based on Assertions SUNY Buffalo	AFRL/IFGA

1999 SREP Final Technical Report Table of Contents

Wright Research Laboratory

Volume 4

Principle Investigator		Report Title University/Institution	Laboratory & Directorate
1	Dr. Farid Ahmed	Image Quality Assessment for ART Applications Using Multiresolional Information Metrics Pennsylvania State University, Erie	AFRL/SNAT
2	Dr. Gregory Buck	Acoustic Disturbance Source Modeling and Development for Hypersonic Receptivity South Dakota School of Mines	AFRL/VAAA
3	Dr. Kevin Belfield	Synthesis of New Two-Photon Absorbing Dyes, Monomers and Polymers University of Central Florida	AFRL/ML
4	Dr. Patrick Gilcrease	Biocatalysis of Biphenyl and Diphenylacetylene in an Aqueous Organic Biphasic Reaction System University of Wyoming	AFRL/MLQ
5	Dr. Jeffrey Johnson	Incorporating Fixed, Adaptive, and Learning Controllers to the Flight Control University of Toledo	AFRL/VACC
6	Dr. Vikram Kapila	Dynamics and control of Spacecraft Formation Flying Polytechnic Institute of New York	AFRL/VACC
7	Dr. Kenneth Kihm	Micro-Scale Flow Field Measurement of the Thin Meniscus of Capillary-Driven Heat Exchanger Devices Using MFW Texas A & M University	AFRL/VAVE
8	Dr. Rongxing Li	Uncertainty Modeling of Target Locations From Multiplatform and Multisensor Data Ohio State	AFRL/SNAR
9	Dr. Chun-Shin Lin	Sensor Fusion w/Passive Millimeter Wave & Laser Radar for Target Detection University of Missouri –	AFRL/MNGS
10	Dr. Chaoqun Liu	Boundary Conditions in Curvilinear Coordinates for Direct Numerical Simulation of Turbulent Flow Louisiana Tech University	AFRL/VAAA

1999 SREP Final Technical Report Table of Contents

Wright Research Laboratory

Volume 4, continued

	Principle Investigator	Report Title University/Institution	Laboratory & Directorate
11	Dr. Carl Mungan	Infrared Spectropolarimetric Directional Reflectance and Emissivity of Mental Surfaces University of Forida	AFRL/MNGS
12	Dr. Amod Ogale	Structural Changes in Mesophase Pitch-Based Carbon Fibers: In SITU & ES SITU Measurements Clemson University	AFRL/MLBC
13	Mr. Ramana Pidaparti	Benchmarking Aerodynamic Panel Methods for Flight Loads in Multidisciplinary Optimization Indiana University	AFRL/VAS
14	Dr. Stephen Saddow	Silicon Carbide Implant Activation & Surface preparation Investigation Mississippi State University	AFRL/PRPE
15	Dr. Paavo Sepri	Computational Study of Unsteady Flow Interactions Between Turbine Blades, Cylinder Wakes, and coolant Injection Florida Institute of Technology	AFRL/PRTT
16	Dr. Hongchi Shi	Developing an efficient Algorithm for Routing Processors of the VGI Parallel Computer for Signal Processing Applications University of Missouri – Columbia	AFRL/MNGI
17	Dr. Mehrdad Soumekh	Signal and Image Processing for FOPEN/GPEN SAR SUNY Buffalo	AFRL/SNRT
18	Mr. Craig Riviello	In-Situ Synthesis of Discontinuously Reinforced Titanium alloy CompoLaboratorys Via Blended Elemental Powder Metallurgy Processing Wright State University	AFRL/MLLM

1999 SUMMER RESEARCH EXTENSION PROGRAM (SREP) MANAGEMENT REPORT

1.0 BACKGROUND

Under the provisions of Air Force Office of Scientific Research (AFOSR) contract F49620-90-C-0076, September 1990, Research & Development Laboratories (RDL), an 8(a) contractor in Culver City, CA, manages AFOSR's Summer Research Program. This report is issued in partial fulfillment of that contract (CLIN 0003AC).

The Summer Research Extension Program (SREP) is one of four programs AFOSR manages under the Summer Research Program. The Summer Faculty Research Program (SFRP) and the Graduate Student Research Program (GSRP) place college-level research associates in Air Force research laboratories around the United States for 8 to 12 weeks of research with Air Force scientists. The High School Apprenticeship Program (HSAP) is the fourth element of the Summer Research Program, allowing promising mathematics and science students to spend two months of their summer vacations working at Air Force laboratories within commuting distance from their homes.

SFRP associates and exceptional GSRP associates are encouraged, at the end of their summer tours, to write proposals to extend their summer research during the following calendar year at their home institutions. AFOSR provides funds adequate to pay for SREP subcontracts. In addition, AFOSR has traditionally provided further funding, when available, to pay for additional SREP proposals, including those submitted by associates from Historically Black Colleges and Universities (HBCUs) and Minority Institutions (MIs). Finally, laboratories may transfer internal funds to AFOSR to fund additional SREPs. Ultimately the laboratories inform RDL of their SREP choices, RDL gets AFOSR approval, and RDL forwards a subcontract to the institution where the SREP associate is employed. The subcontract (see Appendix 1 for a sample) cites the SREP associate as the principal investigator and requires submission of a report at the end of the subcontract period.

Institutions are encouraged to share costs of the SREP research, and many do so. The most common cost-sharing arrangement is reduction in the overhead, fringes, or administrative charges institutions would normally add on to the principal investigator's or research associate's labor. Some institutions also provide other support (e.g., computer run time, administrative assistance, facilities and equipment or research assistants) at reduced or no cost.

When RDL receives the signed subcontract, we fund the effort initially by providing 90% of the subcontract amount to the institution (normally $18,000 for a $20,000 SREP). When we receive the end-of-research report, we evaluate it administratively and send a copy to the laboratory for a technical evaluation. When the laboratory notifies us the SREP report is acceptable, we release the remaining funds to the institution.

2.0 THE 1999 SREP PROGRAM

SELECTION DATA: A total of 381 faculty members (SFRP Associates) and 130 graduate students (GSRP associates) applied to participate in the 1998 Summer Research Program. From these applicants 85 SFRPs and 40 GSRPs were selected. The education level of those selected was as follows:

1998 SRP Associates, by Degree			
SFRP		GSRP	
PHD	MS	MS	BS
83	1	3	19

Of the participants in the 1998 Summer Research Program 65 percent of SFRPs and 20 percent of GSRPs submitted proposals for the SREP. Fifty-four proposals from SFRPs and eleven from GSRPs were selected for funding, which equates to a selection rate of 65% of the SFRP proposals and of 20% for GSRP proposals.

1999 SREP: Proposals Submitted vs. Proposals Selected			
	Summer 1998 Participants	Submitted SREP Proposals	SREPs Funded
SFRP	85	54	34
GSRP	40	11	2
TOTAL	125	65	36

The funding was provided as follows:

Contractual slots funded by AFOSR	36
Laboratory funded	0
Total	36

Four HBCU/MI associates from the 1998 summer program submitted SREP proposals; four were selected (none were lab-funded; all were funded by additional AFOSR funds).

Proposals Submitted and Selected, by Laboratory		
	Applied	Selected
Armstrong Research Site	15	3
Air Logistic Centers	1	0
Arnold Engineering Development Center	1	0
Phillips Research Site	10	8
Rome Research Site	12	7
Wilford Hall Medical Center	1	0
Wright Research Site	25	18
TOTAL	65	36

The 212 1998 Summer Research Program participants represented 60 institutions.

Institutions Represented on the 1998 SRP and 1999 SREP		
Number of schools Represented in the Summer 98 Program	Number of schools represented in submitted proposals	Number of schools represented in Funded Proposals
60	36	29

Thirty schools had more than one participant submitting proposals.

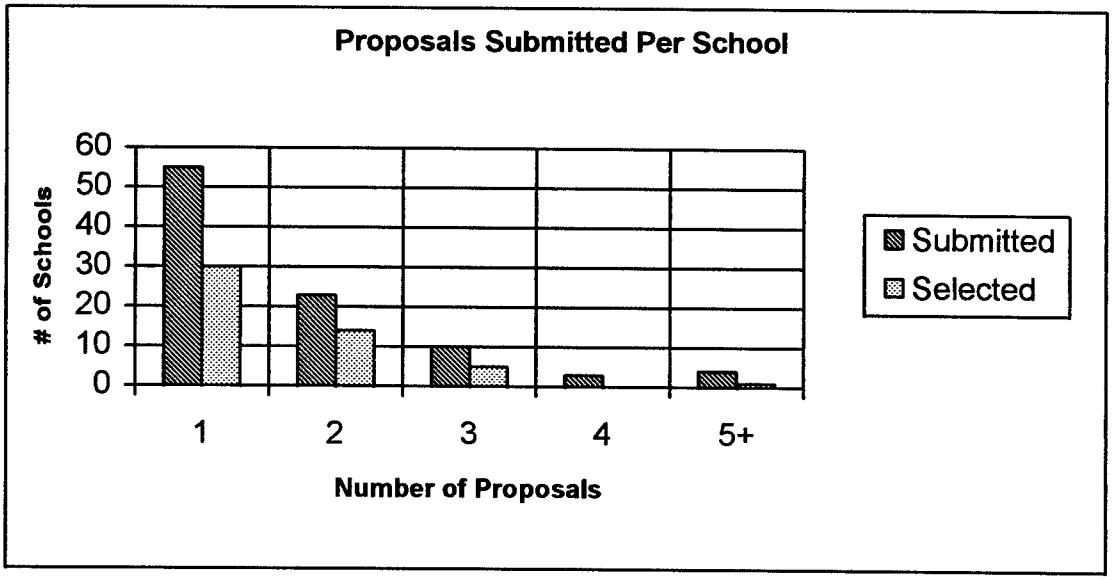

The selection rate for the 60 schools submitting 1 proposal (68%) was better than those submitting 2 proposals (61%), 3 proposals (50%), 4 proposals (0%) or 5+ proposals (25%). The 4 schools that submitted 5+ proposals accounted for 30 (15%) of the 65 proposals submitted.

Of the 65 proposals submitted, 35 offered institution cost sharing. Of the funded proposals which offered cost sharing, the minimum cost share was $1274.00, the maximum was $38,000.00 with an average cost share of $12,307.86.

Proposals and Institution Cost Sharing		
	Proposals Submitted	Proposals Funded
With cost sharing	35	30
Without cost sharing	30	6
Total	65	36

The SREP participants were residents of 31 different states. Number of states represented at each laboratory were:

States Represented, by Proposals Submitted/Selected per Laboratory		
	Proposals Submitted	Proposals Funded
Armstrong Research Laboratory	15	3
Air Logistic Centers	1	0
Arnold Engineering Development Center	1	0
Phillips Research Laboratory	10	8
Rome Research Laboratory	12	7
Wilford Hall Medical Center	1	0
Wright Research Laboratory	25	18

Six of the 1999 SREP Principal Investigators also participated in the 1998 SREP.

ADMINISTRATIVE EVALUATION: The administrative quality of the SREP associates' final reports was satisfactory. Most complied with the formatting and other instructions provided to them by RDL. Thirty-six final reports have been received and are included in this report. The subcontracts were funded by $897,309.00 of Air Force money. Institution cost sharing totaled $356,928.00.

TECHNICAL EVALUATION: The form used for the technical evaluation is provided as Appendix 2. Thirty-two evaluation reports were received. Participants by laboratory versus evaluations submitted is shown below:

	Participants	Evaluations	Percent
Armstrong Laboratory	3	2	95.2
Phillips Laboratory	8	8	100
Rome Laboratory	7	7	100
Wright Laboratory	18	15	91.9
Total	36	32	95.0

Notes:

1: Research on four of the final reports was incomplete as of press time so there aren't any technical evaluations on them to process, yet. Percent complete is based upon 20/21=95.2%

PROGRAM EVALUATION: Each laboratory focal point evaluated ten areas (see Appendix 2) with a rating from one (lowest) to five (highest). The distribution of ratings was as follows:

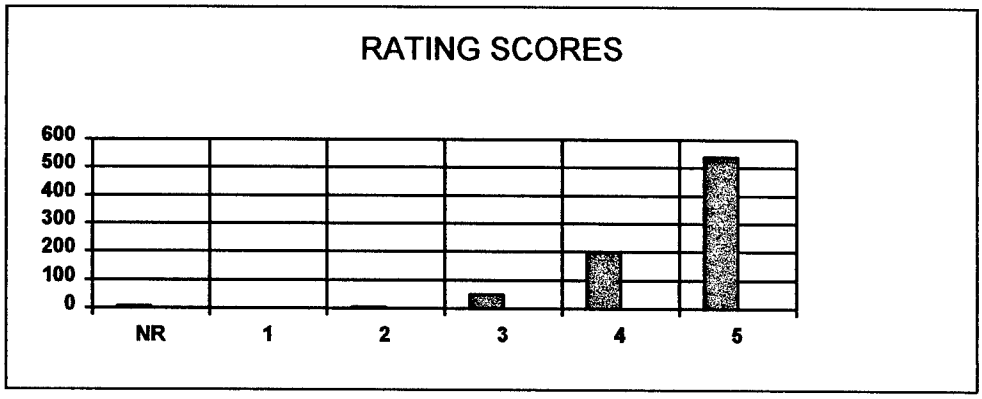

Rating	Not Rated	1	2	3	4	5
# Responses	7	1	7	62 (6%)	226 (25%)	617 (67%)

The 8 low ratings (one 1 and seven 2's) were for question 5 (one 2) "The USAF should continue to pursue the research in this SREP report" and question 10 (one 1 and six 2's) "The one-year period for complete SREP research is about right", in addition over 30% of the threes (20 of 62) were for question ten. The average rating by question was:

Question	1	2	3	4	5	6	7	8	9	10
Average	4.6	4.6	4.7	4.7	4.6	4.7	4.8	4.5	4.6	4.0

The distribution of the averages was:

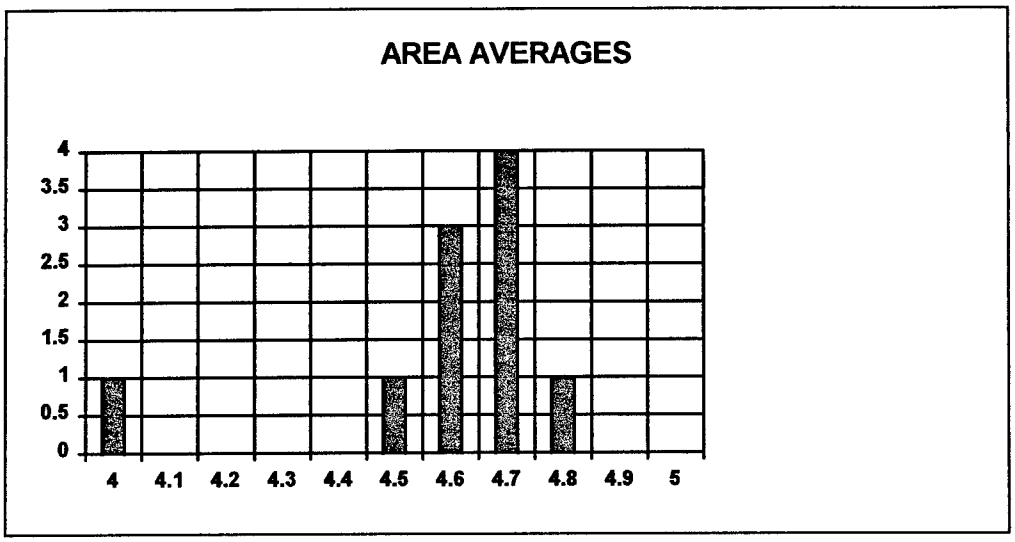

Area 10 "the one-year period for complete SREP research is about right" had the lowest average rating (4.1). The overall average across all factors was 4.6 with a small sample standard deviation of 0.2. The average rating for area 10 (4.1) is approximately three sigma lower than the overall average (4.6) indicating that a significant number of the evaluators feel that a period of other than one year should be available for complete SREP research.

The average ratings ranged from 3.4 to 5.0. The overall average for those reports that were evaluated was 4.6. Since the distribution of the ratings is not a normal distribution the average of 4.6 is misleading. In fact over half of the reports received an average rating of 4.8 or higher. The distribution of the average report ratings is as shown:

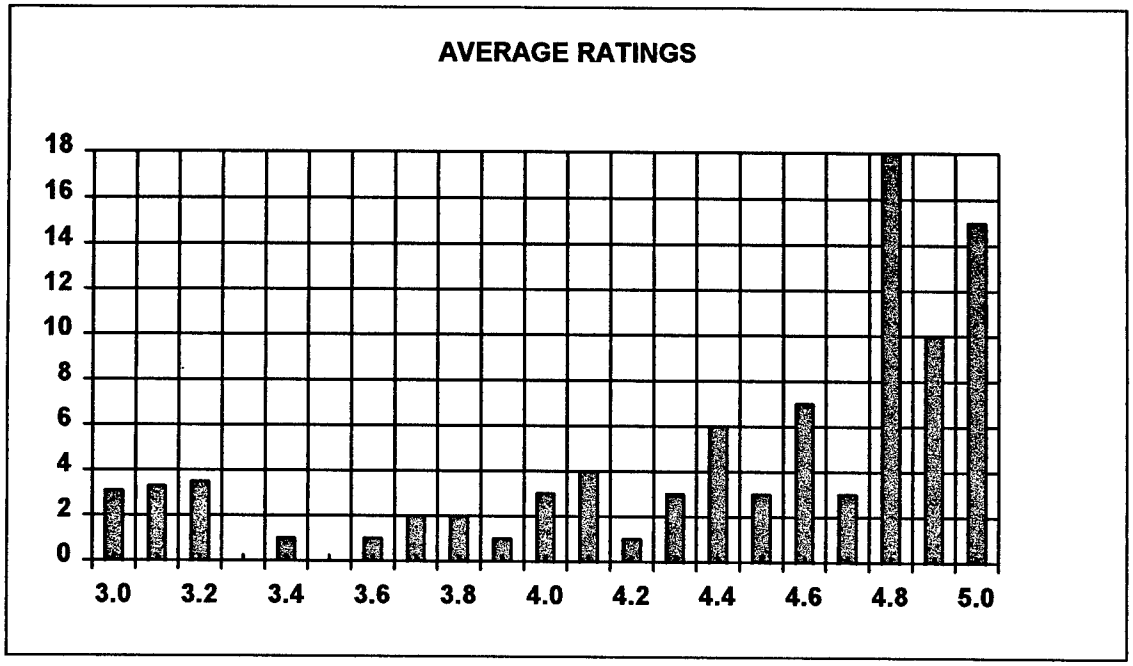

It is clear from the high ratings that the laboratories place a high value on AFOSR's Summer Research Extension Programs.

3.0 SUBCONTRACTS SUMMARY

Table 1 provides a summary of the SREP subcontracts. The individual reports are published in volumes as shown:

Laboratory	Volume
Armstrong Research Laboratory	1
Phillips Research Laboratory	2
Rome Research Laboratory	3
Wright Research Laboratory	4

SREP SUB-CONTRACT DATA

Report Author Author's University	Author's Degree	Sponsoring Lab	Performance Period	Contract Amount	Univ. Cost Share
Graetz , Kenneth Department of Psychology University of Dayton, Dayton, OH	PhD 99-1803	AL/CF	01/01/99 12/31/99 Conflict resolution in distributed Meetingl; Using Collaboration Technology to	$24983.00	$0.00
Kannan , Nandini Statistics Univ of Texas at San Antonio, San Antonio, TX	PhD 99-1804	AL/CF	01/01/98 12/31/98 Altitude decompression Sickness: Modeling and Prediction	$22492.00	$4478.00
Ramesh , Ramaswamy Magement Science/Systems Research Foundation of SUNY, Buffalo, NY	PhD 99-1802	AL/CF	01/01/99 12/31/99 Modeling and Analsis of DMT Systems: Training Effectiveness, Costs, Resource Ma	$24979.00	$0.00
Le , Vanessa Biochemistry Univ of Texas at Austin, Austin, TX	BS 99-1805	AL/CF	01/01/98 12/31/98 a Study on Stress-Induced Alterations In Blood-Brain Barrier Permeability to Pyr	$25000.00	$0.00
Gill , Gurnam EE Naval Postgraduate School, Monterey, CA	PhD 99-1834	PL/VT	01/01/99 12/31/99 Adaptive signal Processing and its Applications in Space based Radar	$25000.00	$0.00
Hinde , Robert Physical Chemistry Univ of Tennessee, Knoxville, TN	PhD 99-1801	WL/PO	01/01/98 12/31/98 Dopant-Induced Infrafed Activity in Solid Hydrogen An AB Initio and Quantum Mont	$25000.00	$3976.00
Jeffs , Brian Electrical Engineering Brigham Young University, Provo, UT	PhD 99-1828	PL/LI	01/01/98 12/31/98 Algebraic Methods for Improved blimd Restoration of Adaptive Optics Images of Sp	$25000.00	$19177.00
Leo , Donald Mechanical & Aerospace Virginia Tech, Blacksburg, VA	PhD 99-1835	PL/VT	01/01/99 12/31/99 Self-Sensing Acoustic Sources for Interior Noise Control in Payload Fairings	$24999.00	$7416.00
Lodhi , M. Arfin Nuclear Physics Texas Tech University, Lubbock, TX	PhD 99-1832	PL/VT	01/01/99 12/31/99 Investigatioin into Time-Dependent Power Losses from AMTEC Components	$25000.00	$0.00
McHugh , John Applied Mechanics University of New Hampshire, Durham, NH	PhD 99-1833	PL/VT	01/01/99 12/13/99 Atmospheric Gravity Waves Near The Tropopause	$25000.00	$7000.00
Steinberg , Stanly Mathematics University of New Mexico, Albuquerque, NM	PhD 99-1829	PL/LI	01/01/99 12/31/99 Lie-Algebraic Representations of Product Integrals of Variable Matrices	$25000.00	$0.00
Stephens II , Kenneth University of North Texas, Denton, TX	MA 99-1830	PL/LI	01/01/99 12/31/99 Simulation of a Magnetized Target Fusion Concept Using MACH2	$25000.00	$16764.00
Arvas , Ercument Electrical Engineering Syracuse University, Syracuse, NY	PhD 99-1808	WL/AA	01/01/99 12/31/99 Realization of Low Noise MMIC Amplifier as a Microwave-to-Optics Link for Radar	$25000.00	$13000.00
Gopalan , Kaliappan Electrical Engineering Purdue Research Foundation, West Lafayette, IN	PhD 99-1814	RL/IR	01/01/99 12/31/99 Detection of Acoustic Correlates of Stress from Modulation Characteristics	$25000.00	$38168.00

SREP SUB-CONTRACT DATA

Report Author Author's University	Author's Degree	Sponsoring Lab	Performance Period		Contract Amount	Univ. Cost Share
Hung , Donald **Electrical Engineering** **Washington State University, Richland, WA**	**PhD** 99-0812	**RL/IR** An Investigation on Accelerating the Ray-Tracing Compputations	**01/01/99**	**12/31/99**	**$25000.00**	**$23008.00**
Lutoborski , Adam **Applied Mathematics** **Syracuse University, Syracuse, NY**	**PhD** 99-0811	**RL/IR** Transform Methods for Watermarking Digital Images	**01/01/99**	**12/31/99**	**$25000.00**	**$1274.00**
Panda , Brajendra **Computer Science** **University of North Dakota, Grand Forks, ND**	**PhD** 99-0810	**RL/IR** Implementation of Petri Nets Based Multi-source Attack Detection Model	**01/01/98**	**12/31/98**	**$24942.00**	**$2600.00**
Potter , Jerry **Computer Science** **Kent State University, Kent, OH**	**PhD** 99-0809	**RL/IR** Algorithms for Data Intensive Knowledge Discovery	**01/01/99**	**12/31/99**	**$25000.00**	**$52767.00**
Upadhyaya , Shambhu **Elec & Comp Engineering** **SUNY Buffalo, Buffalo, NY**	**PhD** 99-0813	**RL/IR** a Distrubuted concurrent Intrusion Detection And recovery Scheme based on Assert	**01/01/98**	**12/31/98**	**$25000.00**	**$6430.00**
Ahmed , Farid **Electrical engineering** **Penn State Uni-Erie, Erie, PA**	**PhD** 99-0806	**WL/AA** Image Quality Assessment for ATR Applications Using Multiresolutional Informatio	**10/10/98**	**12/31/98**	**$25000.00**	**$2396.00**
Belfield , Kevin **Chemistry** **University of Central Florida, Orlando, FL**	**PhD** 99-0816	**WL/ML** Synthesis of New Two-Photon Absorbing Dyes, Monomers and Polymers	**01/01/99**	**12/31/99**	**$25000.00**	**$5765.00**
Buck , Gregory **Mechanical Engineering** **S Dakota School of Mines/Tech, Rapid City, SD**	**PhD** 99-0818	**WL/FI** Acoustic Disturbance Source Modeling and Development for Hypersonic Receptivity	**01/01/99**	**12/31/99**	**$25000.00**	**$7639.00**
Gilcrease , Patrick **Chemical Engineering** **University of Wyoming, Laramie, WY**	**PhD** 99-0815	**WL/ML** Biocatalysis of Biphenyl and Diphenylacetylene in an Aqueous-Organic Biphasic Re	**01/01/99**	**12/31/99**	**$25000.00**	**$28010.00**
Johnson , Jeffrey **Electrical Engineering and** **University of Toledo, Toledo, OH**	**PhD** 99-0823	**WL/FI** Incorporating Fixed, Adaptive, & Learning Controllers to the Flight Control	**01/01/99**	**12/31/99**	**$25000.00**	**$10075.00**
Kapila , Vikram **Aerospace engineering** **Polytechnic Inst of New York, Brooklyn, NY**	**PhD** 99-0820	**WL/FI** Dynamics and Control of Spacecraft Formation Flying	**01/01/99**	**12/31/99**	**$25000.00**	**$17448.00**
Kihm , Kenneth **Mechanical Engineering** **Texas Engineering Experiment Station, College**	**PhD** 99-0821	**WL/FI** Micro-Scale Flow Field Measurement of the Thin Meniscus of Capillary-Driven Heat	**01/01/99**	**12/31/99**	**$25000.00**	**$10310.00**
Li , Rongxing **Photogrammertry & Remote Sensing** **Ohio State University, Columbus, OH**	**PhD** 99-0831	**WL/AA** Uncertainty Modeling of Target Locations From Multiplatform and Multisensor Data	**01/01/98**	**12/31/98**	**$25000.00**	**$13183.00**
Lin , Chun-Shin **Electrical Engineering** **Univ of Missouri - Columbia, Columbia, MO**	**PhD** 99-0826	**WL/MN** Sensor Fusion w/Passive Millimeter Wave & Laser Radar for Target Detection	**01/01/99**	**12/31/99**	**$25000.00**	**$1991.00**
Liu , Chaoqun **Applied Mathematics** **Louisiana Tech University, Ruston, LA**	**PhD** 99-0819	**WL/FI** Boundary Conditions in Curvilinear Coordinates for Direct Numerical Simulation	**01/01/99**	**12/31/99**	**$25000.00**	**$12521.00**

SREP SUB-CONTRACT DATA

Report Author Author's University	Author's Degree	Sponsoring Lab	Performance Period	Contract Amount	Univ. Cost Share
Mungan , Carl **Dept of Physics** **University of Florida, Pensacola, FL**	**PhD** 99-0824	**WL/MN**	**01/01/99 12/31/99** infrared Spectrcpolarimetric Directonal Reflectance and Emissivity of Mental Sur	**$24914.00**	**$3276.00**
Ogale , Amod **Chemical Engineering** **Clemson University, Clemson, SC**	**PhD** 99-0817	**WL/ML**	**01/01/99 12/31/99** Structural Changes in Mesophase Pitch-Based Carbon Fibers:In SITU &ES SITU Measu	**$25000.00**	**$9000.00**
Pidaparti , Ramana **Aeronautics & Astronautics** **Indiana U-Purdue at Indianap, Indianapolis, IN**	**PhD** 99-0822	**WL/FI**	**01/01/99 12/31/99** Benchmarking Aerodynamic Panel Methods for Flight Loads in Multidisciplinary Opt	**$25000.00**	**$10582.00**
Saddow , Stephen **Electrical Engineering** **Mississippi State University, Mississippi State,**	**PhD** 99-0827	**WL/PO**	**01/01/98 12/31/98** Silicon Carbide Implant Activation & Surface preparation Investigation	**$25000.00**	**$0.00**
Sepri , Paavo **Engineering Science** **Florida Inst of Technology, Melbourne, FL**	**PhD** 99-0836	**WL/PO**	**01/01/99 12/31/99** Computational Study of Unsteady Flow Interactions Between Turbine Blades, Cylind	**$25000.00**	**$6519.00**
Shi , Hongchi **Computer Engineering** **Univ of Missouri - Columbia, Columbia, MO**	 99-0825	**WL/MN**	**01/01/99 12/31/99** Developing an efficient Algorithm for Routing Processors of the VGI Parallel Com	**$25000.00**	**$15851.00**
Soumekh , Mehrdad **Elec/Computer Engineering** **SUNY Buffalo, Amherst, NY**	**PhD** 99-0807	**WL/AA**	**01/01/99 12/30/99** Signal and Image Processing for FOPEN/GPEN SAR	**$25000.00**	**$0.00**
Riviello , Craig **Mechanical** **Wright State University, Dayton, OH**	**BS** 99-0837	**WL/ML**	**01/01/99 01/01/99** In-Situ Synthesis of Discontinuously Reinforced Titanium alloy Composites Via Bl	**$25000.00**	**$6304.00**

1. BACKGROUND: Research & Development Laboratories (RDL) is under contract (F49620-93-C-0063) to the United States Air Force to administer the Summer Research Program (SRP), sponsored by the Air Force Office of Scientific Research (AFOSR), Bolling Air Force Base, D.C. Under the SRP, a selected number of college faculty members and graduate students spend part of the summer conducting research in Air Force laboratories. After completion of the summer tour participants may submit, through their home institutions, proposals for follow-on research. The follow-on research is known as the Summer Research Extension Program (SREP). Approximately 61 SREP proposals annually will be selected by the Air Force for funding of up to $25,000; shared funding by the academic institution is encouraged. SREP efforts selected for funding are administered by RDL through subcontracts with the institutions. This subcontract represents an agreement between RDL and the institution herein designated in Section 5 below.

2. RDL PAYMENTS: RDL will provide the following payments to SREP institutions:
   - 80 percent of the negotiated SREP dollar amount at the start of the SREP research period.
   - The remainder of the funds within 30 days after receipt at RDL of the acceptable written final report for the SREP research.

3. INSTITUTION'S RESPONSIBILITIES: As a subcontractor to RDL, the institution designated on the title page will:

a. Assure that the research performed and the resources utilized adhere to those defined in the SREP proposal.

b. Provide the level and amounts of institutional support specified in the SREP proposal..

c. Notify RDL as soon as possible, but not later than 30 days, of any changes in 3a or 3b above, or any change to the assignment or amount of participation of the Principal Investigator designated on the title page.

d. Assure that the research is completed and the final report is delivered to RDL not later than twelve months from the effective date of this subcontract, but no later than December 31, 1998. The effective date of the subcontract is one week after the date that the institution's contracting representative signs this subcontract, but no later than January 15, 1998.

e. Assure that the final report is submitted in accordance with Attachment 3.

f. Agree that any release of information relating to this subcontract (news releases, articles, manuscripts, brochures, advertisements, still and motion pictures, speeches, trade associations meetings, symposia, etc.) will include a statement that the project or effort depicted was or is sponsored by: Air Force Office of Scientific Research, Bolling AFB, D.C.

g. Notify RDL of inventions or patents claimed as the result of this research as specified in Attachment 1.

h. RDL is required by the prime contract to flow down patent rights and technical data requirements to this subcontract. Attachment 2 to this subcontract

contains a list of contract clauses incorporated by reference in the prime contract.

4. All notices to RDL shall be addressed to:

RDL AFOSR Program Office
5800 Uplander Way
Culver City, CA 90230-6609

5. By their signatures below, the parties agree to provisions of this subcontract.

Abe Sopher RDL Contracts Manager	Signature of Institution Contracting Official
	Typed/Printed Name
Date	Title
	Institution
	Date/Phone

ATTACHMENT 2
CONTRACT CLAUSES

This contract incorporates by reference the following clauses of the Federal Acquisition Regulations (FAR), with the same force and effect as if they were given in full text. Upon request, the Contracting Officer or RDL will make their full text available (FAR 52.252-2).

FAR CLAUSES	TITLE AND DATE
52.202-1	DEFINITIONS
52.203-3	GRATUITIES
52.203-5	COVENANT AGAINST CONTINGENT FEES
52.203-6	RESTRICTIONS ON SUBCONTRACTOR SALES TO THE GOVERNMENT
52.203-7	ANTI-KICKBACK PROCEDURES
52.203-8	CANCELLATION, RECISSION, AND RECOVERY OF FUNDS FOR ILLEGAL OR IMPROPER ACTIVITY
52.203-10	PRICE OR FEE ADJUSTMENT FOR ILLEGAL OR IMPROPER ACTIVITY
52.203-12	LIMITATION ON PAYMENTS TO INFLUENCE CERTAIN FEDERAL TRANSACTIONS
52.204-2	SECURITY REQUIREMENTS
52.209-6	PROTECTING THE GOVERNMENT'S INTEREST WHEN SUBCONTRACTING WITH CONTRACTORS DEBARRED, SUSPENDED, OR PROPOSED FOR DEBARMENT
52.212-8	DEFENSE PRIORITY AND ALLOCATION REQUIREMENTS
52.215-2	AUDIT AND RECORDS - NEGOTIATION
52.215-10	PRICE REDUCTION FOR DEFECTIVE COST OR PRICING DATA

52.215-12	SUBCONTRACTOR COST OR PRICING DATA
52.215-14	INTEGRITY OF UNIT PRICES
52.215-8	ORDER OF PRECEDENCE
52.215.18	REVERSION OR ADJUSTMENT OF PLANS FOR POSTRETIREMENT BENEFITS OTHER THAN PENSIONS
52.222-3	CONVICT LABOR
52.222-26	EQUAL OPPORTUNITY
52.222-35	AFFIRMATIVE ACTION FOR SPECIAL DISABLED AND VIETNAM ERA VETERANS
52.222-36	AFFIRMATIVE ACTION FOR HANDICAPPED WORKERS
52.222-37	EMPLOYMENT REPORTS ON SPECIAL DISABLED VETERAN AND VETERANS OF THE VIETNAM ERA
52.223-2	CLEAN AIR AND WATER
52.223-6	DRUG-FREE WORKPLACE
52.224-1	PRIVACY ACT NOTIFICATION
52.224-2	PRIVACY ACT
52.225-13	RESTRICTIONS ON CONTRACTING WITH SANCTIONED PERSONS
52.227-1	ALT. I - AUTHORIZATION AND CONSENT
52.227-2	NOTICE AND ASSISTANCE REGARDING PATIENT AND COPYRIGHT INFRINGEMENT

52.227-10	FILING OF PATENT APPLICATIONS - CLASSIFIED SUBJECT MATTER
52.227-11	PATENT RIGHTS - RETENTION BY THE CONTRACTOR (SHORT FORM)
52.228-7	INSURANCE - LIABILITY TO THIRD PERSONS
52.230-5	COST ACCOUNTING STANDARDS - EDUCATIONAL INSTRUCTIONS
52.232-23	ALT. I - ASSIGNMENT OF CLAIMS
52.233-1	DISPUTES
52.233-3	ALT. I - PROTEST AFTER AWARD
52.237-3	CONTINUITY OF SERVICES
52.246-25	LIMITATION OF LIABILITY - SERVICES
52.247-63	PREFERENCE FOR U.S. - FLAG AIR CARRIERS
52.249-5	TERMINATION FOR CONVENIENCE OF THE GOVERNMENT (EDUCATIONAL AND OTHER NONPROFIT INSTITUTIONS)
52.249-14	EXCUSABLE DELAYS
52.251-1	GOVERNMENT SUPPLY SOURCES

DOD FAR CLAUSES	DESCRIPTION
252.203-7001	SPECIAL PROHIBITION ON EMPLOYMENT
252.215-7000	PRICING ADJUSTMENTS
252.233-7004	DRUG FREE WORKPLACE (APPLIES TO SUBCONTRACTS WHERE THERE IS ACCESS TO CLASSIFIED INFORMATION)
252.225-7001	BUY AMERICAN ACT AND BALANCE OF PAYMENTS PROGRAM
252.225-7002	QUALIFYING COUNTRY SOURCES AS SUBCONTRACTS
252.227-7013	RIGHTS IN TECHNICAL DATA - NONCOMMERCIAL ITEMS
252.227-7030	TECHNICAL DATA - WITHOLDING PAYMENT
252.227-7037	VALIDATION OF RESTRICTIVE MARKINGS ON TECHNICAL DATA
252.231-7000	SUPPLEMENTAL COST PRINCIPLES
252.232-7006	REDUCTIONS OR SUSPENSION OF CONTRACT PAYMENTS UPON FINDING OF FRAUD

APPENDIX 2:

SAMPLE TECHNICAL EVALUATION FORM

SUMMER RESEARCH EXTENSION PROGRAM
TECHNICAL EVALUATION

SREP NO: 99-0828
PRINCIPAL INVESTIGATOR: Dr.Brian Jeffs
Brigham Young University

Circle the rating level number, 1 (low) through 5 (high), you feel best evaluate each statement and return the completed form by fax or mail to:

RDL
Attn: SREP Tech Evals
5800 Uplander Way
Culver City, CA 90230-6608

---

1. This SREP report has a high level of technical merit	1 2 3 4 5
2. The SREP program is important to accomplishing the lab's mission	1 2 3 4 5
3. This SREP report accomplished what the associate's proposal promised	1 2 3 4 5
4. This SREP report addresses area(s) important to USAF	1 2 3 4 5
5. The USAF should continue to pursue the research in this SREP report	1 2 3 4 5
6. The USAF should maintain research relationships with this SREP associate	1 2 3 4 5
7. The money spent on this SREP effort was well worth it.	1 2 3 4 5
8. This SREP report is well organized and well written	1 2 3 4 5
9. I'll be eager to be a focal point for summer and SREP associates in the future	1 2 3 4 5
10.The one-year period for complete SREP research is about right.	1 2 3 4 5

---

11. If you could change any one thing about the SREP program, what would you change:

_____

_____

_____

12. What do you definitely NOT change about the SREP program?

_____

_____

_____

PLEASE USE THE BACK FOR ANY OTHER COMMENTS

Laboratory: AFRL/IFEC
Lab Focal Point: Mr. Stanley Wendt
PHONE: (315) 330-7244

IMAGE QUALITY ASSESSMENT FOR ATR APPLICATIONS USING MULTIRESOLUTIONAL INFORMATION METRICS

Farid Ahmed

Assistant Professor of Electrical Engineering

Pennsylvania State University, Erie

The Behrend College, Erie, PA 16563

Final Report for:
Summer Research Extension Program
Air Force Research Laboratory, Dayton, OH

Sponsored by:
Air Force Office of Scientific Research
Bolling Air Force Base, DC

December 1999

IMAGE QUALITY ASSESSMENT FOR ATR APPLICATIONS USING MULTIRESOLUTIONAL INFORMATION METRICS

Farid Ahmed

Assistant Professor of Electrical Engineering

Pennsylvania State University, Erie

The Behrend College, Erie, PA 16563

Abstract

Determining the quality of an image is an important initial step for the construction of an accurate and robust automatic target recognition (ATR) system. A very smart detection or recognition algorithm may fail, only because the images being used are not of desired quality. Performance measures like probability of detection, probability of false alarms, and probability of identification , do not carry much useful information unless good-quality images are used. This report addresses these problems and proposes to use multi-resolutional information metric to assess the quality of target images for ATR applications. The effects of compression and noise on this metric is studied with the MSTAR data sets.

IMAGE QUALITY ASSESSMENT FOR ATR APPLICATIONS USING MULTIRESOLUTIONAL INFORMATION METRICS

Farid Ahmed

Introduction

In an automatic target recognition (ATR) system, target samples are registered using different types of sensors resulting in synthetic aperture radar (SAR), infra-red (IR), electro-optic (EO), multi-spectral, and hyper-spectral imageries. Images may vary in terms of intensity, resolution, contrast, brightness, and noise content. There may also be some artifacts arising from the sensors. In addition, different operating conditions, such as targets with different configurations and articulations, cover, camouflage, and deception, obscuration result in registered images to be of varying quality. Finally, in order to effectively deal with humongous data set, an ATR system must deal with compressed data. It is therefore of primary interest to know what type of quality distortions are associated with data compression. All of these deliberate and non-deliberate distortion on the acquired data imposes burden on the detection and recognition systems as well as it degrades the system performance. A poor-quality image may result in not-so-robust recognition or detection system. Determination of image quality is therefore of prime importance to the ATR applications.

We here measure the quality by a change in the spatio-temporal information content of the said image. The image sequence here is obtained from the azimuthal sequence of MSTAR data sets. Our attempt is to benchmark the changes in the target, background, and shadow region of a synthetic aperture radar (SAR) image sequence. This information may subsequently be used to either filter out the bad frames or find out the effect on performance degradation of an ATR system. This will also lead to the construction of more reliable and robust ATR systems.

Background

A number of variations of spatial and temporal information features with varying degrees of success is used in literature to determine the quality of an image [1,2,3]. The primary focus of this work is to use a metric mentioned in [4] and to extend the results in a multiresolutional fashion. This work proposes to use a single metric from the spatio-temporal property of image sequences at multiple resolutional decompositions. The motivation towards using multiresolutional feature is to exploit the approximate, horizontal, vertical, and diagonal details of a dynamic change in image quality[7]. This is a natural way of looking at image quality. Human visual system uses the multiresolutional technique to extract information at different scale. Any 'change' in image sequence which may not be evident in one resolution or scale, is expected to be detected at some other resolution.

Analysis of Spatio-temporal metrics

The following analysis is based on a sequence of images. An image sequence may be characterized by some spatial and temporal information contents. Spatial information represents the change in an individual frame, while temporal information characterizes inter-frame changes. Histogram feature is a typically used technique for spatial information in color images. Edge-based technique is also widely used iin spatial feature extraction.

Let us consider k-th frame, *f(i,j,k)* having a total of P pixels. Let *s(i,j,k)* represent the spatial information of the frame. A very widely used spatial information is based on the extraction of edges from an image [5]. A metric representing spatial information content (SIC) is then defined as,

$$SIC(k) = \sqrt{\frac{1}{P}\left(\sum_i \sum_j s^2(i,j,k)\right) - \overline{S(k)^2}}$$

Here *S(k)* is the mean value of spatial information of k -th frame over the total pixels.

A second metric called temporal information, on the other hand, is obtained from the frame differencing as given below.

$$t(i,j,k) = f(i,j,k) - f(i,j,k-1)$$

The metric, temporal information content (TIC) is then defined as follows,

$$TIC(k) = \sqrt{\frac{1}{P}\left(\sum_i \sum_j t^2(i,j,k)\right) - \overline{T(k)^2}}$$

Next. a new metric called velocital information content (VIC) is proposed in [4,6] using spatial and temporal information. Velocital information is obtained from the ratio

$$v(i,j,k) = \frac{t(i,j,k)}{s(i,j,k) + a}$$

Here, a constant a is actually used to take care of the mathematically indeterminate situation, where *s(i,j,k) = 0* . This also acts as a moderator for the specific application of the metric. For example, if we are interested in sharp quality changes, then a should have a relatively smaller value.

Next we apply some statistical treatments on this formulation to extract more generic and robust spatio-temporal features. One of these formulations is based on the variance of the velocital information.

$$VIC(k) = \sqrt{\frac{1}{P}\left(\sum_i \sum_j v^2(i,j,k)\right) - \overline{V(k)^2}}$$

The second one is the entropy-based which is

$$VIC(k) = -\sum_i \sum_j v^2(i,j,k) \ln(v^2(i,j,k))$$

Note that this is an unnormalized definition of entropy. The entropy-based definition is found to result in more discriminatory metric to benchmark the distinction between a slowly-varying quality to a rapidly varying quality change.

Dynamic Changes in the data set

The data set that we tested the metrics is the MSTAR public release data set. The results furnished here are for the T72 15 degree sequence. There are 195 frames in that sequence corresponding to different azimuth angle.

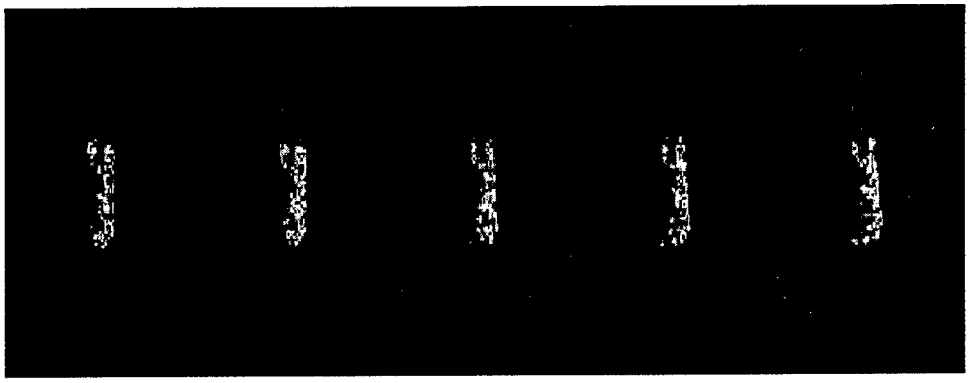

Figure 1: T72 data frames 45-49. The target area does not change much nor does the background.

A SAR image is characterized by three different regions: the target area, the background area and the shadow area. In addition, the speckle noise is the one that complicates the target detection, because the radar reflectivity from non-targets that closely matches the reflectivity of 'target' are basically the speckles.

Depending upon the characteristics in these regions, there are different types of changes in a typical SAR image sequence:

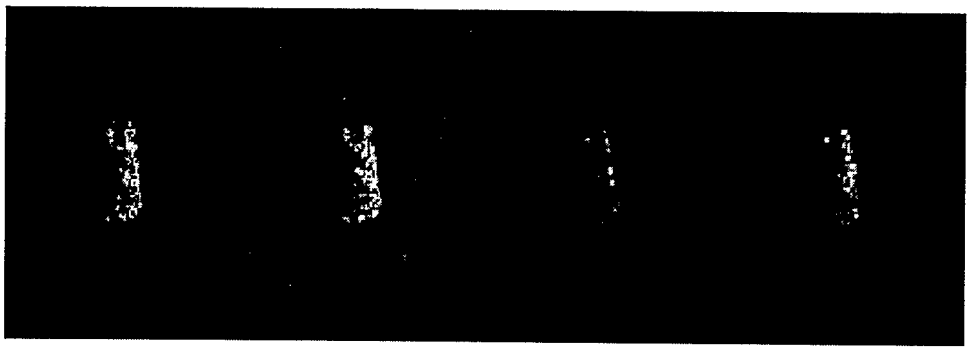

Figure 2: T72 data frames 48-51

i) Global decrease in intensity over the target, background, and shadow area.

ii) Background unchanged, target changing slowly in intensity

iii) A sharp change in target intensity compared to the background.

iv) A sharp change in background, target area remaining almost unchanged.

Frames 45-49 as shown in Fig. 1 does not seem to have any significant change. There is a sharp change in target intensity between frame 49 and 50, which is obvious from fig. 2. Figure 3 shows a sequence where the target area remain almost unchanged, but there is a change in the background intensity. The goals of the current work involves the detection of all these different sorts of changes, although results are furnished only for the sharp target changes.

Figure 4 shows the entropy-based metric values for 195 frames of the T72 sequence. The different values of the metrics represent different types of changes throughout the frames. It is to be noted that as far as the target area is concerned there are two dominant changes. These are frame 49 to 50 and the other one is 110 to 111. It is found that the velocital information metric was able to pick up these two dominant changes.

Figure 3: T72 data frames 79-82

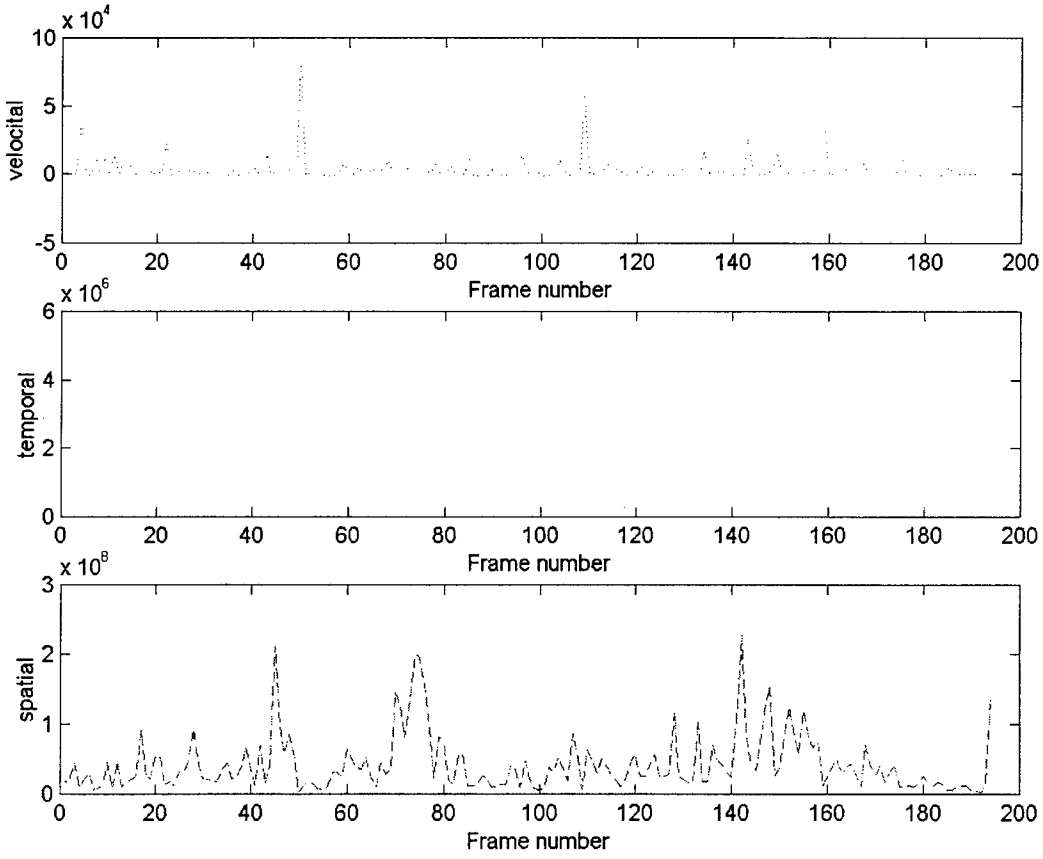

Figure 4: Spatio-temporal metrics with T72 frame sequences

Next we look at how the metrics work with noisy sequence. Figure 5 shows the quality metrics with a sequence that has been corrupted by signal-to-noise ratio of –5 dB Gaussian white noise. As expected the absolute value of the metrics values in general increased while the discrimination ability is decreased. We will furnish some results on this discrimination ability with the wavelet denoising later. Here we get a notion of the metrics. With the addition of random noise in general, the metrics value increase. Figure 6 shows the results after the addition of speckle noise of -5 dB.

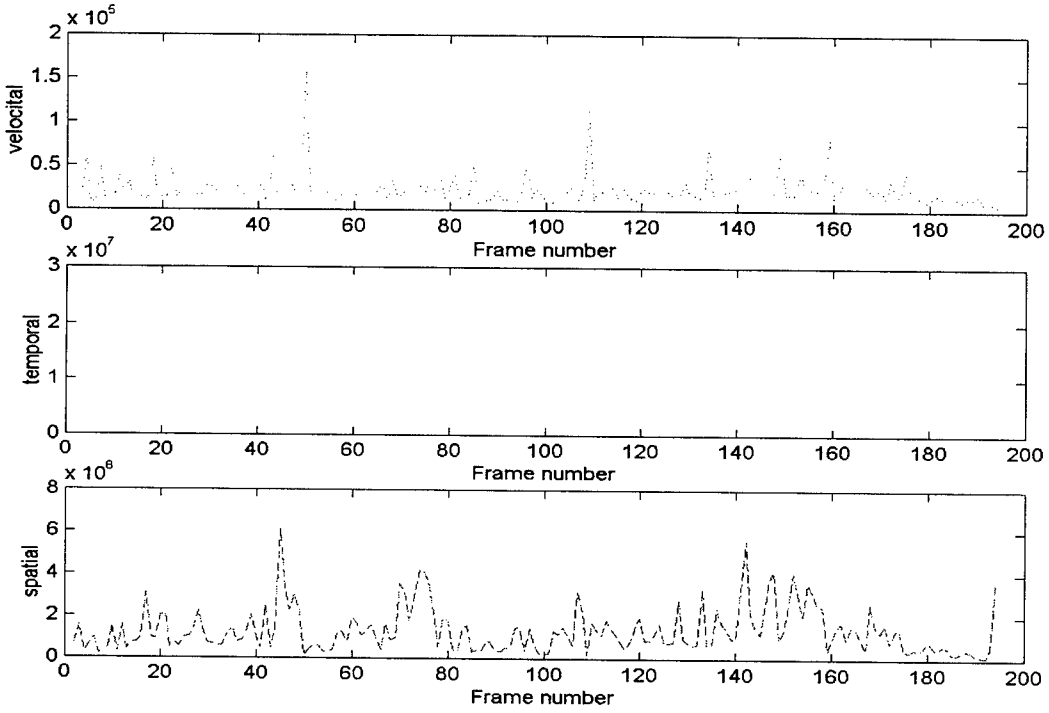

Figure 5: Spatio-temporal metrics with Noisy (GWN –5 dB) T72 frame sequences

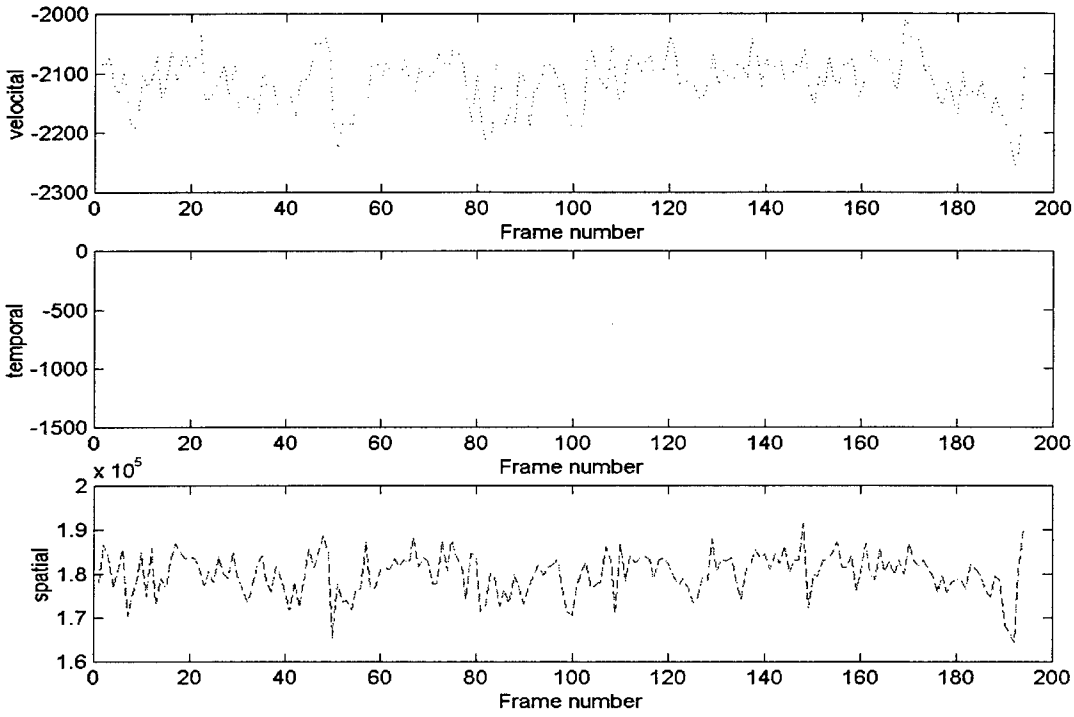

Figure 6: Spatio-temporal metrics with Noisy (Speckle Noise –5 dB) T72 frame sequences

Note that metrics values no longer are representatives of the changes. This is specially because the speckles in a SAR image is very detrimental. In other words, because of the similar radar reflectivity of speckles with the target, the quality metrics become very noisy. This is found to be a very neat way of estimating speckle noise with SAR images.

Quality Assessment after standard image preprocessing

In an ATR system, images usually go through some preprocessing stages. Contrast enhancement with unsharp masking is a widely used preprocessing technique. Next we ran the tests with the unsharp masked image sequences. Figure 7 shows the results. Note a significant change in the spatial information content, because of the extra edge features arising out of the preprocessing. The other two metric values (VIC and TIC) also increased.

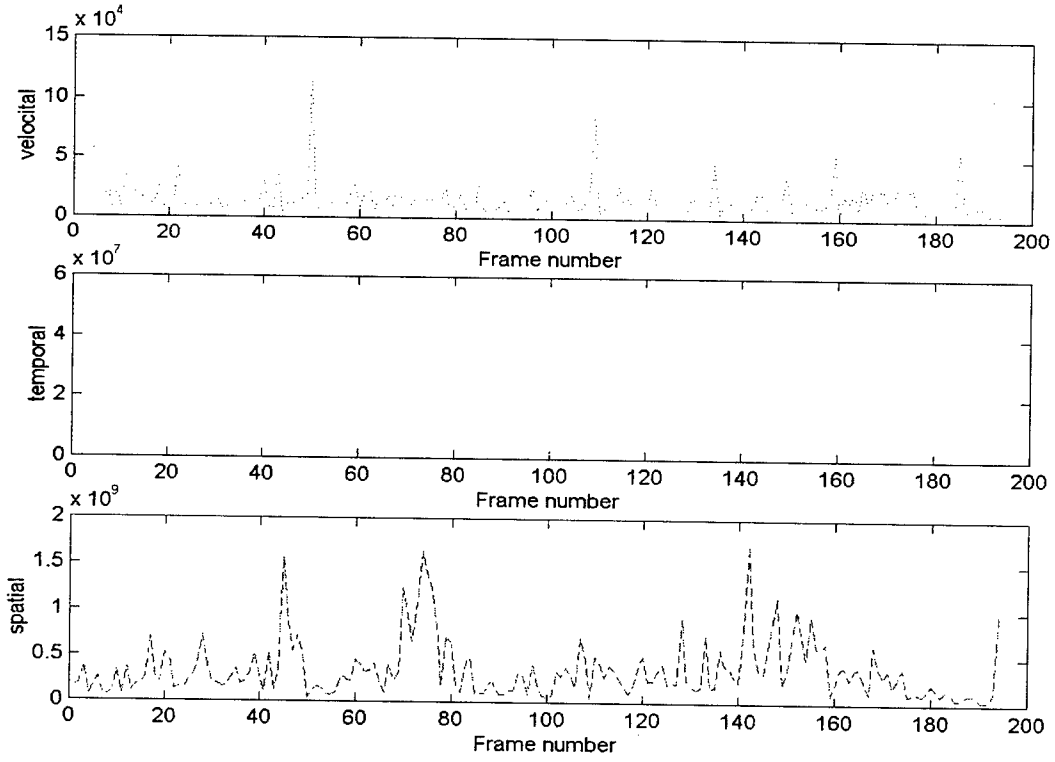

Figure 7: Spatio-temporal metrics with unsharp mask preprocessed T72 frame sequences

Just for the sake of comparison of the spatio-temporal metrics with other standard metrics, we ran the T72 sequence and registered the histogram difference metric, which is a widely used metric for change detection. Figure 8 shows the results.

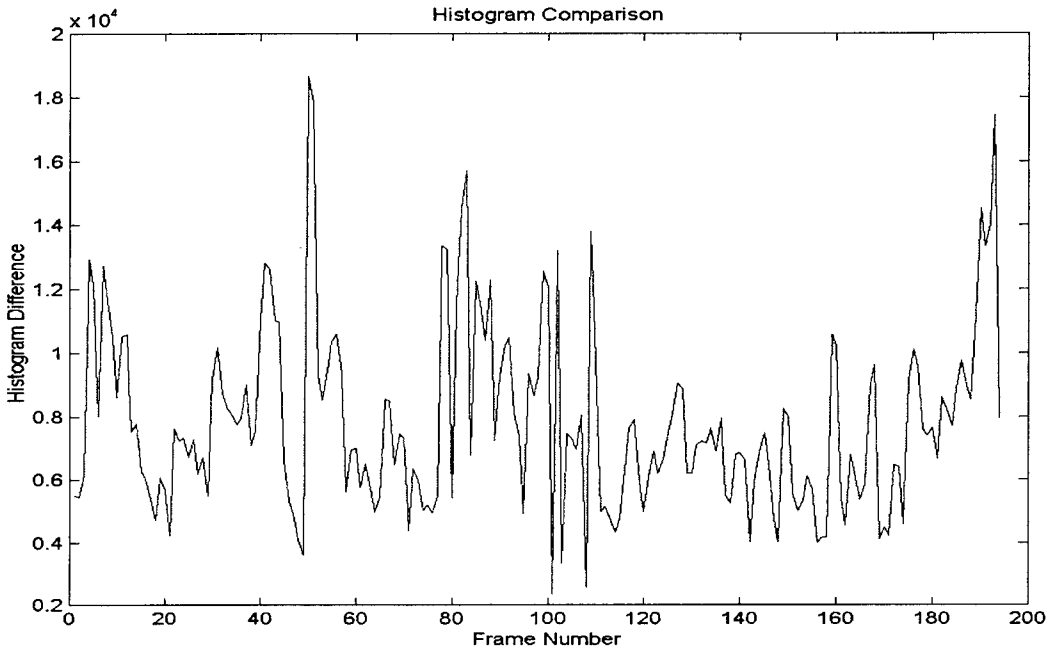

Figure 8: Histogram difference metric for the T72 sequence

Multi-resolutional Information Metric:

Next we turn our focus defining the multiresolutional form of the spatio-temporal metrics

The above-mentioned spatio-temporal features will actually be extracted at different resolutional levels. Each resolutional decomposition demonstrates different interesting characteristics of the dynamic change which are very vital for detection. Wavelet transform has been used as a popular tool for decomposing a signal or an image at different resolution [7]. In the research discrete wavelet transform is used for the multiscale multiresolutional decomposition. An image can be decomposed into a low-resolutional smooth image and detailed image. Let us assume that we are performing one level of decomposition. We denote the smooth image as A1. The detailed image has three components depending upon the directional vector used in the decomposition. Let these be horizontal (H1), vertical (V1), and diagonal (D1). Now suppose the information contents at these resolutional decompositions are represented as I_{A1}, I_{H1}, I_{V1}, and I_{D1} respectively. As mentioned earlier, each of these information metric will exploit different characteristics of quality changes. We then aim at fusing these information into one single metric. The information features at different resolution will be combined to result in a single metric using a data fusion technique. The objective of the fusion is to obtain more discriminatory feature that can identify a change in quality from other slowly varying changes in an image sequence with higher discrimination ratio.

The resulting metric is expected to show sharp peaks at the location of frames

corresponding to sharp change in quality. The fused metric

$$FM = f(I_{A1}, I_{H1}, I_{V1}, I_{D1})$$

Here f(.) is the fusion function.

Figure 9 shows a first-level wavelet decomposition of a typical T72 frame.

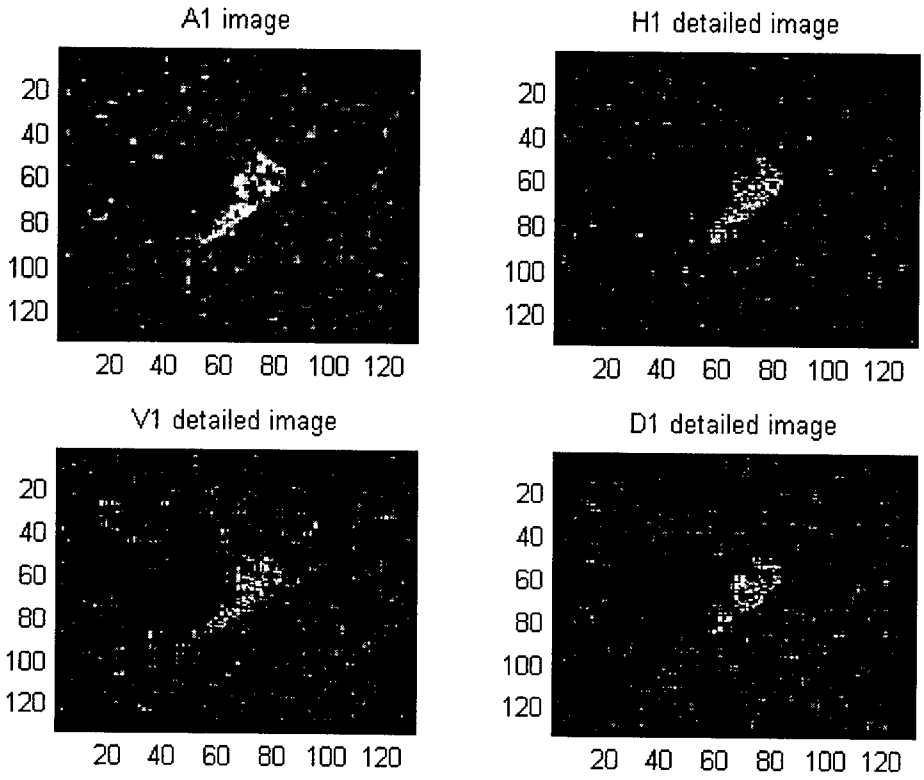

Figure 9: Wavelet decomposition of a T72 frame into approximate (A1) and detailed (H1,V1, D1)

Figure 10 shows the corresponding quality metrics.

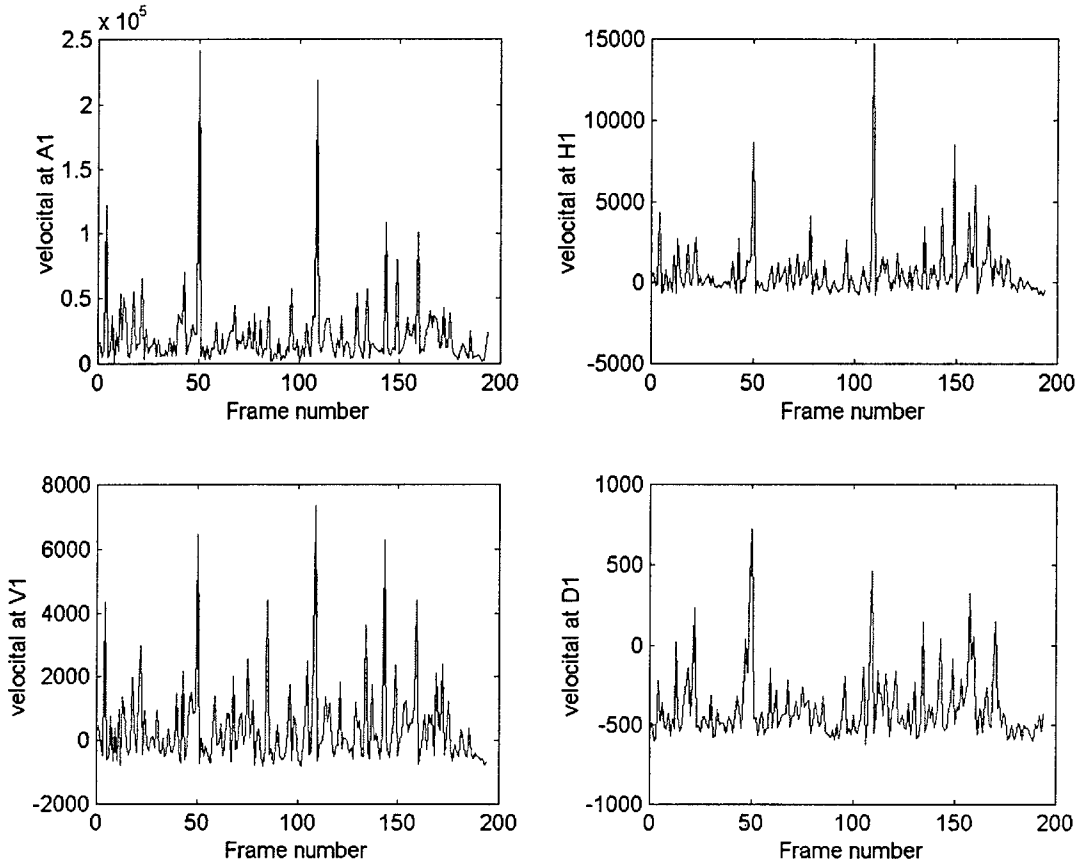

Figure 10: Multiresolutional Velocital Information Content

A simple fusion algorithm is then developed for the exploitation of the metric at different resolutions. Fusion results are also shown in Fig. 11. Note that the fused metrics are even more discriminatory which will prove to be very desirable result in recognition applications.

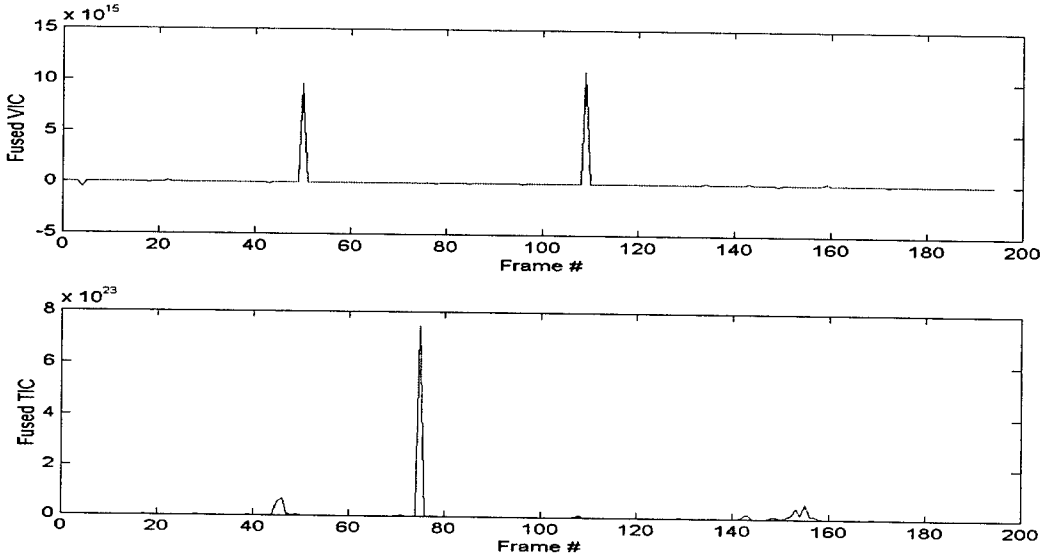

Figure 11: Fusion of Multiresolutional metrics for sharp change detection.

It is a well-known fact that features obtained through wavelet decomposition, by virtue of their de-noising properties, have certain degree of noise tolerance. It will then be interesting to know how noise-tolerant the proposed metrics would be? In other words what is the degree of noise sensitivity? This information can be used to benchmark noise and other artifacts accruing from image sensors. Table 1 shows the discrimination ratio for a GWN of 5 dB at level 1 (A1) and level 2 (A2) approximation of the velocital information content. The decomposition is based on Haar mother wavelet.

	T 72 No Noise	15 Deg Noise (5 dB)	T72 No Noise	17 deg Noise (5 dB)
Original	1.4511		2.1361	
A1 'Haar'	1.6228	1.0106	1.8363	1.0045
A2 'Haar'	1.4352	1.011	2.1614	1.0046
Fused 'Haar'	1.6228	1.0218	1.8363	1.0091
A1 'DB4'	1.2057	1.0085	1.0723	1.0019
A2 'DB4'	1.8382	1.0086	1.4988	1.0019
Fused 'DB4'	1.2057	1.0172	1.0723	1.0038

Table 1: Discrimination ratio of multiresolutional velocital information content

Quality of Compressed Sequence

Our next focus is the effects of compression on the quality metrics. To do this we took wavelet decomposition of the image frames at different levels of resolutions. We then applied a threshold to the wavelet coefficients and then compressed the sequence. This way different frames depending upon their dynamic ranges of wavelet coefficients have gone through different compression ratio.

Figure 12: Spatio-temporal information with the compressed T72 sequence

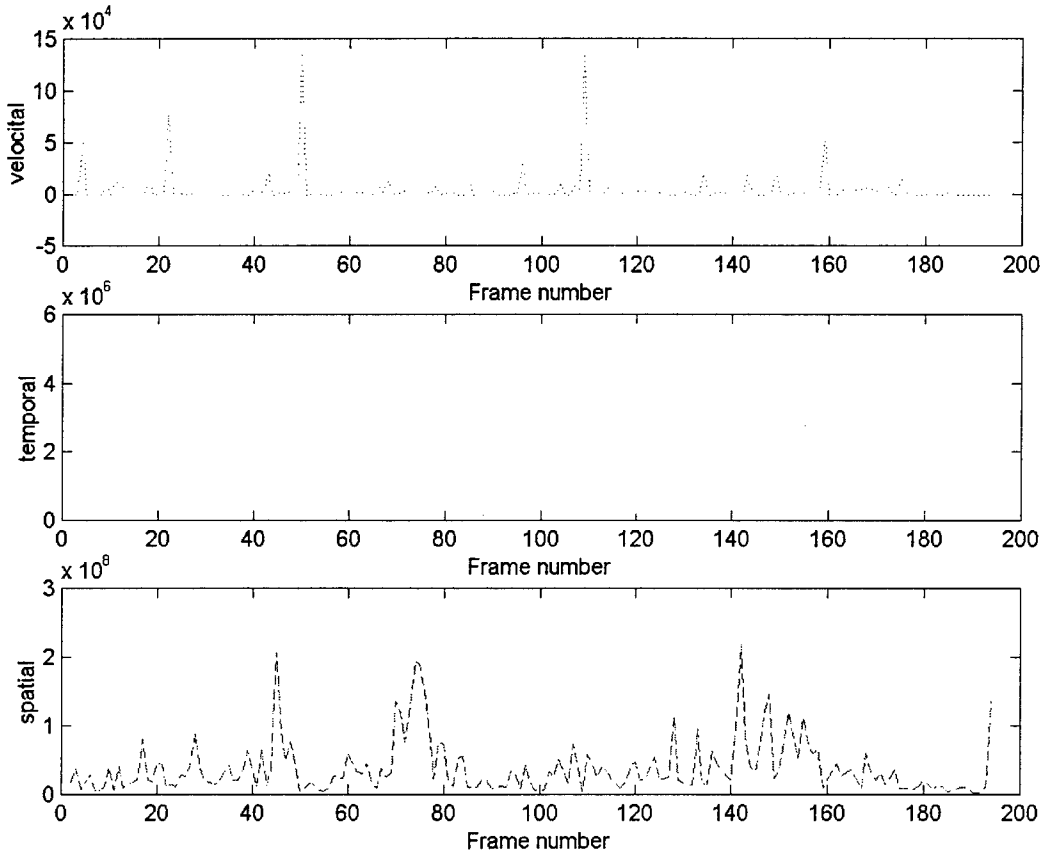

Table 2 shows the effects of mother wavelet choice and levels of decompositions on the compression ratios.

15 Degree with Threshold = 2*median			
Wavelet type	Level of decomposition	Mean compression ratio	Std compression ratio
db3	2	3.3948	0.0606
db3	3	3.6377	0.0721
db3	4	3.6676	0.0740
db5	2	3.7339	0.0691
db5	3	4.0308	0.0818
db5	4	4.1078	0.0845
haar	2	3.1014	0.0474
haar	3	3.2844	0.0559
haar	4	3.3236	0.0580
17 Degree with Threshold = 2*median			
Wavelet type	Level of decomposition	Mean compression ratio	Std compression ratio
db3	2	3.4259	0.0684
db3	3	3.6791	0.0810
db3	4	3.7121	0.0835
db5	2	3.7701	0.0737
db5	3	4.0795	0.0871
db5	4	4.1604	0.0899
haar	2	3.1307	0.0500
haar	3	3.3211	0.0590
haar	4	3.3622	0.0604

Table 2: Effects of wavelet type and levels of decomposition

Quality Assessment with the raw images

The SAR images in the MSTAR data set are processed from the raw data. We applied the inverse processing to get the 'raw' data sequence and applied the spatio-temporal metrics. Figures 13 and 14 show the metrics values for the magnitude and phase sequence respectively. It is found that phase sequence does not give as good a discriminatory metric as the magnitude sequence.

Figure 13: Spatio-temporal metrics for T72 raw Phase sequence

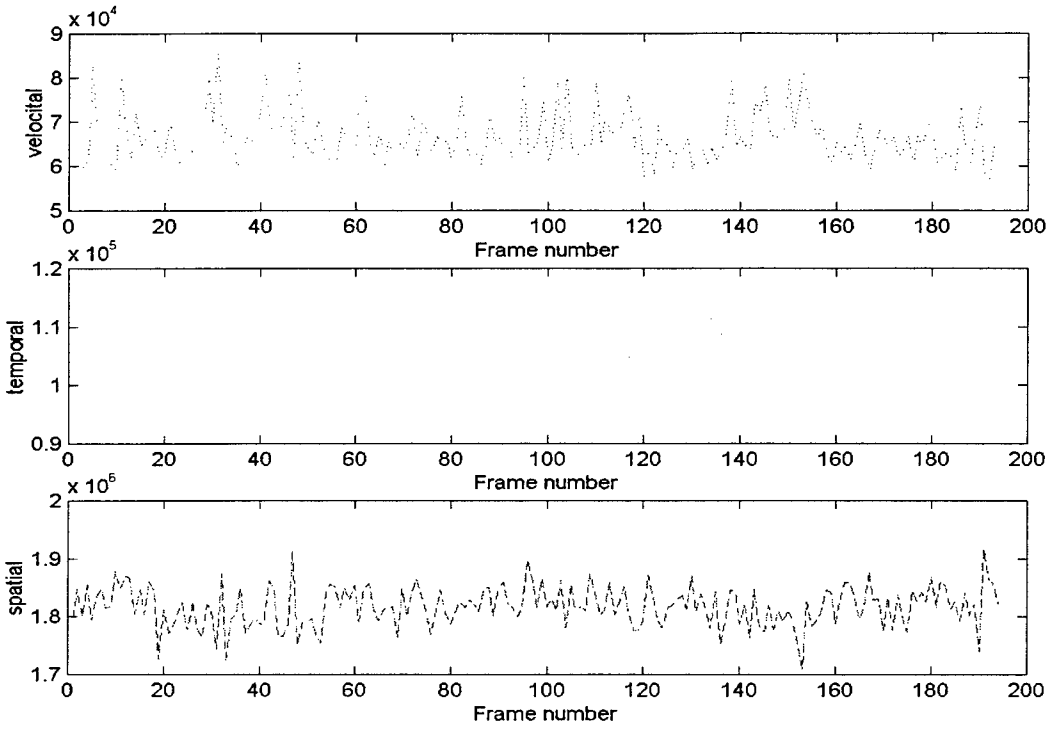

Figure 14: Spatio-temporal metrics for T72 raw magnitude sequence

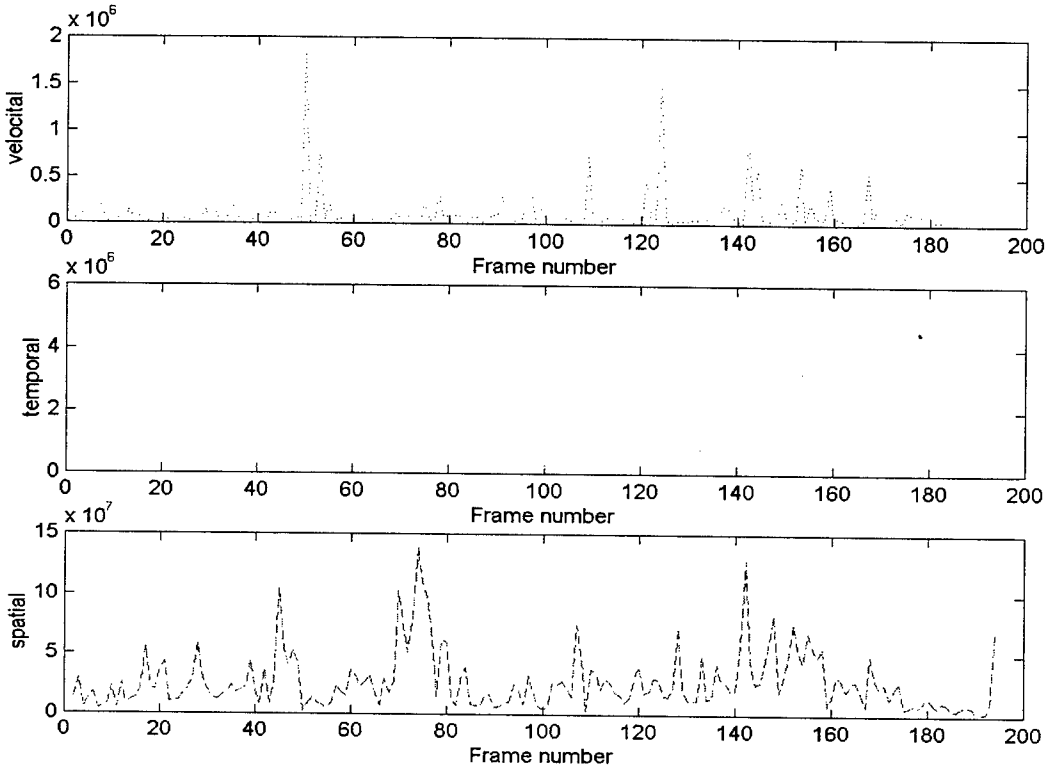

Dissemination of Results

Results were presented at the following SPIE conferences.

1. A compressed-domain spatio-temporal metric for change detection in image sequence, presented at Aerosense, SPIE, paper no. 3716-07, April 1999.
2. Multiresolutional Quality Assessment of SAR Azimuth Sequence Using a Spatio-temporal Analysis technique To be presented at the Photonics West conference, SPIE/IS&T, Jan 2000.

Abstract: The quality degradation of synthetic aperture radar (SAR) images can be primarily attributed to the noise introduced by the imaging sensors, speckle noise due to the coherent property of radar, the approximations done in the image formation algorithm, and any uncompensated motion between the target and the sensor. The last two attributes, sometimes, jointly are referred to as phase error. In this work, we address how speckle noise and phase errors affect SAR image quality. We propose a spatio-temporal metric to benchmark these degradations. The contrast of a particular frame will be included in the metric in the form of the spatial information content. Phase errors are found to be related to the temporal changes of consecutive azimuthal samples. The inclusion of temporal changes in the metric, is therefore, expected to categorize the phase error. Successive decomposition of images into coarser resolution level will minimize the effects of phase error. On the other hand the detailed information at each decomposition can be used to benchmark the noise content. The degree of the noise detection depends among others

on the choice of the mother wavelet filter and the level of decomposition. These will be further explored in this work.

In addition, the PI has organized a technical session on "Image Sequence Analysis" at the International Conference on Imaging Science, Systems, and Technology" (CISST'99) at Las Vegas, NV, July 1999 as well as co-edited a chapter on "Image Sequence Analysis" . Also a manuscript for a journal paper is under preparation.

A web site has been developed with the matlab web server that will run the corresponding matlab programs off the web.

References

[1] S. Wolf, Features for automated quality assessment of digitally transmitted video, Tech. Report, 90-264, *US Department of Commerce, National Telecommunications and Information Administration*, June 1990.

[2] D. J. Lee, Objective Quality Metrics: Applications for partially compensated images of space objects, *Master's thesis, Air Force Institute of Technology*, Wright-Patterson AFB, OH, 1993.

[3] M. J. Swain and D. H. Ballard, Color Indexing, *International Journal of Computer Vision*, Vol. 7, No. 1, pp. 11-32, 1991.

[4] Gregory J. Power, M. A. Karim, and Farid Ahmed, A Velocital Information Feature for Charting Spatio-Temporal Changes in Digital Image Sequences, submitted to *Journal of Electronic Imaging*, June 1998.

[5] R. C. Gonzalez, and P. Wintz, *Digital Image Processing*, Reading, Massachussets, Addison-Wesley Publishing Co., 1987.

[6] Gregory J. Power, Determining a confidence factor for automatic target recognition based on image sequence quality in *Algorithms for Synthetic Aperture Radar Imagery V*, E. G. Zelnio *et al.* eds., Proc. SPIE 3370, Orlando, April 1998.

[7] S. Mallat, A theory for multiresolutional signal decomposition: the wavelet representation, *IEEE PAMI*, vol. 11, no. 7, pp. 674-693, 1993.

ACOUSTIC DISTURBANCE SOURCE MODELING AND DEVELOPMENT FOR HYPERSONIC RECEPTIVITY RESEARCH

Gregory A. Buck
Associate Professor
Department of Mechanical Engineering

South Dakota School of Mines and Technology
501 E. St. Joseph Street
Rapid City, SD 57701

Final Report for:
Summer Research Extension Program

Sponsored by:
Air Force Office of Scientific Research
Bolling Air Force Base, DC

December 1999

ACOUSTIC DISTURBANCE SOURCE MODELING AND DEVELOPMENT FOR HYPERSONIC RECEPTIVITY RESEARCH

Gregory A. Buck
Associate Professor
Department of Mechanical Engineering

Abstract

Transition from a laminar state of fluid motion to a turbulent flow remains one of the most complex as well as one of the most important unsolved problems in fluid mechanics. Among the many challenges that face designers of supersonic and hypersonic aircraft, the issue of boundary layer transition as it spawns from freestream disturbance receptivity is central. Experimental studies of this complex phenomenon require the characterization of acoustic disturbance sources in terms of intensity and spectral content. Among the possible sources for these studies, sparks have been identified as viable candidates, primarily because the impulsive disturbance provides broad spectrum excitation and does not suffer from wave interference issues that plague continuous sources in supersonic flow.

Despite the advantages of spark sources, a number of practical issues arise in their implementation, particularly with regard to electrical noise generated by the high voltage pulse applied to the spark gap. In addition, the low static pressure levels typifying supersonic and hypersonic test sections make the implementation of any acoustic source difficult in terms of signal to noise ratio for the disturbance measurement. This work presents both experimental measurements and numerical predictions of the time-dependent sound pressure field generated by a spark discharge in air at various static pressures ranging from 90 to 3 kPa absolute. The spark discharge was simulated numerically using time dependent sources of both momentum and energy placed within a small region of the air (simulating the spark channel). Code validation runs were conducted using a 2-dimensional, inviscid model for a continuous harmonic point source to compare with acoustic theory, for both still air and a supersonic mean flow. The spark experiments were conducted with 5 different spark gaps to study the influence of gap spacing on sound pressure level as well. The measured data showed peak SPL's above 110 dB at the largest distance (3.5 inches from source) even at the lowest static pressures tested, but revealed the emergence of oscillations at low pressure, speculated to be due to reduced sensor damping under these conditions. It was also observed that the sound pressure decreased slowly with decreasing static pressure, until a threshold of about 10 kPa was reached; static pressures below this threshold resulted in substantial reductions in SPL.

Using the still air spark data to establish impulse energy source levels, the validated code was used to predict freestream spark source characteristics for a Mach 3 flow assuming both inviscid and viscous, laminar flow. The results for the inviscid flow show the impulsive disturbance to propagate into the Mach cone with the spherical wave (cylindrical in the 2-dimensional model) clearly separating into fast and slow components associated with the leading and trailing edges of the disturbance. Arrival times of the computed transient pressure pulses associated with each mode at a fixed point agree to within 1% of those expected from the inviscid theory. The wave is distorted by this spatial variation in phase velocity and its intensity decreases as the expanding wavefront propagates into the freestream. For the viscous flow, the distortion is more pronounced as the subsonic portion of the boundary layer allows the wave to propagate upstream from the source, resulting in significant phase modulation of the slow mode. No significant change in the phase of the fast mode was observed in the viscous numerical results, but amplitude modulation on the order of 50% over the inviscid case was observed.

ACOUSTIC DISTURBANCE SOURCE MODELING AND DEVELOPMENT FOR HYPERSONIC RECEPTIVITY RESEARCH

Gregory A. Buck

Introduction and Background

Transition from a laminar state of fluid motion to a turbulent flow remains one of the most complex, as well as one of the most important, unsolved problems in fluid mechanics. In the design of supersonic and hypersonic aircraft, prediction of boundary layer transition is of paramount importance because the turbulence dramatically increases both heat transfer and skin friction drag, with attendant increases in weight and cost, and decreases in aerodynamic performance and flight range. For military aircraft, hypersonic flight improves both weapon survivability and response time. Predicting boundary layer transition to turbulence is essential in hypersonic vehicle design primarily because the higher heat transfer generally requires higher-performance thermal protection systems, at the price of increased weight and cost. Transition also impacts engine and aerodynamic performance due to large increases in drag from turbulent skin friction, particularly important for vehicles with large wetted areas and extended flight times. In addition, commercial hypersonic aircraft are under study as the next generation in civilian air transport, and therefore it is imperative that the basic mechanisms underlying the transition process be fully understood. Future hypersonic vehicle designs require reliable prediction and (ultimately) control of this phenomenon.

Although a number of theories currently exist to predict transition, they rest heavily on knowledge of initial disturbance amplitudes in the boundary layer, which are coupled in some manner to the freestream fluctuations. The process by which freestream disturbances generate instabilities in the boundary layer is referred to as receptivity, and plays a pivotal role in transition. Freestream disturbances will have energy distributed over some range of wavelength and frequency (or equivalently wavelength and phase velocity), and the wavelength of a freestream disturbance will not, in general, match the wavelength of a boundary layer instability of the same frequency. For example, a critical issue in low-speed receptivity theory is the mismatch between acoustic wavelengths and Tollmein-Schlichting (TS) wavelengths, which may be two orders of magnitude smaller. Also, the amplitude distribution of the disturbance in the boundary layer will not necessarily match the eigenfunction of the boundary layer instability, computed from the homogeneous disturbance equations without regard to the freestream environment. Details of this evolution from freestream disturbance to boundary layer instability, including the amplitude of the engendered boundary layer instability, are the principal objectives of receptivity studies.

Freestream disturbances in a compressible flow are often represented as three independent modes: they are: 1) an entropy mode, 2) a vorticity mode, and 3) an acoustic mode. The entropy mode in a wind tunnel, for example, is typically described as "temperature spottiness", i.e. a fluctuation in the fluid total temperature and density due to nonuniform upstream heating. It convects at the freestream velocity and has a pressure equal to the freestream. The vorticity mode arises from sources of vorticity in the flow (turbulence, wakes, boundary layers, etc.) and also has constant pressure and freestream convection velocity. The acoustic mode is distinguished from the vorticity and entropy modes in that it consists of isentropic pressure, density and temperature fluctuations which propagate at some velocity not necessarily equal to the freestream velocity. A point on a sound wave created by a stationary source propagates normal to the wavefront at the sound speed, a, and convects with the freestream velocity, U. The points on the wavefront directly upstream and downstream of a stationary source in supersonic flow propagate downstream at U-a (slow acoustic wave) and U+a (fast acoustic wave), respectively.

The ideal acoustic source should produce disturbances with a well-defined and independently variable frequency and wave number spectrum, and independently variable amplitude, from the linear to non-linear range. Maslov, et al. [12,13,23] have conducted experiments at Mach 2 using a glow discharge to provide a harmonic acoustic source. In the first version of this experiment, a discharge in a flat splitter plate created acoustic radiation, which impinged on the test boundary layer developing on an adjacent flat plate. In a second version of this experiment, the test flat plate was rolled 180°, so that the test boundary layer was now on the side opposite to the acoustic source on the splitter plate. The test boundary layer was thus shielded from direct radiation from the source. The leading edge of the test flat plate thus appeared as a line acoustic source to the test boundary layer, in emulation of previous theoretical studies in the Russian literature. Oblique input waves inclined 20 to 40 degrees to the freestream were found to give maximum boundary layer response.

The second experiment was repeated at Mach 6 using point and line glow discharge sources on the splitter plate. Input disturbances of 31.6 and 50 kHz were created. The largest boundary layer oscillations in this case were created by oblique waves inclined approximately 60 degrees to the freestream. The glow-discharge used in this experiment tended to produce a rather complex three-dimensional wave number spectrum due to sound created by traveling waves in the splitter-plate boundary layer.

Acoustic frequencies of interest in supersonic and hypersonic flows can be well into the ultrasonic range. A typical non-dimensional frequency $F = 10^{-4}$ would coincide with a dimensional frequency of 11.4 kHz for freestream Mach 4, with ambient stagnation conditions. At Mach 8 conditions, the "most dangerous" second mode frequencies as predicted by the theory of Mack [11] are on the order of 100 kHz.

A ubiquitous problem in stability experiments is determination of the required acoustic amplitude. The amplitude of the disturbance must be large enough to be reliably detected, but not so large as to introduce non-linear effects (if comparison with linear stability theory is sought). Nishioka and Morkovin [16], often cited in low-speed receptivity work, state that a threshold for nonlinear effects is 95 dB (SPL = 1.1 Pa). Saric [19] has shown that for flows with low freestream turbulence, the threshold for nonlinearity depends on the background vorticity level, and has shown linear response up to 110 dB (SPL = 6.3 Pa) for narrow band acoustic input. The influence of compressibility on these threshold levels is uncertain, but order-of-magnitude sound levels in conventional supersonic facilities, where acoustic noise is known to influence transition locations, provide some guidance. Hot-wire measurements by Laufer [9] in the JPL supersonic tunnel showed broadband pressure fluctuations of approximately 0.04-0.06% of freestream dynamic pressure over a Mach range of 1.6 to 5.0. For conditions typical of the Mach 4 Quiet Flow Ludweig Tube at Purdue University, this would be a sound pressure level of 70 to 105 Pa (131 to 134 dB).

Among the principal difficulties in supersonic and hypersonic acoustic receptivity experiments is the generation of sufficiently high-amplitude, high-frequency sound in a low-density environment. For a planar acoustic wave, the sound pressure level, p', may be related to the fluid velocity after the wave passage, U', via the acoustic impedance of the medium, ρa, where ρ and a are the undisturbed density and sound speed, respectively, as $p' = \rho a U'$. At a loudspeaker sound source for example, U' is velocity of the speaker surface. For the same speaker in a low-density environment, the sound pressure level at the speaker will thus scale on ρa.

In subsonic stability experiments, acoustic disturbances have typically been generated using speakers. In Saric's experiments [19,20], the speakers were located around the circumference of the plenum of the wind tunnel and were phased so as to generate planar acoustic waves normal to the freestream velocity. In studies of traveling disturbances in 3-dimensional flows, Buck and Takagi [4] used a speaker coupled to a small hole to introduce a point source of disturbances into a rotating disk boundary layer. Previous research has identified several methods for introducing acoustic disturbances into the settling chamber of

a supersonic wind tunnel [6,10,14]. Several factors however, complicate the introduction of acoustic waves into the settling chamber. One issue is that only fast waves can pass the sonic throat, potentially altering the receptivity that would be observed for sources in a supersonic flow with both waves present. In addition. sound levels are attenuated through the throat passage [6] and for these reasons recent work has focused on sources placed in the supersonic test section.

As mentioned above, one drawback of continuous stationary sources in supersonic flow is that they create a pattern of constructive/destructive interference between the fast and slow portions of the acoustic waves emanating from the source. Therefore any receptivity study using such a source would need to take into account this interference, and would also require some technique to isolate the two waves. Because of the inherent time delay, fast and slow components of impulsive sources, such as blast waves and sparks, are more easily separated. Impulsive disturbance sources have been investigated as viable candidates for receptivity studies, and for purposes of practical implementation fall into two generic categories. The first is a spark discharge, and the second is laser-induced breakdown [18]. In studies performed in the Purdue Quiet Flow Ludweig Tube, the acoustic wave from a laser-induced breakdown was resolved using interferometry. However, the acoustic wave could not be resolved using a hot-wire anemometer [21]. Sparks and double diaphragm shock tubes were investigated in the 1960's [10,14,25] principally as sources for dynamic blast-loading effects, and a number of more recent studies have examined sparks as acoustic sources [1,2,7,8,24]. This work is directed towards a better understanding of spark source characterization, and describes both experimental and numerical studies of sparks under various static pressure and flow conditions.

Physically a spark discharge creates an impulsive source of heat, light and sound (energy) as a high voltage (typically greater than 10000 volts) is applied across two electrodes separated by gap, ionizing the gas between the electrodes, causing a spark to jump across the gap. Preliminary studies [5] were conducted to examine the acoustic structure of a typical spark using a Xenon Corporation Model 437-B Nanopulse ™ system, originally designed as a light source for high-speed image capture. Schlieren photographs taken at 50 and 100 microseconds after spark firing were presented in [5] for a spark gap of 0.050 inch and clearly show the expected spherical wave structure moving at slightly supersonic Mach number. Akram [1] presents numerical results for a 2-dimensional simulation of a spark discharge in air at atmospheric pressure and reports voltage, current and energy transients during the spark firing. Neglecting the departure from local thermodynamic equilibrium during the initial spark formation (first 10 nanoseconds) and using the experimental measurements of Borghese et al [3] for the current transient. Akram computes an energy of about 12 mJ delivered to the gas in the spark channel (0.05 inch diameter x 0.050 length) over a 60 nanosecond time interval. White et.al [24] describe numerical simulations of sparks using energy sources in the compressible Navier-Stokes equations to study spark generated shocks passing through a stationary glow discharge.

Distortions of the acoustic waves due to the flowfield around the source, also introduce unknown consequences, in particular the influence of viscous effects as the waves pass through the test section wall boundary layer. These effects have been studied in the present work, for comparison with the inviscid results with the same impulsive disturbance passing through a laminar boundary layer.

Development and Validation of the Numerical Model

Numerical models for various types of acoustic sources under various flow conditions were developed using the two-dimensional version of the Fluent CFD code. Fluent 5.1 is a mature finite-volume code. which solves the full, unsteady, compressible Navier-Stokes equations and allows for great flexibility in terms of sources in the conservation equations and boundary conditions. The previous work of Akram [1], White et al [24] and others, indicated that successful computation of the acoustic pressure field could

be obtained by modeling the spark as an impulsive (time-dependent) source of energy input to the gas over an extremely small time interval into a very small region of space simulating the spark channel. It was also recognized that a source of momentum in this region might provide a reasonable representation of the physics as well. Before attempting to model the spark source however, it was acknowledged that any model should be validated against existing theoretical solutions. Neglecting the influence of viscosity and thermal conductivity, Morse and Ingard [15] develop theoretical solutions for harmonic point sources in still air and moving supersonically, which were used to validate the model. Schmisseur et al [22] provide transformed solutions from the theory of Morse and Ingard for a stationary source placed in a supersonic flow which they also compared with experimental data at Mach 2.8. Their theoretical results were also used in model validation.

Time-dependent sources of energy and/or momentum are input to the Fluent code through user-defined functions. Momentum sources require the additional specification of the momentum source direction (two direction cosines for the 2-D code). An energy source gives rise to a radial outflow rather than flow in a specified direction as is the case with momentum sources. The point source theory was developed for a pulsating sphere, and such a radial momentum source cannot be modeled simultaneously with the user-defined function necessary in Fluent. In addition, previous work gave credence to the use of an impulsive point source of energy as a reasonable spark model, so the choice was made to employ an energy source disturbance model for this work. In support of this decision, Figures 1 and 2 show the velocity vectors for impulsive sources of both energy and y-momentum at nearly the same instant in time, as computed by Fluent. The energy source shows a radial outflow from the source, while the y-momentum source shows an obvious preferred direction, not representative of the physics. In order to test this concept, model validation began with a continuous harmonic energy source at 25 kHz in still air. The Fluent results were compared with the analytical solution developed by Morse and Ingard [15] for stationary point sources. The amplitude of the energy source was chosen to be 20 million W/m^3 and solutions were computed on a nonuniform 401 x 27 grid in a physical domain 24 inches long x 2.5 inches high. The size of the source was chosen to be 0.05 x 0.05 inch. The Fluent inviscid model was invoked and the resulting time-dependent compressible flow field computed for the harmonic disturbance input. The computation was carried out to 800 μsec, i.e. 20 cycles of the 25 kHz source oscillation. As described in the theory, for regions near the source (i.e. the radius of the location of interest small compared to the wavelength of the acoustic disturbance ($r<\lambda$)), a phase shift exists between radial velocity and pressure. Reference [15] describes the theoretical relationship between radial velocity and pressure for a point source (pulsating sphere of very small radius), with phase and amplitude relations given by:

$$u_r = \frac{p}{\rho c}\left(1 + \frac{i\lambda}{2\pi r}\right)$$

$$\varphi = \arctan\left(\frac{\lambda}{2\pi r}\right) * \frac{T}{2\pi}$$

$$|u_r| \cdot \rho c \Big/ \sqrt{1 + (\lambda/2\pi r)^2} = |p|$$

where

φ	=	phase shift (sec)
λ	=	wavelength (m)
T	=	period of source (sec)

r	=	distant from observed point to the source(m)
P	=	disturbance Pressure (Pa)
ρ	=	density (kg/m^3)
c	=	sound speed (m/sec)

Far from the source ($r>>\lambda$) the theory predicts the pressure and velocity to be in-phase and simply related as:

$$u_r = \frac{p}{\rho c}$$

Figures 3 and 4 show computed pressure and y-velocity as a function of time at a two points on the y-axis (hence y-velocity is equivalent to radial velocity), one near the source on the y-axis (x = 0 m, y = 3.21e-03 m) and one far from the source (x = 0, y = 3.55e-02 m) for a static absolute pressure of 101325 Pa and a temperature of 300K. These x and y coordinates are referenced to the source location. As predicted by the theory, a phase shift between pressure and velocity is observed near the source, with these functions gradually becoming in-phase farther from the source. The computed average phase shift near the source was φ = 3.6 μsec as compared to φ = 3.86 μsec from the theory of Morse and Ingard. Figure 5 compares the computed disturbance pressure with the computed r-velocity times ρc, divided by the square root of $(1+(\lambda/2\pi r)^2)$ at a location near the source (x = 0 m, y = 3.21e-03 m). Figure 6 shows the periodic numerical disturbance velocity far from the source (x = 0, y = 3.55e-02 m) compared with $P/\rho c$ at the same location. Both figures confirm the numerical results against the inviscid point source theory. Additional confirmation is obtained from Figure 7 which shows contours of the instantaneous pressure perturbation for the 25 kHz harmonic source in still air (at the end time of 800 μsec), clearly indicating the expected wavelength of 0.01389 m for the acoustic disturbance.

Having validated the ability to properly resolve acoustic disturbances in still air, the energy source model was used to simulate a 25 kHz harmonic point source in a supersonic flow, by introducing the disturbance into the same channel (24 x 2.5 inch) carrying a Mach 3 inviscid flow. The physics of this disturbance flow field are complicated considerably by the presence of the two (fast and slow) traveling waves, as described above. Schmissuer et al. [22] have used the theory of Morse and Ingard [15] to plot the spatial variation of amplitude and phase for a fixed harmonic point source at 28 kHz in a supersonic flow at Mach 2.8. Their equations were used to compute theoretical amplitude and phase distributions that were then compared with the numerical results. As described above and detailed in their paper, the flow field in the Mach cone downstream of the source results from the interaction between the fast and slow acoustic waves. The disturbance pressure field downstream of the source can be considered as a periodic disturbance having the same frequency as the source with a modulated amplitude and phase. In order to make valid comparisons with this supersonic flow theory, the source region must be small enough to truly represent a point source. The source size and grid chosen for the harmonic source in still air turned out to be too large to properly resolve the disturbance for the supersonic case. After refining the grid adjacent to the wall, the size of the source was decreased to 0.2 x 0.1 mm. The source power input was then modified to comprehend this change; the amplitude of the energy source was ultimately chosen to be 1400 million W/m^3, although two other values, 100 million and 500 million W/m^3, were also studied with no qualitative change in the results. For a source frequency of 25kHz and an energy input of 1400 million W/m^3, the rms sound pressure amplitude at x = 0.015, y = 0 was computed to be about 3 Pa (105 dB) (coordinates referenced to source location at (0,0)). Figure 8 shows the contours of pressure amplitude and Figure 9 the contours of instantaneous pressure at a time of 500 μs. These figures agree well with those presented in Schmisseur et al [22]. Figure 10 shows time plots of the pressure disturbance at the indicated spatial locations downstream. The relative phase of the pressure at each point was computed using the cross-correlation function in Matlab. Phase shifts computed near the source exhibit a slight

discrepancy with the phase predicted by the theory, improving at points farther downstream. For example, the theory predicts a relative phase between x = 0.015 m and x = 0.035 m of about 1.8π, whereas the numerical solutions give a phase of 2.1π; between 0.035 and 0.055 the theory predicts 2.7π, while the numerical results gave 2.7π; between 0.055 and 0.075 the prediction is 2.6π, and the numerical results gave 2.7π. These results are documented in the cross-correlation functions shown in Figures 11 through 13, which were compared with the unwrapped phase from the inviscid theory, shown in Figure 14 (vertical axis in multiples of π) as a function of distance from the source along the x-axis. The dashed curve in each of these figures is the cross-correlation of the upstream function with itself, to confirm a reference. Since the theory was developed for a point source of radial momentum (pulsating sphere), it is expected that the energy input at the source will require some region of equilibration before the proper disturbance momentum phase is observed. Despite this small discrepancy in phase, these results do provide acceptable validation of the energy source model that was subsequently used to simulate impulsive spark disturbances as described in the following section.

Numerical Results for Impulsive Energy Sources

After validation of the energy source model in Fluent for harmonic sources, an impulsive source was simulated in still air for comparison with the experimental data presented and discussed later in this report. The energy-input level was varied but was always assumed to be input over a 60-nanosecond time interval (after ref [1]) into a region 0.1875 inch long x 0.050 inch high. The solutions were computed on a staggered 401 x 27 grid, 24 inches long and 2.5 inches high, with high resolution near the source and along the lower wall. Figure 15 shows plots of the transient pressure pulse generated by an energy source of 2.21 E+10 W/m^3 (corresponding to 7.9 mJ into the gas) for the spark gap of 0.1875 inch at various distances from the source, for a static pressure of 3 kPa. This static pressure corresponds roughly to the static pressure expected at Mach 3 conditions in the AFIT wind tunnel. Figure 16 shows plots of the experimental data for the same spark gap (0.1875 inch) at the same distances from the source. The oscillation observed in the data not present in the numerical solution is discussed in greater detail in the experimental results section below. It is the peak pulse amplitude that is of principal concern to energy-input level, and these plots show a difference of about 30 %, between theory and computation. Comparison of the variation of this peak SPL vs. distance from the source, however, is made in Figure 17, and reveals this energy input choice to be a reasonable compromise for this spark gap. Additional insight is gained by re-examining the transient pressure plots at various distances from the source, for both numerical and experimental results in Figures 15 and 16. The experimental data show that although the peak amplitude of the pressure pulse decays with increasing distance, the pulse width remains fairly constant, with sharp leading and trailing edges as would be expected for a spherical wave. On the other hand the numerical results show the pulse to widen as it propagates, consistent with cylindrical wave behavior expected for the 2-D model.

Detailed results for this impulsive energy input in still air are best described by examining Figure 18, which shows static pressure contours at 6 instants in time as the wave moves out from the source. The time for each contour is given in the inset and the height of the channel is 2.5 inches as before. Figure 19 shows the same data with the contouring interval kept constant at each time, to more clearly illustrate amplitude changes. From these figures it can be seen that the wave moves away from the source initially at supersonic Mach number (M = 1.22) and gradually begins to slow and weaken as the energy is distributed over an expanding wavefront. The computation was stopped when the wave reached the top of the channel, i.e. when reflection was first observed. These results are consistent with the previous experimental observations of Buck et al [5] for spark generated disturbances, and laid the foundation for simulating the spark disturbance in a supersonic flow.

The spark model was first employed to study impulsive disturbances in an inviscid supersonic flow at Mach 3. Figure 20 shows contours of static pressure during the evolution of the impulsive disturbance as it propagates and convects downstream into the Mach cone. Here again the contour interval for each display is chosen to enhance visualization of the disturbance, and varies from contour to contour. Figure 21 shows disturbance velocities at the same 6 instants in time and is particularly instructive as to the physics of this phenomenon. This sequence of contours reveals that the wavefront is really comprised of two parts – the slow mode associated with the upstream front (blue color) and the fast mode associated with the downstream front (red color). Because of the difference in phase velocities they separate more as time passes, distorting the wavefront shape. Of particular interest are the transient pressures that result from the impulsive disturbance, shown in Figure 23. Here the pressure at three different points on an arc of radius 2 inches centered at the source (hence at the same distance from the source), namely a) along the wall, b) in the center of the Mach cone, and c) above the Mach cone are plotted. For the stagnation conditions assumed here (P_0 = 125 kPa and T_0 = 300 K), the freestream mean velocity and sonic velocity are 623 m/sec and 207 m/sec respectively. At a point 2 inches from the source, the fast mode should therefore arrive in 61 μsec and the slow mode in 121 μsec. The numerical solutions predict these same arrival times to less than 1% difference. Along the wall for this inviscid case, the larger x-component of phase velocity allows the wave to arrive slightly sooner and drop to lower values in the rarefaction behind the wave as expected. The absence of any computed disturbance above the Mach cone provides additional validation of the acoustic nature of this impulse disturbance. Similar plots at distances of 3 and 4 inches from the source are shown in Figures 24 and 25 indicating the same behavior, delayed for longer times.

Of paramount interest to any future receptivity experiment is the influence of viscosity on the wave characteristics of an impulsive disturbance. In order to study this effect, the inviscid solutions were compared with numerical results obtained for the same impulsive energy input to a laminar flow at Mach 3. Figures 26 and 27 show contours of disturbance pressure and velocity at 6 instants in time as the wave moves out the same channel, solved on the same grid. The reference point is the source location indicated by the small circle in Figure 26. Two observations from these contours are unrelated to the impulsive disturbance behavior but require a brief comment. First is the Mach wave emanating from the disturbance created at the leading edge of the lower channel wall as a result of suddenly enforcing the no-slip condition there, and second is the small region near the lower right corner where the (unknown) pressure outlet condition influences the subsonic portion of the boundary layer. These effects are far removed from the disturbance under study and should have no significant influence on the conclusions. These contours indicate additional distortion of the wavefront due to changing phase velocity through the boundary layer and a strong disturbance amplitude modulation. In Figure 27 the boundary layer is much too thin to reveal details of the disturbance behavior; however near the wall the disturbance must move upstream and downstream at the sonic velocity, but begin to exhibit the same dual-mode behavior in the outer supersonic regions of the boundary layer. Of course the disturbance velocity must also satisfy the no-slip condition at the wall, which makes interpretation of zoomed velocity contours difficult. Figure 28 however, shows zoomed contours of the disturbance pressure for the laminar boundary layer, at the same 6 instants in time as in Figure 26. Of course the position of the zoomed disturbance changes from instant to instant but can be located using the reference point in Figure 26. The complex wave behavior in the boundary layer is clearly evident in the distorted pressure profiles that are observed.

Perhaps more instructive are the transient pressures computed at the same three points on a 2 inch radius arc as were shown above for the inviscid flow. These are displayed in Figure 29 and immediately reveal a number interesting changes for the viscous flow. First an amplitude modulation of approximately 50% is revealed, perhaps better illustrated in Figures 30 and 31 where the viscous results are compared with the inviscid solutions, at the same points on the wall and in the center of the Mach cone. From these results it is also evident that there is almost no influence on the phase of the fast mode due to the presence of the boundary layer, but the slow mode is phase delayed by nearly 15 μsec in the Mach cone. Figures 32

through 35 show the same comparisons of viscous and inviscid disturbance pressures for points 3 and 4 inches from the source. Also apparent in Figure 29 is a broadening of the slow mode peak in the Mach cone compared to along the wall, not present in the inviscid solution as well as a much stronger amplitude modulation for the point near the wall, as expected.

Because the incorporation of viscosity into the model significantly complicates the physics of the acoustic wave propagation in a supersonic flow, results for the laminar boundary layer are difficult to verify beyond the simple checks mentioned above. However, the model validation done using the inviscid theory gives confidence that these extended results are reasonable. Additional experimental confirmation in a supersonic facility would of course be desirable and should be continued with an appropriate sound pressure sensor, as per the experimental observations discussed in the next section. Moreover, the influence of a turbulent boundary layer on the acoustic pulse is of great practical interest and pending future funding, is planned for the next phase of this work.

Experimental Apparatus and Procedure

Design and development of a repeatable experiment created a number of technical challenges, involving not only sensing/noise questions, but fabrication issues as well. Figures 36 and 37 show photographs of the apparatus as finally used to generate spark disturbances and acquire all sound pressure measurements, and it is worthwhile to describe and document the development history. The vacuum chamber is comprised of an aluminum base, 5/8-inch thick and 12 inches in diameter, with a 2-inch evacuation hole, feeding into 2-inch copper tube, reduced to 3/8-inch Tygon tubing for connection to a standard mechanical vacuum pump (Sargeant-Welsh, Model 8810). A 10-inch diameter bell jar, 24 inches high (18-inch vertical sides) sits on the base, which has tapped holes for two ½-inch diameter threaded rods which support the spark electrodes and the sensors. Two ¾-NPT holes were tapped in the base to permit the high voltage leads and the pressure sensor signals to pass through. Shielded BNC cables were used for the sound pressure sensors; the high voltage leads were 8 mm automotive spark plug wires with right angle boots. It turned out that the best combination of cables here was to have a resistive wire (carbon core) on the high voltage supply and a metallic wire-wound core on the ground side. Electrical noise was observed to increase significantly when both leads were metallic core and if both leads were resistive core, the spark tended to jump to undesired locations at low pressures. Grounding the base also gave rise to similar problems with unwanted spark jumps.

Several high voltage power supplies were considered using high-turn ratio transformer coils from simple designs that were published on the Internet. A number of low cost Tesla coil construction details and other high voltage power supply designs were discovered at the following URLs:

URL 1	http://www.geocities.com/CapeCanaveral/Lab/5322/hv2.html
URL 2	http://bs.cyty.com/menschen/e-etzold/archiv/spark.htm
URL 3	http://www.voltnet.com/
URL 4	http://junitec.ist.utl.pt/einfo_psu.html
URL 5	http://home.earthlink.net/~jimlux/hv/hvmain.htm
URL 6	http://freeweb.pdq.net/headstrong/ind2.htm

Although simple and inexpensive, most of these designs do not permit controlled triggering of the spark. At the first web site a triggerable design using two standard automotive coils connected in anti-parallel was described (see Appendix A). This design was built and tested but the triggering scheme was unsatisfactory because the voltage is applied across the electrodes continuously during the entire grounded half of the trigger cycle, so that the sparks fire repeatedly as breakdown occurs and recurs during this half cycle (sizzling spark). However a commercially available automotive ignition system

(Holley HP Annihilator 800-100, w/Laser Shot Pro coil) designed to produce controlled repetition of single sparks was also tested. Implementation of this unit proved to be quite convenient because it is designed to be triggered by either points or electronic distributors, so was easily adapted for square wave function generator input. Despite the fact that it is designed to produce multiple sparks at each trigger, triggering could be set at frequencies low enough to permit complete damping of the sound from the last spark before the first spark of the next trigger was fired. For a trigger frequency of 3 Hz, the built-in time between multiple sparks for this unit was measured to be 1.2 msec (at 3 Hz the unit is designed to produce 6 sparks). However, the maximum trigger frequency capability of the unit is over 650 Hz, which could be useful for ensemble averaging in blow-down wind tunnels. The number of multiple sparks is reduced as the trigger frequency increases and at the highest frequency, a single spark is produced. For all data reported herein, the trigger frequency was 3 Hz, and the number of ensemble averages was 32. The latter was chosen based on no observable change in the time signal for larger number of averages.

Fabrication of an easily adjustable spark head was also one of the objectives of this project. Electrode fabrication presents difficulties because a highly insulating dielectric material must surround each of them, particularly important at the low pressures. Standard automotive spark plugs have excellent ceramic insulators and provide a low cost solution, but the high voltage electrode is much too close to the metallic threaded portion to be useful in this application. However it was discovered that the center electrode is easily removed by cutting away the hex/threaded portion (with the ground electrode) and extracting the insulated center. Holders were then fabricated from plexiglas and nylon C-clamps with nylon machine screws to hold this center electrode in place on the vertical threaded rod extending from the base. Electrical connections were made with standard booted clip contacts, designed to fit tightly around the ribbed insulator. Both resistor and non-resistor spark plugs were tried, but it was discovered that the resistor plugs again create unwanted spark jump problems. In fact at the low pressures, current bleeding could be observed at numerous locations including, around the boots, through the epoxied base plugs and even through the lead wire insulation itself when the total resistance of the spark gap/electrode/lead combination became too large. Due to time and money constraints, electrical measurements were not attempted on the high voltage side, but it is planned to devise an experiment to measure voltage and current transients during the spark firing at the next phase of this work. Knowledge of the actual energy delivered to the gas would be quite useful for comparison with the numerical predictions described above.

Finding a suitable sensor for these short duration, low pressure pulses that would not be overwhelmed by the intense spike of electromagnetic noise created at each spark firing was perhaps the most challenging of all the experimental difficulties. In addition to a Kulite XCW-093 low-pressure piezoresistive sensor, two condenser microphone configurations were tried, one externally powered (RS 270-090C with a 5V DC excitation) and an Optimus 33-3013 powered by a 1.5 V battery. Signals from the microphones were mV level and could be read directly by the 8-bit HP 54645A digital scope. The Kulite bridge was supplied with 15 V DC excitation from an HP 3630A DC power supply and the differential output signal was amplified using a Burr-Brown instrumentation amplifier INA103 configured for a gain of 100.

From the previous summer 1998 work, high frequency ringing in the Kulite sensor signal for static conditions was known to exist (see e.g. Figures 16 and 18, ref. [5]). Although the source of this ringing was unknown, it was speculated that this might be due to either sound reflections in the spark cavity or dynamic response of the sensing element. To eliminate the cavity influence, the present experiment was conducted with the electrodes centered in the bell jar, with the sensor placed closer to the source than any adjacent reflecting surfaces. Figure 38 shows signals from both the Kulite and the Optimus mic under static atmospheric pressure, clearly indicating the presence of this ringing in the Kulite signal, not present in the condenser mic signal. The figure also reveals another problem with the Kulite sensor, namely much more susceptibility to induced noise from the spark firing. Because of this, and the persistent oscillations in the Kulite signal, it was concluded that this sensor would not be the best choice to resolve the sound pressure pulse, and therefore all data reported herein are for the Optimus mic. It was also

observed that this battery powered mic performed much better than the externally powered RS 270-090C condenser mic in terms of induced noise in the signal, ostensibly because the power cables supplying the mic, were also observed to pick up the noise created by the spark firing. This electromagnetic noise coupling was also observed to be sensitive to the relative positions of the power, high voltage wires and signal cabling. This observation also provided support for the decision to use the Optimus mic.

The experiments were conducted for 5 different spark gaps ranging from 0.1875 inch (4.76 mm) to 1.5 inches (38.1 mm), at 7 different static pressures ranging from 95 to 3 kPa nominal. The transient sound pressures produced by the spark were measured with the Optimus mic placed at various locations from the source ranging from 0.5 inch (12.7 mm) to 3.5 inches (88.9 mm). It was discovered that for lower pressures, the mic could not be placed too near the source or the spark would jump to the mic body, the limiting distance being roughly ($\sqrt{3}$ / 2) x (the length of the spark gap), as expected for the geometry (i.e. the mic would then be closer to the high voltage electrode than the ground electrode). As mentioned above, all spark data were taken using a 3 Hz trigger, and at each trigger 2000 point ensembles were sampled at 2 MHz (1 msec total sampling time per ensemble) and averaged in the time domain over 32 ensembles using an HP 54645A digital oscilloscope. The averaged data was then downloaded to a PC for post processing using the HP BenchLink software.

Experimental Results and Discussion

Figures 39 and 40 shows results from typical sound pressure measurements for a spark gap of 0.1875 inch, for pressures of 91.3 kPa and 3.45 kPa, respectively. Each curve represents the SPL for a different distance from the source. The shape of the pulses is as expected, with a large overpressure associated with the initial wavefront, followed by a rarefaction region behind the compression wave. The duration of the positive pulse is about 15 μsec, consistent with the previous measurements of Wright and Medendorf [27], and in good agreement with the numerical predictions described above, for points close to the source. Time zero is the trigger event and the small glitch observable in the signals prior to the large rise, is the spark-firing event, typically occurring 60 μsec after the trigger. Also evident in the plots are smaller peaks much later in time (about 700 μsec or so after the spark firing) that were verified to be reflections from the bell jar glass (by moving the jar these pulses were observed to shift in time). The very low amplitude oscillations discernable at about 400 μsec from spark fire were verified to be reflections from the electrode holders. It can also be observed that the peak overpressure decreases with decreasing static chamber pressure from 125 Pa at 91.3 kPa to 26.4 Pa at 3.45 kPa as expected. The behavior of peak pulse amplitude with distance from the source is also as expected, but an interesting change in the signal is observed for the low-pressure case, namely the appearance of oscillations at about 35 kHz. This phenomenon was observed for all gaps and all distances from the mic: it was also observed for the other condenser mic, although the frequency of these oscillations was observed to be sensor dependent. This is evidence that the sensor response itself is probably the cause of this ringing, with the speculation that at the higher static pressures enough air is present to damp this ringing to unobservable levels. A summary description and significant observations from all spark data are discussed in the following paragraphs.

One observation worthy of note (and one that remains unexplained), is the zero drift/shift that begins to appear in some measurements where the mic is very close to the spark gap (more prevalent for larger gaps). It is believed that the condenser element of the mic may be picking up some charge from the ionized gas created during the sparking that remains on the mic after the spark dies out. Farther from the spark gap, ion concentrations are probably low enough to prevent this phenomenon from affecting the measurement. The peak pressure may still be captured adequately, but this observation indicates that other sensing techniques should be attempted in the next phase of this work, to obtain confidence in the

SPL measurements near the spark. The photo-acoustic detector (PAD) described by White et al [27] is one promising possibility although they did not attempt measurements very close to the spark. Moreover, this sensor has an extremely rapid rise time and these additional measurements would also serve to confirm the Optimus mic data, particularly with regard to any transient response concerns.

Of major significance are the summary plots provided in Figure 41. Here the measured maximum sound pressure pulse in dB for each spark gap is plotted as a function of static pressure for fixed distance from the source. One of the first points to make is the fact that for the larger spark gaps, high static pressure data is not available, because the spark could not be made to jump the gap under these conditions. For a gap of 25.4 mm data could only be taken below 69 kPa and for the largest gap of 38.1 mm, a 34 kPa maximum was observed (38.1 mm gap summary results are not presented). As expected the maximum sound pressure level decreases with decreasing pressure, but it is instructive to examine the nature of this dependence, namely, the sharp drop-off that occurs below about 10 kPa. Static pressures above this provide only modest decreases in sound pressure with decreasing static pressure. This finding important in choosing stagnation conditions for any future receptivity experiment. Figure 42 shows the same data, with the maximum sound pressure pulse now plotted as a function of distance from the source, for fixed static pressure. Recognizing the dB scale for these plots, it is apparent that the peak sound pressure drops exponentially with distance from the source, as expected. This spatial data for the 0.1875 inch (4.76 mm) gap was used to choose the energy source level for the numerical model of the spark source as described above.

In addition to these quantitative measures of spark sound pressures, a few observations on the qualitative nature of the spark formed are worthy of note. Figures 43 and 44 show photographs of the spark channel captured during the discharge at static pressures of 91 and 3.4 kPa, respectively for a spark gap of 1.5 inches. At the higher pressure the spark forms a narrow bright channel, which takes a random, curved path between the electrodes. In addition to the condenser mic problems discussed above for the larger spark gaps, this also makes it difficult to pinpoint the precise location of the cylindrical source. At low pressure the spark forms a broad straight-sided channel of ionized air that gives off a distinctive purple glow. The initial appearance of this type of spark coincides with the threshold pressure of 10 kPa, described above. With the proper resistance in the high voltage system, the location of this spark channel is much more repeatable.

Conclusions and Recommendations

Numerical and experimental studies of spark-induced, impulsive acoustic disturbances in still air and under supersonic flow conditions have been conducted. The numerical models were validated against inviscid theory for a harmonic point source in still air and at Mach 3 using a time-dependent energy source in an unsteady, inviscid, 2-D model. The results are in excellent agreement with the theory and existing literature. An impulsive energy source of 1400 W/m^3 into a very small spark channel region was used to model the spark, based on measured sound pressure levels at low static pressure. In order to obtain these measurements an experiment was designed and built to produce a spark discharge in air at pressures ranging from 91 kPa to 3.4 kPa. The latter static pressure is representative of that expected in a typical supersonic blow-down wind tunnel at Mach 3. The high voltage discharge creates a spike of electromagnetic noise that renders the use of traditional sound pressure sensors difficult. The experiment also examined the influence of spark gap and distance from the source. It was discovered that a threshold static pressure of about 10 kPa exists below which, significant decreases in sound pressure are observed. Larger spark gaps produce higher sound pressure levels but beyond about a 1-inch gap, other difficulties arise particularly with regard to consistency of spark location and condenser microphone measurements. Peak sound pressure levels of over 110 dB were recorded even for the smallest spark gap at the lowest pressure.

Numerical results for the impulse disturbance were obtained for both inviscid and laminar flow at Mach 3. The inviscid computations clearly revealed the presence of the fast and slow acoustic modes in the Mach cone. Arrival times of the computed transient pressure pulses associated with each mode at a fixed point agree to within 1% of those expected from the inviscid theory. The wave is distorted by this spatial variation in phase velocity and its intensity decreases as the expanding wavefront propagates into the freestream. For the laminar flow, the distortion is more pronounced as the subsonic portion of the boundary layer allows the wave to propagate upstream from the source, resulting in significant phase modulation of the slow mode. No significant change in the phase of the fast mode was observed in the viscous numerical results, but amplitude modulation on the order of 50% over the inviscid case was observed.

Although these numerical results are presented with reasonable confidence, additional insight would certainly be gained though careful experimental measurements in a supersonic flow facility. Such measurements were attempted using spark sources by the author and colleagues at AFRL in the summer of 1998, but the lessons learned in this study will be of value in designing and improving an extended experiment. It is certain that a sound pressure sensor with acceptable dynamic response to such impulsive excitation should be employed for any future studies. As a first step, the PAD technique of White et al. should be examined for this application and tested in the vacuum chamber used for the present experiment. This work will be proposed in a future study.

In addition, as mentioned in the body of this report, it would be desirable to obtain detailed information on the transient electrical characteristic of the spark discharge. Fast response voltage and current sensors on the high voltage discharge should be employed in the next phase of the experimental work to determine more precisely the energy delivered into the gas at each spark. This is planned for the next phase of this work as well.

On the numerical side, there is of course always more sophistication to be added. The influence of a turbulent shear layer on the wave structure and phase velocity is of paramount concern to most receptivity experiments and would be the next logical extension of this study. Fluent 5.1 offers a number of choices for turbulence models including simple one-equation models, standard k-e models, six component Reynolds stress models, large eddy simulation and of course direct solution of the compressible Navier-Stokes equations. The latter would most likely require substantially bigger and faster hardware than was currently employed for this study, but should be considered among the other alternatives listed for future numerical refinement of this study. In addition the influence of 3-dimensional effects, in particular, spherical vs. cylindrical waves, should be studied in future phases of the numerical work.

References

1.) Akram, M. "Two-Dimensional Simulation for Spark Discharge in Air", AIAA J., v. 34, no. 9, Sept. 1996.

2.) Baronets, P.N. "Cylindrical Shock Waves Generated by a Spark Discharge and Their Interaction with the Shock Waves from a Pulsed Induction Discharge", Fluid Dynamics, v.29, no. 1, 1994.

3.) Borghese, A., D'Alessio, A., Diana, M., and Venitozzi, C., "Development of Hot Nitrogen Kernel, Produced by a Very Fast Spark Discharge", 22nd Symposium (International) on Combustion, Combustion Inst., Pittsburgh, PA, pp. 1651-1659, 1988.

4.) Buck, G.A. and Takagi, S., "Observations of Traveling Disturbances from a Point Source in Rotating Disk Flow", AIAA 97-2299, June, 1997.

5.) Buck, G.A., Kimmel, R.L. and Schmisseur, J.D., "Characterization of Acoustic Sources for Hypersonic Receptivity Research, AIAA 99-3708, June 1999.

6.) Candel, S. M., "Acoustic Conservation Principles and an Application to Plane and Modal Propagation in Nozzles and Diffusers," Journal of Sound and Vibration, vol. 41, no. 2, 1975, pp., 207-232.

7.) Korolev, S.V. and Krylov, V.V., "Waveforms of Acoustic Pulses Generated in a Solid by Spark Discharge", Sov. Phys. Acoust., 36(2), Mar-Apr 1990.

8.) Lafleur, L.D., Matese, J.J and Spross, R.L., "Acoustic Refraction by a Spark Discharge in Air", J. Acoust. Soc. Am., 81(3), Mar. 1987.

9.) Laufer, J., "Some Statistical Properties of the Pressure Field Radiated by a Turbulent Boundary Layer," *The Physics of Fluids*, vol. 7, no. 8, August 1964, pp. 1191-1197.

10.) Lemcke, B., "Double-Shock Shock Tube for Simulating Blast Loading in Supersonic Flow," *AIAA J.* vol. 1, no. 6, June 1963, pp. 1417-1418.

11.) Mack, L. M., "Boundary-Layer Stability Theory," *Special Course on Stability and Transition of Laminar Flow*, edited by R. Michel, AGARD Report No. 709, pp. 3-1 to 3-81, 1984.

12.) Maslov, A. A., and Semenov, N. V., "Excitation of Natural Oscillations in a Boundary Layer by an External Acoustic Field," translated from *Izvestiya Akademii Nauk SSSR, Mekhanika Zhidkosti I Gaza*, no. 3, pp. 74-78, May-June, 1986.

13.) Maslov, A. A., Shiplyuk, A. N., Sidorenko, A. A., and Arnal, D., "Leading Edge Receptivity of the Hypersonic Boundary Layer on a Flat Plate," Preprint no. 1-98, Institute of Theoretical and Applied Mechanics, Russian Academy of Sciences Siberian Branch, Novosibirsk, 1998.

14.) Miller, H. R. "Shock-on-Shock Simulation and Hypervelocity Flow Measurements with Spark-Discharge Blast Waves," *AIAA J.* vol. 5, no. 9, September 1967, pp. 1675-1677.

15.) Morse, P.M. and Ingard, K.U., Theoretical Acoustics, McGraw-Hill, 1968.

16.) Nishioka, M., and Morkovin, M. V., "Boundary-Layer Receptivity to Unsteady Pressure Gradients: Experiments and Overview," *Journal of Fluid Mechanics*, vol. 171. 1986.

17.) Phillips, O.M., "On the Generation of Sound by Turbulent Supersonic Shear Layers", Journal of Fluid Mechanics, vol. 9, 1960, pp. 1-28.

18.) Salyer, T. R., Randall, L. A., Collicott, S. H., and Schneider, S. P., "Use of Laser Differential Interferometry to Study Receptivity on a Hemispherical Nose at Mach 4," AIAA 98-0238, January 1998.

19.) Saric, W. S., and White, E. B., "Influence of High-Amplitude Noise on Boundary-Layer Transition to Turbulence," AIAA 98-2645, June, 1998.

20.) Saric, W. S., Reed, H. L., and Kerschen, E. J., "Leading Edge Receptivity to Sound: Experiments, DNS and Theory," AIAA 94-2222, June, 1994.

21.) Schmisseur, J. D., "Receptivity of the Boundary Layer on a Mach-4 Elliptic Cone to Laser-Generated Localized Freestream Perturbations," Doctoral Dissertation, Purdue University School of Aeronautics and Astronautics, December 1997.

22.) Schmisseur, J.D., Poggie, J. and Kimmel, R.L., "Acoustic Source for Compressible Flow Receptivity Experiments", AIAA 2000-0285, January, 2000.

23.) Semionov, N. V., Kosinov, A. D., and Maslov, A. A., "Experimental Investigation of Supersonic Boundary-Layer Receptivity," *Transitional Boundary Layers in Aeronautics*, Proceedings of the colloquium "Transitional Boundary Layers in Aeronautics," Amsterdam, 6-8 December 1995, Henkes, R. A. W. M., and van Ingen, J. L., ed, Royal Netherlands Academy of Arts and Sciences, P.O. Box 19121, 1000 GC Amsterdam, the Netherlands, 1996, pp.413-420.

24.) White, A.R., Aithal, S.M. and Subramaniam, V.V., "Experimental Studies of Spark Generated Shock Waves", AIAA 99-3670, June 1999.

25.) Wright, W.M., and Medendorf, N.W., "Acoustic Radiation from a Finite Line Source with N-Wave Excitation", J. Acoust. Soc. Am., 43(5), 1968.

Acknowledgements

The author wishes to acknowledge the Air Force Office of Scientific Research for their support of this research under the Summer Research Extension Program, contract SREP 99-0818 and for the opportunity to initiate this work at the Air Force Research Laboratory, Wright-Patterson AFB during the summer of 1998. A sincere debt is owed to many fine colleagues and associates at AFRL and AFOSR for their support during the initial stages of this work. Special thanks go to Dr. Roger Kimmel, Dr. Jon Poggie and Dr. John Schmisseur of the Aerodynamic Components Branch of AFRL for numerous and sundry contributions and many fruitful discussions.

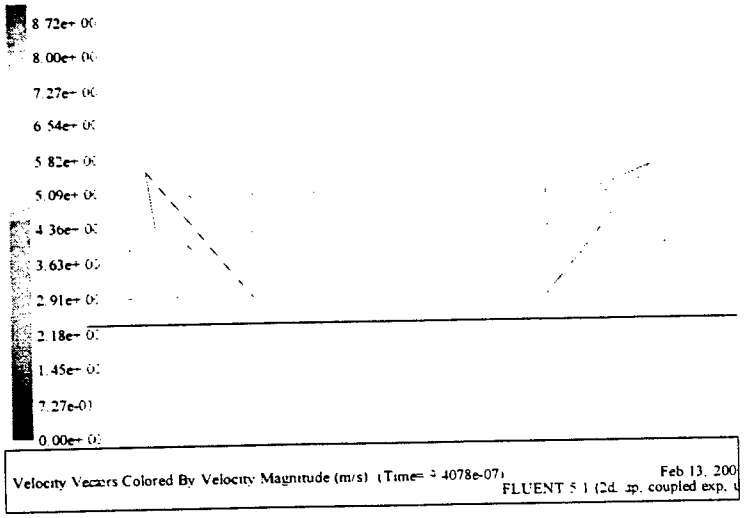

Figure 1 Velocity vector field from energy source

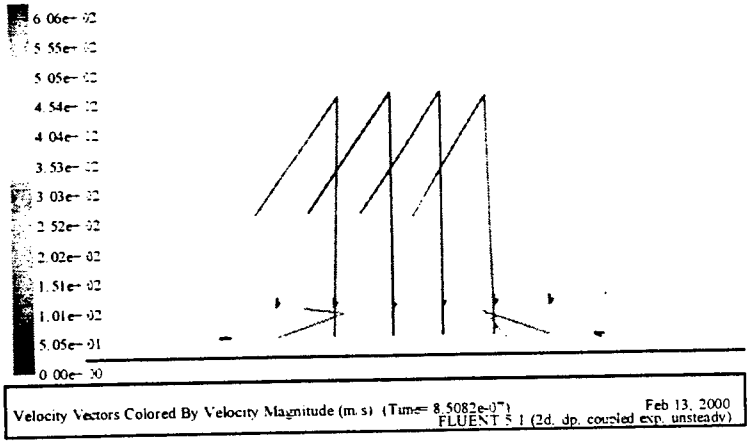

Figure 2 Velocity vector field from momentum source

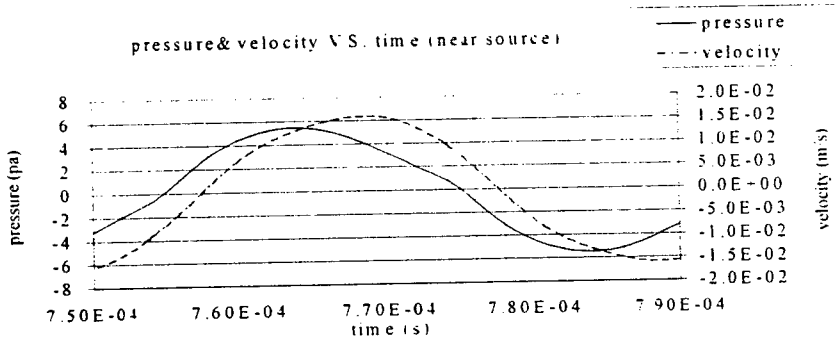

Figure 3 Computed velocity and pressure near the source (r = 3.2 mm)

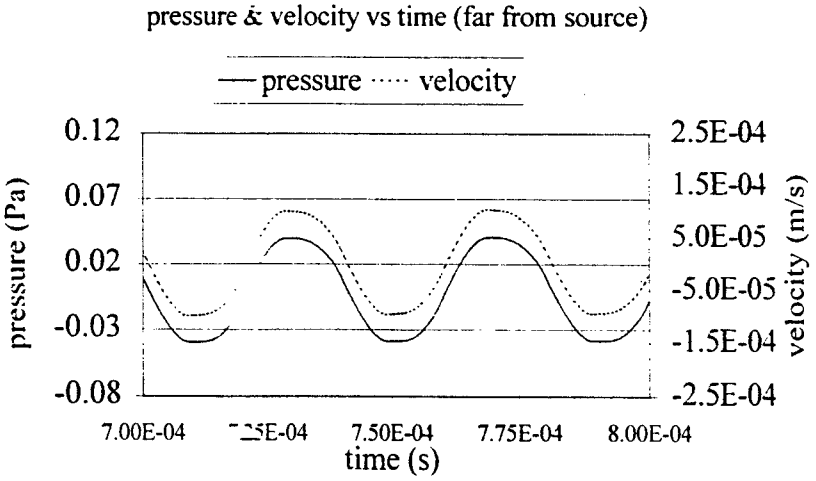

Figure 4 Computed velocity and pressure far from the source (r = 35 mm)

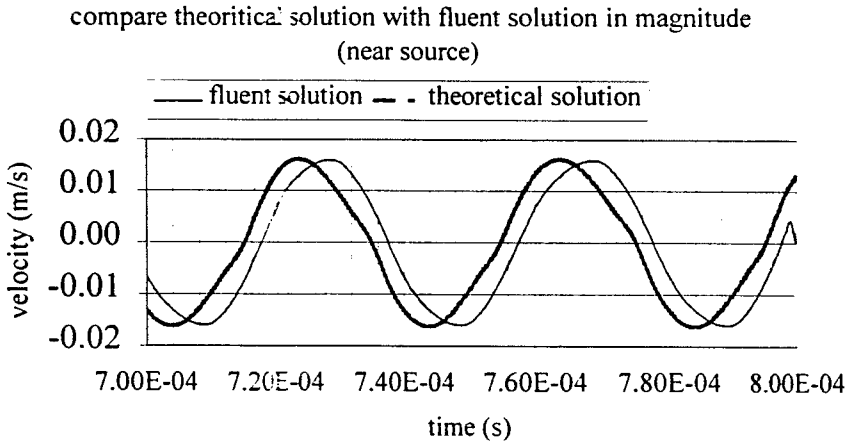

Figure 5 Pressure and velocity amplitude validation – near source (r = 3.2 mm)

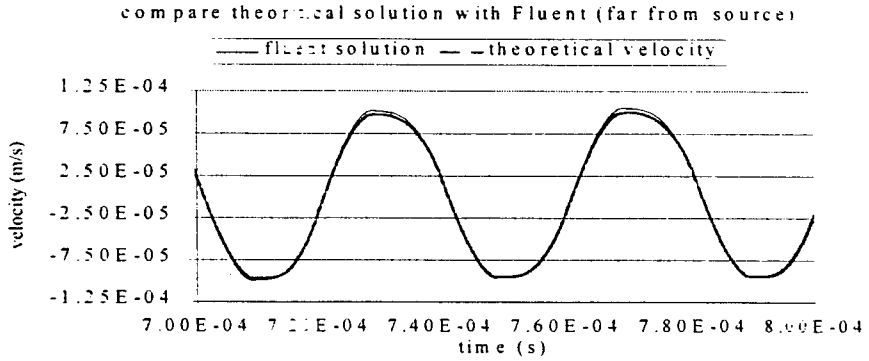

Figure 6 Pressure and velocity amplitude validation – far from source (r = 35 mm)

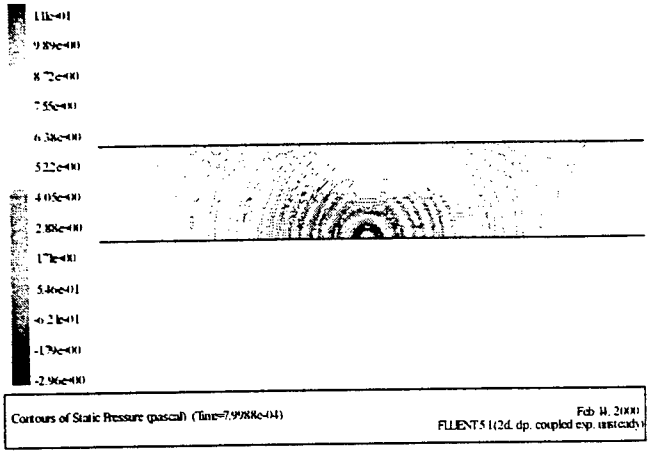

Figure 7 Contours of sound pressure in still air – 25 kHz harmonic point source

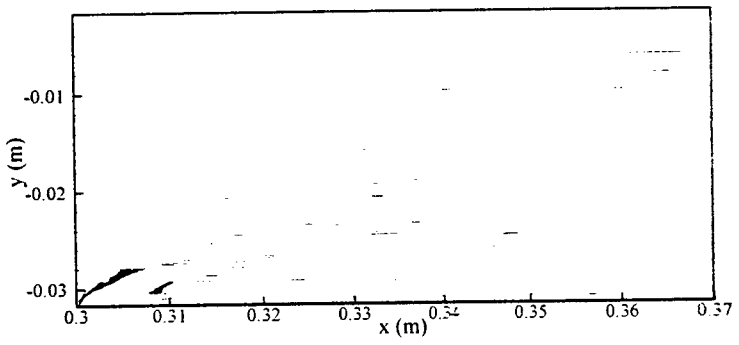

Figure 8 Contours of sound pressure amplitude downstream at Mach 3 – 25 kHz harmonic point source. Contour interval 0.2, amplitude reference to x ≈ 0.32 m.

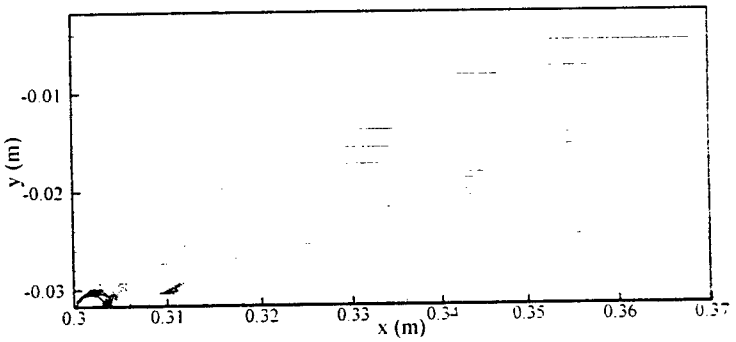

Figure 9 Contours of instantaneous sound pressure amplitude downstream at Mach 3 – 25 kHz harmonic point source. Contour levels 0.1, amplitude referenced to value at x ≈ 0.32 m.

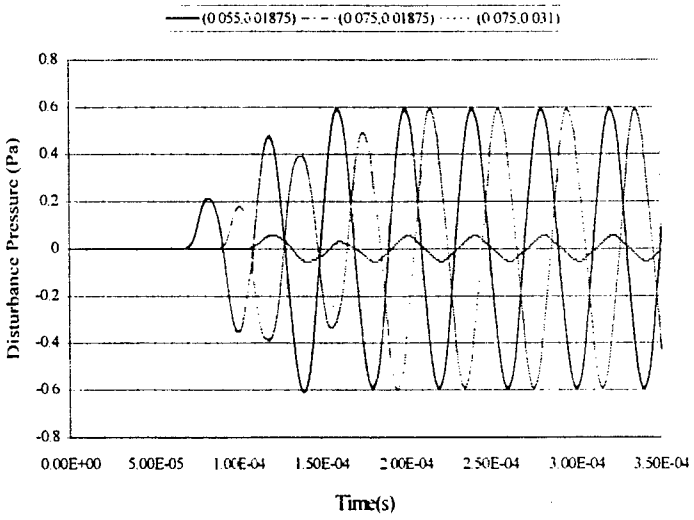

Figure 10 Computed Pressure Disturbances for 25kHz harmonic source at Mach 3 Spatial location indicated on legend

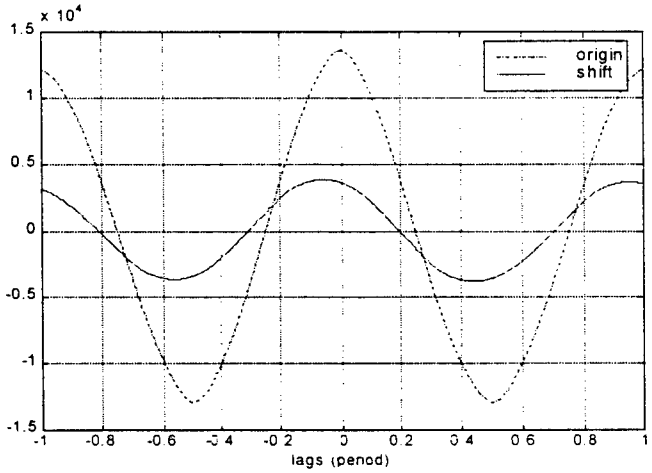

Figure 11 Cross correlation $X_1 = 0.015$ m to $X_2 = 0.035$ m

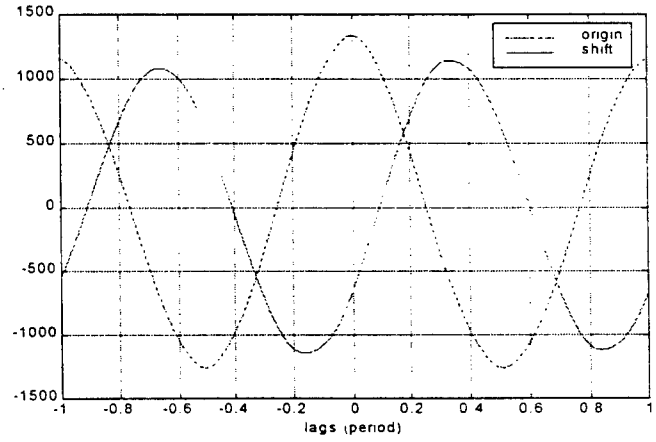

Figure 12 Cross correlation $X_1 = 0.035$ m to $X_2 = 0.055$ m

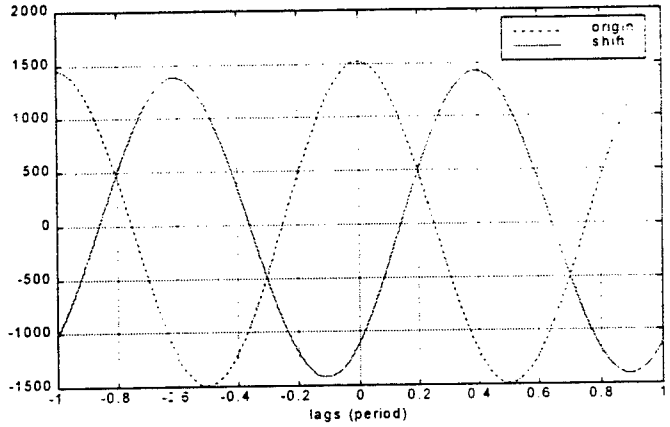

Figure 13 Cross correlation $X_1 = 0.055$ m to $X_2 = 0.075$ m

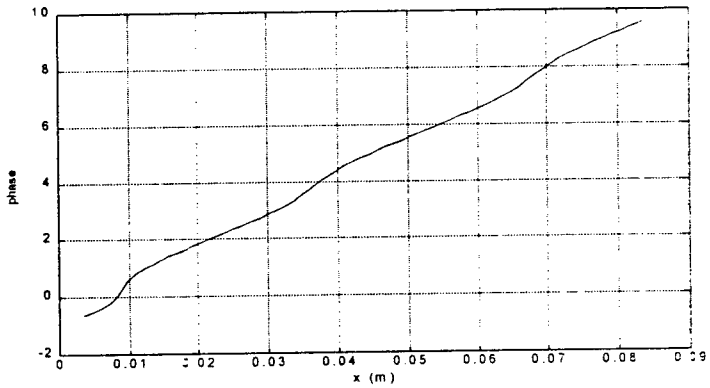

Figure 14 Unwrapped phase from inviscid theory

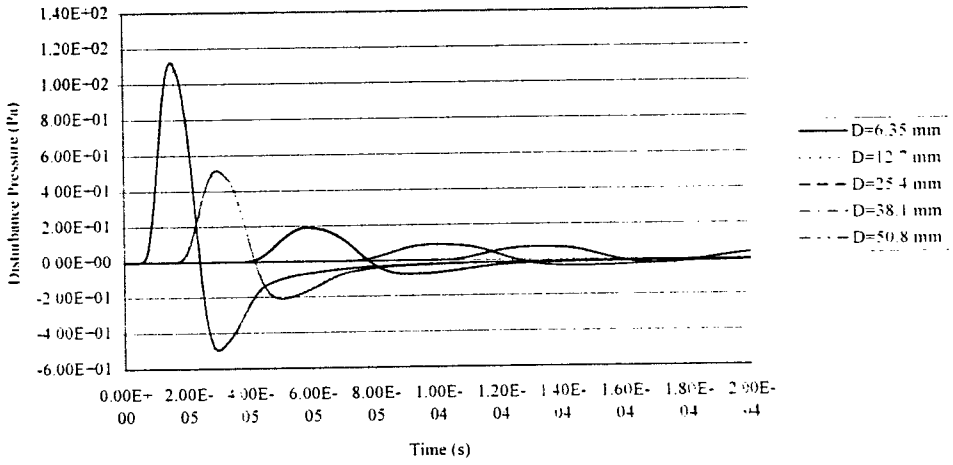

Figure 15 Computed transient sound pressure pulse, P_{static}= 3 kpa. Location indicated.

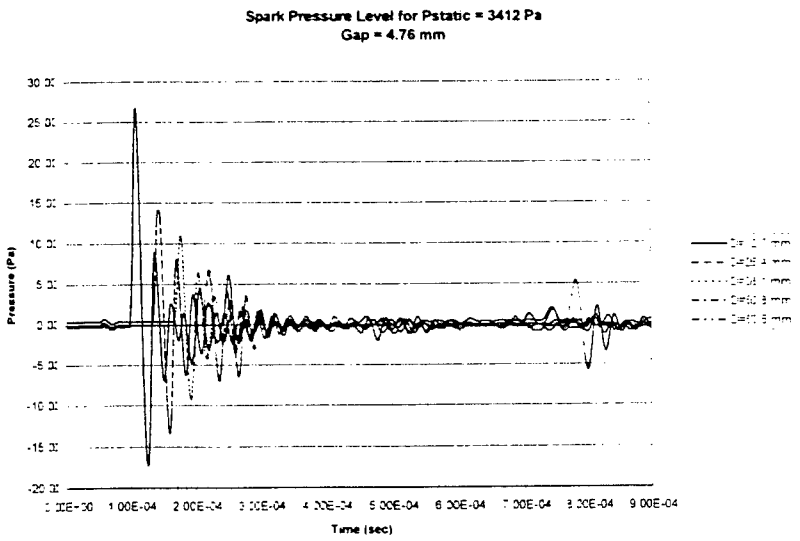

Figure 16 Experimental transient sound pressure pulse, P_{static} =3 kpa. Location indicated.

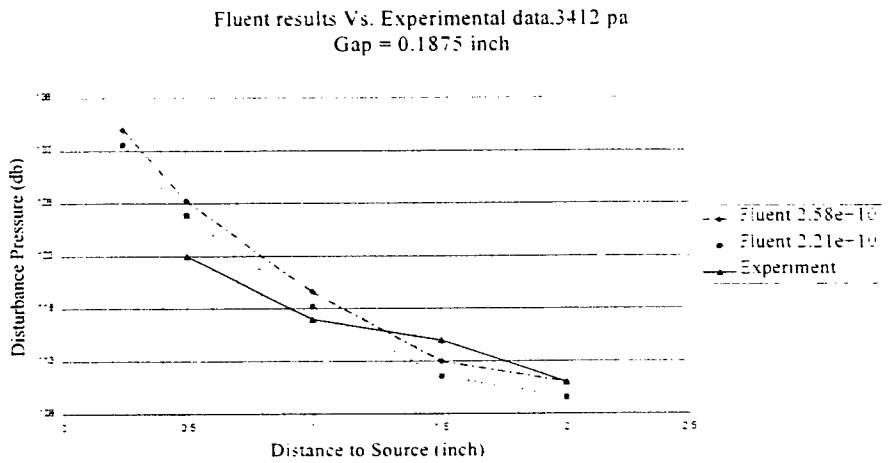

Figure 17 SPL vs. distance from source numerical and experimental for P_{static}=3 kpa.

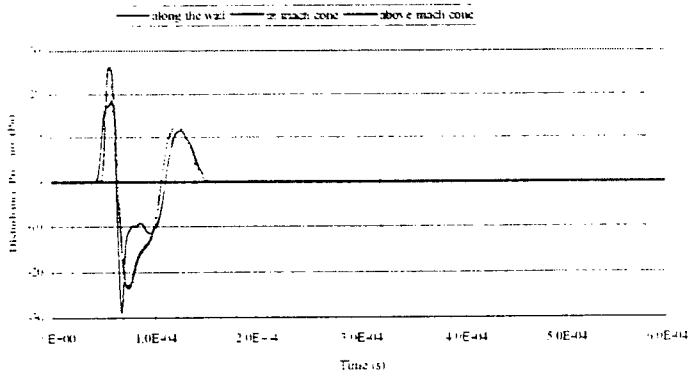

Figure 23 Computed transient pressure at 3 different points on an arc of radius 2 inches, inviscid model.

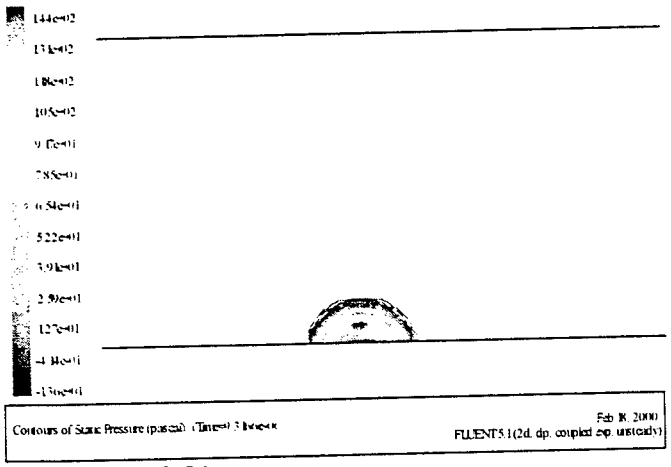

At time = 9.31 μs

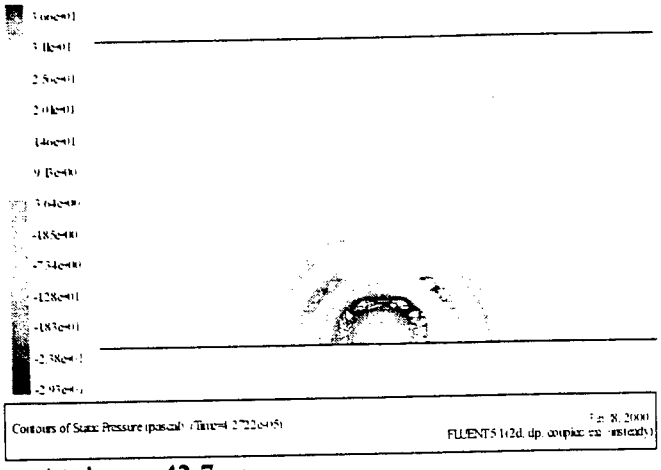

At time = 42.7 μs

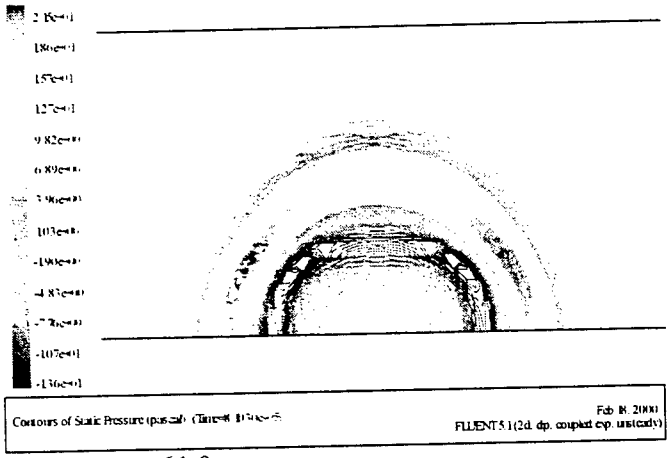

At time = 61.0 μs

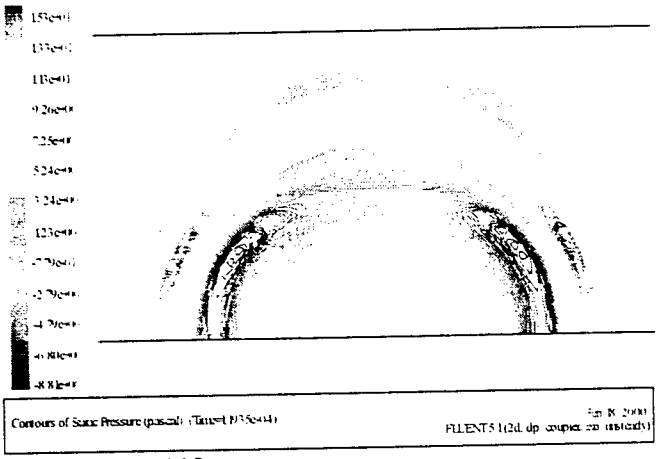

At time = 119 μs

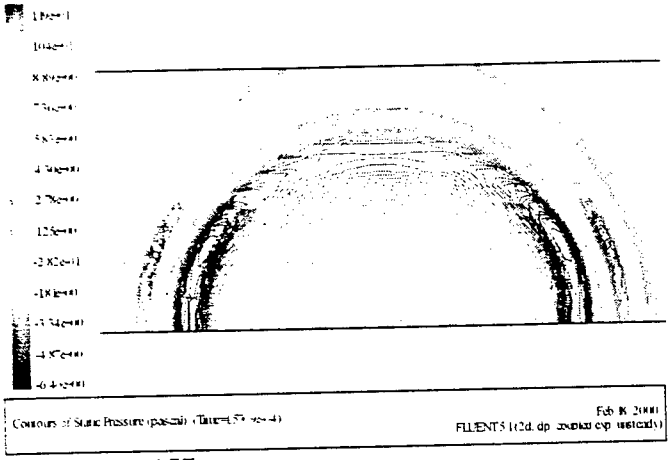

At time = 157 μs

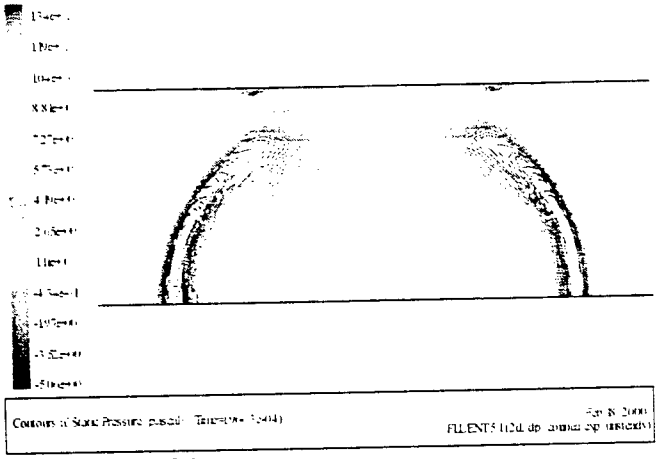

At time = 196 μs

Figure 18 Contours of instantaneous static pressure after introducing a pulse in still air.

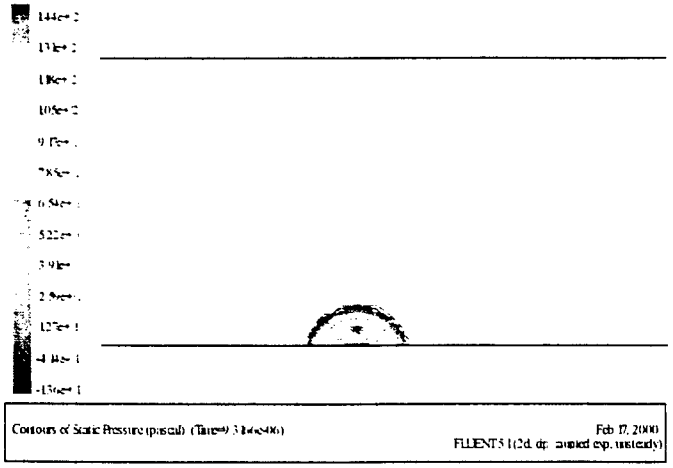

At time = 9.36 μs

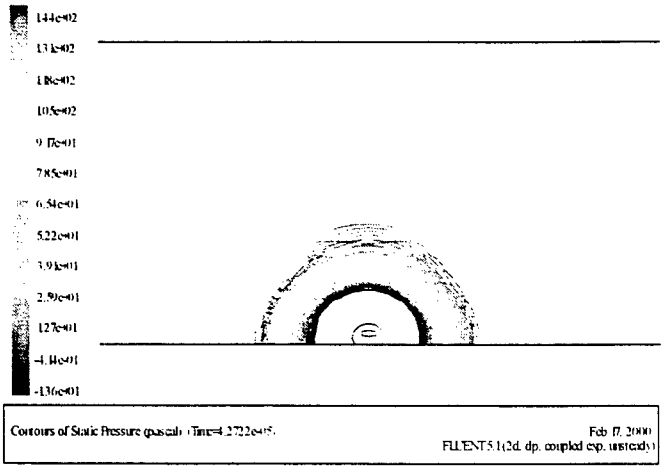

At time = 42.7 μs

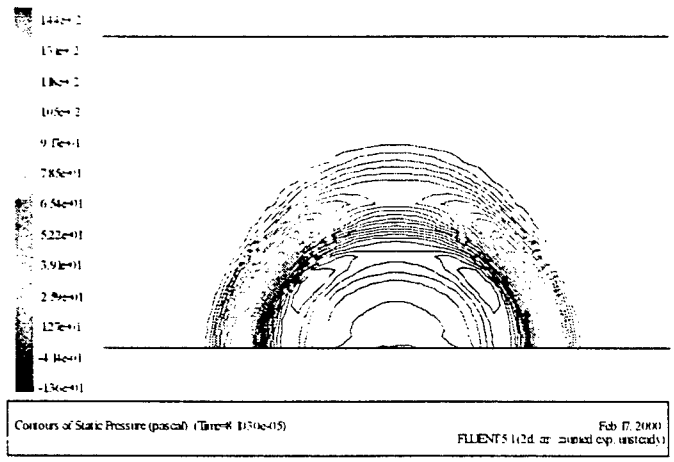

At time = 61.0 μs

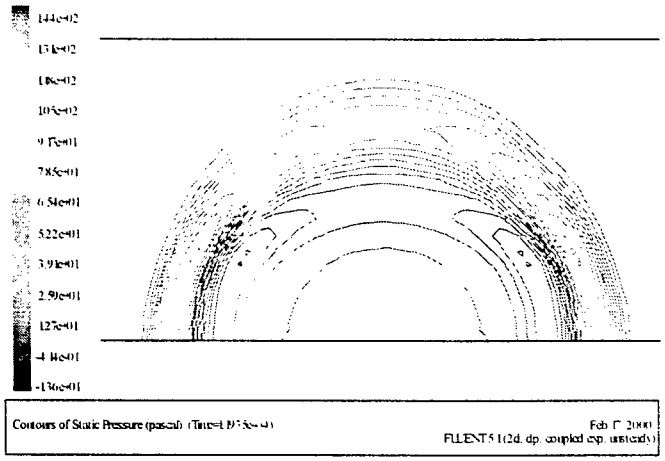

At time = 119 μs

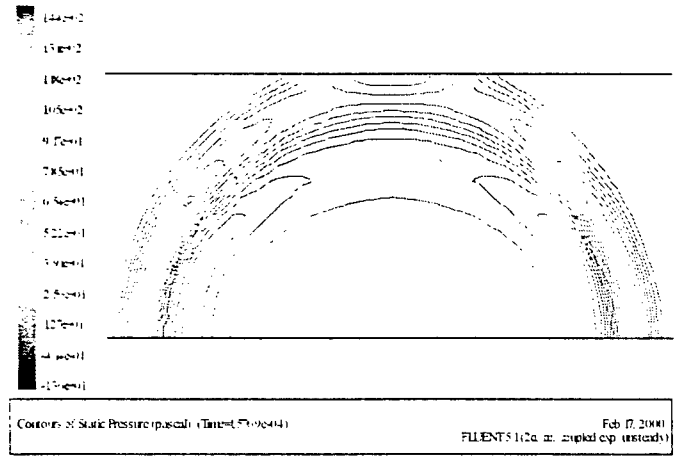

At time = 157 μs

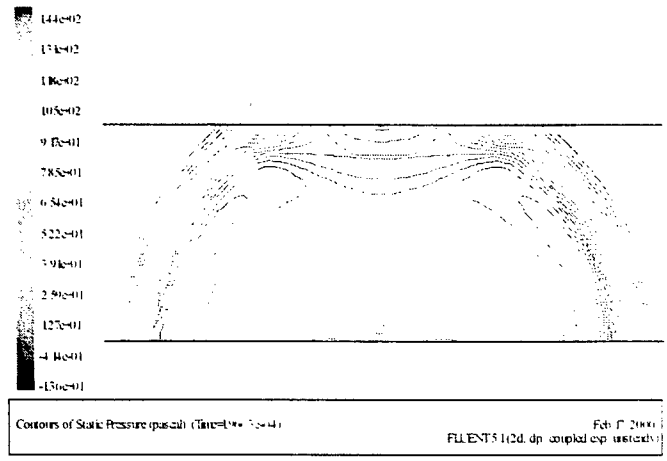

At time = 196 μs

Figure 19 Contours of instantaneous static pressure after introducing a pulse, still air. Contouring interval fixed.

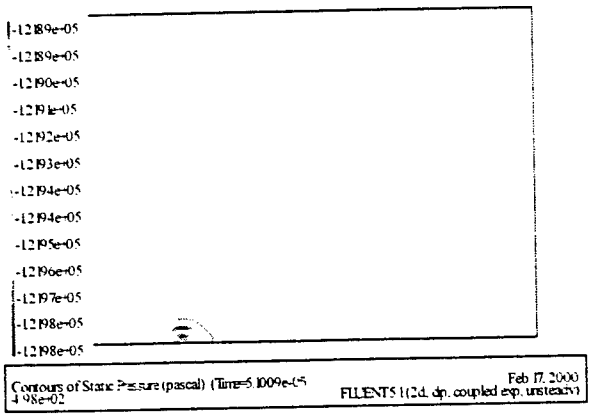

At time = 61 μs

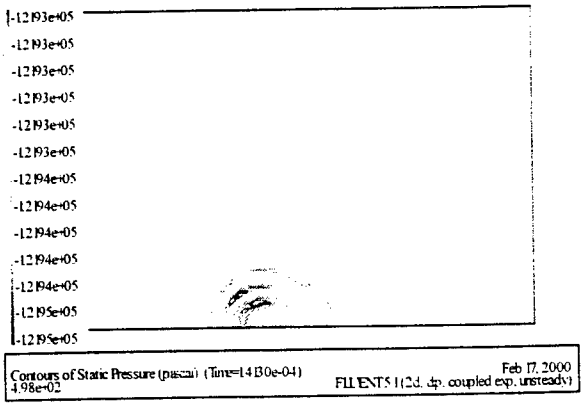

At time = 51 μs

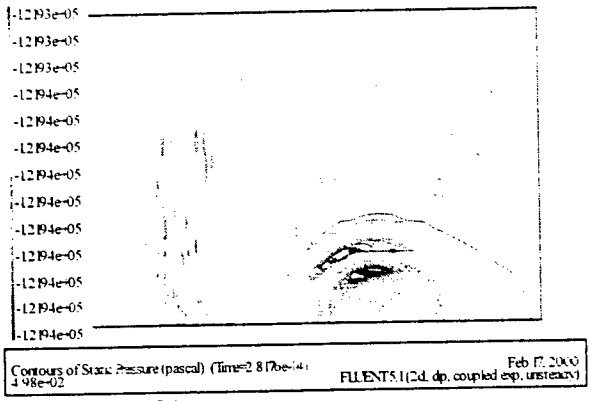

At time = 281 μs

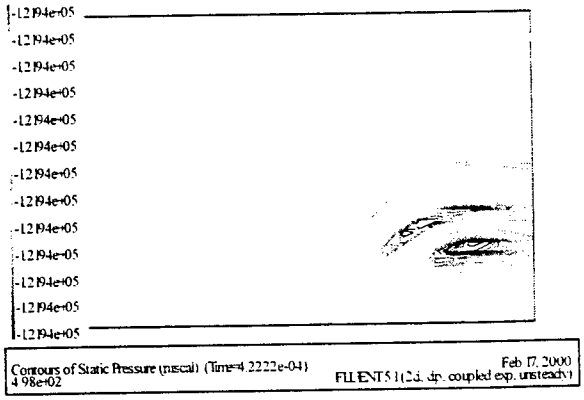

At time = 423 μs

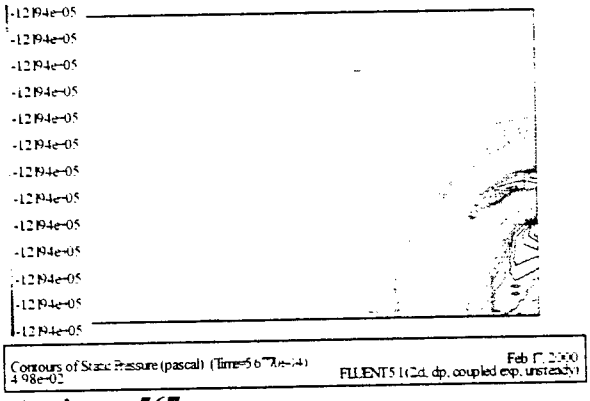

At time = 567 μs

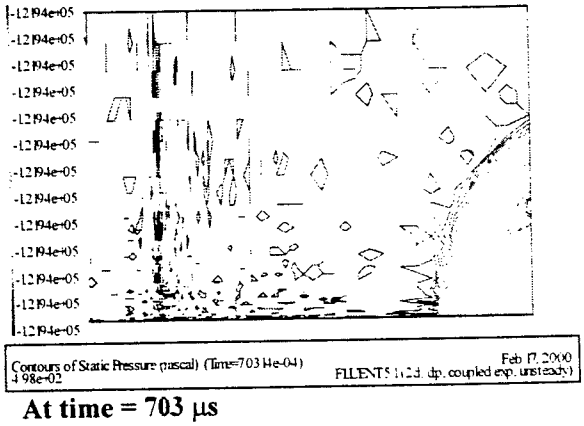

At time = 703 μs

Figure 20 Contours of instantaneous static pressure downstream at Mach 3, inviscid flow.

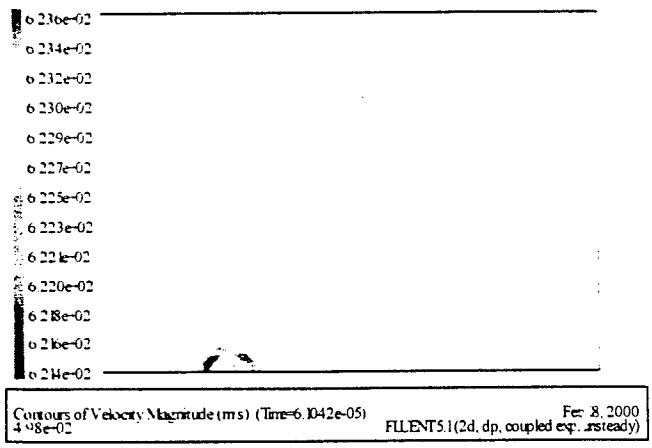

At time = 61 μs

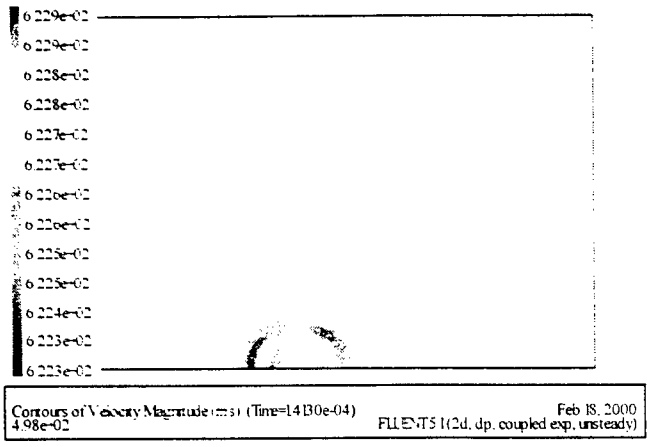

At time = 141 μs

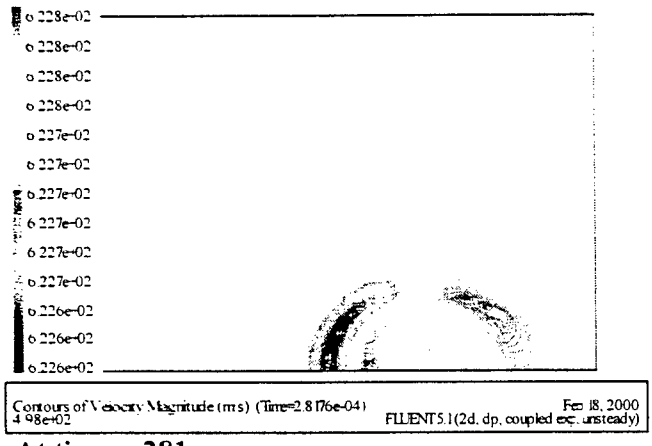

At time = 281 μs

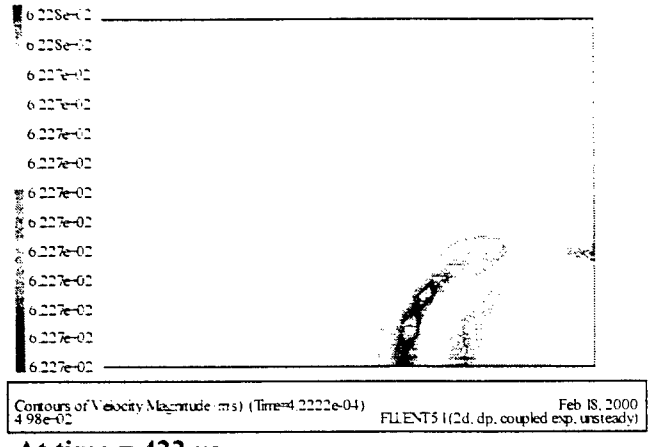

At time = 422 μs

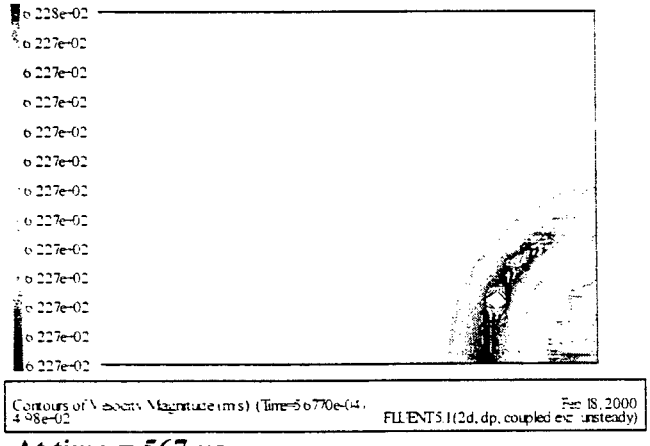

At time = 567 μs

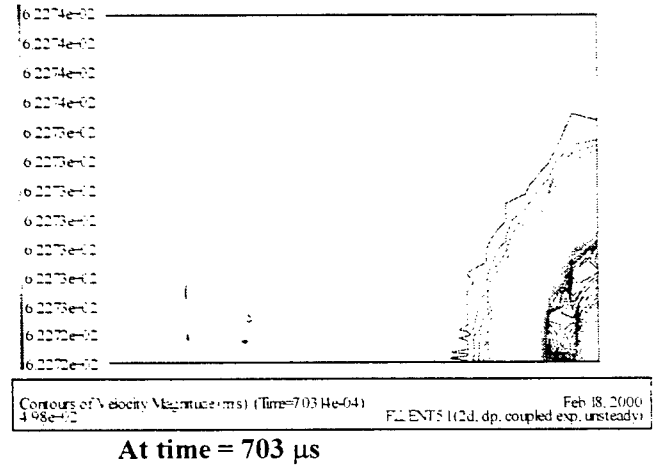

At time = 703 μs

Figure 21 Contours of instantaneous velocity downstream at Mach 3, inviscid flow.

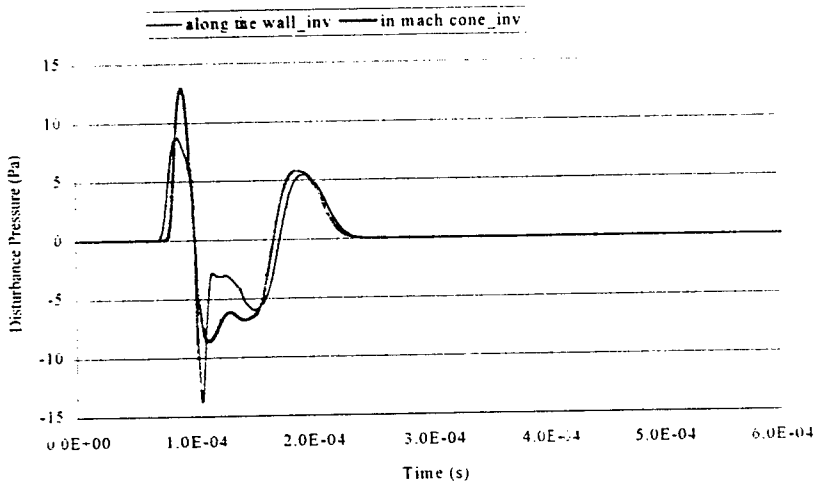

Figure 24 Computed transient pressure at 2 different points on an arc of radius 3 inches. Inviscid model.

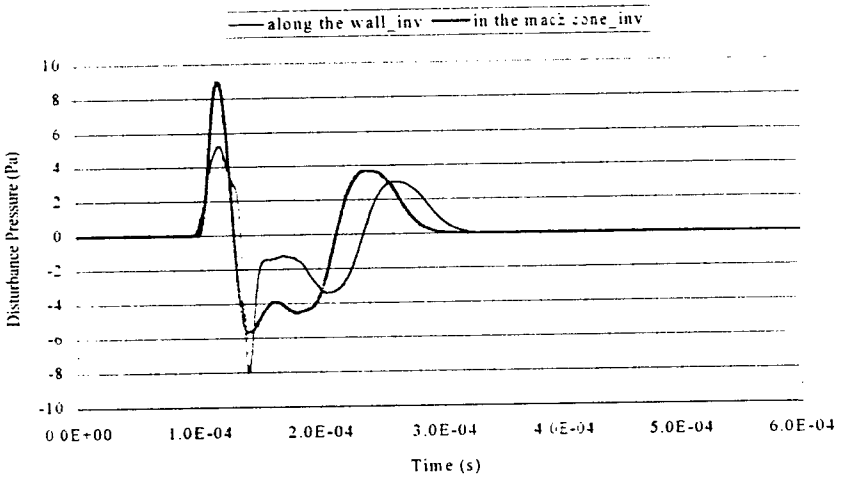

Figure 25 Computed transient pressure at 2 different points on an arc of radius 4 inches. Laminar model.

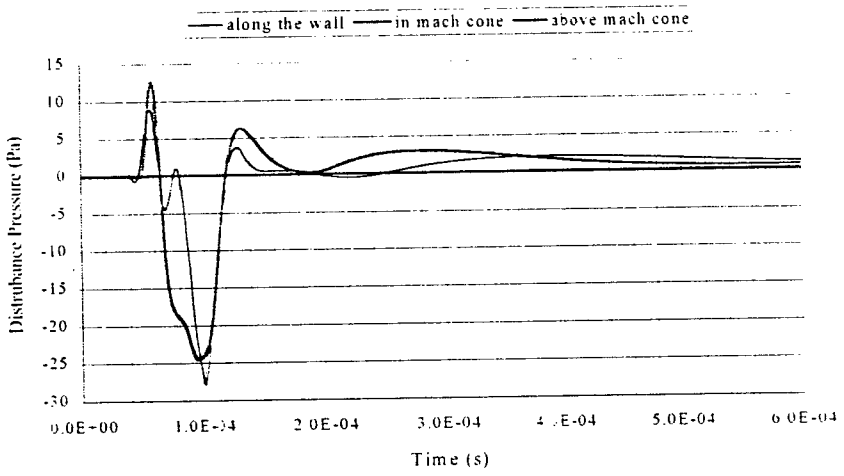

Figure 29 Computed transient pressure at 3 different points on an arc of radius 2 inches. Laminar flow.

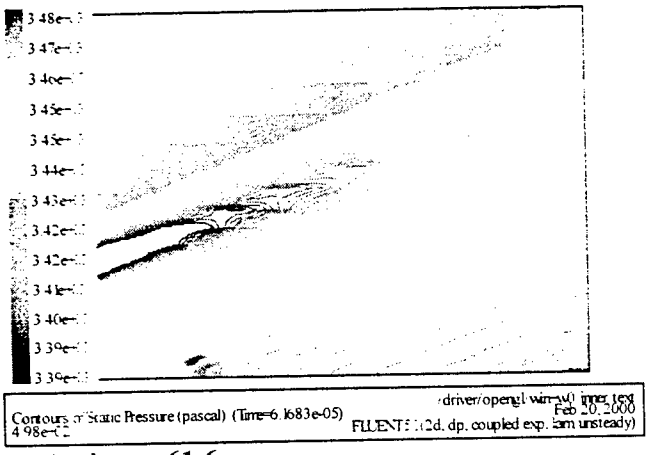

At time = 61.6 μs

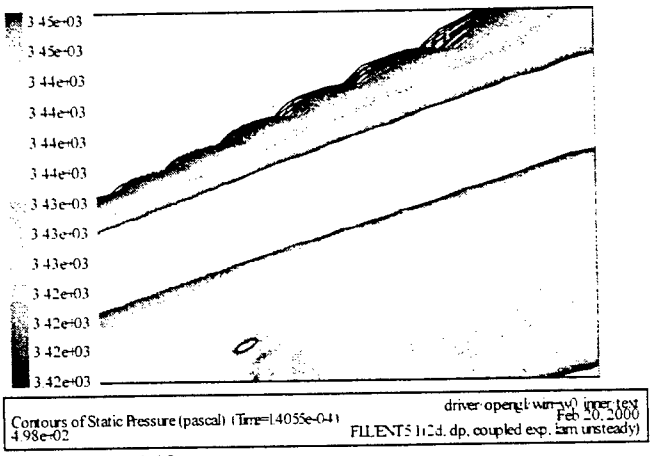

At time = 140 μs

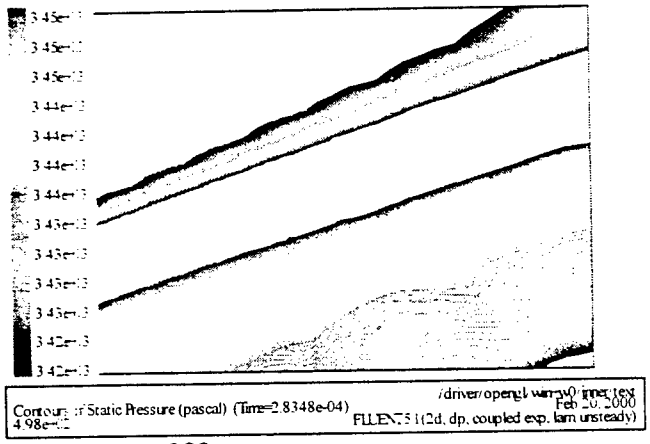

At time = 283 μs

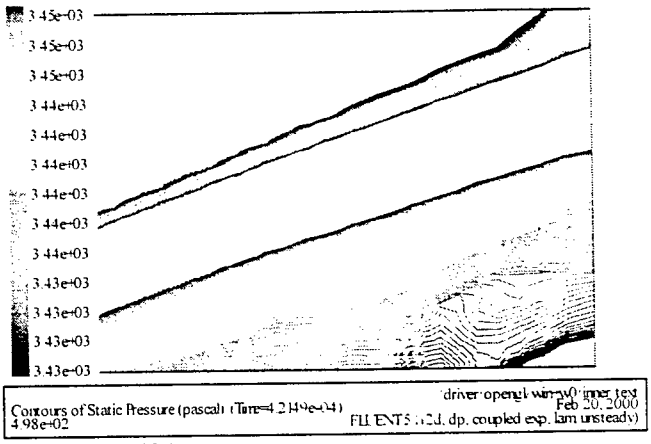

At time = 421 μs

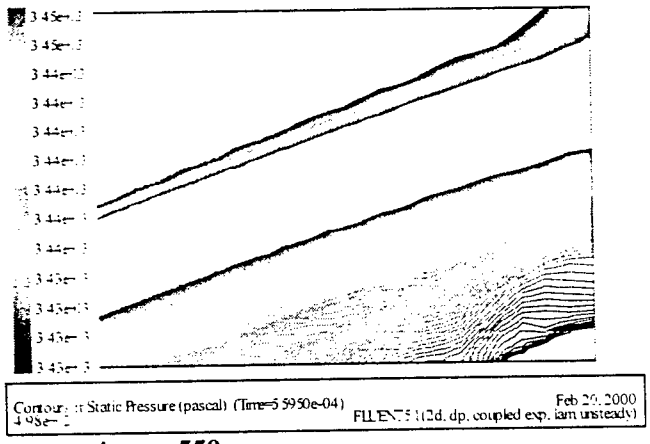

At time = 559 μs

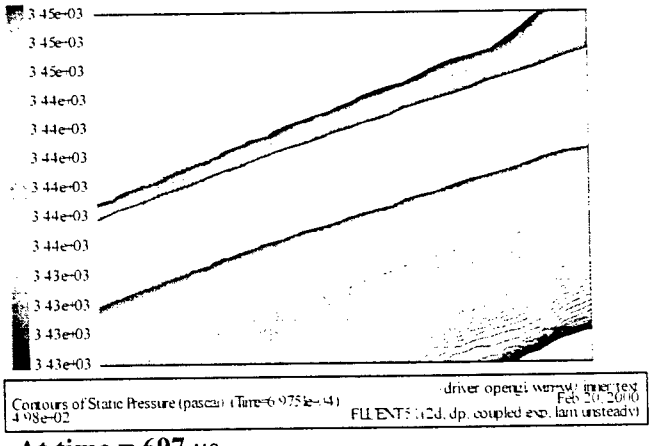

At time = 697 μs

Figure 26 Contour of instantaneous static pressure downstream at Mach = 3, laminar flow. (source reference point indicated).

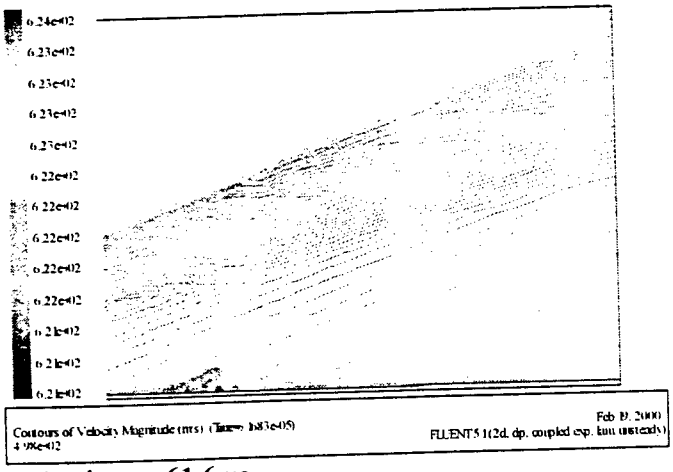

At time = 61.6 μs

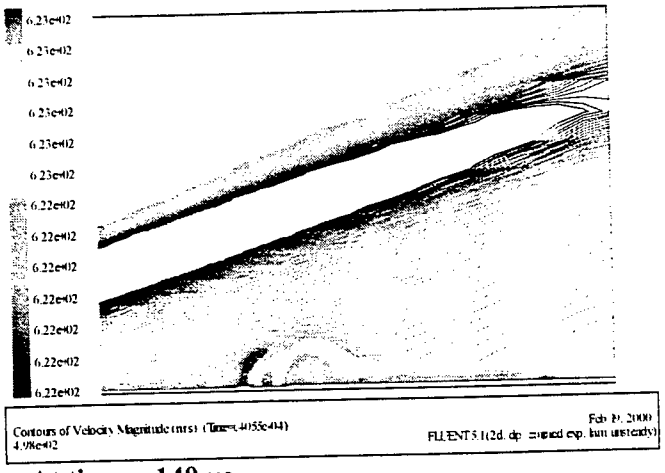

At time = 140 μs

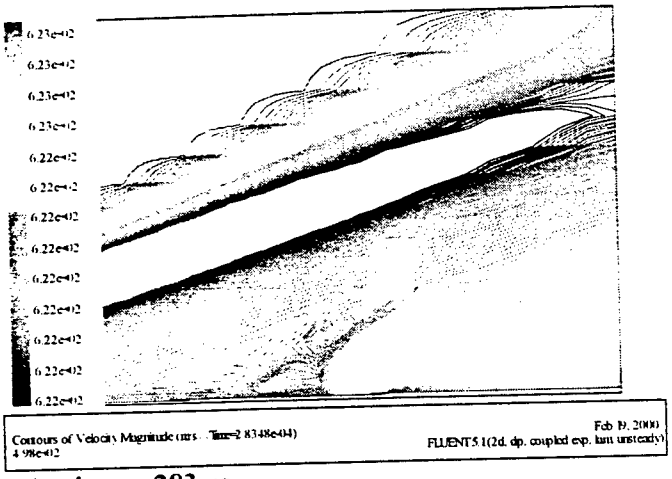

At time = 283 μs

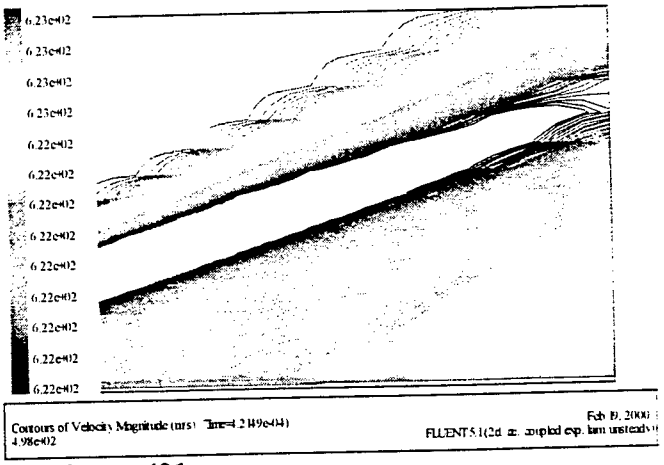

At time = 421 μs

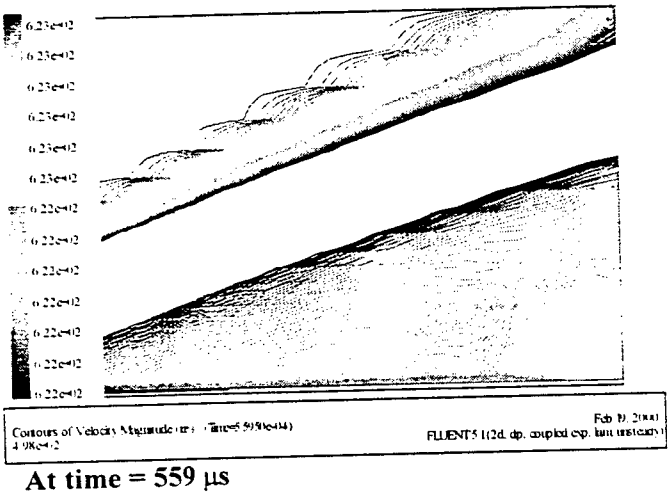

At time = 559 μs

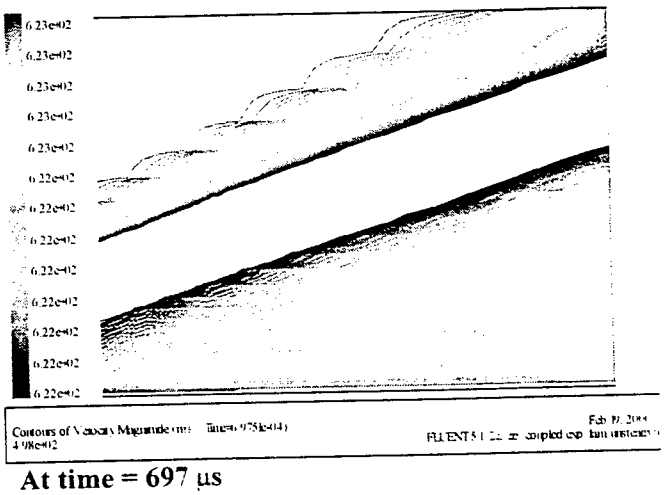

At time = 697 μs

Figure 27 Contours of instantaneous velocity magnitude downstream at Mach = 3, laminar flow.

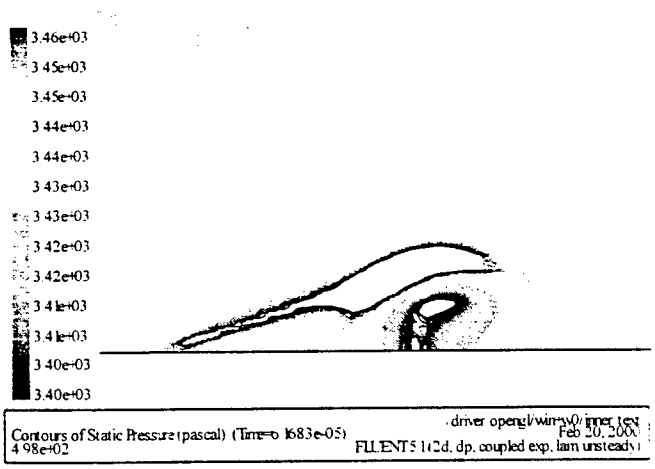

At time = 61.6 μs

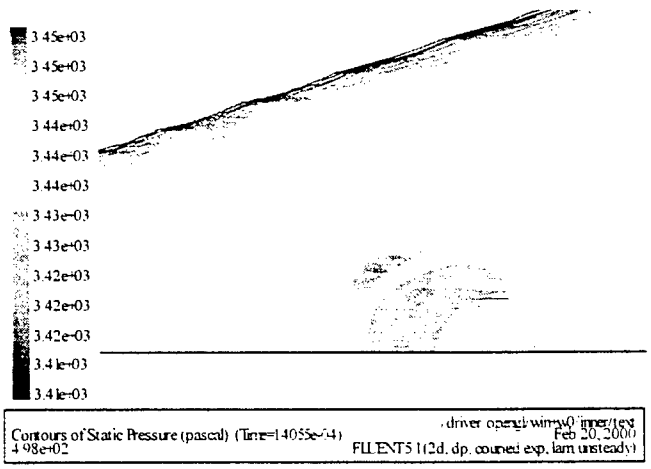

At time = 140 μs

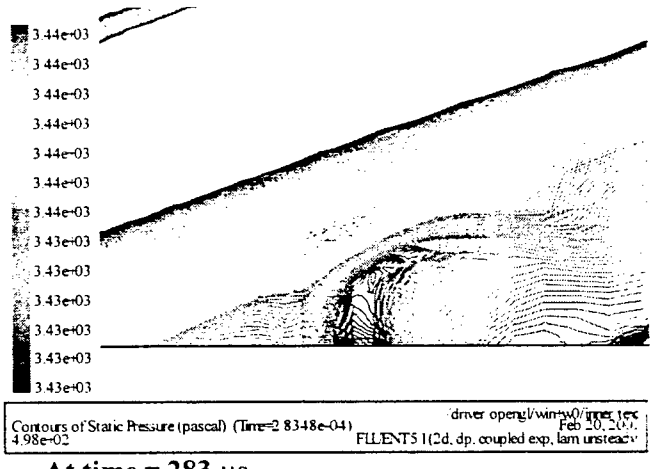

At time = 283 μs

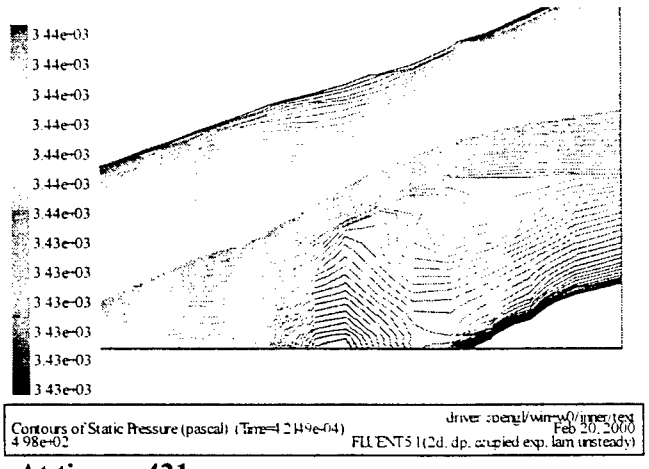

At time = 421 μs

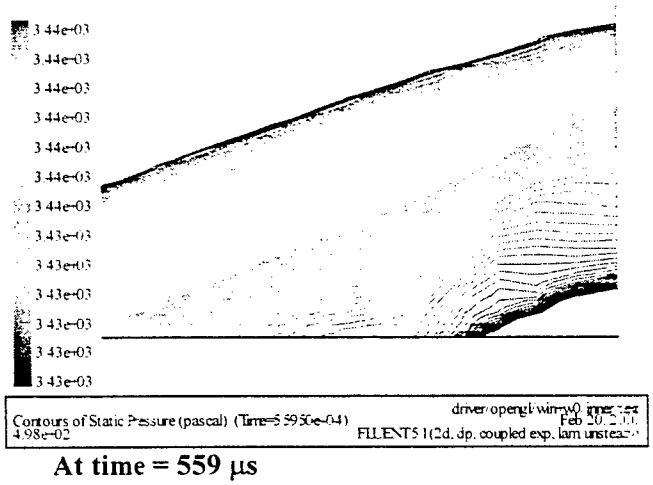

At time = 559 μs

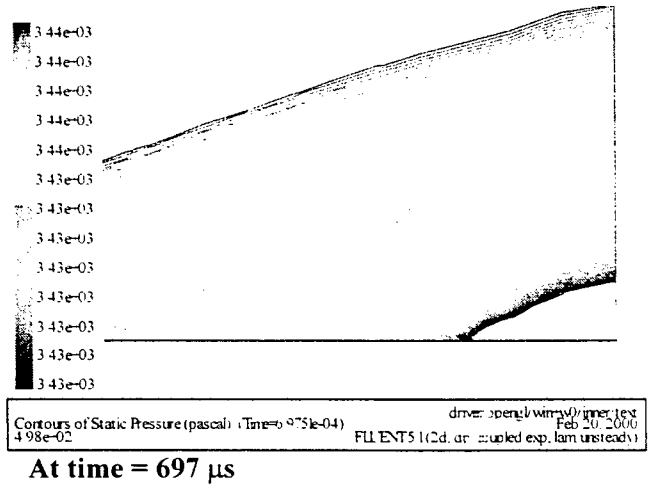

At time = 697 μs

Figure 28 Zoomed contours of instantaneous static pressure downstream at Mach = 3, laminar flow.

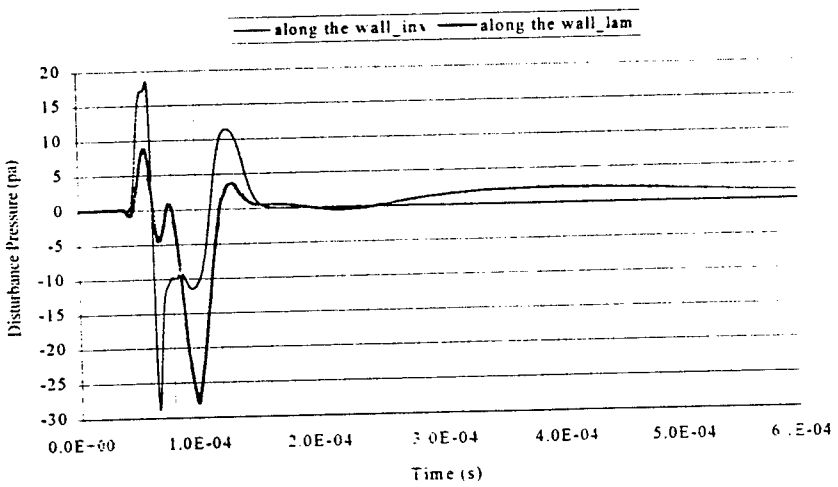

Figure 30 Computed transient pressure: inviscid vs. laminar on an arc of radius 2 inches along the wall.

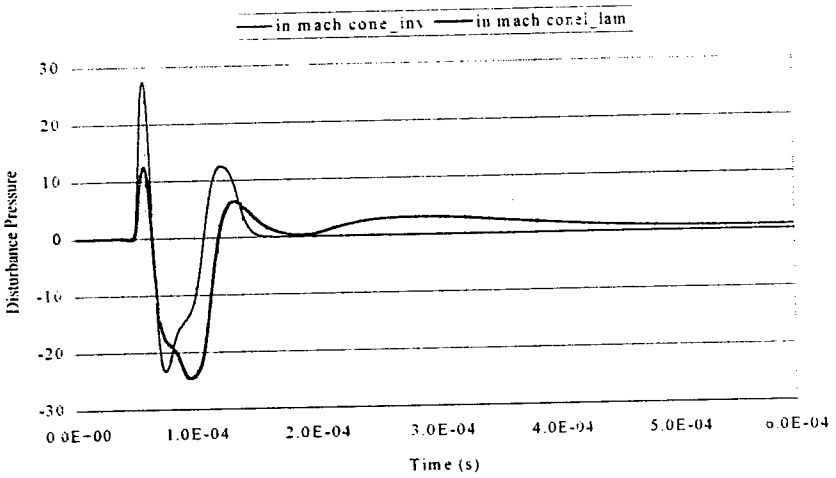

Figure 31 Computed transient pressure: inviscid vs. laminar on an arc of radius 2 inches in mach cone.

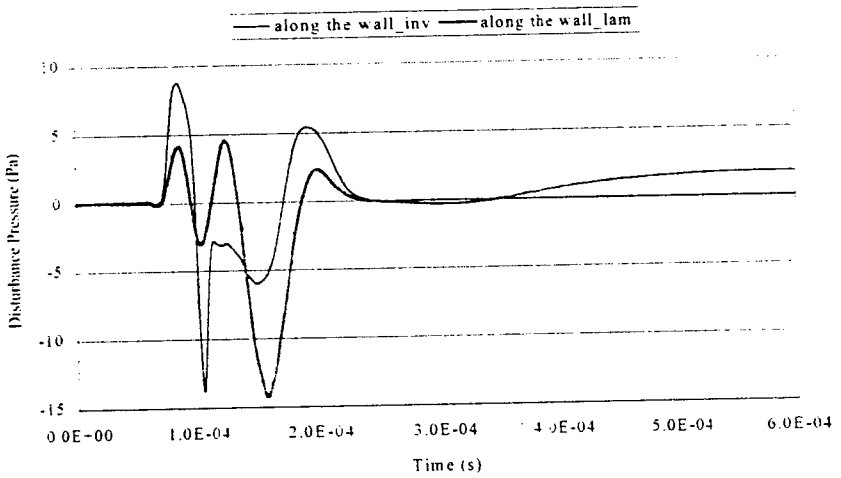

Figure 32 Computed transient pressure: inviscid vs. laminar on an arc of radius 3 inches along the wall.

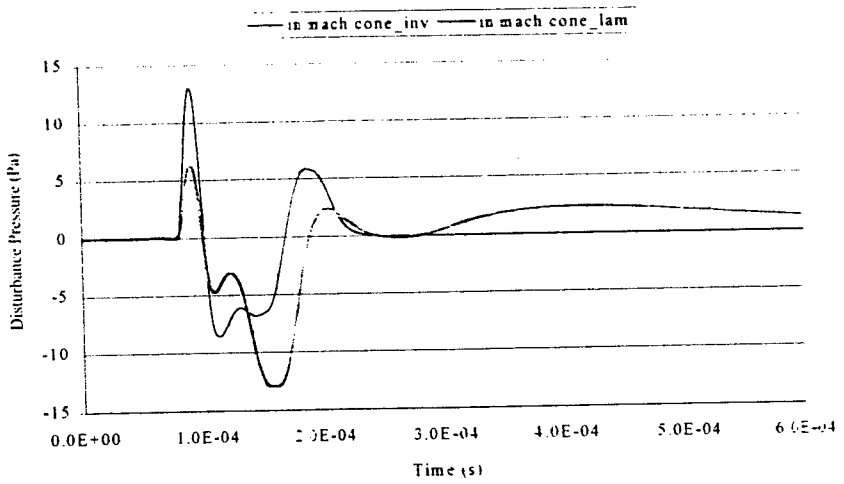

Figure 33 Computed transient pressure: inviscid vs. laminar on an arc of radius 3 inches in mach cone .

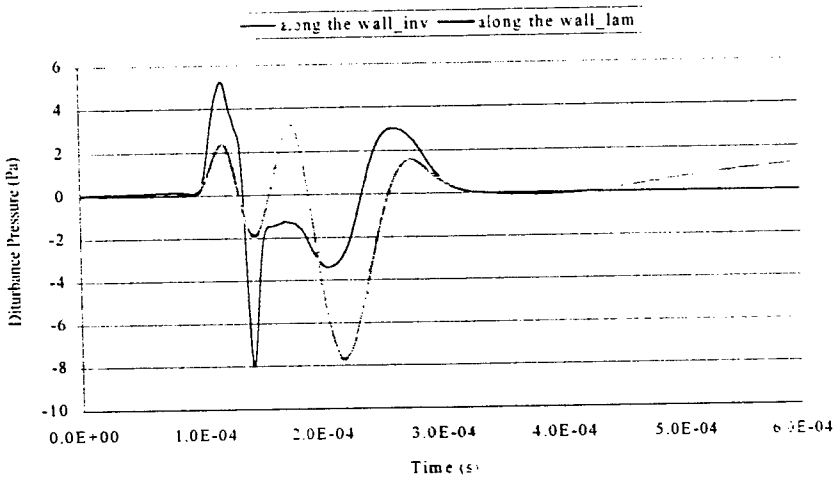

Figure 34 Computed transient pressure: inviscid vs. laminar on an arc of radius 4 inches along the wall.

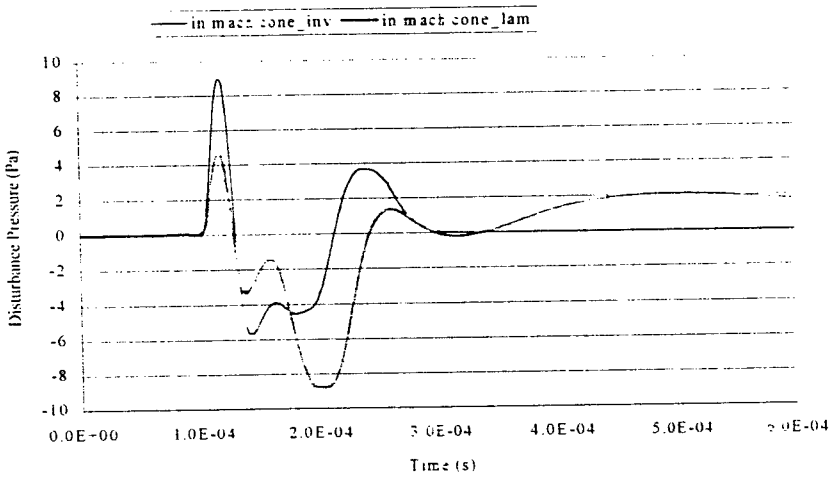

Figure 35 Computed transient pressure: inviscid vs. laminar on an arc of radius 4 inches in mach cone.

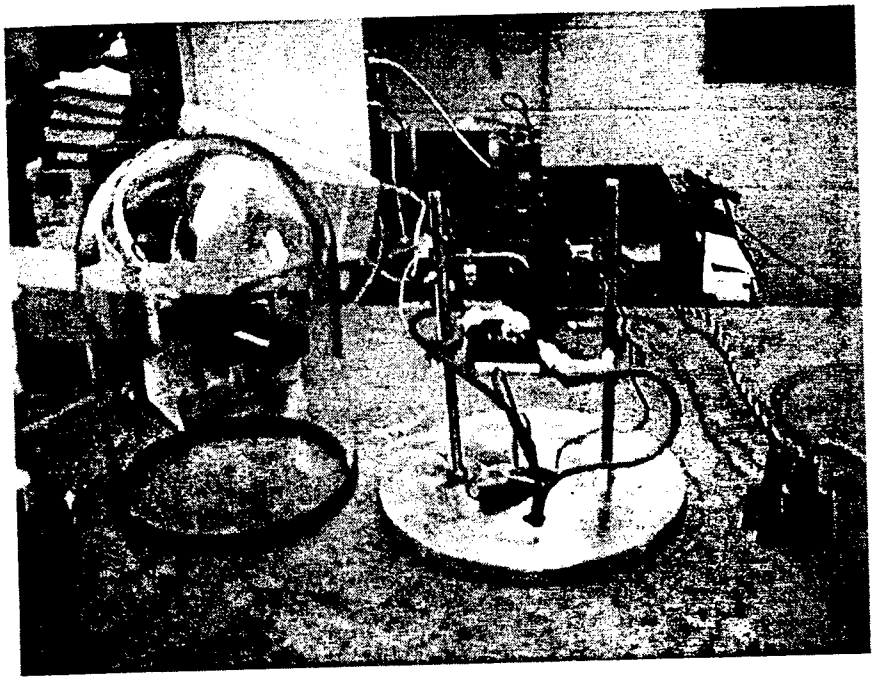

Figure 36 Apparatus with bell jar removed – Holley 40 kV coil on right

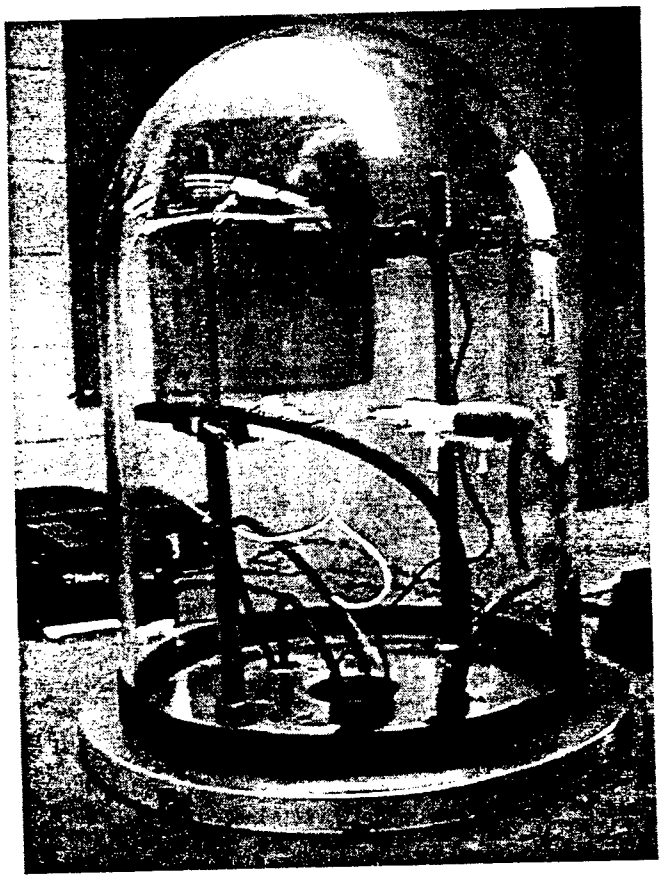

Figure 37 Apparatus with bell jar installed – Holley trigger box behind

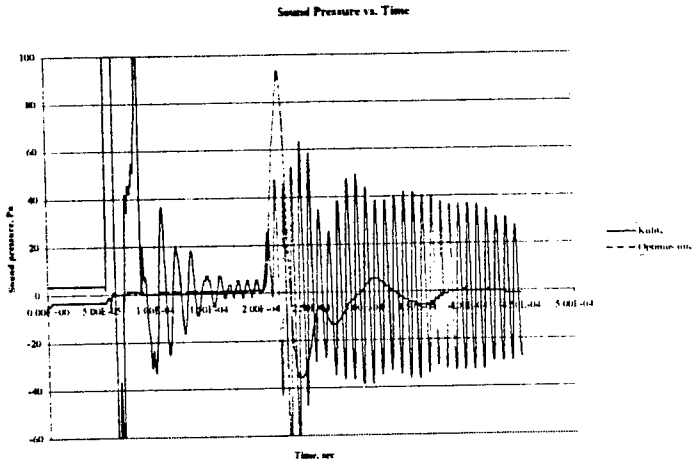

Figure 38 Sound pressure measurements- 0.5 inch spark gap, 2 inches from source Kulite and Optimus mic

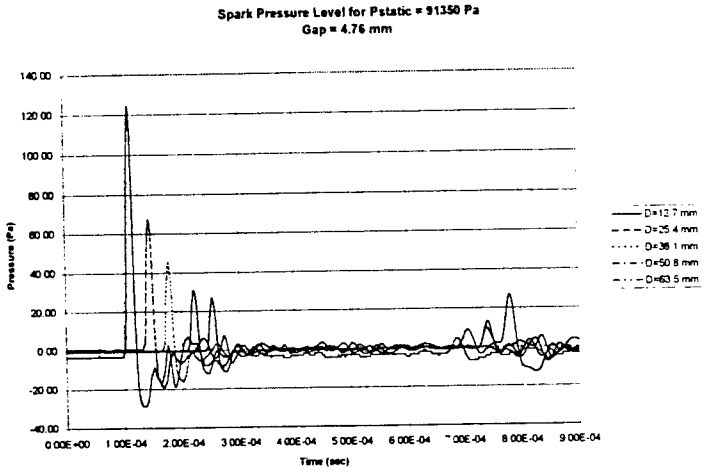

Figure 39 Sound pressure measurements for Pstatic = 91.3 kPa (gap = 0.375 inch)

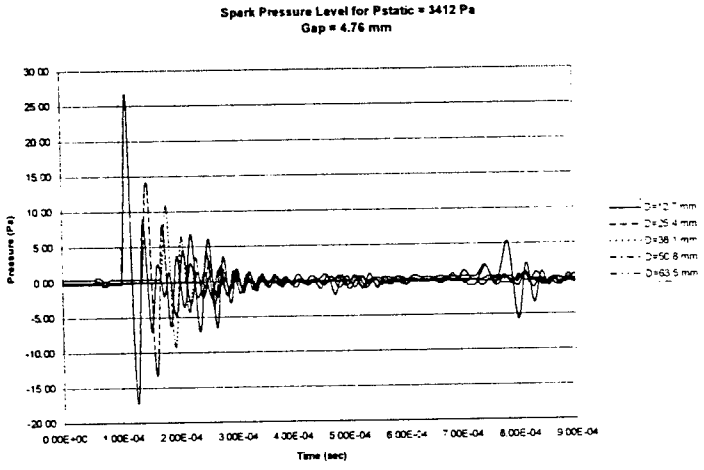

Figure 40 Sound pressure measurements for Pstatic = 3.45 kPa (gap = 0.1875 inch)

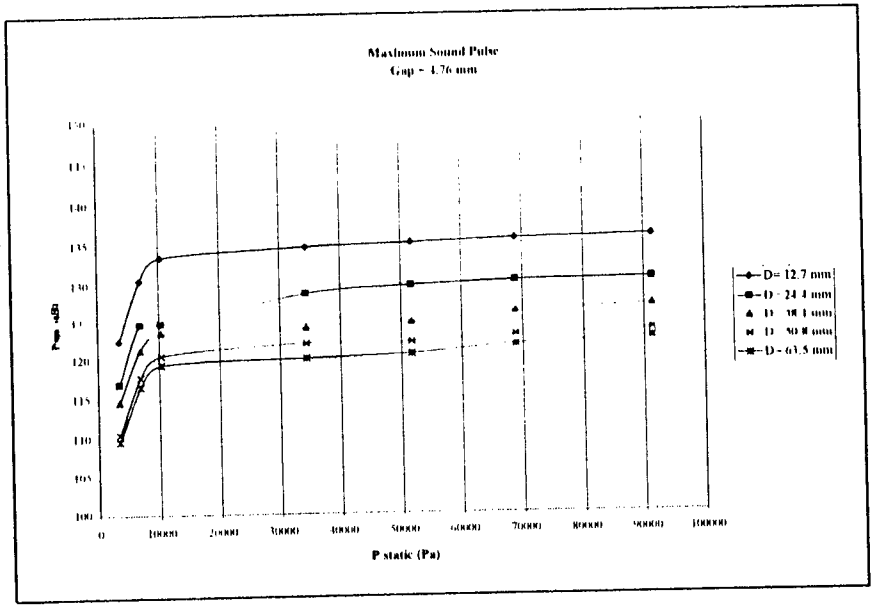

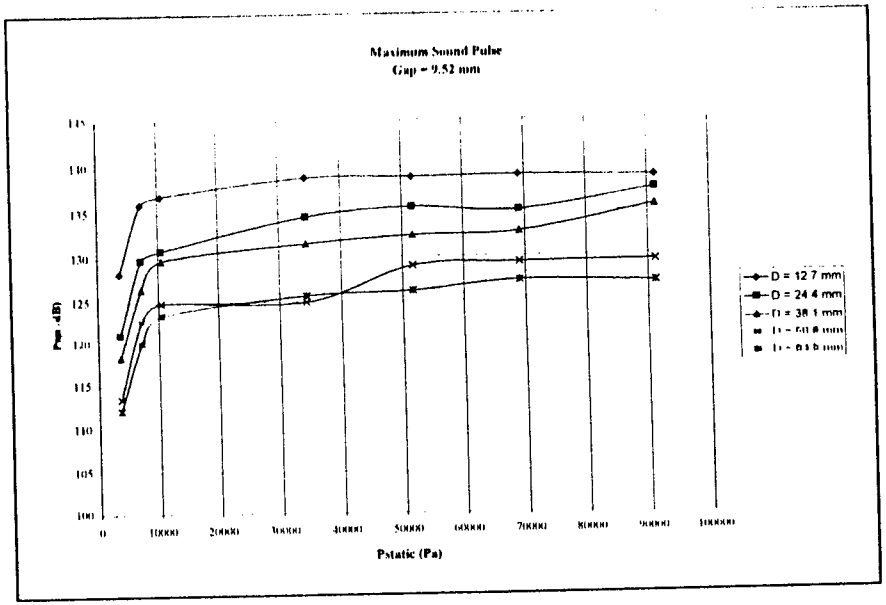

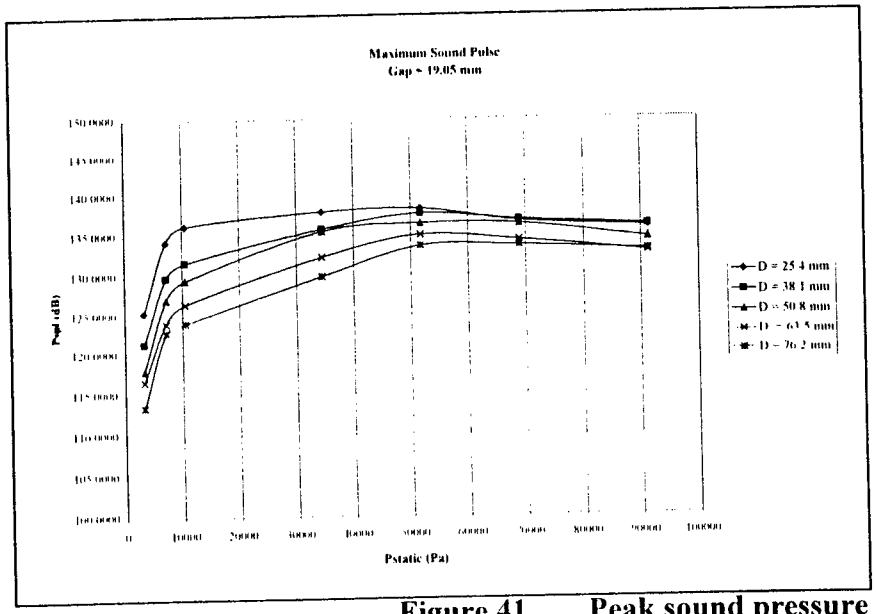

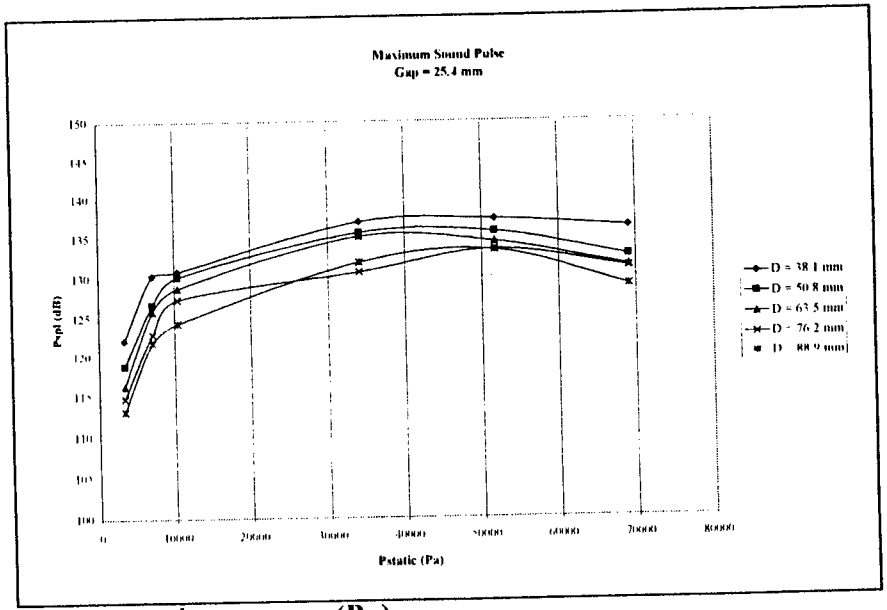

Figure 41 Peak sound pressure level (dB) vs. static pressure (Pa)

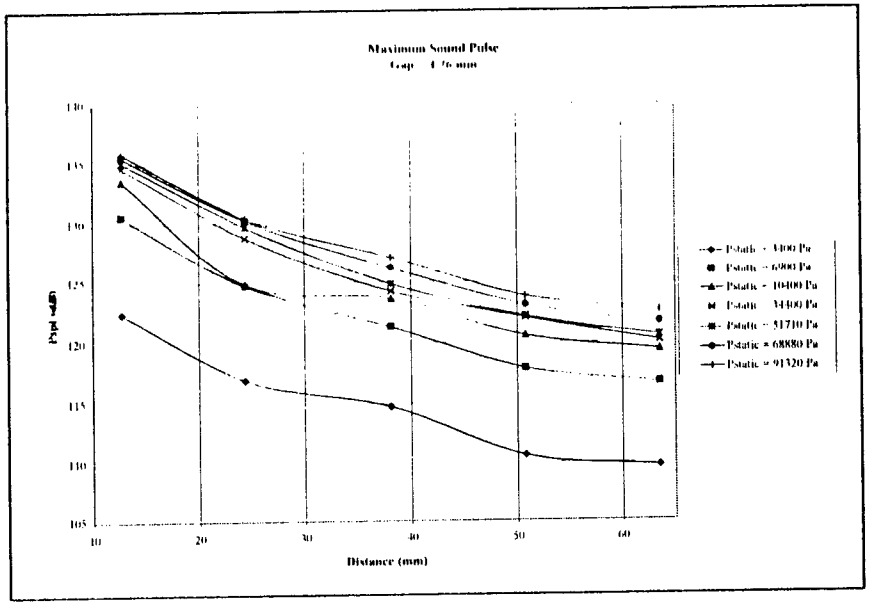

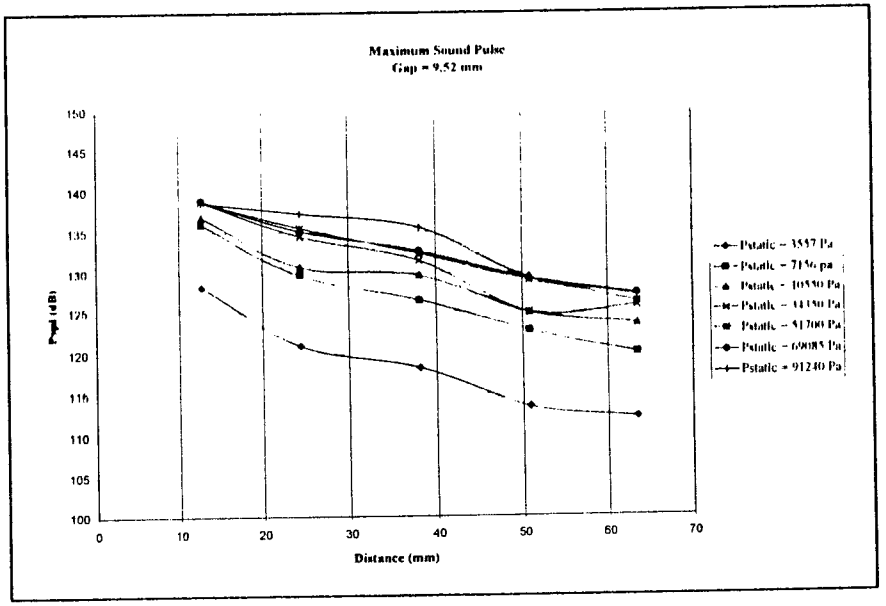

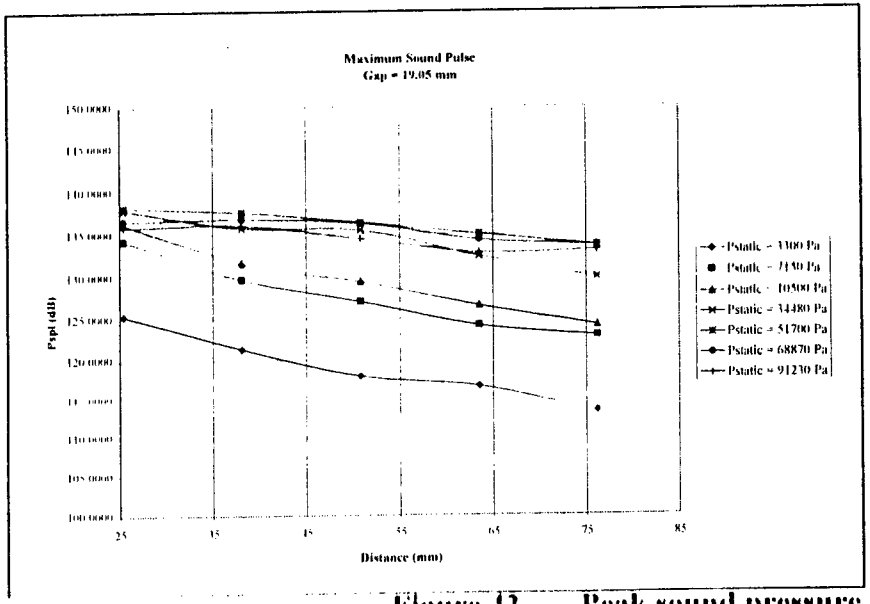

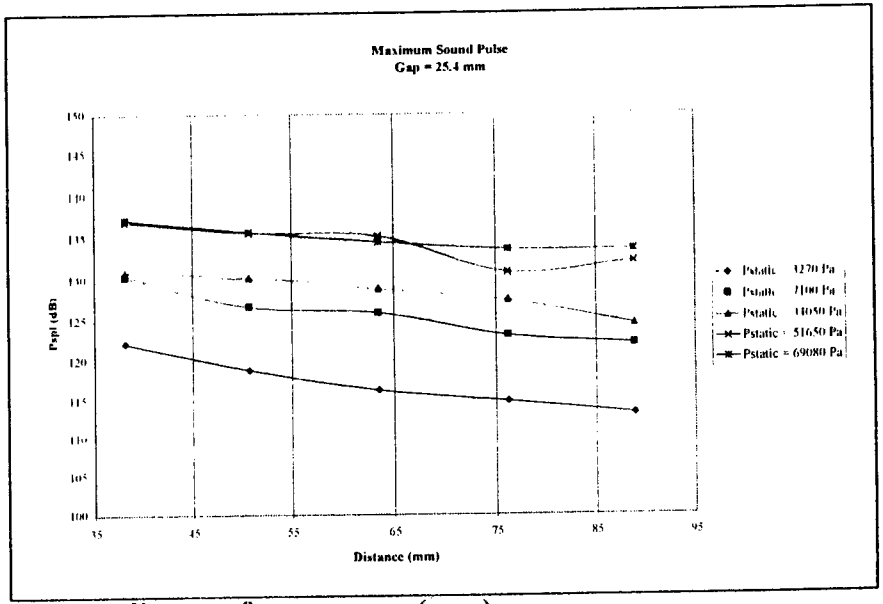

2-36

Figure 42 Peak sound pressure level (dB) vs. distance from source (mm)

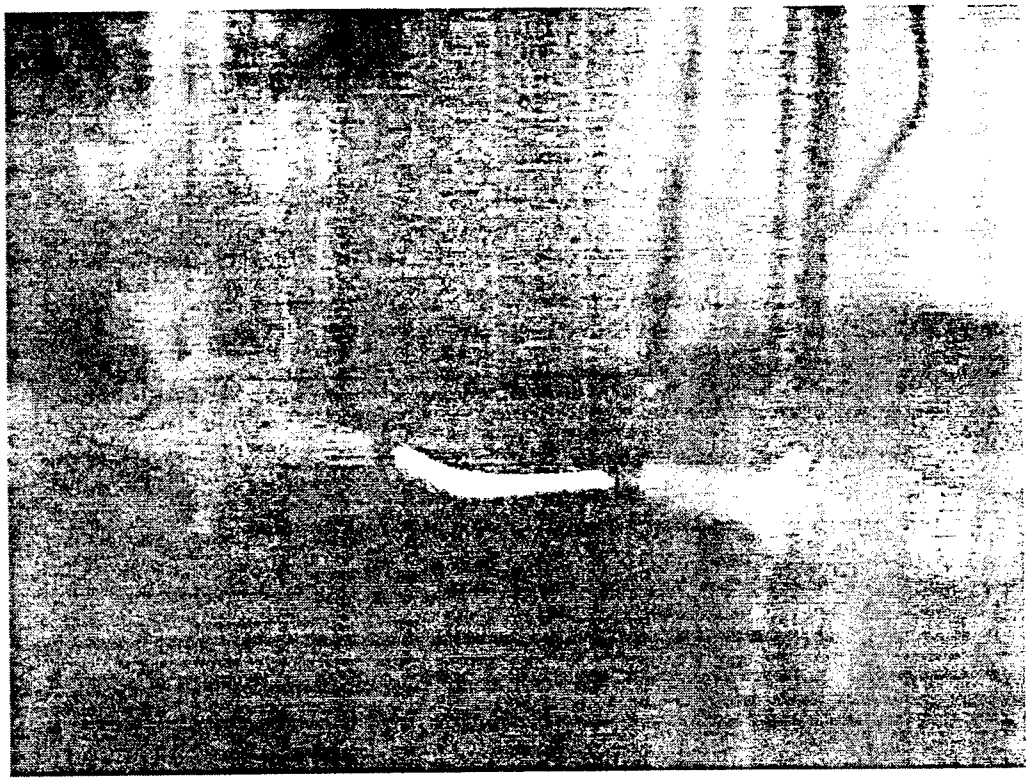

Figure 43 Spark discharge at 93 kPa static pressure

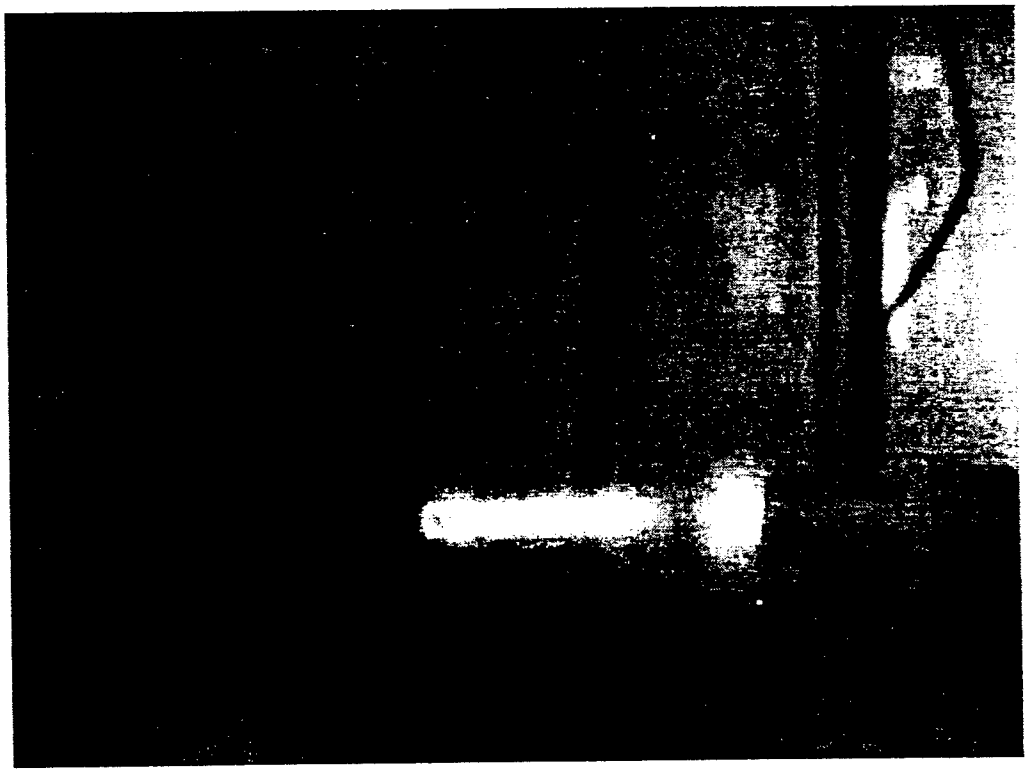

Figure 44 Spark discharge at 3.4 kPa static pressure

Appendix A – Two-Ignition Coil Spark Power Supply

The following excerpts were taken from the URL #1, listed in the body of this report, and include links to other web sites which were used to construct a two-coil HV spark power supply:

Here is probably the best ignition coil driver circuit that I have seen. As far as I know it was designed by Jochen Kronjaeger. You can find the original at Jochen's High Voltage Page This circuit is designed to run from 230V, but I have came up with a circuit that will run from 120V about just as well. You will need to find two ignition coils (preferably of the same type), a 100uF with at least a 200VDC rating, a full-wave bridge rectifer with a rating of about 5A at 200VDC. A large power resistor with at about 150-200ohms resistance and a power capability of at least 100W, or you can use an aquarium immersion heater. The next two things are optional, but they will make the project a lot more interesting. You might want to get about three 6A 200VDC SCRs. You can get these from Radio Shack. You might also want a simple square wave pulse generator. This can be just a simple 555 timer circuit. Make sure you can vary the frequency on it.

Ok, here is a simple schematic showing my project:

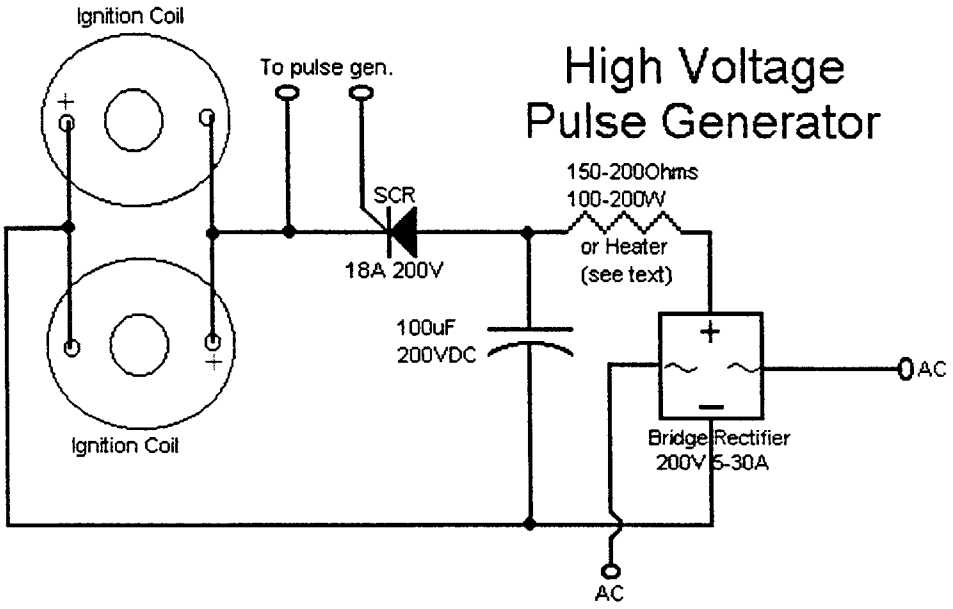

This circuit is fairly easy to build. If you can't get an SCR, you may also use a TRIAC as a substitute. If you can't get either then you can use a relay, switch, or just two pieces of wire to trigger it. The contacts will probably be burned out soon though. The resistor or heater is used so that the power doesn't need to be cut when you discharge the capacitor. It limits the current to a safe value when discharging the capacitor. If you choose not to use the current limiter, the power will have to be unplugged every time you discharge the capacitor. If you cannot find a heater or power resistor you can also use a common household lightbulb. This will also give you a visual indication when the capacitor is charged. The bulb will go out when the capacitor is fully charged.

The following is from the Jochen's High Voltage Page link above:

60 kV pulses

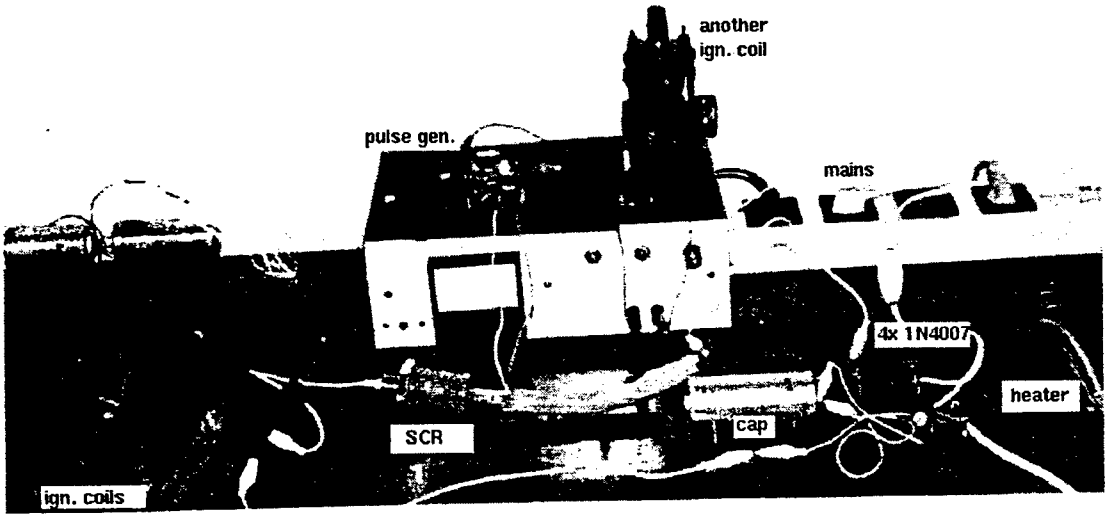

This is a slightly different kind of HV source, it produces single pulses only, but at considerably high voltage and output current. It's simple to build, but you need a special component, namely a high-current SCR (Thyristor). I found mine by chance in an electronic components store (It's got a 1cm diameter cable!). You also need two car igniton coils, preferably "high power" ones, and an immersion heater or similar device. Connect the two coil primaries anti-parallel, so that the secondaries give voltages of different sign. You will probably have to step up the insulating rim around the secondary terminals with some plastic pipe and epoxy glue.

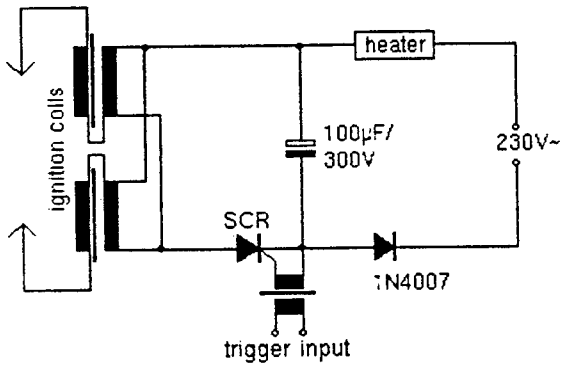

Charge a cap (electrolytic is o.k.) of about 100uF with rectified mains voltage (300V) through the heater (to limit current) and discharge it in an instant through the SCR and the ignition coils. You don't have to disconnect the mains if you use a one-way rectifier (single diode). Trigger the SCR by hand or with a pulse generator at about one pulse per second max. Don't leave out the gate transformer, as the SCR is on mains voltage. NOTE: Michael Huff adapted this circuit to 120V. He also reports success using a standard SCR.
If you can't find a suitable SCR, you can also use a relay, switch or just two blank cable ends. This actually works almost as nice as a SCR, but the (relay-, switch-, cable-) contacts will "burn" soon.

These coils give you 8 cm or longer sparks of high energy. You can use up to 1000uF caps to increase this. See the "things to do" section for further experiments.

SYNTHESIS OF NEW TWO-PHOTON ABSORBING DYES, MONOMERS AND POLYMERS

Kevin D. Belfiled
Associate Professor
Department of Chemistry

University of Central Florida
4000 Central Florida Blvd.
Bldg. 5, Room 117
Orlando, FL. 32816-2366

Final Roport for:
Summer Faculty Research Program
Wright-Patterson Laboratory

Sponsored by:
Air Force Office of Scientific Research
Bolling Air Force Base, DC

and

Wright-Patterson Laboratory

December, 1999

SYNTHESIS OF NEW TWO-PHOTON ABSORBING DYES, MONOMERS AND POLYMERS

Kevin D. Belfiled
Associate Professor
Department of Chemistry
University of Central Florida

Abstract

The quest for organic materials exhibiting high nonlinear optical (NLO) absorptivities has increased dramatically over the past several years. Specifically, the nonlinear process of two-photon absorption is the subject of intense interest in the chemistry, photonics, and biophotonics communities. Two-photon absorption (TPA or 2PA) can be defined as the simultaneous absorption of two photons via virtual states in a medium. The process requires high peak power, which is available from pulsed lasers. Several current and emerging technologies exploit the two-photon absorption phenomenon, including optical power limiting materials, two-photon fluorescence imaging, photodynamic cancer therapy, and two-photon microfabrication.

The two-photon process considered here involves the simultaneous absorption of two photons, either degenerate or nondegenerate, at wavelengths well beyond the linear absorption spectrum of a particular molecule. Unfortunately, the criteria for the design of molecules with large TPA cross-sections, δ, have not been well developed, impeding the full potential of TPA-based applications. Herein, the synthesis and characterization of new near-IR TPA dyes are presented. The synthetic methodology developed facilitates the systematic preparation of derivatives with varying electronic character. The dyes employ fluorene as a thermally and photochemically stable π-conjugated system from which the 2, 7, and 9-postions can be readily functionalized. Nondegenerate, TPA spectra of select dyes were obtained using a recently developed "NLO spectrometer". Their respective δ values, a measurement of the efficiency of the TPA process, are reported. Finally, comparisons of the nonlinear data have generated preliminary trends of the TPA process as a function of wavelength and chemical structure.

SYNTHESIS OF NEW TWO-PHOTON ABSORBING DYES, MONOMERS AND POLYMERS

Kevin D. Belfield

Introduction

Organic materials exhibiting significant nonlinear optical effects have been a subject of intense investigation recently.[1] In particular, compounds that are strong nonlinear, multiphoton absorbers are being investigated as materials for a wide variety of potential applications in areas of study ranging from optical sciences, biophotonics, materials sciences, and photochemistry, to name a few. Multiphoton absorption can be defined as simultaneous absorption of two or more photons through virtual states in a medium.[2] More specifically, the nonlinear process of two-photon absorption (2PA) has been a subject gaining greater interest among these multidisciplinary areas.

The theory of the simultaneous absorption of two photons was developed by Goeppert-Mayer in 1931[2], but remained mainly a conceptual curiosity. This is because the process requires a light source of suitably high intensity. Hence, it was not until the advent of the pulsed laser providing very high intensity light, that the two-photon absorption process was experimentally verified by Kaiser and Garrett in the early 1960s using a focused, pulsed ruby laser beam.[1] Since then, the ever-improving development of lasers providing increasing peak pulse powers has provided a wide range of experimental information on TPA dynamics in a broad range of materials ranging from inorganic crystals, organometallics, polymers, organic and biological materials.[1] However, due to the relatively small TPA cross sections of most materials, and particularly of complex organic materials, multiphoton processes are far from reaching their full application potential. This premature condition may be due to the lack of understanding and consistence existing among the various multidiciplinary fields to adequately explain details of the energy states and structures of compounds upon undergoing two-photon absorption. Hence, a driving motivation currently exists in carefully probing the effects of molecular structure variation on two-photon processes, with the expectation that knowledge of structural requirements to elicit tailored nonlinearity can be acquired.

Molecules exposed to high intensity light can undergo simultaneous absorption of two photons through "virtual" intermediate states. This process is generally termed "two-photon absorption" (TPA), and an immediate distinction must be made from the process involving two *sequential* absorptions of single photons. Two-photon absorption involves the *concerted* interaction of both photons (mediated by a so called virtual state) that combine their energies to produce an electronic excitation that is conventionally caused by a single photon with a correspondingly shorter wavelength (Figure 1).

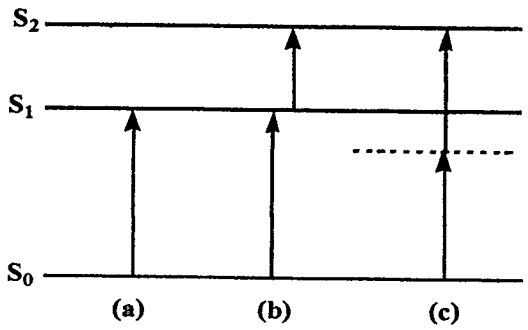

Figure 1. Simplified diagram displaying the singlet energy levels involved in (a) single-photon absorption, (b) sequential absorption of two photons, and (c) simultaneous two-photon absorption.

Some significant differences of TPA from conventional single photon absorption must be noted. As TPA occurs through the concerted act of two photons, it would necessarily dictate both photons to essentially pass simultaneously through the region of space occupied by a molecule. Hence, unlike single photon absorption, the TPA process depends on both a spatial and temporal overlap of the incident photons. A key distinguishing feature arises then, from considering the rate of photon absorption for each process. In the single photon process, the rate of photon absorption is directly proportional to and linearly dependent on the incident intensity ($dw/dt \propto I$), and is independent of the rate of photons passing through the molecule. Contrary to this, as two photons are required in the TPA process, the rate of absorption takes on a quadratic dependency on the incident intensity ($dw/dt \propto I^2$).[1, 3]

Selection rules dictate that excitation transitions allowed for one-photon absorption are not allowed for two-photon absorption, and that the nature of the excitation leaves the molecule in the second excited state, S_2.[4] Much of the theoretical aspects discerning symmetry operations and parity restrictions pertaining to the TPA process have been explored in great detail, notably within the work by McClain[5,6], Mortensen and Svendsen[7], and Birge[8]. Consequently, the greatest manifestation and application of these results were in multiphoton spectroscopy, where the TPA spectrum was uniquely different than that of the single photon spectrum. Hence, spectroscopic developments have led to the probing of transitions that were forbidden under one-photon excitations. Yet, the density of vibrational states for complex molecules in solution often allows significant overlap between the allowed one-photon and two-photon transitions, and some similarities between the linear and nonlinear spectra can exist.[8] Even with this overlap, differences between the linear and nonlinear spectra are often observed.

An interesting feature in TPA is that two photons of wavelength λ_0 striking the molecule simultaneously and absorbed by it, can be regarded similarly as one photon of wavelength $\lambda_0/2$, as for instance, two photons of red light exciting a UV-absorbing chromophore. Hence, two near-IR photons from an intense light undergoing simultaneous absorption mediated by a virtual transition can raise the molecule to an excited state at, or near, energy equivalence to that of the two photons. From this the

molecule decays like any excited state, either nonradiatively to the ground state, or to a fluorescing state and then to the ground state (Figure 2).[5]

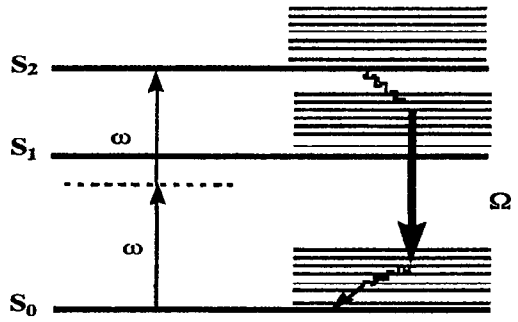

Figure 2. Simplified energy diagram of upconverted fluorescence via two-photon absorption. Excitation of a molecule from the ground state (S_0) to the second excited state (S_2) with nonradiative decay to the first excited state (S_1), is followed by the spontaneous emission back down to the ground state at an energy Ω greater than that of the individual wavelength ω.

Consequently, two near-IR photons can achieve essentially similar electronically excited singlet state as would be obtained through resonant single-photon absorption at or near the λ_{max} of a particular molecule. The molecule then would be expected to exhibit the same photochemical and photophysical behavior as when excited by the one-photon process.

Applications

Particular molecules can undergo upconverted fluorescence through nonresonant two-photon absorption using near-IR radiation, resulting in an energy emission greater than that of the individual photons involved. The use of a longer wavelength excitation source for fluorescence emission affords advantages not feasible using conventional UV or visible fluorescence techniques.[9] The quadratic rate dependency of light absorption in the TPA process has enormous implications for a wide range of applications. The advantage of this quadratic dependency on the illumination intensity means absorption is localized to the immediate vicinity of the focal point of a light beam of appropriate energy, with the two-photon absorption outside the focal region falling off with the fourth power of the distance along the beam path. This allows spatial resolution about the beam axis as well as radially, and depth discrimination at deeper sample penetrations.

These properties have greatly enhanced two-photon laser scanning fluorescence microscopy as a valuable imaging tool in both biophotonics and in the material sciences. Use of near-IR radiation as the excitation source to induce fluorescence in biological samples containing fluorophores has the capability of imaging dynamic processes in living cells.[10] The TPA process greatly reduces photobleaching of the

fluorophore and photodamage of cells, as would occur using conventional UV, or short wavelength excitation sources. This makes it possible to image and study intracellular processes and structures in living cells.

Two-photon laser scanning microscopy could be a employed as a nondestructive diagnostic and evaluation tool to probe surfaces, interfaces, and fractures in polymers, glass, or composite systems. Recently, fractures in poly(methyl methacrylate) (PMMA) doped with organic fluorophores were reportedly imaged by this method.[11] TPA fluorescent imaging provided a three dimensional image of the fractures, demonstrating the possibility of the method as a valuable tool in failure analysis of materials. Similarly, two-photon multichannel fluorescence microscopy was used to probe and construct images of multilayered polymeric coatings (Figure 3)[11].

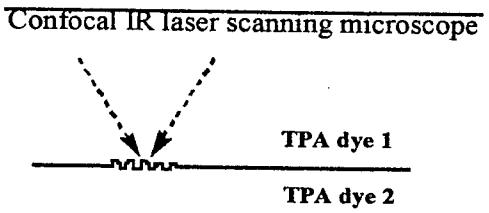

Figure 3. Interfacial imaging of coatings using two-photon absorbing coatings and multichannel confocal laser scanning microscopy.

A bilayer of two PMMA coatings was prepared, each containing a fluorphore that exhibited emission at different wavelengths (green and yellow). The interface of the two layers was imaged with the a multichannel two-photon laser scanning fluorescence microscopy system, again demonstrating the possibility of two-photon microscopy methods as a nondestructive tool for the imaging of interfacial subsurface features.

Two-photon absorption for optical power limiting has also been suggested for potential application in the protection of sensors and human eyes from intense laser radiations.[1] Figure 4 depicts the response of an ideal optical power limiter[14], where it should have linear transmittance at lower light intensities and becomes opaque at some threshold level (higher light intensity) where the transmittance remains at a constant value. Most available materials suffer from speed, concentration, and solubility problems. Organic compounds with large TPA cross-sections may be used, to take advantage of their inherent nonlinear optical properties applied to optical limiters. Many other applications of two-photon absorption have been suggested, ranging from their use as three-dimensional optical data storage devices, optical switching devices for optical computing and telecommunications applications, as dyes in laser technology, optical storage devices and microfabrication, photochemistry, and photodynamic cancer therapy, to name a few.[12, 13, 14] This is by no means an exhaustive list and only demonstrates the importance of TPA in emerging technologies.

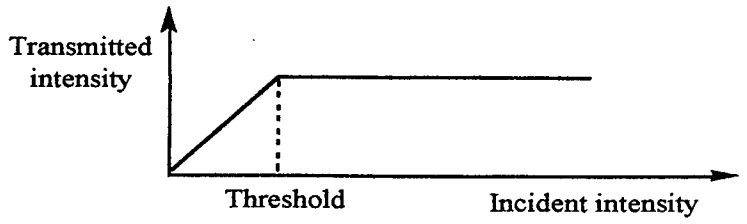

Figure 4. Optical response of an ideal optical power limiter.

Fluorene-based two-photon absorbing chromophores

Molecules with large two-photon absorption cross sections (δ) are in great demand because of their wide range of application as, for example, those listed previously. It became apparent that in order to fully realize the potential developments of these applications, major improvements need to be made in the design and preparation of more active dyes. Unfortunately, most known dyes have relatively small δ values, and the criteria for the design of molecules with large cross sections have not been well established, impeding the full realization of TPA applications.

A driving necessity arose then, to establish an empirical body of two-photon absorption cross sections as a function of molecular structure. This may be attained by collecting nonlinear absorption spectra of judiciously selected compounds, and correlating them to their respective linear UV-visible absorption spectra. From this, observation of trends in the spectral shifts of TPA bands and strengths as they depend on structural changes could be established, leading to the development of scaling relationships, similar to those already existing for the conventional linear absorption process. The ultimate goal is to develop a predictive capability for the nonlinear optical properties of a variety of organic compounds, in terms of the linear optical or structural properties of the material.

The effort to establish well-defined structure/TPA property relationships for large complex organic dyes has been ongoing among a limited number of research groups. Perry et al.[15] have investigated two-photon absorption properties of organic compounds based on bis-donor/acceptor containing stilbenes, as for example, those shown in Figure 5. A series of derivatives with donor-π-donor (D-π-D), donor-acceptor-donor (D-A-D), and acceptor-donor-acceptor (A-D-A) structural motifs were prepared and their two-photon absorption cross sections measured.

High two-photon absorption cross sections were reported on those with extended conjugation lengths on the order of 500 to 1100 x 10^{-50} cm^4 s $photon^{-1}$ $molecule^{-1}$, relative to bis-1,4-(2-methylstyryl)benzene for which δ is 55 x 10^{-50} cm^4 s $photon^{-1}$ $molecule^{-1}$ using both nanosecond and femtosecond pulses at 605 nm excitation wavelength.[15] Quantum chemical calculations performed on the compounds studied provided δ values in relatively good agreement with experimental values, and indicated

that substantial symmetric charge redistribution occurs upon excitation which correlates with a substantial increase in the S_1 to S_2 transition dipole moments.

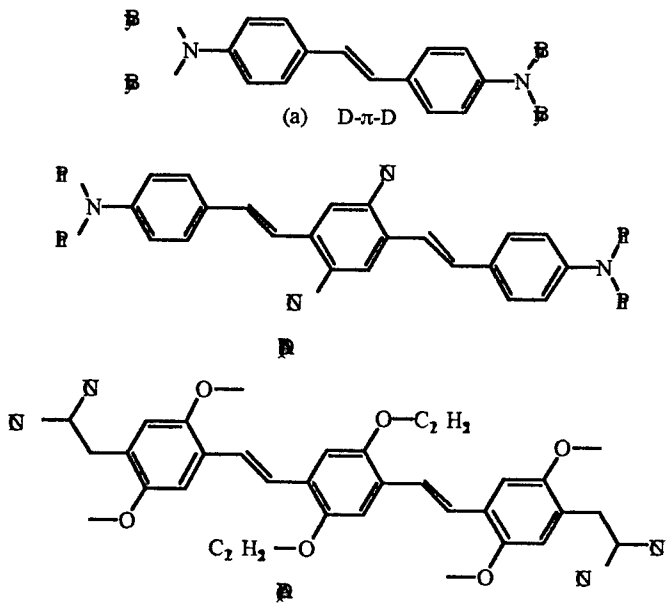

Figure 5. Examples of the bis-donor/acceptor containing stilbene compounds prepared and studied.

Reinhardt et al. have prepared and characterized a number of asymmetric fluorene-based dyes that exhibit TPA at 800 nm.[16] Two types of chromophores were prepared (Figure 6), where Type I (a) was symmetrical in nature consisting of a π-electron rich thiophene aromatic bridge flanked by two electron withdrawing heterocyclic benzothiazole group, and Type II (b) was of the asymmetrical type consisting of a π-electron rich aromatic/olefinic bridge flanked by a thiophene or diarylamine electron donor and by a pyridine heterocyclic electron withdrawing groups. It was determined that the chomophores of the Type II provided higher two-photon absorption cross sections and that systems with strong electron-donating functionality conjugated effectively with strong electron-withdrawing functionality enhanced the TPA molecular cross section.

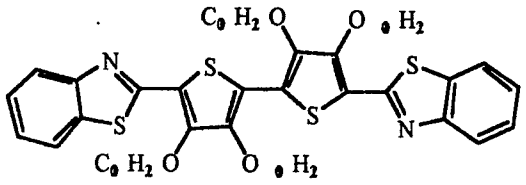

(a) A-π-A

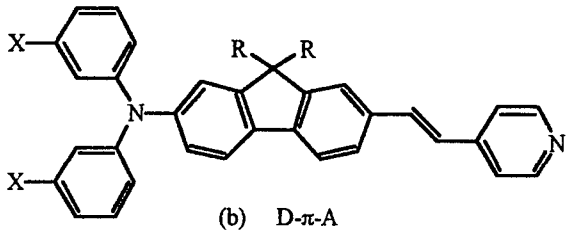

(b) D-π-A

Figure 6. Type I chromophore (a) of a symmetrical π electron rich bridge consisting of two electron withdrawing group, and Type II chromophore (b) of an asymmetrical π electron bridge consisting of an electron donor and withdrawing groups, and where R = pendant alkyl chains.

Research objectives

As a result of a collaboration with Reinhardt, the design and synthesis of the Type II compounds were continued, with the intent to prepare versatile intermediates which possessed the fluorene π-electron bridge, from which efficient and relatively easy derivations could be achieved. The fluorenyl ring system offers some advantages, in that it is a thermally and photochemically stable π-conjugated structural system, that will not undergo isomerization (such as cis/trans isomerization). Moreover, the 2, 7, and 9 positions of the ring system can be readily functionalized, facilitating the systematic preparation of derivatives with varying electronic character (Figure 7).

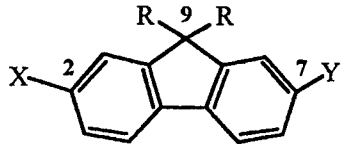

Figure 7. Basic π-conjugated fluorenyl ring system. Modification at the 2, 7, and 9 positions can be such that X = electron donors, Y = electron withdrawers, or X = Y of either donors or withdrawers, and R = n-alkyl groups.

Additionally, the R alkyl groups will be decyl substituents to impart solubility in common solvents, prevent aggregation, and inhibit crystallization of the chromophores, and in suitably derivatized compounds, lead to the formation of amorphous glasses. Preparation of key intermediates should be

efficient and afford a synthetic methodology readily adaptable for rapid functionalization via established procedures. Hence, by simply altering the fluorenyl structure, derivatives with a range of absorption and emission characteristics can be obtained.

Both the linear UV-visible absorption as well as the nonlinear two-photon absorption spectrum of target dyes will be obtained for spectral comparison studies. The resonant, linear spectra will be collected using a conventional UV-visible spectrophotometer. Nondegenerate, nonresonant TPA spectra will be obtained using a recently developed Titanium: sapphire based "NLO spectrometer", the detailed description of which has been reported elsewhere.[17] Two-photon absorption will be performed using an excitation beam far beyond the expected linear absorption range of all compounds proposed. TPA cross sections will be determined (a fundamental measure of the efficiency of the TPA process), as a function of wavelength and structural variation. Photoluminescence spectra will also be obtained, as the fluorene derivatives are expected to undergo upconverted fluorescence upon near-IR two-photon absorption. As such, this class of compounds could be useful as two-photon fluorophores, providing new materials for imaging and other processes requiring fluorescence emission. However, the ultimate long-term goal will be to deduce basic structure/TPA property relationships and establish predicative criteria for the nonlinear optical properties of organic compounds, in terms of the linear optical or structural properties of the material.

Results and discussion of fluorenyl derivatives

The synthesis and characterization of a series of new fluorene derivatives will be discussed. The preparation of key intermediates was efficient from readily available fluorene. The fluorenyl ring system was chosen to suffice as a thermally and photochemically stable π-conjugated system, that can be readily functionalized on the 2, 7, and/or 9-positions. Such versatility in this methodology facilitates the systematic preparation of derivatives of varying electronic character. Hence, various electron withdrawing and/or donating groups incorporated at the 2 and/or 7-position of the π-conjugated central fluorene ring system were designed to probe the effect of the electronic character of the compounds on nonlinear absorption. In addition, long alkyl groups at the 9-position were incorporated to impart solubility and inhibit aggregation and crystallization. Full spectroscopic and, in most cases, CHN, analysis were performed. In suitably derivatized compounds, thermal behavior was recorded for further characterization. This is followed by the presentation of preliminary results and discussion on nonlinear absorption exhibited by select fluorenyl compounds.

2-Nitrofluorene (**1**) (Scheme 1) was prepared in 80% yield by regiospecific nitration of fluorene with nitric acid in AcOH at 85 °C. The melting point (160-163 °C) was comparable with the literature value (157 °C)[18], while CHN analysis were in agreement with calculated values. Regiospecific iodonation of 2-nitrofluorene followed with iodine, sodium nitrite, AcOH, and H_2SO_4 at 115 °C, afforded 7-iodo-2-nitrofluorene (**2**) in 77% yield after recrystallization from AcOH. Again, the melting point (245-246 °C) was consistent with the literature value (244-245 °C)[19] and CHN analysis were in good agreement with

calculated values. Dialkylation of **2** was accomplished by generation of the fluorenyl anion with KOH in DMSO and subsequent alkylation with 1-bromodecane in the presence of KI at room temperature.[16]

7-Iodo-9,9-didecyl-2-nitrofluorene (**3**) was obtained as a yellow solid in 77% isolated yield after column chromatography. MS, CHNI analysis, ^{1}H and ^{13}C NMR confirmed the formation of the desired product, with CHNI analysis in good agreement with the calculated values. Figure 28 shows the ^{1}H NMR of **3** where the didecyl CH_2 protons are clearly observable with the CH_2 protons α to the C9 carbon of the fluorene ring system observed at 2.0 ppm. The internal CH_2 protons are observed as two broad multiplets at 1.18 and 1.05 ppm, with the terminal CH_3 protons and the CH_2 protons α to the CH_3 observed as a triplet and broad multiplet at 0.83 and 0.56 ppm, respectively.

Scheme 1

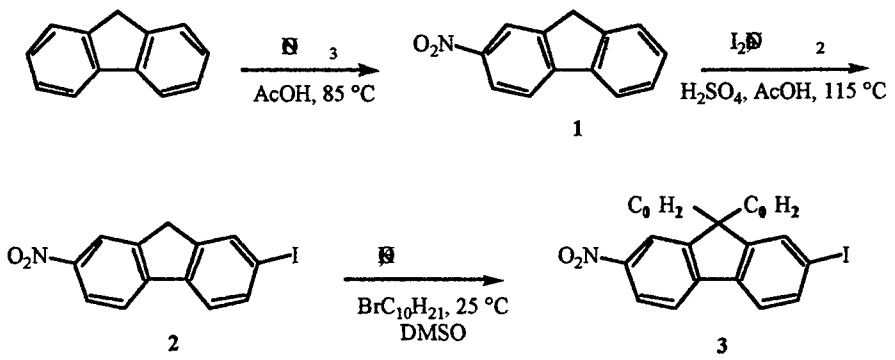

These resonances are characteristic of the presence of the didecyl groups and are observed in all the fluorene derivatives containing the dialkyl group. ^{13}C NMR of **3** (Figure 29) also displays the C9 carbon of the fluorene ring system observable at 55.9 ppm, characteristically observed in all didecylated fluorene derivatives. Also observed is the C2 carbon to which the iodine atom is directly attached at 95.5 ppm.

A Stille coupling procedure was employed to prepare **5**, as illustrated in Scheme 2. (2-Tri-n-butylstannyl)benzothiazole (**4**) was prepared in 90% yield by treating benzothiazole with n-BuLi in THF at -75 °C, followed by addition of tri-n-butyltin chloride.[20] Pd-catalyzed coupling was subsequently performed between **4** and 7-iodo-9,9-didecyl-2-nitrofluorene (**3**) in refluxing toluene with either tetrakis(triphenyl phosphine)palladium (0) or dichlorobis(triphenylphosphine)palladium (II).[21] 2-(9,9-Didecyl-7-nitrofluoren-2-yl)benzothiazole (**5**) was obtained as yellow crystals in 61% isolated yield after column chromatography (mp = 94-95 °C). Clearly evident in the FT-IR spectrum were absorptions attributable to the asymmetric and symmetric NO_2 stretching vibrations at 1519 and 1337 cm^{-1}, respectively. Also present was the benzothiazole C=N stretching vibration at 1589 cm^{-1}. Nitro derivative **5** exhibited a linear UV-visible absorption ranging from 220-420 nm with λ_{max} at 365 nm. The diagnostic ^{13}C NMR (Figure 31) resonance of the carbon in the 2-positon in the benzothiazole ring was present at 168 ppm.[31]

Scheme 2

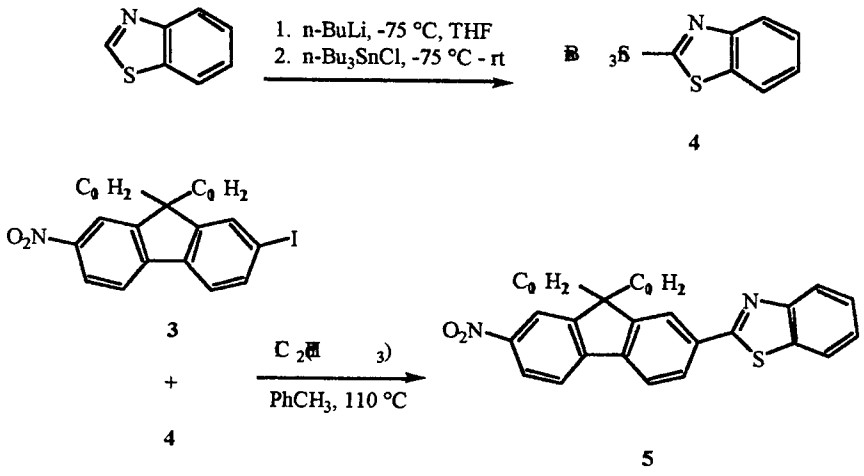

Fast, quantitative reduction of **5** was achieved using hydrazine hydrate and 10% Pd/C in a 1:1 mixture of EtOH and THF at 70 °C (Scheme 3)[22], providing 7-benzothiazole-2-yl-9,9-didecylfluoren-2-ylamine (**6**) as a bright yellow, sticky, viscous oil. The UV-visible spectrum of **6** ranged from 210-450 nm, with the λ_{max} = 380 nm, exhibiting an expected 15 nm bathochromic shift in its spectrum relative to **5**. The amine also display a brilliant blue fluorescence in solution upon irradiation with long wavelength UV radiation. The FT-IR spectrum of **6** characteristic stretching absorptions for NH_2 (3741 and 3383 cm^{-1}) and benzothiazole C=N (1603 cm^{-1}). MS, ^1H and ^{13}C NMR provided additional structural confirmation of the compound.

Scheme 3

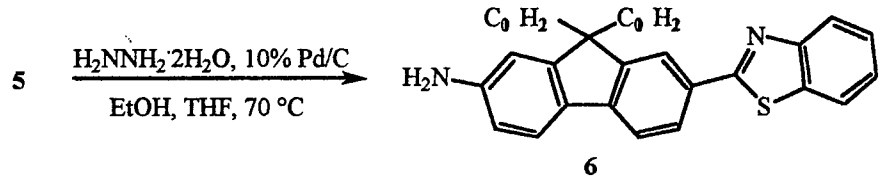

The ^{1}H NMR spectrum of **6** in Figure 32 show aromatic protons *ortho* to the amine on the fluorene ring structure at 6.67 ppm, with the NH_2 protons as a broad singlet at 3.82 ppm. Conclusive proof of the product was secured by the anticipated upfield shift in the ^{13}C NMR spectrum (Figure 33) of carbons *ortho* and *para* to the amine in the fluorene ring of **6**. *Ortho*-carbons 3 and 1 were observed at 109.8 and 114.3 ppm, respectively, compared to the corresponding carbons in **5** at 118.6 and 122.0 ppm, respectively. Even more pronounced was the chemical shift of the *para*-carbon 11 of **6** at 125.0 ppm relative to that of **5** at 147.9 ppm.

Amine **6** was a key intermediate from which facile funcitonalization of the structure was performed on the 2-position of the fluorene ring. A new TPA dye was attained via a copper meditated Ullmann condensation of 7-benzothiazol-2-yl-9,9-didecylfluoren-2-ylamine (**6**) with iodobenzene in *o*-DCB using K_2CO_3 as base and 18-crown-6 at 180 °C (Scheme 4).[23] (7-Benzothiazol-2-yl-9,9-didecyl-fluoren-2-yl)-diphenylamine (**7**) was obtained in 80% yield as a yellow viscous oil after column chromatographic purification. The UV-vis spectrum of **7** in THF ranges from 239-450 nm with a λ_{max} of 392 nm, and also fluoresces to a brilliant yellow-green in solution upon exposure to long range UV radiation. The FT-IR spectrum revealed the complete disappearance of the NH_2 stretching vibrations observed in **6**. Conclusive determination of the structure was secured by CHN analysis which were in accord with calculated values as well as by ^{1}H and ^{13}C NMR. Clearly evident in the ^{1}H NMR spectrum in Figure 34 is the complete disappearance of the NH_2 proton resonance at 3.82 ppm observed in **6**.

Also evident is the dramatic downfield shift of the *ortho* protons on the fluorene ring system to the NH_2 in **6** from 6.67 ppm to 7.16 and 7.07 ppm observed in **7**. ^{13}C NMR spectrum (Figure 35) reveal the downfield shift of *ortho*-carbons 3 and 1 at 118.7 and 120.9 ppm, respectively, compared to the corresponding carbons in **6** at 109.8 and 114.3 ppm, respectively. Also observed was the appearance of the diphenylamine carbons, most notably of the *para*-carbon of the diphenylamine at 122.7 ppm not present in **6**.

The amine **6** was used to prepare another TPA dye with the aim to increase the electron density of the donor was increased relative to that of **7**. Hence, **6** underwent similar Ullmann conditions with 4-iodoanisole to provide (7-benzothiazol-2-yl-9,9-didecyl-fluoren-2-yl)-bis-(4-methoxy-phenyl)amine (**8**) (Scheme 4) as a bright yellow viscous oil obtained in 82% yield after column chromatography.

Scheme 4

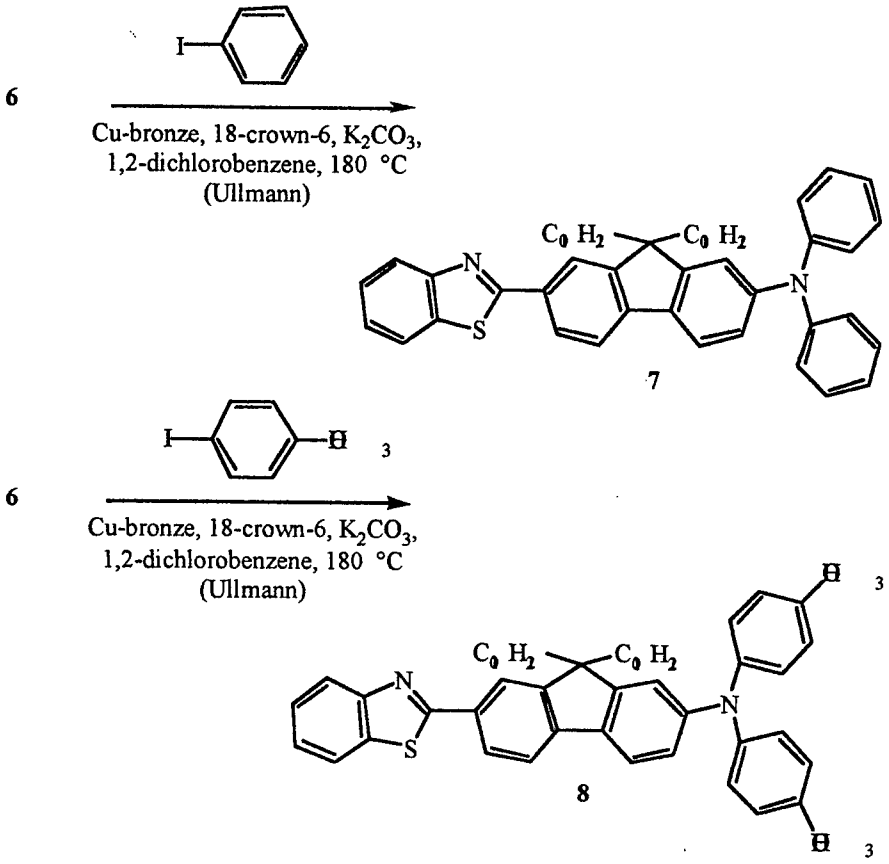

The UV-visible spectrum of **8** (Figure 8) in THF ranges from 239-480 nm with a λ_{max} at 408 nm. CHN Analysis were in good agreement with calculated values and FT-IR revealed the asymmetric and symmetric C-O-C stretches at 1241 and 1038 cm^{-1} respectively. The ^1H NMR spectrum in Figure 36 shows the -OCH_3 protons as a sharp singlet at 3.78 ppm. Likewise, in ^{13}C NMR (Figure 37), the *para*-carbon of the 4-methoxy-phenylamine is at 155.7 ppm while the -OCH_3 carbon is observed at 55.4 ppm.

7-Iodo-9,9-didecyl-2-nitrofluorene (**3**) was also employed as a key intermediate whereby both the 2 and 7 position of the nitro and iodo group respectively allowed for relatively easy derivitization of the fluorene ring system. The same Ullmann condition was applied to **3** with diphenylamine to obtain (9,9-didecyl-7-nitro-fluoren-2-yl)diphenylamine (**9**) (Scheme 5) as an orange oil in ca. 80% yield.

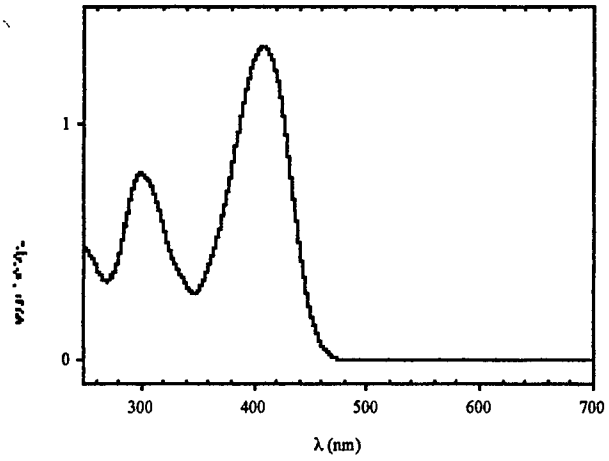

Figure 8. UV-visible spectrum of **9** in THF.

The UV-visible spectrum of **9** ranged from 220-520 nm with a λ_{max} of 300 nm in THF. CHN Analysis were found to be in good agreement with calculated values and FT-IR displayed the presence of the asymmetric and symmetric NO_2 stretches at 1519 and 1334 cm^{-1}, respectively. The ^1H NMR spectrum in Figure 38 of **9** reveals the diphenylamino aromatic protons from 7.32-7.03 ppm. Further certainty of the structure was confirmed by ^{13}C NMR shown in Figure 39, where the most dramatic chemical shift observed is the C2 carbon of the fluorene ring system to which the diphenylamine was substituted for the iodine. The C2 carbon of **9** was observed at 147.5 ppm, whereas the comparable carbon of **3** was at 95.5 ppm. This dramatic shift was expected due to increased deshielding of the amino substituent relative to iodine. The diphenylamino aromatic carbons are observed at 147.6, 129.3, 122.6, and 118.1 ppm for the *ipso, meta, para* and *ortho* carbons, respectively. Also observed are the upfield shifts of the carbons *ortho* to the diphenylamine in the fluorene ring of **9**. *Ortho*-carbons 1 and 3 are at 121.9 and 117.7 ppm, respectively, compared to the corresponding carbons in **3** at 138.3 and 132.5 ppm, respectively. Also notable was the upfield-shifted *para*-carbon 11 on the fluorene ring of **9** at 132.8 ppm relative to that of **3** at 136.5 ppm.

Fast, quantitative reduction of **9** was achieved using hydrazine hydrate and 10% Pd/C in a 3:1 mixture of EtOH and THF at 70 °C (Scheme 5), providing 9,9-didecyl-N,N-dipheynl-fluoren-2,7-diamine (**10**) as a faint yellow viscous oil. Compound **10** displayed a UV-visible spectrum ranging from 210-390 nm with its λ_{max} at 335 nm in THF, a bathochromic shift relative to that of **9**, expected for a change from the electron-withdrawing nitro to the electron-donating amine group. Characteristic NH_2 stretching absorptions were observed at 3462 and 3374 cm^{-1} by FT-IR. Further confirmation of **10** was secured by ^1H and ^{13}C NMR spectra in Figures 40 and 41, respectively. Clearly evident is the chemical shift of the NH_2 protons observed as a broad singlet at 3.72 ppm. Also pronounced are the chemical shifts of the protons *ortho* to the amine on the fluorene ring structure upfield at 6.63 ppm relative to those observed in **9**. The ^{13}C NMR displayed a confirming spectrum, whereby the carbons *ortho* to the amine

underwent an upfield shift relative to those in **9**. *Ortho*-carbons 1 and 3 are observed at 113.9 and 109.8 ppm for **10**, whereas the corresponding carbons for **9** were at 124.6 and 118.7 ppm. The *para*-carbon 11 of **10** displays a pronounced upfield shift to 123.3 ppm, relative to that of **9** at 146.2 ppm.

Scheme 5

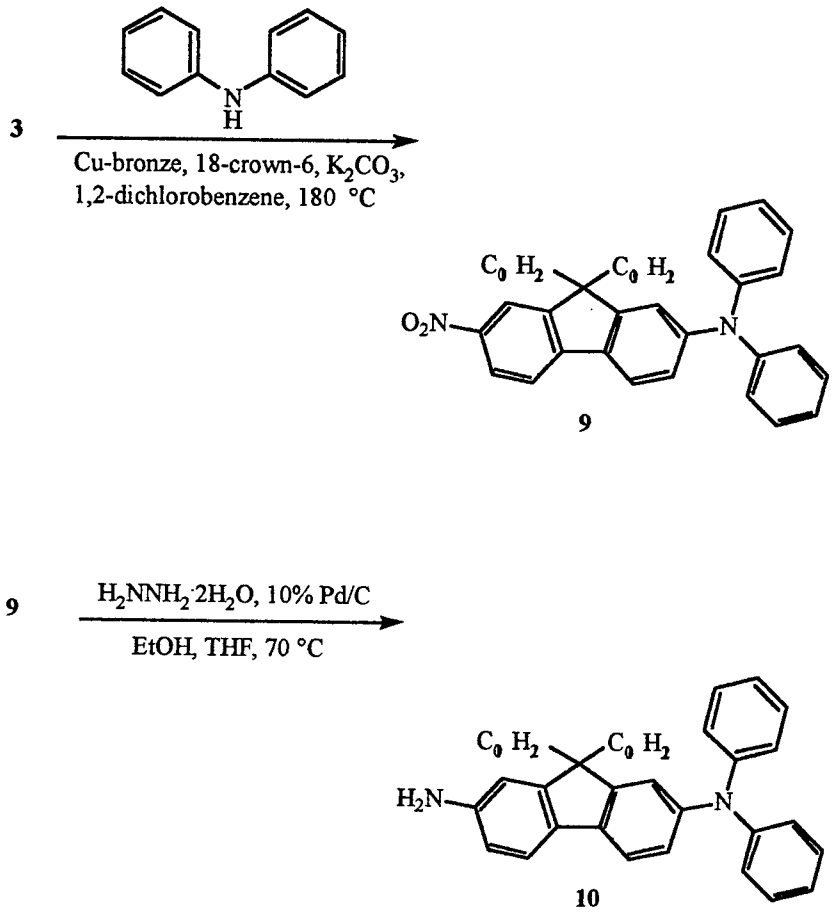

In an effort to synthesize a longer wavelength absorbing dye, 3,4,9,10-perylenetetracarboxylic dianhydride was chosen for $Zn(OAc)_2$-catalyzed condensation imidization with amines **6** and **10**. Condensation of 7-benzothiazole-2-yl-9,9-didecyfloren-2-ylamine (**6**) and perylenetetracarboxylic dianhydride was attempted in the presence of $Zn(OAc)_2{\cdot}2H_2O$ in quinoline (Scheme 6).[24] The resulting 2,9-bis-(7-benzothiazol-9,9-didecyl-fluoren-2-yl)-perylene dye (**11**) was isolated as a deep red solid after column chromatographic purification. The symmetrical perylene-based dye containing two didecyl-fluorene moieties with the benzothiazole electron withdrawing group was fully characterized via conventional methods. CHN analysis results were well within acceptable tolerances from calculated values, and FT-IR revealed the presence of C=O stretching vibrations from the formed imide bonds at 1701 and 1665 cm^{-1}. The benzothiazole C=N stretching vibration at 1593 cm^{-1} was also present. Further structural determination was secured via ^1H and ^{13}C NMR.

Scheme 6

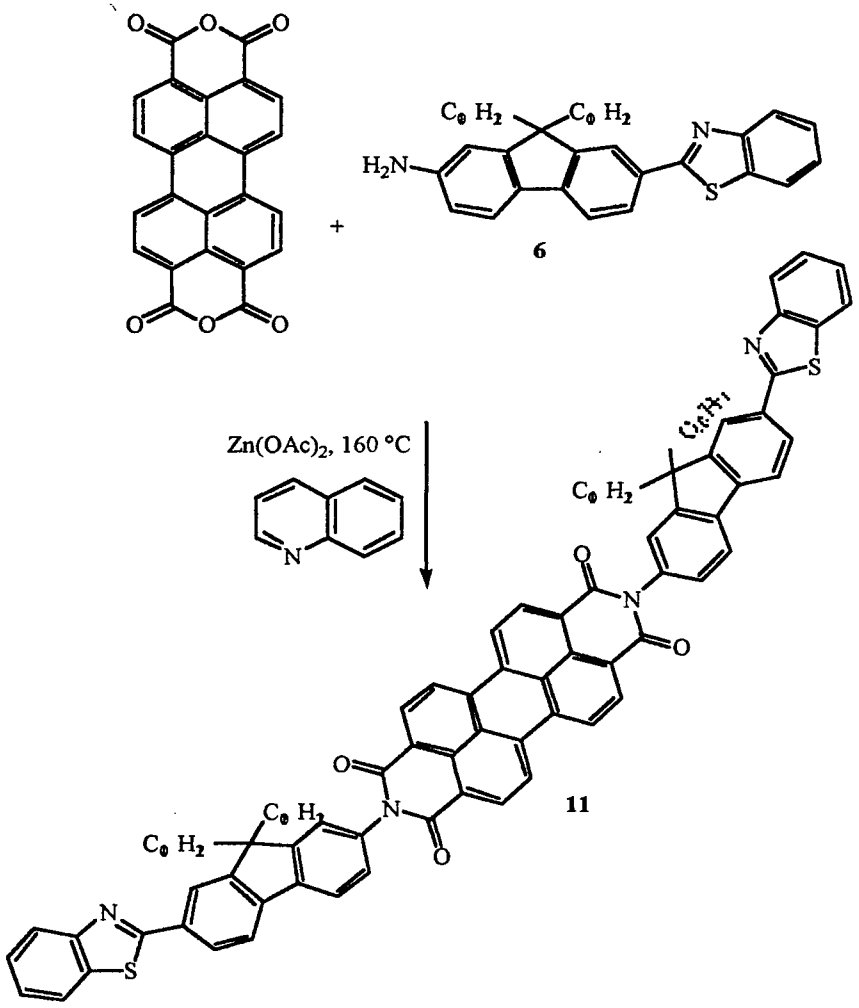

Very obvious in the ^{1}H NMR spectrum in Figure 42 of **11** was the complete disappearance of the NH_2 protons present in **6** at 3.82 ppm. There is also a pronounced downfield chemical shift observed for the fluorene protons on carbons 1 and 2 *ortho* to the imide bond to 7.93 and 7.76 ppm, respectively, compared to the corresponding protons in **6** at 6.67 ppm. Also notable is the appearance of the two doublets attributable to the eight protons on the perylene ring system from 8.80 to 8.30 ppm. The ^{13}C NMR in Figure 43 of **11** proved to be equally informative as the carbonyl carbon of the imide bond was observed at 163.0 ppm. Carbons 8 and 6 *ortho* to the imide in the fluorene ring of **11** are shifted downfield to 121.0 and 120.6 ppm, respectively, compared to the corresponding carbons in **6** observed at 114.3 and 118.6, respectively. The carbon 12, *para* to the imide in the fluorene ring of **11,** was also observed with an upfield shift at 132.4 ppm, compared to the same carbon in **6** observed at 125.0 ppm. Finally, the perylene carbon 18 displayed a chemical shift at 134.1 ppm which was not present in **6**. Interestingly, the dye **11** exhibited two strong, UV-visible absorption bands (Figure 9), one in the UV

from 270-385 nm (λ_{max} = 345 nm) and another in the visible from 410-545 nm with λ_{maxima} at 457, 486, and 522 nm. The first absorption band is likely due to the fluorenyl groups, as it is similar to the absorption range exhibited by the amine **6** from 210-450 nm with a λ_{max} = 380 nm, while the absorption in the visible range is due to the central perylene ring system.

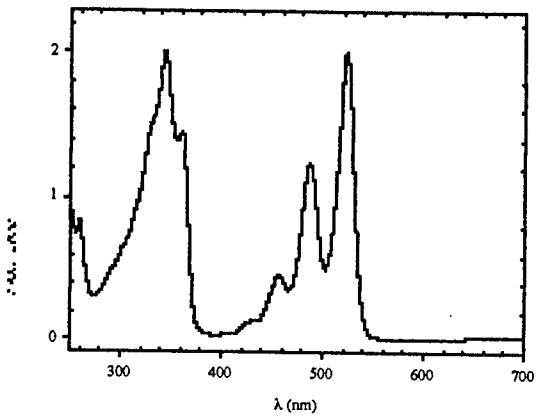

Figure 9. UV-visible spectrum of **11** in THF.

Fluorescence emission spectra of **11** was obtained and is shown in Figure 10, where excitation was performed at λ_{ex} = 325 nm, resulting in an unexpectedly remarkable emission λ_{maxima} at 540, 585, and 625 nm. Another excitation at λ_{ex} = 500 nm resulted in a similar emission λ_{maxima} profile as that obtained with the λ_{ex} = 325 nm. However, this was expected as the excitation was done within the λ_{max} of the visible absorption range and hence should generate a characteristically similar vibrational structure of the lower excited state at a lower frequency, and therefore, the fluorescence spectrum is expected to closely resemble the mirror image of the absorption spectrum. The resulting emission profile from the first excitation may indicate an efficient internal energy transfer process whereby the expected emission of the fluorescence from the fluorenyl groups is absorbed by the perylene ring system in the visible range, which then undergoes excitation followed by its own fluorescence emission.

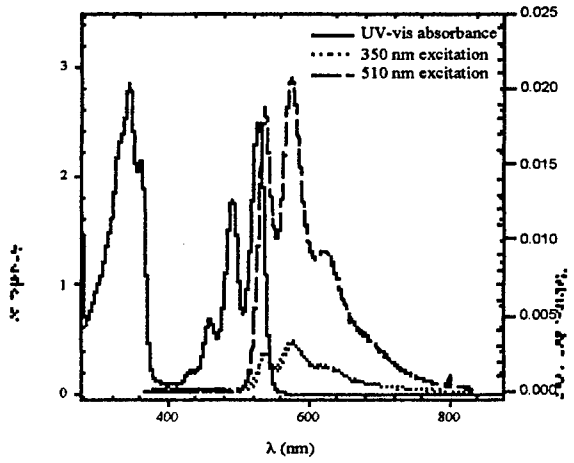

Figure 10. Overlap of UV-visible spectrum and fluorescence emission spectra of **11** excited at 350 nm and 510 nm.

This then generates a similar fluorescence spectrum as that obtained from the λ_{ex} = 500 nm, although the relative intensity of the fluorescence from this energy transfer process is much weaker than that of the corresponding fluorescence obtained from the excitation performed at the visible maxima. This is not be surprising since the energy transfer process is not 100 % efficient.

Thermal studies were performed on **11** in order to ascertain its thermal behavior, as the obtained information would be of importance in its possible application. TGA analysis was performed under N_2 atmosphere at a heating rate of 20 °C/min from room temperature to 650 °C, the result of which is shown in Figure 44. Compound **11** exhibited high thermal stability up to 382 °C, upon which the greatest weight % loss of 57 % was observed up to 650 °C, with a remaining residue of 39 % upon completion.

Repeated DSC scans of controlled heating and cooling were also performed on **11** under N_2 atmosphere at constant rate of 10 °C/min. The DSC trace in Figure 45 revealed a slight endothermic transition that was detected and identified as a glass transition, T_g, at 111 °C. No melting transition was detected, even as the temperature was brought up to 380 °C, before its decomposition temperature. Controlled cooling was accomplished by manually adding liquid N_2, which explains the higher baseline noise at the onset of cooling. An obvious exotherm was detected from 111 °C to 90 °C which likely correlates with the T_g endotherm. The DSC trace indicated that **11** behaved much like a glassy material would, where no clear melting or crystallization transitions are detected.

Another longer wavelength absorbing dye was prepared under the same $Zn(OAc)_2$ catalyzed conditions with the primary amine **10** and 3,4,9,10-perylenetetracarboxylic dianhydride. The condensation imidization resulted in the symmetrical 2,9-bis(9,9-didecyl-7-diphenylamino-fluoren-2-yl)-perylene dye (**12**) (Scheme 7), where the electronic character of the dye was dramatically changed by the presence of the electron-donating

Scheme 7

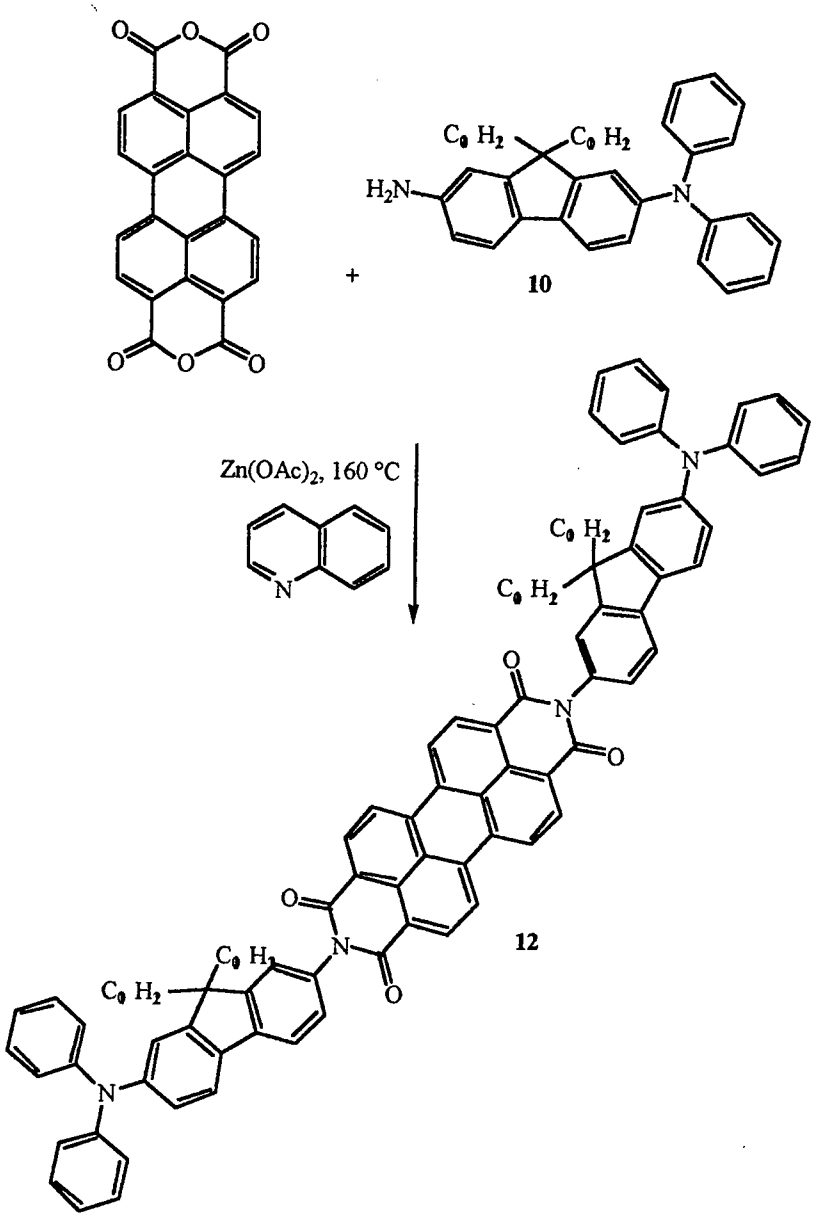

diphenylamines, compared to that of **11** containing the electron-withdrawing benzothiazoles. The desired product was isolated via column chromatography as a deep red solid and was fully characterized. Interestingly, small circular crystalline regions had developed randomly throughout the bulk sample over time. Two apparently different looking crystals had evolved, where one type appeared as metallic-greenish crystals, and the other as orange crystals. However, CHN analysis of the bulk sample were in good agreement with calculated values and FT-IR displayed the characteristic C=O stretching vibrations at 1703 and 1665 cm^{-1}.

The UV-visible spectrum of **12** in THF is shown in Figure 11, and displayed two strong absorption bands, similar to that of **11**. A broad band in the UV ranging from 275 to 395 nm (λ_{max} = 355 nm) and a broad band in the visible from 425 to 586 nm (λ_{maxima} = 455, 488, and 523 nm) were exhibited. Interestingly, the three λ_{maxima} in the visible range of **12** are comparatively similar to the corresponding bands observed in **11** (λ_{maxima} = 457, 486, and 522 nm) without much notable shifts in wavelengths.

Conclusive determination of the structure was secured by ^{1}H and ^{13}C NMR. The ^{1}H NMR spectrum of **12** in Figure 46 clearly showed the complete disappearance of the NH_2 protons observed in **10** at 3.53 ppm. As consistent with the perylene protons in **11**, the corresponding protons of **12** displayed characteristically similar doublets from 8.72 to 8.55 ppm.

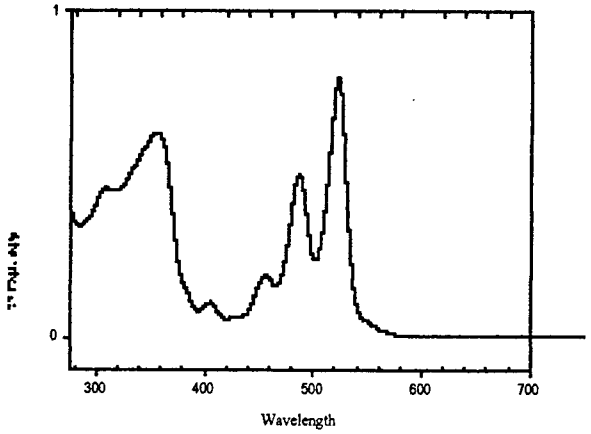

Figure 11. UV-visible spectrum of **12** in THF.

The ^{13}C NMR spectrum in Figure 47 of **12** proved to be equally confirming. The expected downfield shifts of the *ortho*-carbons 8 and 6 to the imide on the fluorene ring of **12** were observed at 120.8 and 119.2 ppm, respectively, compared to the corresponding carbons of **10** at 113.9 and 109.8 ppm, respectively. Also evident was the chemical shift of the carbonyl carbon of the imide group at 163.1 ppm, not present in **10**.

Thermal studies were also performed on **12** using the same conditions as those applied to **11**. TGA analysis of the bulk sample was executed under N_2 atmosphere at a heating rate of 20 °C/min from room temperature to 650 °C, the thermogram of which is shown in Figure 48. Similarly to **11**, compound **12** exhibited high thermal stability up to 377 °C upon which the greatest weight % loss of 66 % was observed up to 650 °C, with a remaining residue of 27 % upon completion. The TGA thermogram also displayed a 4 weight % loss from 80 to 140 °C, which most likely is due to the presence of residual solvents and/or water.

Repeated DSC scans of controlled heating and cooling were also performed on **12** under N_2 atmosphere at a constant rate of 10 °C/min. However, curiosities arising from the appearance of the circular crystals induced isolated thermal studies of the crystalline and noncrystalline samples. The "green" and "orange" crystals were crudely separated, with DSC scans performed on both as well as on the noncrystalline sample, and their corresponding

curves are shown in Figure 49, 50, and 51, respectively. In general, all three samples exhibited similar thermal behavior, whereby the same transitions were consistently observed in all three samples, with slight shifts in the temperature range of occurrence.

Surprisingly, the overall calorimetric thermal behavior of **12** was dramatically different than that observed for **11**. Two endothermic transitions were observed in all three samples upon heating, the first occurring from 128 to 148 °C, 154 to 166 °C, and 151 to 163 °C in the noncrystalline, orange, and green crystals, respectively. The second transition was identified to be the melting transition, T_m, occurring as a large, sharp endotherm near 298 °C in all three samples. Observation of a T_m event in **12** was interesting, as no such transition occurred in the corresponding structurally similar dye **11**. Most intriguing and interesting was the first endothermic transition, as it is uncharacteristic of a T_g, and resembles, rather, that of a small melting transition. A possible explanation may reside in investigating whether **12** exhibits liquid crystalline behavior, although this is currently purely speculative. However, liquid crystals have been known to exhibit similar transitions while going through various microcrystalline phase changes, prior to undergoing a complete isotropic melt.[31, 32]

Upon cooling, two exothermic transitions were observed in all three samples, correlating to the two endothermic transitions noted during heating. A large, sharp exotherm occurring near 243 °C was identified as a crystallization transition, again, not discernible in dye **11**. The more interesting second exotherm occurred from 114 to 92 °C, 136 to 120 °C, and 85 to 62 °C in the noncrystalline, orange, and green samples respectively. Again, it may be possible for **12** to undergo further microcrystalline organization that may be indicative of a liquid crystal. However, the unexpected thermal behavior of **12** warrants further, careful, and detailed investigation into the phase structure of the compound near these temperature ranges. If the exothermic event occurring at the lower temperature is indicative of mesophase transitions, than careful examination of the samples under an optical polarising microscope may provide information on the phase structure at the temperature range of interest per sample.

As stated previously, key intermediates were prepared to easily modify the electronic character of target derivatives. While the synthesis of the aforementioned fluorenyl compounds has been successfully isolated and characterized, not all attempts of acquiring target derivatives were as successful. For instance, further derivitation of 7-benzothiazole-2-yl-9,9-didecylfluoren-2-ylamine (**6**) was attempted by *p*-TsOH-catalyzed condensation with 4-(*N*,*N*-diphenylamino)benzaldehyde (**13**) (previously prepared by Vilsmeier formylation of triphenylamine) (Scheme 8).[25]

Scheme 8

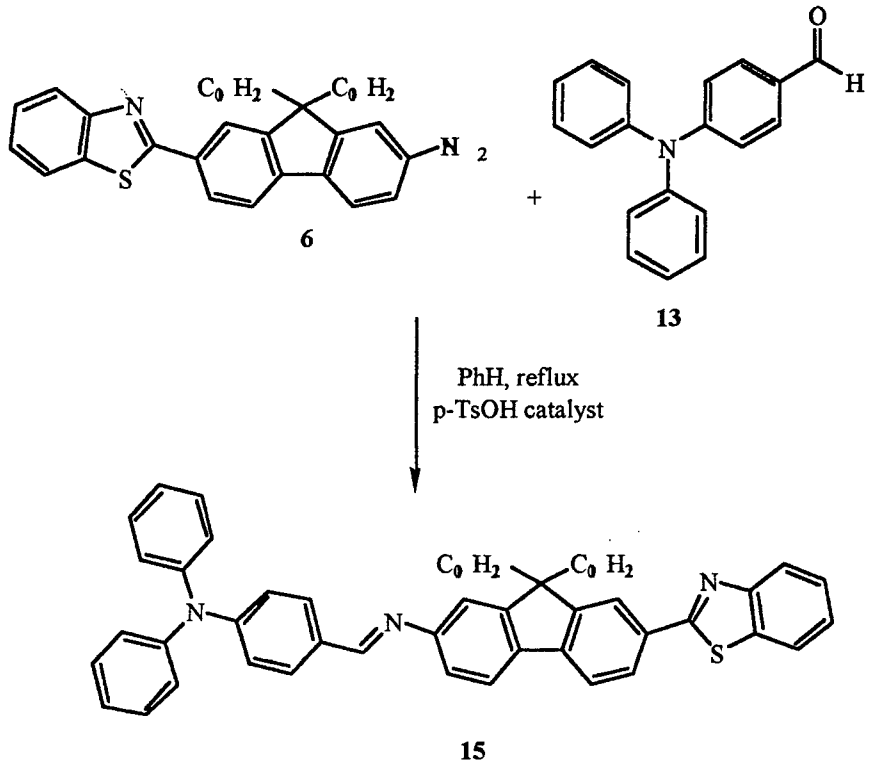

An orange yellow solid was obtained, presumably of 4-(*N*,*N*-diphenylamino) benzaldehyde/7-benzothiazol-2-yl-9,9-didecylfluoren-2-ylamine azomethine dye (**15**). To maximize the reaction yield, a repeat of the same reaction was performed in reflux toluene. The reaction was monitored via TLC (alumina), and was found to be incomplete even after 52 h, as indicated by the persistent presence of the starting amine **6**. The crude was passed through a basic alumina column, resulting in an unsuccessful isolation of the desired product. Interestingly, pale yellow crystals had grown in the recollected fractions, and after recrystallization, were identified to be the starting monoaldehyde **13** by ^{1}H NMR spectrum. The aromatic aldehyde CHO proton from the isolated crystals were clearly evident, with its resonance observed at 9.8 ppm. The ^{1}H NMR spectrum of the starting **13** was obtained for comparison and was found to match that of the crystal spectrum .

Another attempt to isolate the desired product **15** was unsuccessful, even after inclusion of pyridine to the eluent through a basic alumina column. The ^{1}H NMR of the semi-crude oil from recombined fractions revealed the presence of the aldehyde CHO proton at 8.82 ppm along with the imine HC=N proton observed as a singlet at 8.48 ppm. The FT-IR of the same oil was complex, possibly detecting the aldehyde CH and C=O stretching vibrations at 2725 cm^{-1} and 1693 cm^{-1} respectively. Unsuccessful isolation efforts due to the hydrolytically unstable imine bond resulted in termination of the attempted synthesis of **15**.

A similar pyridinium toluene sulfonate-catalyzed condensation of **6** with triphenylamine biscarboxaldehyde (**14**) prepared previously by Vilsmeier bisformylation of triphenylamine (Scheme 9).[26] It was hoped the desired triphenylamine biscarboxaldehyde/7-benzothiazole-2-yl-9,9-didecylfluoren-2-ylamine azomethine dye (**16**) could be

isolated to study the effects of two symmetrically placed fluorenyl groups on the linear and nonlinear absorption processes. However, due to the difficulties arising from the isolation of **15**, further attempts to prepare additional Schiff base dyes were discontinued.

Scheme 9

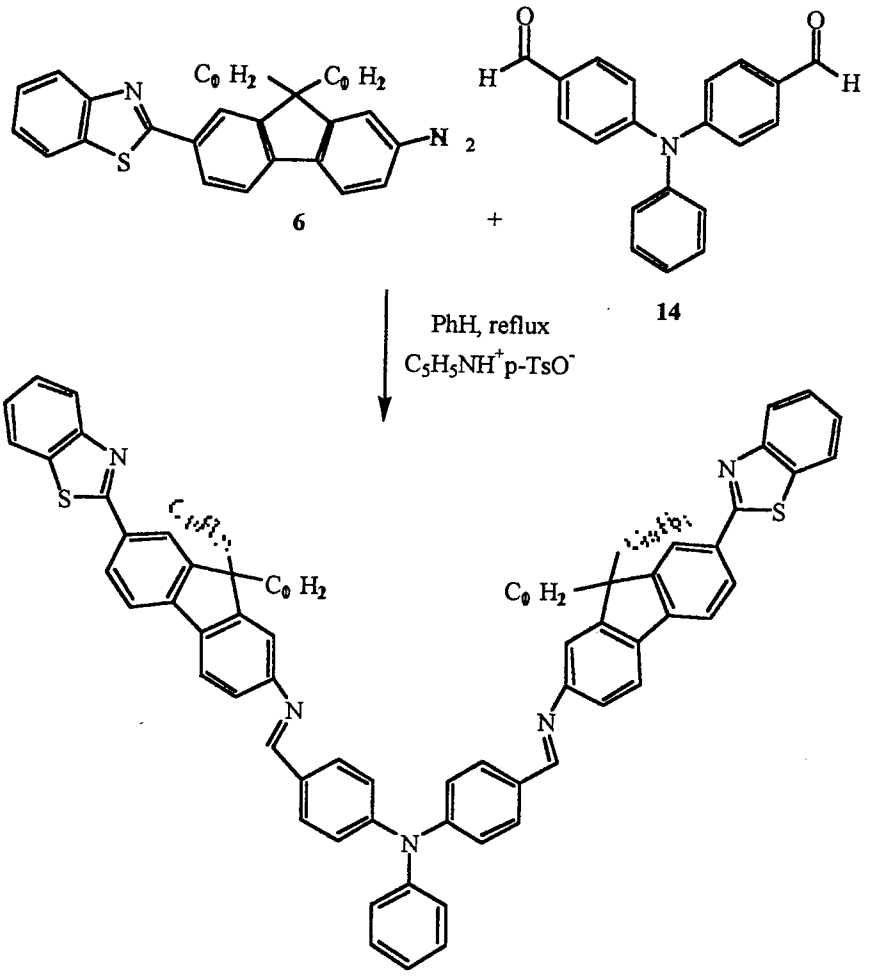

6 + **14**

16

Additional derivatives with a slight variation on the electronic character from the presented dyes were prepared. Structures containing long conjugation lengths may lead to large two-photon absorptivities.[1] Hence, three stilbene derivatives bearing electron-withdrawing groups (phosphonate and nitro) of varying strengths were prepared and recently published.[33] Heck coupling chemistry was employed to prepare model stilbene and fluorenyl-stilbene based derivatives with extended conjugation lengths which may lead to large TPA cross sections. The preparation of the model stilbene, 4-diethyl-4'-*N*,*N*-dimethylaminostilbenephosphonate (**19**) was previously reported (Scheme 10).[28]

Briefly, Pd-catalyzed Heck cross coupling of 4-bromo-*N,N*-dimethylaniline and 4-vinylbenzenephosphonic acid diethyl ester (**17**) (prepared in three steps involving $NiCl_2$-mediated Arbuzov-type reaction, $NaBH_4$ reduction, followed by elimination over $KHSO_4$)[26] yielded the bright fluorescent yellow compound which was fully characterized via ^1H NMR and high resolution MS (EI). The UV-visible spectrum of **19** in THF revealed a λ_{max} of 365 nm over the absorption range of 280 - 455 nm.

Scheme 10

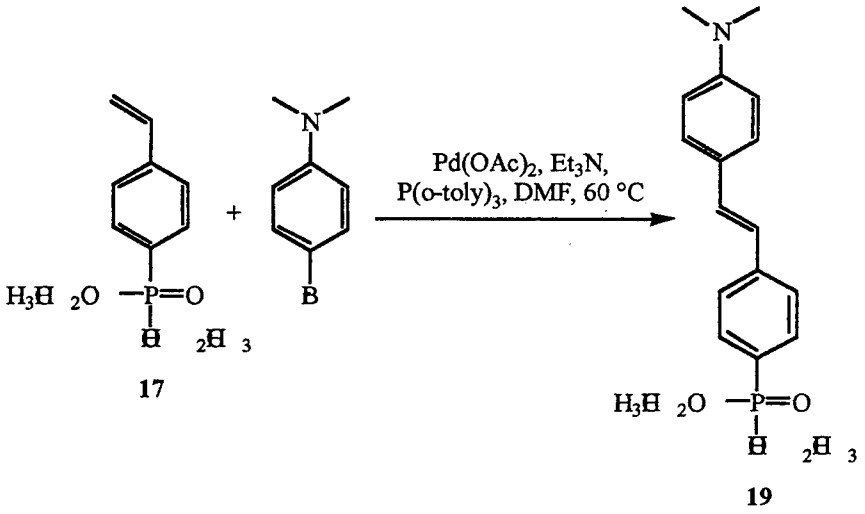

In similar fashion, two fluorenyl-stilbene derivatives bearing different electron-withdrawing groups (phosphonate and nitro) were prepared utilizing the Pd-catalyzed Heck coupling conditions used for the model compound **19** (Scheme 11).[33] Briefly, 2-bromo-7-*N,N*-diphenylamino-9,9-diethylfluorene (**20**) (prepared in three steps from fluorene via dibromination, diethylation, and Ullmann-type coupling with dipheynlamine as previously reported[16]) was subjected to Heck coupling conditions with either 4-vinylbenzene phosphonic acid diethyl ester (**17**) or 4-nitrostyrene prepared from 4-nitroacetophenone by established procedures.[29]

The phosphorylated fluorene derivative **21** was isolated as a bright yellow solid and fully characterized. The UV-visible absorption of **21** in CH_3CN extended out to 480 nm, with λ_{maxima} at 308 and 383 nm. Likewise, the nitro-containing fluorene derivative **22** was obtained as a bright orange-red solid and fully characterized. The UV-visible absorption of **22** in CH_3CN extended out to 550 nm, and also had two λ_{maxima} at 309 and 414 nm. Nonlinear two-photon absorption studies were performed on both compounds, the results of which will be discussed with those of select fluorenyl compounds in the next section, in which similar TPA studies were also performed.

Scheme 11

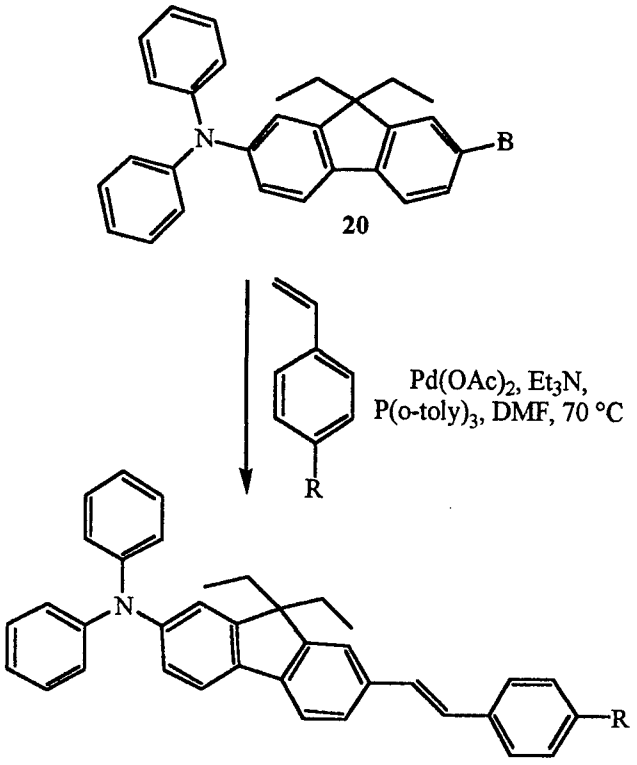

R = $P(O)(OCH_2CH_3)_2$ (**21**), NO_2 (**22**)

Results and discussion of TPA absorption and TPA cross sections (δ) of select fluorenyl derivatives

Linear and nonlinear absorption (nondegenerate 2PA) spectra of select fluorenyl derivatives will be discussed. Details of the nonlinear absorption measurements and the "NLO spectrometer" have been described elsewhere.[17] These measurements were performed in collaboration with professors Eric Van Stryland and David Hagan of CREOL and Raluca Negres (physics graduate student). Briefly, femtosecond pump probe experiments were performed in which a strong excitation pump beam wavelength was selected to be at low enough energy (longer wavelength) to prevent degenerate 2PA. The probe beam consisted of a femtosecond white light continuum (WLC) generated by irradiation of a sapphire window able to produce an output in the range of the near IR radiation. In short, the pump (excitation) beam along with the WLC probe beam is exposed together to the sample of interest, with the WLC split to provide a reference beam to monitor the nonlinearity induced by the pump beam. Hence, the output of the two probe and reference pulses can be recorded, providing both the linear and nonlinear absorption transmission spectra respectively, of the chromaphore under study.

Depending upon the linear behavior of the compound, a particular wavelength is selected to be the excitation beam. The excitation wavelength used to study the nonlinearity of select fluorenyl derivatives was 1210 nm, with the WLC used as the probe beam. Since the pump and probe are of different frequencies, the nonlinear absorption spectrum is also nondegenerate. By examination of the linear UV-visible spectra of the fluorenyl derivatives, degenerate absorption is not expected to occur at the pump wavelength. The resulting nonlinear spectra provides TPA cross section (δ) values which are of practical importance, as benchmark values for applications such as dyes for two-photon fluorescence microscopy. More importantly, the spectra may aid in the understanding of the relationship between molecular structure and optical nonlinearity.

Select derivatives were chosen to study the nonlinear absorption behavior and obtain TPA cross sections as a function of electron density variation on the fluorenyl ring system. These can be regarded as polarizable compounds of different electronic character provided by the systematic variation of electron donating (donor) or withdrawing (acceptor) functional groups attached to the fluorene ring. Hence, linear and nonlinear spectra of end-chain donor and acceptor group substituted (D-π-D, A-π-D, A-π-A) compounds can be examined to assess the relative effect of electronic strength of these groups on nonlinear absorption. All fluorene dyes were dissolved in THF and their TPA spectra obtained using the "NLO spectrometer".

The linear UV-visible spectra of compounds 7 and 9 are shown in Figure 12, comparing the relative effects of electron withdrawing groups on absorption. The nonlinear spectra was subsequently obtained, from which the largest TPA cross section value measured was over 1600 x 10^{-50} cm^4 s $photo^{-1}$ $molecule^{-1}$ at the spectral maximum for compound 7 in Figure 13.

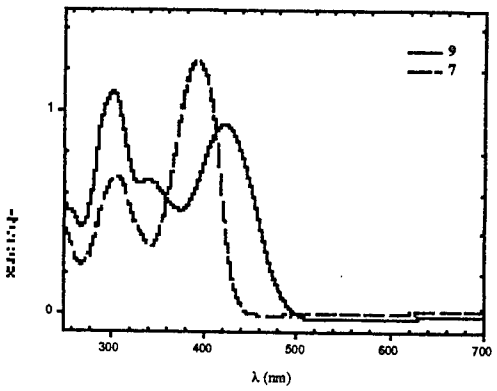

Figure 12. Linear UV-visible spectra for compounds 7 and 9.

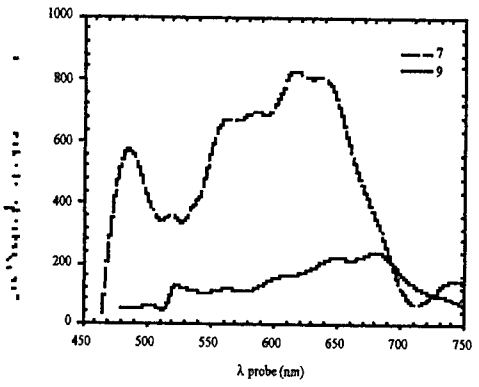

Figure 13. Nondegenerate TPA spectra for compounds 7 and 9 using a 1210 nm pump beam.

This δ value is comparable in magnitude to large TPA cross sections that were recently reported by Albota et al. for another class of conjugated organic compounds (on the order of 500 to 1100 x 10^{-50} cm^4 s $photon^{-1}$ $molecule^{-1}$).[15] In examining the nonlinear spectra of compounds 7 and 9 in Figure 13, a D-π-A system wherein the effect of the relative strength of the acceptor on δ value was obtained, a strong

enhancement of the cross section was observed in **7** containing the weaker electron-withdrawing benzothiazole group.

Conversely, the nonlinear spectral comparison of derivatives **6** and **7** of the D-π-A configuration type in Figure 15 also displays enhanced TPA cross section in compound **7** containing the stronger donor group. A contrasting comparison of a D-π-A and an A-π-A system is shown in Figure 17 for compounds **6** and **5**, respectively, with the maximum TPA cross section of ca. 600 x 10^{-50} cm^4 s $photon^{-1}$ $molecule^{-1}$ and ca. 400 x 10^{-50} cm^4 s $photon^{-1}$ $molecule^{-1}$, respectively. The slightly higher δ of **6** seems to reinforce the observed trend of higher electron density containing compounds exhibiting larger 2PA cross sections.

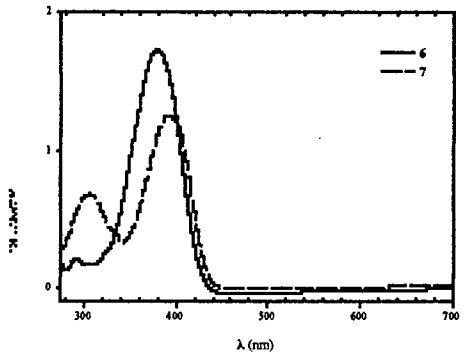

Figure 14. Linear UV-visible spectra of compounds **6** and **7**.

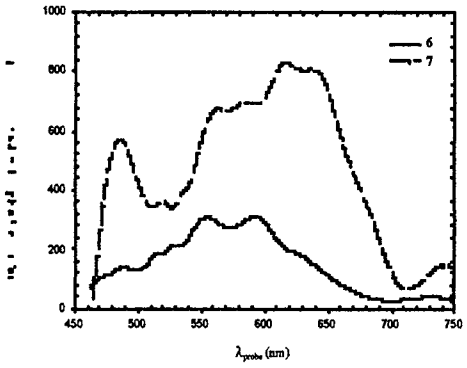

Figure 15. Nondegenerate TPA spectra for compounds **6** and **7** using a 1210 nm pump beam.

enhancement of the cross section was observed in 7 containing the weaker electron-withdrawing benzothiazole group.

Conversely, the nonlinear spectral comparison of derivatives **6** and **7** of the D-π-A configuration type in Figure 15 also displays enhanced TPA cross section in compound **7** containing the stronger donor group. A contrasting comparison of a D-π-A and an A-π-A system is shown in Figure 17 for compounds **6** and **5**, respectively, with the maximum TPA cross section of ca. 600 x 10^{-50} cm^4 s $photon^{-1}$ $molecule^{-1}$ and ca. 400 x 10^{-50} cm^4 s $photon^{-1}$ $molecule^{-1}$, respectively. The slightly higher δ of **6** seems to reinforce the observed trend of higher electron density containing compounds exhibiting larger 2PA cross sections.

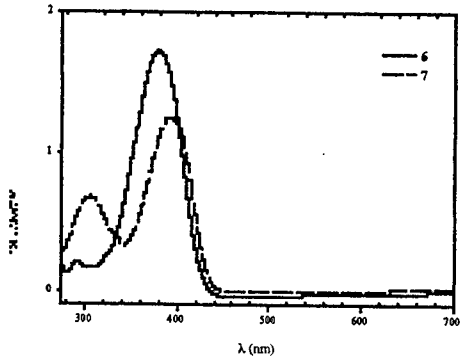

Figure 14. Linear UV-visible spectra of compounds **6** and **7**.

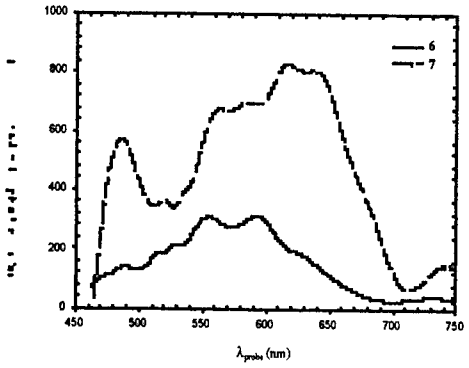

Figure 15. Nondegenerate TPA spectra for compounds **6** and **7** using a 1210 nm pump beam.

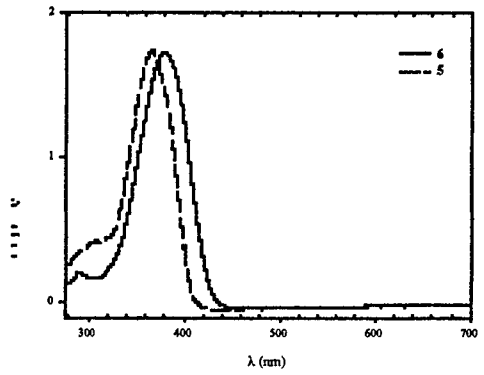

Figure 16. Linear UV-visible spectrum for compounds **5** and **6**.

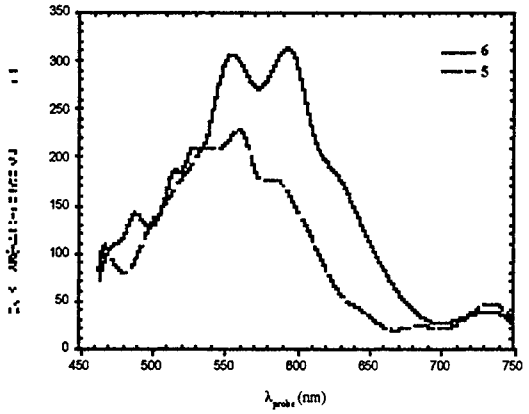

Figure 17. Nondegenerate TPA spectra for compounds **5** and **6** using a 1210 nm pump beam.

A direct comparison of one-photon (linear) and two-photon (nonlinear) absorption spectra may be examined by regarding the total energy of the photons absorbed in the process. Figures 18 - 21 display the linear and nonlinear spectra of derivatives **5**, **6**, **7**, and **9**, respectively, plotted as absorption (arbitrary units) vs. total photon energy in eV (the nonlinear wavelengths of the pump and probe beams were converted to photon energy and summed for the TPA spectra). Red-shifting of the nonlinear spectrum with respect to the linear spectrum was observed along with additional features in all of the compounds, indicating the two-photon states are somewhat different from the one-photon states. However, a relatively good overlap between the nonlinear and linear spectrum seem to be apparent.

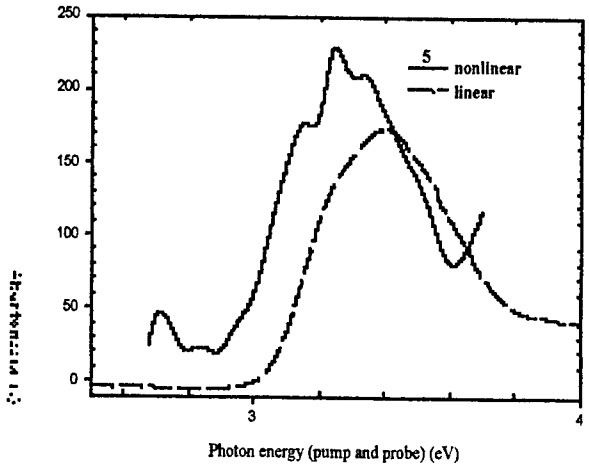

Figure 18. Comparison between linear and nonlinear absorption spectra of compound **5**.

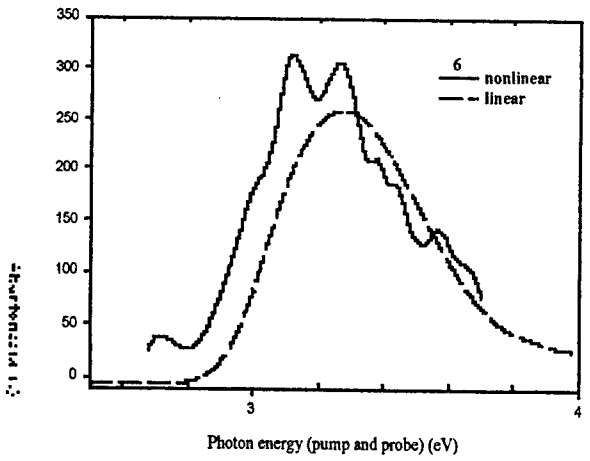

Figure 19. Comparison between linear and nonlinear absorption spectra of compound **6**.

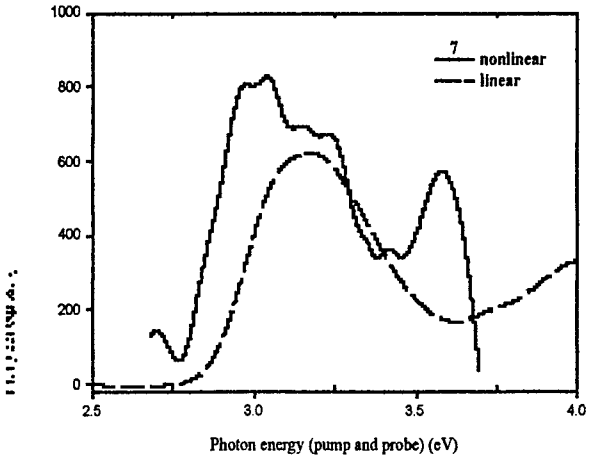

Figure 20. Comparison between linear and nonlinear absorption spectra of compound **7**.

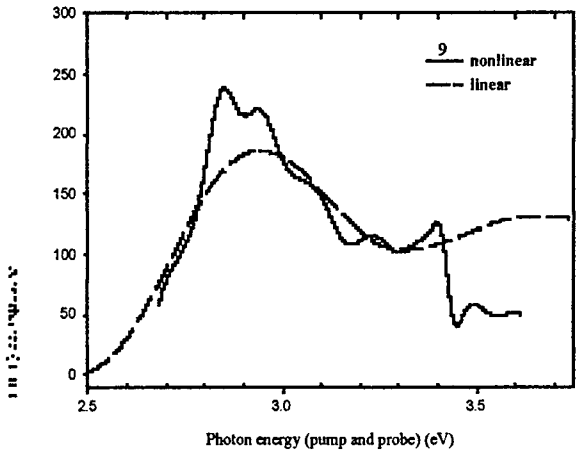

Figure 21. Comparison between linear and nonlinear spectra of compound **9**.

This may be due to large conjugated systems undergoing mixing of their parity such that the spectra of one and two-photon allowed states overlap. Further overlap of the one and two-photon spectra arise from the near degeneracy of one and two photon allowed states and the vibronic structure of the molecules.[4] However, more investigations on the energy level structure of these compounds are needed, and is currently underway, to gain key insights required to correlate the nonlinear spectra to molecular structures.

Complementary to the studies of the effect of electron strengths of donors and acceptors, the relative effects of the nitro and phosphonate ester was examined. Figure 22 shows the linear absorption spectra of fluorenyl compounds **21** and **22**, while the nondegenerate nonlinear absorption spectra of both are shown in Figure 23.

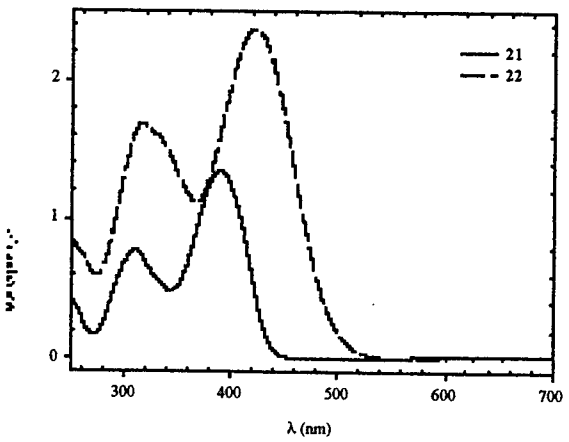

Figure 22. Linear UV-visible spectra of compounds **21** and **22**.

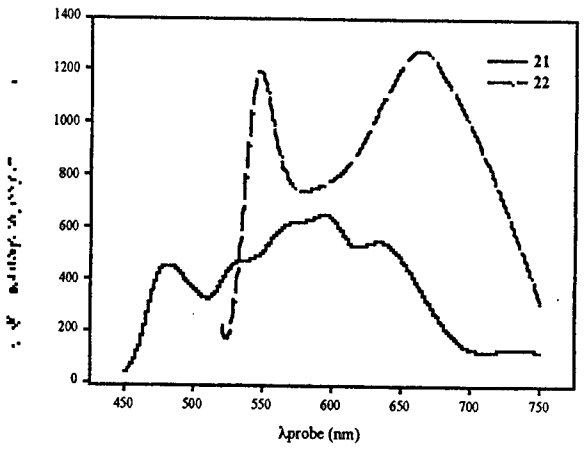

Figure 23. Nondegenerate TPA spectra for compounds **21** and **22** using a 1210 nm pump beam.

The maximum TPA cross section, δ, from Figure 23 of **21** was ca. 650 x 10^{-50} cm^4 s $photon^{-1}$ $molecule^{-1}$ at the WLC wavelength of 605 nm, while that of **22** was much higher at ca. 1300 x 10^{-50} cm^4 s

photon^{-1} molecule^{-1} at the WLC wavelength of 670 nm. The TPA cross section of **22** was also comparable to the large TPA cross sections reported by Albota et al.[15]

The effect of π-conjugation length on the nonlinear absorption was also examined, and an even more interesting comparison of the linear and nonlinear absorption is shown in Figure 24 and Figure 25 of compounds **9** and **22**, respectively. Here, a direct comparison can be made of a D-π-A system, where an extension in the π-conjugation length on the effect of the TPA cross section can be observed.

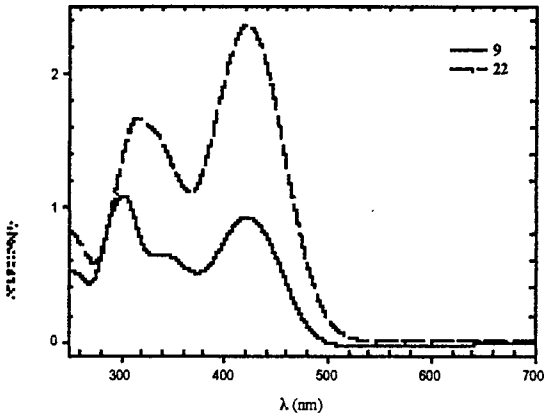

Figure 24. Linear UV-visible spectra for compounds **9** and **22**.

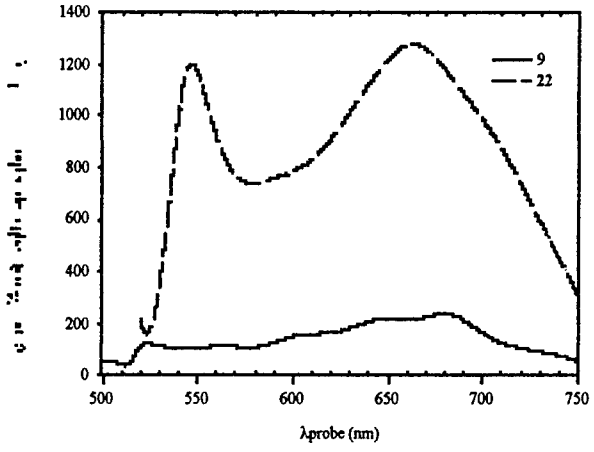

Figure 25. Nondegenerate TPA spectra for compounds **9** and **22** using a 1210 nm pump beam.

The difference in the n-alkyl groups present (diethyl or didecyl) on the 9 position of the two fluorenyl derivatives **9** and **22** can be disregarded, as the contribution to absorption due to the presence of alkyl groups can be considered nominal compared to the contributions arising from the conjugated ring

system. Inspection of Figure 25 shows a dramatic increase in the δ value observed in **22** containing the extended conjugation length provided by the vinyl stilbene group, compared to that of **9**. This may be expected for compounds having an extended π-conjugated system exhibiting high TPA cross section values.[1]

Figures 26 and 27 display the linear and nonlinear spectra of derivatives **21** and **22**, respectively, plotted as absorption (arbitrary units) vs. total photon energy in eV for a direct comparison of one-photon (linear) and two-photon (nonlinear) absorption spectra.

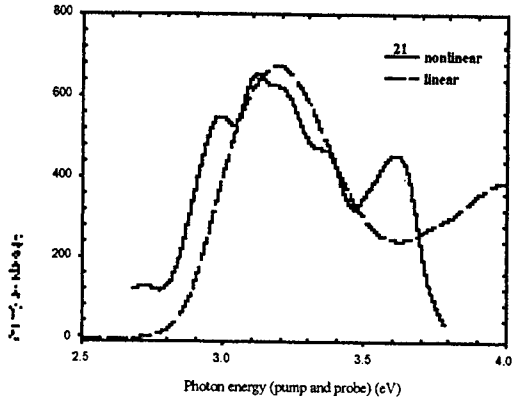

Figure 26. Comparison between linear and nonlinear absorption spectra of compound **21**.

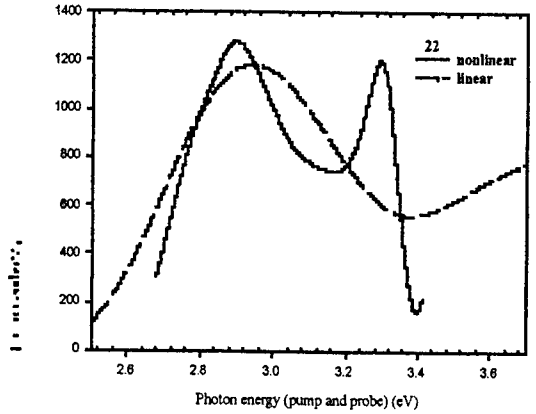

Figure 27. Comparison between linear and nonlinear absorption spectra of compound **22**.

Relatively good correlation between the linear and nonlinear spectra was observed with additional fine absorption features present in the nonlinear spectra. Similar preponderant speculation proposed to explain the linear and nonlinear spectra of compounds **5**, **6**, **7**, and **9** may also be applied for compounds **21** and **22**.

Some general trends do seem to be appearing upon an overview of the presented spectra. There seems to be evidence that the TPA may be enhanced by the presence of strong electron donating groups on the π-conjugated fluorene ring system, while electron withdrawing groups seem to have an opposing effect on TPA, though some anomalies exist. Hence, molecules of high electron density are expected to exhibit high TPA cross sections. A logical next step then, is to study and compare the linear and nonlinear spectra of D-π-D type compounds, an aspect currently being pursued. In addition to the enhancing effect of electron donors on TPA, another enhancement was observed with a compound containing an extended conjugation length when compared to a compound of similar structure lacking the conjugation extension. This was most dramatically presented in Figure 26 with compounds 9 and 22. Likewise, with similar intention to study D-π-D systems, the next step is to synthesize derivatives of already presented compounds that contain extended π-conjugation lengths. This effort is also currently in progress.

References

1. Kershaw, S. In *Characterization Techniques and Tabulations for Organic Nonlinear Optical Materials*; Kuzyk, M. G.; Dirk, C. W. Eds.; Marcel Dekker: New York, 1998, Chapter 7.

2. Goeppert-Mayer, M. *Ann. Physik* **1931**, *9*, 273.

3. Bhawalkar, J. D.; He, G. S.; Prasad, P. N. *Rep. Prog. Phys.* **1996**, *59*, 1041

4. Birge, R. R. In *Ultrasensitive Laser Spectroscopy*; Kliger, D. S., Ed.; Academic Press: New York, 1983, Chapter 2.

5. McClain, W. M.; Harris, R. A. *Excited States*, **1977**, 2.

6. McClain, W. M.; Friedrich, D. M. *Ann. Rev. Phys. Chem.* **1980**, *31*, 559.

7. Mortensen, O. S.; Svendsen, E. N. *J. Chem. Phys.* **1981**, *74*, 3185.

8. Piston, D. W. In *Fluorescence Imaging Spectroscopy and Microscopy*; Wang, X. F.; Herman, B. Eds.; John Wiley: New York, 1996, pp 253-257.

9. White, J. G.; Centonze, V. E.; Wokosin, D. L. In *Microscopy and Microanalysis*; Bailey, G.; Corbett, J. M.; Dimlich, R. V. M.; Michael, J. R.; Zaluzec, N. J. Eds.; San Francisco Press: Minneapolis, 1996, pp. 280-281.

10. Herman, B.; Wang, X. F.; Wodnicki, P.; Perisamy, A.; Mahajan, N.; Berry, G.; Gordon, G. In *Applied Fluorescence in Chemistry, Biology, and Medicine*; Rettig, W.; Strehmel, B.; Schrader, S.; Seifert, H. Eds.; Springer: New York, 19999, pp 496-500.

11. Bhawalkar, J. D.; Shih, A.; Pan, S. J.; Liou, W. S,; Swiatkeiwicz, J.; Reinhardt, B. A.; Prasad, P. N.; Cheng, P. C. *Bioimaging* **1996**, *4*, 168.

12. Strickler, J. H.; Webb, W. W. *Opt. Lett.* **1991**, *16*, 1780.

13. Maruo, S.; Nakamura, O.; Kawata, S. *Opt. Lett.* **1997**, *22*, 132.

14. Wang, X.; Krebs, L. J.; Al-Nuri, M.; Pudavar, H. E.; Ghosal, S.; Liebow, C.; Nagy, A. A.; Schally, A. V.; Prasad, P. N. *Proc. Natl. Acad. Sci. USA* **1999**, *96*, 11081.

15. Albota, M; Beljonne, D.; Bredas, J-L.; Ehrlich, J. E.; Fu, J-y.; Heikal, A. A.; Hess, S. E.; Kogej, T.; Levin, M. D.; Marder, S. R.; McCord-Moughon, D.; Perry, J. W.; Rockel, H.; Rumi, M.; Subramaniam, G.; Webb, W. W.; Wu, X-L.; Xu, C. *Science*, **1998**, *281*, 1653.

16. Reinhardt, B. A.; Brott, L. L.; Clarson, S. J.; Dillard, A. G.; Bhatt, J. C.; Kannan, R.; Yuan, L.; He, G. S.; Prasad, P. N. *Chem. Mater.* **1998**, *10*, 1863.

17. Negres, R. A.; Van Stryland, E. W.; Hagan, D. J.; Belfield, K. D.; Schafer, K. J.; Przhonska, O. V.; Reinhardt, B. A. *Proc. SPIE - Int. Soc. Opt. Eng.* **1999**, 3796.

18. Kuhn, W. E. *Organic Synthesis, Coll. Vol. 2*; Blatt, A. H., Ed.; Wiley: New York, 1943, pp. 447.

19. Markevka, V. C.; Ebner, N. A.; Sehon, R. D.; Hanna, P. E. *J. Med. Chem.* **1985**, 28, 18.

20. Kosugi, M.; Koshiba, M.; Atoh, A.; Sano, H.; Migita, T. *Bull. Chem. Soc. Jpn.* **1986**, 59, 677.

21. Hark, R. R,; Hauze, D. B.; Petrovskaia, O.; Joullie, M. M.; Jaouhari, R.; McComiskey, P. *Tet. Lett.* **1994**, 35, 7719.

22. Yang, C. P.; Lin, J. H. *J. Polym. Sci.: Part A: Polym. Chem.* **1994**, 32, 369.

23. Gauthier, S.; Frechet, J. M. J. *Syntheis* **1987**, 383.

24. Bohm, A.; Arms, H.; Henning, G.; Blaschka, P. WO97/22608, World Patent Application.

25. Belfield, K. D.; Najjar, O. N. unpublished results.

26. Zhuang, H.; Pearce, E. M.; Kwei, T. K. *Macromolecules* **1994**, *27*, 6398.

27. Hartmann, M.; Hiplar, U.-CH.; Carlsohn, H. *Acta Polym.* **1980**, *31*, 165.

28. Belfield, K. D.; Chinna, C.; Schafer, K. J. *Tet. Lett.* **1997**, *38*, 6131.

29. Belfield, K, D.; Chinna, C.; Najjar, O. *Macromolecules* **1997**, *31*, 2918.

30. Yang, C.-P.; Lin, J.-H. *J. Polym. Sci.: Part A: Polym. Chem.* **1994**, *32*, 369.

31. Collings, P. J.; Hird, M. In *Introduction to Liquid Crystals Chemistry and Physics*; Taylor & Francis: London, 1997, pp 191-193.

32. Finkelmann, H. In *Polymer Liquid Crystals*; Ciferri, A.; Krighaum, W. R.; Meyer, R. Eds.; Academic Press: New York, 1982, pp 40-43.

33. Belfield, K. D.; Hagan, D. J.; Van Stryland, E. W.; Schafer, K. J.; Negres, R. A. *Organic Letters* **1999**, *1*, (in press).

EFFECTS OF IMMISCIBLE ORGANIC SOLVENTS ON THE WHOLE-CELL BIOCATALYSIS OF BIPHENYL

Patrick C. Gilcrease

Department of Chemical & Petroleum Engineering
University of Wyoming
P.O. Box 3295
Laramie, WY 82071

Final Report for:
Summer Research Extension Program

Sponsored by:
Air Force Office of Scientific Research
Bolling Air Force Base, DC

February 2000

EFFECTS OF IMMISCIBLE ORGANIC SOLVENTS ON THE WHOLE-CELL BIOCATALYSIS OF BIPHENYL

Gene T. Coryell, II and Patrick C. Gilcrease
Department of Chemical & Petroleum Engineering
University of Wyoming

Abstract

The *meta* isomer of hydroxybiphenyl (*m*-HBP) is an important precursor in the synthesis of temperature resistant epoxy resins. Such resins may have important aerospace applications as high temperature structural materials with upper workable temperatures of 265°C. In contrast to chemical hydroxylation, biocatalysis favors production of the *meta* isomer; *m*-HBP yields as high as 90% have been observed. Because of this high regiospecificity, biocatalysis may offer a cost-effective method for the large-scale production of *m*-HBP by significantly reducing downstream separation/purification requirements.

Biocatalysis experiments were conducted with whole-cell recombinant *Pseudomonas aeruginosa* strains; the toluene monooxygenase enzymes expressed by these strains are also capable of hydroxylating biphenyl. Preliminary work conducted at Tyndall AFB showed that while favorable *m*-HBP yields were obtained, very low specific activities were observed (9.2×10^{-4} μmol/mg protein·min for solid biphenyl vs. 230×10^{-4} μmol/mg protein·min for a 3 mM control solution of toluene). For the biocatalysis of solid biphenyl, the overall rate may be limited by either (1) the low dissolution rate of solid biphenyl, or (2) the low aqueous solubility of biphenyl. Benchtop fermentor experiments performed in the presence of excess biphenyl solids showed that the intrinsic biocatalysis rate, not the solid-liquid mass transfer rate, was limiting the overall rate of *m*-HBP production. A two-liquid phase system was investigated as a means of increasing the effective substrate concentration through partitioning of the bacteria to the organic/aqueous interface. The concentration of biphenyl in the organic phase was ~1000× higher than the bulk aqueous concentration. Higher activities were not observed in shake flask experiments utilizing a two-phase system as compared to an excess solids system. In fermentor studies, the two-phase biocatalysis rate was unaffected by increasing the agitation rate from 300 to 600 rpm. For the low cell/enzyme concentrations investigated in this study, mass transfer was not limiting the overall rate of hydroxylation. However, enhanced biocatalysis rates may be achieved in the two-phase system with larger organic to aqueous phase ratios, though. Additionally, a newly developed *Escherichia coli* host that has been overexpressed for the toluene monooxygenase enzyme may shift the two-phase system into a mass transfer-limited regime.

Background

Biocatalysis can be defined as the use of biological cells or their enzymes in the production of chemicals for commercial uses. Bacteria are the most common organisms in biocatalysis, but yeasts, molds, algae, plant cells and even animal cells are also used. Biocatalysis is not a new concept; it has been used for centuries in the production of cheese, wine, and beer, and more recently to produce antibiotics and other pharmaceuticals. Scientists are now discovering that microorganisms can also transform a wide range of unnatural or man-made compounds; thus, they can be used in the production of specialty organic chemicals. There are several advantages to using biocatalysis for organic syntheses: (1) mild temperatures and pressures are used, making the process energy efficient, (2) specific compounds can be produced, often with very few byproducts being formed, (3) biocatalysis can promote reactions that are difficult or impossible to produce by conventional catalysis, and (4) reactions are normally conducted in aqueous solutions, reducing the need for toxic organic solvents [Roberts, et. al 1995].

An organic synthesis of interest to polymer scientists is the hydroxylation of biphenyl. Hydroxybiphenyl (HBP) forms the backbone of specific phenolic resins used to synthesize epoxy thermosets and aromatic polyesters. These high performance polymers can have exceptional thermal resistance with working temperatures of up to 265°C. The U.S. Air Force Material Science directorate and NASA have recognized the potential aerospace applications for such polymers. The mechanical properties of these important polymers are dependent upon the purity of the phenolic isomer used. Unfortunately, the regiospecific hydroxylation of aromatic compounds by purely chemical methods is notoriously difficult [Faber, 1997]; thus, extensive purification is required to obtain a pure isomer.

An alternative method of producing hydroxylated aromatic compounds is biocatalysis. Oxygenase enzymes from various bacterial strains can hydroxylate a number of aromatic substrates [Gibson, 1988]. Unlike most conventional catalysts, enzymes exhibit a high regiospecificity, favoring the production of one isomer over others. Previous work described the characterization of two multicomponent monooxygenases from *Burkholderia* sp. Strain JS150 that hydroxylate a broad range of aromatic compounds [Johnson and Olsen, 1995; Johnson and Olsen, 1997]. Recent work at the Air Force Research Laboratory (Tyndall AFB) showed recombinant *Pseudomonas aeruginosa* strains carrying genes for individual monooxygenases (Tb2m and Tb4m) also hydroxylate biphenyl [Gilcrease, 1998]. Biocatalysis experiments with biphenyl resulted in a hydroxybiphenyl product consisting of 75 to 90% *meta* isomer, depending on which enzyme

was used. The formation of *m*-HBP is quite fortuitous; *meta* hydroxylation of aromatic rings is uncommon by either chemical or biochemical means [Faber, 1997]. Phenolic resins synthesized using *meta*-substituted phenols provide polymer chains with a narrow molecular weight distribution; this results in an increased glass transition temperature for the final polymers [Zampini et al., 1995]. The Tb2m enzyme can further catalyze HBP to form dihydroxybiphenyl; this compound is also an important polymer intermediate [Abramowicz et al., 1990].

Preliminary Work

While the regiospecificity of the above reactions was quite promising, the overall specific activity was very low (up to 8.1×10^{-4} μmol/mg protein·min for biphenyl at 50 μM vs. 230 × 10-4 μmol/mg protein·min for toluene at 3 mM – see *Table 1*). Bacterial fermentations are normally conducted in the aqueous phase, which requires the substrate be in aqueous solution. Unfortunately, the solubility of biphenyl in water is quite low (~50 μM). The results summarized in *Table 1* indicate that higher specific hydroxylation activities were observed for substrates with higher aqueous solubilities. While not conclusive (the steric effects of different substrates can increase or decrease enzyme affinity), this suggests that agents that increase the aqueous concentration of biphenyl may also increase the specific hydroxylation activity. Of the three alternate substrates in *Table 1*, the molecular structure of HBP is closest to that of biphenyl. Aqueous concentrations of HBP were three to four times that of biphenyl, and the corresponding specific enzyme activity for HBP was two to four times greater than that observed for biphenyl.

Table 1: Specific activities observed with toluene monooxygenase enzymes for various substrates. Listed in order of increasing solubility [Gilcrease, 1998].

Substrate	Aqueous Concentration	Specific activity × 10^4 [μmol/mg protein·min]
DPA	5 μM	0.9 to 2.0
Biphenyl	50 μM	2.1 to 8.1
HBP	160 to 190 μM	16 to 30
Toluene	3 μM	110 to 230

Table 1 activity values for biphenyl and diphenylacetylene (DPA) were obtained in the presence of excess solid substrate; a number of studies have shown that the biocatalysis of solid substrates may be limited by the dissolution rate (solid-aqueous mass transfer rate) [Stucki and Alexander, 1987; Bachmann et al., 1988; Kohler et al., 1994; Gilcrease, 1997]. In particular, Abramowicz et al. (1990) used a fine suspension of 4-

bromobiphenyl particles (~5 μm diameter) to synthesize 4-bromo-4'-hydroxybiphenyl using *Aspergillus parasiticus* cultures. As the cell mass was decreased from 10 to 0.6 g/L, the specific activity increased from 7×10^{-4} to 62×10^{-4} mol/g cells·day, respectively. This increase in specific activity suggests the hydroxylation may have been mass transfer limited at the higher cell mass concentration. For comparison, the specific biphenyl activity was estimated at 5×10^{-4} mol/g cells·day for our *P. aeruginosa* cultures (approximately 0.7 g cell mass/L and 1000 μm biphenyl particle diameter). Since this value for specific activity was comparable to the lower *A. parasiticus* value, we speculated that higher activities might be possible with improved agitation/mass transfer.

The addition of organic solvents which are immiscible in water (defined as a biphasic system) may be one method of increasing biocatalysis rates for sparingly soluble substrates under proper conditions [Faber, 1997]. Two separate phenomena may contribute to higher activities in a biphasic system: cell partitioning and high liquid/liquid mass transfer rates. In cell partitioning, the interfacial tension between the two immiscible phases may cause the cells to adhere to the interface. This partitioning is due to a spontaneous surface energy minimization of the system, but may also be due to extracellular adhesins excreted by the cell [Rosenberg and Rosenberg, 1981; Rosenberg, 1991]. The interfacial substrate concentration, which is determined by the thermodynamic partition coefficient, may be much higher than the aqueous substrate concentration. Cells that partition to the interface are exposed to this higher substrate concentration, and a higher biocatalysis rate may be seen. Water miscible solvents can also be used to increase the ***aqueous*** concentration of substrate, but they tend to be much more toxic to whole cells than water immiscible solvents. Additionally, enzyme activity tends to be higher for immiscible organic co-solvents when compared to more polar co-solvents [Nikolova and Ward, 1993].

Vigorous agitation of a biphasic system disperses the organic phase into tiny droplets, maximizing the surface area for substrate mass transfer from the organic to the aqueous phase. This effect was illustrated in biodegradation experiments where a phenanthrene substrate was dissolved in heptamethylnonane; biodegradation rates were directly related to the interfacial surface area, which increased with agitation speed [Kohler et al., 1994]. Mass transfer rates are generally higher in liquid/liquid biphasic systems compared to solid/liquid systems. If solid-liquid mass transfer is controlling the hydroxylation rate, then the higher mass transfer rates associated with a liquid-liquid system may increase the overall hydroxylation rate.

The first objective of this study was to measure intrinsic kinetics for the enzymatic hydroxylation of biphenyl in aqueous solution. As a first approach to modeling the kinetics, a simple Michaelis-Menten enzyme kinetic expression was used, although the exact kinetic expression could have some substrate or product inhibition terms. Once the biocatalysis rate as a function of aqueous biphenyl concentration is known, an overall mass balance that combines mass transfer rates with enzymatic kinetics can be used to predict whether the system will be mass transfer limited. The second objective was to evaluate a biphasic aqueous-organic system as a means of enhancing biphenyl hydroxylation rates. For enzymatic reactions that are mass transfer limited, higher mass transfer rates can be achieved in biphasic systems [Woodley, 1990]. If the biocatalysis rate is limited by low aqueous substrate concentrations, cell partitioning to the aqueous-organic interface may increase the effective biphenyl concentration at the cell wall.

Materials and Methods

Microorganism

A recombinant strain of *Pseudomonas aeruginosa*—PAO 4032 (pRO2038, pRO2369)—was used in all biocatalysis experiments. This strain carries individual genes on its plasmid DNA encoding for the monooxygenase enzyme (Tb4m) and the required native regulatory proteins. Both of these genes were isolated from *Burkholderia* sp. strain JS150 [Johnson and Olsen, 1995; Johnson and Olsen, 1997]. The DNA fragment also carries resistance genes for trimethoprim and carbenicillin/ticarcillin; growth in the presence of these antibiotics selects for bacteria possessing the monooxygenase genes. Preliminary research at Tyndall AFB has demonstrated the ability of this strain to hydroxylate biphenyl and DPA [Gilcrease, 1998].

Culture Techniques

Growth media for the *P. aeruginosa* strain consisted of Stanier's Mineral Salts Broth [Stanier et al., 1966] plus the following: 5 g/L glucose, 2.5 g/L casamino acids, 0.3 g/L trimethoprim, and 0.25 g/L carbenicillin (or 0.125 g/L ticarcillin). The media was autoclaved after addition of glucose and casamino acids, then cooled to room temperature before adding the antibiotics. Freshly prepared media was innoculated immediately with a thawed culture (~1.0 mL innoculum) taken from frozen (-70 °C) stock. The frozen stock culture was prepared from equal volumes of glycerol and mid-log phase ($A_{540} = 0.3$)

liquid culture prepared from the same media. After growth to mid-log phase (A_{540} 0.25 – 0.4), the fermentation broth was induced by adding toluene to the liquid phase (~2.5 mM) and 150-μL of toluene to a vapor tube (to saturate the headspace with toluene). Induction with toluene for 6 hours maximized production of the monooxygenase enzyme [Gilcrease, 1998]. While the toluene monooxygenase enzyme can also hydroxylate biphenyl, only ***toluene*** is capable of inducing monooxygenase expression. After induction, the cells were harvested via centrifugation and rinsed twice in reaction buffer (20-mM potassium phosphate solution, pH 8.0). Freshly washed cells were then resuspended in a small amount of the reaction buffer used for the biocatalysis experiments.

Materials

Biocatalysis experiments were conducted in 500-mL baffled shake flasks or in an Applikon® 3-L fermentor system. Temperature and agitation speed was controlled in the fermentor; dissolved oxygen was monitored, and pH was maintained at 8.0 with the buffered reaction solution. The Applikon® 3-L bioreactor used two 2" axially placed Rushton turbines to agitate the reaction broth.

Biocatalysis experiments utilizing excess biphenyl solids were performed in reaction buffer only; the two-phase biocatalysis experiments were conducted in a mixture of reaction buffer and an immiscible organic solvent. The amount of reaction buffer used in all experiments was 150-mL (shake flask) or 2000-mL (bioreactor). Dodecane and decanol were screened as potential organic solvents. In these screening experiments, each solvent was tested for its tendency to form an emulsion. The organic solubility of biphenyl and *m*-HBP was also measured. Additionally, the organic solvent had to be compatible with normal-phase HPLC analysis. Decanol formed a very stable emulsion when agitated with an aqueous culture broth; it was eliminated because of potential sampling problems. Dodecane was chosen as the organic solvent because gravity separation from the aqueous phase occurred relatively quickly in abiotic tests; however, the addition of the cell culture increased the phase separation time and capacity to emulsify significantly. The solubility of biphenyl in dodecane was approximately 125 g/L. For values of the logarithm of the octanol/water partition coefficient (log P), it has been observed that solvents with values of log P ≥ 4 generally are not toxic to the cells. Since the log P value for dodecane is approximately 12, cell toxicity and/or enzyme inactivation should be minimal in this two-phase system. Enzyme inactivation and cell toxicity has been observed in other biphasic systems, though [Harrop et al., 1992].

Analytical

Hydroxybiphenyl products in both the aqueous and organic phases were analyzed using HPLC. 750-μL samples of the aqueous phase were drawn and immediately diluted with an equal volume of acetonitrile. These samples were then microfuged for 5 minutes to remove cellular material. The HPLC analysis used an Alltech Adsorbosphere HS C18 (d_p = 5 μm, L = 250 mm, ID = 4.6 mm) reverse-phase column with a gradient elution program; the mobile phases were acetonitrile and 10-mM trifluoroacetic acid. The total flowrate was constant at 1 mL/min, and the gradient elution profile was as follows: 0-4 min, 90% TFA-10% CH_3CN; 5-16.5 min, 50% TFA-50% CH_3CN; 17.5-21.5 min, 15% TFA-85% CH_3CN; 22.5-25 min, 90% TFA-10% CH_3CN. Changes between compositions were made via a linear ramp over 1 minute. The organic phase was sampled similarly, but these samples were diluted with an equal volume of n-heptane. Organic phase samples were analyzed by HPLC using a Waters μBondapak NH_2 (d_p = 10 μm, L = 300 mm, ID = 3.9 mm) normal-phase column with a 75% heptane/25% 2-propanol mobile phase at 2 mL/min (isocratic). Unknown compounds were identified by comparison to known standards obtained from Fisher Scientific and Ultra Scientific.

1-mL aqueous samples were collected for measurement of total protein. These samples were microfuged for 5 minutes, and the supernatant was discarded. The cell pellet was then dissolved in a 0.1 N NaOH solution and analyzed using the BCA protein assay method [Smith et al., 1985]. Protein standards were prepared from Bovine Serum Albumin (BSA). Since a specific monooxygenase enzyme assay was unavailable for enzyme quantitation, the reported specific activities are reported on a total cell protein basis. For some of the early intrinsic kinetic experiments, a large variance in the average measured protein was observed; this was due to inadvertently diluting some of the protein samples with acetonitrile.

Reaction Conditions

For clarity, the reaction conditions used in these experiments are shown in Table 2.

Experiment	Type of Vessel	Method of Supplying Biphenyl Substrate to Reaction Medium	Reaction Temperature (°C)	Agitation Speed	Sparge Air Flowrate	Reaction Vessel Pressure
Vapor-Phase Addition Testing	3-L Applikon® Bioreactor	Saturated Vapor-Phase Addition	30 ± 1	300 RPM	5 LPM	5 psig
Intrinsic Kinetic Experiment #1	3-L Applikon® Bioreactor	Saturated Vapor-Phase Addition	30 ± 1	300 RPM	5 LPM	5 psig
Intrinsic Kinetic Experiment #2	3-L Applikon® Bioreactor	Finely-Ground Excess Biphenyl Solids	30 ± 1	600 RPM	2 LPM	3 psig
Two-Phase Screening Experiment	Two 500-mL baffled shake flasks	Flask 1: Excess biphenyl solids Flask 2: Biphenyl dissolved in dodecane	30 ± 1	Both flasks 250 RPM on orbital shaker/incubator	None	Flask 1: 0 psig Flask 2: 0 psig
Two-Phase Parallel Bioreactor Experiment	Two 3-L Applikon® Bioreactors	Both reactors: Biphenyl dissolved in dodecane (two-phase system)	30 ± 1	Reactor 1: 300 RPM Reactor 2: 600 RPM	1.5 LPM	3 psig

Experiment	Protein Concentration (mg BSA/L)	Initial Volume of Organic Dodecane Phase	Initial Mass of Biphenyl Added
Vapor-Phase Addition Testing	Abiotic	N/A	N/A – Vapor Phase Addition
Intrinsic Kinetic Experiment #1	35 ± 12	N/A	N/A – Vapor Phase Addition
Intrinsic Kinetic Experiment #2	77 ± 6	N/A	14 g
Two-Phase Screening Experiment	Flask 1: 347 ± 24 Flask 2: 355 ± 52	Flask 1: None Flask 2: 50 mL	Flask 1: 0.75 g Flask 2: 0.75 g
Two-Phase Parallel Bioreactor Experiment	Not Reported—Same in both reactors.	Reactor 1: 100 mL Reactor 2: 100 mL	Reactor 1: 10 g Reactor 2: 10 g

Table 2: Reaction Conditions

Results and Discussion

Intrinsic Kinetics

Intrinsic kinetic experiments were conducted in an aqueous potassium phosphate reaction buffer (no dodecane). Initial experiments utilized the vapor-phase addition of biphenyl [Reineke and Knackmuss, 1984; Spain and Nishino, 1987] in an attempt to maintain a constant aqueous biphenyl concentration; the sparge air was passed through a column of biphenyl solids prior to entering the bioreactor. By measuring the specific activity at different aqueous biphenyl concentrations, the rate vs. substrate concentration curve could be used to regress Michaelis-Menten kinetic parameters. As shown in Figure 1, only low aqueous-phase biphenyl concentrations were attainable with this technique; a low vapor-phase biphenyl concentration limited the equilibrium aqueous biphenyl concentration. Efforts to increase the vapor-phase biphenyl concentration included preheating the air prior to contacting it with the biphenyl solids, as well as using a molten biphenyl bath (90 °C) to saturate the sparge air. The effects of preheating the air and using the liquid biphenyl bath are also shown in Figure 1.

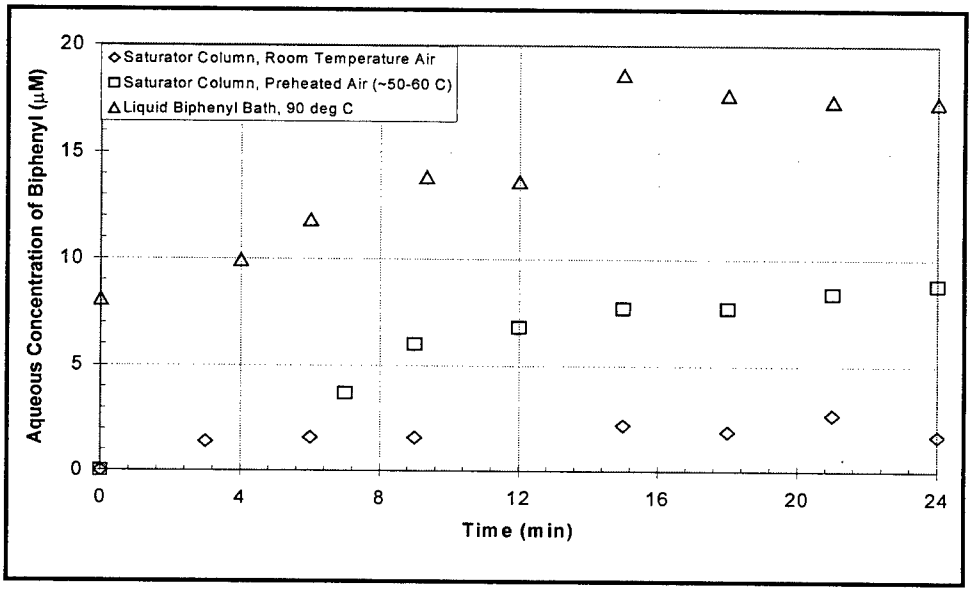

Figure 1: Abiotic Vapor Phase Addition of Biphenyl

Even with reasonable aqueous-phase biphenyl concentrations (~18 µM using the molten biphenyl bath), the vapor-phase addition of biphenyl was severely mass transfer limited at the bubble-liquid interface. Figure 2 shows an intrinsic kinetic experiment using the vapor-phase addition apparatus; an immediate drop in the aqueous-phase biphenyl concentration from 16 to 11 µM was observed when the cells were

added (t = 0), indicating that the system was mass transfer limited. Only after the monooxygenase activity ceases, as indicated by a plateau in the *m*-HBP profile after 30 minutes, does the aqueous phase biphenyl concentration return to the equilibrium value.

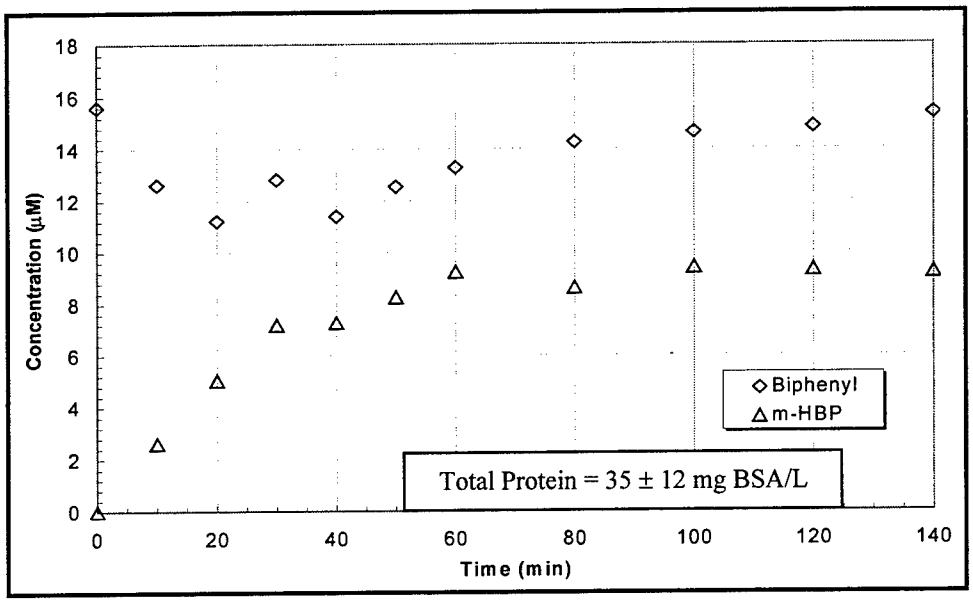

Figure 2: Intrinsic Kinetic Experiment #1 (Vapor-Phase Addition of Biphenyl)

Subsequent intrinsic kinetic experiments used finely ground biphenyl solids (~100/200 Tyler mesh size) to obtain a large surface area for mass transfer; mass transfer rates with these fine solids were sufficient to maintain a constant aqueous biphenyl concentration during biocatalysis. Aqueous HPLC samples were filtered with 1 µm glass Acrodisk® syringe filters to remove any solid biphenyl particles. Figure 3 shows that this technique of supplying substrate to the aqueous phase was not mass-transfer limited as indicated by a constant aqueous biphenyl concentration after the cells were added.

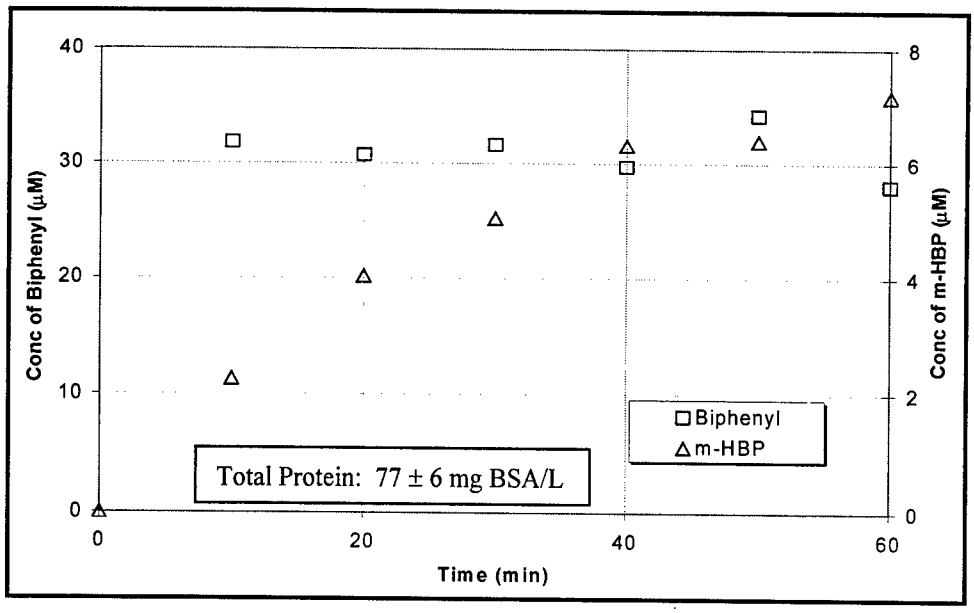

Figure 3: Intrinsic Kinetic Experiment #2 (Finely-Ground Biphenyl Solids)

Figure 4 shows the first experimentally determined points on the specific activity vs. substrate concentration curve. Note that the specific activity *decreases* as the substrate concentration increases, contrary to what was expected. A Michaelis-Menten enzyme kinetics curve with no substrate or product inhibition is shown in Figure 5. The unexpected behavior of the intrinsic kinetics was attributed to variation of enzyme expression from batch to batch, as well as an improper sampling technique (see Methods and Materials section). Because the *P. aeruginosa* strain uses native enzyme regulation, the fraction of enzyme produced in the cells is very sensitive to the point of induction (A_{540}) as well as the length of induction (~ 6 hours). Therefore, developing the V vs. S curve from separate batches of cells is not practical with this strain. A technique that obtains the kinetic parameters in one batch experiment will provide more accurate kinetic data.

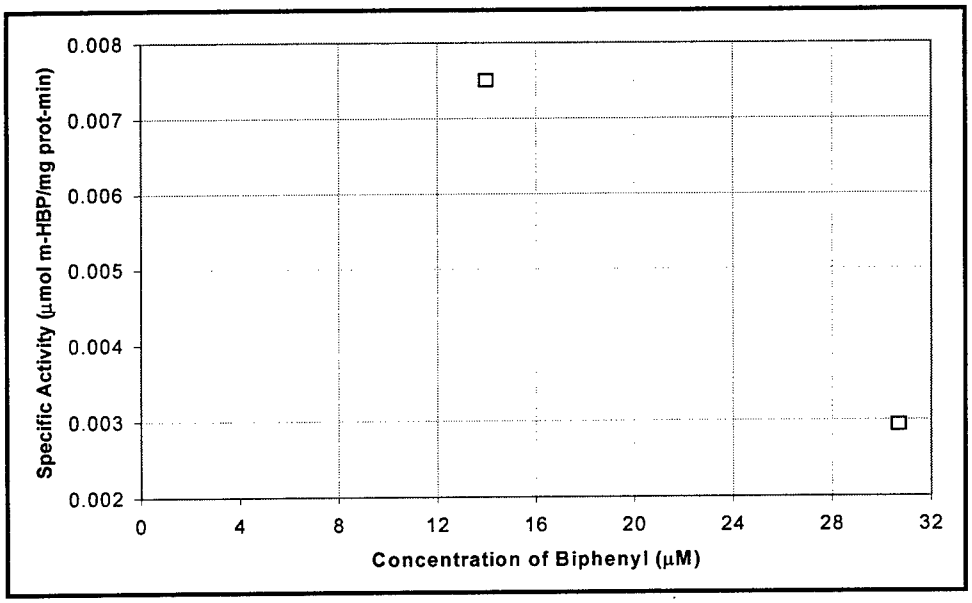

Figure 4: Specific Activity vs. Substrate Concentration

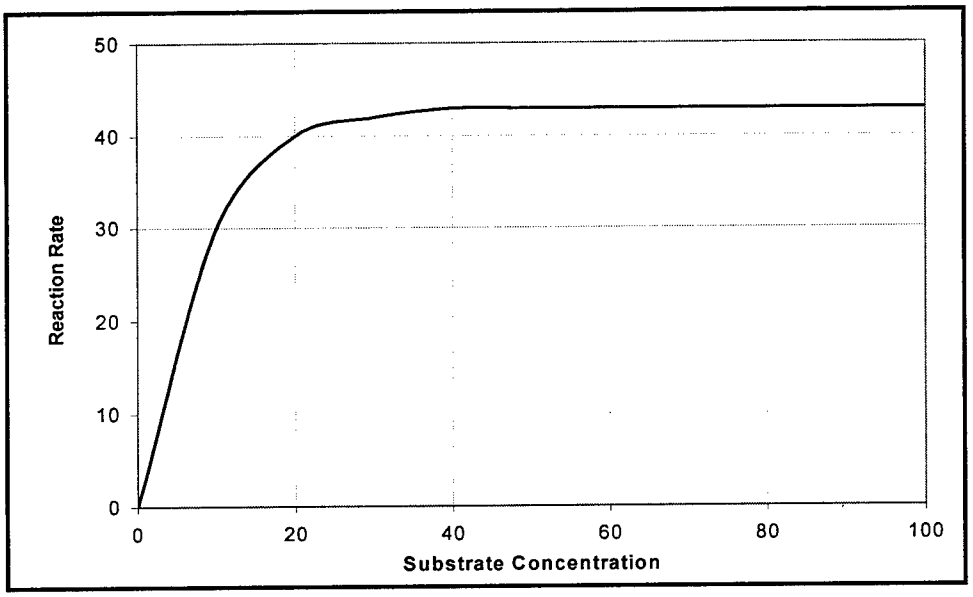

Figure 5: Sample Uninhibited Michaelis-Menten Enzyme Kinetics Curve

Solids/2-Phase Screening Experiments

Screening experiments were conducted in baffled shake flasks to compare specific activities for different methods of supplying substrate to the aqueous phase. Excess biphenyl solids were used in one flask to provide a saturated solution of biphenyl (~50 µM), while a 2-phase dodecane/potassium phosphate

buffer system was evaluated in the other flask. Figure 6 shows a comparison of the amount of *m*-HBP produced vs. time for both the excess solids and 2-phase system.

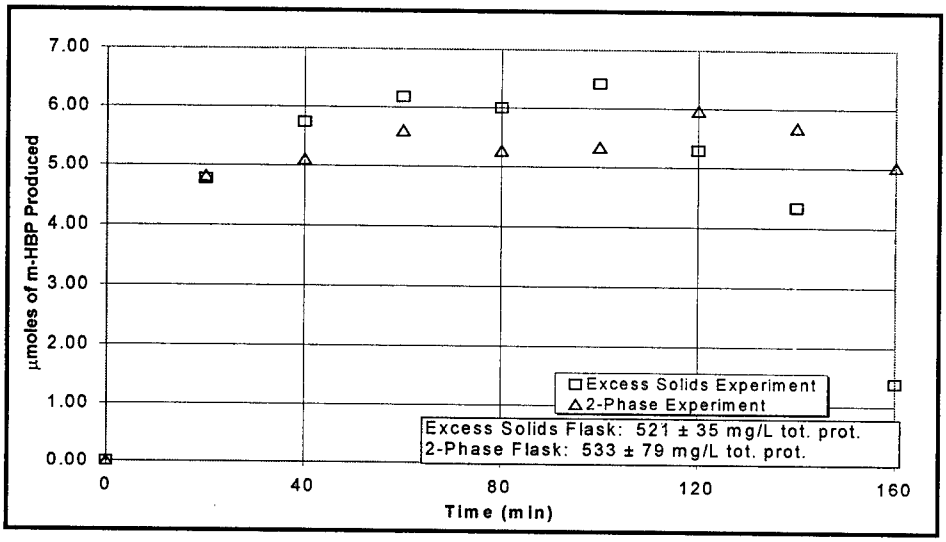

Figure 6: Screening Experiment (Excess Solids vs. a 2-Phase System)

The aqueous biphenyl concentration remained at saturation (~50 µM) in the excess solids flask. Thus, there was no mass transfer limitation in the excess solids system. Also, note the amount of *m*-HBP produced in the 2-phase system was similar to that produced with excess biphenyl solids. This suggests in the 2-phase flask that (1) mass transfer was not limiting the overall hydroxylation rate (no ***reduced*** rate compared to the excess solids), and (2) cells were ***not*** partitioning to the interface as anticipated (no ***increased*** rate compared to the excess solids). After enzyme activity was lost (~30 to 40 minutes), the excess solids experiment shows a ***decrease*** in *m*-HBP over time. Conversely, the 2-phase experiment shows the *m*-HBP concentration remained constant after activity was lost.

The decline in *m*-HBP concentration in the excess solids experiment was investigated further to determine its fate. A student's t-test and replicate filtered vs. non-filtered HPLC samples were used to determine if *m*-HBP product was being sorbed to the Acrodisk® syringe filters used to remove excess biphenyl solids during sampling. For an $\alpha = 0.05$ confidence level, no *m*-HBP was sorbed to the Acrodisk® syringe filters. A second hypothesis was that some of the *m*-HBP product was being hydroxylated a second time to yield *m,m*'-, *p,p*'-, or *m,p*'-dihydroxybiphenyl (DHBP) products. Comparison of aqueous HPLC samples to *m,m*'- and *p,p*'-DHBP standards (no *m,p*'-DHBP standard available) showed this was not the case (no unknown chromatogram peaks). In previous biocatalysis

experiments starting with *m*-HBP or *p*-HBP as the substrate, 97% of the initial substrate remained after 3 hours using the Tb4m strain [Gilcrease, 1998]. Another hypothesis was that part of the *m*-HBP was being volatilized from solution in the shake flask. Testing of this hypothesis showed that after 40 hours of air sparging (5 LPM) a 50 μM *m*-HBP solution in the bioreactor, no stripping occurred. Alternatively, *m*-HBP could have sorbed to residual organic compounds on the glassware; baking the glassware in a muffle furnace may eliminate this problem.

2-Phase Biocatalysis Experiments

Parallel two-phase biocatalysis experiments were conducted in two bioreactors using equal amounts of biocatalyst from the same batch of cells. These experiments were designed to determine the effect of agitation rate on the biocatalysis of biphenyl. In Figure 7 the production of *m*-HBP vs. time for the parallel bioreactor experiment is shown.

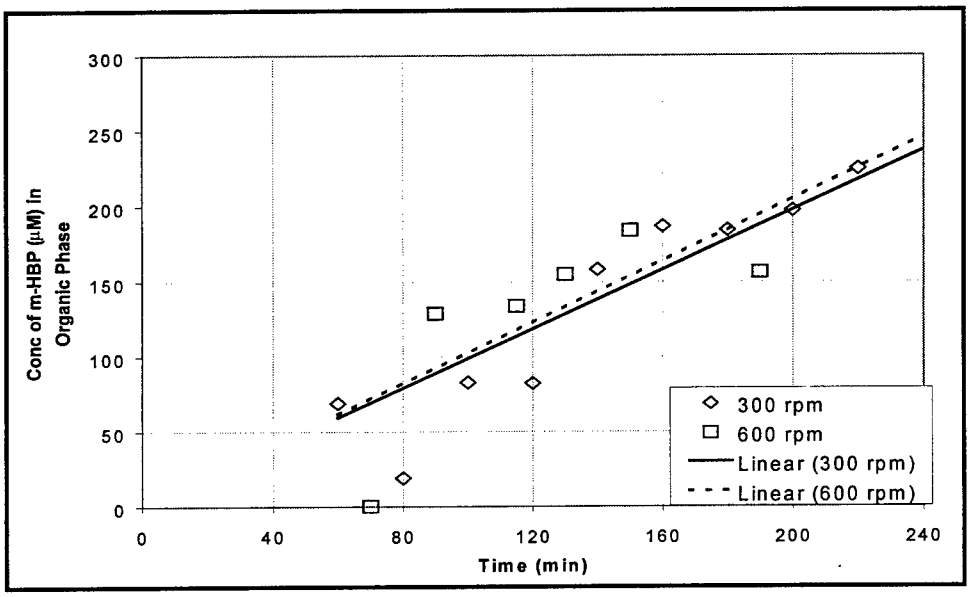

Figure 7: 2-Phase Parallel Bioreactor Experiment (300 vs. 600 RPM)

Note that the production of *m*-HBP was essentially the same in both runs, as evidenced by the statistically identical slopes of the experimental data; a t-test on both regression lines shows the time-averaged concentration is statistically the same. The large scatter in the experimental data is indicative of the difficulty in sampling the emulsified two-phase system. Because of the stable emulsion, aqueous and organic samples were microfuged to break the emulsion prior to dilution for HPLC analysis. Since an enhanced rate was not observed when the agitation rate was increased from 300 to 600 rpm, one could

argue that this two-phase system was not mass transfer limited. If there had been a mass transfer limitation, an enhanced rate would have been seen at the higher rpm. Additionally, since there was no enhanced rate observed between the two agitation levels, one could argue that (1) cell partitioning is not occurring in this system, or (2) any cell partitioning that does occur is not contributing to a net increase in hydroxylation activity. If cell partitioning had occurred, an enhanced rate would have been observed at either 300 or 600 rpm, depending on the effect of increased agitation on cell partitioning. At the higher agitation level, two phenomena are acting in opposition: (1) greater dispersion of the organic phase at the higher agitation level creates a larger surface area for cell partitioning, and (2) greater turbulence at the higher agitation level may create enough shearing to prevent cell partitioning.

To maintain enzymatic activity past 30 minutes, 5 g/L glucose was added to the reaction mixture in these parallel bioreactor experiments. Note that this supplementary glucose is used to provide reducing equivalents of nicotinamide adenine dinucleotide phosphate (NADPH) in its reduced form; these electrons are used in the monooxygenase-catalyzed hydroxylation reaction. Enzyme activity was maintained after 4 hours, contrary to the loss of activity after 20-30 minutes in experiments without glucose.

Conclusions and Recommendations

The results of this research show that the immiscible two-phase dodecane/potassium phosphate buffer system (for the limited set of conditions investigated) does not enhance the overall hydroxylation rate compared to an excess solids in buffer system. While this suggests that it is not advantageous to utilize the two-phase system, other factors need to be considered. Product recovery can be greatly facilitated through the use of liquid/liquid extraction because of the large partitioning of *m*-HBP back into the organic phase. Partition coefficients for *m*-HBP in the dodecane/buffer system were on the order of 50 to 100; this could potentially be utilized to recover the *m*-HBP product from the aqueous phase. This may be important for a new overexpressed *E. coli* strain recently developed by Dr. Glenn Johnson at Tyndall AFB, as the product *m*-HBP is toxic to the *E. coli* cells. Thus, in-situ product recovery may become essential with this new strain to prevent inactivation of the biocatalyst. Lastly, quiescent (low-agitation) reactor conditions in the two-phase system may allow the cells to partition to the interface; in this case, an enhanced activity may be seen. An increase in phase ratio (organic to total liquid volume) may also allow cell partitioning to occur.

As cell concentrations and enzyme activities are increased, interphase mass transfer may eventually control the overall hydroxylation rate. Because of the higher mass transfer rates, the two-phase system may allow higher hydroxylation activities to be realized when cell and enzyme concentrations are high. Future research will concentrate on enhancing the cell and substrate concentrations through genetic engineering and proper two-phase reactor design.

Acknowledgements

We would like to thank Dr. Jim Spain and Dr. Glenn Johnson (Armstrong Laboratory, Tyndall AFB, Florida) for their genetic-engineering work on both the *P. aeruginosa* strain and the new *E. coli* strain; this collaboration between microbiologist and engineer has helped us better understand that both scientist and engineer are crucial in formulating a working model that can be used to scale up this process.

References

Abramowicz, D.A., C.R. Keese, and S.H. Lockwood, Regiospecific hydroxylation of biphenyl and analogs by Aspergillus parasiticus, in *Biocatalysis*, D.A. Abramowicz, Editor, 1990. New York: Van Nostrand Reinhold, p. 63-92.

Bachmann, A., et al.(1988). Aerobic biomineralization of alpha-hexachlorocyclohexane in contaminated soil. *Applied and Environmental Microbiology*. **54**(2): p. 548-554.

Faber, K., *Biotransformations in organic chemistry. 3rd ed.* 1997, Berlin: Springer-Verlag.

Gibson, D.T., Microbial metabolism of aromatic hydrocarbons and the carbon cycle, in *Microbial metabolism and the carbon cycle*, S.R. Hagedorn, S. Hanson, and D.A. Kunz, Editor. 1988, Chur, Switzerland: Harwood Academic Publishers, p. 43-52.

Gilcrease, P.C. (1997). *Mass transfer effects on the bioreduction of TNT solids in slurry reactors*. Ph.D. Dissertation, Colorado State University.

Gilcrease, P.C. (1998). *Biocatalysis of Biphenyl and Diphenylacetylene to Synthesize Polymer Precursors*. Final Report for: Summer Faculty Research Program, Tyndall Research Site, Tyndall AFB, FL. September 1998.

Harrop, A., et al. (1992). Production of naphthalene-*cis*-glycol by Pseudomonas putida in the presence of organic solvents. *Enzyme and Microbial Technology*. **14**: p. 725-730.

Johnson, G.R. and R.H. Olsen (1995). Nucleotide sequence analysis of genes encoding a toluene/benzene-2-monooxygenase from Pseudomonas sp. Strain JS150. *Applied and Environmental Microbiology*. **61**(9): p. 3336-3346.

Johnson, G.R. and R.H. Olsen (1997). Multiple pathways for toluene degradation in Burkholderia sp.strain JS150. *Applied and Environmental Microbiology*. **63**: p. 4047-4052.

Kohler, A., et al. (1994). Enhanced biodegradation of phenanthrene in a biphasic culture system. *Biodegradation.* **5**: p. 93-103.

Nikolova, P. and O.P. Ward (1993). Whole cell biocatalysis in nonconventional media. *Journal of Industrial Microbiology.* **12**: p. 76-86.

Reineke, W. and H. Knackmuss (1984). Microbial Metabolism of Haloaromatics: Isolation and Properties of a Chlorobenzene-Degrading Bacterium. *Applied and Environmental Microbiology.* **47**(2): p. 395-402.

Roberts, S.M., et al., *Introduction to biocatalysis using enzymes and micro-organisms.* 1995, Cambridge: Cambridge University Press.

Rosenberg, M. and E. Rosenberg (1981). Role of Adherence in Growth of Acinetobacter calcoaceticus RAG-1 on Hexadecane. *Journal of Bacteriology.* **148**(1): p. 51-57.

Rosenberg, M. (1991). Basic and Applied Aspects of Microbial Adhesion at the Hydrocarbon:Water Interface. *Critical Reviews in Microbiology.* **18**(2): p. 159-173.

Smith, P.K., *et al.* (1985), Measurement of protein using bicinchoninic acid. *Analytical Biochemistry.* **150**: p. 76-85.

Spain, J. and S. Nishino (1987). Degradation of 1,4-Dichlorobenzene by a Pseudomonas sp. *Applied and Environmental Microbiology.* **53**(5): p. 1010-1019.

Stanier, R.Y., N.J. Palleroni, and M. Doudoroff (1966). The aerobic pseudomonads: a taxonomic study. *Journal of General Microbiology.* **43**: p. 159-271.

Stucki, G. and M. Alexander (1987). Role of dissolution rate and solubility in biodegradation of aromatic compounds. *Applied and Environmental Microbiology.* **53**(2): p. 292-297.

Woodley, J. M. (1990). Two-liquid phase biocatalysis reactor design. In *Biocatalysis*, D. A. Abramowicz, ed., New York: Van Nostrand Reinhold.

Zampini, A., et al. *Esterification product of aromatic novolak resin with quinone diazide sulfonyl group.* 1995. US Patent 5589553.

INVESTIGATING LEARNED AVOIDANCE BEHAVIOR AND ITS APPLICATION TO UNMANNED AIR VEHICLES

Final Report for:

Summer Research Extension Program

Acknowledgement:

Air Force Office of Scientific Research, Bolling, AFB

Air Vehicles Directorate, AFRL, WPAFB, OH

The University of Toledo, Toledo, OH

Jeffrey D. Johnson, Ph. D and Jinghong Li

Department of Bioengineering

The University of Toledo

Toledo, OH 43606

28 February 2000

INVESTIGATING LEARNED AVOIDANCE BEHAVIOR AND ITS APPLICATION TO UNMANNED AIR VEHICLES

Jeffrey D. Johnson Jinghong Li
Department of Bioengineering
The University of Toledo
Toledo, OH 43606

ABSTRACT

Unmanned air vehicles (UAVs) will be an increasingly important component of the U.S. Air Force arsenal. The traditional mission of the UAV as a reconnaissance platform will be augmented by its role in surveillance, target acquisition, and, ultimately, as unmanned combat vehicles. One of the challenges facing UAV deployment is its survivability. Removing the pilot from the air vehicle may remove the risk to human life but it also removes the intelligence and experience needed to maximize the survivability of the weapon system. In this report, we investigate methods to augment the UAV with a simple form of the intelligent behavior that is lacking in an unmanned system. Specifically, we seek to improve the survivability of the UAV by incorporating an algorithm designed to imbue the system with a fundamentally important form of intelligence: learned avoidance behavior. Learned avoidance behavior is the ability of an animal to use past experience to develop a decision policy that allows it to avoid an impending aversive situation. In this report, we propose a model of learned avoidance behavior and test it in a variety of learned avoidance experiments. We find that the model faithfully recreates observable animal behavior an also maps well to the brain structures believed to be responsible for learned avoidance behavior.

1. Introduction

Unmanned air vehicles (UAVs) will be an increasingly important component of the U.S. Air Force arsenal [1]. The traditional mission of the UAV as a reconnaissance platform will be augmented by its role in surveillance, target acquisition, and, ultimately, as unmanned combat vehicles [2]. One of the challenges facing UAV deployment is its survivability. Removing the pilot from the air vehicle may remove the risk to human life but it also removes the intelligence and experience needed to maximize the survivability of the weapon system. As mission parameters become more hostile, and UAV technology becomes more expensive, the need for improved survivability will rise significantly. While efforts are being made in the areas of automatic target recognition, path planning, and low-observable technology, this report focuses on increasing the behavioral repertoire of the UAV. That is, we investigate methods to augment the UAV with a simple form of the intelligent behavior that a pilot would provide in a manned system. Specifically, we seek to improve the survivability of the UAV by incorporating an algorithm designed to provide the system with a fundamentally important form of intelligence: learned avoidance behavior.

Learned avoidance behavior is the ability of an animal to use past experience to develop a decision policy that allows it to avoid an impending aversive situation. Specifically, learned avoidance is the ability to remember an aversive event, identify what preceding events can act as a predictor of the aversive event, and formulate a decision policy removes the threat of the aversive event

In this report, we first introduce theories of whole animal behavior. propose a model of learned avoidance behavior and test it in a variety of learned avoidance experiments. We find that the model faithfully recreates observable animal behavior an also maps well to the brain structures believed to be responsible for learned avoidance behavior.

2. Learned Avoidance Behavior and the Basal Ganglia

All animal behaviors can be categorized into *approach* behavior and *avoidance* behavior. Both categories of behavior are important for an animal to survive. However, avoidance behavior is much less studied both in psychology [3] and in animal learning but it is the principal behavior needed to improve survivability.

In this section, we introduce the experimental observations of learned avoidance behavior and review the proposed theories that seek to explain the behavior. We then describe the basal ganglia, which are believed to be the brain structures responsible for learned avoidance behavior. The behavioral learning theories and physiological processes discussed in this chapter serve as the bases for the biologically-plausible computational model of learned avoidance behavior proposed in the report.

2.1 Learned avoidance behavior

Learned avoidance behavior is an animal's acquired response used to avoid an aversive event. It can be divided into two classes: active and passive avoidance. In active avoidance, the animal must learn a response to avoid punishment while in the passive case the animal has to suppress a response. This work is on the former case and hereafter the active avoidance is simply referred to as avoidance. While there exist many paradigms of experiments for avoidance learning, this report focuses on shuttle-box avoidance experiments. In this section, we first describe the experiment, and then describe some proposed theories explaining the avoidance learning.

2.1.1 A representative experiment: One-way shuttle-box avoidance experiment

In one-way shuttle-box avoidance experiment, the subject is usually a rat (or a dog [4]) and the apparatus is a shuttle-box with two rectangular compartments separated by a barrier or a door. An electric shock can be applied to the feet of the rat via the metal floor grid. A light is placed on the ceiling of one side of the chamber (Side A) and it can be used to signal the coming of the shock. Figure 2.1 shows the setup of the experiment.

At the start of each trial, the rat is placed into Side A of the shuttle-box and is allowed to *habituate* to the environment. Habituation is a procedure that makes an animal's response to repeated stimulus gradually decrease. After habituation, the light in Side A is turned on. If the rat remains in the Side A for a specified period of time (a few seconds) it would receive a shock and the trial end would end. The rat would be removed from the shuttle-box for a predetermined period before being placed again in Side A and the sequence repeated. However, if after the light came on but before shock is applied, the rat is able to flee to the safety side (Side B), then shock would be avoided and the trial would end. Fleeing from Side A to Side B is the necessary response to avoid shock.

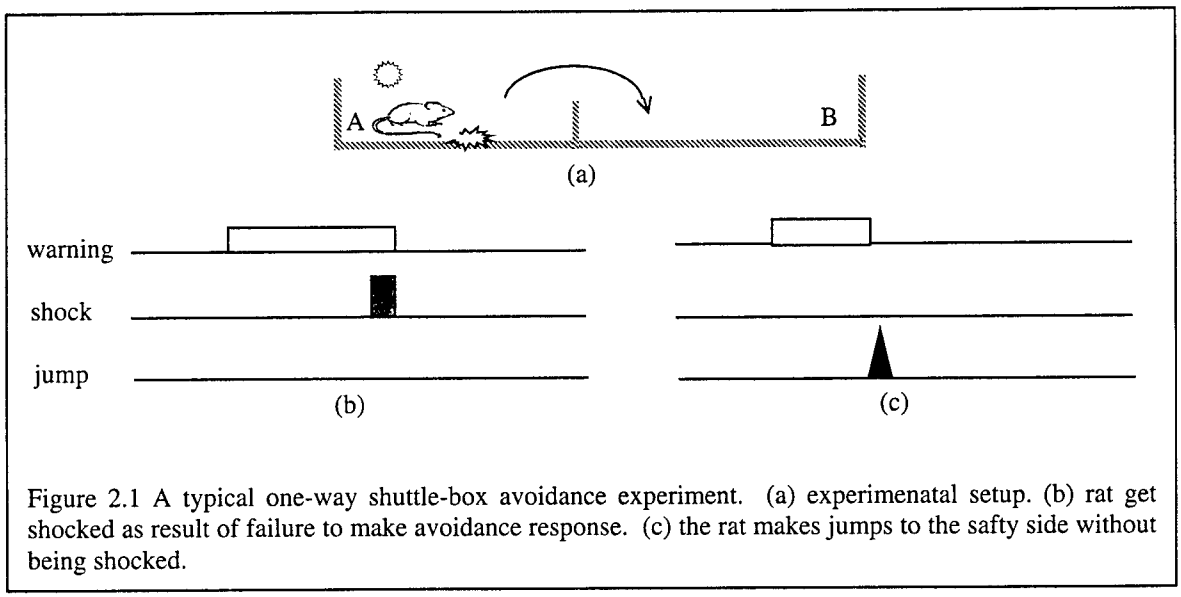

Figure 2.1 A typical one-way shuttle-box avoidance experiment. (a) experimenatal setup. (b) rat get shocked as result of failure to make avoidance response. (c) the rat makes jumps to the safty side without being shocked.

On each trial, the latency of the avoidance response is measured. The latency is defined as the interval between the warning light coming on and the generation of the avoidance response. For the first several trials, the latency are usually as long as the period between light and shock indicating the animal failed to make the correct avoidance response. With more trials, the latency would decrease, that is, the rat learns to make *avoidance* response before a shock is applied. With the progress of the experiment, the latency of the rat would decrease steadily. After a number of trials, the rat learns to run to the safe side as soon as the warning signal comes on and virtually never gets shocked. At the end of the experiment, recorded data are analyzed and performance is evaluated. The performance of a group of rats over blocks of trials is shown in Figure 2.2.

A fundamental question in the avoidance learning is how the absence of shock can provide reinforcement for the animal's avoidance behavior. In the following section we review the proposed theories that try to explain the phenomenon. But before reviewing, we need to briefly review the two fundamental learning paradigms of classical and instrumental conditioning because they form the basis of the proposed theories of avoidance learning.

2.1.2 Classical and instrumental conditioning

Classical conditioning is the association of two stimuli [5]. One of the two stimuli can be a biologically important stimulus that reliably evokes a reflexive reaction. Such stimuli are called unconditioned stimulus because the animal does not have to condition (learn) to respond to it and the unconditioned response (UR) is the innate reaction triggered by the by the US.. The other stimulus is called the conditioned stimulus (CS) because it is an initially innocuous or weak stimulus [6]. Through conditioning, the CS acquires the ability to elicit from the animal a conditioned response (CR), that is similar in nature to that of the UR.

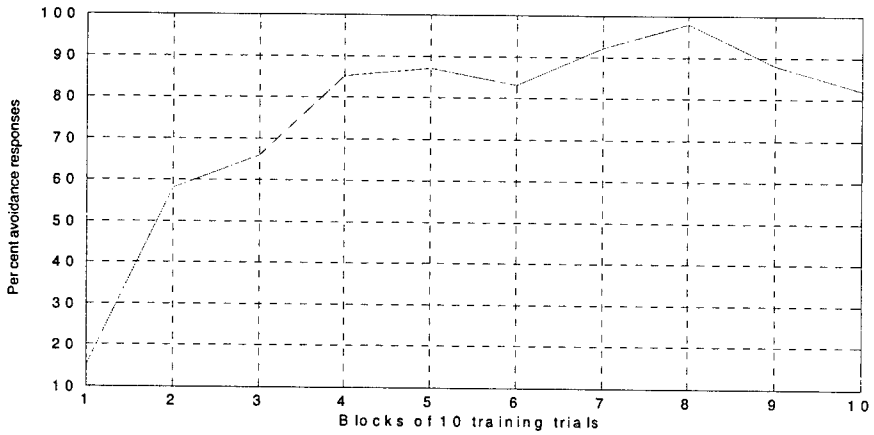

Figure 2.2 Kamin's experiment on performance in the shuttle-box (adapted from *[3]*).

Instrumental conditioning occurs when the stimulus that an animal receives is contingent on the animal's behaviors [7]. Compared with classical conditioning, instrumental conditioning is a closed-loop process because the animal, through its actions, has an influence over the stimuli it receives. Thus, what is learned in instrumental conditioning is the association between a previously innocuous stimulus (CS) and the action needed to elicit (in learned approach behavior) or avoid (in learned avoidance behavior) an unconditioned stimulus (US).

Instrumental conditioning typically involves a reinforcer or punisher. A punisher is defined as any outcome or event that, when made contingent on a prior response, decrease the probability of that response. A reinforcer acts oppositely on behavior as to that of a punisher. Based on the presentation or omission of reinforcers punishers, four basic types of instrumental conditioning procedures can be identified. Avoidance learning is the case of learning the behavior that leads to the omission of the punisher.

2.1.3 Theories of learned avoidance behavior

Several theories prevail in explaining the learned avoidance behavior. Each theory can account for certain characteristics of the complex behavior but no theory accounts for all aspects of the behavior.

2.1.3.1 Two-factor theory

Mowrer's two-factor theory posits that both classical conditioning and instrumental conditioning processes are necessary in avoidance learning [8]. Fear is a critical assumption for this theory. It is believed to be the conditionable component of the unconditional response to an aversive stimulus [9]. The two-factor theory holds that fear itself is aversive and the aversive property of fear gives fear a motivating property because it induces an animal to generate escape (from fear) responses. Because of the importance of fear, two-factor theory is often referred to as fear theory. Through classical conditioning, this fear response is transferred from US to CS. Through instrumental conditioning, the avoidance behavior is reinforced by the reduction of in fear that

accompanies the removal of the fear-eliciting CS. In the shuttle-box avoidance experiment, the fear is transferred from the shock (the US) to the warning light (the CS) that signals eventual shock.

One problem with two-factor theory is accounting for the resistance to extinction that is a characteristic of an avoidance response. According to this theory, the animal's fear should eventually extinguish after multiple successful avoidances because the fear is conditioned to the shock. But, with the extinction of fear, the actual avoidance response should also extinguish because fear is the motivator for the response. However, animals have been shown to be highly resistant to the extinction of an avoidance response with consecutive avoidance responses numbering into the several hundreds [4, 10]. This discrepancy between prediction and observation has led fear theorist to adopt the belief that fear obeys the laws of classical conditioning in its establishment but it disobeys those laws in its extinction. They argue that a residual level of fear, protected from extinction by various factors, remains conditioned to the CS even after hundreds of extinction trials and that this level of fear is sufficient to motivate the animal to maintain the avoidance response [11, 12].

2.1.3.2 Revised Two-factor Theory

Mowrer's eventually revised his two-factor theory by removing the second factor (drive-reduction) from his earlier theory. In its place, Mowrer allowed for conditioning to be a result of primary drives of decremental reinforcement (punishment) and incremental reinforcement (reward) or of the secondary drives of fear, relief, disappointment, or hope. In addition, Mowrer postulated that hope and fear can be conditioned not just to environmentally produced stimuli, but also to response-contingent (proprioceptive) stimuli. These changes removed the role of S-R bonds in the establishment of habits. Instead behavior was predicated on those responses that had hope conditioned to their proprioceptive stimuli. Responses that had fear conditioned to their proprioceptive stimuli were suppressed. Revised two-factor theory made response generation voluntary and selective, instead of the reflexive function of S-R bond strength that characterized the original two-factor theory. However, Mowrer's original two-factor theory had gained such support that even his defection to a cognitive theory has not lessened its popularity. A decade after Mowrer's revised two-factor theory, Bolles [13] and others proposed theories of avoidance that better defined the constructs of expectancy. Each theory has interesting characteristics, however, Seligman & Johnston's [14] cognitive theory will be reviewed in this section, as it incorporates many of the characteristics of its predecessors.

2.1.3.3 Cognitive theory

Cognitive theory proposes that it is the hypothetical construct of expectancy, not the equally hypothetical construct of fear that governs avoidance behavior [14]. According to this theory, the cognitive component develops two expectations during avoidance learning. The first is the expectation that the specific response, when generated in the presence of the specific stimulus, leads to an outcome; the second expectation developed is that not performing the response to the stimulus leads to another outcome. The theory states that for the

animal to generate the response, it must have an a priori preference for the outcome that occurs as a result of its response over the other outcome that occurs in the absence of a response. These expectancies are strengthened if the animal's experiences confirm them and are weakened if the animal's experiences disconfirm them.

However, this theory does not totally remove the fear component because it has both an expectancy-based cognitive component and a fear-based emotional component (although the role of fear in this theory is relatively minor when compared to its role in two-factor theory). Cognitive theory agrees with two-factor theory in the premises that fear motivates an animal to elicit responses, is classically conditioned, and obeys the conditioning laws of acquisition and extinction. However, it explicitly state that fear plays no role in the reinforcement of behavior. The role of fear is confined to eliciting the responses from which the animal can begin to develop its expectancies. Subsequent avoidance responses are a function of the expectancy that a given response will lead to the animal's preferred outcome, not a function of the fear experienced by the animal.

Cognitive theory explains the resistance to extinction of avoidance behavior concomitant with the extinction of fear. After each successful avoidance, the expectancy that the avoidance response is followed by no shock is always strengthened through confirmation. Conversely, because non-avoidance responses are never generated, the expectancy that such responses are followed by shock is never weakened by disconfirmation. With the expectancies determining behavior, the fear associated with aversive outcomes can extinguish during repeated avoidance without altering behavior.

2.1.3.4 One-factor theory

One-factor theory states that only the instrumental process is necessary in avoidance learning [15]. The avoidance of shock itself can serve as the reinforcer for the avoidance behavior and hence the unnecessary assumption of fear signal as in the two-factor theory. This theory has a simple explanation of the slow extinction of avoidance response [16]: The subjects just cannot discriminate the change in experimental conditions and hence no change in (avoidance) behavior. This theory is supported by experiments made by Herrnstein and Hineline [17] who showed that animals can learn an avoidance behavior when neither an external CS nor the passage of time is a reliable signal for shock.

2.1.3.5 Approach theory

Other researchers, including Bolles [18] and Gray [19], regard avoidance learning as an approach to a positive goal (safety) rather than an escape from fear. In Gray's theory, safety signal is independent of the level of fear. Hence the persistence of avoidance response is independent of the decreased fear.

2.1.3.6 Summary of the theories

Despite the apparent success of expectancy theory in accounting for the experimentally observed behaviors, two-factor theory is still the dominant theory of avoidance learning and behavior. McAllister [20] examined many of the evidences that are proposed to be against the fear theory and found them inadequate to "put the fear theory to rest". To cope with some of the difficulties as to the parallelism of fear and avoidance behavior, some modification of fear-reduction has been made including the proposing of the effective reinforcement theory [20].

While each of the theories has its strength and weakness in explaining the learned avoidance behavior, their ultimate validity lies in its physiological plausibility. In the following section, we describe a brain structure, the basal ganglia, that are believed to play a role in avoidance learning.

2.2 Functional anatomy of the Basal ganglia

The basal ganglia may be the most complicated structures in the brain. The research on them is mostly motivated by the Parkinson Disease (PD), a disease caused by the degeneration of the dopaminergic transmission in the basal ganglia [21, 22]. Over the years, much progress has been made in the understanding of the basal ganglia, both normal and disordered [21-26]. In this section we briefly review the functional anatomy of the basal ganglia with a bit more in-depth description of the striatum, an important component. Recent reviews in detail of the functional anatomy of the basal ganglia can be found in the publication [27-30].

The basal ganglia are several extensively interconnected subcortical nuclei that are located directly under the cerebral cortex. They include caudate nucleus, putamen, globus pallidus, subthalamic nucleus, and substantia nigra. The first two, caudate nucleus and putamen, are jointly termed as the striatum (STR). The globus pallidus (GP) is divided into external and internal segments (GPe and GPi, respectively) while the substantia nigra (SN) is divided into the pars compacta (SNc) and reticulata (SNr) both functionally and anatomically.

There are complex external and internal connections in the basal ganglia and the pathways related to motor function are illustrated in Figure 2.3. The striatum serves as the major input station for the basal ganglia and receives input from virtually the entire cerebral cortex including the motor, sensory, association, and limbic areas. The other inputs to the striatum include projections from the intralaminar nuclei of the thalamus and the amygdala. The striatum projects to the GP and to the SN. The STN is the second input station of the basal ganglia. It receives direct input from the motor and premotor cotices, as well as the output of the GPe. STN projects to GPi and SNr and projects back to GPe.

The striatum also receives dopaminergic projection from the SNc. The output pathway of the basal ganglia is from the GPi and the SNr to the ventral lateral, ventral anterior, and mediodorsal nuclei in the thalamus. These

nuclei project back to prefrontal, premotor, the supplementary motor, and motor cortices, and hence formed the *cortico-striato-pallido-thalamo-cortical* loops. Of the loops, two major pathways can be identified – an inhibitory one called direct pathway and an excitatory one called indirect pathway. The inhibitory direct pathway begins from the STR that projects to the GPi and the SNr. The excitatory indirect pathway also begins from the STR, which, however, projects to GPe, through STN, and finally ends on SNr and GPi. It should be noted that the projections from STR to GPe and from GPe to SNr/GPi are inhibitory in nature. In addition to these major pathways, there is a loop from the striatum to the SNc and back to the STR, and also reciprocal inhibitory connections between the GPi and GPe.

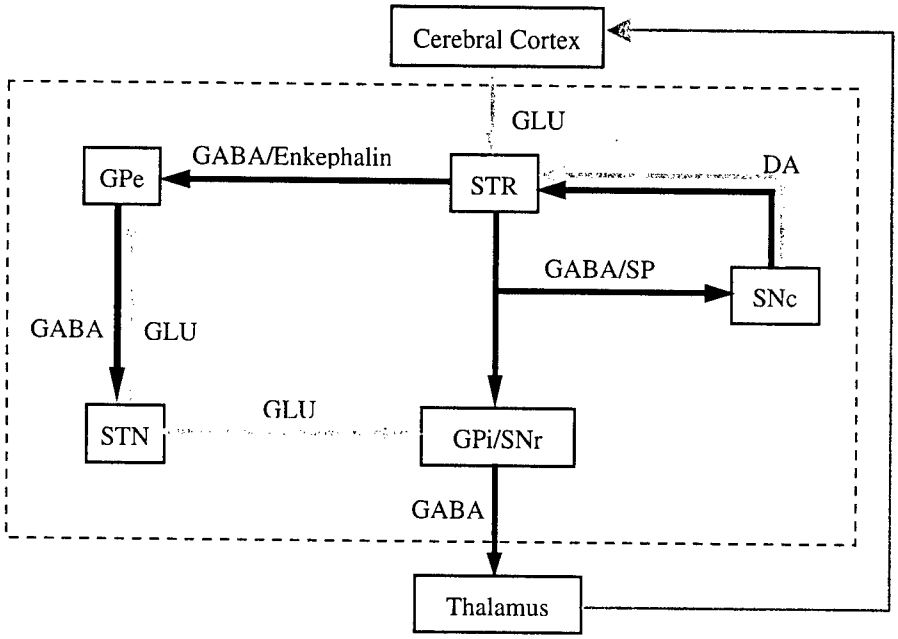

Figure 2.3 Components and circuits of the basal ganglia (from [30]). In the figure, gray connections are excitatory and black ones inhibitory connections. See text for an explanation.

All of the pathways described above have a topographic nature. That is to say that specific cortical areas map to specific parts of the striatum, which, again, project to specific parts in its targets, the other components of the basal ganglia. There is a relative segregation among the pathways and this segregation is maintained throughout the basal ganglia and back to the cortical areas [30]. Hence there are multiple closed loop pathways in the basal ganglia. However, there may exist some degree of divergence and overlapping among projections of the pathways. And cortical inputs to the basal ganglia may be dispersed within the striatum and then brought back again at the next stage in the information processing [31]. The circuit functions by the interactions of inhibitory or excitatory neurotransmitters or neuromodulators that include γ-aminobutyric acid (GABA), glutamate (GLU), enkephalin, substance P (SP), and dopamine (DA). DA has a differential effect on the two pathways: it tends to excite the indirect pathway and inhibit the direct pathway.

As the major input station as well as an information-integration component of the basal ganglia, the striatum plays an important role in avoidance learning. It can be divided into two functionally and chemically distinct modules, called matrix and striosomes. Striosomes receive input from limbic and prefrontal cortex; whereas matrisomes in matrix receive input from virtually the whole cerebral cortex. These two also differ in their projection targets – matrisomes project to the GPe and SNr, whereas striosomes project to SNc. There is also evidence that striosomes can affect matrisomes via large aspiny interneurons, though these two are relatively segregated. In both modules, there are two categories of cells – the medium spiny neurons and aspiny neurons, each of which has distinct neurochemical substance contents and firing pattern. Aspiny inter-neurons also receive excitatory inputs and contributes to determining whether projection neurons (i.e., the medium spiny neurons) fire or not [32, 33]. Medium spiny neurons comprise about 95% of striatal neurons [34]. Their dendritic spines are chemically and electrically segregated compartments that are the sites for the interaction of the glutamate of cortical inputs and the dopamine released from the SNc. Activation of such neurons would require coordinated spatial and temporal convergence of cortical inputs and extensive interaction of glutamate and dopamine [35-40]. As will be discussed in section 2.4, the neuronal activity in the striatum is critical for the avoidance learning mechanism in the basal ganglia.

Investigation into the functional anatomy of the basal ganglia is still ongoing [21, 29, 41-46]. New findings are cropping-up and the old hypotheses are being challenged. For example, STN also receives a large mass of excitatory projections from the cerebral cortex and has dopamine receptors with density similar to that of STR and hence may have afferents from SNc; GPe may be an internal control device as well as a output control device because of its extensive connections with all of the other nuclei in the basal ganglia [27, 28]. Apparently more realistic models are called for to accommodate the new evidences [43].

2.3 Proposed roles of dopamine and the basil ganglia in learned avoidance behavior

Motivated by the research on Parkinson's Disease, the motor functions of the basal ganglia have been the historic focus. For example, the basal ganglia have been believed to be responsible for the selection of actions [47-50] and initiation of movement [23, 45, 51]. Recent findings suggest that they are also involved in learning [52-57], especially when biologically significant rewarding events like food or drink, are involved [58-63].

The basal ganglia also play an important role in the aversive event related behavioral learning. However, this has been neglected until recently. As reviewed by Chudler and Dong [64], electrophysiological, metabolic and blood flow studies show that the basal ganglia are involved in processing noxious somatosensory information. Many neurons in striatum, SN and GP may encode the intensity of noxious stimulus and these may be associated

with the escape or avoidance behaviors. Other neurons in the basal ganglia respond uniquely to noxious stimuli and may signal the occurrence of damaging stimuli or coordinate the response to such stimuli.

A major proportion of evidences concerning the involvement of the basal ganglia in learned avoidance behavior are correlated with the function of the dopamine. The conventional view of role of the dopamine, with respect to the basal ganglia, is that its release correlates with reward-related learning [58, 60, 65, 66] but only recently this point of view is being challenged [57, 67, 68]. The controversy may be caused by the discrepancy between neurophysiological recording of dopamine signal activity and transmitter measurements of dopamine release (Beninger, 1999, personal communication) or the temporal moment when the measurement is made in conditioning (Schultz, 1999, personal communication).

Dopaminergic neurons may respond to stimuli that serve as signals of biologically significant events in both appetitive and defensive (including avoiding) behavior cases [69]. However, dopamine response may be different for appetitive and aversive conditioning. For example, Besson and Louilot noted a rapid and marked dopamine increase and a delayed dopamine decrease in rats presented to the appetitive and the aversive olfactory stimulus respectively [68].

The role of dopamine in avoidance learning is also revealed in lesion tests that disrupt the dopaminergic neurotransmission [70] or dopamine antagonist application that impairs dopamine release [69, 71]. In avoidance tests, for pre-trained rats, the US (e.g., shock) retains their ability to elicit escape behavior; however, repeated trials would make the avoidance response lost gradually; non-pre-trained rats have an impaired ability to learn the avoidance response [71]. Another line of evidence about the dopamine release is obtained with microdialysis that is a sampling method used to measure extracellular concentration of neurotransmitters [72]. In an experiment with aversive (light/tone-shock pairing) conditioning, increases in extracellular dopamine in the nucleus accumbens and striatum were observed when an association is formed between two stimuli of which neither is a biological reinforcer nor, prior to formation of the association, affects dopamine levels [73]. It is suggested that dopamine plays a role in the modulation of associative learning in general, not just that involving reinforcement.

A number of researches have been also conducted on the dopamine release in avoidance learning, targeting the brain structures *other than* the basal ganglia (e.g., [69-71, 74-79]). For instance, increased dopamine release in prefrontal cortex, the working memory [80], has also been observed during avoidance learning [77, 81-83]. It is reasonable to assume that some of these results may lend themselves to explanation of the activities of the dopamine in the basal ganglia, since a large portion of the dopamine released in the mid-brain area including SNc and nucleus accumbens do reach the striatum (and possibly other components) of the basal ganglia as well.

Another notable brain structure related with the basal ganglia is the amygdala. The amygdala is identified as the interface between the sensory system that carry information about the CS and US, and the different motor and autonomic systems that control the conditioned fear reactions [84-86]. As described in Section 2.1, the *fear signal* has a considerable influence on avoidance learning, albeit not without controversy among the avoidance learning theorists. Fear learning is a nonspecific kind of learning that involves many different kinds of responses, particularly of the sympathetic nervous system and hypothalamus-pituitary-adrenal system, as well as behaviors like freezing or fleeing [87]. Since the amygdala has connections with the striatum of the basal ganglia and SN in the midbrain, it provides additional a path for the integration of information in the basal ganglia.

A closely related issue in avoidance learning is the temporal information processing. A number of reaction time experiments have been conducted, which exhibit the role of dopamine in modulating the learning process that involve not only external (environmental) stimuli but also the internal (proprioceptive) stimuli that elicit responses [88-101]. The internal clock used to time duration in the seconds-to-minutes range appears linked to dopamine function in the basal ganglia. Dopamine D_2 receptors plays an important role in determining the rate of temporal integration for time perception, dopamine releasing neurons are involved in temporal integration, and neuroleptic drugs decrease the speed of the internal clock while stimulant drugs increase the clock's speed [102]. Specific levels of dopamine activity (neither too low nor too high) in STR are necessary for correct execution of the movement in a conditioned motor task with temporal constraint. Blockade of D_2 receptors produce an increased number of delayed responses and lengthened reaction time. Intracerebral injection of dopamine in STR has an opposite effect [103], for example, PD patients tend to underestimate time intervals [104].

The mechanism of how the basal ganglia process the vast amount of information fed by the cerebral cortex and what the role of dopamine is during avoidance learning is examined in the next section.

2.4 The learning mechanism in the basal ganglia (Qualitative models)

Although much progress has been made in determining the functional anatomy of the basal ganglia, the information processing mechanisms undertaken by this structure are still largely unknown. The reason that the basal ganglia is difficult to understand is that there is extensive connections between the components of the basal ganglia and between the basal ganglia and other brain structures. This section summarizes some of the recent proposals as to how the basal ganglia perform information processing and learning, paying special attention to the role of the neuromodulator dopamine. It should be pointed out both the reward-related learning and punishment-related learning (including avoidance learning, of course) will be reviewed, not only because of the large amount of literatures are towards the former, but also there is the possibility that both processes may be are subserved by the same mechanism [105].

It has been repeatedly proposed that the corticostriatal synapses where the dopamine and glutamate interact are the site for learning [30, 34, 106-110]. Intense high frequency stimulation induces both long-term depression (LTD) and long-term potentiation (LTP) at the corticostriatal synapses. And the LTD/LTP are regarded as the substrate for learning and memory [111]. Both LTD and LTP at the corticostriatal synapses depend on the interaction between the neurotransmitter glutamate and neuromodulator dopamine and until recently has research shown that dopamine and glutamate affect each other both on a presynaptic and postsynaptic level [35-40, 106]. Normally, the generation of LTD/LTP requires the co-activation of both D_1-like and D_2-like dopamine receptors through dopamine released by nigrostriatal afferents [107]. Graybiel proposed that the modular corticostriatal projection patterns produce the re-coded templates for the gradual selection on new input-output relations [47]. Thus the striatum re-codes the cortically derived information. Graybiel also observed that the modular structure of the corticostriatal complex resembles the adaptive mixture of expert architecture [112], which are similar to multiple model control systems (see [113, 114] for details). Redgrave proposed that the basal ganglia are a centralized selection and switching mechanism, specialized to resolve conflicts or competition over access to limited motor and cognitive resources [115]. In this model, dopamine regulates the frequency and timing of behavioral selections, facilitate or retard switching, or put the basal ganglia into a state of readiness to modify selections based on subsequent experience. Baev used control theory concepts to describe the basal ganglia-thalamocortical loops as modeling and prediction loops and their dopamine enervation as an error distribution system [116].

Kropotov [49], based on data recorded from patients with Parkinson's Disease, proposed a hypothesis of action programming that requires the separation of sensory, motor, and cognitive functions. Kropotov proposed that an action may demand several motor components for its implementation, hence the program for this action should be distributed across the association areas of the cortex. The fact that vast areas of the cortex project to the basal ganglia seems to fit this requirement (while the input source of the cerebellum does not). The theory proposes that the basal ganglia-thalamus circuits play a critical role in initiation of, preparation for, and suppression of actions while the plan of action is stored in inter-cortical network. The execution of action is via the concurrent activation of the basal ganglia loops: initialization and preparation of action is via the direct pathway, while the termination of action is via the indirect pathways. Modules in the striatum are selected if their activity is above a threshold and dopamine is proposed to set the level of the threshold.

Houk et al [61, 117] proposed an influential model of how the basal ganglia predict the occurrence of a rewarding event (stimulus). In their model, the basal ganglia learns to associate patterns of neuronal activity generated by the cortex with the action that must be generated in response to that pattern. Houk et al propose that each striosome in the striatum recognizes, and is enabled by, a distinct pattern of activity generated by the cortex. The pattern of activity generated by the cortex encodes both external (environmental) and internal

(proprioceptive) information. The striosome and matrix modules are responsible for learning, via trial-and-error, the behavior that must be generated in response to the specific cortical activities. The trial-and-error learning is mediated by an internally generated reinforcement signal carried by the dopamine signal that arises from SNc. For goal-directed behavior, the dopamine signal is believed to be an error signal that encodes the difference between expected and actual outcomes of the behavior. This model has been associated with Barto, Sutton, and Anderson's actor-critic reinforcement learning model [118, 119].

Kimura [52] proposed a behavioral learning model of the basal ganglia involving the integration of motivational and motor functions. In this model, limbic input, which conveys information related to reinforcement or incentive, contributes to the acquisition and expression of learned activity in the striatum. Limbic system input either affects the striatum directly or indirectly through the nigrostriatal dopamine system. Kimura proposes that striatal neurons require a phasic supply of nigrostriatal dopamine for learning a new behavioral act as well as a basic tonic supply of dopamine for maintenance of the learned act.

There is a consensus on the role of dopamine in learning: dopamine release in the striatum may be a mechanism by which specific synapses are modified after significant environmental events. Those synapses that were recently active tend to be strengthened, whereas those that were inactive tend to be weakened. As a result, previously innocuous stimuli that precede the occurrence of an unconditionally rewarding stimulus acquire the ability to stimulate dopamine release. These stimuli are now conditioned to eventual reward and become predictors to its occurrence. Wickens and Kotter proposed heterosynaptic reinforcement learning rule involving three factors, presynaptic activity in corticostriatal afferent (carrying situation or state information), postsynaptic activity in striatal output neurons (encoding action), and phasic activity in dopaminergic afferent (the reinforcement signal) [63]. They propose that the interactions among the three factors require strict timing. They suggest that there is competition among pathways in the cortico-striatal-thalamic-cortical loop that can be used to select the cortical cell assemblies that maximize expected reinforcement.

The dominant view is that the output of dopaminergic neurons encode an error in the learning system's prediction of reward. Thus they may provide an excellent reinforcement signal for inducing synaptic changes necessary for learning reward-directed behavior [120, 121]. In behavioral experiments with primates, Schultz and his team observed that dopamine neurons are activated by unpredicted rewards, are not influenced by predicted rewards, and are depressed when a predicted reward is omitted. After conditioning, they respond to reward-predicting stimuli in a similar manner [58, 60, 66, 121, 122].

Beninger et al associate the role of the dopamine signal with incentive motivational learning that is similar to reinforcement learning [123]. They proposed a model of the interaction of dopamine and glutamate in the striatum to explain incentive learning (see [124]). They regard the conditioning process as the shifting of

affective value of reward from unconditioned stimuli to conditioned stimuli. This affective value is critical for a stimulus to induce response. They further differentiated the roles of dopamine signals at D_1-like and D_2-like receptors based on the inferences drawn from a series of psychopharmacological experiment [55, 123, 125]. They concluded that actions of D_1-like receptor may be related more closely to their motor effects whereas D_2-like dopamine receptor antagonists may reduce reward. A rewarding signal at D_1-like receptors may mediate both the acquisition of rewarding properties by neutral stimuli and their ability to control behavior [125].

Different views exist opposing the role of dopamine as reinforcement signal. By examining the most commonly used reinforcement learning algorithms and the basal ganglia architectures, Pennartz [126] summarized several criteria that are critical to reinforcement signals and then compared each of them to the characteristics of dopamine. He concluded that dopamine does not fit all of the criteria and may not represent a reinforcement signal. However, it is possible that dopamine signal constitutes only one of the different reward signals existing in the central nervous system. All the reward signals including dopamine may function cooperatively to make optimal use of rewards for learning and behavior [121].

As mentioned in last section, a closed related issue in avoidance learning is the temporal information processing. While many brain structures may be responsible for this [104], specifically, the basal ganglia has been proposed as a timing mechanism [102, 127] responsible for the scale of second. Meck proposed a three-component clock-counter system existing in the basal ganglia based on scalar timing theory. In his model, SNc is the pacemaker, while STR gating, and GPi would be the integration component. D_2 play a major role in determining the rate of temporal integration for time perception.

While the descriptive models accounted above describe some features of the information processing in the basal ganglia, they are imprecise. Computational models are called for to order to resolve this problem. In next section we will review the computational models related to behavioral learning and the basal ganglia function.

2.5 Computational models of Basal ganglia and the learned avoidance behavior

Despite of the importance of the learned avoidance behavior, the number of computational models accounting for it is limited. Even for the limited number of models, none is biologically plausible. In this chapter, we first review these models and then review the computational models concerning the functions of dopamine and the basal ganglia. The latter would provide biological constraints as to how the computational model should work [128] and also provide biological insight into how the model should be built [129]. Consider the controversies about the factors involved in explaining the learned avoidance behavior, a computational model can, to some extent, help to resolve this problem from a computational point of view.

2.5.1 Computational models of the learned avoidance behavior

Behavioral learning modeling requires either classical conditioning modeling or instrumental conditioning modeling or both. For instance, the modeling of avoidance learning using two-factor theory needs modeling both the classical and instrumental conditioning processes. Of the classical conditioning models, Klopf's drive-reinforcement (DR) neuronal model [130] may be the most biologically rigorous model [131]. Adopting a modified hebbian learning rule [132], the DR model can predict seventeen classical conditioning phenomena including the S-shaped learning curve, that is much more realistic and more comprehensive than the other classical conditioning models. A class of classical conditioning models including DR model was reviewed and formalized by Malaka [133].

Using DR neuron model as a building block, Klopf et al [134] further developed a learning structure called associate control process network (ACP) that meant to model the nervous system function during classical and operant conditioning. This model was then modified and simplified by Baird and Klopf [135]. Despite of their capability, these models have difficulty in accounting for learned avoidance behavior.

Johnson et al [136] built computational model of avoidance behavior by extending the ACP model. This model can mimic a rat's avoidance behavior in a one-way shuttle-box experiment and can be roughly mapped to the structure of the basal ganglia. The proposed research is based upon this work, as is discussed in next chapter.

Another notable computational model of avoidance behavior was by Schmajuk [137]. His model is based on the two-factor theory and has a classical conditioning component (to learn an internal model of environment) and an instrumental conditioning component (to learn behavioral strategies). Although this model can account for many features that characterize avoidance behavior, it lacks biological plausibility.

While many models use neural networks (see [138] for an introduction) as a form of representation, it does not necessarily mean that the neural networks can be mapped to certain brain structures. In the following subsection, we examine the features of computational models related with the basal ganglia structure and dopamine function.

2.5.2 Computational Models related with the Basal Ganglia and dopamine

Compared with the number of qualitative models that lack analytical exploration, there are fewer computational models of the basal ganglia. A computational model would allow us to explore the functions of the basal ganglia extensively in a predictive manner. In this chapter, we will briefly review those models in this section. Suri and Schultz [139] implemented a temporal-difference reinforcement learning algorithm (see [140] an explanation) to learn a sequence of actions. Associating the internal reinforcement signal with characteristics of the DA signal, this model resembles Houk's qualitative model [61]. Another model that employs the structure of

Houk's model is by Salum et al [141]. It models the function of the striatal dopamine in attentional learning. In a model that predict the effect of neuroleptics on motor responses, dopamine was coded as a gain factor in an artificial neuron's activation function [142]. A change in the dopamine level would change the slope and threshold of the transfer function, which accordingly affects the performance at the behavioral level. The same concept has also been implemented in a neural network model that tests the effects of dopamine on selective attention [143].

Berns and Sejnowski [144] proposed a computational model of the basal ganglia that resembles a dual circuit model except the addition of corticosubthalamic pathway and the omission of SNc/SNr. They propose that the corticosubthalamic pathway inhibits actions that have recently been selected. This model can learn to select an action, store it in the prefrontal cortex, and also generate sequences of actions. A recent model built by the Berns and Sejnowski [145] proposed that DA projects diffusely to almost every component of the basal ganglia and that it represents a prediction error. They propose that the recursive loop between the GPe and STN functions as local working memory, although no evidence was cited to support their hypothesis.

Jackson and Houghton proposed a neural network model that addressed spatial attention problem [48]. They proposed that one information processing role was to highlight difference between active and suppressed regions of the basal ganglia. Their model functions as an attentional amplifier, enhancing behaviorally relevant neuronal activity and suppressing irrelevant activity.

Each of the computational models reviewed above describes some features of the basal ganglia structure or the functions of dopamine. In next chapter, we will describe the proposed computational model that has these features and can explain the learned avoidance behavior as well.

3. A New Computational Model of Learned Avoidance Behavior

The new computational model of learned avoidance behavior is based upon the ACP model proposed by Klopf, Morgan and Weaver [134]. It is a control-theoretic model of sensorimotor, limbic, and hypothalamic nervous system function. Their model consists of a learning system that is composed of input sensors, output effectors, and a hierarchical network of control systems. Each control system is capable of learning and is called an associative control process (ACP). The model incorporates three characteristics of animal learning: time, goal-driven behavior, and a closed-loop between the learning system and the environment. Klopf, et al [134] proposed that learning is dependent on two different processes. The first is modeled by a reinforcement center that utilizes the drive-reinforcement learning mechanism [130]. The second is modeled as a motor center that associates the current stimuli with a learned response. The ACP model is conceptually similar to the actor-critic models that have been previously proposed [118, 119, 125, 140].

In this research, we extend the capabilities of the ACP network to include learned avoidance behavior. We account for the unique temporal characteristics of learned avoidance behavior by incorporating proprioceptive stimuli and utilizing Anger's theory of conditioned aversive temporal stimuli [146]. We then try to map the learning mechanism to the structure of the basal ganglia.

3.1 The model

Our computational model of avoidance behavior consists of a learning system engaged in real-time, closed-loop, goal-directed interactions with the environment. The learning system, shown in Figure 3.1, is composed of a reinforcement element, a behavior element, sensors, and a tapped delay-line and decoder. The set of sensors can detect externally produced stimuli and proprioceptive feedback. The output of the decoder represents the current state of the learning system and environment as a pair (as sensed by the learning system).

The learning system has one behavior element for each class of behaviors available to it. We propose that, at least at the level of the control system modeled here, behaviors are grouped into classes by the similarity of the goal of the behavior not by the similarity of the behavior itself. The role of the behavior element is to generate a prediction of future benefit that is based on the current state of the learning system and the characteristic behavior of the element. Such a prediction has been labeled Q-learning [147]. In these experiments, it was assumed that the learning system performs the behavior that has the greatest prediction of future benefit.

In this paper we focus on the role of the reinforcement element. The equations that govern a reinforcement element are from Baird and Klopf [135]. The input output equation is:

$$V_i(t) = f\left[\sum_j \left(w_{ij}^+(t) + w_{ij}^-(t)\right)x_j(t)\right] \qquad (1)$$

where f is a ramp function with minimum and maximum limits of 0 and 1, respectively. The output, $V_i(t)$, is the predicted future reinforcement of the i^{th} behavior from the current state.

An ACP is a temporal-difference [140] learning mechanism that adapts to eliminate errors between temporally

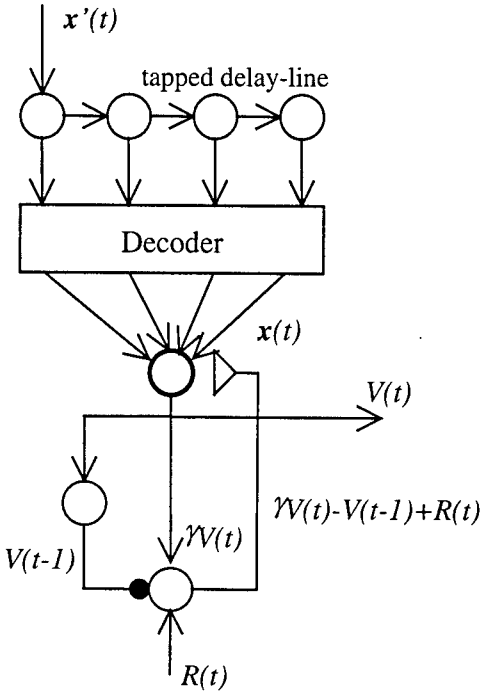

Figure 3.1 Diagram of an ACP. Thin circles are delay elements, or simple computing elements. Thicker circle is the site of learning. The stimulus $\boldsymbol{x}'(t)$ is transformed via a tapped delay-line to $\boldsymbol{x}(t)$. The prediction of the ACP is $V(t)$.

successive predictions. The learning equation is

$$\Delta w_{ij}(t) = \alpha(i) e \sum_{k}^{\tau} c_k \left| w_{ij}(t-k) \right| x(t-k), \tag{2}$$

where e is short-hand notation for

$$\gamma V(t) - V(t-1) + R(t). \tag{3}$$

3.1.1 Tapped delay-line and decoder

Time plays a significant role in learning. In experiments in which explicit information on the passage of time is not supplied, subjects are still able to condition to the duration of a stimulus or the duration of the offset of a stimulus, as in an avoidance schedule [148]. Anger [146] considered the role of time in learning when he proposed his theory of Conditioned Aversive Temporal Stimuli as an explanation of Sidman avoidance behavior. Anger suggested that animals have an internal mechanism that generated events that "change in a consistent way

with time after the last response, reinforcement, etc. These events *function* like external stimuli, at least to the extent that differences in responding can be conditioned to these organism differences" (italics his, p 479). The internally generated temporal stimuli provide the animal with additional cues for conditioning.

A tapped delay-line and decoder can simulate the internal mechanism postulated by Anger. The tapped delay-line receives input from sensory systems and feedback from motor neurons generating behavior. The tapped delay-line samples the output of the neurons at a constant interval as determined by cell function. The decoder translates this information into a pattern of activity that is a function of the externally and proprioceptive stimuli and time. This structure provides a type of counter that resets after the occurrence of each external stimulus. Tapped delay-lines and decoders have been hypothesized by Zisper [149]; implemented in a model of classical conditioning by Moore, Desmond, and Berthier [150]; and possible tapped delay-line structures have been noted in the brain [151-153].

3.1.2 Generalization

Reinforcement in an instrumental conditioning experiment is a function of stimulus (state) and response (action) of the subject while reinforcement in a classical conditioning experiment is a function of the stimulus, alone. The ACP network stores information in state-action pairs thus allowing it to master the instrumental conditioning paradigm. But it, or any learning system that stores information in state-action pairs, or Q-values [147], will have difficulty mastering classical conditioning experiments because of the learning system's inability to generalize across the action space. Without generalization, to learn state dependent information, the ACP network must attempt each of its possible behaviors in every state it experiences. This is not a biologically plausible explanation of animal learning. The ability to generalize over actions is a critical trait of animal learning.

Generalizing over actions is accomplished by changing the weights of all ACPs by an amount equal to half the error in the prediction. Thus, half of the error is independent of action, making it state dependent. This approach to generalization is attractive because it does not require additional ACPs, learning equations, memory, or interconnections. A single set of weights for each ACP can incorporate both the action and state dependent knowledge. The only change to the learning equation is the addition of a learning parameter, $\alpha(i)$, that is a function of the current action.

3.3 Method

In the following experiments, the learning system has thee classes of behaviors: foraging, freezing (remaining still), and fleeing. In the absence of a learned preference for behavior, there is a prior (innate) priority of behavior. Foraging is the preferred behavior in naïve animals. That is, all things being equal, the animal would forage before freeze, and freeze before flee.

3.3.1 One-way shuttle-box avoidance experiment

The learning system was trained in a simulation of a one-way shuttle-box. The shuttle-box had two sides, A and B. The experiment consisted of multiple trials with each trial beginning by placing the learning system in Side A. The learning system was allowed to habituate to its placement in Side A by presenting the learning system with the same decoder output, $\boldsymbol{x}(t)$, for τ time-steps. Although theoretically impossible, this simple step prevented the learning system from conditioning to the start of the trial and allowed us to avoid the complex issues of selective attention.

The warning signal was presented to the learning system after habituation. If the learning system did not perform the avoidance response (flee) within eight time-steps, shock was applied and the trial was ended. If the learning system generated the avoidance response within the allotted time, the learning system moved into Side B, the warning signal was terminated, and shock was avoided. The trial ended with the learning system in Side B. Figure 3.2(a) is a state transition diagram of the one-way shuttle-box environment.

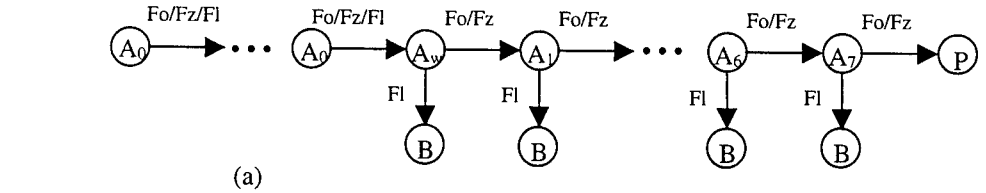

(a)

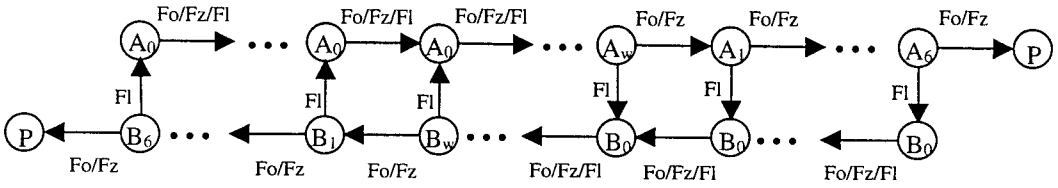

(b)

Figure 3.2 State transition diagram of (a) one-way shuttle-box experiment and (b) two-way shuttle-box experiment. Allowable behaviors are forage (Fo), freeze (Fz) and flee (Fl). Multiple A_0 and B_0 states result in habituation of the learning system to its environment. States A_w and B_w correspond to the warning lights, state P corresponds to punishment, and state B corresponds to the safety side in the one-way shuttle-box experiment.

3.3.2 Two-way shuttle-box avoidance experiment

In the two-way shuttle-box experiment, the learning system could receive shock in both sides of the shuttle-box. The learning system was allowed sufficient time to habituate to side A before warning signal was presented.

Shock was applied and the trial was ended if the learning system did not make the avoidance response (flee) within six time-steps. If the learning system generated the avoidance response, it would enter side B, the warning signal would be terminated, and shock would be avoided. However, the trial did not end. Instead, the learning system was allowed to habituate to side B before a second warning signal, different from the warning signal in side A, was presented. The learning signal had six time-steps to make the avoidance response (flee) before shock was applied. If the learning system made the avoidance response, it would enter side A, the warning signal would be terminated, and shock would be avoided. Again, the learning system would be allowed to habituate to side A before the cycle repeated itself. A single trial could continue indefinitely as long as the learning system continues to make the avoidance response. Figure 2(b) is a state-transition diagram of the two-way shuttle-box experiment.

3.4 Experimental Results

3.4.1 One-way shuttle-box experiment

Figure 3.3 is a graph of the response latency versus trial number for the one-way shuttle-box experiment. The dashed line indicates the onset of shock, and thus the end of the trial. The first two trials ended in punishment. The next three trials showed progressively faster response times. In all subsequent trials the learning system generated the avoidance response within one time step after the presentation of the warning signal. Figure 3.4 is a graph of the rate of correct responses versus trial number for the one-way shuttle-box experiment.

3.4.2 Two-way shuttle-box experiment

Figure 3.5 is a graph of the total time of shock avoidance versus trial number. The learning system avoided shock for progressively longer times until after the fourth trial when it avoided shock until the experimenter terminated the trial. The graph shows that on the third trial, the learning system made its first successful avoidance to side B but it failed to avoid shock while in side B. This is to be expected because the experiment reduced the possibility of any generalization by using different warning signals.

3.5 Discussion

We have presented a computational model of a process that controls the selection of voluntary behavior during avoidance conditioning. A model such as this is only useful if it helps us understand the neural mechanism responsible for these processes. To that end we attempt to map our model to the neuroanatomy and neurophysiology thought to govern the initiation of voluntary motor responses.

There is increasing evidence in neural science research that suggests that dopamine neurons in the basal ganglia provide internal reinforcement signals during motor learning (see [61] for an excellent reference). Houk et al [61] has drawn an analogue of cerebral cortex and striatum structure to Barto and Suton's [119] actor-critic

architecture. In this section, we wish also to map our model to the known neurophysiology. The simplified schema of interactions of cerebral cortex and components of basal ganglia is shown in Figure 3.6.

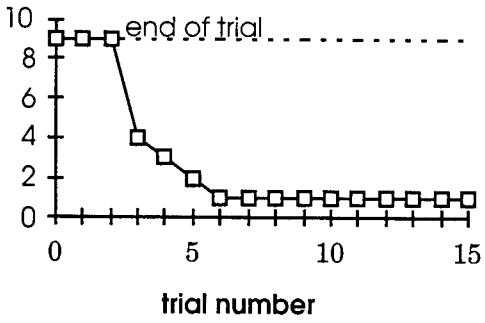

Figure 3.3. Graph of response latency versus trial number for the one-way shuttlebox experiment.

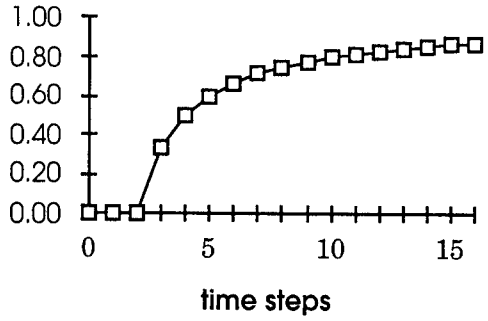

Figure 3.4 Graph of correct response frequency versus trial number for the one-way shuttle-box experiment.

In Figure 3.6, the bottom right module is believed to act as a reinforcement center (RC) which provides an internal reinforcement signal for the motor centers (MC) shown in the bottom left module and itself. The large number of projections from the cells in cerebral cortex to the SP_s in the basal ganglia represent the decoded sensory input patterns, and SP_s provide the sites for pattern recognition [117].

As proposed by other researchers, we also propose that the dopamine neuron is the site for error signal detection. Its inputs include the primary reinforcement signal, excitatory signals from SP_s and an inhibitory component of last time step's output. Our model predicts that it is the output of the SP_s, not the dopamine neurons that influence learning in the motor centers. The primary support for our approach is the fact that an error signal does not provide a useful method for reinforcing appropriate behavior, only suppressing incorrect behavior.

While each matrix SP generates a behavioral signal (Forage, Freeze, or Flee, as in Figure 2), there is competition among them because of lateral inhibition. The winning matrix, that is the matrix whose behavior controlled the learning system, would modify its synaptic strengths facilitated by internal reinforcement input.

There exists another possibility that the action, or command, signals from the pallidal neurons act upon SP_s either through direct pathways or via other components in the striatum or cortex. The neurons of the frontal cortex are believed to be the site of working memory as it is there where behavioral information generated by matrix modules is registered. In this case, the function of SP_s would be to select from its inputs (using temporal-difference methods) according to the maximum output of SP_m neurons, then transmit the result to DA neurons to generate the internal reinforcement signal.

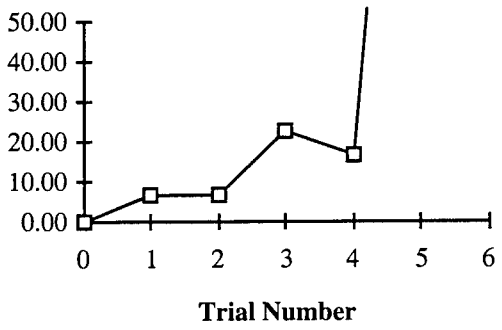

Figure 3.5 Graph of time of avoidance versus trial number for the two-way shuttle-box experiment.

The above explanation is clearly a simplistic one considering that there are a large number of connections between the cerebral cortex and the basal ganglia and we show only a few. In addition, we only briefly discuss the role of other components such as the thalamus. However, supporting evidences on the side of the basal ganglia are listed in the following:

- STR is site for information integration. As the target of most extrinsic and intrinsic striatal afferents from cerebral cortex, the thalamus, and SNc, the medium spiny neurons (SP_s) in the striatum are believed to be the site where the interaction between nigral dopaminergic and corical glutamatergic inputs [27]. SP_s neurons can be regarded as relatively isolated biochemical compartments and their activities have been suggested to be mutually inhibitory. This can be modeled as a winner-take-it-all mechanism [144].

- STR can be divided into two large segregated compartments according to both chemical make-ups and projection targets [31]. One compartment is called the striosome module and it receives afferents from limbic system and SNc and projects back to SNc. The striosomes are believed to be the site where motivation-related information is processed. The second compartment is called the matrix module that receives afferents from vast areas of the cerebral cortex and project to the globus pallidus. The two types of compartments in the striatum are represented in our model by the reinforcement and motor centers.

- The firing patterns of DA signal from SNc has the characteristic of showing the error of the prediction and the actually the reinforcement outcome [58, 60, 66, 121]. In our model, it has been modeled as the TD factor.

- Eligibility: DA chemical may leave a trace for the recently activated synapses to be modified. DA receptivity is a potential for reinforcement that becomes elevated after and decays slowly over time [61]. The cortical presynaptic activity and concurrent striatal postsynaptic activation may elevate spine calcium concentration that could persist for tens or hundreds of milliseconds. This elevated calcium could serve as the physical basis of the eligibility trace [63]. The firing patterns of DA signal from SNc has the characteristic of showing the error of the prediction and the actually the reinforcement outcome [58, 60, 66, 121]. In our model, it has been modeled as the TD factor.

- The evidence for the mutual inhibitory properties among the RCs and MCs in our model is that the neuronal modules in the striatum can be mutually inhibitory as shown by computer simulation [154].

- The mechanism of generalization in the action space employed in our model can be realized through the activity of tonically active neurons which are thought to be inter-neurons in the striatum [52, 155, 156].

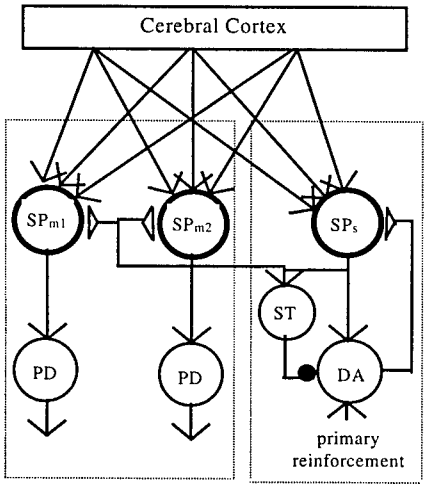

Figure 3.6. Schema of interactions of cerebral cortex and components of the basal ganglia. Some side loops and pathways are not shown. SP_s: spiny neuron in striasome; Sp_m:spiny neuron in matrix module; PD: pallidal neuron; DA: dopamine neuron; ST: subthalamus; other symbols are the same as in figure 3.1.

Despite the above mappings, there exists some mismatching between the ACP structure and the basal ganglia. For example, the multiple copies of past values of each connection weight (the set of $w(t\text{-}j)$ in Equation 2) have to be kept for learning. Another is the requirement of both excitatory and inhibitory weights are needed for each synaptic connection (w^+ and w^- in Equation 1). These requirements are not physiologically plausible. Further work is needed to make the model more biologically plausible.

4. Conclusion

We have shown the psychological models believed to be the basis for learned avoidance behavior. We have implemented a model of such behavior that replicates known observable animal behavior and also maps well to the brain structures believed to be responsible for this behavior. We believe that this report documents an important step toward imbuing unmanned air vehicles with learned avoidance behavior, and ability critical to the improved survivability of the aircraft.

Bibliography

1. Wall, R., *Recon Architecture Presages Changes*, in *Aviation Week & Space Technology*. 1998. p. 48-49.

2. Roos, J.G., *Expanding: US unmanned aerial vehicle programs now range from lightweight reconnaissance aircraft to heavyweight attack platforms*, in *Armed Forces Journal International*. 1998. p. 26-28.

3. Overmier, J.B. and T. Archer, *Historical perspectives on the study of aversively motivated behavior: history and new look*, in *Aversion avoidance, and anxiety: perspective on aversively motivated behavior*, T. Archer and L.G. Nilsson, Editors. 1989, Hillsdale, N.J. : Lawrence Erlbaum Associates. p. 3-15.

4. Solomon, R.L., L.J. Kamin, and L.C. Wynne, *Traumatic avoidance learning: The outcomes of several extinction procedures with dogs.* Journal of Abnormal and Social Psychology, 1953. **48**: p. 291-302.

5. Pavlov, I.P., *Conditioned reflexes*. 1927, London: Oxford University Press.

6. Tarpy, R.M., *Contemporary learning theory and research*. 1997: New York : McGraw-Hill. 625.

7. Thorndike, E.L., *Animal intelligence. An experimental study of the associative process in animals.* Psychological Monographs, 1898. **2**(8).

8. Mower, O.H., *On the dual nature of learning: A re-interpretation of "conditioning" and "problem-solving"*. Harvard Educational Review, 1947. **17**: p. 102-148.

9. Miller, N.E., *Studies of fear as an acquirable drive: I. Fear as motivation and fear-reduction as reinforcement in the learning of new responses.* Journal of Experimental Psychology, 1948. **38**: p. 89-101.

10. Solomon, R.L. and L.C. Wynne, *Traumatic avoidance learning: The principles of anxiety conservation and partial irreversibility.* Psychological Review, 1954. **61**: p. 353-385.

11. Kamin, L.J., C.J. Brimer, and A.J. Black, *Conditioned suppression as a monitor of fear of CS in the course of avoidance training.* Journal of comparative and physiological psychology, 1963. **56**: p. 497-501.

12. Smith, J.E. and D.J. Levis, *Is fear present following sustained avoidance responding?* Behavioral Processes, 1991. **24**: p. 37-47.

13. Bolles, R.C., *Reinforcement expectancy, and learning.* Psychological Review, 1972. **79**: p. 394-409.

14. Seligman, M.E.P. and J.C. Johnston, *A cognitive theory of avoidance learning*, in *Contemporary approaches to conditioning and learning*, F.J. McGuigan and D.B. Lumsden, Editors. 1973, Winston-Wiley: Washington, DC.

15. Herrnstein, R.J., *Method and theory in the study of avoidance.* Psychological review, 1969. **76**: p. 49-69.

16. Mazur, J.E., *Learning and behavior*. third ed. 1994, NJ: Prentice Hall.

17. Herrnstein, R.J. and H.P. N., *negative reinforcement as shock-frequency reduction.* Journal of experimental analysis of behavior, 1966. **9**: p. 421-430.

18. Bolles, R.C., *Species-specific defense reactions*, in *Aversive conditioning and learning*, F.R. Brush, Editor. 1970, Academic Press: New York. p. 183-233.

19. Gray, J.A., *The psychology of fear and stress*. 1987: Cambridge ; New York : Cambridge University Press.

20. McAllister, D.E. and W.R. McAllister, *Fear theory and aversively motivated behavior: some controversial issues*, in *Fear, avoidance, and phobias : a fundamental analysis*, M.R. Denny, Editor. 1991, Hillsdale, N.J. : L. Erlbaum Associates. p. 135-163.

21. Lee, *et al.*, *The anatomy of the basal ganglia and Parkinson's disease: a review.* Singapore Med J, 1995. **36**(1): p. 74-6.

22. Marsden, C., *Function of the basal ganglia as revealed by cognitive and motor disorders in Parkinson's disease.* Can J Neurol Sci, 1984. **11**(1 Suppl): p. 129-35.

23. Albin, R.L., A.B. Young, and J.B. Penney, *The functional anatomy of basal ganglia disorders.* TRENDS IN NEUROSCIENCES, 1989. **12**(10): p. 366-375.

24. Obeso, J.A., *The basal ganglia and new surgical approaches for Parkinson's disease.* Advances in neurology. Vol. 74. 1997.

25. Obeso, J.A., M.C. Rodriguez, and M.R. DeLong, *Basal Ganglia Pathophysiology: A Critical Review*, in *The basal ganglia and new surgical approaches for Parkinson's disease*, J.A. Obeso, Editor. 1997: Philadelphia: Lippincott-Raven. p. 3-18.

26. Wiesendanger, *Motor functions of the basal ganglia.* Appl Neurophysiol, 1986. **49**(5): p. 269-77.

27. Parent, A. and L.-N. Hazrati, *Functional anatomy of the basal ganglia. I. The cortico-basal ganglia-thalamo-cortical loop.* Brain Research Reviews, 1995. **20**(1): p. 91-127.

28. Parent, A. and L.-N. Hazrati, *Functional anatomy of the basal ganglia. II. The place of subthalamic nucleus and external pallidum in basal ganglia circuitry.* Brain Research Reviews, 1995. **20**(1): p. 128-154.

29. Smith, Shink, and Sidibé, *Neuronal circuitry and synaptic connectivity of the basal ganglia.* Neurosurg Clin N Am, 1998. **9**(2): p. 203-22.

30. Strick, P.L., R.P. Dum, and N. Picard, *Macro-organization of the circuits connecting the basal ganglia with the cortical motor areas*, in *Models of information processing in the basal ganglia*, J.C. Houk, J.L. Davis, and D.G. Beiser, Editors. 1995, Cambridge, Mass. : MIT Press. p. 117-130.

31. Graybiel, A.M. and M. Kimura, *Adaptive neural networks in the basal ganglia*, in *Models of information processing in the basal ganglia*, J.C. Houk, J.L. Davis, and D.G. Beiser, Editors. 1995, Cambridge, Mass. : MIT Press. p. 103-116.

32. Kawaguchi, Y. and Y. Kubota, *Local circuit neurons in the frontal cortex and the neostriatum*, in *Functions of the cortico-basal ganglia loop*, M. Kimura and A.M. Graybiel, Editors. 1995: Tokyo ; New York : Springer. p. 73-88.

33. Kawaguchi, Y., *Neostriatal cell subtypes and their functional roles.* Neuroscience Research, 1997. **27**(1): p. 1-8.

34. Groves, P.M., *et al.*, *Elements of the Intrinsic Organization and Information Processing in the Neostriatum*, in *Models of information processing in the basal ganglia*, J.C. Houk, J.L. Davis, and D.G. Beiser, Editors. 1995, Cambridge, Mass. : MIT Press. p. 51-96.

35. Calabresi, P., *et al.*, *Synaptic plasticity and physiological interactions between dopamine and glutamate in the striatum.* Neurosci Biobehav Rev, 1997. **21**(4): p. 519-23.

36. Amalric, M., *et al.*, *Functional interactions between glutamate and dopamine in the rat striatum.* Neurochem Int, 1994. **25**(2): p. 123-31.

37. Greenamyre and Jt, *Glutamate-dopamine interactions in the basal ganglia: relationship to Parkinson's disease.* J Neural Transm Gen Sect, 1993. **91**(2-3): p. 255-69.

38. Lange, K.W., J. Kornhuber, and P. Riederer, *Dopamine/Glutamate Interactions in Parkinson's Disease.* Neuroscience & Biobehavioral Reviews, 1997. **21**(4): p. 381-524.

39. Starr, M., *Editorial to the special issue on the interaction of dopamine and glutamate in the Basal Ganglia.* Neuroscience & Biobehavioral Reviews, 1997. **21**(4): p. 1-1.

40. Wan, F.J., M.A. Geyer, and N.R. Swerdlow, *Presynaptic dopamine-glutamate interactions in the nucleus accumbens regulate sensorimotor gating.* Psychopharmacology (Berl), 1995. **120**(4): p. 433-41.

41. Levy, *et al.*, *Re-evaluation of the functional anatomy of the basal ganglia in normal and Parkinsonian states.* Neuroscience, 1997. **76**(2): p. 335-43.

42. Féger, *Updating the functional model of the basal ganglia [letter; comment].* Trends Neurosci, 1997. **20**(4): p. 152-3.

43. Albin, R.L., A.B. Young, and J.B. Penney, *The functional anatomy of disorders of the basal ganglia.* TRENDS IN NEUROSCIENCES, 1995. **18**(2): p. 63-64.

44. Wichmann, T. and M. DeLong, *Functional and pathophysiological models of the basal ganglia.* Curr Opin Neurobiol, 1996. **6**(6): p. 751-8.

45. Chesselet, M.-F. and J.M. Delfs, *Basal ganglia and movement disorders: an update.* Trends In Neurosciences, 1996. **19**(10): p. 417-422.

46. Bergman, H., *et al.*, *Physiological aspects of information processing in the basal ganglia of normal and parkinsonian primates.* Trends In Neurosciences, 1998. **21**(1): p. 32-38.

47. Graybiel, A., *The basal ganglia and chunking of action repertoires.* Neurobiol Learn Mem, 1998. **70**(1-2): p. 119-36.

48. Jackson, S. and G. Houghton, *Sensorimotor Selection and the Basal Ganglia: A Neural Network Model*, in *Models of information processing in the basal ganglia*, J.C. Houk, J.L. Davis, and D.G. Beiser, Editors. 1995, Cambridge, Mass. : MIT Press. p. 337-374.

49. Kropotov, J.D. and S.C. Etlinger, *Selection of actions in the basal ganglia-thalamocortical circuits: review and model.* International Journal Of Psychophysiology, 1999. **13**(3): p. 197-217.

50. Mink, J.W., *The basal ganglia: focused selection and inhibition of competing motor programs.* Progress in Neurobiology, 1996. **50**(4): p. 381-425.

51. Brooks, D.J., *The role of the basal ganglia in motor control: contributions from PET.* Journal of the Neurological Sciences, 1995. **128**(1): p. 1-13.

52. Kimura, M., *Role of basal ganglia in behavioral learning.* Neuroscience Research, 1995. **22**(4): p. 353-358.

53. Pennartz, C.M.A., *Reinforcement learning by hebbian synapses with adaptive thresholds.* Neuroscience, 1995. **81**(2): p. 303-319.

54. Hasselmo and Me, *Neuromodulation and cortical function: modeling the physiological basis of behavior.* Behav Brain Res, 1995. **67**(1): p. 1-27.

55. Beninger, R.J. and R. Miller, *Dopamine D1-like Receptors and Reward-related Incentive Learning.* Neuroscience & Biobehavioral Reviews, 1998. **22**(2): p. 335-345.

56. Beninger, R.J., *The role of dopamine in locomotor activity and learning.* Brain Res, 1983. **287**(2): p. 173-96.

57. Spanagel, R. and F. Weiss, *The dopamine hypothesis of reward: past and current status.* Trends in Neurosciences, 1999. **22**(11): p. 521-527.

58. Schultz, *Predictive reward signal of dopamine neurons.* J Neurophysiol, 1998. **80**(1): p. 1-27.

59. Graybiel, *et al.*, *The basal ganglia and adaptive motor control.* Science, 1994. **265**(5180): p. 1826-31.

60. Schultz, W., P. Dayan, and P.R. Montague, *A neural substrate of prediction and reward.* Science, 1997. **275 (Mar. 14 '97)**((Mar. 14 '97)): p. 1593-9.

61. Houk, J.C., J.L. Adams, and A.G. Barto, *A model of how the basal ganglia generate and use neural signals that predict reinforcement*, in *Models of information processing in the basal ganglia*, J.C. Houk, J.L. Davis, and D.G. Beiser, Editors. 1995, Cambridge, Mass. : MIT Press. p. 249-270.

62. Houk and Jc, *On the role of the cerebellum and basal ganglia in cognitive signal processing.* Prog Brain Res, 1997. **114**: p. 543-52.

63. Wickens, J. and R. Kotter, *Cellular Models of Reinforcement*, in *Models of information processing in the basal ganglia*, J.C. Houk, J.L. Davis, and D.G. Beiser, Editors. 1995, Cambridge, Mass. : MIT Press. p. 187-214.

64. Chudler, E.H. and W.K. Dong, *The role of the basal ganglia in nociception and pain.* Pain, 1995. **60**(1): p. 3-38.

65. Mirenowicz, J. and W. Schultz, *Preferential activation of midbrain dopamine neurons by appetitive rather than aversive stimuli.* Nature, 1996. **379**(6564): p. 449-51.

66. Schultz, W., *et al.*, *Reward-related Signals Carried by Dopamine Neurons*, in *Models of information processing in the basal ganglia*, J.C. Houk, J.L. Davis, and D.G. Beiser, Editors. 1995, Cambridge, Mass. : MIT Press. p. 233-248.

67. Redgrave, P., T.J. Prescott, and K. Gurney, *Is the short-latency dopamine response too short to signal reward error?* Trends in Neurosciences, 1999. **22**(4): p. 146-151.

68. Besson, C. and A. Louilot, *Striatal dopaminergic changes depend on the attractive or aversive value of stimulus.* Neuroreport, 1997. **8**(16): p. 3523-6.

69. Blackburn, J.R., J.G. Pfaus, and A.G. Phillips, *Dopamine functions in appetitive and defensive behaviours.* Prog Neurobiol, 1992. **39**(3): p. 247-79.

70. Cooper, B.R., *et al.*, *Effects of 6-hydroxydopamine treatments on active avoidance responding: evidence for involvement of brain dopamine.* J Pharmacol Exp Ther, 1973. **185**(2): p. 358-70.

71. Beninger, R.J., *The role of serotonin and dopamine in learning to avoid aversive stimuli*, in *Aversion avoidance, and anxiety : perspective on aversively motivated behavior /*, T. Archer and L.G. Nilsson, Editors. 1989, Hillsdale, N.J. : Lawrence Erlbaum Associates. p. 265-282.

72. Westerink, B.H.C., *Brain microdialysis and its application for the study of animal behaviour.* Behavioural Brain Research, 1995. **70**(2): p. 103-124.

73. Young, A.M., *et al.*, *Increased extracellular dopamine in the nucleus accumbens of the rat during associative learning of neutral stimuli.* NEUROSCIENCE, 1998. **83**(4): p. 1175-1183.

74. White, I.M. and G.V. Rebec, *Performance on a lever-release, conditioned avoidance response task involves both dopamine D1 and D2 receptors.* Eur J Pharmacol, 1994. **253**(1-2): p. 167-9.

75. Talalaenko, A.N., *et al.*, *The role of dopaminergic mechanisms on the brain in various models of anxious states.* Neurosci Behav Physiol, 1994. **24**(3): p. 284-8.

76. Taboada, M.E., *et al.*, *The actions of dopaminergic and noradrenergic antagonists on conditioned avoidance responses in intact and 6-hydroxydopamine- treated rats.* Psychopharmacology (Berl), 1979. **62**(1): p. 83-8.

77. Sokolowski, J.D., L.D. McCullough, and J.D. Salamone, *Effects of dopamine depletions in the medial prefrontal cortex on active avoidance and escape in the rat.* Brain Res, 1994. **651**(1-2): p. 293-9.

78. Salamone, J.D., *The involvement of nucleus accumbens dopamine in appetitive and aversive motivation.* Behav Brain Res, 1994. **61**(2): p. 117-33.

79. Koob, G.F., *et al.*, *Neuroleptic-like disruption of the conditioned avoidance response requires destruction of both the mesolimbic and nigrostriatal dopamine systems.* Brain Res, 1984. **303**(2): p. 319-29.

80. Gabrieli, J., *Contribution of the Basal Ganglia to Skill Learning and Working Memory in Humans*, in *Models of information processing in the basal ganglia*, J.C. Houk, J.L. Davis, and D.G. Beiser, Editors. 1995, Cambridge, Mass. : MIT Press. p. 277-294.

81. Yoshioka, M., *et al.*, *Effect of conditioned fear stress on dopamine release in the rat prefrontal cortex.* Neuroscience Letters, 1996. **209**(3): p. 201-203.

82. Stark, H., A. Bischof, and H. Scheich, *Increase of extracellular dopamine in prefrontal cortex of gerbils during acquisition of the avoidance strategy in the shuttle-box.* Neurosci Lett, 1999. **264**(1-3): p. 77-80.

83. Ware, *et al., Disease-avoidance model: factor analysis of common animal fears.* Behav Res Ther, 1994. **32**(1): p. 57-63.

84. Fendt, M. and M.S. Fanselow, *The neuroanatomical and neurochemical basis of conditioned fear.* Neuroscience and biobehavioral reviews, 1999. **23**: p. 743-760.

85. Holland, *Amygdala circuitry in attentional and representational processes.* Trends in Cognitive Sciences, 1999. **3**(2): p. 65-73.

86. Young, A.M. and K.R. Rees, *Dopamine release in the amygdaloid complex of the rat, studied by brain microdialysis.* Neuroscience Letters, 1998. **249**(1): p. 49-52.

87. Thompson, R.F., *The brain: a neuroscience primer.* 2nd ed. 1993: New York : W.H. Freeman & Co. 475.

88. Amalric, M. and G.F. Koob, *Depletion of dopamine in the caudate nucleus but not in nucleus accumbens impairs reaction-time performance in rats.* J Neurosci, 1987. **7**(7): p. 2129-34.

89. Amalric, M., *et al., Complex deficits on reaction time performance following bilateral intrastriatal 6-OHDA infusion in the rat.* Eur J Neurosci, 1995. **7**(5): p. 972-80.

90. Blokland, A., *Reaction Time Responding in Rats.* Neuroscience & Biobehavioral Reviews, 1998. **22**(6): p. 847-864.

91. Brown, V.J. and T.W. Robbins, *Simple and choice reaction time performance following unilateral striatal dopamine depletion in the rat. Impaired motor readiness but preserved response preparation.* Brain, 1991. **114**(Pt 1B): p. 513-25.

92. Brown, V.J., *et al., Dopamine dependent reaction time deficits in patients with Parkinson's disease are task specific.* Neuropsychologia, 1993. **31**(5): p. 459-69.

93. Cunnington, R., R. Iansek, and J. L. Bradshaw, *Relationships between movement initiation times and movement-related cortical potentials in Parkinson's disease.* Human Movement Science, 1999. **18**(2-3): p. 443-459.

94. Gauntlett-Gilbert, J. and V.J. Brown, *Reaction Time Deficits and Parkinson's Disease.* Neuroscience & Biobehavioral Reviews, 1998. **22**(6): p. 865-881.

95. Kutukcu, Y., *et al., Simple and choice reaction time in Parkinson's disease.* Brain Research, 1999. **815**(2): p. 367-372.

96. Mayfield, R.D., *et al., Selective D1 and D2 dopamine receptor antagonists produce differential effects on reaction time in the rat.* Pharmacol Biochem Behav, 1993. **46**(4): p. 759-68.

97. Mayfield, R.D., *et al., Apomorphine and amphetamine produce differential effects on the speed and success of reaction time responding in the rat.* Pharmacol Biochem Behav, 1993. **46**(4): p. 769-75.

98. Rammsayer, T., *Is there a common dopaminergic basis of time perception and reaction time?* Neuropsychobiology, 1989. **21**(1): p. 37-42.

99. Spirduso, W.W., *et al., Reactive capacity: a sensitive behavioral marker of movement initiation and nigrostriatal dopamine function.* Brain Res, 1985. **335**(1): p. 45-54.

100. Zappia, M., *et al., Short-term levodopa test assessed by movement time accurately predicts dopaminergic responsiveness in Parkinson's disease.* Mov Disord, 1997. **12**(1): p. 103-6.

101. Zhuang, *et al., Implicit and explicit learning in an auditory serial reaction time task.* Acta Neurol Scand, 1998. **97**(2): p. 131-7.

102. Meck, W.H., *Neuropharmacology of timing and time perception.* Cognitive Brain Research, 1996. **3**(3-4): p. 227-242.

103. Baunez, C., A. Nieoullon, and M. Amalric, *Dopamine and complex sensorimotor integration: further studies in a conditioned motor task in the rat.* Neuroscience, 1995. **65**(2): p. 375-384.

104. Hazeltine, *Neural mechanisms of timing.* 1997.

105. Berridge, K.C. and T.E. Robinson, *What is the role of dopamine in reward: hedonic impact, reward learning, or incentive salience?* Brain Research Reviews, 1998. **28**(3): p. 309-369.

106. Garcia-Munoz, M., *et al.*, *Glutamate-dependent long-term presynaptic changes in corticostriatal excitability.* Neuroscience, 1996. **73**(1): p. 109-119.

107. Calabresi, P., *et al.*, *Coactivation of D1 and D2 dopamine receptors is required for long-term synaptic depression in the striatum.* Neurosci Lett, 1992. **142**(1): p. 95-9.

108. Calabresi, P., *et al.*, *Role of dopamine receptors in the short- and long-term regulation of corticostriatal transmission.* Nihon Shinkei Seishin Yakurigaku Zasshi, 1997. **17**(2): p. 101-4.

109. Calabresi, P., *et al.*, *Glutamate-triggered events inducing corticostriatal long- term depression.* J Neurosci, 1999. **19**(14): p. 6102-10.

110. Wilson, C.J., *The contribution of cortical neurons to the firing pattern of striatal spiny neurons*, in *Models of information processing in the basal ganglia*, J.C. Houk, J.L. Davis, and D.G. Beiser, Editors. 1995, Cambridge, Mass. : MIT Press. p. 29-50.

111. Kandel, E.R., J.H. Schwartz, and T.M. Jessell, eds. *Essentials of neural science and behavior.* . 1995, Norwalk, CT : Appleton & Lange.

112. Jacobs, R.A., *et al.*, *Adaptive mixtures of local experts.* Neyral Computation, 1991. **3**: p. 79-87.

113. Murray-Smith, R. and T.A. Johansen, eds. *Multiple model approaches to modelling and control.* . 1997, London ; Bristol, PA : Taylor & Francis.

114. Narendra, K.S., *adaptive control using multiple models.* IEEE transactions on Automatic Control, 1997. **42**(2): p. 171-187.

115. Redgrave, P., T.J. Prescott, and K. Gurney, *The basal ganglia: a vertebrate solution to the selection problem?* Neuroscience, 1999. **89**(4): p. 1009-1023.

116. Baev, K.V., *Highest level automatisms in the nervous system: A theory of functional principles underlying the highest forms of brain function - II. Monkey.* Progress In Neurobiology, 1997. **51**(2): p. 129-166.

117. Houk, J.C., *Information processing in modular circuits linking basal ganglia and cerebral cortex*, in *Models of information processing in the basal ganglia*, J.C. Houk, J.L. Davis, and D.G. Beiser, Editors. 1995, Cambridge, Mass. : MIT Press. p. 3-9.

118. Barto, A.G., *Adaptive Critics and the Basal Ganglia*, in *Models of information processing in the basal ganglia*, J.C. Houk, J.L. Davis, and D.G. Beiser, Editors. 1995, Cambridge, Mass. : MIT Press. p. 215-232.

119. Barto, A.G., R.S. Sutton, and C.W. Anderson, *Neuronlike adaptive elements that can solve difficult learning control problems.* IEEE Transactions on Systems, Man & Cybernetics, 1983. **13**(5): p. 834-846.

120. Houk, J.C., J.L. Davis, and D.G. Beiser, eds. *Models of information processing in the basal ganglia.* . 1995, Cambridge, Mass. : MIT Press.

121. Schultz, W., L. Tremblay, and J.R. Hollerman, *Reward prediction in primate basal ganglia and frontal cortex.* Neuropharmacology, 1998. **37**(4-5): p. 421-429.

122. Schultz, W., *et al.*, *Context-dependent Activity in Primate Striatum Reflecting Past and Future Behavioral Events*, in *Models of information processing in the basal ganglia*, J.C. Houk, J.L. Davis, and D.G. Beiser, Editors. 1995, Cambridge, Mass. : MIT Press. p. 11-27.

123. Beninger, R.J. and M.C. Olmstead, *The role of dopamine in the control of locomotor activity and reward-related incentive learning*, in *Brain dynamics and the striatal complex*, R. Miller and J. Wickens, Editors. 1999, Harward academic Press, Switzerland (in press). p. 29-50.

124. Balleine, B.W. and A. Dickinson, *Goal-directed instrumental action: contingency and incentive learning and their cortical substrates.* Neuropharmacology, 1998. **37**(4-5): p. 407-419.

125. Sutton, M.A. and R.J. Beninger, *Psychopharmacology of conditioned reward: evidence for a rewarding signal at D1-like dopamine receptors (in press).* Psychopharmacology, 1999.

126. Pennartz, C.M.A., *The ascending neuromodulatory systems in learning by reinforcement: comparing computational conjectures with experimental findings.* Brain Research Reviews, 1995. **21**(3): p. 219-245.

127. Harrington, D., K. Haaland, and N. Hermanowicz, *Temporal processing in the basal ganglia.* Neuropsychology, 1998. **12**(1): p. 3-12.

128. Aakerlund, L. and R. Hemmingsen, *Neural Networks as Models of Psychopathology.* Biological Psychiatry, 1998. **43**(7): p. 471-482.

129. Sejnowski, T.J., *Computational Neuroscience*, in *MIT Encyclopedia of the Cognitive Science*. 1998, MIT Press: Cambridge MA. p. 165-168.

130. Klopf, A.H., *A neuronal model of classical conditiong.* Psychobology, 1988. **16**: p. 85-125.

131. Caudill, M., *Neural networks primer*, in *AI Expert*. 1989. p. 51-58.

132. Hebb, D.O., *The Orginization of Behavior.* 1949, New York: Wiley.

133. Malaka, R., *Models of Classical Conditioning.* Bulletin Of Mathematical Biology, 1999. **61**(1): p. 33-83.

134. Klopf, A.H., J.S. Morgan, and S.E. Weaver, *A hierarchical network of control systems that learn: modeling nervous system function during classical and instrumental condintioning.* Adaptive Behavior, 1993. **1**: p. 263-319.

135. Baird, L.C. and A.H. Klopf, *A hierarchical network of provably optimal learning control systems: extensions of the associative control process (ACP) network.* Adaptive Behavior, 1993. **1**: p. 321-352.

136. Johnson, J.D., *et al. A computational model of avoidance behavior.* in *International Joint Conference on Neural Networks*. 1998. Anchorage, Alaska.

137. Schmajuk, N.A. *Behavioral Dynamics of Escape and Avoidance: A Neural Network Approach.* in *International Conference on Simulation of Adaptive Behavior (3rd : 1994 : Brighton, England).* 1994.

138. Lippmann, R.P., *An introduction to computing with neural nets.* IEEE ASSP Magzine, 1987: p. 4-22.

139. Suri, R. and J.R. Schultz, *Learning of sequential movements by neural network model with dopamine-like reinforcement signal.* Exp Brain Res, 1998. **121**(3): p. 350-4.

140. Sutton, R.S., *Learning to predict by methods of temporal differences.* Machine Learning, 1988. **3**: p. 9-44.

141. Salum, C., A. Roque da Silva, and A. Pickering, *Striatal dopamine in attentional learning: A computational model.* Neurocomputing, 1999. **26-27**: p. 845-854.

142. Servan-Schreiber, D. and J. Blackburn, *Neuroleptic effects on acquisition and performance of learned behaviors: a reinterpretation.* Life Sci, 1995. **56**(25): p. 2239-45.

143. Servan-Schreiber, D., *et al., Dopamine and the Mechanisms of Cognition: Part I. A Neural Network Model Predicting Dopamine Effects on Selective Attention.* Biological Psychiatry, 1998. **43**(10): p. 713-722.

144. Berns, G.S. and T.J. Sejnowski, *How the Basal Ganglia Make Decisions*, in *The Neurobiology of Decision Making*, A.R. Damasio, H. Damasio, and Y. Christen, Editors. 1996, Springer-Verlag: Berlin. p. 101-113.

145. Berns, G.s. and T.j. Sejnowski, *A computational model of how the basal ganglia produce sequences.* J Cogn Neurosci, 1998. **10**(1): p. 108-21.

146. Anger, D., *The role of temporal discriminations in the reinforcement of Sidman avoidance behavior.* Journal of Experimental Analysis of Behavior, 1963. **6**: p. 477-506.

147. Watkins, C.H., *Learning from delayed rewards*, . 1989, The University of Cambridge: Cambridge.

148. Sidman, M., *Avoidance behavior*, in *Operant behavior: areas of research and application*, W.K. Konig, Editor. 1966, Appelton-Century-Crofts: New York. p. 448-498.

149. Zisper, D., *A model of hipocampal learning during classical conditioning.* Behavioral Neuroscience, 1986. **100**: p. 764-776.

150. Moore, J.W., J.E. Desmond, and N.E. Berthier, *Adaptively timed conditioned responses and the cerebellum: a neural network approach.* Biological Cybernetics, 1989. **62**: p. 17-28.

151. Schiebel, M.E. and M.A. Schiebel, *Structural substrates for integrative patterns in the brain stem reticular core.*, in *Reticular information of the brain*, H. Jasper, *et al.*, Editors. 1958, Little, Brown: Boston. p. 31-55.

152. Schiebel, M.E. and M.A. Schiebel, *Anatomical basis of attention mechanisms in vertebrate brains.*, in *The neurosciences: a study program*, G.C. Quarton, T. Melnechuk, and F.O. Schmitt, Editors. 1967, Rockefeller University Press: New York. p. 577-602.

153. Braitenberg, V., *Is the cerebellar cortex a biological clock in the millisecond range?* Prog Brain Res, 1967. **25**: p. 334-46.

154. Kötter, R. and J. Wickens, *Striatal mechanisms in Parkinson s disease: new insights from computer modeling.* Artificial Intelligence In Medicine, 1998. **13**(1-2): p. 37-55.

155. Kimura, M. and N. Matsumoto, *Neuronal Activity in the Basal Ganglia: Functional Implications*, in *The basal ganglia and new surgical approaches for Parkinson's disease*, J.A. Obeso, Editor. 1997: Philadelphia: Lippincott-Raven. p. 111-118.

156. Kimura, M. and A.M. Graybiel, *Role of basal ganglia in sensory motor association learning*, in *Functions of the cortico-basal ganglia loop*, M. Kimura and A.M. Graybiel, Editors. 1995: Tokyo ; New York : Springer. p. 2-17.

Dynamics and Control of Spacecraft Formation Flying

Vikram Kapila
Assistant Professor
Department of Mechanical, Aerospace,
and Manufacturing Engineering

Polytechnic University
Six Metrotech Center
Brooklyn, NY 11201

Final Report for:
Summer Faculty Research Extension Program
Wright Research Site

Sponsored by:
Air Force Office of Scientific Research
Bolling Air Force Base, DC

and

Polytechnic University

December 1999

Dynamics and Control of Spacecraft Formation Flying

Vikram Kapila
Assistant Professor
Department of Mechanical, Aerospace,
and Manufacturing Engineering
Polytechnic University

Abstract

A novel concept of distributed array of small, low-cost, cooperative, and highly coordinated micro-spacecraft is vigorously being pursued for several future space missions. Implementation of the distributed coordinated spacecraft concept will require tight control of the relative distances and phases between the participating spacecraft. In this research, we developed a unified treatment of relative spacecraft position modeling and linear quadratic control that is suitable for further advancement in autonomous multiple spacecraft formation flying technology. In previous research literature, impulsive control based dynamic models for relative spacecraft position had been developed. In addition, a linear quadratic control algorithm had been developed for impulsive feedback control of relative positioning of two spacecraft. Unfortunately, however, it is not possible to guarantee the closed-loop stability with these previously developed impulsive controllers in a mathematically rigorous manner. Thus, in this research, we developed a mathematically rigorous control design framework for linear quadratic control of spacecraft relative position dynamics. Specifically, we developed and analyzed a pulse control based methodology to design linear quadratic controllers for spacecraft formation keeping.

The formation control schemes that are based on linearized relative spacecraft position model are unlikely to yield good precision for spacecraft in general elliptical orbits for long durations. Thus, in this research, we developed nonlinear dynamics describing the motion of a follower spacecraft relative to a leader spacecraft for the case where the leader spacecraft is in an elliptical orbit. In addition, a formation initialization constraint is developed for the ideal, unperturbed, periodic relative motion of the spacecraft formation which serves as a desired, relative motion trajectory. Next, a Lyapunov-based, nonlinear, adaptive control law is designed which guarantees global asymptotic convergence of the position tracking error in the presence of unknown, constant or slow-varying spacecraft masses and exogenous disturbance forces. Simulation results are provided to illustrate the efficacy of the formation initialization methodology and the adaptive controller performance.

Finally, additional research issues addressed as part of this AFOSR sponsored effort are briefly summarized.

Dynamics and Control of Spacecraft Formation Flying

Vikram Kapila

1. Introduction

A novel concept of distributing the functionality of large spacecraft among smaller, less expensive, cooperative spacecraft is seriously being considered for numerous space missions [1–3, 5]. A practical implementation of the concept relies on the control of relative distances and orientations between the participating spacecraft. A ground-based command and control system for relative positioning of multiple spacecraft will be excessively burdened and complex and may not be able to provide sufficiently rapid corrective control commands for formation reconfiguration and collision avoidance. Thus, the concept of autonomous formation flying of spacecraft clusters is vigorously being studied by numerous researchers. In particular, multiple spacecraft formation flying (MSFF) has been identified as an enabling technology by the U.S. Air Force and NASA for future space missions [1, 5, 15, 21, 22, 27]. For example, U.S. Air Force's TechSat-21 program [1, 22, 27] and NASA's Earth Orbiter-I (EO-I) and the New Millennium Interferometer (NMI) programs [5, 15, 21, 25], among others, rely on successful development and deployment of MSFF technologies. In particular, MSFF is expected to enable the Earth and space science missions, such as the distributed aperture radar, enhanced stellar optical interferometer, virtual co-observing and stereo-imaging platforms for space science and Earth observing, etc. For a recent collection of related research, the reader is referred to the proceedings of the Air Force-MIT workshop on spacecraft formation flying and micropropulsion [3].

A majority of the current MSFF control designs utilize simplifying modeling assumptions to aid the control synthesis due to inherent difficulties associated with the structure of the full, nonlinear dynamic model of MSFF. These simplifications result in the well-known Clohessy-Wiltshire (C-W)

linear, dynamic equations [8, 9, 18] for the relative positioning of MSFF. The Clohessy-Wiltshire model has formed the basis for the application of various linear control techniques to the MSFF position control problem [23, 24, 31]. Specifically, [31] presented the concept of formation keeping of spacecraft, using C-W equations, for a ground-based terrestrial laser communication system whereas [24] considered station keeping for the space shuttle Orbiter, using C-W equations. In addition, recently [21] considered MSFF control for NASA's NMI mission which relies on separated spacecraft interferometry. Similarly, [15] considered MSFF control for NASA's EO-I mission which is scheduled to demonstrate a stereo imaging concept in 1999.

Reviewing the current state of MSFF control, it appears that in contrast to linear control, nonlinear control theory has not been exploited to its full potential in MSFF. To the best of our knowledge, one of the few results on nonlinear control of MSFF can be found in [16, 32, 33] using a Lyapunov-based approach. In particular, [32] designed a class of control laws based on exact knowledge of the MSFF model that yield local asymptotic position tracking and global exponential attitude tracking. The application of the controllers proposed in [32] to formation rotation of MSFF about a given axis and synchronization of individual spacecraft rotation was later reported in [33]. More recently, [16] developed an adaptive position controller that compensates for unknown, constant disturbances while producing globally asymptotically decaying position tracking errors. This controller, however, requires exact knowledge of the spacecraft parameters.

In this research, we developed a complete set of nonlinear relative spacecraft position dynamic equations as well as the linearized dynamic equations. These dynamic equations form the basis for the development of a mathematically rigorous control design framework for full-state feedback (FSFB) and output feedback (OFB) control of spacecraft relative position dynamics. Specifically, we developed and analyzed discrete-time, pulse control-based methodologies to design FSFB linear quadratic controllers for MSFF. We also considered the fully nonlinear dynamics of relative

spacecraft position to develop a class of nonlinear control laws for MSFF. In particular, these nonlinear controllers account for *i)* noisy, incomplete state measurement (i.e., OFB design), *ii)* system uncertainties, and *iii)* exogenous disturbances. To facilitate the theoretical development of these novel control design tools, we exploited Lyapunov-based design and analysis techniques. Finally, a formation initialization constraint was developed for the ideal, unperturbed, periodic relative motion of the spacecraft formation which serves as a desired, relative motion trajectory.

The principal objective of this summer research extension program has been to advance the state-of-the-art in linear and nonlinear control design for MSFF. This report is an outcome of our one year effort and it provides:

- Linear/nonlinear modeling of spacecraft relative motion dynamics.
- Analysis of the nonlinear relative motion equations.
- Development of the pulse-based, linear quadratic control algorithms.
- Development of the nonlinear, Lyapunov-based control algorithms for the nonlinear MSFF dynamics.
- A formation initialization constraint for the ideal, unperturbed, periodic relative motion of the spacecraft formation which may serve as a desired, relative motion trajectory.

We note that all the results provided in this report constitute original research and have resulted in several conference papers [11, 13, 19] and journal articles [12, 19, 34].

2. Linear Pulse Control

In previous research, to minimize fuel consumption in MSFF, [24, 31] have proposed the use of sampled-data, full-state feedback impulsive control schemes. Specifically, a discrete-time model

for the linearized spacecraft relative position dynamics has been derived in [31] assuming that the control is applied impulsively at the sampling instant (as opposed to the standard zero-order, sample-and-hold technique where the control is held constant over the entire sampling interval [20]). However, the approach of [24, 31] fails to provide rigorous, *a priori* guarantees of the closed-loop system stability. This technique also fails to take advantage of recent developments in propulsion technologies. In particular, high performance Hall thrusters, pulse plasma thrusters, etc. are currently being developed to meet the requirements for future MSFF missions [28]. These low weight, high performance thrusters are expected to provide continuous thrusting capabilities for short time intervals, several times every day (if necessary). These advancements in propulsion technologies necessitate the development of novel *pulse-based*, spacecraft relative position and orientation control laws. In this research, we developed pulse-based, discrete-time feedback control laws. Specifically, we designed full-state feedback controllers that ensure closed-loop stability in the presence of pulse-type actuators which provide only intermittent control action. Before proceeding with the development of pulse-based control scheme, in the next subsection, we review the modeling of spacecraft relative position dynamics.

2.1. Spacecraft Relative Position Dynamic Modeling

In this subsection, we begin with the classical C-W equations [9] that describe the motion of a follower spacecraft relative to a leader spacecraft. In order to present the C-W equations we assume that *i)* the leader spacecraft is in a circular orbit around the Earth with an angular velocity ω and *ii)* a rectangular moving coordinate frame is attached to the leader spacecraft with the x-axis pointing opposite to the instantaneous tangential velocity of the leader spacecraft, the y-axis pointing along the instantaneous position vector from Earth center to the leader spacecraft, and the z-axis is mutually perpendicular to the x and y axis and x-y-z form a right handed coordinate frame. Thus, it follows that the z-axis is perpendicular to the orbital plane. Next, let $\overline{\rho}$ denote

the position vector of the follower spacecraft relative to the leader spacecraft. In addition, let $\overline{\rho} = x\hat{\imath} + y\hat{\jmath} + z\hat{k}$ and $\overline{\omega} = \omega\hat{k}$ be the vector representations of $\overline{\rho}$ and $\overline{\omega}$, respectively, in the moving reference x-y-z. Then, it follows from [18,31] that the linearized dynamic equations governing the motion of the follower spacecraft relative to the leader spacecraft are given by

$$\ddot{x} - 2\omega\dot{y} = F_x, \tag{1}$$

$$\ddot{y} + 2\omega\dot{x} - 3\omega^2 y = F_y, \tag{2}$$

$$\ddot{z} + \omega^2 z = F_z, \tag{3}$$

where F_i, $i = x, y, z$, is the i^{th} component of the resultant specific external disturbance and/or specific control force (i.e., force per unit mass) acting on the relative motion dynamics.

Note that (1)–(3) are known as the C-W equations and were originally derived in the context of the spacecraft rendezvous problem [9]. Also note that it has been shown in [18,31] that the open-loop spacecraft relative position dynamics are inherently unstable and in the absence of any control input, a nonzero initial condition or a nonzero exogenous disturbance will cause the two spacecraft to drift apart with the passage of time.

Next, to design pulse-based, discrete-time controllers that accomplish the spacecraft formation flying objective, we begin with a continuous-time, state-space description of (1)–(3). Thus, we define the state variables $x_1 \triangleq x$, $x_2 \triangleq \dot{x}$, $x_3 \triangleq y$, $x_4 \triangleq \dot{y}$, $x_5 \triangleq z$, and $x_6 \triangleq \dot{z}$. Using these state variables and observing the fact that the in-plane (x-y) dynamics are decoupled from the out-of-plane (z) dynamics, the state-space description for the combined in-plane and out-of-plane dynamics is given by

$$\dot{\mathbf{x}}(t) = \begin{bmatrix} A_1(\omega) & 0_{4\times 2} \\ 0_{2\times 4} & A_2(\omega) \end{bmatrix} \mathbf{x}(t) + \begin{bmatrix} B_1 & 0_{4\times 1} \\ 0_{2\times 2} & B_2 \end{bmatrix} u(t), \tag{4}$$

where $\mathbf{x} \triangleq [x_1 \ x_2 \ x_3 \ x_4 \ x_5 \ x_6]^T$, $u \triangleq [u_x \ u_y \ u_z]^T$, and

$$A_1(\omega) \triangleq \begin{bmatrix} 0 & 1 & 0 & 0 \\ 0 & 0 & 0 & 2\omega \\ 0 & 0 & 0 & 1 \\ 0 & -2\omega & 3\omega^2 & 0 \end{bmatrix}, \quad B_1 \triangleq \begin{bmatrix} 0 & 0 \\ 1 & 0 \\ 0 & 0 \\ 0 & 1 \end{bmatrix}, \quad A_2(\omega) \triangleq \begin{bmatrix} 0 & 1 \\ -\omega^2 & 0 \end{bmatrix}, \quad B_2 \triangleq \begin{bmatrix} 0 \\ 1 \end{bmatrix}, \tag{5}$$

with u_i for $i = x, y, z$ being the control input.

Next, we obtain a sampled-data representation of the above continuous-time, state-space model of spacecraft relative position dynamics [20]. Thus, let T_1 and T_2 be the in-plane and out-of-plane sampling intervals, respectively, and define

$$A_{1d}(\omega) \triangleq e^{A_1(\omega)T_1}, \qquad B_{1d}(\omega) \triangleq \int_0^{T_1} e^{A_1(\omega)(T_1-s)}dsB_1,$$
$$A_{2d}(\omega) \triangleq e^{A_2(\omega)T_2}, \qquad B_{2d}(\omega) \triangleq \int_0^{T_2} e^{A_2(\omega)(T_2-s)}dsB_2.$$

With the above notation, the combined in-plane and out-of-plane sampled-data spacecraft relative position dynamics are given by

$$\mathbf{x}(k+1) = \begin{bmatrix} A_{1d}(\omega) & 0_{4\times 2} \\ 0_{2\times 4} & A_{2d}(\omega) \end{bmatrix} \mathbf{x}(k) + \begin{bmatrix} B_{1d}(\omega) & 0_{4\times 1} \\ 0_{2\times 2} & B_{2d}(\omega) \end{bmatrix} u(k), \tag{6}$$

where

$$\mathbf{x}(k) \triangleq [x_1(kT_1) \ x_2(kT_1) \ x_3(kT_1) \ x_4(kT_1) \ x_5(kT_2) \ x_6(kT_2)]^T,$$
$$u(k) \triangleq [u_1(kT_1) \ u_2(kT_1)u_3(kT_2)]^T.$$

2.2. Linear Pulse Control

Note that an asymptotically stabilizing feedback controller for the relative motion dynamics of (6) can be developed using discrete-time, linear quadratic regulator (LQR) theory [14]. However, application of the standard LQR scheme to (6) necessitates prohibitive amount of fuel. Furthermore, as discussed in [28], a number of advanced pulse-type actuation technologies are currently being developed for spacecraft propulsion. Finally, it appears that, at least for the Earth-centric

MSFF missions, it is wiser to exploit Kepler than to fight Kepler [30]. Thus, the various leader and follower spacecraft in the cluster of cooperative spacecraft can be typically parked in their natural orbits between useful mission operation periods. Next, for useful mission operation, the participating spacecraft can achieve the desired formation while still in their natural orbits. However, in order to extend the formation life for each cycle, it will be necessary to provide control thrust to mitigate the destabilizing influence of gravitational perturbation, differential drag, solar pressure disturbance, etc. In this section, in order to minimize control action while simultaneously ensuring the asymptotic stability, we develop pulse-based controllers that utilize continuous thrusting, for possibly short intervals. The proposed pulse-based control design methodology is outlined next.

Consider a general, $\hat{n}^{\text{th}}$-order, time-invariant, pulse-based, discrete-time feedback control system

$$\mathbf{x}(k+1) = \Phi\mathbf{x}(k) + \Gamma u(k), \quad k = 0, 1, \ldots, \tag{7}$$

$$\begin{aligned} u(k) &= K\mathbf{x}(k), \quad k = nN, \ldots, nN+p-1, \\ &= 0, \quad k = nN+p, \ldots, nN+p+q-1, \end{aligned} \tag{8}$$

where $\mathbf{x}$ is the system state vector, u is the control input vector, Φ is the system dynamic matrix, Γ is the input matrix, $n = 0, 1, 2, \ldots$, and $N = p+q$ is the number of samples in one complete cycle over which the control is first turned on for p samples and then off for the remaining q samples. In this case, using a recursive solution procedure, it can be shown that

$$\mathbf{x}(nN) = [\Phi^q(\Phi + \Gamma K)^p]^n \mathbf{x}(0), \ n = 1, 2, \ldots. \tag{9}$$

Note that the stability of the closed-loop system (7), (8) can be guaranteed by requiring that the solution of (9) decay. To this end, it follows that for the case when $p = 1$, (9) can be rewritten as

$$\mathbf{x}(nN) = \left[(\Phi^{(q+1)} + \Phi^q\Gamma K)\right]^n \mathbf{x}(0), \ n = 1, 2, \ldots. \tag{10}$$

In order to ensure that the solutions of (10) decay, we require that $\Phi^{(q+1)} + \Phi^q\Gamma K$ be asymptotically stable. When the pair $(\Phi^{(q+1)}, \Phi^q\Gamma)$ is stabilizable, this condition can be satisfied by designing the

feedback gain K, for example, using the LQ control design technique [14]. Alternatively, one can use the standard pole placement algorithms [20] to design K such that

$$\rho(\Phi^{(q+1)} + \Phi^q \Gamma K) < 1, \tag{11}$$

where $\rho(X)$ is the spectral radius of a square matrix X (i.e., the maximum absolute value among all eigenvalues of X).

Next, for the pulse-based LQ control of (7), consider the stabilizable auxiliary system

$$\mathbf{z}(k+1) = \hat{\Phi}\mathbf{z}(k) + \hat{\Gamma}v(k), \tag{12}$$

where $\mathbf{z}(k)$ and $v(k)$ correspond to the state and control, respectively, of the auxiliary system, $\hat{\Phi} \triangleq \Phi^{(q+1)}$ and $\hat{\Gamma} \triangleq \Phi^q \Gamma$. Now design

$$v(k) = K\mathbf{z}(k), \tag{13}$$

that satisfies the following design criteria: *i)* the closed-loop system (12), (13) is globally asymptotically stable and *ii)* the quadratic performance functional

$$J(K) \triangleq \sum_{k=0}^{\infty} \mathbf{z}^T(k) R_1 \mathbf{z}(k) + v^T(k) R_2 v(k), \tag{14}$$

where R_1 is a nonnegative-definite, state weighting matrix and R_2 is a positive-definite, control weighting matrix, [14] is minimized. Note that it follows from (11) that the state feedback controller gain K that stabilizes the auxiliary closed-loop system (12), (13) also stabilizes the pulse-based, state feedback control system (7), (8). Thus, we now determine the pulse-based, state feedback control gain K by designing an LQ state feedback gain K for the auxiliary system. Finally, note that the case when $p > 1$ is significantly more involved and is addressed later in this report by replacing the time-invariant, state feedback controller (8) by a periodic, state feedback controller.

2.3. Illustrative Numerical Simulation

In this subsection, we provide illustrative numerical simulations to demonstrate the proposed pulse-based, discrete-time, linear control scheme for the relative position control of two spacecraft. The problem data is adopted from [31]. Consider a leader-follower spacecraft pair to be in the geosynchronous orbit of radius $r = 42,241$ km. Let the orbital period be 24 hours, thus $\omega = 7.2722 \times 10^{-5}$ radians/sec. The control objective is to regulate the relative x position component to 100 meters, the relative y and z position components to zero, and the relative x, y, and z velocities to zero with the in-plane control (u_x, u_y) and the out-of-plane control u_z applied every one hour and four hours, respectively. The in-plane control and the out-of-plane control are each turned on for a 2 minute duration at the beginning of their respective cycles. The control gains for the in-plane and out-of-plane dynamics are designed using the standard LQ regulation method with quadratic performance criteria [14]

$$J_{ip} = \sum_{k=0}^{\infty} \mathbf{z}_1^2(k) + \frac{1}{\omega^2}[v_x^2(k) + v_y^2(k)], \tag{15}$$

$$J_{op} = \sum_{k=0}^{\infty} \mathbf{z}_5^2(k) + \frac{1}{\omega^2}\, v_z^2(k), \tag{16}$$

where $\mathbf{z}_i$ and v_i are transformations of $\mathbf{x}_i$ and u_i to the auxiliary coordinate system described in subsection 2.2. For convenience, we scale the time units in (4), (5), (15), and (16) from seconds to minutes. This is accomplished by replacing ω by $\hat{\omega} = 60\omega$. Now we design the in-plane state feedback gain K_{ip} using $(\hat{\Phi}_1(\hat{\omega}), \hat{\Gamma}_1(\hat{\omega}))$ and the quadratic performance criterion (15) where $\hat{\Phi}_1(\hat{\omega}) \triangleq [A_{1d}(\hat{\omega})]^{(q+1)}$, $\hat{\Gamma}_1(\hat{\omega}) \triangleq [A_{1d}(\hat{\omega})]^q B_{1d}(\hat{\omega})$, $T_1 = 2$ minutes and $q = 29$. In addition, we design the out-of-plane state feedback gain K_{op} using $(\hat{\Phi}_2(\hat{\omega}), \hat{\Gamma}_2(\hat{\omega}))$ and the quadratic performance criterion (16) where $\hat{\Phi}_2(\hat{\omega}) \triangleq [A_{2d}(\hat{\omega})]^{(q+1)}$, $\hat{\Gamma}_2(\hat{\omega}) \triangleq [A_{2d}(\hat{\omega})]^q B_{2d}(\hat{\omega})$, $T_2 = 2$ minutes and $q = 119$. The system response to nonzero initial condition $\mathbf{x}(0) = \begin{bmatrix} 200 & 0 & -100 & 0_{3\times 1} \end{bmatrix}^T$ and periodic solar pressure differential described in [18,31] (with appropriate time scaling to minutes) is given in

Figure 1. Unlike the unstable response in [18,31] for the open-loop system, the closed-loop response in Figure 1 is bounded. However, the system response in Figure 1 represents oscillatory behavior. This is due to the fact that, since the system is subjected to periodic solar pressure differential, the pulse-based controller is unable to reject the periodic disturbance. If the solar pressure differential is assumed to be absent, the closed-loop response asymptotically tracks the desired set-point.

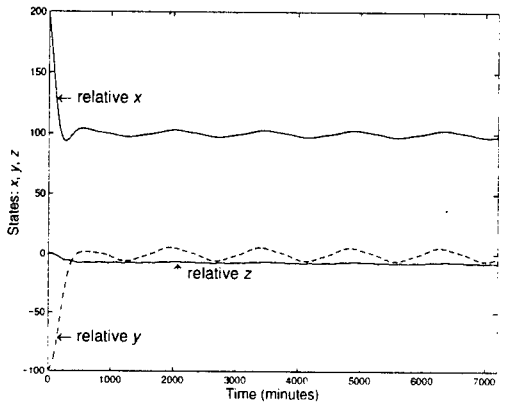

Figure 1: Pulse-Based Spacecraft Relative Position Control

2.4. Pulse-Based Linear Periodic Control

In this subsection, in order to overcome the difficulty in the design of constant gain matrix K for the stabilization of $\Phi^q(\Phi + \Gamma K)^p$, we reformulate the pulse-based control design problem for (7), and replace the control law (8) by a periodic controller

$$\begin{aligned} u(k) &= K(k)\mathbf{x}(k), \qquad && k = nN, \ldots, nN + p - 1, \\ &= 0, && k = nN + p, \ldots, nN + p + q - 1. \end{aligned} \tag{17}$$

Note that $K(k)$ in (17) is a periodic gain, i.e., $K(nN + i) = K(i)$ for $i = 0, 1, \ldots, p - 1$ and $n = 0, 1, 2, \ldots$. Using a recursive procedure, it can be shown that

$$\mathbf{x}(nN) = [\Phi^q(\Phi + \Gamma K(p-1)) \cdots (\Phi + \Gamma K(0))]^n \mathbf{x}(0), \quad n = 1, 2, \ldots. \tag{18}$$

Now, the asymptotic stability of the closed-loop system (7), (17) can be guaranteed by requiring that the solution of (18) decay. To this end, we require that the state transition matrix of the closed-loop system (7), (17) over one period

$$\tilde{\Phi} \triangleq \Phi^q(\Phi + \Gamma K(p-1)) \cdots (\Phi + \Gamma K(0)), \tag{19}$$

be discrete-time asymptotically stable.

Next, we propose a constructive solution to the problem of stabilizing $\tilde{\Phi}$. First, define

$$\begin{aligned} \hat{\Phi}(i) &\triangleq \Phi^{\frac{q}{p}}\hat{\Phi}(i+1)\Phi + \Phi^{\frac{q}{p}}\hat{\Phi}(i+1)\Gamma K(i), \qquad i = 0, 1, \ldots, p-1, \\ \hat{\Phi}(i) &\triangleq I, \qquad i = p. \end{aligned} \tag{20}$$

Let $i = p-1$ and assume $(\Phi^{\frac{q}{p}}\hat{\Phi}(i+1)\Phi, \Phi^{\frac{q}{p}}\hat{\Phi}(i+1)\Gamma)$ is stabilizable. Then, we can design $K(i)$, $i = p-1$, using LQR [14] or pole placement [20] techniques. This procedure can be repeated recursively for $i = p-2, \ldots, 0$, to obtain $K(p-2), \ldots, K(0)$.

Alternatively, we can use periodic LQR theory [6] to design the periodic gains $K(i)$, $i = 0, \ldots, p-1$, in order to stabilize $\tilde{\Phi}$. Now, we provide a brief overview of the periodic LQR theory. Given the $\hat{n}^{\text{th}}$-order stabilizable, linear time periodic (LTP) controlled system

$$\mathbf{x}(k+1) = \Phi(k)\mathbf{x}(k) + \Gamma(k)u(k), \quad k = 0, 1, \ldots, \tag{21}$$

where $u \in \mathbb{R}^m$, design a full-state feedback periodic controller

$$u(k) = K(k)\mathbf{x}(k), \quad k = 0, 1, \ldots, \tag{22}$$

which satisfies the following design criteria:

i) the transition matrix over one period of the closed-loop system (21), (22) is asymptotically stable; and

ii) the performance functional

$$J(K(\cdot)) \triangleq \lim_{\hat{K}\to\infty} \sum_{k=0}^{\hat{K}} [\mathbf{x}^T(k)R_1(k)\mathbf{x}(k) + u^T(k)R_2(k)u(k)], \tag{23}$$

is minimized.

Remark 1. Note that the periodicity assumption on the plant implies $\Phi(k+N) = \Phi(k)$, $k = 0, 1, \ldots$, and similarly for the control matrix $\Gamma(\cdot)$. Finally, in order to account for our periodicity assumption in the system dynamics, we assign a periodic structure to the state and control weighting matrices (i.e., $R_1(k+N) = R_1(k)$ and $R_2(k+N) = R_2(k)$, $k = 0, 1, \ldots$) as well as to the gain matrix $K(\cdot)$ (i.e., $K(k+N) = K(k)$, $k = 0, 1, \ldots$).

The solution to the full-state feedback, LTP control design problem can be obtained via Lagrange multiplier optimization [17]. In order to state the principal result, we define the notation

$$P_a(i) \triangleq \Gamma^T(i)P(i+1)\Phi(i),$$

$$R_{2a}(i) \triangleq R_2(i) + \Gamma^T(i)P(i+1)\Gamma(i),$$

for arbitrary $P(i) \in \mathbb{R}^{\hat{n}\times\hat{n}}, i = 0, \ldots, N-1$. Then, the periodic, full-state feedback gain $K(i)$ is given by

$$K(i) = -R_{2a}^{-1}(i)P_a(i), \tag{24}$$

where $P(i) \in \mathbb{R}^{\hat{n}\times\hat{n}}$, $i = 0, \ldots, N-1$, are nonnegative-definite matrices satisfying the periodic, matrix Riccati difference equation

$$P(i) = \Phi^T(i)P(i+1)\Phi(i) + R_1(i) - P_a^T(i)R_{2a}^{-1}(i)P_a(i). \tag{25}$$

Now, interpreting (7), (17), as (21), (22) yields

$$\begin{aligned} \Phi(k) &= \Phi, & k &= 0, 1, \ldots, \\ \Gamma(k) &= \Gamma, & k &= 0, \ldots, p-1, \\ &= 0_{n\times m}, & k &= p, \ldots, p+q-1. \end{aligned} \tag{26}$$

Using, the plant and input matrices $\Phi(k), \Gamma(k)$ given by (26) and selecting the appropriate state and control weighting matrices $R_1(k)$ and $R_2(k)$, respectively, we can now compute the periodic, full-state feedback control law (17) via (24), (25).

2.5. Pulse-Based Trajectory Tracking Control

For ideal MSFF, the initial conditions for the formation flying spacecraft must be chosen to enable the spacecraft to undergo periodic motions such that a relative spatial pattern persists for several orbits with minimal propellant expenditure [7]. Using the linearized dynamics of relative motion between a leader-follower spacecraft pair, *viz.*, C-W equations (1)–(3), (also known as Hill's equations), recently, [27] identified the set of feasible initial conditions that annihilate the secular growth in time in the solution of Hill's equations; thus, yielding periodic relative motion between the leader-follower spacecraft pair. Based on the work in [27], spatial patterns for formation design have been proposed in [26]. Next, note that even though the above pulse control framework has been developed for the stabilization of the discretized version of Hill's equations (1)–(3), it is directly applicable for trajectory tracking control via an error system formulation. Specifically, beginning with an initial condition from the set of feasible initial conditions yielding no-thrust periodic solution to Hill's equations (1)–(3) [27], we can compute the desired formation trajectory via the evolution of

$$\dot{\mathbf{x}}_d(t) = \begin{bmatrix} A_1(\omega) & 0_{4\times 2} \\ 0_{2\times 4} & A_2(\omega) \end{bmatrix} \mathbf{x}_d(t). \tag{27}$$

Now, for the actual MSFF dynamics, $\mathbf{x}(0) \neq \mathbf{x}_d(0)$ will necessitate feedback control. Note that the actual MSFF dynamics is given by (1)–(3), or, equivalently, by

$$\dot{\mathbf{x}}(t) = \begin{bmatrix} A_1(\omega) & 0_{4\times 2} \\ 0_{2\times 4} & A_2(\omega) \end{bmatrix} \mathbf{x}(t) + \begin{bmatrix} B_1 & 0_{4\times 1} \\ 0_{2\times 2} & B_2 \end{bmatrix} u(t). \tag{28}$$

Next, define $e(t) \triangleq \mathbf{x}(t) - \mathbf{x}_d(t)$. Then, it follows from (27), (28) that

$$\dot{e}(t) = \begin{bmatrix} A_1(\omega) & 0_{4\times 2} \\ 0_{2\times 4} & A_2(\omega) \end{bmatrix} e(t) + \begin{bmatrix} B_1 & 0_{4\times 1} \\ 0_{2\times 2} & B_2 \end{bmatrix} u(t). \tag{29}$$

Now, the discretization of (29) leads to a dynamic system of the form (6) with the state vector $\mathbf{x}(k)$ of (6) replaced by the error vector $e(k)$. The pulse control scheme proposed for the stabilization of (7) can thus be applied for trajectory tracking.

3. Nonlinear Control

To reiterate from subsection 2.5, for ideal MSFF, the initial conditions for the formation flying spacecraft must be chosen to enable the spacecraft to undergo periodic motions such that a relative spatial pattern persists for several orbits with minimal propellant expenditure [7]. Furthermore, as mentioned in subsection 2.5, recently, [27] identified the set of feasible initial conditions that yield periodic relative motion between the leader-follower spacecraft pair whereas [26] proposed feasible relative spatial patterns for formation. Unfortunately, however, a caveat of [26, 27] is that their results are based on the linearization of nonlinear dynamics of spacecraft relative motion. In fact, it can be shown that the ideal, no-thrust, formation initialization methodology of [27] fails to hold the *designed* formations [26] for the nonlinear dynamics of spacecraft relative motion.

As mentioned previously, a majority of the MSFF control designs also utilize the aforementioned Hill's linearized relative motion equations to aid in the control synthesis [24, 31]. This linearized spacecraft relative motion dynamics model [9]) was originally developed for spacecraft rendezvous problem in circular orbits and is valid for short period maneuvers. Thus, to reiterate, formation initialization, formation deign, and formation control schemes based on Hill's equations are unlikely to yield good precision for MSFF in general elliptical orbits for long durations.

It is clear from the preceding discussion that there exists an urgent need for developing MSFF nonlinear dynamic modeling, formation initialization, and control schemes. Reviewing the current state of MSFF control research, [32] developed an exact model knowledge relative position controller with local asymptotic position tracking errors. More recently, as part of this AFOSR sponsored

effort, in [11, 12], we proposed a nonlinear, adaptive controller which ensures global asymptotic position tracking errors. However, the framework of [11, 12] is based on the assumption that the leader spacecraft remains in a circular orbit.

In this research, we developed the nonlinear dynamic model describing the relative positioning of MSFF for the case where the leader spacecraft is in an elliptical orbit. In addition, we developed a formation initialization scheme, which in the ideal case yields a no-thrust, periodic relative motion between the leader-follower spacecraft pair, and serves as a desired, relative motion trajectory. Next, a Lyapunov-based, nonlinear adaptive control law is designed which guarantees global asymptotic convergence of the position tracking error in the presence of unknown, constant or slow-varying spacecraft masses and exogenous disturbance forces. In comparison to the previous works [11, 12, 26, 27], the proposed formation initialization, desired trajectory generation, and adaptive nonlinear control schemes exploit the orbital mechanics (neglecting the Earth's oblateness effects) to aid in formation keeping and thus minimize propellant consumption. In fact, as demonstrated by the illustrative numerical simulation, the proposed controller utilizes the natural orbits of the leader-follower spacecraft pair for formation keeping and exactly cancels the unknown exogenous perturbations.

3.1. System Model

We begin with the consideration of a MSFF composed of two spacecraft, i.e., a *leader* spacecraft and a *follower* spacecraft. The leader spacecraft provides the basic reference motion trajectory and is considered to be in an ideal elliptical orbit around the Earth. The follower spacecraft navigates in proximity of the leader spacecraft. In this section, we will focus on MSFF such that the relative trajectory of the follower spacecraft with respect to the leader spacecraft is periodic, while the two spacecraft orbit a perfectly spherical Earth according to Keplerian Laws.

A schematic drawing of the MSFF system is given in Figure 2 where we make the following

considerations *i*) the inertial coordinate frame $\{X, Y, Z\}$ is attached to the center of the Earth, *ii*) $R(t) \in \mathbb{R}^3$ denotes the position vector from the origin of the inertial coordinate frame to the leader spacecraft, *iii*) the coordinate frame $\{x_l, y_l, z_l\}$ is attached to the leader spacecraft (see Figure 2) with the x_l-axis perpendicular to the instantaneous vector R, the y_l-axis pointing along the direction of the vector R, and the z_l-axis being mutually perpendicular to the x_l and y_l axes such that $\{x_l, y_l, z_l\}$ forms a right-hand coordinate frame, and *iv*) $\rho(t) \in \mathbb{R}^3$ denotes the position vector from the origin of the moving coordinate frame $\{x_l, y_l, z_l\}$ to the follower spacecraft.

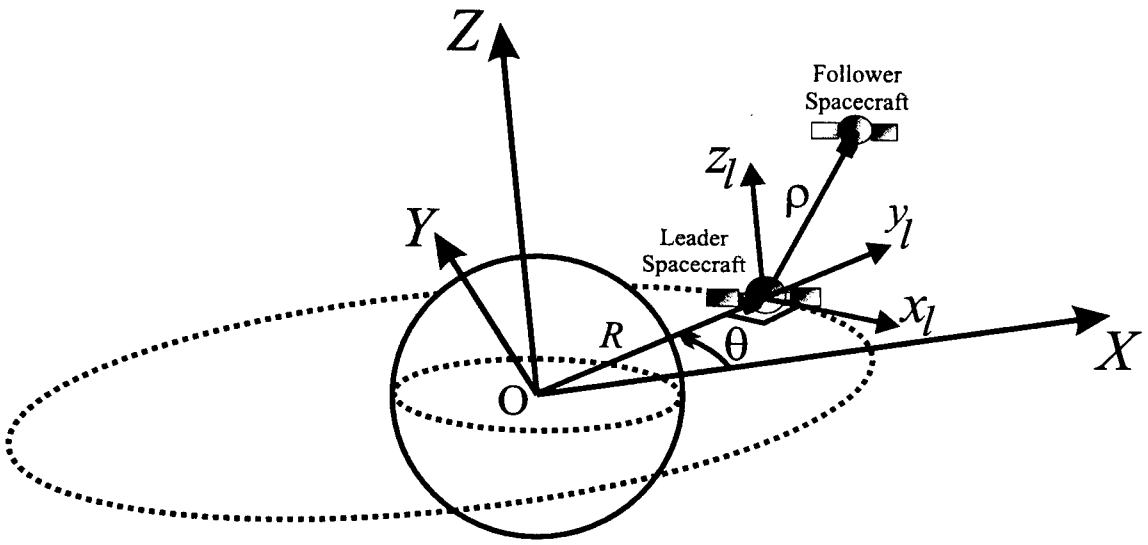

Figure 2: Schematic representation of the MSFF system

The nonlinear position dynamics of the leader and follower spacecraft in the inertial coordinate frame $\{X, Y, Z\}$ are given by [11, 12, 31]

$$m_l \ddot{R} + m_l \left(M + m_l\right) G \frac{R}{\|R\|^3} + F_{dl} = u_l \tag{30}$$

and

$$m_f(\ddot{R} + \ddot{\rho}) + m_f \left(M + m_f\right) G \frac{R + \rho}{\|R + \rho\|^3} + F_{df} = u_f, \tag{31}$$

respectively, where m_l, m_f are the masses, $F_{dl}, F_{df} \in \mathbb{R}^3$ are disturbance force vectors, and $u_l(t), u_f(t) \in \mathbb{R}^3$ are the actual control input vectors of the leader and follower spacecraft, respectively, M is

the Earth's mass, and G is the universal gravity constant. Since $M >> m_l, m_f$, (30) and (31) can be simplified to

$$m_l\ddot{R} + m_l\mu\frac{R}{\|R\|^3} + F_{dl} = u_l \tag{32}$$

and

$$m_f(\ddot{R} + \ddot{\rho}) + m_f\mu\frac{R+\rho}{\|R+\rho\|^3} + F_{df} = u_f, \tag{33}$$

respectively, where $\mu \triangleq MG$. After some simple algebraic manipulations on (32) and (33), the dynamic equation describing the position of the follower spacecraft relative to the leader spacecraft in the coordinate frame $\{X, Y, Z\}$ can be written as

$$m_f\ddot{\rho} + m_f\mu\left(\frac{R+\rho}{\|R+\rho\|^3} - \frac{R}{\|R\|^3}\right) + \frac{m_f}{m_l}u_l + F_{df} - \frac{m_f}{m_l}F_{dl} = u_f. \tag{34}$$

In the above model, we consider that the spacecraft masses vary slowly in time due to fuel consumption and payload variations. Furthermore, we consider that the disturbance forces result from solar radiation, aerodynamics, and magnetic fields, and hence, are also slow time-varying quantities [11, 12, 32]. As such, we can assume m_l, m_f are constant parameters and F_{dl}, F_{df} are constant vectors. The case where F_{dl}, F_{df} have known time-varying characteristics with unknown amplitudes can be handled as in [13].

To write the dynamics of (34) in terms of the moving coordinate frame $\{x_l, y_l, z_l\}$, we must obtain an expression for $\ddot{\rho}$ in the moving coordinate frame $\{x_l, y_l, z_l\}$. In order to do so, we consider the homogeneous form of (32) given by

$$\ddot{R} + \mu\frac{R}{\|R\|^3} = 0. \tag{35}$$

Next, using a polar coordinate frame fixed at the center of the Earth (see the R-θ coordinate frame in Figure 2), the motion of the leader spacecraft given by the vector differential equation (35) can be alternatively characterized by the planar dynamics,

$$\ddot{r}_l - r_l\dot{\theta}^2 + \mu\frac{r_l}{{r_l}^3} = 0, \tag{36}$$

$$r_l\ddot{\theta} + 2\dot{r}_l\dot{\theta} = 0, \tag{37}$$

where $r_l \triangleq \|R\|$. Now, employing standard orbital mechanics techniques, simple manipulations of (36), (37) yield

$$r_l(t) = \frac{a_l(1-{e_l}^2)}{1+e_l\cos\theta(t)}, \tag{38}$$

$$\dot{\theta}(t) = \frac{n(1+e_l\cos\theta(t))^2}{(1-{e_l}^2)^{3/2}}, \tag{39}$$

where a_l is the semi-major axis of the elliptical orbit of the leader spacecraft, e_l is the orbital eccentricity of the leader spacecraft, and n is the average orbital angular velocity defined by

$$n \triangleq \frac{2\pi}{T}, \tag{40}$$

with T as the orbital period. Finally, differentiating (39), we obtain

$$\ddot{\theta}(t) = \frac{-2n^2e_l(1+e_l\cos\theta(t))^3\sin\theta(t)}{(1-{e_l}^2)^3}. \tag{41}$$

Next, note that the relative position vector $\rho(t)$ expressed in $\{x_l, y_l, z_l\}$ is given by

$$\rho = x\hat{\imath}_l + y\hat{\jmath}_l + z\hat{k}_l, \tag{42}$$

where $\hat{\imath}_l, \hat{\jmath}_l, \hat{k}_l$ denote the unit vectors, while the angular velocity of the moving coordinate frame $\{x_l, y_l, z_l\}$ is given by $\dot{\theta}\hat{k}_l$. Hence, the relative acceleration vector $\ddot{\rho}(t)$ is given by

$$\ddot{\rho} = (\ddot{x} - 2\dot{\theta}\dot{y} - \dot{\theta}^2x - \ddot{\theta}y)\hat{\imath}_l + (\ddot{y} + 2\dot{\theta}\dot{x} - \dot{\theta}^2y + \ddot{\theta}x)\hat{\jmath}_l + \ddot{z}\hat{k}_l. \tag{43}$$

After substituting the right-hand side of (43) into (34), the nonlinear position dynamics of the follower spacecraft relative to the leader spacecraft can be arranged into the following advantageous form

$$m_f\ddot{q} + C(\dot{\theta})\dot{q} + N(q, \dot{\theta}, \ddot{\theta}, R, u_l) + F_d = u_f. \tag{44}$$

Note that, in (44), $q(t) \in \mathbb{R}^3$ is the relative position vector $q(t) \in \mathbb{R}^3$

$$q(t) \triangleq [x(t) \quad y(t) \quad z(t)]^T, \tag{45}$$

$C : \mathbb{R} \rightarrow \mathbb{R}^{3\times 3}$ is the Coriolis-like matrix given by

$$C(\dot{\theta}) \triangleq 2m_f\dot{\theta}\begin{bmatrix} 0 & -1 & 0 \\ 1 & 0 & 0 \\ 0 & 0 & 0 \end{bmatrix}, \tag{46}$$

and $N : \mathbb{R}^3 \times \mathbb{R} \times \mathbb{R} \times \mathbb{R}^3 \times \mathbb{R}^3 \rightarrow \mathbb{R}^3$ is a nonlinear term defined as

$$N(q,\dot{\theta},\ddot{\theta},R,u_l) \triangleq \begin{bmatrix} m_f\mu\dfrac{x}{\|R+q\|^3} - m_f(\dot{\theta}^2x + \ddot{\theta}y) + \dfrac{m_f}{m_l}u_{lx} \\ m_f\mu\left(\dfrac{y+\|R\|}{\|R+q\|^3} - \dfrac{1}{\|R\|^2}\right) - m_f(\dot{\theta}^2y - \ddot{\theta}x) + \dfrac{m_f}{m_l}u_{ly} \\ m_f\mu\dfrac{z}{\|R+q\|^3} + \dfrac{m_f}{m_l}u_{lz} \end{bmatrix}, \tag{47}$$

with u_{lx}, u_{ly}, u_{lz} being the components of the leader control input vector u_l. In addition, in (44), $F_d \in \mathbb{R}^3$ is the total, constant perturbing force vector given by

$$F_d \triangleq F_{df} - \frac{m_f}{m_l}F_{dl} \tag{48}$$

and R in the moving coordinate frame $\{x_l, y_l, z_l\}$ is given by

$$R = [0 \quad r_l \quad 0]^T. \tag{49}$$

Finally, note that r_l, $\dot{\theta}$, and $\ddot{\theta}$ in (44)–(49) are computed from (38), (39), and (41), respectively.

The dynamic model of (44)–(48) has the following property which will be exploited in the subsequent adaptive control design. The left-hand side of the dynamic equation (44) can be linearly parameterized as

$$m_f\xi + C(\dot{\theta})\dot{q} + N(q,\dot{\theta},\ddot{\theta},R,u_l) + F_d = W(\xi,\dot{q},q,\dot{\theta},\ddot{\theta},R,u_l)\phi, \qquad \forall\xi(t) \in \mathbb{R}^3, \tag{50}$$

where $W : \mathbb{R}^3 \times \mathbb{R}^3 \times \mathbb{R}^3 \times \mathbb{R} \times \mathbb{R} \times \mathbb{R}^3 \times \mathbb{R}^3 \rightarrow \mathbb{R}^{3\times 5}$ is the regression matrix which is composed of known functions and $\phi \in \mathbb{R}^5$ is the system's constant parameter vector. From the form of (44)–(48),

we can define $W(\cdot)$ and ϕ as

$$W(\xi,\dot{q},q,\dot{\theta},\ddot{\theta},R,u_l) \triangleq \begin{bmatrix} \xi_x - 2\dot{\theta}\dot{y} - \dot{\theta}^2 x - \ddot{\theta}y + \mu\dfrac{x}{\|R+q\|^3} & u_{lx} & 1 & 0 & 0 \\ \xi_y + 2\dot{\theta}\dot{x} - \dot{\theta}^2 y + \ddot{\theta}x + \mu\left(\dfrac{y+\|R\|}{\|R+q\|^3} - \dfrac{1}{\|R\|^2}\right) & u_{ly} & 0 & 1 & 0 \\ \xi_z + \mu\dfrac{z}{\|R+q\|^3} & u_{lz} & 0 & 0 & 1 \end{bmatrix}, \quad (51)$$

$$\phi \triangleq \begin{bmatrix} m_f & \dfrac{m_f}{m_l} & F_{dx} & F_{dy} & F_{dz} \end{bmatrix}^T, \quad (52)$$

where ξ_x, ξ_y, ξ_z and F_{dx}, F_{dy}, F_{dz} are the components of the vectors ξ and F_d, respectively.

3.2. Initialization Constraint for Formation Design

As discussed in subsection 2.5, it has recently been shown in [26, 27] that the solutions of the unperturbed Hill's equations of spacecraft relative motion yield periodic relative motion for initial conditions that annihilate secular growth in time. Inspired by the results of [26,27], in this research we analyze the feasibility of periodic relative motion resulting via the unperturbed relative motion dynamics

$$m_f\ddot{q} + C(\dot{\theta})\dot{q} + N(q,\dot{\theta},\ddot{\theta},R,u_l) = 0, \quad (53)$$

with $u_l \equiv 0$.

We begin by considering the homogeneous form of (32) given by

$$\ddot{\Re}(t) + \mu\frac{\Re(t)}{\|\Re(t)\|^3} = 0, \qquad \forall \Re \in \mathbb{R}^3. \quad (54)$$

It follows from [8] that (54) can be manipulated to yield

$$\frac{v^2(t)}{2} - \frac{\mu}{\|\Re(t)\|} = -\frac{\mu}{2a}, \quad (55)$$

where $v \triangleq \|\dot{\Re}\|$ and a is the semi-major axis of the spacecraft elliptical orbit.

Now, consider a pair of leader-follower spacecraft in an ideal, central gravitational force system. Furthermore, let the leader and follower spacecraft be in natural, elliptical orbits with orbital

periods T_l and T_f, respectively. Then, the relative motion between the two spacecraft will exhibit periodic characteristic if and only if $T_l = kT_f$ or $T_f = kT_l$, $k = 1, 2, \ldots$. In this research, we will focus on the case where $T_l = T_f$, i.e., $k = 1$. For the cases where $k \geq 2$, the relative distance between the leader and follower spacecraft will be quite large, and are not of particular interest for spacecraft formation flying.

Using Kepler's third law, we have that

$$\frac{a^3}{T^2} = \frac{\mu}{4\pi^2}, \tag{56}$$

which, with the constraint $T_l = T_f = T$, yields $a_l = a_f = a$. Using (55), we obtain a constraint on the initial condition of the leader-follower spacecraft pair which yields periodic, desired, relative motion between the two spacecraft. Specifically, the aforementioned initial condition constraint is given by

$$v_l^2(0) - \frac{2\mu}{\|R(0)\|} = v_f^2(0) - \frac{2\mu}{\|R(0) + q(0)\|}, \tag{57}$$

where $v_f \triangleq \|\dot{R} + \dot{q}\|$.

Next, let $\mathbf{v}_l$ and $\mathbf{v}_f$ denote the absolute velocities of the leader and follower spacecraft, respectively, expressed in the moving coordinate frame $\{x_l, y_l, z_l\}$. In addition, let $\mathbf{v}_{\rm rel}$ denote the velocity of the follower spacecraft relative to (as measured in) the moving coordinate frame $\{x_l, y_l, z_l\}$. Finally, let $\mathbf{v}_{l0}$, $\mathbf{v}_{f0}$, $\mathbf{v}_{{\rm rel}0}$, θ_0, and q_0 denote $\mathbf{v}_l(0)$, $\mathbf{v}_f(0)$, $\mathbf{v}_{\rm rel}(0)$, $\theta(0)$, and $q(0)$, respectively. Then, it follows, that

$$\mathbf{v}_{f0} = \mathbf{v}_{l0} + \mathbf{v}_{{\rm rel}0} + \dot{\theta}_0 \hat{k}_l \times q_0, \tag{58}$$

where

$$\mathbf{v}_{l0} = -r_{l0}\dot{\theta}_0 \hat{\imath}_l + \dot{r}_{l0}\hat{\jmath}_l, \tag{59}$$

$$\mathbf{v}_{{\rm rel}0} = \dot{x}_0 \hat{\imath}_l + \dot{y}_0 \hat{\jmath}_l + \dot{z}_0 \hat{k}_l, \tag{60}$$

$$q_0 = x_0 \hat{\imath}_l + y_0 \hat{\jmath}_l + z_0 \hat{k}_l. \tag{61}$$

Substituting (58)–(61) into (57) and rearranging terms, yields the following initial condition constraint for (53) to exhibit periodic solutions

$$2\mu\left[\frac{1}{({x_0}^2+(y_0+r_{l0})^2+{z_0}^2)^{\frac{1}{2}}}-\frac{1}{r_{l0}}\right] = \dot{x}_0^2+\dot{y}_0^2+\dot{z}_0^2+\dot{\theta}_0^2({x_0}^2+{y_0}^2+2y_0r_{l0}) \\ +2\dot{\theta}_0(-\dot{x}_0(r_{l0}+y_0)+x_0(\dot{r}_{l0}+\dot{y}_0))+2\dot{y}_0\dot{r}_{l0}, \qquad (62)$$

where r_{l0} and $\dot{r}_{l0}$ are determined from (38) and $\dot{\theta}_0$ is determined from (39).

3.3. Adaptive Control Law Design

In this section, we develop an adaptive feedback control law that asymptotically tracks a prespecified spacecraft relative position trajectory. In particular, we consider that a desired position trajectory $q_d(t) \in \mathbb{R}^3$ for the follower spacecraft relative to the leader spacecraft is given. Furthermore, we assume that $q_d(t)$ and its first two time derivatives are bounded functions of time. Now, an adaptive control law is to be designed to produce u_f such that $\lim_{t\to\infty} q(t) \to q_d(t)$.

In order to state the main result of this section, we define the following notation. The position tracking error $e(t) \in \mathbb{R}^3$ is defined as

$$e(t) \triangleq q_d(t) - q(t), \qquad (63)$$

and filtered tracking error $\zeta(t) \in \mathbb{R}^3$ is defined as

$$\zeta(t) \triangleq \dot{e}(t) + \Lambda e(t), \qquad (64)$$

where $\Lambda \in \mathbb{R}^{3\times 3}$ is a constant, diagonal, positive-definite matrix. Finally, a new regression matrix $W_d(\cdot)$ is defined as

$$W_d(\cdot) \triangleq W(\ddot{q}_d + \Lambda\dot{e}, \dot{q}, q, \dot{\theta}, \ddot{\theta}, R, u_l), \qquad (65)$$

where $W(\cdot)$ was defined in (51).

Theorem 1. Let $K \in \mathbb{R}^{3\times 3}$ and $\Gamma \in \mathbb{R}^{5\times 5}$ be constant, diagonal, positive-definite matrices. Then, the adaptive control law

$$u_f = W_{\rm d}(\cdot)\hat{\phi} + K\zeta, \tag{66}$$

$$\dot{\hat{\phi}} = \Gamma W_{\rm d}^T(\cdot)\zeta, \tag{67}$$

where $\hat{\phi} \in \mathbb{R}^5$ denotes the dynamic estimate of the unknown parameter vector ϕ defined in (52), ensures the global asymptotic convergence of the relative position and relative velocity tracking errors as illustrated by

$$\lim_{t\to\infty} e(t), \dot{e}(t) = 0. \tag{68}$$

Proof. We begin by rewriting the spacecraft relative position dynamics (44) in terms of the filtered tracking error variable (64). To this end, differentiating (64) with respect to time, multiplying both sides of the resulting equation by m_f, using $\ddot{e} = \ddot{q}_d - \ddot{q}$ from (63), and rearranging terms yields

$$m_f\dot{\zeta} = m_f\left(\ddot{q}_d + \Lambda\dot{e}\right) - m_f\ddot{q}. \tag{69}$$

Next, we substitute for $m_f\ddot{q}$ from (44) in (69), to obtain

$$\begin{aligned} m_f\dot{\zeta} &= m_f(\ddot{q}_d + \Lambda\dot{e}) + C(\dot{\theta})\dot{q} + N(q,\dot{\theta},\ddot{\theta},R,u_l) + F_d - u_f \\ &= W_{\rm d}(\cdot)\phi - u_f, \end{aligned} \tag{70}$$

where we used (50) and (65). The above first-order, nonlinear, differential equation represents the open-loop dynamics of $\zeta(t)$.

Next, define the parameter estimation error vector $\tilde{\phi}(t) \in \mathbb{R}^5$ as

$$\tilde{\phi}(t) \triangleq \phi - \hat{\phi}(t). \tag{71}$$

Now, substituting (66) into (70) and using (71) yields the closed-loop dynamics for $\zeta(t)$ given by

$$m_f\dot{\zeta} = -K\zeta + W_{\rm d}(\cdot)\tilde{\phi}. \tag{72}$$

Finally, note that differentiating (71) with respect to time and using (67), produces the closed-loop dynamics for the parameter estimation error

$$\dot{\tilde{\phi}} = -\Gamma W_{\mathrm{d}}^T(\cdot)\zeta. \tag{73}$$

Now, we utilize the error systems of (72) and (73) along with the positive-definite, candidate Lyapunov function $V : \mathbb{R}^3 \times \mathbb{R}^5 \rightarrow \mathbb{R}$ defined by

$$V(\zeta, \tilde{\theta}) = \frac{1}{2}\zeta^T m_f \zeta + \frac{1}{2}\tilde{\phi}^T \Gamma^{-1} \tilde{\phi} \tag{74}$$

to prove the above stability result for the position and velocity tracking errors. Specifically, differentiating (74) with respect to time yields

$$\dot{V}(\zeta, \tilde{\phi}) = \zeta^T m_f \dot{\zeta} + \tilde{\phi}^T \Gamma^{-1} \dot{\tilde{\phi}}\,. \tag{75}$$

Now, substitution of the closed-loop dynamics (72) into (75), yields

$$\dot{V}(\zeta, \tilde{\phi}) = -\zeta^T K \zeta + \tilde{\phi}^T \left(W^T(\cdot)\zeta + \Gamma^{-1} \dot{\tilde{\phi}} \right). \tag{76}$$

Finally, substituting (73) into the parenthetical term of (76), we obtain

$$\dot{V}(\zeta, \tilde{\phi}) = -\zeta^T K \zeta \ \leq -\lambda_{\min}\{K\} \|\zeta\|^2 \ \leq 0, \tag{77}$$

where $\lambda_{\min}\{\cdot\}$ denotes the minimum eigenvalue of a matrix.

Due to the form of (77), we know that $V(\zeta, \tilde{\phi})$ is either decreasing or constant. Since $V(\zeta, \tilde{\phi})$ of (74) is a non-negative function, we can conclude that $V(\zeta, \tilde{\phi}) \in \mathcal{L}_\infty$; hence, $\zeta(t) \in \mathcal{L}_\infty$ and $\tilde{\phi}(t) \in \mathcal{L}_\infty$. Since $\zeta(t) \in \mathcal{L}_\infty$, we can utilize Lemma 1.4 of [10] to show that $e(t), \dot{e}(t) \in \mathcal{L}_\infty$; hence, due to the boundedness of $q_d(t)$ and $\dot{q}_d(t)$, we can use (63) to conclude that $q(t), \dot{q}(t) \in \mathcal{L}_\infty$. Since $\tilde{\phi}(t) \in \mathcal{L}_\infty$ and ϕ is a constant vector, (71) can be used to show that $\hat{\phi}(t) \in \mathcal{L}_\infty$. From the above boundedness statements and the fact that $\ddot{q}_d(t)$ is assumed bounded, the definitions of (51) and (65) can be used to show that $W_{\mathrm{d}}(\cdot) \in \mathcal{L}_\infty$. It is now easy to see from (66) that the

control input $u_f(t) \in \mathcal{L}_\infty$. The above information can be applied to (44) and (72) to illustrate that $\ddot{q}(t), \dot{\zeta}(t) \in \mathcal{L}_\infty$. Thus, we have explicitly illustrated that all signals in the adaptive controller and system remain bounded during the closed-loop operation.

From (77), it is now easy to show that $\zeta(t) \in \mathcal{L}_2$. Since we have already proved that $\zeta(t), \dot{\zeta}(t) \in \mathcal{L}_\infty$, we can apply Barbalat's Lemma [10,29] to conclude that

$$\lim_{t \to \infty} \zeta(t) = 0. \tag{78}$$

Finally, Lemma 1.6 of [10] can be applied to (78) and (64) to obtain the result of (68). □

Remark 2. In the case that the parameter vector ϕ of (52) is perfectly known, the proposed control law (66) with $\hat{\phi} = \phi$ (i.e., an exact model knowledge controller) would ensure global exponential convergence of the position and velocity tracking errors in the sense that

$$\|\zeta(t)\| \leq \|\zeta(0)\| \exp\left(-\frac{\lambda_{\min}\{K\}}{m_f} t\right). \tag{79}$$

This result can be proven by selecting a candidate Lyapunov function $V = \frac{1}{2}\zeta^T M_f \zeta$ and utilizing similar arguments as in the proof of Theorem 1 along with Lemma 1.5 of [10].

3.4. Simulation Results

The adaptive control law described in Theorem 1 was simulated for a two spacecraft MSFF problem having the following parameters [11,12,31]

$$\begin{aligned} &M = 5.974 \times 10^{24} \text{ kg}, \quad m_f = 410 \text{ kg}, \quad m_l = 1550 \text{ kg}, \quad G = 6.673 \times 10^{-11} \tfrac{\text{m}^3}{\text{kg}\cdot\text{s}^2}, \\ &u_l = F_{dl} = 0 \text{ N}, \quad F_d = [1.9106, -1.9106, -1.517] \times 10^{-5} \text{ N}. \end{aligned} \tag{80}$$

The orbital elements and initial position for the leader spacecraft were selected as

$$T_l = 24 \text{ hours}, \quad e_l = 1.425 \times 10^{-5}, \quad \theta_0 = 0 \text{ rad}. \tag{81}$$

The initial condition for the desired, no-thrust, periodic trajectory $q_d(t)$ is selected using (62). Note that, given an initial relative position, we can choose different sets of initial relative velocity

vectors for the follower spacecraft satisfying (62). Next, by integrating (53) for the sets of valid initial conditions, we can obtain different periodic, relative motion geometries. In this research, the following initial conditions satisfying (62) were chosen to compute $q_d(t)$

$$q_d(0) = [-100 - 50 - 0.2] \text{ m}, \quad \dot{q}_d(0) = [-26.1805, 10.6574, 0.0398]^T \tfrac{\text{m}}{\text{sec}}. \tag{82}$$

Next, by integrating (53) with the initial condition (82), we obtained the desired, no-thrust, periodic trajectory $q_d(t)$ in the moving frame $\{x_l, y_l, z_l\}$.

In this simulation, the actual initial condition for the follower spacecraft were chosen the same as the desired initial condition while the parameter estimates were initialized to zero. The control and adaptation gains were tuned by trial and error until a good tracking performance was achieved, and are as follows

$$\begin{aligned} &\Gamma = \text{diag}\,(2.549, 16.85, 14.10, 20.20)\,, \quad K = \text{diag}\,(30.345, 25.475, 31.361)\,, \\ &\Lambda = \text{diag}\,(24.798, 17.50, 33.4)\,, \end{aligned} \tag{83}$$

where Γ is chosen as a reduced $\mathbb{R}^{4\times 4}$ form since $u_l = 0$ in this simulation.

The phase portrait of the actual trajectory $q(t)$ of the follower spacecraft relative to the leader spacecraft is illustrated in Figure 3 where "*" represents the leader spacecraft at the origin of the moving frame. Figure 4 depicts the position tracking error $e(t)$ which approaches zero as $t \to \infty$. Four components of the parameter estimate vector $\hat{\phi}(t)$ are shown in Figure 5. It is interesting to note that the controller estimates the unknown, constant perturbation force F_d accurately and exactly cancels it as shown in Figure 6. In addition, note that the follower spacecraft traces the ideal, desired, periodic trajectory exactly in steady-state, despite the presence of the unknown constant perturbations.

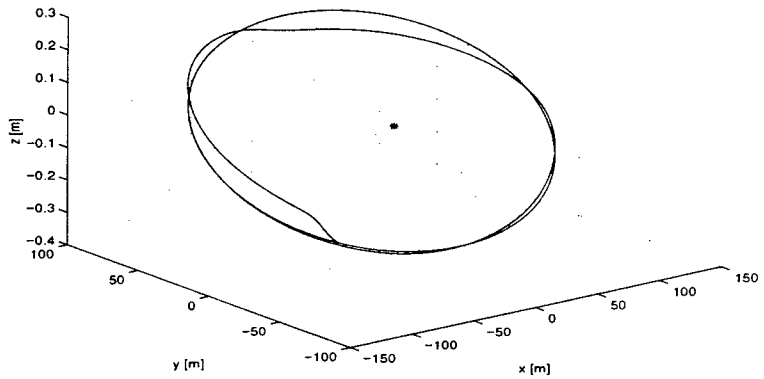

Figure 3: Actual trajectory of follower spacecraft relative to leader spacecraft ('*' denotes the leader spacecraft)

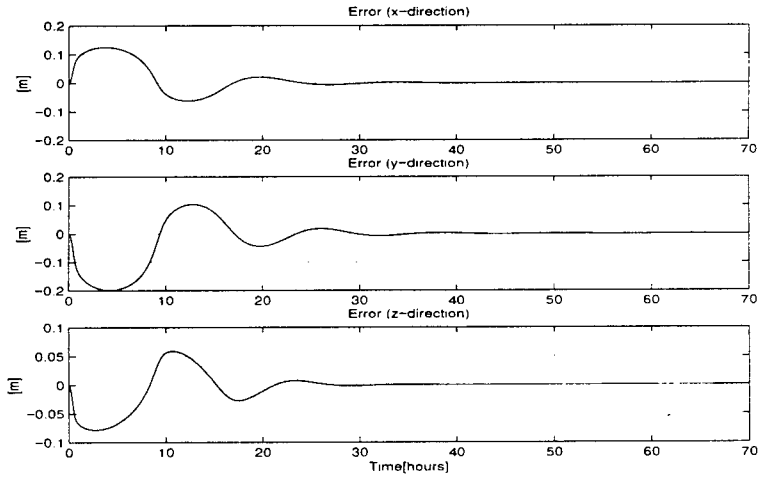

Figure 4: Position tracking error

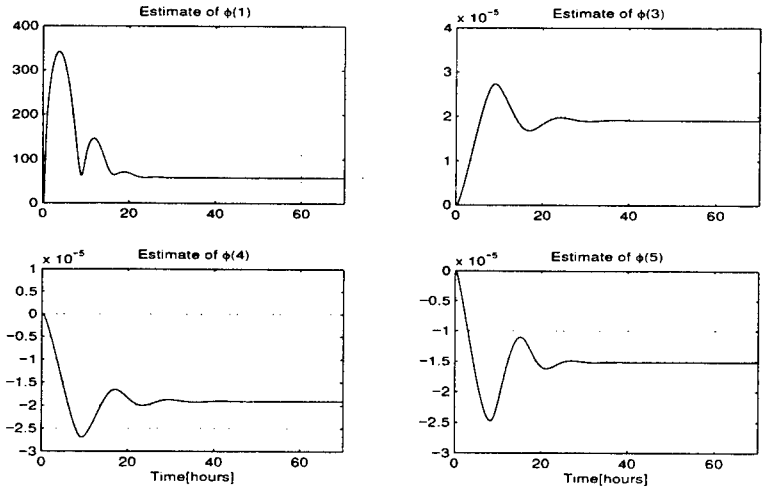

Figure 5: Sample of parameter estimates

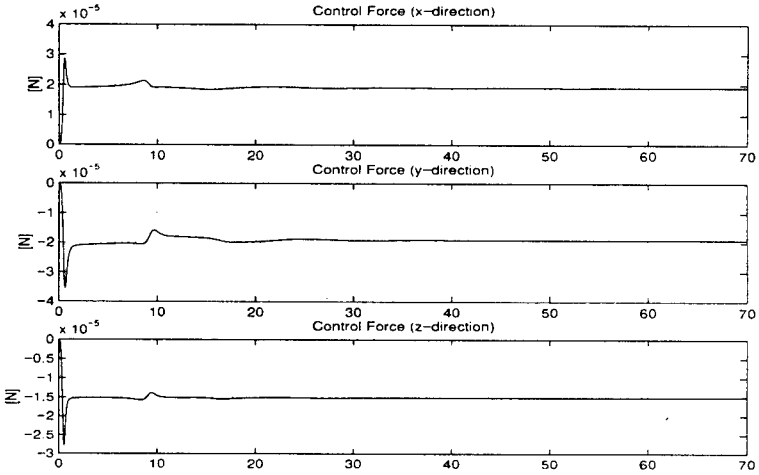

Figure 6: Control Input in x, y, and z directions

4. Additional Research Results

Next, we briefly summarize some additional MSFF control designs and related issues addressed in this research.

In an early effort [11, 12], we considered the problem of nonlinear relative position control for multiple spacecraft formation flying. Specifically, the full nonlinear dynamics describing the relative positioning of multiple spacecraft formation flying (with the leader spacecraft in a circular orbit around the Earth) were used to develop a Lyapunov-based, nonlinear adaptive control law that guarantees global asymptotic convergence of the position tracking error in the presence of unknown, constant or slow-varying spacecraft masses, disturbance forces, and gravity forces. Simulation results were developed to illustrate the controller performance for formation reconfiguration maneuver.

In [13], we considered the problem of relative position control for multiple satellite formation flying (MSFF) without velocity measurements. Specifically, in [13], we used the nonlinear dynamics describing the relative positioning of MSFF to develop a nonlinear, output feedback control law that guarantees the global uniform ultimate boundedness of the position and velocity tracking errors, despite the lack of velocity feedback and the presence of unknown satellite masses and disturbance force parameters. Simulation were conducted to illustrate the controller performance.

In [34], we addressed the attitude tracking problem of uncertain rigid spacecraft without angular velocity measurements. The adaptive control law, which incorporates a velocity-generating filter from attitude measurements, is shown to ensure the asymptotic convergence of the attitude and angular velocity tracking errors despite unknown spacecraft inertia. Simulation were carried to illustrate the theoretical results.

5. Concluding Remarks

In this research, we developed several linear and nonlinear MSFF control design methodologies. In particular, we developed a mathematically rigorous control design framework for linear control of spacecraft relative position dynamics with guaranteed closed-loop stability. A pulse-based control architecture has been proposed which can potentially lower the fuel consumption in MSFF. An illustrative numerical simulation demonstrated the efficacy of the proposed approach. In addition, we proposed a generalization of the pulse-based, discrete-time feedback control law to the case $p > 1$ via a periodic control architecture.

We also developed the dynamic equation of relative motion for MSFF when the leading spacecraft is in an elliptical orbit. This dynamic model has wider application and yields greater precision compared with the linearized Hill's equation model which is restricted to circular spacecraft orbits. Furthermore, we derived an initial condition constraint which enables ideal, no-thrust, periodic relative motion trajectory. Next, using a Lyapunov-based design and analysis framework, we developed an adaptive controller which was shown to guarantee global asymptotic position tracking errors in the presence of unknown spacecraft masses and exogenous perturbing forces. Simulation results were provided to demonstrate the efficacy of the formation initialization methodology and the adaptive controller performance.

Finally, in related research, we also developed a FSFB, nonlinear, adaptive control law and an OFB, nonlinear, robust control law for MSFF. In addition, an OFB control law was developed for spacecraft attitude control.

References

1. Available on the Web at http://www.vs.afrl.af.mil/factsheets/TechSat21.html.

2. Available on the Web at **http://origins.jpl.nasa.gov/missions/overview.html**.

3. *Proceedings of the Air Force Research Laboratory - Formation Flying and Micro-Propulsion Workshop*, Lancaster, CA, 1998.

4. "Shuttle 7 to Fly Approaches to Payload," *Aviation Week and Space Technology*, **118**-19, 51–57, 1983.

5. Bauer, F. *et al.*, "Satellite Formation Flying using An Innovative Autonomous Control System (AUTOCON) Environment," *Proceedings of the AIAA Guidance, Navigation, and Control Conference*, New Orleans, LA, 1997, pp. 657–666.

6. Bittanti, S., Colaneri, P., and DeNicolao, G., "The Periodic Riccati Equation," *The Riccat Equation*, Springer-Verlag, 1991, pp. 127–162.

7. Chao, C. C., Pollard, J. E., and Janson, S. W., "Dynamics and Control of Cluster Orbits for Distributed Space Missions," *Proceedings of the AAS/AIAA Space Flight Mechanics Meeting*, 1999, Paper No. AAS99-126.

8. Chobotov, V. A., (Ed.) *Orbital Mechanics*, AIAA, Washington, DC, 1996, pp. 31-33.

9. Clohessy, W. H. and Wiltshire, R. S., "Terminal Guidance System for Satellite Rendezvous," *Journal of Aerospace Science*, Vol. 27, No. 9., 1960, pp. 653-658.

10. Dawson, D.M., Hu, J., and Burg, T.C., *Nonlinear Control of Electric Machinery*, Marcel Dekker, New York, NY, 1998, pp. 1-19.

11. de Queiroz, M.S., Kapila, V., and Yan, Q., "Adaptive Nonlinear Control of Satellite Formation Flying," *AIAA Guidance, Navigation, and Control Conference*, Portland. OR, August 1999, AIAA paper no. 99–4270, pp. 1596–1604.

12. de Queiroz, M.S., Kapila, V., and Yan, Q., "Adaptive Nonlinear Control of Multiple Spacecraft Formation Flying," *AIAA J. Guid. Contr. Dyn.*, to appear.

13. de Queiroz, M.S., Yan, Q. , Yang, G., and Kapila, V., "Global Output Feedback Tracking Control of Spacecraft Formation Flying with Parametric Uncertainty," *Proc. IEEE Conf. Dec. Contr.*, Phoenix, AZ, December 1999, pp. 584–589.

14. Dorato, P., Abdallah, C., and Cerone, V., *Linear-Quadratic Control: An Introduction*, Prentice-Hall, Englewood Cliffs, NJ, 1995, pp. 174–176.

15. Guinn, J. R., "Autonomous Navigation for the New Millennium Program Earth Orbiter 1 Mission," *Proceedings of the AIAA Guidance, Navigation, and Control Conference*, New Orleans, LA, 1997, pp. 612–617.

16. Hadaegh, F.Y., Lu, W.M., and Wang, P.C., "Adaptive Control of Formation Flying Spacecraft for Interferometry," *IFAC Conference on Large Scale Systems*, Rio Patras, Greece, 1998, pp. 97-102.

17. Haddad, W.M., Kapila, V. and Collins, Jr., E.G., "Optimality Conditions for Reduced-Order Modeling, Estimation, and Control for Discrete-Time Linear Periodic Plants," *J. Math. Syst. Est. and Contr.*, **6**, 1996, pp. 437–460.

18. Kapila, V., "Spacecraft Formation Flying: A Survey." Tech. Rep., Air Force Office of Scientific Research–Summer Faculty Research Program 1998, pp. 7.1–7.19.

19. Kapila, V., Sparks, A. G., Buffington, J. M., and Yan, Q., "Spacecraft Formation Flying: Dynamics and Control," *Proc. Amer. Contr. Conf.*, San Diego, CA, June 1999, pp. 4137 4141; see also *AIAA J. Guid. Contr. Dyn.*, to appear.

20. Kuo, B. C., *Digital Control Systems*, Saunders HBJ, New York, NY, 1992, pp. 55–59 and 556–566.

21. Lau, K. *et al.*, "The New Millennium Formation Flying Optical Interferometer," *Proceedings of the AIAA Guidance, Navigation, and Control Conference*, New Orleans, LA, 1997, pp. 650–656.

22. Leitner, J., Beck, J., and Bell, K., "Advanced Guidance, Navigation, and Control for Remote Sensing," 1997, AIAA Paper.

23. Leonard, C. L., Hollister, W. M., and Bergmann, E. V., "Orbital Formationkeeping with Differential Drag," *Journal of Guidance, Control, and Dynamics*, Vol. 12, No. 1, 1989, pp. 108–113.

24. Redding, D. C., Adams, N. J., and Kubiak, E. T., "Linear-Quadratic Stationkeeping for the STS Orbiter," *Journal of Guidance, Control, and Dynamics*, Vol. 12, No. 2, 1989, pp. 248–255.

25. Robertson, A., Corazzini, T., and How, J. P., "Formation Sensing and Control Technologies for a Separated Spacecraft Interferometer," *Proceedings of the American Control Conference*, 1998, pp. 1574–1579.

26. Sabol, C., Burns, R., and McLaughlin, C., "Formation Flying Design and Evolution," *Proceedings of the AAS/AIAA Space Flight Mechanics Meeting*, 1999.

27. Sedwick, R. J., Wong, E. M. C., and Miller, D. W., "Exploiting Orbital Dynamics and Micropropulsion for Aperture Synthesis using Distributed Satellite Systems: Applications to TechSat 21," 1998, AIAA Paper No. 98-5289.

28. Schilling, J. and Spores, R., "Comparison of Propulsion Options for TechSat 21 Mission," presented at the *Air Force Research Laboratory–Formation Flying and Micro-Propulsion Workshop*, Lancaster, CA, Oct 20, 21, 1998.

29. Slotine J.J. and Li, W., A*pplied Nonlinear Control* , Prentice Hall, Englewood Cliff, NJ, 1991, pp. 122-126.

30. Vadali, S. R., "Analysis and Distributed Control of a Formation of Intelligent Satellites," presented at the *Air Force Research Laboratory–Formation Flying and Micro-Propulsion Workshop*, Lancaster, CA, Oct 20, 21, 1998.

31. Vassar, R. H. and Sherwood, R. B., "Formationkeeping for a Pair of Satellites in a Circular Orbit," *Journal of Guidance, Control, and Dynamics,* Vol. 8, No. 2, 1985, pp. 235–242.

32. Wang, P.K.C. and Hadaegh, F.Y., "Coordination and Control of Multiple Microspacecraft Moving in Formation," *Journal of Astronautical Sciences*, Vol. 44, No. 3, 1996, pp. 315 355.

33. Wang, P.K.C., Hadaegh, F.Y., and Lau, K., "Synchronized Formation Rotation and Attitude Control Of Multiple Free-Fyling Spacecraft," *Journal of Guidance, Control, and Dynamics*, Vol. 22, No. 1, 1999, pp. 1582-1589.

34. Wong, H., de Queiroz, M.S., and Kapila, V., "Adaptive Attitude Tracking Control without Velocity Measurements," *Automatica*, submitted (1999).

MICRO-SCALE FLOW FIELD MEASUREMENT OF THE THIN MENISCUS OF CAPILLARY-DRIVEN HEAT EXCHANGER DEVICES USING MOLECULAR FLUORESCENCE VELOCIMETRY (MFV)

Kenneth D. Kihm
Associate Professor
Department of Mechanical Engineering

Texas A&M University
College Station, TX 77843-3123

Final Report for:
Summer Faculty Research Program

Sponsored by:
Air Force Office of Scientific Research
Wright-Patterson Air Force Research Laboratory

April 2000

MICRO-SCALE FLOW FIELD MEASUREMENT OF THE THIN MENISCUS OF CAPILLARY-DRIVEN HEAT EXCHANGER DEVICES USING MOLECULAR FLUORESCENCE VELOCIMETRY (MFV)

Kenneth D. Kihm
Associate Professor
Department of Mechanical Engineering
Texas A&M University, College Station, Texas

Abstract

The purpose of this study is to develop Molecular Fluorescent Velocimetry (MFV), which is a nonintrusive visualization method that uses a caged dye called Photo-Activated Fluorophores (PAF's) for the visualization and measurement of velocity flow fields in micro-scale flows. The Photo-Activated Fluorophores are a caged dye that is optically uncaged and tracked by triggering its fluorescence. When the PAF's are caged they are not fluorescent but once they are uncaged with ultraviolet light, the dye is then able to fluoresce. This fluorescence is activated with visible light and it displays an image of the velocity profile of the fluid flow. The PAF's are mixed at relatively low concentrations in a fluid such as water and an ultraviolet laser beam tags a specific region in a flow field which uncages the dye in that region of the flow. The uncaged dye is then illuminated with 488 nm wavelength (blue) light, pumping the dye's fluorescence at an approximately 518 nm wavelength (yellow) of light in the shape of the velocity profile of the flow field. The flooding light and the induced fluorescence produce a contrast for easy visualization of the flow field. From these images, the shape and velocity of the flow field may be determined by using a CCD camera in conjunction with a computer to capture pictures of the flow for post-data analysis. This type of information has been unavailable in the past due to ineffective imaging techniques for micro-scale flows and has value for a variety of applications such as ongoing research of heat transfer augmentation of capillary pumped heat transport devices.

Introduction

Molecular Fluorescent Velocimetry (MFV) is a new technique that is being developed for the study of microscale flow fields. With a lack of such a technique today, MFV will prove to be an exciting means of studying such flows, of which the behavioral properties are currently virtually unknown. MFV utilizes a caged fluorescent dye (Photo-Activated Fluorophores or PAF's) that upon uncaging and illumination, fluoresces at a high intensity. A line of this dye is uncaged and illuminated so that it can be tracked as the flow of the fluid progresses. This allows for the determination of the velocity vectors of the flow field and for the visualization of these microscale flows. The size of the dye particles is on the order of a few nanometers, so it is easily used for microscale flows where other commonly used flow field mapping techniques such as Particle Image Velocimetry cannot be applied.

Technology is constantly and ever more quickly changing and in every industry and discipline there is a push to make things smaller. With such demands comes a need for new techniques and methodologies that can properly be applied to the microscale so the design of small components and systems can be very precise. Such a scenario is just one example of the necessity of knowledge about microscale flows. Others include fluid dynamic research, heat transfer and thin film evaporation research, etc. Molecular Fluorescent Velocimetry (MFV) is a technique that in the future will prove very valuable for the study of microscale flows for a variety of applications.

MFV utilizes a caged fluorescent dye that upon uncaging and activation fluoresces visible light. The migration of a line of this fluorescing dye allows for the determination of the velocity profile of a flow field for microscale flows. The dye is dextran caged fluorescein that is initially unable to fluoresce, but upon exposure to ultraviolet radiation, the caging chemical group on the compound is cleaved and the molecule regains its affinity to fluoresce. This fluorescence is activated upon exposure to blue light and the molecule then fluoresces yellow light. The yellow images are easily seen be the naked eye and captured using video capturing equipment. The digitized images of the fluorescent line's progression through a capillary pore allow for the study of the flow fields in millimeter and even micron scale flows.

Methodology

Molecular Fluorescent Velocimetry utilizes a state of the art experimental setup. No equipment is currently manufactured for the explicit use of this type of experiment, so the entire apparatus was designed

and built from scratch. The summer of 1999 was spent building and testing the experimental apparatus. The fall of 1999 was utilized modifying and tweaking the experimental apparatus and doing initial testing of the technique that is presented in this report.

Figure 1 illustrates a schematic of the basic experimental setup for MFV. A triple harmonic Nd:YAG ultraviolet laser beam (with a wavelength of 355 ranging from 100 μJ to approximately 1 mJ) initially exits the laser as a pulse with a diameter of 8 mm and a duration of 5 to 6 nanoseconds. The Nd:YAG laser is capable of emitting three different wavelengths of light, 355 nm, 532 nm, and 1064 nm. The 532 nm, or green light is used for alignment of the experimental apparatus. It allows for easy visualization of the position of the beam and does not harm any of the equipment.

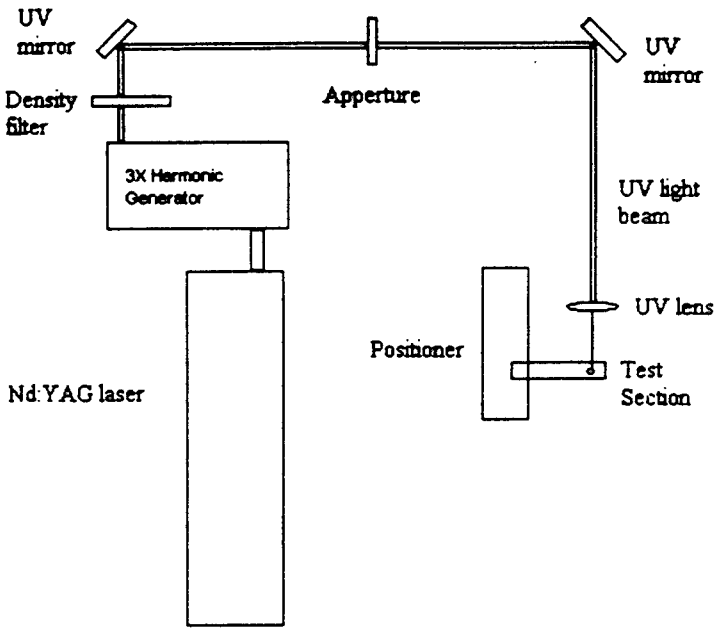

Figure 1: Schematic of basic experimental apparatus set up.

To conduct the experiment, the Nd:YAG laser is fired and the laser beam passes through a density filter and then reflects off an ultraviolet mirror at a 90° angle and passes through an aperture (see Figure 2 for a picture of the actual setup). The density filter ensures that the power of the beam is not too high to try to avoid damage to the equipment. The aperture decreases the beam's size and eliminates noise and diffused light from the edge of the beam as it passes through the aperture's 5 mm diameter opening. The

beam reflects off another ultraviolet mirror at a 90° angle so that it is aligned to hit the test section which is positioned parallel to the Nd:YAG laser. An ultraviolet lens focuses the laser beam from 5 mm in diameter, to 20 μm in diameter at the beam waist where it contacts the test section. About 26% of the power losses for the UV beam occur at the first mirror, 38% at the aperture, 14% at the second mirror and 22% at the UV lens.

Figure 2: Picture of experimental apparatus. At the back is the Nd:YAG, to the left the Argon-ion laser, in the center is the test section and the visualization equipment.

The test section is a capillary pore held with a three-degree-of-freedom positioner. The positioner allows for alignment of the centerline of the test section with the ultraviolet beam. An argon-ion blue laser (which emits 488nm wavelength beam at 40 mW with a 1.5 mm diameter) illuminates the test section from the opposite side as that of the ultraviolet laser. The blue beam is filtered by a narrow band pass interference filter to remove extraneous wavelengths of light incidentally produced by the laser that can induce uncaging of the fluorescent dye. A cylindrical lens creates a laser sheet parallel to the capillary pore that illuminates the test section along the pore's centerline. The blue beam excites the dye that is uncaged by the ultraviolet laser pulse so that it fluoresces at 518 nm (yellow light).

To induce flow in the test section, a coil wire heater is wrapped around the capillary pore and attached to a power source. Typically 3W from the power source was used to heat the fluid and the heater was placed both below the meniscus of the fluid and above to observe the effects of different heating conditions on the induced flow.

The fluorescent images in the test section are captured using a CCD camera with a macro lens for magnification. The magnification required depends on the size of the test section and is chosen so that the fluorescent images fill the entire field of view. Extension pieces are easily added to the lens to increase or decrease the magnification as desired. A longpass color glass filter is aligned in the front of the CCD camera to prevent wavelengths of light other than the 518 nm wavelength emitted by the fluorescent dye to be captured by the camera. The CCD camera transmits the images to a video capture board in a PC and to video capture software. The Asymetrix Digital Video Producer software was used for this purpose and served its function well. The software captures 10 frames per second as digital video in the form of .avi files. These digital images are then edited to remove background noise from extraneous uncaged dye and is later analyzed to determine the velocity vectors in the flow field.

The fluorescent dye used for this experiment is a dextran caged fluorescein with a molecular weight of 10,000 grams/mole (product number D-3310) manufactured by Molecular Probe, Inc. this dye has an optimal excitation wavelength of 494 nm and an emission wavelength of 518 nm. The probe is water-soluble and is mixed to a concentration of 0.05 grams per liter of distilled, deionized water. At this low concentration, the properties of the water are not changed to any significant degree. This concentration is sufficient to induce images that are bright enough to be easily seen by the naked eye and captured by the camera. Extensive testing has not completed to determine the optimal concentration of the probe, and lower concentrations will most likely also be sufficient. Lempert, et al. (1995) used a concentration ranging between 1 and 5 mg per liter, however this concentration proved to be far too low for these experiments. Also, Paul, et al. (1998) recommended 5 mg dissolved in 3 mL of 0.1 molar sodium carbonate buffer with a pH 9.0. The dextran used for this experiment is easily dissolved in water and the concentration Paul recommends is far too high. Concentrations are easily recognizable as being too high if the yellow characteristic color of the uncaged dye is visible without exposure to blue light.

The probe must be carefully handled and stored. The caging compound is inherently unstable and its instability is increased with exposure to high temperatures and ultraviolet light sources, including ambient light. The probe should be handled in a dark environment and stored at temperatures around –7 °C to minimize uncaging. The heating of the probe to induce the flow for this experiment causes significant uncaging of the probe, which does decrease the clarity of the images, though as seen in Figures 3 and Figure 5, the probe uncaged by the ultraviolet beam is significantly brighter. The images can be digitally edited to remove the background uncaged dye by "subtracting" an initial frame that is illuminated by the blue laser, but not yet uncaged by the ultraviolet laser from all subsequent frames in the video footage. Such editing is easily accomplished by using a software package such as Adobe Photoshop.

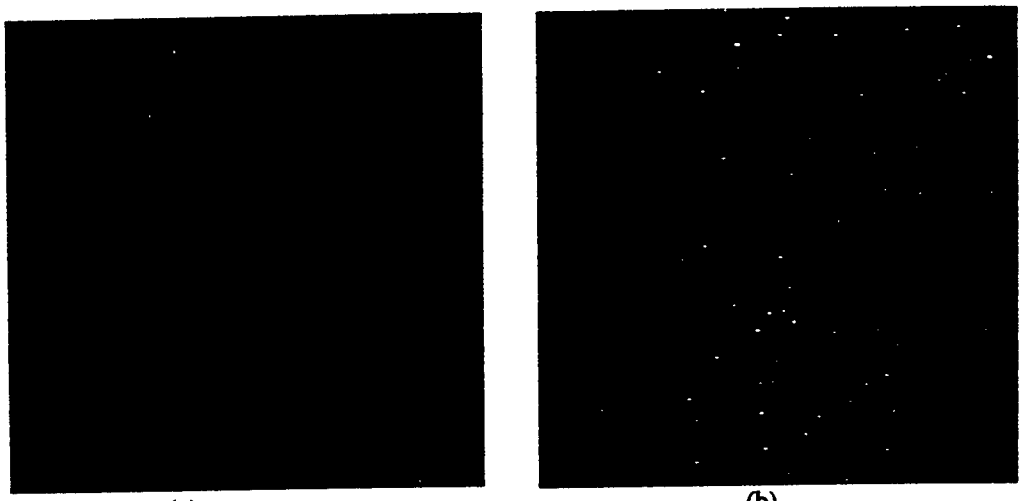

(a) (b)

Figure 3: (a) initial frame, (b) image with background subtracted, compare to images in Figure 5.

Experimental Procedure

The basic procedure for MFV is fairly simple and straightforward. The difficulty lies in the alignment of the uncaging, ultraviolet beam and the illuminating blue beam with each other and with the test section. The test section can be oriented in two different manners, horizontal for study of capillary bulk flow or tilted at a low angle from the horizontal for study of milli and microscale flows around the meniscus (as seen in Figure 4). Alignment with the tilted test section is much easier than using a small diameter capillary tube oriented horizontally for examining the smaller scale flows.

Figure 4: Test section orientation for tilted case.

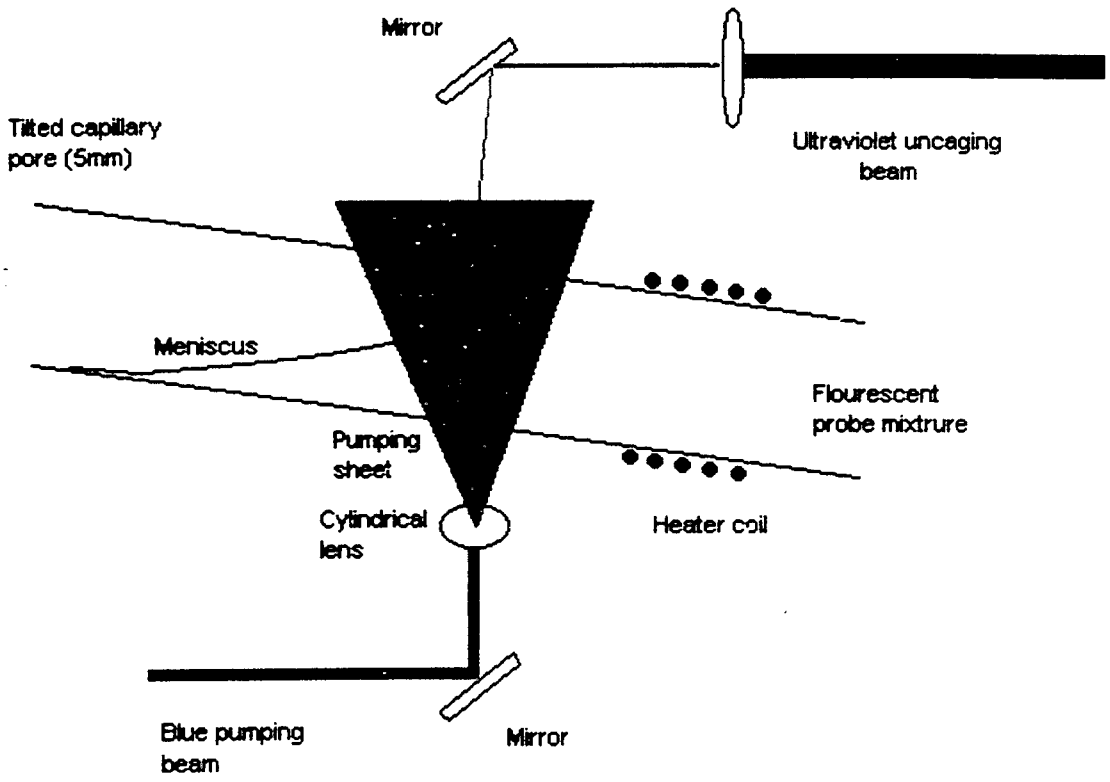

Before beginning the experiment, the lasers need to be turned on and all settings properly determined and set. The Nd:YAG is not run at full power because of damage that can occur to the

ultraviolet mirrors and the capillary tube itself. For optimal uncaging and minimized damage to the apparatus, the ultraviolet laser is set to 100 μJ output. The argon-ion laser is run at full intensity to maximize the brightness of the fluorescence. The higher the intensity of the incident blue beam, the brighter the yellow, fluorescent images. Before uncaging, the lasers also must be properly aligned, which can be a delicate process. If the ultraviolet beam and the blue beam are not coincident in the capillary tube, then the uncaged dye may move out blue laser sheet, which eliminates the fluorescence.

The imaging system must also be properly set up, ensuring proper focus and alignment. Image acquisition will begin just before uncaging.

The probe should be pre-mixed to the proper concentration and is stored at –7 °C. Before removing the probe from the refrigerator, the room must be darkened to minimize any uncaging from ambient light. The probe should be exposed to heat and light for as minimal a time as possible. Connect the heater on the capillary tube to the power source and allow the temperature of the probe to reach steady state, but keep it well below the boiling point of the fluid. Once steady state has been attained, flood the test section with the blue light and then quickly begin data acquisition. After a few frames, pulse the probe once with the ultraviolet beam, and then again at regular time intervals until the imaging sequence is complete. The initial frame before uncaging will be used as a datum to remove background noise and images from the captured fluorescent images. Stop the flooding of the probe with the blue laser, turn off the power source to the heater and return the probe to the refrigerator. Continue with image editing and analysis of the flow fields.

Results and Discussion

The results of the preliminary stages of implementing MFV have been very favorable. Successful visualization of flows on a 5 mm scale and 1 mm scale has been completed as well as studies of bulk and meniscus flow for different heating arrangements. Figure 5 shows typical images collected for bulk and thin film flow with different heater orientations. Generally it was determined from these images that for the tilted case, the flow in the meniscus region is toward the meniscus when the heater is placed below the meniscus and the flow is away from the meniscus when the heater is placed above the fluid meniscus. Bulk flow in the capillary pore circulates up (towards the meniscus) at the center of the pore and then down

along the sides of the pore. Research is continuing in adjusting the MFV technique for smaller and smaller flows as well as for the visualization of the flow fields off the centerline of the pore.

MFV has evolved immensely since work on the work on the experimental technique and apparatus began in June of 1999. A number of problems have arisen since then and been successfully resolved. Others are continually being worked on and improved.

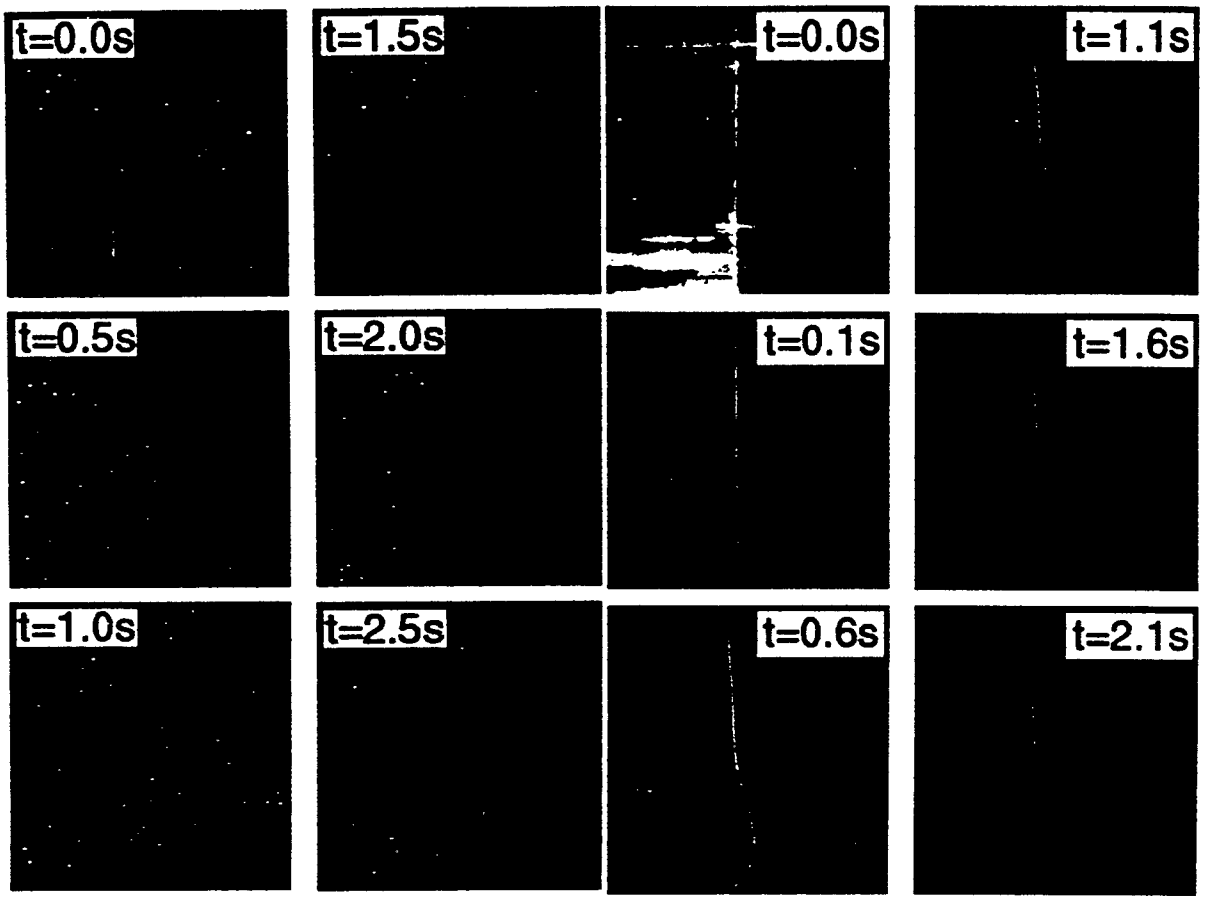

(a) (b)

Figure 5: a) Meniscus flow with the heater oriented above the meniscus (to the right), approximately 1-mm scale. b) Bulk flow with the heater oriented below the meniscus (to the left), 5-mm scale.

The fluorescent probe used for this experiment is a complicated and delicate technology. As previously mentioned, the dextran caged fluorescein (10,000 M; 10 to 15 nm in size when caged; ~3 nm when uncaged) is an inherently unstable molecule that is susceptible to degradation from heat, light, and time. The probe consists of a molecule that naturally has the ability to fluoresce, but that fluorescence is quenched, or "caged", by the addition of a specific chemical group. The chemical bond of this group is destroyed in the presence of the ultraviolet radiation. However, lower wavelengths of light may also cause uncaging, although not to the same degree. For instance, it is recommended that the probe be exposed to ambient light for no more than 15 minutes or significant uncaging could occur. Fluorescent lights are especially damaging, although sunlight is not as bad because the glass in windows usually filters most of the ultraviolet radiation. Also, continuous heating increases the rate of spontaneous uncaging although quantitative information on the effects of heating is not yet available. The probe is most stable when stored and handled at temperatures near freezing.

The probe is also hydroscopic, so its original powder form can easily turn into a type of paste in a humid environment. However, this characteristic does not harm the normal function of the probe. The uncaged probe is also inherently yellow in color, but this color is not visible in the concentrations used for these experiments and does not hinder the proper visualization of the fluorescent images. The probe also has two wavelength peaks at which its fluorescence may be induced. The first is at 485 nanometers and the second is in the 250-300 nanometer range. However, exposure for any length of time to the second range also destroys the molecules and is not recommended to induce fluorescence.

Once the probe is exposed to the ultraviolet beam, there is a delay in the millisecond range before uncaging begins and uncaging is complete within half of a second (Lempert et al. 1995). The delay on the fluorescence once the dye is pumped is in the nanosecond range and the fluorescent lifetime is 4 nanoseconds. Since the Nd:YAG laser is triple harmonic, it produces small levels of the other two wavelengths (532 and 1064). However, these wavelengths will not pump the dye since the pulses only have a 7-nanosecond duration, which is not enough time for uncaging to occur. The fluorescence, on the other hand, occurs nearly instantaneously.

Another area essential to the proper functioning of the technique is the pumping light intensity. As mentioned earlier, an Argon-ion blue laser is used to induce the fluorescence of the dye. This, however,

was not the original planned configuration for pumping the fluorescence. A halogen lamp in conjunction with a blue filter was to be used, but the light intensity was not strong enough to be captured by the camera, and was only dimly visible to the naked eye. For the proper intensity, an Argon-ion laser or a mercury vapor lamp is recommended. Lempert recommends a pulse intensity of 3×10^5 Watts/cm^2. For these experiments, the Argon-ion laser has performed very well.

Problems also arose with the use of the capillary pore. Obviously there is some reflection and refraction of the laser beams and the images as they pass through the pore walls, but the effects were not significantly detrimental for the scales studied thus far. Some testing was completed on a 1-mm capillary pore and the reflection, refraction, and diffusion problems were significant and the images were dim and blurry. To address these issues, the orientation of the 5-mm pore was changed to allow for study of flows on the 1 mm scale. The pore is tilted to a small angle from the horizontal to create a long this meniscus along the capillary wall. A schematic of these two orientations and different heater orientations are shown in Figure 6. The use of the tilted pore also addressed another issue.

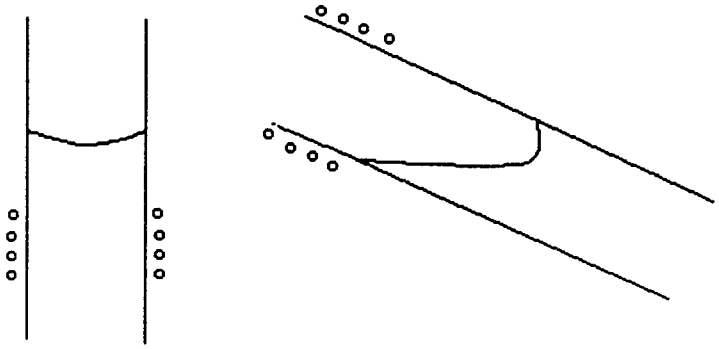

Figure 6: Capillary and heater orientations, vertical and tilted, and below and above the meniscus, respectively.

For the upright section, the meniscus reflects most of the pumping light so those images in only one half of the meniscus region are visible (see Figure 7). The pore is illuminated from the left of the test section, so

the meniscus area on the right remains dark. With the tilted pore, only one side of the meniscus is uncaged and illuminated, so it eliminates these problems.

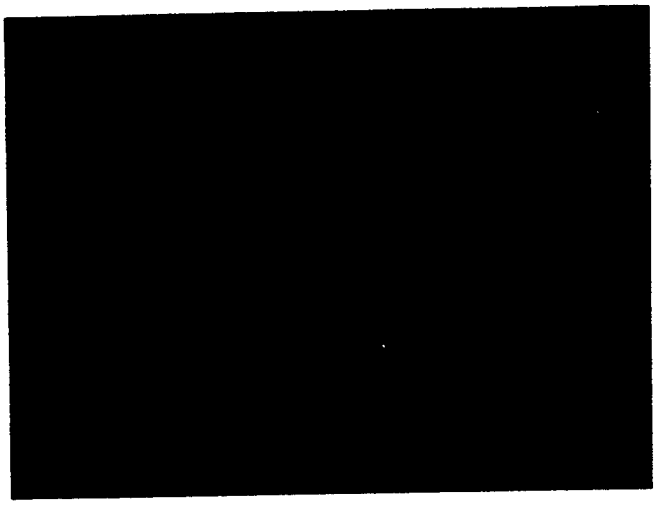

Figure 7: Fluorescence blackout due to meniscus.

Also, a macro lens is favored over an objective for the size of the flows studied. A Mitutoyo objective was originally used, but this high-powered lens also decreased the intensity of the images captured by the CCD camera. A macro lens with the use of extension tubes easily created enough magnification for the images to fill the entire field of view of the camera. The use of a Mitutoyo objective will be necessary, however, at smaller scales when magnification for the macro lens is no longer sufficient.

The entire experimental apparatus is currently placed on one worktable. table and the imaging system is located on another. Modifications will need to be made to this arrangement, however, when higher power magnification is required for the study of smaller scale flows. At high magnifications, small vibrations inherent to the equipment being used and the building become very apparent. To eliminate these vibrations, an optical table is required and will soon be implemented.

Overall the initial testing of Molecular Fluorescent Velocimetry has been very successful and promises more success in the future. MFV is still in its developmental stage, but it will soon prove to be an exciting and important technique for the study of microscale flows.

Comparison to Other Techniques

Currently, the most widely used method for visualizing flow fields in fluid flow is Particle Image Velocimetry (PIV). PIV utilizes small particles that are several microns in diameter, which scatter laser light for the visualization of flow fields. This scattering allows for simple visualization and tracking of the particles so that the velocity vectors of the flow field may be determined. However, the particles that are several microns in diameter are far too large to be used for microscale flows and are even difficult to use for a 1-mm scale. On the 1-mm scale, only a few particles are in the field of view that can be tracked and not enough data is available for proper analysis. See Figure 8 for a comparison of the results from PIV and MFV for a 5-mm capillary tube bulk flow. Molecular Fluorescent Velocimetry allows for the study of flows that is impossible for Particle Image Velocimetry.

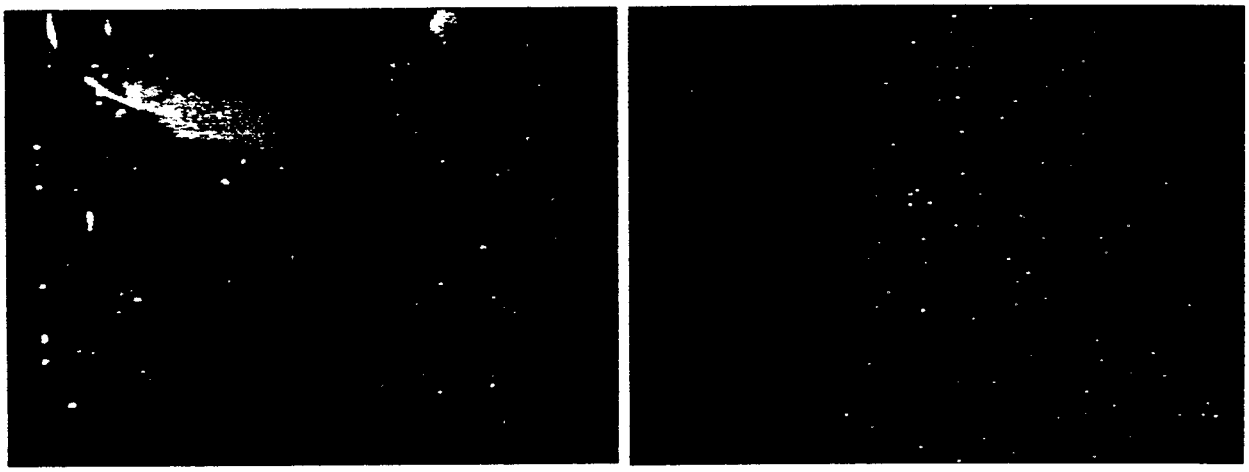

Figure 8: Comparison of PIV and MFV for 5-mm bulk flows. (The MFV image is rotated 90°.)

Conclusions

Molecular Fluorescent Velocimetry has successfully allowed for the visualization of millimeter scale flows. Further research will continue to refine the technique so that it may be applied to the extent possible to even smaller scale flows. This technique is very promising for aiding the study of microscale flows in the near future.

References

1. Edmund Scientific Company: Industrial Optics Division, Barrington, NJ; Catalog N991B.

2. Gendrich, C.P.; Koochesfahani, M. M. "A Spatial Correlation Technique for Estimating Velocity Fields Using Molecular Tagging Velocimetry (MTV)," *Experiments in Fluids*, Vol. 22, pp. 67-77, 1996.

3. Kihm, Kenneth; Personal Communication, Associate Professor, Department of Mechanical Engineering, Texas A&M University, 1999.

4. Lempert, W.R.; Magee, K.; Ronney, P.; Gee, K.R.; Haugland, R.P. "Flow Tagging Velocimetry in Incompressible Flow Using Photo-Activated Nonintrusive Tracking of Molecular Motion (PHANTOMM)," *Experiments in Fluids*, Vol. 18, pp. 249-257, 1995.

5. Molecular Probe Inc., Eugene, OR; www.probes.com.

6. Okamotao, Koji; "Future of Particle Imaging Velocimetry," Invited Seminar Presentation, Department of Nuclear Engineering, University of Tokoyo, July 19, 1999; Texas A&M University.

6. Paul, P.H.; Garguilo, M.G.; Rakestraw, D.J. "Imaging of Pressure- and Electrokinetically Driven Flows through Open Capillaries," *Analytical Chemistry*, Vol. 70, pp. 2459-2467, 1998.

7. Webb, A.; Maynes, D. "Velocity Profile Measurements in Microtubes," AIAA 99-3803, 30th AIAA Fluid Dynamics Conference, Norfolk, VA, 28 June – 1 July 1999.

Uncertainty Modeling of Target Locations from Multiplatform and Multisensor Data

Project Report (SREP 99-0831)

January 1, 1999 - February 29, 2000

Submitted to
Air Force Office of Scientific Research (AFOSR)

By

Principal Investigator: Dr. Rongxing Li
Researchers: Ruijing Ma and Jason Blevins

Department of Civil and Environmental Engineering
And Geodetic Science
The Ohio State University

February 2000

Table of Contents

1. Introduction 1

2. Experimental data.....2

2.1 Image data.....2

2.2 Metric camera parameters 3

2.3 Network configuration 6

2.4 Ground control.....7

2.5 Photogrammetric triangulation and DTM generation.....9

2.5.1 Photogrammetric triangulation.....9

2.5.2 DTM generation.....11

2.5.3 Orthophoto generation.....13

3. Conclusions.....14

4. Acknowledgements.....16

References.....16

Appendix A. Standard deviations of all points (original printout of ERDAS).....18

Appendix B. Detailed computational information in the iterative process.....21

1. Introduction

This research project has been concentrated on modeling the geometry of sensors and associated uncertainties. The ultimate goal is to reduce uncertainties of target locations derived from data that are acquired by using multisensors and multiplaforms. In this project we focused on processing of a data set of optical images acquired at the Elgin Air Force Base. Our tasks were to (a) reconstruct the geometric configuration of the sensors during the imaging process, (b) build a photogrammetric bundle adjustment model that includes images taken at different positions, and (c) reconstruct the location and orientation of the sensors, generate a digital terrain model, and analyze uncertainties involved in the output.

The project started with Mr. Jason Blevens, an MS research associate. He had reviewed the literatures, worked on the mathematical model, and initiated the image processing of the optical images. Mr. Ruijing Ma, a Ph.D. research associate, continued working on the project after Mr. Blevans left for a company in Columbus, Ohio.

During this year, we have been intensively working on the mathematical model for uncertainty modeling of the optical images, application of the model for Eglin test site images, and analysis of processing result. Supported by other projects funded by NOAA, NASA, and NSF in the Mapping and GIS Lab of OSU, we have obtained extensive knowledge, data, software and hardware systems that also make this project so efficient and cost effective. For example, the SGI O2 UNIX workstation and IMAGINE and OthoMax software packages from ERADS Inc. were purchased without charging to this project. However, it was also extensively used for data processing for this project.

The project has investigated the characteristics of radial and tangential lens distortions of the camera; we have tested a variety of tie point and GCP distributions to achieve the high quality accuracy of the sensor orientation parameters and ground point locations; multiple images are used to build an image network to improve the geometric strength for

precise ground target localization; and finally, a high quality digital terrain model of the area is generated from the all images covering the area.

2. Experimental data

2.1 Image data

A large data set of aerial photography over the study area, Eglin Air Force Base, was acquired by using a high quality optical metric camera. Such a mapping camera usually provides characteristics of very high optical quality, calibrated camera model for photogrammetric processing and very fine resolution for metric applications. The images were acquired in the analog form and scanned into a digital form. Nine images centering around the test field with vehicles are selected for investigation. An aerial photograph is shown in Figure 1.

Figure 1: An aerial photograph of the study area

The ground covered by the images is relative flat. Therefore, the displacement caused by elevation differences is not significant. There is a river running from North to South in the west part of the area. A significant portion of the test field is covered by dense and high woods, which create difficulties for recognition of features for photogrammetric triangulation. A whole view of the test field is depicted by a mosaic of the nine photographs.

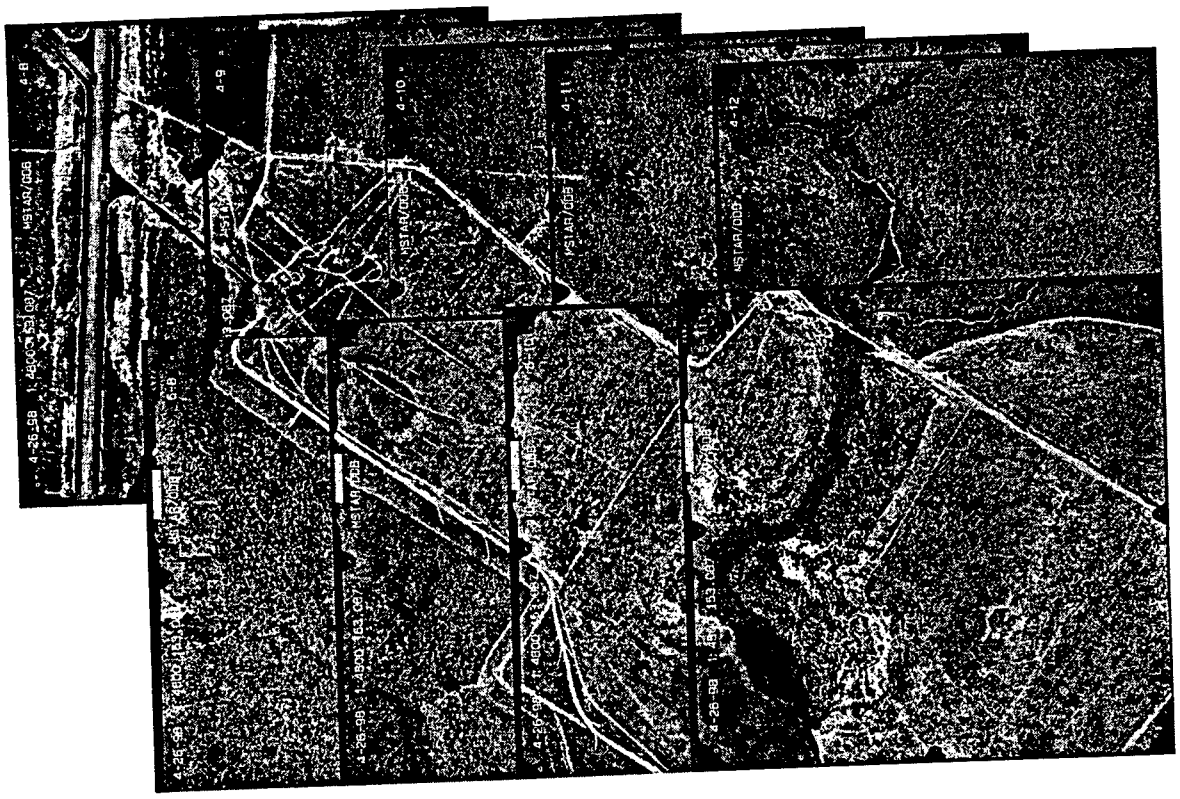

Figure 2. A mosaic of the study area

2.2 Metric camera parameters

The RC30 camera manufactured by Wild in Switzerland has a lens of Wild Universal Aviogon A4-F. The calibrated focal length is 153.087mm. The symmetric radial distortion parameters are

$K_0 = 5.527e\text{-}5$

$K_1 = -1.072e-8$

$K_3 = 0$

$K_4 = 0$

The decentering distortion parameters are

$P_1 = -1.397e-7$

$P_2 = 1.411e-7$

$P_3 = 0$

$P_4 = 0$

The calibrated principal point is at

$x_p = 0.001mm$

$y_p = -0.012mm$

There are eight fiducial marks on each photograph. Their distribution is depicted in Figure 3.

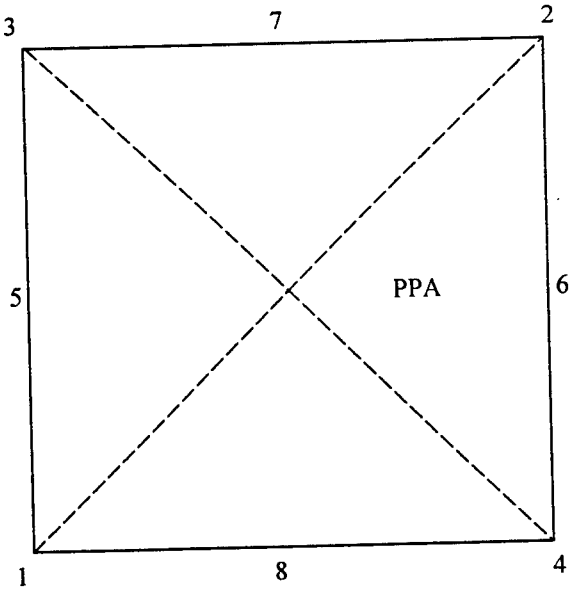

Figure 3: Fiducial mark distribution

The image coordinates of the fiducial marks in the image coordinate system are listed in the following table.

Fiducial Marks	X(mm)	Y(mm)
1	-106.008	-106.003
2	105.992	105.994
3	-106.004	105.996
4	105.990	-106.003
5	-110.009	-0.002
6	109.994	-0.004
7	-0.007	109.998
8	-0.009	-110.005

Table 1. Fiducial mark coordinates

The distances between fiducial marks and diagonal intersection angles are presented in Table 2. These data can be used to execute interior orientation and determine image resolution.

Fiducial Marks	Distance (mm)	Intersection angle (degree)
1-2	299.810	90
3-4	299.809	90
5-6	220.003	
7-8	220.004	
1-3	211.998	
1-4	211.998	
2-3	211.996	
2-4	211.997	

Table 2. Distances between fiducial marks and intersection angles

2.3 Network configuration

In the project area nine aerial photographs are selected to build a block of two strips (Figure 4). The upper strip has four photographs and the lower one has five strip. The along-track overlapping is about 60% and the sidelapping is around 30%. The initial positions and attitudes, also called exterior orientation parameters, are listed in Table 3. They are provided by Woolpert LLP in Dayton, Ohio. The average ground resolution of the photographs is calculated by the relationship between the flying height, focal length, image size, and ground coverage (Figure 5).

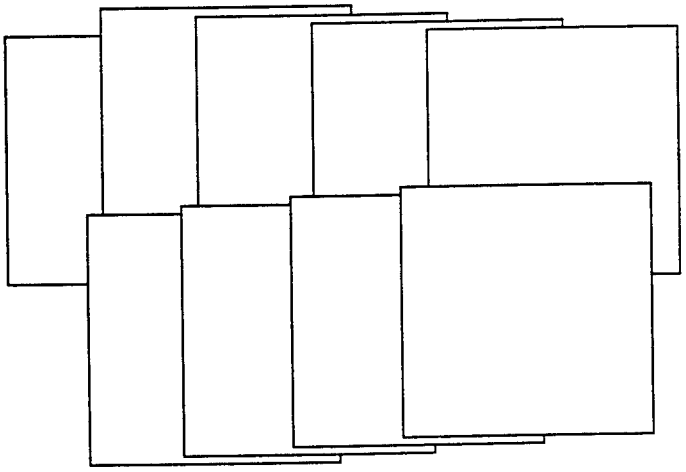

Figure 4: The nine-image block with along-track and side overlapping

Photo_ID	X(m)	Y(m)	Z(m)	Omega(d)	Phi(d)	Kappa(d)
4-8	562662.279	3392353.850	842.528	-0.72918	-1.24430	3.00538
4-9	563105.301	3392355.850	846.034	-0.39231	-2.35485	5.46202
4-10	563541.501	3392357.875	845.970	-1.71447	-2.35485	4.81922
4-11	563984.173	3392354.290	851.555	-0.59889	-0.53472	5.30481
4-12	564425.774	3392346.110	840.881	-1.43574	0.42834	4.34985
5-8	563008.098	3391600.923	822.454	-0.89805	0.13783	178.52662

5-9	563438.230	3391597.444	817.126	-0.04890	-0.14017	177.42933
5-10	563879.295	3391595.875	834.170	-0.47819	0.71800	176.57069
5-11	564319.990	3391593.668	837.284	-0.93087	1.31523	175.60902

Table 3. Initial exterior orientation parameters

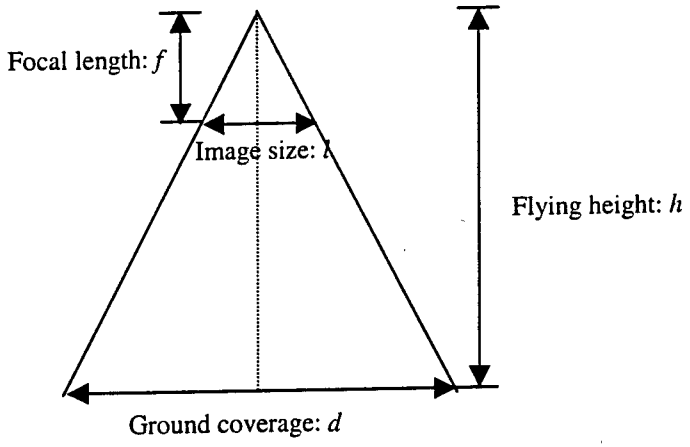

Figure 5. Image coverage and ground resolution

Suppose that the image size is l, corresponding to n pixels. The ground resolution can be calculated by

$$r = \frac{h \times l}{f \times n}$$

Taking Photo 4-9 as an example, the flying height h is 846.034m, focal length f 0.153087m, image size l 0.211988m and number of pixels n 8835. The ground resolution r is about 0.13m.

2.4 Ground control

There are 123 ground control points (GCPs) in this area. They are located on 41 vehicles. For each vehicle, points at the center, left front corner and right rear corner are measured using GPS to provide precise three-dimensional ground coordinates. The GCPs only

cover a small portion of the study area where the vehicles are located (Shaded area in Figure 6). Figure 7 depicts the distribution of the GCPs in the shaded area of Figure 6.

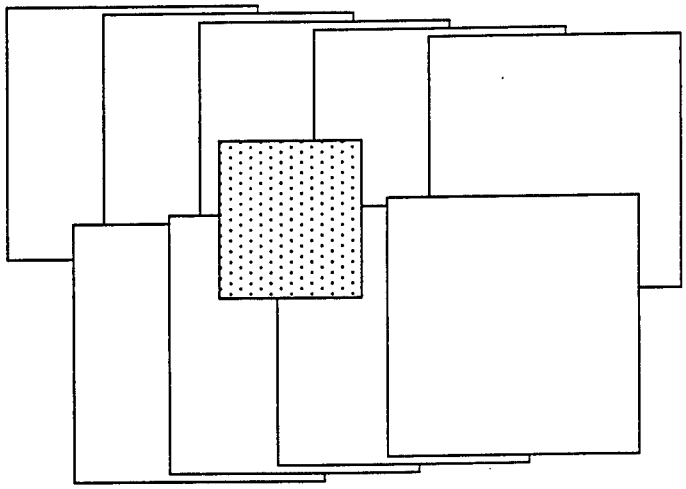

Figure 6. GCPs are only available in the central area of the study site

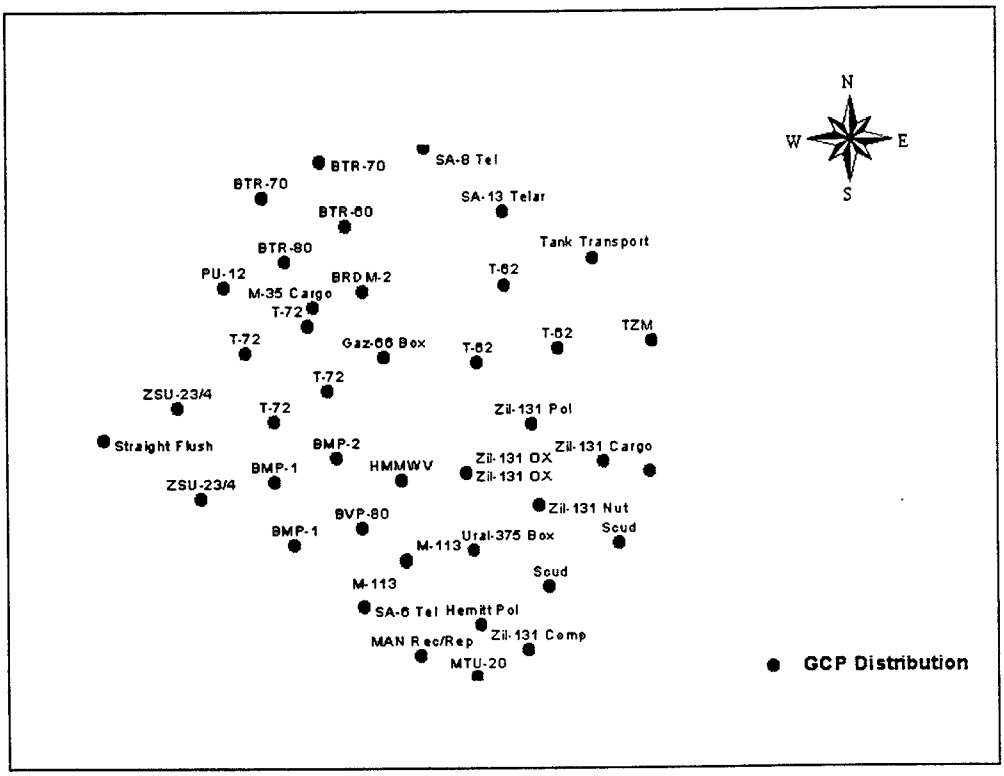

Figure 7. Distribution of GCPs

2.5 Photogrammetric triangulation and DTM generation

2.5.1 Photogrammetric triangulation

Totally, 8 ground control points and 61 tie points are selected in the photogrammetric triangulation. The tie points are mainly used to connect the images to build strips along the track and to form the block across the track. These control points and tie points are shown in Figure 8 with the background of an orthophoto.

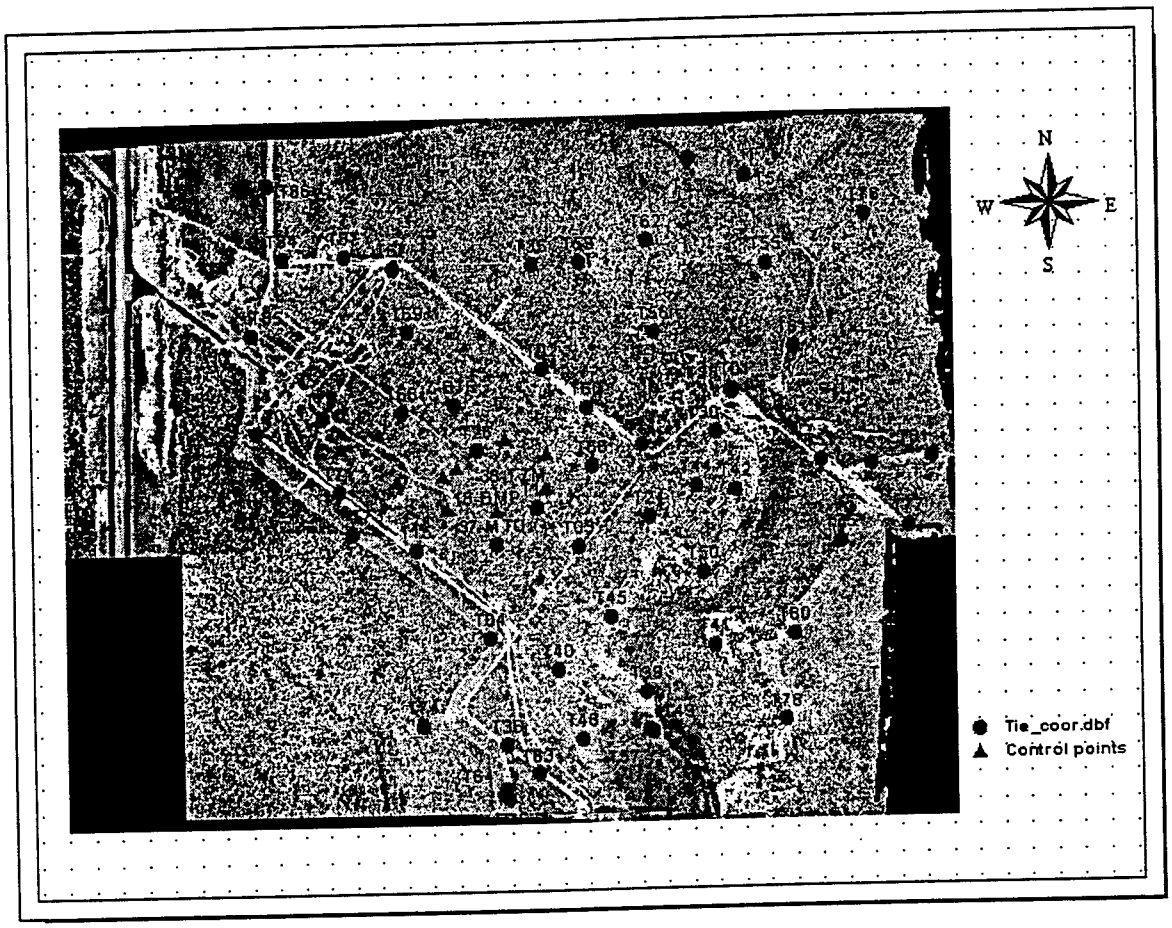

Figure 8. Control points and tie points used for photogrammetric triangulation

The photogrammetric triangulation system has 717 equations and 261 unknowns, with a degree of freedom of 456. A least squares adjustment was performed to estimate the unknowns using the ERDAS Orthomax model on an SGI O2 UNIX workstation. Residuals of the coordinates of the eight GCPs and the RMS (root mean square errors)

are listed in Table 4. The residuals are calculated by comparing the photogrammetrically estimated coordinates of the GCPs and those of known coordinates. The RMS in X, Y and Z directions are 0.6m, 0.9m and 0.5m, respectively.

GCP	ΔX(m)	ΔY(m)	ΔZ(m)
1-SFD	-0.152	-1.484	0.525
38-TZM	-0.005	1.356	0.256
25-T-62	-0.364	0.514	0.906
12-T-72	-0.023	-0.346	0.656
11-T-72	-0.071	-0.535	0.652
18-BMP	0.625	-0.679	-0.065
36-URAL	0.902	1.132	-0.380
29-URAL	1.030	0.053	-0.404
Average	0.396	0.762	0.481
RMS	0.551	0.898	0.540

Table 4: Residuals and RMS of GCPs

The standard deviations of the exterior orientation parameters of all nine frames are listed in Table 5.

Frame	ΔX(m)	ΔY(m)	ΔZ(m)	ΔOmega(d)	ΔPhi(d)	ΔKappa(d)
4-8	0.463	0.440	0.412	0.021812	0.020646	0.018879
4-9	0.348	0.360	0.344	0.020707	0.018430	0.018629
4-10	0.321	0.335	0.327	0.020259	0.018030	0.018556
4-11	0.381	0.372	0.366	0.020261	0.018015	0.018533
4-12	0.509	0.459	0.442	0.021046	0.019539	0.019045
5-8	0.372	0.375	0.356	0.020552	0.019281	0.018757
5-9	0.318	0.341	0.325	0.020543	0.018060	0.018494
5-10	0.363	0.365	0.353	0.020453	0.018014	0.018571

5-11	0.476	0.446	0.424	0.021461	0.018923	0.018851
Average	0.394556	0.388111	0.372111	0.020788	0.018771	0.018702
RMS	0.070305	0.047256	0.04312	0.000543	0.000915	0.00019

Table 5. Standard deviations of exterior orientation parameters of nine frames

The standard deviations of the exposure center coordinates are 7cm, 5cm, and 4cm in X, Y and Z direction, respectively. The standard deviations of three rotation angles of ω, φ and κ are around 1 arc-minute, which are of high accuracy. The estimated standard deviations of all points, including GCPs and tie points, are given in Appendix A (original printout of the software system). It is to note that the internal uncertainties of the standard deviations (Appendix A) are much smaller than thaose of the exterior measures of RMS of GCPs (Table 4).

Appendix B gives the detailed information of the photogrammetric bundle adjustment computation in iterations.

2.5.2 DTM generation

After the triangulation was completed, a DTM of the area was generated using the results of the triangulation. Two adjacent photographs in the same track were selected to form a stereo pair to generate a portion of the DTM. In this way, four stereopairs in the upper track and three in the lower track were used to build the DTM in piecewise. Finally, the seven DTM pieces were mosaiced to build the entire DTM with a 0.5m grid spacing in X and Y directions. The DTM has a dimension of 4226 by 3930, namely, 16608180 grid points.

The DTM was generated using the automatic image matching technique that depends heavily on image features. Areas where only homogeneous gray values are available have poor image matching results and thus, the DTM has low quality. One example of such areas is the river. Handling of elevation information at grid points with mismatches has

two alternatives: (a) placing a code, for instance, -9999 indicating non-observations, or (b) interpolating elevation using those of surrounding grid points. Other areas with rich image features have high quality image matching results and subsequently have high quality elevation information in he DTM.

Figure 9 is a shaded relief map of the area derived from the DTM. Figure 10 displays a 3-D view of the DTM with an exaggeration factor of two in the Z direction.

Figure 9. Shaded relief map derived from the DTM

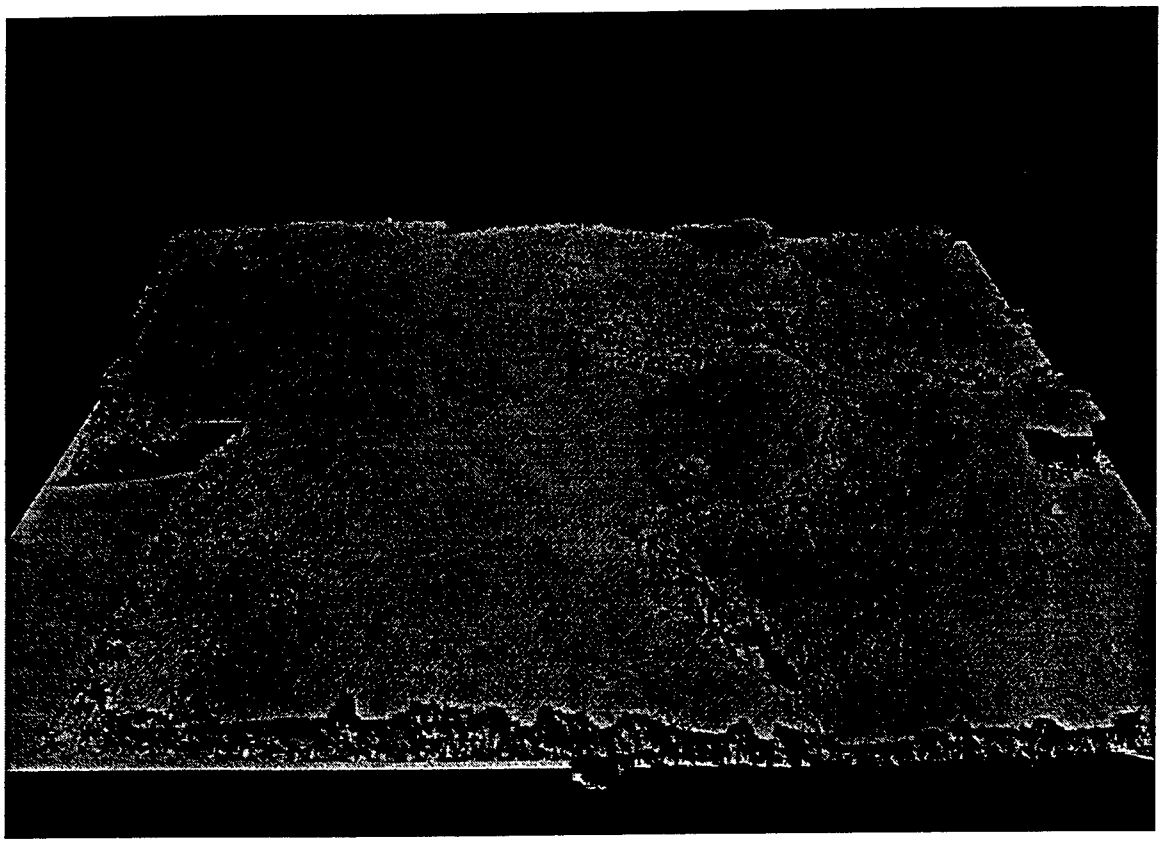

Figure 10. 3-D perspective view of the study area using the computed DEM

2.5.3 Orthophoto generation

Finally, an othorphoto of the study area is generated. The orthophoto eliminated the terrain relief displacement so that it can be treated as a map. For example, distances and azimuths can be measured on the map. Technically, it is a projection from the aerial photographs to the horizontal datum plane through the exterior orientation parameters of the images and the computed DTM. Figure 11 displays one of the orthophotos. Figure 12 shows the DTM draped with the mosaic of the area with an elevation exaggeration of factor two.

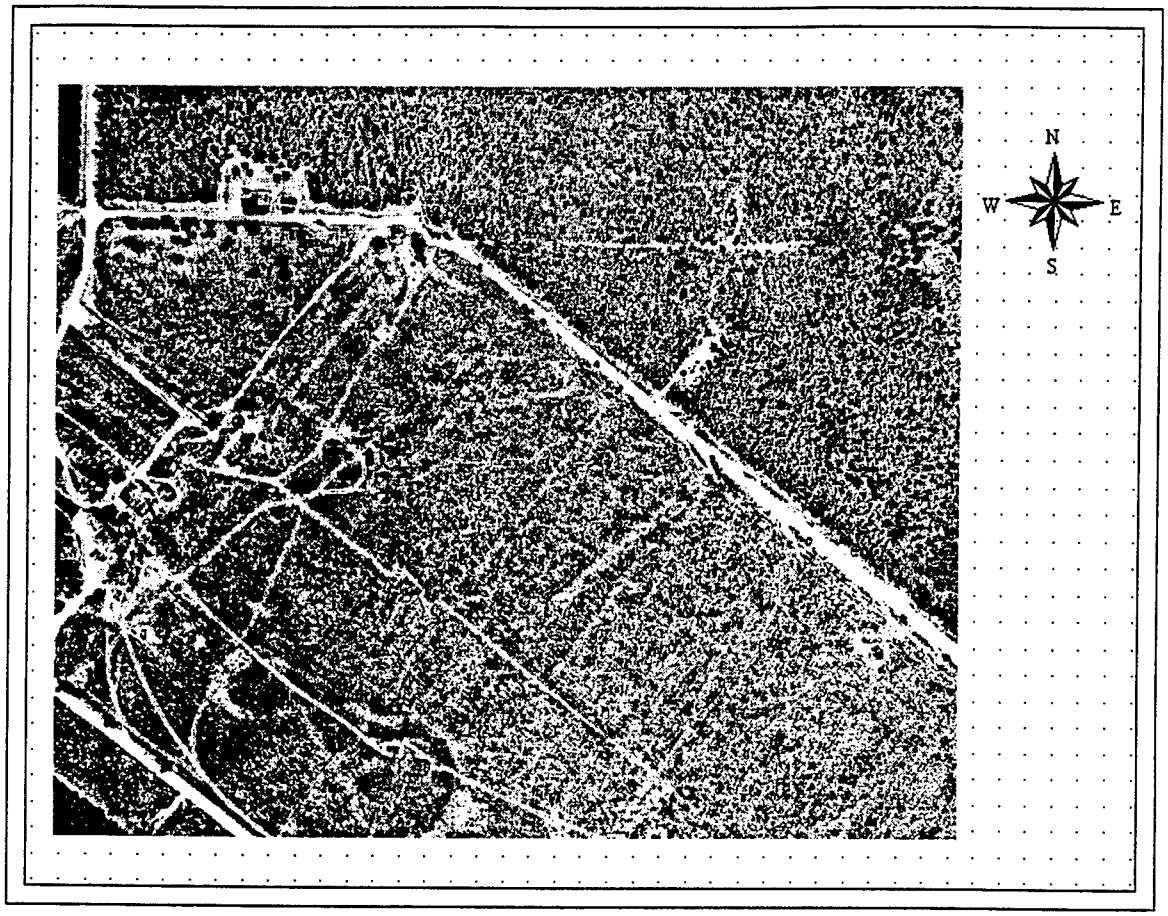

Figure 11. One of the othorphotos

3. Conclusions

The optical images investigated in this research project has high quality metric characteristics, for example, fiducial marks, principle point position, calibrated focal length and lens distortion parameters (very small). The along-track and side overlapping rates of 60% and 30% make it possible to form a photogrammetric bundle block that provides very strong geometry for determination of 3-D ground coordinates from measured 2-D image coordinates. Based on the above modeling, computation and analysis results, we can draw the following conclusion:

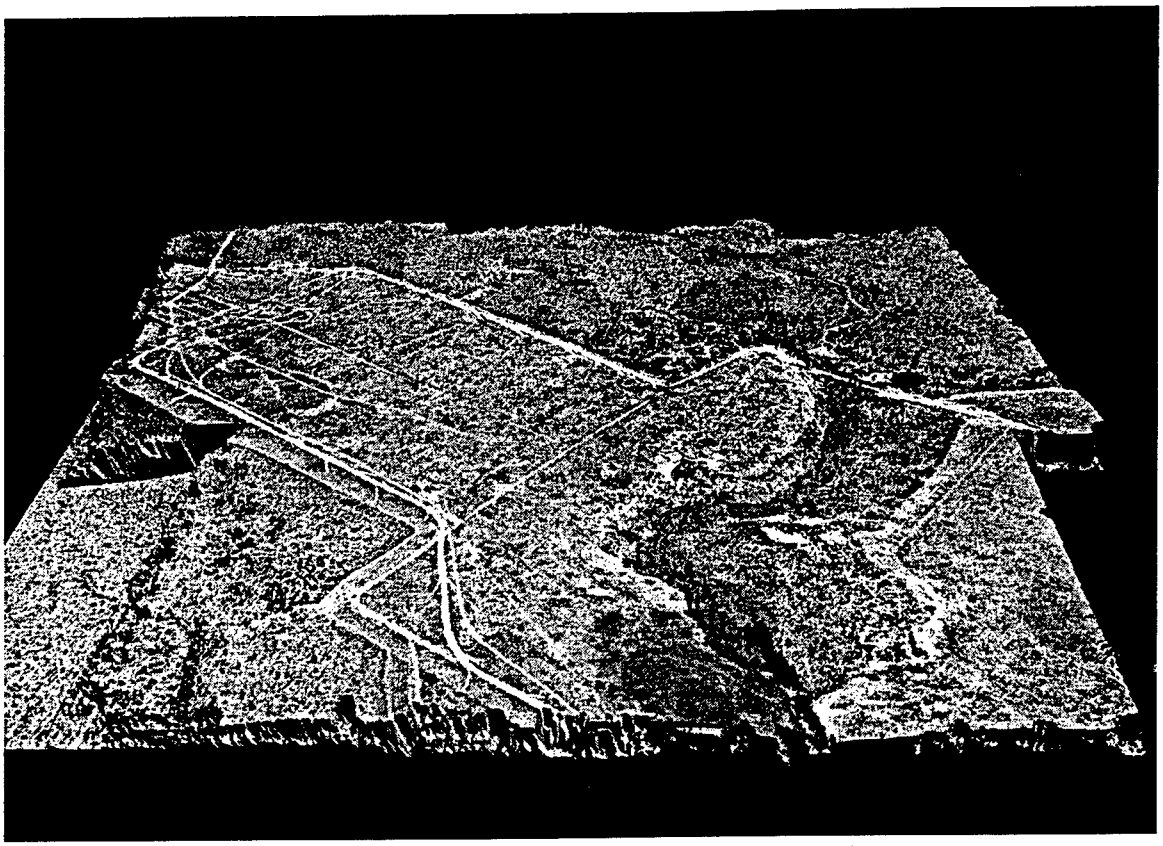

Figure 12. 3-D perspective view of the DTM draped with the mosaic

- Standard deviations of 30cm to 40cm for ground object locations can be achieved.
- Selection of tie points is critical to the final standard deviations of the ground points. They should be well-defined points and possibly, be evenly distributed in the entire area covered.
- The GCPs are centrally distributed in a small area. They would provide a much better ground control if spread widely.
- The DTM generated is of good quality with a grid spacing of 0.5 meter that matches the point accuracy of 30~40 cm.
- The sensor locations and orientations (exterior orientation parameters of the camera in Table 5) computed by the bundle adjustment demonstrated that we are able to estimate the parameters with a low uncertainty (between 40 cm and 1 meter).

In future research, the following topics should be investigated:

- In addition to optical sensors, geometry of other sensors and configurations consisting of multiplatforms should be investigated. It is expected that not only the geometric strength, but also the capability of sensing in different situations will be improved.
- Automation of the recognition/selection of the tie points should be researched. This process should give a set of tie points that are visually distinct and evenly distributed in the area.
- An improved bundle adjustment method that can integrate various types of sensors and process images acquired in different time periods should be developed and implemented.

4. Acknowledgements

We would like to thank Mr. James Leonard and Mr. Todd Jenkins of the Air Force Research Laboratory (AFRL) for providing the data and cooperation. Funding from the Air Force Office of Scientific Research (AFOSR) is greatly appreciated.

References

Berning, S., P. Howe and T.Jenkins 1998. Theater-wide Reference Information Management. AFRL,WPAFB, OH. 4pp

Curlander, J.C and R.N. McDonough 1991. Synthetic Aperture Rada Systems and Singnal Processing. John Wiley & Sons, Inc

Carrara, W.G., R.S. Goodman and R.M. Majewski 1995. Spotlight Synthetic Aperture Radar. Artech House, Inc. MA.

Leick, A.1995. GPS Satellite Surveying. John Wiley & Sons, Inc

Li, R. 1997. Mobile Mapping: An Emerging Technology for Spatial Data Acquisition. Journal of Photogrammetric Engineering and Remote Sensing, Vol. 63, No.9, pp.1085-1092.

Li. R. 1998. A Study of Referencing Issues in Multiplatform and Multisensor Based Object Location. Project Report submitted to AFOSR, 20pp.

Mikhail, E.M. and G. Gracie 1981. Analysis and Adjustment of Survey Measurements, Van Nostrand Reinhold Company.

Moffitt, F.H. and E.M. Mikhail 1980. Photogrammetry. Harper & Row, Publishers, Inc., New York.

Appendix A

Standard deviations of all points (original printout of ERDAS)

Statistics Summary

Number of Equations: 717
Number of Unknowns: 261
Degrees of Freedom: 456

Standard Deviation of Unit Weight: 0.718338

Category	VTPV Sum	Ratio	Sigma0
a priori photo	10.874	0.614	0.449
a priori point	4.982	0.073	0.155
collinearity equations	219.444	1.466	0.694

Point Standard Deviations and Correlations (Unit is Meter)

Point_ID	X	Y	Z	XY	XZ	YZ
1-SFD	0.331	0.318	0.334	0.0112	0.1034	0.0037
7-BTR	0.311	0.311	0.328	-0.0295	0.0591	-0.0333
38-TZM	0.290	0.296	0.313	0.0011	-0.0060	-0.0080
37-MTU	0.301	0.309	0.323	0.0273	0.0328	0.0466
T02	0.306	0.317	0.330	-0.0066	-0.0071	-0.0518
T03	0.302	0.313	0.326	-0.0035	-0.0354	0.0459
T04	0.334	0.355	0.360	0.0525	0.0210	0.0867

T11	0.316	0.317	0.330	0.0081	-0.0856	-0.0107
T14	0.292	0.299	0.315	0.0075	0.0002	0.0251
T15	0.330	0.325	0.340	0.0538	0.0895	0.0477
T24	0.321	0.324	0.334	-0.0197	-0.0906	0.0268
T26	0.299	0.299	0.317	-0.0046	0.0516	-0.0129
T28	0.372	0.362	0.369	0.0410	-0.1207	-0.0214
T30	0.356	0.347	0.354	0.0177	-0.1223	-0.0123
25-T-62	0.294	0.298	0.315	-0.0061	0.0284	-0.0203
12-T-72	0.304	0.302	0.319	0.0023	0.0675	-0.0027
11-T-72	0.309	0.305	0.322	0.0070	0.0776	0.0023
18-BMP	0.309	0.307	0.324	0.0249	0.0730	0.0242
T35	0.347	0.376	0.372	-0.0200	-0.0161	-0.0930
T01	0.375	0.364	0.383	0.0360	-0.1437	-0.0063
T36	0.386	0.434	0.419	0.0506	-0.0154	0.1099
T39	0.377	0.410	0.401	-0.0515	-0.0881	0.0847
T40	0.344	0.376	0.374	0.0067	-0.0386	0.0920
T41	0.389	0.401	0.393	-0.0798	-0.1175	0.0579
T42	0.368	0.355	0.361	-0.0165	-0.1324	0.0103
T44	0.342	0.336	0.345	-0.0113	-0.1164	0.0090
T45	0.333	0.353	0.368	-0.0257	-0.0661	0.0671
T48	0.384	0.435	0.425	-0.0080	-0.0515	0.1179
T49	0.401	0.444	0.434	-0.0640	-0.1023	0.1053
T50	0.360	0.361	0.365	-0.0527	-0.1169	0.0377
T51	0.436	0.404	0.404	0.0005	-0.1438	-0.0021
T52	0.479	0.435	0.431	-0.0022	-0.1452	-0.0018
T53	0.444	0.493	0.474	0.0858	-0.1017	-0.1157
T54	0.461	0.492	0.467	0.1077	-0.1109	-0.0779

T55	0.433	0.437	0.427	0.0989	-0.1221	-0.0575
T56	0.344	0.355	0.371	0.0453	-0.0822	-0.0542
T57	0.398	0.439	0.422	-0.0560	-0.0905	0.0886
T58	0.419	0.483	0.456	0.0503	-0.0264	0.1152
T59	0.353	0.382	0.389	0.0050	-0.0202	-0.1030
T60	0.302	0.310	0.325	0.0078	-0.0425	-0.0241
T61	0.428	0.411	0.410	0.0693	-0.1363	-0.0320
T62	0.380	0.411	0.411	0.0540	-0.0762	-0.0986
T63	0.402	0.460	0.438	0.0250	-0.0399	0.1107
T64	0.420	0.484	0.464	0.0702	0.0035	0.1411
T65	0.414	0.475	0.450	0.0526	-0.0233	0.1147
T66	0.298	0.303	0.319	0.0012	-0.0468	0.0005
T67	0.381	0.393	0.390	-0.0986	0.0563	-0.0987
T68	0.333	0.323	0.339	-0.0356	0.0930	-0.0318
T69	0.349	0.351	0.358	-0.0747	0.0690	-0.0766
T70	0.435	0.387	0.401	-0.0293	0.1338	-0.0230
T71	0.368	0.341	0.358	0.0198	0.1205	0.0105
T72	0.383	0.353	0.368	-0.0402	0.1203	-0.0342
T73	0.365	0.344	0.360	0.0517	0.1149	0.0366
T74	0.397	0.430	0.431	0.1089	0.0434	0.1273
T75	0.456	0.423	0.419	-0.0545	-0.1439	0.0180
T76	0.528	0.520	0.507	0.1347	-0.1340	-0.0678
T77	0.516	0.465	0.458	-0.0474	-0.1434	0.0129
T78	0.466	0.482	0.467	-0.1174	-0.1246	0.0733
T79	0.535	0.519	0.505	-0.1349	-0.1539	0.0536
T80	0.439	0.431	0.431	-0.0961	-0.1323	0.0431
T81	0.536	0.476	0.470	0.0012	-0.1456	-0.0025

T82	0.591	0.517	0.508	-0.0395	-0.1424	0.0066
T83	0.633	0.544	0.537	-0.0085	-0.1454	-0.0028
36-URAL	0.290	0.297	0.313	0.0042	-0.0041	0.0139
29-URAL	0.296	0.300	0.317	0.0171	0.0381	0.0276
T84	0.455	0.444	0.452	-0.1390	0.0972	-0.1104
T85	0.456	0.417	0.435	-0.1018	0.1279	-0.0648
T86	0.499	0.510	0.501	-0.1670	0.0841	-0.1433
T87	0.412	0.418	0.425	-0.1174	0.0627	-0.1166

Appendix B

Detailed computational information in the iterative process

Pre-Triangulation Facts:

Total Number of Frames: 9
Total Number of Active Frames: 9
Total Number of Points: 137
Total Number of Active Points: 69
Total Number of Elements: 9
Maximum Number of Correlations: 8
Unsorted Element Bandwidth: 9

Frame Parameter Residuals (Unit is Meter and degrees)

Frame	Description	Cam	X	Y	Z	Omega	Phi	Kappa

1	4_10	1	0.230	0.140	-0.298	-0.016908	0.016996	0.003094
2	4_11	1	0.156	-0.144	-0.552	-0.012401	0.007821	0.009585
3	5_9	1	-1.609	-1.350	-0.638	0.063699	-0.062976	0.025111
4	5_10	1	-0.920	0.734	0.361	0.075010	0.052981	0.000128
5	4_9	1	0.336	0.237	-0.141	-0.023432	0.019384	0.005556
6	5_8	1	1.117	-2.290	0.048	-0.024500	-0.139373	0.001232
7	4_12	1	0.041	-0.201	-0.664	-0.007367	0.009094	0.012931
8	5_11	1	0.302	0.318	-0.386	-0.012320	0.029435	0.005029
9	4_8	1	0.336	0.614	0.124	-0.028624	0.039659	0.004162

		Point Residuals (Meter)					Image Residuals			
Point ID	Type	X	Y	Z			Frame ID	Sample	Line	Image X	Image Y
1-SFD	C	-0.152	-1.484	0.525							
							4_10	0.33	-0.29	8.0	7.1
							5_9	0.40	-0.26	9.5	6.2
							4_9	-0.26	-0.04	-6.3	0.9
							5_8	-0.35	-0.23	-8.4	5.4
							4_8	-0.16	0.81	-3.8	-19.4
7-BTR	T										
							4_10	0.04	0.32	1.1	-7.7
							4_9	-0.19	0.61	-4.6	-14.7
							4_8	0.11	-0.95	2.7	22.8
38-TZM	C	-0.005	1.356	0.256							
							4_10	-0.37	0.42	-9.0	-10.0
							4_11	0.48	0.83	11.5	-20.0
							5_9	-0.08	0.48	-1.8	-11.4
							5_10	0.15	-0.23	3.6	5.5
							4_9	-0.15	-0.66	-3.7	15.9
							5_8	-0.09	-0.80	-2.4	19.1

37-MTU	T				
		4_10	-0.94	-0.32	-22.6	7.5
		5_9	0.55	0.07	13.2	-1.5
		5_10	0.49	0.15	11.8	-3.6
		4_9	0.01	0.47	0.2	-11.2
		5_8	-0.13	-0.47	-3.3	11.3
T02	T				
		4_10	-0.31	-0.22	-7.4	5.2
		4_11	0.14	0.24	3.4	-5.7
		4_9	0.17	-0.02	4.2	0.5
T03	T				
		4_10	0.30	0.05	7.2	-1.2
		4_11	-0.31	-0.13	-7.5	3.1
		5_9	-0.16	-0.05	-4.0	1.3
		5_10	0.20	0.12	4.8	-2.9
T04	T				
		5_9	-0.07	0.14	-1.6	-3.4
		5_10	0.05	0.32	1.3	-7.6
		5_8	0.03	-0.45	0.7	10.9
T11	T				
		4_10	0.37	-0.28	8.9	6.7
		4_11	-0.04	-0.09	-0.9	2.2
		5_9	0.04	0.03	0.9	-0.7
		5_10	-0.07	-0.12	-1.6	3.0
		4_9	-0.33	0.47	-7.9	-11.4
T14	T				
		4_10	0.24	0.15	5.7	-3.5
		4_11	0.15	0.38	3.6	-9.2
		5_9	0.13	0.08	3.1	-2.0
		5_10	-0.18	-0.06	-4.3	1.3
		4_9	-0.19	-0.26	-4.5	6.2

					5_8	-0.18	-0.26	-4.4	6.3
T15	T								
					4_10	0.38	0.31	9.3	-7.4
					5_9	-0.20	0.20	-4.7	-4.9
					4_9	0.33	-0.03	8.0	0.8
					5_8	-0.52	-0.39	-12.5	9.3
T24	T								
					4_10	0.16	-0.21	3.7	5.1
					4_11	0.23	0.01	5.6	-0.2
					5_9	0.08	-0.04	1.9	0.9
					5_10	-0.18	0.05	-4.3	-1.1
					5_11	-0.25	0.25	-5.9	-6.0
T26	T								
					4_10	0.18	0.06	4.3	-1.5
					5_9	0.20	0.18	4.7	-4.3
					4_9	0.01	-0.12	0.2	2.8
					5_8	-0.41	-0.40	-10.0	9.5
					4_8	0.03	0.31	0.7	-7.4
T28	T								
					4_10	-0.07	0.15	-1.7	-3.7
					4_11	0.14	-0.23	3.2	5.4
					4_12	-0.06	0.08	-1.5	-1.8
T30	T								
					4_11	0.16	0.13	3.9	-3.2
					5_10	-0.20	0.43	-4.7	-10.3
					4_10	0.18	-0.61	4.3	14.7
					5_9	0.12	-0.60	2.9	14.4
					4_12	-0.21	0.20	-5.1	-4.8
					5_11	0.01	0.46	0.3	-11.0
25-T-62	C	-0.364	0.514	0.906					
					4_10	-0.63	0.36	-15.0	-8.8

					5_9	-0.03	0.75	-0.6	-18.0
					5_10	0.09	-0.39	2.1	9.3
					4_9	0.91	-0.55	21.9	13.1
					5_8	-0.28	-0.16	-6.7	3.7
12-T-72	C	-0.023	-0.346	0.656					
					4_10	0.04	-0.17	0.8	4.0
					5_9	0.75	-0.12	17.9	3.0
					4_9	-0.38	-0.40	-9.2	9.6
					5_8	-0.41	-0.28	-9.9	6.7
					4_8	-0.01	0.94	-0.3	-22.4
11-T-72	C	-0.071	-0.535	0.652					
					4_10	-0.95	-0.66	-22.9	15.7
					5_9	-0.92	-1.24	-22.3	29.6
					4_9	-0.65	-0.60	-15.7	14.4
					5_8	2.93	2.35	70.9	-55.7
					4_8	-0.40	-0.10	-9.6	2.4
18-BMP	C	0.625	-0.679	-0.065					
					4_10	-0.59	0.47	-14.0	-11.2
					5_9	0.20	-0.46	4.7	11.2
					4_9	-0.37	0.42	-8.9	-10.0
					5_8	0.01	1.04	0.4	-25.0
					4_8	0.76	-1.56	18.2	37.4
T35	T								
					4_10	-0.32	-0.12	-7.6	3.0
					4_11	0.18	-0.12	4.3	2.9
					4_9	0.15	0.25	3.5	-6.1
T01	T								
					4_10	-0.03	0.33	-0.7	-8.0
					4_11	0.03	-0.33	0.8	7.8
T36	T								
					5_9	0.18	0.03	4.3	-0.7

		5_10	-0.09	0.06	-2.2	-1.4
		5_8	-0.09	-0.09	-2.2	2.1
T39	T					
		5_9	0.02	0.07	0.5	-1.6
		5_10	-0.04	0.10	-0.9	-2.4
		5_11	0.01	-0.17	0.3	4.2
T40	T					
		5_9	0.24	-0.14	5.7	3.5
		5_10	-0.12	0.13	-2.9	-3.1
		5_8	-0.12	0.02	-3.0	-0.5
T41	T					
		5_9	-0.08	-0.05	-1.8	1.3
		5_10	0.15	-0.05	3.6	1.2
		5_11	-0.07	0.11	-1.8	-2.6
T42	T					
		5_9	-0.21	-0.15	-5.1	3.5
		5_10	0.01	0.08	0.3	-2.0
		4_10	0.15	0.03	3.5	-0.6
		4_11	0.06	0.07	1.5	-1.7
T44	T					
		4_10	0.03	0.11	0.8	-2.7
		4_11	0.09	0.38	2.1	-9.2
		5_9	0.03	0.11	0.7	-2.7
		5_10	-0.16	0.49	-3.8	-11.8
		4_12	-0.03	-0.51	-0.7	12.2
		5_11	0.03	-0.59	0.7	14.1
T45	T					
		5_9	0.00	0.06	0.1	-1.4
		5_10	0.00	-0.06	-0.1	1.5
T48	T					
		5_9	0.00	0.06	0.0	-1.5

		5_10	0.00	-0.06	0.0	1.5
T49	T					
		5_9	0.00	0.04	0.0	-0.9
		5_10	0.00	-0.04	0.0	1.0
T50	T					
		5_9	-0.06	0.18	-1.3	-4.3
		5_10	0.12	-0.27	2.8	6.4
		5_11	-0.06	0.09	-1.5	-2.1
T51	T					
		4_11	0.03	-0.38	0.6	9.1
		5_10	0.22	0.05	5.3	-1.3
		4_12	0.27	0.31	6.5	-7.5
		5_11	-0.50	0.06	-11.9	-1.3
T52	T					
		4_11	0.01	0.43	0.2	-10.2
		5_10	0.10	-0.11	2.5	2.7
		4_12	-0.36	-0.60	-8.5	14.3
		5_11	0.25	0.23	6.1	-5.5
T53	T					
		4_10	0.04	-0.36	0.9	8.6
		4_11	-0.04	0.37	-0.9	-8.8
T54	T					
		4_10	0.13	0.28	3.1	-6.6
		4_11	-0.29	-0.23	-7.0	5.4
		4_12	0.16	-0.05	3.8	1.3
T55	T					
		4_10	-0.10	0.39	-2.4	-9.4
		4_11	0.14	-0.23	3.4	5.4
		4_12	-0.04	-0.16	-1.0	3.8
T56	T					
		4_10	-0.03	0.32	-0.7	-7.7

		4_11	0.03	-0.32	0.8	7.6
T57	T					
		5_9	-0.01	0.16	-0.2	-3.9
		5_10	0.03	0.12	0.7	-2.8
		5_11	-0.03	-0.29	-0.7	6.9
T58	T					
		5_9	0.16	0.03	3.8	-0.7
		5_10	-0.08	-0.07	-2.0	1.6
		5_8	-0.08	0.04	-1.9	-0.9
T59	T					
		4_10	0.01	-0.05	0.1	1.2
		4_11	-0.01	0.05	-0.1	-1.2
T60	T					
		4_10	0.22	-0.33	5.2	8.0
		4_11	-0.11	0.19	-2.7	-4.6
		4_9	-0.11	0.14	-2.6	-3.4
T61	T					
		4_10	-0.04	-0.12	-1.0	2.8
		4_11	0.16	-0.51	3.8	12.2
		4_12	-0.11	0.61	-2.6	-14.8
T62	T					
		4_10	-0.04	0.37	-0.9	-8.8
		4_11	0.04	-0.37	0.9	8.9
T63	T					
		5_9	-0.03	-0.07	-0.8	1.7
		5_10	0.01	-0.12	0.3	2.9
		5_8	0.02	0.19	0.4	-4.6
T64	T					
		5_9	0.00	0.01	0.0	-0.3
		5_10	0.00	-0.01	0.0	0.3
T65	T					

		5_9	-0.06	-0.19	-1.4	4.4
		5_10	0.03	0.00	0.6	-0.1
		5_8	0.03	0.19	0.7	-4.5
T66	T					
		4_10	0.37	-0.21	9.0	5.0
		4_11	-0.23	-0.09	-5.6	2.1
		5_9	0.15	-0.09	3.6	2.3
		5_10	-0.12	0.25	-2.9	-5.9
		4_9	-0.15	0.14	-3.5	-3.3
T67	T					
		4_9	0.01	-0.55	0.2	13.2
		4_10	0.00	0.19	0.1	-4.7
		4_8	0.00	0.35	0.1	-8.5
T68	T					
		4_9	-0.05	-0.23	-1.2	5.5
		4_10	0.05	-0.21	1.2	5.1
		4_8	0.01	0.44	0.4	-10.7
T69	T					
		4_9	-0.01	-0.38	-0.2	9.2
		4_10	0.00	0.20	0.1	-4.8
		4_8	0.01	0.18	0.3	-4.3
T70	T					
		4_9	0.14	0.14	3.3	-3.3
		5_8	-0.10	-0.03	-2.5	0.8
		4_8	-0.04	-0.09	-1.0	2.2
T71	T					
		4_9	0.33	0.04	7.9	-0.8
		5_8	-0.33	-0.03	-7.9	0.7
		4_8	0.00	0.04	0.0	-0.9
T72	T					
		4_9	0.00	0.10	-0.1	-2.3

		5_8	0.19	-0.09	4.6	2.3
		4_8	-0.21	-0.01	-5.0	0.3
T73	T					
		4_9	0.27	0.03	6.4	-0.8
		5_8	-0.15	-0.08	-3.6	1.9
		4_8	-0.12	0.08	-3.0	-1.8
T74	T					
		5_8	0.00	-0.06	0.0	1.4
		5_9	0.00	0.06	0.1	-1.4
T75	T					
		4_11	-0.53	0.11	-12.7	-2.6
		4_12	0.17	0.14	4.1	-3.4
		5_10	-0.07	-0.19	-1.6	4.7
		5_11	0.37	-0.11	8.9	2.6
T76	T					
		4_11	0.01	-0.08	0.2	1.9
		4_12	-0.01	0.08	-0.2	-1.8
T77	T					
		4_11	-0.36	0.03	-8.6	-0.8
		4_12	-0.04	0.08	-1.0	-1.9
		5_11	0.36	-0.17	8.6	4.1
T78	T					
		5_10	0.00	-0.08	-0.1	1.9
		5_11	0.00	0.08	0.1	-2.0
T79	T					
		5_10	0.00	0.04	0.1	-1.1
		5_11	0.00	-0.04	-0.1	1.1
T80	T					
		5_10	-0.01	-0.14	-0.2	3.4
		5_11	0.01	0.14	0.2	-3.4
T81	T					

						4_11	-0.12	0.27	-2.8	-6.4
						4_12	0.14	-0.21	3.3	5.0
						5_11	-0.04	-0.05	-0.9	1.2
	T82	T								
						4_12	0.03	0.01	0.8	-0.2
						5_11	-0.03	0.00	-0.8	0.1
	T83	T								
						4_12	0.09	0.02	2.1	-0.5
						5_11	-0.08	-0.01	-2.0	0.2
	36-URAL	C	0.902	1.132	-0.380					
						4_9	-0.01	-0.11	-0.3	2.6
						4_10	0.73	0.50	17.5	-11.9
						4_11	-0.06	-0.42	-1.4	10.0
						5_9	-0.37	0.56	-8.9	-13.5
						5_10	-0.27	-0.44	-6.6	10.6
	29-URAL	C	1.030	0.053	-0.404					
						4_10	0.53	-0.87	12.7	20.9
						5_9	-0.97	0.18	-23.3	-4.4
						5_10	-0.06	0.08	-1.4	-2.0
						4_9	0.55	0.73	13.3	-17.5
	T84	T								
						4_8	0.00	-0.05	0.1	1.3
						4_9	-0.01	0.05	-0.1	-1.2
	T85	T								
						4_8	0.02	-0.40	0.5	9.5
						4_9	-0.04	0.39	-0.9	-9.3
	T86	T								
						4_8	0.00	0.02	0.0	-0.5
						4_9	0.00	-0.02	0.1	0.5
	T87	T								
						4_8	0.00	0.00	0.0	0.1

			4_9	0.00	0.00	0.0	-0.1
Averages:	0.396	0.762	0.481				
RMS:	0.551	0.898	0.540				

Averages:	0.18	0.25	4.3	6.0
RMS:	0.32	0.37	7.8	8.8

----- Results for Iteration 3 -----

Statistics Summary

Number of Equations: 717
Number of Unknowns: 261
Degrees of Freedom: 456

Standard Deviation of Unit Weight: 0.718338

Category	VTPV Sum	Ratio	Sigma0
a priori photo	10.874	0.614	0.449
a priori point	4.982	0.073	0.155
collinearity equations	219.444	1.466	0.694

Frame Parameters (Unit is Meter and degrees)

Frame	Description	Cam	X	Y	Z	Omega	Phi	Kappa
1	4_10	1	563544.351	3392353.600	843.655	-1.576571	-2.000420	4.371216
2	4_11	1	563986.947	3392346.529	849.036	-0.443646	-0.485225	4.851641
3	5_9	1	563435.540	3391594.517	812.753	0.134335	-0.119353	-3.014453
4	5_10	1	563876.288	3391589.366	829.459	-0.290347	0.766061	-3.874165
5	4_9	1	563108.475	3392354.706	843.907	-0.235441	-2.327800	5.004695

6	5_8	1	563005.462	3391601.512	818.308	-0.723163	0.162966	-1.928319
7	4_12	1	564428.579	3392334.980	837.921	-1.260918	0.508562	3.891165
8	5_11	1	564317.005	3391583.536	832.095	-0.726107	1.390870	-4.839534
9	4_8	1	562665.590	3392356.174	840.491	-0.567182	-1.244299	2.545722

Point Results for Iteration 3

			Current Correction			Current Position		
Point ID	Type	Description	X	Y	Z	X	Y	Z
1-SFD	C	RR	0.000	0.000	0.000	563049.614	3391963.453	62.505
7-BTR	T		0.000	0.000	0.000	563213.626	3392174.687	66.993
38-TZM	C		0.000	0.000	0.000	563473.750	3392034.771	63.254
37-MTU	T		0.000	0.000	0.000	563330.382	3391779.027	61.116
T02	T		0.000	0.000	0.000	563465.232	3392275.754	63.195
T03	T		0.000	0.000	0.000	563561.766	3391772.261	55.458
T04	T		0.000	0.000	0.000	563309.429	3391514.769	51.513
T11	T		0.000	0.000	0.000	563745.607	3392057.623	49.273
T14	T		0.000	0.000	0.000	563448.699	3391882.912	60.014
T15	T		0.000	0.000	0.000	563103.970	3391766.497	55.805
T24	T		0.000	0.000	0.000	563763.892	3391848.645	49.354
T26	T		0.000	0.000	0.000	563278.368	3392045.932	60.902
T28	T		0.000	0.000	0.000	563998.925	3392198.878	51.062
T30	T		0.000	0.000	0.000	563954.528	3392086.689	52.413
25-T-62	C		0.000	0.000	0.000	563357.902	3392079.808	62.930
12-T-72	C		0.000	0.000	0.000	563221.297	3392000.211	61.387
11-T-72	C		0.000	0.000	0.000	563179.914	3391976.606	61.320
18-BMP	C		0.000	0.000	0.000	563194.145	3391881.680	60.252
T35	T		0.000	0.000	0.000	563436.966	3392570.114	68.238
T01	T		0.000	0.000	0.000	564001.795	3392205.378	51.230
T36	T		0.000	0.000	0.000	563353.104	3391213.897	49.600

T39	T	0.000	0.000	0.000	563748.876	3391356.992	30.904
T40	T	0.000	0.000	0.000	563501.473	3391424.072	51.664
T41	T	0.000	0.000	0.000	563947.997	3391484.483	45.933
T42	T	0.000	0.000	0.000	564008.502	3391922.885	50.529
T44	T	0.000	0.000	0.000	563898.042	3391937.055	53.111
T45	T	0.000	0.000	0.000	563652.610	3391569.436	42.511
T48	T	0.000	0.000	0.000	563569.122	3391229.480	48.403
T49	T	0.000	0.000	0.000	563766.341	3391244.966	34.315
T50	T	0.000	0.000	0.000	563916.873	3391691.466	42.924
T51	T	0.000	0.000	0.000	564254.649	3392001.672	38.872
T52	T	0.000	0.000	0.000	564394.308	3391991.210	44.155
T53	T	0.000	0.000	0.000	563885.213	3392858.610	38.954
T54	T	0.000	0.000	0.000	564042.048	3392807.548	47.922
T55	T	0.000	0.000	0.000	564101.082	3392557.439	43.365
T56	T	0.000	0.000	0.000	563780.161	3392373.978	58.198
T57	T	0.000	0.000	0.000	563758.036	3391250.757	35.674
T58	T	0.000	0.000	0.000	563358.104	3391064.496	47.719
T59	T	0.000	0.000	0.000	563573.540	3392574.450	63.742
T60	T	0.000	0.000	0.000	563588.931	3392162.274	58.273
T61	T	0.000	0.000	0.000	564176.064	3392321.466	33.910
T62	T	0.000	0.000	0.000	563763.978	3392629.197	57.465
T63	T	0.000	0.000	0.000	563441.303	3391132.173	47.759
T64	T	0.000	0.000	0.000	563343.266	3391076.414	48.178
T65	T	0.000	0.000	0.000	563350.165	3391087.764	48.363
T66	T	0.000	0.000	0.000	563604.204	3391997.040	54.052
T67	T	0.000	0.000	0.000	563045.749	3392564.151	70.323
T68	T	0.000	0.000	0.000	563068.327	3392159.416	63.171
T69	T	0.000	0.000	0.000	563086.392	3392386.451	69.008
T70	T	0.000	0.000	0.000	562649.720	3392103.951	64.074
T71	T	0.000	0.000	0.000	562888.464	3391935.705	63.356
T72	T	0.000	0.000	0.000	562839.568	3392144.112	66.020

T73	T	0.000	0.000	0.000	562919.749	3391814.561	58.237
T74	T	0.000	0.000	0.000	563116.728	3391270.519	46.861
T75	T	0.000	0.000	0.000	564305.612	3391771.120	49.509
T76	T	0.000	0.000	0.000	564383.463	3392691.815	59.136
T77	T	0.000	0.000	0.000	564499.041	3391811.815	54.782
T78	T	0.000	0.000	0.000	564147.940	3391270.268	54.926
T79	T	0.000	0.000	0.000	564425.508	3391337.630	47.969
T80	T	0.000	0.000	0.000	564172.418	3391512.699	53.478
T81	T	0.000	0.000	0.000	564563.331	3392006.704	42.946
T82	T	0.000	0.000	0.000	564713.797	3391845.051	60.903
T83	T	0.000	0.000	0.000	564827.282	3391964.802	55.287
36-URAL	C	0.000	0.000	0.000	563468.291	3391935.012	62.820
29-URAL	C	0.000	0.000	0.000	563332.132	3391875.170	63.434
T84	T	0.000	0.000	0.000	562729.512	3392593.565	70.220
T85	T	0.000	0.000	0.000	562640.919	3392381.618	68.325
T86	T	0.000	0.000	0.000	562689.593	3392802.170	70.081
T87	T	0.000	0.000	0.000	562908.081	3392596.723	73.560

Timing Information (in minutes):

Time in Pre-Triangulation: 0.00
Time in Estimation: 0.02
Time in Initialization: 0.00
Time in Solution: 0.00
Average Time Per Iteration: 0.00
Time in Error Propagation: 0.00
Total Triangulation Time: 0.02

Dr. Chun Shin Lin's report was unavailable at the time of publication.

Dr. Chaoqun Liu's report was unavailable at the time of publication.

INFRARED SPECTROPOLARIMETRIC DIRECTIONAL REFLECTANCE AND EMISSIVITY OF METAL SURFACES

Carl E. Mungan
Assistant Professor
Department of Physics

The University of West Florida
11000 University Parkway
Pensacola, FL 32514-5751

Final Report for:
Summer Research Extension Program
Air Force Research Laboratory / Munitions Directorate

Sponsored by:
Air Force Office of Scientific Research
Bolling Air Force Base, DC

and

Air Force Research Laboratory / Munitions Directorate
Eglin Air Force Base, FL

December 1999

INFRARED SPECTROPOLARIMETRIC DIRECTIONAL REFLECTANCE AND EMISSIVITY OF METAL SURFACES

Carl E. Mungan
Assistant Professor
Department of Physics
The University of West Florida

Abstract

The bidirectional reflectance distribution function function (BRDF) is a measure of the amount of light scattered by some medium from one direction into another. Integrating it over specified incident and reflected solid angles defines the reflectance, which can be easily related to the emissivity of a sample. The BRDF can thus be taken as a fundamental quantity for the optical characterization of an object and it correspondingly is important in a large variety of applications. When a beam of electromagnetic radiation (visible, infrared, radar, etc.) strikes a body, it can scatter off the top or first surface, as well as from the volume or subsequent interfaces. However, the total amount of light reflected from the first surface depends primarily on the complex index of refraction of the illuminated medium (relative to that of the incident medium) and is often sufficiently large that this dominates the scattering from the material. On the other hand, the topography of this interface determines the angular distribution of the scattered radiation—smooth surfaces reflect almost entirely into the specular direction, while with increasing roughness the light tends to diffract into all possible directions. Ultimately an object will appear equally bright throughout the outgoing hemisphere if its surface is perfectly diffuse (i.e., Lambertian). Measuring and modeling the BRDF can thus give valuable information about the nature of a target sample.

INFRARED SPECTROPOLARIMETRIC DIRECTIONAL REFLECTANCE AND EMISSIVITY OF METAL SURFACES

Carl E. Mungan

Introduction

Measurements of the reflectances of a variety of different lidar target samples and building construction materials have been performed under ambient conditions for a variety of incident and scattering angles in the near-infrared over all possible polarization states. This gives what is called the spectropolarimetric bidirectional reflectance. The target samples are of interest for laser radar calibrations, while the building materials are applicable to remote sensing applications. A Fourier-transform spectrometer (shown in Fig. 1) fitted with an external reflectance goniometer and with an incident and scattered polarization generator and analyzer, respectively, was used for this purpose at Eglin AFB.

Fig. 1. Photograph of the Fourier transform interferometer at Eglin AFB.

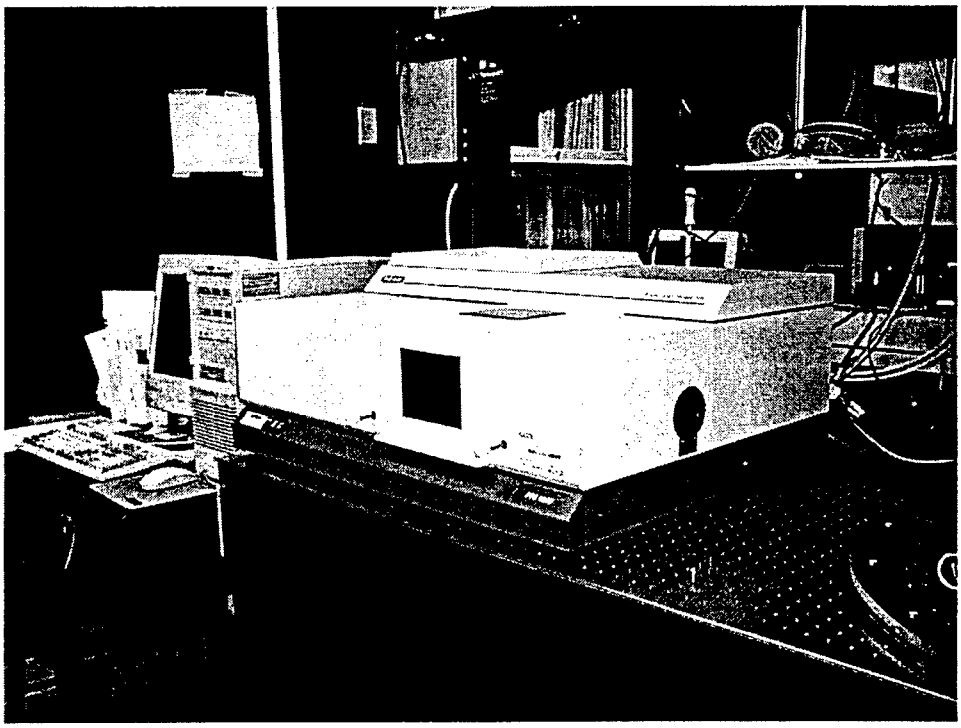

Experimental Setup

Three attenuators (labeled #1 through #3) were used to avoid saturating the silicon detector in the spectrometer. Although these are nominally neutral density in the visible range, their transmittances were decidely not flat in the near-infrared, as can be seen in Figs. 2–4 below. The light-colored, jagged traces are the transmission spectra measured using the BioRad interferometer. The bold, smooth traces are polynomial fits to these spectra. The lowest order polynomials which give acceptable fits are the quartics

$$T = A + B\lambda + C\lambda^2 + D\lambda^3 + E\lambda^4 \tag{1}$$

where T is the fractional transmittance and λ is the wavelength in microns. The coefficients and average transmittances of these three attenuators are listed in Table 1.

Table 1. Coefficients for fits to the attenuator transmittances.

Attenuator	$\bar{T}$	A	B	C	D	E
1	11.3%	-26.655	119.97	-199.24	145.62	-39.626
2	22.7%	-39.904	183.03	-308.04	227.33	-62.283
3	5.6%	-16.985	75.996	-125.22	90.496	-24.253

These fitted transmittances are used to correct the measured reflectances of the samples. For example, if for some particular sample, the reference data were collected with attenuator #2 in place but the sample data were collected with no attenuator, the actual reflectance would be computed by multiplying the measured reflectance by the transmittance given by Eq. (1) using the data from the appropriate row of Table 1.

Fig. 2. Transmission spectrum of attenuator #1.

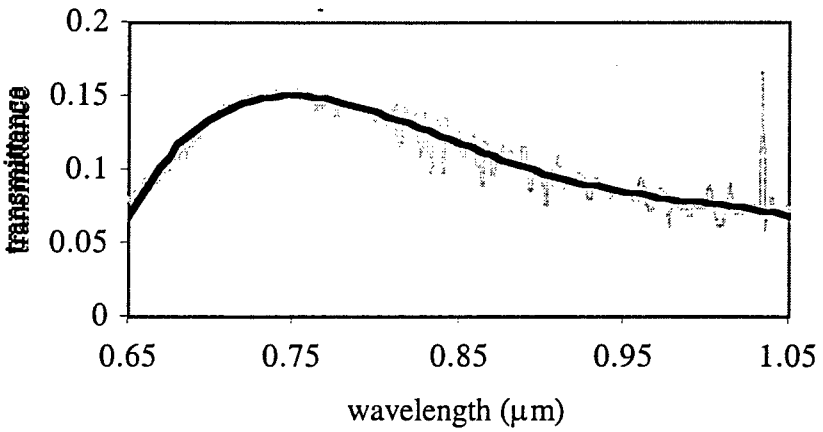

Fig. 3. Transmission spectrum of attenuator #2.

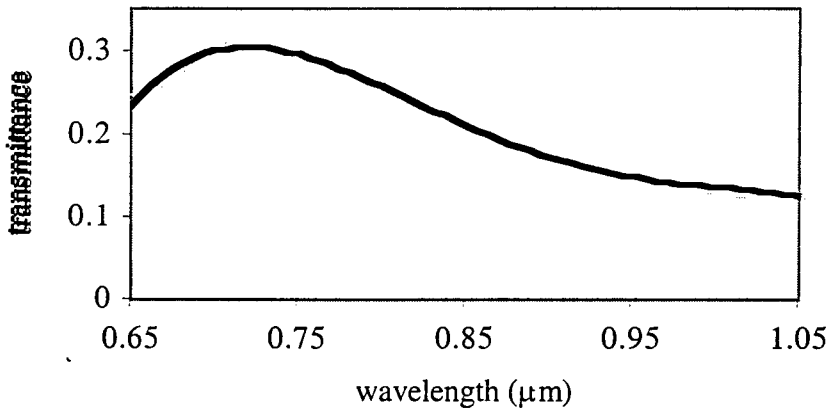

Fig. 4. Transmission spectrum of attenuator #3.

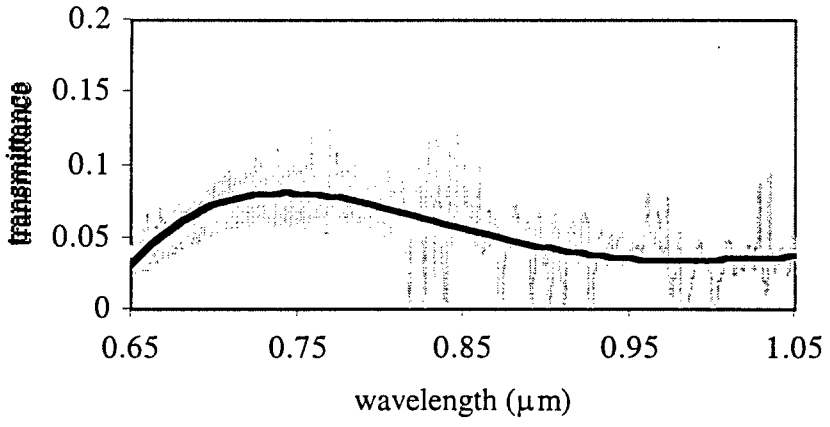

Fig. 5. Raw intensity spectrum of the source.

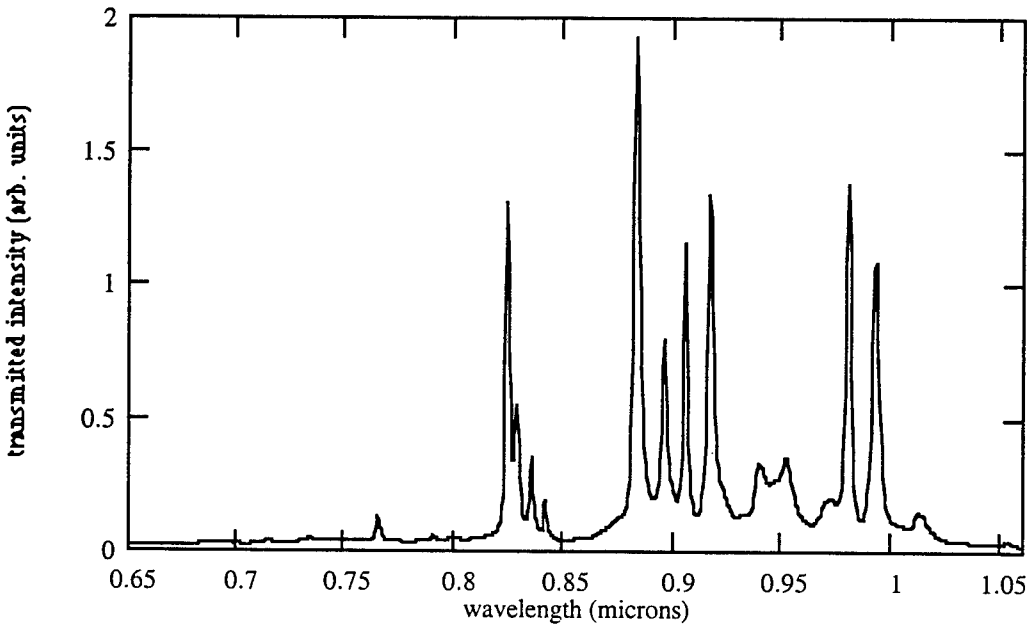

The Xe arc lamp spectrum in Fig. 5 shows discrete atomic emission lines, superimposed on top of a smooth thermal background. This blackbody background spectrum looks weak only because of the sharpness of the atomic lines; in fact, the thermal spectrum has enough strength for spectroscopy and the sharp lines are not of interest. In order to eliminate residual unratioed features at these strong lamp spectral peaks, the reflectance data were smoothed slightly.

The most general mapping of the bidirectional reflectance distribution function (BRDF) of a flat sample requires that four angles be continuously variable over the hemisphere about the sample's normal: the incident polar and azimuthal angles, θ_i and ϕ_i, and the reflected angles, θ_r and ϕ_r. These angles are sketched in Fig. 6. Note that the sample normal defines the z-axis, while the x-axis can be chosen to coincide with some preferred surface feature of the sample, such as striations, a crystallographic direction, or an optical axis. For an isotropic surface, having no such preferred features, the BRDF is a function only of $\phi_r - \phi_i$ and not of the two azimuthal angles

individually. The samples investigated in the present study are assumed to be isotropic when averaged over the area of illumination scattered into the detector aperture. Arbitrarily fixing ϕ_i at 0° by suitable choice of the coordinate system, this means that the BRDF only depends on ϕ_r.

Fig. 6. General geometry of the incident and reflected beams.

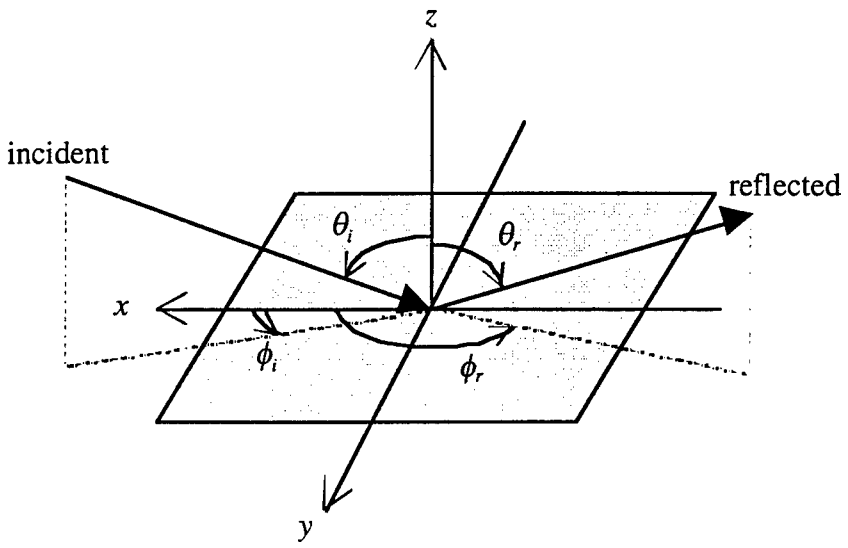

The spectropolarimetric reflectometer at Eglin AFB has the following geometry, as sketched in Fig. 7. The output retarder and polarizer, together with the mirror and detector, rotate around the sample on a motor-driven stage. The sample also rotates on an independently driven stage. A particular choice of the detector and sample positions fixes the incident and reflected polar angles. (Note carefully that the z-axis in Fig. 6 has been rotated by 90° in Fig. 7, so that rotations of the two stages determine the polar not the azimuthal angles.) In principle, out-of-plane azimuthal measurements can be performed by tilting the sample about the axis parallel to the optical bench in the plane of the sample. However, in the present work, only in-plane measurements (i.e., $\phi_r = 180°$) were made, in which the sample normal lies in the plane of the incident and reflected beams.

Fig. 7. Block diagram of the spectropolarimetric reflectometer.

Legend: A = attenuators, P = linear polarizer, R = achromatic retarder,

M = off-axis parabolic mirror, D = silicon detector.

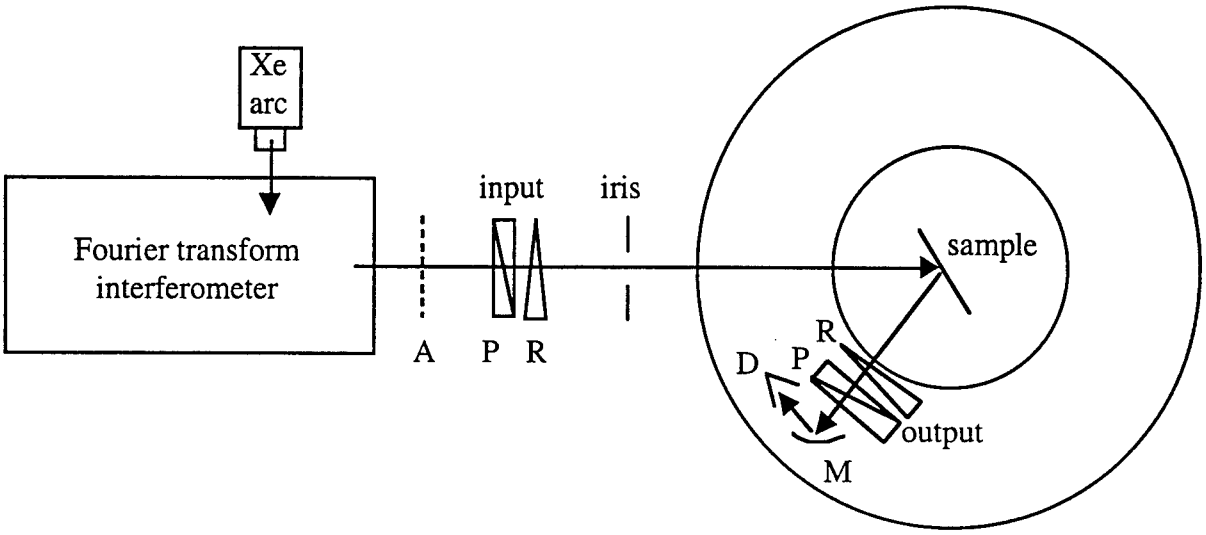

The device in Fig. 7 can be conceptually divided into three parts: a spectrometer, a polarimeter, and a reflectometer. The spectrometer modulates the radiation from the Xe arc source using a scanning Michelson-Morley interferometer with a quartz beamsplitter. The parameters for the spectrometer are as follows:

- speed of the scanning mirror = 5 kHz
- electronic filter = 5 kHz
- undersampling ratio = 1
- resolution = 16 cm^{-1}
- aperture = fully open
- number of scans to co-add = 64
- wavelength range = 0.65–1.06 μm

The modulated beam exits the spectrometer through its external port. Attenuators can be inserted or removed into this beam, as needed to limit the signal strength which ultimately falls on the detector to ±10 V. In addition, the sensitivity (which is an electronic gain) can be adjusted to boost weak signals; typically a sensitivity of 1 was used for the reference scans and a value of 16 for the sample scans.

The polarimeter consists of two matched pairs of polarizers and retarders. On the input side, the unpolarized incident beam first passes through a dichroic sheet linear polarizer, and the resulting linearly polarized beam next traverses an achromatic two-plate MgF_2 retarder, whose slow axis is delayed by a quarter wavelength compared to its fast axis. By rotating the optical axis of the retarder, it is possible to encode any desired elliptical polarization state into the harmonics of the intensity signal (Chenault *et al.*, 1998), i.e., with the major axis oriented at any desired angle, of either handedness, and with any desired ellipticity between 0 (circular) and 1 (linear). On the output side, the reflected beam passes through a matching polarizer-retarder combination in the opposite order. By suitably rotating the optical axis of the retarder, it is possible to transform any elliptical polarization state into a linearly polarized wave which can be analyzed by the linear polarizer. The polarimetric properties of a sample can be described in terms of its Mueller matrix, which is a 4×4 matrix $\mathbf{M}$ defining the transformation of the incident polarization state into the reflected polarization state—cf. Eq. (14) below.

Finally, the reflectometer consists of the rotating sample and detector stages. There are two ways of specifying the incident and reflected angles (cf. Fig. 8): either relative to the sample normal, or absolutely with respect to the optical bench. The former pair are the polar angles θ_i and θ_r defined previously in Fig. 6. By choice of our x-axis, θ_i is always positive. Taking ϕ_r to always be equal to 180° implies that θ_r is positive whenever the reflected beam lies on the other side of the sample normal than the incident beam, which is hereafter referred to as forward scattering. On the other hand, θ_r is taken to be negative for backward scattering, when the

incident and reflected beams both lie within the same x-z quadrant. Although this is contrary to the usual convention for the specification of polar angles, it simplifies the notation in the present work. The absolute angles θ_d and θ_s are measured with reference to the incident direction, using the convention that positive angles are measured in the clockwise direction and negative angles in the counter-clockwise direction. (This is not actually contrary to the standard convention for plane polar angles, because the incident beam points in the $-x$ direction according to Fig. 6.) With these definitions, the conversion formulae from relative to absolute angles are

$$\theta_s = -\theta_i \text{ and}$$
$$\theta_d = 180° - \theta_i - \theta_r. \tag{2}$$

Fig. 8. Specification of the incident and reflected angles.

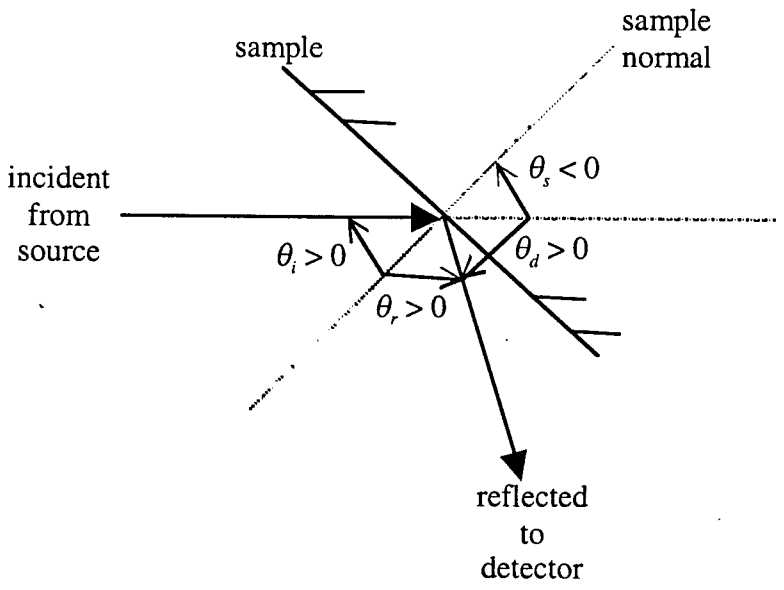

It is conventional in optics to employ the relative angles; for example, specular scattering corresponds to the case of $\theta_r = \theta_i$, while monostatic scattering (also referred to as backscattering) corresponds to $\theta_r = -\theta_i$, so called because in radar work it corresponds to using the same antenna

both as the source and as the detector (as opposed to separate transmitting and receiving dishes for the bistatic case). However, it is simpler from the point of view of the experimental setup of Fig. 7 to use the absolute angles in practice. The absolute zero angle can be found for θ_d by peaking up the signal in the absence of a sample, and for θ_s by replacing the sample with a flat mirror and checking that the incident beam is reflected straight back toward the source.

Combining the spectrometer, polarimeter, and reflectometer components, it is evident that a single data run consists of measuring a 4×4 array of spectra for each of a variety of different incident and reflected angles. Each data run is begun by collecting calibration data with no sample in place and with the detector looking straight back at the source through the spectrometer (i.e., $\theta_d = 0°$). This generates both a background reference spectrum for determination of the reflectance, and error corrections for the retarders and polarizers. There are five possible errors, indicated as small angles ε in Fig. 9: discrepancies in the 90° retardances δ of the quarter-wave plates and orientation misalignments of the output polarization axis and of the retarder optical axes. (The input polarization axis is not crucial because the source beam is unpolarized and the polarizers remain fixed in orientation during the runs, in order to eliminate any possible polarization dependence of the optics either before the input polarizer or following the output polarizer.) Fortunately, the procedure for collecting the data and performing the Mueller matrix calculations is automated. Nevertheless, it requires large amounts of time, generally on the order of a couple of days per sample. A wealth of information can in principle be extracted from this large quantity of data.

Fig. 9. Polarization and retardation errors.

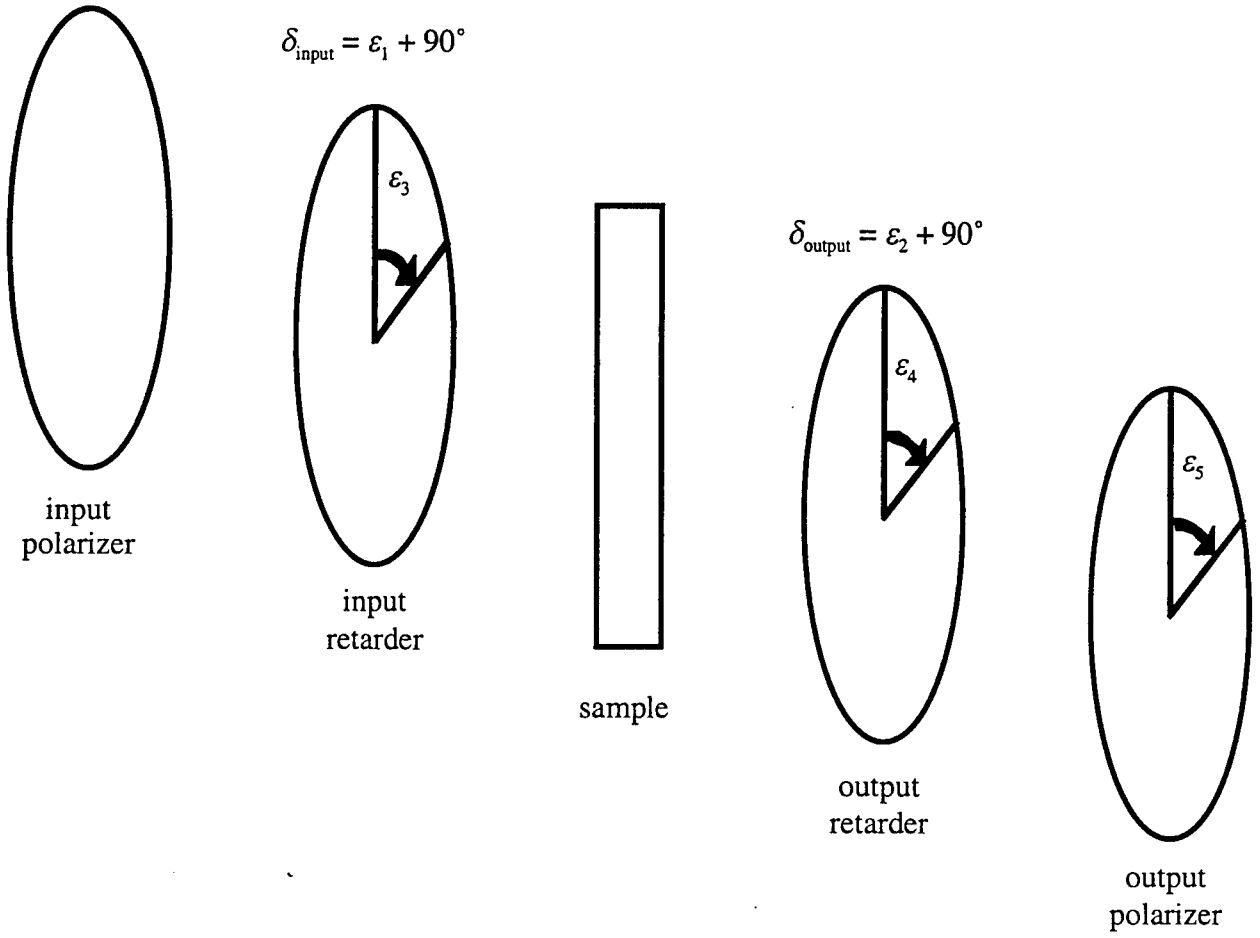

Thirteen samples were selected for study in the present work, six construction materials and seven lidar target board samples. They are all flat, square items measuring several inches on a side. A brief description of each is presented in Table 2 below.

Table 2. Description of samples studied.

Sample	Description
Construction Materials	
Foam	Blue polystyrene housing insulation labeled sample #819.
Drywall	Standard housing drywall material labeled sample #914.
Rubber	Piece of soft black rubber labeled sample #10A.
Wood	Piece of plywood labeled sample #719.
Shingle	Speckled grey roof shingle labeled sample #6A.
Steel	Steel plate painted military grey labeled sample #2A.
Target Board Samples	
2%	black paint
5%	black paint with slight sparkles
10%	black paint with more sparkles
A	grey paint with a sandpaper texture
B	grey-black paint with a sandpaper texture
E	grey-white paint with a sandpaper texture
Resolution	flat grey paint

The total reflectances $\tilde{M}_{00}$ (cf. Eq. 15 below) of these 13 samples are plotted in Fig. 10 over the near-infrared wavelength range of 0.75–1 μm for specular scattering at $\theta_i = \theta_r = 45°$. (In this report, the term "reflectance" always refer to the bidirectional reflectance, wherein light incident from one direction—within a narrow element of solid angle Ω_i defined by the iris—is reflected into some other direction—within a narrow element of solid angle Ω_r defined by the detector aperture. Dividing the bidirectional reflectance by the projected reflection solid angle, $\Omega_r \cos\theta_r$, gives the BRDF.) Since these spectra are quite flat, it is reasonable to average them over this wavelength range. The results are given in Table 3, in the same top to bottom order of samples as they are graphed in Fig. 10.

Table 3. Average reflectances in the near-infrared for 45° specular scattering.

Sample	**Average Reflectance** (10^{-7})
Resolution	1300
Foam	670
Drywall	140
Rubber	84
E	79
Wood	74
Shingle	31
A	24
Steel	24
10%	23
B	23
2%	8.5
5%	4.8

A couple of general comments can be made about these results. The reflectances of the target board samples span the range of reflectances of the construction materials. Hence, these target boards can be usefully employed to gauge typical scattering from man-made objects of military interest, at least at medium specular angles. However, the reflectances of a number of the materials are not in the same order in the near-infrared as they appear to be by eye in the visible. For example, the black rubber sample reflects more than the grey-painted steel, the 2% target more than the 5% target, and so on. Hence, one should be careful not to assume that a reflectance calibration at one wavelength holds true at another wavelength. Infrared lidars generally require infrared standard targets rather than the more commonly available visible targets.

Fig. 10. Total reflectances of the 13 samples investigated for 45° specular scattering.

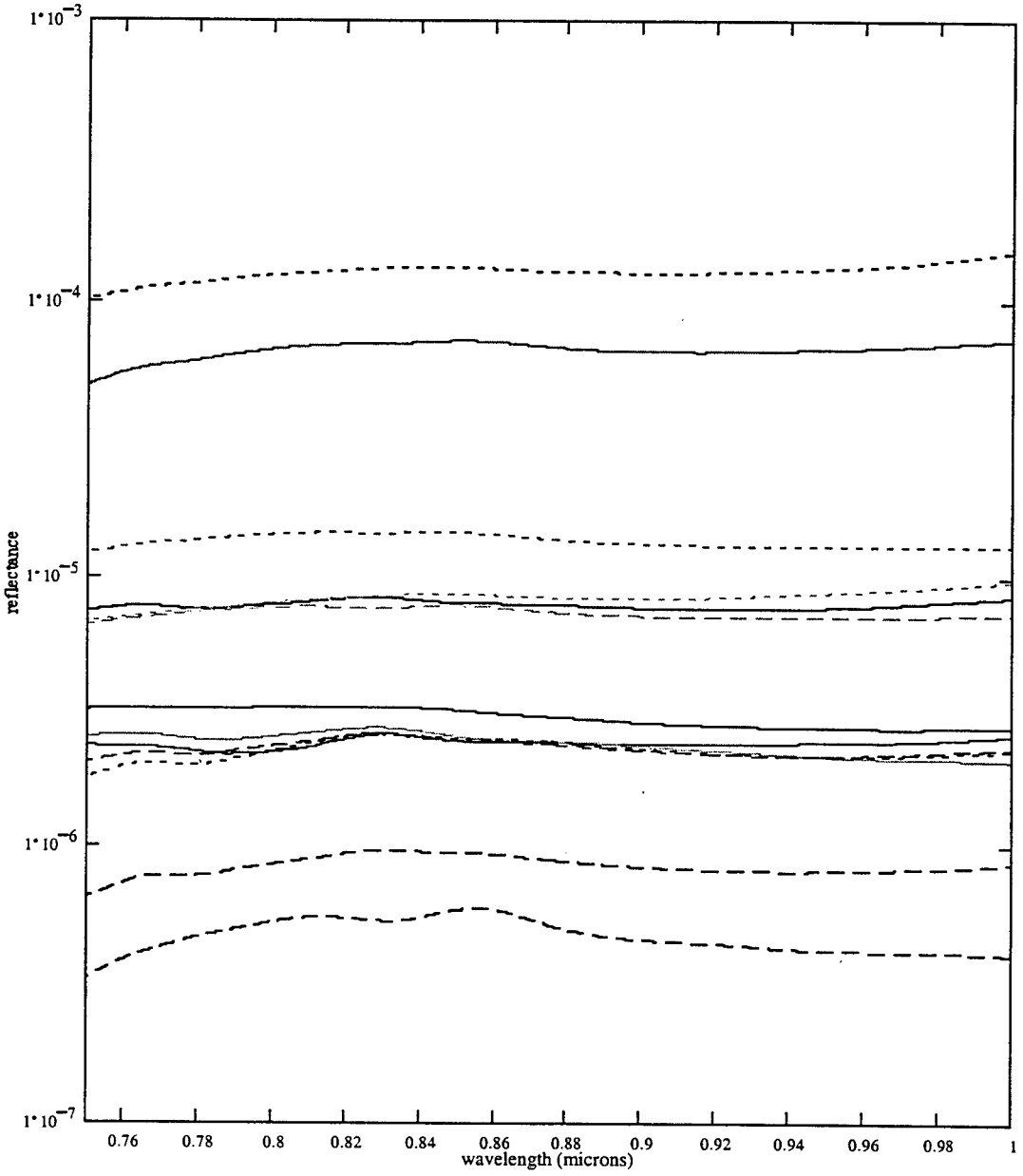

Theory of Polarized Light Scattering

The incident optical power P per unit illuminated area A of an object is known as the illuminance $H \equiv dP/dA$ in units of W/m^2; the corresponding scattered quantity is called the exitance. [Note that the element dA of area is taken to be small on the macroscopic scales of interest, but large compared to the sub-resolution irregularities in the sample surface, and is taken to be perpendicular to the macroscopic surface normal (Nicodemus, 1965).] When it is desired to speak of either the illuminance or the exitance, without specifying which, this report will refer to the irradiance of the surface. This is to be distinguished from the intensity of the irradiating beam, $I \equiv dP/(dA \cos\theta)$, where the $\cos\theta$ term projects the element of surface area dA into the direction of propagation of the beam, which is inclined at polar angle θ to the (macroscopic) surface normal. The irradiance per unit projected solid angle is called the radiance or luminance, which corresponds to the photometric concept of brightness, $L \equiv dH/(\cos\theta\, d\Omega) = dI/d\Omega$ in units of W/m^2/sr. Here the element of solid angle is $d\Omega \equiv \sin\theta\, d\theta\, d\phi$; sometimes (Nicodemus *et al.*, 1977) a separate symbol is also introduced for the element of projected solid angle $\cos\theta\, d\Omega$, though I will not do so here. Let the subscript i refer to incident quantities and r to reflected (scattered) terms. The bidirectional reflectance distribution function (BRDF) can now be defined as

$$f(\theta_i,\phi_i;\theta_r,\phi_r) \equiv \frac{dL_r}{dH_i} = \frac{dP_r}{dP_i \cos\theta_r d\Omega_r} \tag{3}$$

with units of sr^{-1}; here dP_i is the incident power illuminating dA from direction (θ_i,ϕ_i) and dP_r is the radiant power reflected from dA into the outgoing solid angle $d\Omega_r$ centered about the direction (θ_r,ϕ_r). In the present work, all of the sample surfaces are macroscopically planar and the incident beam has a spatially uniform ("top hat") intensity profile, so that one can integrate Eq. (3) over a macroscopic area A of the sample to get

$$f(\theta_i;\theta_r,\phi_r-\phi_i)=\frac{dP_r}{P_i\cos\theta_r d\Omega_r} \tag{4}$$

where now P_i is the incident power illuminating A and dP_r is the flux reflected from A into $d\Omega_r$. Since the surfaces investigated here are taken to be isotropic, f is a function only of $\phi_r - \phi_i$ (which is fixed at 180° in this study) as explained previously. Unlike reflectances, which cannot exceed unity, the BRDF can be very large, becoming infinite for a purely specular reflector.

By integrating the BRDF over all scattered angles, one gets the dimensionless directional-hemispherical reflectance

$$\rho(\theta_i,\phi_i;2\pi)=\int_{2\pi} f(\theta_i,\phi_i;\theta_r,\phi_r)\cos\theta_r d\Omega_r\,, \tag{5}$$

which gives the fractional amount of power reflected into the entire hemisphere out of that incident from a particular direction. (The integral over 2π is a shorthand meaning integrate θ from 0 to $\pi/2$ and ϕ from 0 to 2π, for a total solid angle of 2π.) If instead one averages over all incident angles, the hemispherical-directional reflectance is obtained as

$$d\rho(2\pi;\theta_r,\phi_r)=\frac{\cos\theta_r d\Omega_r}{\pi}\int_{2\pi} f(\theta_i,\phi_i;\theta_r,\phi_r)\cos\theta_i d\Omega_i\,. \tag{6}$$

Note that the denominator is π and not 2π because of the $\cos\theta_i$ projection factor. In the spirit of Eqs. (5) and (6), the bihemispherical reflectance (or albedo) is given by

$$\rho(2\pi;2\pi)=\frac{1}{\pi}\iint_{2\pi} f(\theta_i,\phi_i;\theta_r,\phi_r)\cos\theta_i d\Omega_i\cos\theta_r d\Omega_r\,. \tag{7}$$

Other similar quantities, such as the conical-hemispherical reflectance, have been tabulated by Judd (1967) and by Nicodemus *et al.* (1977). If the prefactor before the integral in Eq. (6) is left off, the resulting quantity is instead called the hemispherical-directional reflectance factor, which is defined as the ratio of the flux reflected by the sample to that which would be reflected by an ideal Lambertian reflector for the same geometry, because $f = 1/\pi$ for the latter (Mungan, 1998).

From the definition of the BRDF, the scattered radiance can be related to the incident radiance by

$$L_r(\theta_r,\phi_r) = \int_{\Omega_i} L_i(\theta_i,\phi_i) f(\theta_i,\phi_i;\theta_r,\phi_r)\cos\theta_i d\Omega_i , \tag{8}$$

which can be rather complicated to evaluate analytically. The emissivity is given by Kirchhoff's law as

$$\varepsilon(\theta_i,\phi_i) = 1 - \int_{2\pi} f(\theta_i,\phi_i;\theta_r,\phi_r)\cos\theta_r d\Omega_r \tag{9}$$

and is thus determined by the BRDF. Hence a separate measurement of the emissivity is not required.

According to the Helmholtz reciprocity theorem, $f(\theta_i,\phi_i;\theta_r,\phi_r) = f(\theta_r,\phi_r;\theta_i,\phi_i)$, so that either direction may be that of the incident beam with the other the reflected beam. Note from Eqs. (5) and (6) that this would imply that the directional-hemispherical reflectance equals the hemispherical-directional reflectance factor; interestingly enough, however, equality of these two reflectance terms remains true even when Helmholtz reciprocity does not (Nicodemus, 1970). There has been considerable discussion about the conditions under which reciprocity holds (Clarke and Parry, 1985; Kriebel, 1996; Shirley *et al.*, 1997; Snyder, 1998)—for example, it clearly does not apply to a Faraday isolator. It is generally accepted however that the theorem is obeyed by most materials (including compound objects) under ordinary conditions and hence models which are not reciprocal are generally considered unphysical and experimental failures

are often attributed to measurement errors or limitations.

Equation (4) contains no polarization information and relates only the total incident and reflected optical fluxes to each other. In order to quantify the polarimetric scattering, we need to retain the phase information about the electric fields associated with the beams and not simply their intensities. There are two alternative representations for doing so (Hecht, 1998). The Jones calculus writes each electric field as a vector of two complex components, and the scattering is then described by a 2 × 2 matrix. This formalism is not applicable to the present work, as it implicitly assumes that each beam is fully polarized and coherent. To instead handle incoherent light which is partially polarized in general, as we need here, each beam can be represented by a column vector of four real components. This vector is called the Stokes vector **S** and its four components are called the Stokes parameters $\{S_0,S_1,S_2,S_3\}$. These parameters can be defined either operationally or from electromagnetic theory. To get the former, imagine a set of three ideal polarizers, i.e., they perfectly transmit a specific polarization state and perfectly block the complementary polarization state. (That is, their diattenuations, as defined below, for the appropriate polarization states are 100%.) Note that each polarizer therefore transmits half of the intensity of incident unpolarized light. Filter 1 is a linear polarizer whose pass axis is horizontal; filter 2 is another linear polarizer but with a pass axis inclined at +45°; and filter 3 is a right-handed circular polarizer. (For the present case of surface scattering, these axes are defined relative to the plane of incidence or reflection, as appropriate. That is, horizontal means *s*-polarized and vertical means *p*-polarized.) Let I_0 be the incident beam intensity, and denote the intensities transmitted by each polarizer as I_1, I_2, and I_3, respectively. Then the normalized Stokes parameters are given by

$$\begin{aligned} S_0 &= 1 \\ S_1 &= 2I_1 / I_0 - 1 \\ S_2 &= 2I_2 / I_0 - 1 \\ S_3 &= 2I_3 / I_0 - 1 \end{aligned} \tag{10}$$

so that S_1, S_2, and S_3 each vary between –1 and +1 and specify the state of polarization: $S_1 > 0$ means the beam is preferentially horizontally (H) polarized, while $S_1 < 0$ indicates it is predominantly vertically (V) polarized; S_2 refers to the tendency to be linearly polarized at +45° ($S_2 > 0$) or –45° ($S_2 < 0$); and finally S_3 indicates preferential right-handed circular (RHC) versus left-handed circular (LHC) polarizations by its sign. If the normalized Stokes vector is multiplied by the total beam intensity, then the unnormalized Stokes vector (denoted by a tilde) results,

$$\tilde{\mathbf{S}} = I_0 \mathbf{S} \tag{11}$$

so that $\tilde{S}_0 = I_0$. Alternatively, from an electromagnetic point of view, if the complex amplitude of an electric field vector is written as $(E_{0x}e^{i\varphi_x}, E_{0y}e^{i\varphi_y})$, then

$$\begin{aligned} S_1 &= \left\langle E_{0x}^2 - E_{0y}^2 \right\rangle \Big/ \left\langle E_{0x}^2 + E_{0y}^2 \right\rangle \\ S_2 &= \left\langle 2E_{0x}E_{0y}\cos\varphi \right\rangle \Big/ \left\langle E_{0x}^2 + E_{0y}^2 \right\rangle \\ S_3 &= \left\langle 2E_{0x}E_{0y}\sin\varphi \right\rangle \Big/ \left\langle E_{0x}^2 + E_{0y}^2 \right\rangle \end{aligned} \tag{12}$$

where $\varphi \equiv \varphi_y - \varphi_x$ and the angular brackets denote time averages. From this we see that if the beam is unpolarized, then $\left\langle E_{0x}^2 \right\rangle = \left\langle E_{0y}^2 \right\rangle$ and $\langle \varphi \rangle = 0$ independently of the real amplitudes, so that $S_1 = S_2 = S_3 = 0$. At the other extreme, for fully polarized light Eq. (12) implies that $S_1^2 + S_2^2 + S_3^2 = 1$. In general, the degree of polarization of a beam is defined as

$$DOP \equiv \frac{I_{pol}}{I_0} = \frac{\sqrt{\tilde{S}_1^2 + \tilde{S}_2^2 + \tilde{S}_3^2}}{\tilde{S}_0} = \sqrt{S_1^2 + S_2^2 + S_3^2}\,, \tag{13}$$

where the total intensity I_0 is equal to the sum of its polarized portion, I_{pol}, and its unpolarized portion, I_{unpol}. For example, $DOP = 0$ for an unpolarized beam, while $DOP = 1$ for fully polarized light.

Now, the incident and reflected beams are related by a 4 × 4 matrix called the unnormalized Mueller matrix,

$$\tilde{\mathbf{S}}_r = \tilde{\mathbf{M}}\tilde{\mathbf{S}}_i \tag{14a}$$

which we can write out explicitly in component form using Eq. (11) as

$$\begin{bmatrix} I_{0r} \\ \tilde{S}_{1r} \\ \tilde{S}_{2r} \\ \tilde{S}_{3r} \end{bmatrix} = \begin{bmatrix} \tilde{M}_{00} & \tilde{M}_{01} & \tilde{M}_{02} & \tilde{M}_{03} \\ \tilde{M}_{10} & \tilde{M}_{11} & \tilde{M}_{12} & \tilde{M}_{13} \\ \tilde{M}_{20} & \tilde{M}_{21} & \tilde{M}_{22} & \tilde{M}_{23} \\ \tilde{M}_{30} & \tilde{M}_{31} & \tilde{M}_{32} & \tilde{M}_{33} \end{bmatrix} \begin{bmatrix} I_{0i} \\ \tilde{S}_{1i} \\ \tilde{S}_{2i} \\ \tilde{S}_{3i} \end{bmatrix}. \tag{14b}$$

Comparing this to Eq. (3), we see that for incident and reflected unpolarized beams,

$$\tilde{M}_{00} = f(\theta_i, \phi_i; \theta_r, \phi_r) \cos\theta_r d\Omega_r, \tag{15}$$

i.e., the top leftmost element of the unnormalized Mueller matrix is equal to the bidirectional reflectance. The other elements in the matrix give polarimetric information. Thus, the Mueller matrix can be thought of as a generalization of the BRDF to polarized scattering (Flynn and Alexander, 1995). It is conventional to normalize the Mueller matrix by ratioing out the unpolarized reflectance,

$$\mathbf{M} \equiv \tilde{\mathbf{M}} / \tilde{M}_{00}. \tag{16}$$

From this normalized Mueller matrix, all polarization properties of interest can be calculated. For example, if unpolarized light is incident on the sample, then Eq. (14b) becomes

$$\begin{bmatrix} \tilde{S}_{0r} \\ \tilde{S}_{1r} \\ \tilde{S}_{2r} \\ \tilde{S}_{3r} \end{bmatrix} = \begin{bmatrix} \tilde{M}_{00} & \tilde{M}_{01} & \tilde{M}_{02} & \tilde{M}_{03} \\ \tilde{M}_{10} & \tilde{M}_{11} & \tilde{M}_{12} & \tilde{M}_{13} \\ \tilde{M}_{20} & \tilde{M}_{21} & \tilde{M}_{22} & \tilde{M}_{23} \\ \tilde{M}_{30} & \tilde{M}_{31} & \tilde{M}_{32} & \tilde{M}_{33} \end{bmatrix} \begin{bmatrix} I_{0i} \\ 0 \\ 0 \\ 0 \end{bmatrix} = I_{0i} \begin{bmatrix} \tilde{M}_{00} \\ \tilde{M}_{10} \\ \tilde{M}_{20} \\ \tilde{M}_{30} \end{bmatrix} \tag{17}$$

so that the scattered beam is in general polarized. The degree of polarization of the reflected beam for an unpolarized incident beam defines the polarizance, P (Sornsin and Chipman, 1996). Using Eq. (13), this is seen to be

$$P = \frac{\sqrt{(I_{0i}\tilde{M}_{10})^2 + (I_{0i}\tilde{M}_{20})^2 + (I_{0i}\tilde{M}_{30})^2}}{I_{0i}\tilde{M}_{00}} = \sqrt{M_{10}^2 + M_{20}^2 + M_{30}^2} \tag{18}$$

and is thus determined by the first column of the Mueller matrix. It is a fraction varying between 0 and 1, and is thus conveniently expressed as a percentage. For example, $P = 1$ for an ideal

polarizer, while $P = 0$ for an ideal retarder. An ideal polarizer, as previously mentioned, fully passes one polarization state while completely blocking the complementary polarization state. This is described by a quantity called the diattenuation, D, that quantifies variations in the scattered power as a function of the incident polarization state. The diattenuation vector **D** has three components, each of which can vary from –1 to +1: $D_1 = M_{01}$ which describes H–V diattenuation, $D_2 = M_{02}$ which describes ±45° diattenuation, and $D_3 = M_{03}$ which describes RHC–LHC diattenuation. The overall magnitude of this vector is

$$D = \sqrt{M_{01}^2 + M_{02}^2 + M_{03}^2}\,, \tag{19}$$

determined by the first row of the Mueller matrix. Like P, it is a fraction conveniently expressed as a percentage between 0 and 100%.

In studying the polarimetry of materials, an important question is the extent to which the polarization state of a beam is preserved by the interaction with the sample or device. This is described by the general concept of "depolarization." Unfortunately, two distinct definitions of depolarization are used in the literature. To avoid this confusion, I will here coin two alternate names for these processes. On the one hand, one can ask for the degree to which a polarized beam becomes unpolarized; this will be called the unpolarizance, U. On the other hand, one can ask about changes from one state to another state of polarization; let's term this the transpolarizance. For example, suppose an s-polarized beam is incident on some device or material, and the exiting beam is 10% s, 20% p, 40% RHC, and 30% unpolarized. Then we would say that the s-unpolarizance is 30% and the s-transpolarizance is 60%. A measure of the unpolarizance is given by (Sornsin and Chipman, 1996)

$$U = 1 - \sqrt{\frac{\left(\sum_{i,j=0}^{3} M_{ij}^2\right) - 1}{3}}\,, \tag{20}$$

expressed as a percentage between 0 and 100%. If $U = 0$, then the exiting light is fully polarized

for any incident polarization state; this occurs when $\left\langle M_i^2 \right\rangle = 1$, where $\mathbf{M}_i$ is the i^{th} row vector of the Mueller matrix and the average is over all four rows. For example, $U = 0$ for an ideal polarizer or retarder. Note that since the sum of M_{ij}^2 equals the trace of $\mathbf{M}$ multiplied by its transpose, this definition is equivalent to Eq. (29) of Kim *et al.* (1987).

If a material does not unpolarize light, then its Mueller matrix can be uniquely decomposed into the product of a diattenuating component and a retarding component (Chenault *et al.*, 1998). While the diattenuation vector **D** measures the relative changes in the real amplitudes of the scattered electric field components for complementary polarization states, the retardance vector **R** measures the relative changes in their phases. The overall magnitude of the retardance is given by a fairly involved expression,

$$R = \cos^{-1}\left[\frac{\left(\sum_{i=1}^{3} M_{ii}\right) - \left(\sum_{i=1}^{3} M_{i0}M_{0i}\right) \Big/ \left(1+\sqrt{1-D^2}\right)}{2\sqrt{1-D^2}} - 0.5\right] \tag{21}$$

which can vary between 0 and 180°. For example, this expression gives $R = 90°$ for a quarter-wave plate for any orientation of its fast axis, but an indeterminate answer for any ideal polarizer, as expected because the complex number $z = 0$ has an undefined phase angle.

Experimental Results

The data for the polarizance, diattenuation, retardance, and unpolarizance were found for all samples to be relatively constant over the 800–1000 nm spectral range. Consequently they were averaged over this interval and are reported in the following tables.

In Table 4, three pairs of angles are specular, $\theta_i = \theta_r$. In Table 5, as in many cases, most angles were chosen to correspond to forward scattering, for which interesting polarimetric behavior is expected.

Table 4. Averaged results for the 2% lidar target sample.

θ_i	θ_r	P	D	R	U
45°	45°	73.5%	69.8%	92.9°	15.1%
75°	75°	40.7%	41.5%	89.7°	6.2%
75°	0°	54.4%	64.9%	111.8°	12.6%
20°	20°	15.0%	16.1%	90.2°	7.7%
45°	75°	77.8%	77.5%	93.7°	13.0%

Table 5. Averaged results for the 5% lidar target sample.

θ_i	θ_r	P	D	R	U
45°	45°	47.1%	48.8%	100.0°	34.1%
75°	75°	38.0%	37.6%	87.2°	6.5%
45°	75°	66.6%	66.9%	93.0°	20.4%

Table 6. Averaged results for the 10% lidar target sample.

θ_i	θ_r	P	D	R	U
45°	45°	31.9%	31.7%	93.1°	17.7%
75°	75°	43.5%	43.7%	89.6°	14.4%
75°	0°	57.7%	62.4%	119.4°	–
0°	75°	16.8%	34.8%	111.3°	12.5%
20°	20°	5.7%	5.8%	93.4°	8.7%

In Table 6, the 75°–0° data afford a test of reciprocity, wherein the incident and reflected beams are swapped. Note however from Eq. (15) that this requires a correction for the projection factor and has not been pursued in this report. The dash indicates a small value, but the data were too noisy to permit a reliable determination of it.

Table 7. Averaged results for lidar target sample A.

θ_i	θ_r	P	D	R	U
45°	45°	18.3%	18.0%	113.1°	76.6%
45°	75°	39.2%	40.3%	107.1°	56.4%
20°	20°	2.7%	3.8%	116.8°	85.6%

Note in Table 7 how large the unpolarizance values are. As discussed in connection with Eq. (21), this renders the determinations of the retardance questionable.

Table 8. Averaged results for lidar target sample B.

θ_i	θ_r	P	D	R	U
45°	45°	45.8%	46.3%	104.8°	43.4%
75°	75°	54.2%	54.4%	89.6°	6.3%
60°	0°	34.3%	26.8%	116.7°	30.1%

Note in Table 8, as is the case for most of the samples, that the retardance is about 100° for any pair of angles.

Table 9. Averaged results for lidar target sample E.

θ_i	θ_r	P	D	R	U
45°	45°	4.5%	4.3%	137.0°	34.5%
45°	25°	2.4%	2.4%	137.1°	38.9%
45°	75°	14.5%	17.1%	90.4°	3.5%
20°	20°	2.2%	11.3%	103.5°	44.1%
75°	45°	10.1%	18.4%	95.5°	12.5%
75°	60°	13.8%	22.2%	94.8°	–
75°	75°	18.1%	26.3%	95.4°	–
45°	45°	4.7%	4.4%	100.3°	32.1%
75°	–45°	0.7%	0.7%	106.3°	44.9%
75°	75°	19.2%	18.9%	93.1°	28.5%
75°	85°	22.3%	22.2%	91.4°	22.8%

Two sets of runs in Table 9 were repeated many months apart, after the spectropolarimeter had been moved to a new lab and realigned from scratch, resulting in a substantial improvement in signal-to-noise for the later runs below the double line. In view of this, the reproducibility of the data is seen to be fairly good in these two cases. One might thus reasonably expect self-consistency among the runs for the other samples, which were collected as a set either with the old or the new setup.

Table 10. Averaged results for the resolution board sample.

θ_i	θ_r	P	D	R	U
45°	45°	83.4%	85.4%	90.5°	2.5%
75°	75°	48.2%	50.2%	88.1°	1.4%
75°	0°	1.1%	11.5%	117.4°	86.8%
20°	20°	16.6%	17.0%	93.8°	10.6%

Note the surprisingly large range of values for P, D, and U in Table 10.

Table 11. Averaged results for the construction samples for $\theta_i = \theta_r = 45°$.

Sample	P	D	R	U
foam	54.7%	67.9%	101.3°	25.9%
wood	17.0%	20.8%	113.7°	72.3%
drywall	19.4%	24.7%	112.3°	72.2%
rubber	68.7%	80.9%	88.7°	12.3%
shingle	11.5%	16.2%	116.3°	83.3%
steel	58.5%	69.3%	92.1°	18.8%

It is easier to understand these data visually. A number of different graphs are possible and presented below.

Fig. 11. Lidar target samples at $\theta_i = 45°$ and $\theta_r = 45°$.

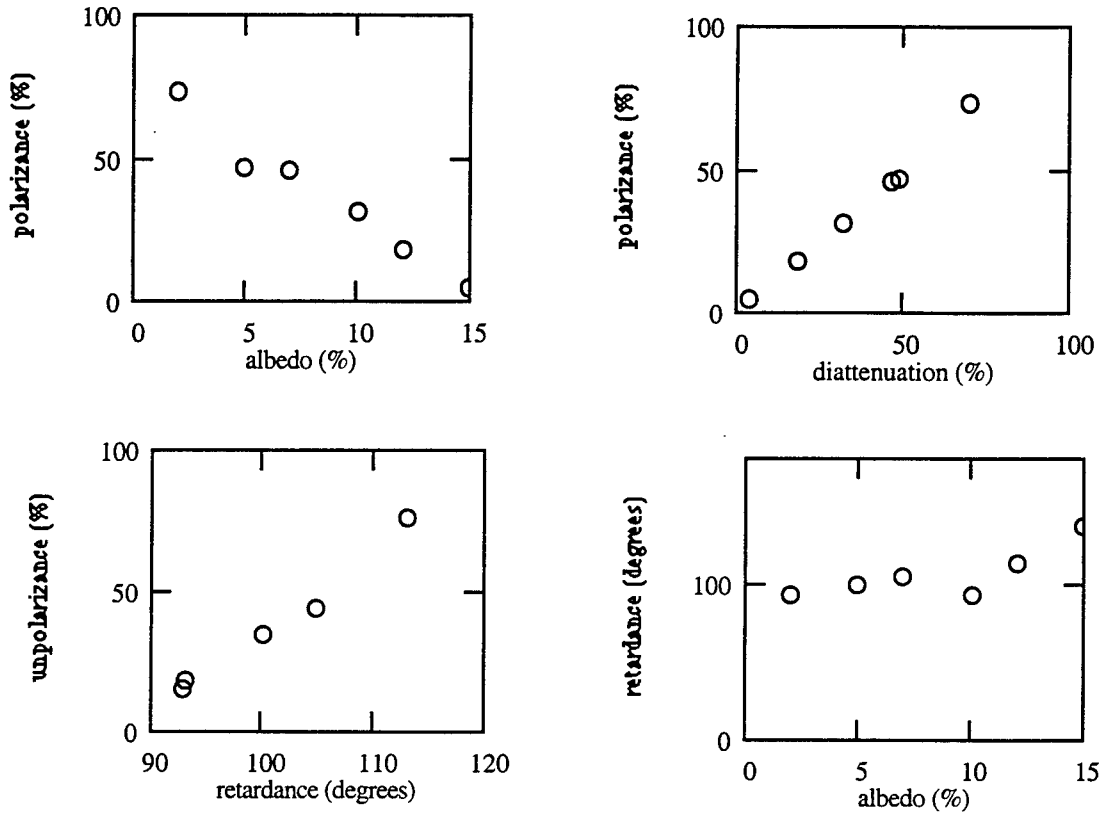

In Fig. 11, I have plotted the averaged data for the lidar samples for the important case of 45° specular scattering. The albedos are estimated from their nominal ratings or visual appearances, as listed in Table 12.

We see from the top left graph in Fig. 11 that the polarizance decreases with the reflectance. More highly absorbing samples polarize the light more efficiently. The explanation for this is the well-known fact that the reflectance of *p*-polarized light is lower than that of *s*-polarized light at any oblique angle (Hecht, 1998). In particular, the former equals zero at the Brewster angle for a dielectric medium such as the paint coating on the samples. (Even for metal surfaces, the *p*-reflectance has a minimum, albeit not a zero, at the pseudo-Brewster angle.) Thus, as the sample

absorptance increases, and hence the reflectance decreases (since the reflectance and absorptance sum to unity for an opaque sample), only the *s*-polarized beam survives. The top right graph in Fig. 11 shows that the polarizance is strongly linearly correlated to the diattenuation, confirming this conclusion.

In the lower right graph in Fig. 11, it can be seen that the retardance hovers around 90° at low sample reflectances, but rises at larger reflectances. In fact, perfect mirror-like reflection can be obtained for a real surface at 180° forward scattering (i.e., specular scattering at grazing incidence), whether a dielectric or a conductor. We might then be tempted to predict a simple 180° phase shift upon reflection from a high albedo sample for any polarization state, following a consideration of the electromagnetic boundary conditions for grazing scattering (Hecht, 1998). However, this line of reasoning can be seen to be incorrect by examining the lower left graph in Fig. 11: at high retardances, the samples unpolarize an incident beam, in striking contradistinction to the effect of a mirror. At high albedos, our samples become perfect diffuse not specular reflectors, i.e., they are more nearly Lambertian than mirror-like and hence it is no surprise that the scattered light is unpolarized.

Table 12. Estimated bihemispherical reflectances of the lidar samples.

Target Sample	Estimated Albedo
2%	2%
5%	5%
B	7%
10%	10%
A	12%
E	15%

Fig. 12. Construction samples at $\theta_i = 45°$ and $\theta_r = 45°$.

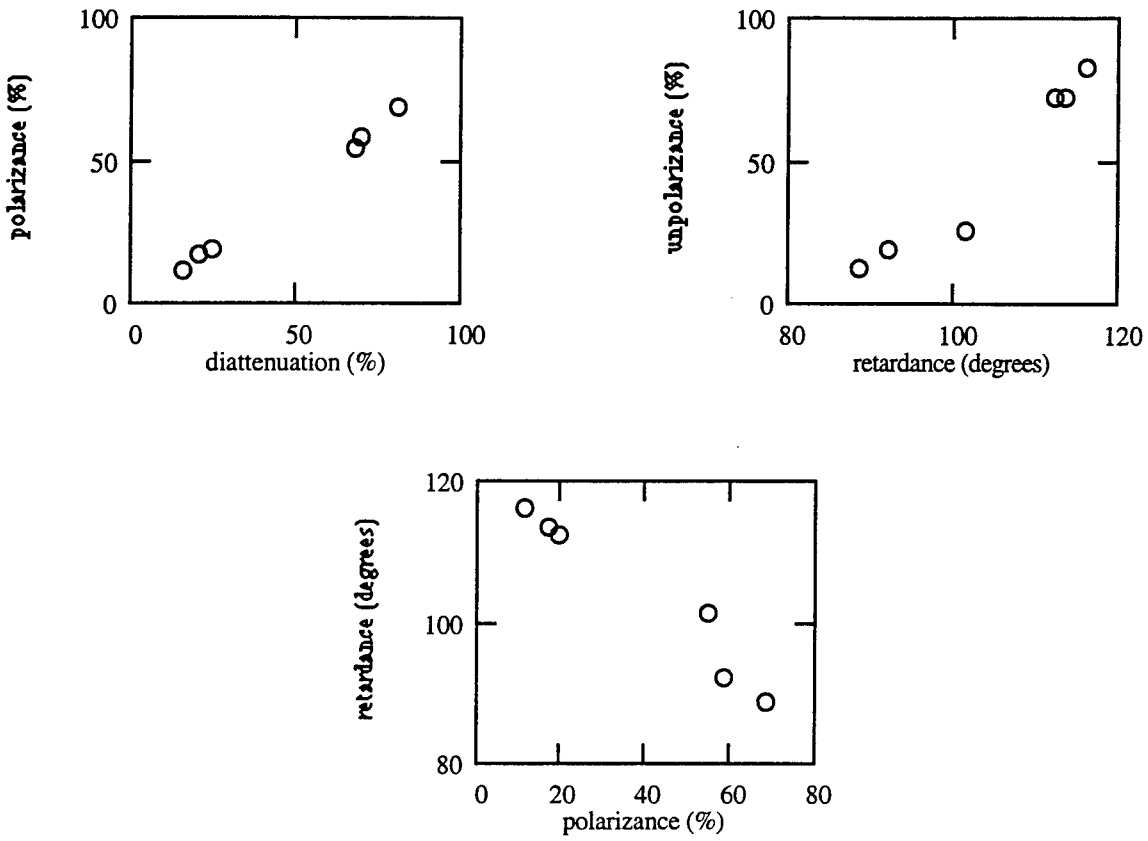

Figure 12 presents results for the construction materials at 45° specular scattering. The upper two graphs are similar in their trends to the corresponding graphs in Fig. 11. Since it is difficult to estimate the albedos for these samples, the other two graphs in Fig. 11 have been combined into the lower graph in Fig. 12. The retardance appears to approach 90° as the polarizance and hence the diattenuation rises toward 100%. An average retardance of 90° can result if the *p* component of the scattered light has a 0° phase shift while the *s* component has a 180° shift, as is true for specular reflection from a dielectric at angles of incidence below the Brewster angle (Hecht, 1998).

Figure 13 plots target sample E for three different cases of specular reflection, $\theta_i = \theta_r$.

Fig. 13. Lidar sample E for specular scattering.

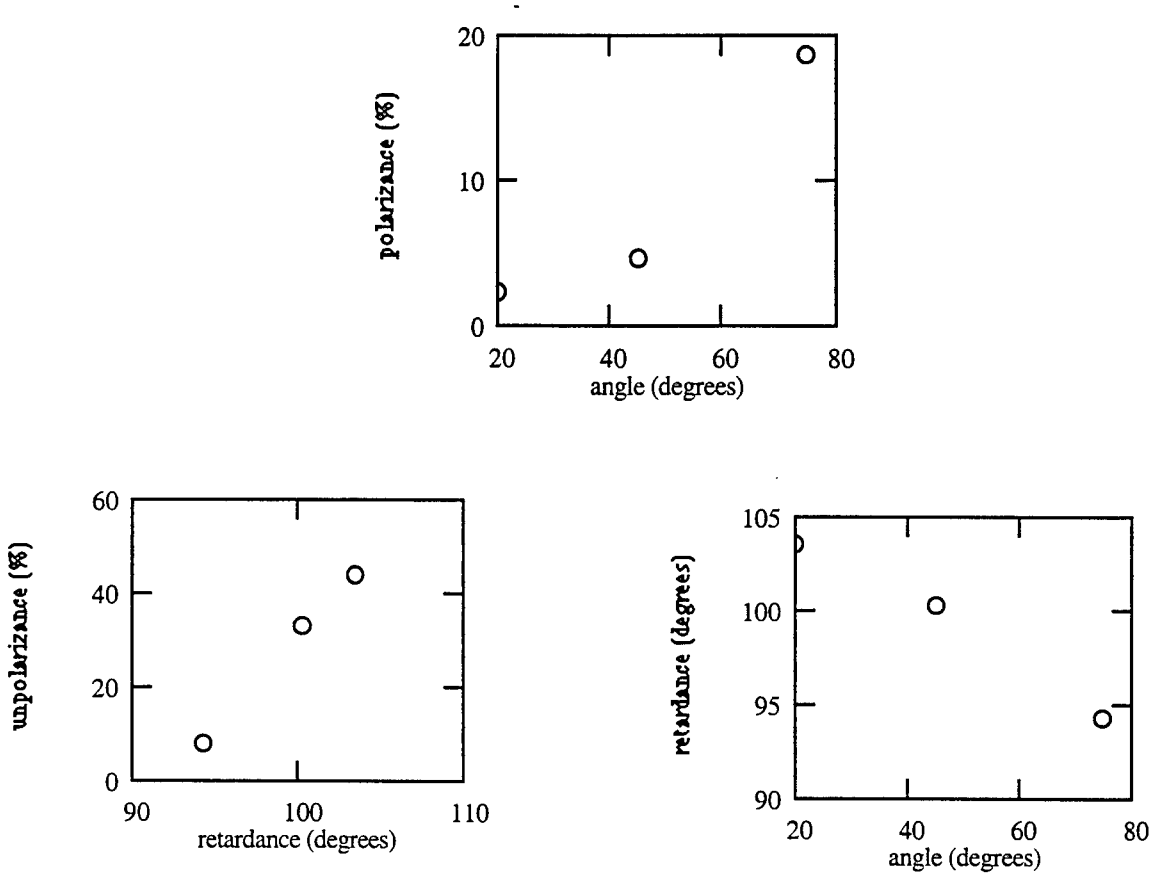

The top graph in Fig. 13 implies that the polarizance rises with the specular angle. This suggests a rather high Brewster angle and hence real part of the index of refraction of the surface, just as the glare off the surface of a lake is preferentially horizontally polarized. Surprisingly, the retardance is seen in the lower right graph in Fig. 13 to decrease with the scattering angle, in contrast to the 180° phase shift expected for a mirror.

Similar behavior is observed for specular scattering from the 2%, 10%, and resolution board lidar samples. On the other hand, Fig. 14 shows what happens if we fix the angle of incidence at 45° and allow the angle of reflection to sweep through the specular direction.

Fig. 14. Lidar sample E at $\theta_i = 45°$.

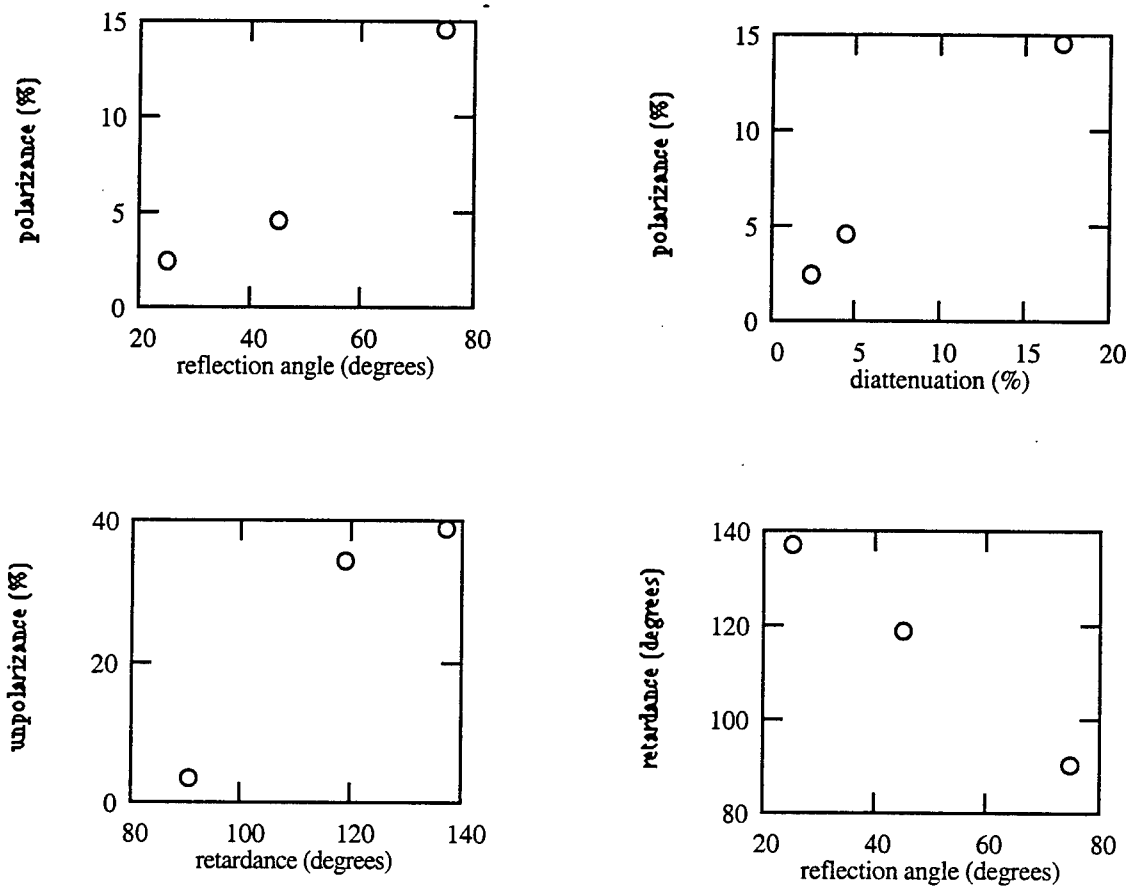

The polarizance increases as θ_r moves toward grazing, and correspondingly the diattenuation rises in step. The lower two plots in Fig. 14 resemble those of Fig. 13, indicating that the polarimetric dependence of the specular and off-specular beams are very similar, which is perhaps not surprising for diffuse scattering. Similar, although noisier, results are found for $\theta_i = 75°$. In further confirmation of this, the lidar target samples for $\theta_i = 45°$ and $\theta_r = 75°$ give graphs like those of Fig. 11.

Conclusions

A preliminary presentation on some of the results in this report was presented at the APS March Meeting, as summarized in the Appendix, for which AFOSR's support was gratefully acknowledged. In bullet form, the three key results of this study, as discussed in this report, are as follows.

• Seven laser radar calibration targets and six different common construction materials have been characterized polarimetrically from 0.65 to 1.06 μm for a number of different incident and reflected angles relevant to bistatic remote sensing applications.

• A novel spectropolarimetric reflectometer at Eglin AFB has been optimized for operation and described here in detail along with the associated theory, for the benefit of future workers at this facility.

• The huge amount of data collected in this study has been boiled down into average values of the polarizance, diattenuation, retardance, and unpolarizance. These have been both tabulated and graphed. Possible interpretations of these results have been suggested, along with some questions deserving further study.

References

D.B. Chenault, D.H. Goldstein, and D.M Hayes (1998), "Fourier transform spectropolarimetry for optical diagnostics of transmissive materials," SPIE Proc. **3425**, 258.

F.J.J. Clarke and D.J. Parry (1985), "Helmholtz reciprocity: Its validity and application to reflectometry," Light. Res. & Tech. **17**, 1.

D.S. Flynn and C. Alexander (1995), "Polarized surface scattering expressed in terms of a bidirectional reflectance distribution function matrix," Opt. Eng. **34**, 1646.

E. Hecht, "Optics," 3rd ed. (Addison-Wesley, Reading MA, 1998).

D.B. Judd (1967), "Terms, definitions, and symbols in reflectometry," J. Opt. Soc. Am. **57**, 445.

K. Kim, L. Mandel, and E. Wolf (1987), "Relationship between Jones and Mueller matrices for random media," J. Opt. Soc. Am. A **4**, 433.

K.-T. Kriebel (1996), "On the limited validity of reciprocity in measured BRDFs," Remote Sens. Environ. **58**, 52.

C.E. Mungan, (1998), "Bidirectional reflectance distribution functions describing first-surface scattering," AFOSR Final Report for the Summer Faculty Research Program.

F.E. Nicodemus (1965), "Directional reflectance and emissivity of an opaque surface," Appl. Opt. **4**, 767.

F.E. Nicodemus (1970), "Reflectance nomenclature and directional reflectance and emissivity," Appl. Opt. **9**, 1474.

F.E. Nicodemus, J.C. Richmond, J.J. Hsia, I.W. Ginsberg, and T. Limperis (1977), "Geometrical considerations and nomenclature for reflectance," NBS Monograph 160.

P. Shirley, H. Hu, B. Smits, E. Lafortune (1997), "A practitioners' assessment of light reflection models," Proceedings of the Pacific Graphics Conference.

W.C. Snyder and Z. Wan (1996), "Surface temperature correction for active infrared reflectance measurements of natural materials," Appl. Opt. **35**, 2216.

E.A. Sornsin and R.A. Chipman (1996), "Polarization BRDF of satellite materials," Proceedings of the Workshop on Infrared and Millimeter Wave Polarimetry.

Appendix

Abstract for a poster presentation at the American Physical Society Centennial Meeting in Atlanta on 3/24/99, as published in Bull. Am. Phys. Soc. **44**, 1289 (1999).

Infrared Spectropolarimetric Directional Reflectance and Emissivity of Metal Surfaces

C.E. Mungan (cmungan@uwf.edu),
Dept. of Physics, Univ. of West Florida, Pensacola, FL 3251
and
D.H. Goldstein (goldstei@eglin.af.mil),
Air Force Research Lab, Eglin AFB, FL 32542

The bidirectional reflectance distribution function (BRDF) is a measure of the amount of light scattered by a surface from one direction into another. Integrating it over specified incident and reflected solid angles defines the reflectance, which is related to the emissivity via Kirchhoff's law. The spectral, angular, and polarization dependences of the BRDF permit the nature and topography of a target surface to be characterized. An infrared spectropolarimeter has been constructed for this purpose: the modulated beam from a Fourier-transform interferometer illuminates an external sample on a motorized rotation stage, while a cooled detector revolves around it. The incident and reflected beams each pass through a linear polarizer and variable retarder to enable a complete measurement of the Mueller matrix. Separate emissivity experiments are being set up in a large cryogenic vacuum chamber. Experimental progress in studying gold-plated cylinders and plates (as a first step toward recognition of military targets) will be described.

STRUCTURAL CHANGES IN MESOPHASE PITCH-BASED CARBON FIBERS

Amod A. Ogale
Professor
Department of Chemical Engineering

Clemson University
203 Earle Hall
Clemson, SC 29634-0909

Final Report for:
Summer Research Extension Program

Sponsored by:
Air Force Office of Scientific Research

and

Wright Patterson Air Force Research Labs

February 2000

STRUCTURAL CHANGES IN MESOPHASE PITCH-BASED CARBON FIBERS

Amod A. Ogale
Professor
Department of Chemical Engineering
Clemson University

Abstract

The structure and tensile properties of pitch-based carbon fibers are reported in this study. During the first phase of the study, conducted at Wright Patterson Air Force Research Labs (WPAFRL) in 1998, the dimensional changes of AR-mesophase pitch fibers were measured for fiber subjected to heat treatment temperatures (HTT) that ranged from 300°C to 3000°C. The unique aspect of this follow-up study is the characterization of dimensional changes of the same set of fibers at several different temperatures, and the structural characterization using micro-Raman technique.

Single-filament testing indicates that the average tensile strength of the fibers ranged from 1.0 GPa to 2.0 GPa, the modulus ranged from 100 to 600GPa, whereas the strain-to-failure ranged from 0.4% to 0.8%. The structure of the fibers was probed in this study by the micro-Raman technique. Starting from the stabilized state, the heights of the D (1360 cm^{-1}) and G (1580 cm^{-1}) bands were found to decrease up to HTTs of 900°C. For higher HTTs, the peaks started to become sharper and taller. The limited long-range order of disordered phase is evident as the additional band at 1620 cm^{-1}. Wide-angle x-ray scattering (WAXS) measurements, independently conducted by Dr. Dave Anderson WPAFRL, indicate that the misorientation angles display a small peak (maximum) at an HTT of 900°C.

The dimensional measurements for AR fibers suggest that starting from an oxidized state, the length of the fibers shrinks about 8% at a HTT of 900°C. Above 900°C, the length does not reduce any further, instead it increases slightly. Thus, fibers heat treated to 2400°C shrink less (7%) than those heat treated to 900°C. The slight increase in length of fibers heat treated to high temperatures (greater than 900°C) can be explained by the alignment of the graphene layer planes along the fiber axis that can result in an expansion along the longitudinal direction.

STRUCTURAL CHANGES IN MESOPHASE PITCH-BASED CARBON FIBERS

Amod A. Ogale

Background

Recently, a considerable attention has been directed toward pitch-based carbon fibers/composites. These liquid crystalline mesophase pitches result in fibers that have thermal conductivity, which is about three times that of copper [1-3].

The processing of carbon-carbon composite materials presents several technical and economic challenges. These materials must be heat treated at temperatures exceeding 2000C, and the resulting high processing costs of these materials lead to their limited use to such applications where performance is the critical controlling factor [4].

In carbon-carbon composites, severe internal stresses are generated during processing, the primary reason being that the shrinkage of the precursor material when noncarbon constituents (oxygen, nitrogen, CO, CO_2) are evolved during carbonization. This shrinkage results in matrix/fiber cracks and leads to deterioration of physical and mechanical properties.

The science of simultaneous carbonization of fibers and matrix is not well understood. The microstructure and properties of pitch-based fibers have been investigated by a number of researchers [5-10]. However, only a limited number of studies have dealt with dimensional changes [11,12].

Consequently, a study was initiated by the PI and the MLBC Branch of the AFRL at WPAFB during the summer of 1998 [13]. The primary objective of the study was the quantitative measurement of the dimensional changes in pitch-based fibers during carbonization. Results indicated that the shrinkage is fairly anisotropic, since the

reduction in length after carbonization was approximately 8% whereas that in diameter is over 20%.

This project sought to elucidate further the structural changes taking place in the mesophase precursor during the various heat treatment steps. The specific objectives of the proposed project were to process pitch-based carbon fibers, monitor dimensional changes as a function of heat treatment temperatures (HTT), characterize the microstructure, and measure the tensile properties of the fibers.

Experimental

Materials

All experiments in this study were conducted on AR-mesophase, provided by Mitsubishi Gas Chemical Company, Japan. The pitch fibers were melt extruded in the Carbon Fiber Labs at Clemson University.

Stabilization

Whereas thin (10 micrometer diameter) AR pitch fibers can be stabilized in a temperature range of 180°C to 280°C within a few hours, the fibers used in the present study, about 50-100 μm, had to be oxidized for about 3 days at 200°C. The thicker fibers facilitate accurate diameter and length measurements.

Heat Treatment

Carbonization was carried out in a Lindberg furnace (model 51442) equipped with a temperature controller and a vacuum pump. After loading the stabilized samples, the furnace was purged with nitrogen and vacuumed for 30 min; this purge and vacuum step was repeated three times. The furnace was then heated in nitrogen atmosphere to 900°C at a rate of 3 °C/min and held there for 1 hour, and finally cooled down to room temperature.

Graphitization was performed in an Astro graphite furnace equipped with a temperature controller and an ultra-vacuum pump. After loading the carbonized samples, the furnace was purged with helium and vacuumed three times, and each time vacuum was controlled below 0.1 Torr. The furnace was heated in helium atmosphere to 1800°C at a rate of 20°C/min, to 2400 °C at a rate of 10 °C/min, and then soaked at 2400 °C for 15 min before being cooled with cooling water to room temperature.

Attempts to investigate the *in situ* monitoring of length in thermogravimetric analyzer (TG171, Cahn Instruments) was unsuccessful because of the technical difficulties encountered in mounting pitch fibers in a fixture. The pitch fibers are extremely fragile and could not be mounted without getting crushed.

Characterization

Tensile Properties

The tensile modulus, strength, and strain-to-failure of fibers were measured by conducting single-fiber tests in a MTI single-fiber testing machine at Clemson University. A standard gage length of 25.4 mm and an extension rate of 0.0508 mm/min was used. To obtain statistically significant values, a large number of samples (20 replicates or more) were used for single-filament testing.

Dimensional

The dimensions were measured, both before and after the heat treatment cycle, in a Olympus BX60 optical microscope. The fibers were placed individually on glass slides and the length and diameter were measured with the aid of a Microcode indexer with a resolution of 1 μm. For carbonization, the fibers were placed on graphite plates (approx. 6 inches long, 3 inches wide, and 0.25 inch thick) and the position of each fiber was carefully noted. For graphitization, the fibers were placed in small tubes made of GrafoilTM graphite sheet. After heat treatment, the fibers were carefully removed from the graphite plates or the tubes and placed on the glass slides.

Microstructural

The micro-Raman spectroscopy was conducted using a Renishaw Raman Microscope System 1000 at Clemson University. The Raman system was equipped with a CCD (charge coupled device) detector and a near infrared diode laser excitation (782 nm). The fiber samples were mounted on an aluminum slide and focused with a 50X objective microscope.

The crystalline content and structure (d002 spacing, Lc, and La) of fibers processed was independently measured by Dr. Dave Anderson at the WPAFRL using wide angle X-ray scattering (WAXS) on a Huber Instrument.

Results and Discussion

Tensile Properties

The tensile properties were measured by single-filament testing. The tensile strength, modulus, and strain-to-failure data for AR fibers are displayed in Figs. 1-3. Starting from the lowest HTT of 300°C, the strength increases for higher HTTs and levels off at about 1.5 GPa; the significantly higher value at a HTT of 2875°C cannot be explained. The tensile modulus, on the other hand, increases successively as the HTT increases, although the very high value of 600GPa at 2875°C cannot be explained. The strain-to-failure values at the lower HTTs are about 0.8%, but decrease to about 0.5% at the higher HTTs. The properties from successive HTTs are not statistically significant at the 95% confidence level, but the properties at the highest and lowest HTTs are significantly different. The strength and moduli measured in this study are lower than the values of 2-3 GPa and 300-800 GPa reported in the studies of Mochida et al. [7] and Pencock, et al. [8]. The probable reason for the lower values is that the fibers chosen for this study were considerably thicker than those used in most other studies. Also, optical microscopy revealed that the thick fibers tend to have more defects and the characteristics "Pac-man" splitting. It is noted that the thicker fibers facilitated accurate measurement of the dimensional changes and were purposely chosen for the present study.

Dimensional Changes

Since carbonization involves the removal of noncarbon species from the organic precursors, a considerable shrinkage takes place during processing. It was established in the first phase of this study (conducted at WPAFRL) that the fiber length could be measured consistently with an error of about ±10 μm. Repeated measurements of fiber lengths (after removing and replacing the fibers on the glass slide) have an error of no ≈0.2%, with much of the error arising from the waviness of fibers. The ratio of the fiber length before and after heat treatment is reported as "L/Lo".

Tables 1 and 2 display data from the length and diameter measurements. A summary of the results is presented in Figures 4 and 5 for the length ratio and diameter ratio, respectively, as a function of the heat treatment temperatures. Starting from the stabilized state, the length of the fibers shrinks about 8% at a HTT of 900°C. However, at 2400°C, the fibers display a shrinkage of about 7% as compared with 8% at the intermediate temperature of 900°C. Although the two values are not significant at a 95% confidence level, the trend is clear that the fibers increase slightly in length at higher HTTs as compared with the length at 900°C.

Considerably larger changes are observed in the diameter of the fibers, as displayed in Figure 5. It was established in the first phase of the study (at WPAFB) that the role of surface oxidation was not significant in the diameter reduction. Starting from the oxidized state, a significant drop of 15% is observed in the diameter till a HTT of 900°C. At a HTT of 2400°C, the diameter reduces by 27%.

X-Ray Diffraction

The microstructure of the fibers heat treated to various temepartures in the first phase of the study (at WPAFRL) was independently characterized by Dr. Dave Anderson using wide angle x-ray scattering (WAXS). The presence of a (103) peak confirmed the existence of 3-dimensional crystallinity (as opposed to turbostratic structure).

The orientation angle, as determined by the "full-width at half-max", is displayed in Fig. 6. It is noted that an orientation angle of 0° represents perfect alignment of the basal planes in the fiber direction. Data presented in Fig. 6 suggests that the misalignment is fairly large before heat treatment but decreases as HTT increases. However, a slight increase in misalignment is observed as the HTT increases from 300°C to 900°C, followed by an eventual decrease of misalignment at highest HTTs.

Micro-Raman Spectroscopy

Raman measurements were performed in the frequency range from 1250 to 1750 cm^{-1}. Raman spectra obtained from these AR pitch fibers are shown in Figures 7 and 8. The Raman spectrum of crystalline graphite has a resonance-enhanced first-order G-band at 1580 cm^{-1} [14], which is due to the in-plane E_{2g} stretching mode of the graphite layer. For disordered carbon with limited long-range order, there are additional broad bands found at 1360 cm^{-1} (the D band) and at 1620 cm^{-1} (the D' band), which are attributed to a disorder-induced relaxation for finite-size crystallites [15].

AR pitch fibers heat-treated below 900°C contain residual amounts of hydrocarbons. However, as can be seen in Figures 7, the Raman peak at 1580 cm^{-1} and 1360 cm^{-1} are still evident at the lowest temperatures. In fact, with increasing HTT, the height of the peaks decrease and the width increases up to a HTT of 900 °C. At higher HTTs, the intensity increases and the peaks become sharper. Thus, disorder seems to go through a maximum at the intermediate temperature of 900C. The disorder, as represented by the width of the peaks, is displayed in Fig. 9. Although the magnitude of this disorder is not large, the phenomenon is consistent with WAXS results, which show a maximum in the misorientation angle at the intermediate HTT of 900C. At HTTs higher than 2100C, the Raman spectra suggest that the size of disordered micro-crystallites of carbon (1360 cm^{-1} D band and at 1620 cm^{-1} D' band) decrease and these get converted to ordered graphitic crystallites (G band) starting about 2400 °C. It has been demonstrated in the literature [16] that the linewidth of the Raman peak at 1580 cm^{-1} correlates with the planar crystallite size of graphite, L_a, obtained by WAXS.

Conclusions

For AR mesophase pitch fibers, a shrinkage of 8% occurs in the length of fibers at a heat treatment temperature of about 900°C. For the same set of fibers, heat treated to a higher temperature of 2400°C, the length shrinkage (relative to the stabilized state) was only ≈7%. Thus, the length of fibers increases slightly as the HTT is increased from 900°C to 2400°C. The slight increase from 900 to 2400°C may result from the alignment of the graphene planes from the initial out-of-plane orientation to the very highly aligned state at 2400°C. The shrinkage in diameter is about 27% at a HTT of 2400°C. These values establish the anisotropic nature of the dimensional changes during carbonization of AR mesophase pitch.

Wide angle x-ray diffraction and micro-Raman spectroscopy results indicate that the AR pitch fibers heat treated to 900°C have the highest molecular misorientation and broadest peak-widths. Thus, as molecular orientation improves with higher HTTs, the alignment of the graphene planes along the fiber length could explain the small increase in length of the fibers.

Acknowledgments

Funding from AFOSR through the Summer Faculty Research Program Contract Number F49620-93-C-0063 is gratefully acknowledged. The technical and organizational support provided by the Carbon Group of the Nonmetallic branch of the Materials Directorate, Wright Patterson Air Force Research Labs, Dayton, is highly appreciated. Special thanks to Scott Thiebert (Lab Focal Point), Kris Kearns, and Dave Anderson.

References

1. D. Schmidt, K. E. Davidson, L. S. Thiebert, "Evolution of Carbon-Carbon Composites," SAMPE Journal, 32 (4), 44-50, 1996.

2. E. Fitzer and L. M. Manocha, "Carbon Reinforcements and Carbon/Carbon Composites, " Springer-Verlag Publishers, 1998.

3. J. D. Buckley and D. D. Edie, "Carbon-Carbon Materials and Composites, "NASA Reference Publication 1254, 1992.

4. H. G. Mahs, W. L. Vauhn, "Four Advances in C-C Composites," NASA CP 3249 361 (1994).

5. I. Mochida, et al., "Microstructure of Mesophase Pitch-Based Carbon Fiber and Its Control," Carbon, 34 (8), 941-956, 1996.

6. S. P. Jones, C. C. Fain, and D. D. Edie, "Structural Development in Mesophase Pitch Based Carbons Fibers Produced From Naphthalene," Carbon, 35(11), 1553-43, 1997.

7. I. Mochida, K. Shimizu, Y. Korai, and Y. Sakai, "Mesophase Pitch Catalytically Prepared From Anthracene," Carbon, 30(1), 55-61, 1992..

8. G. M. Pencock, G. H. Taylor, and J. D. Fitzgerald, "Microstructure in a Series of Mesophase Pitch-Based Fibers from du Pont," Carbon, 31 (4), 591-609, 1993.

9. X. Bourrat, E. J. Roche, and J. G. Lavin, "Structure of Mesophase Pitch Fibers," Carbon, 28 (2/3), 435-446, 1990.

10. D. J. Johnson, I. Tomizuka, and O. Watanabe, "The Fine Structure of Pitch-Based Carbon Fibres," Carbon, 13, 529-534, 1975.

11. L. M. Manocha, H. Bhatt, and S. M. Manocha, "Development of Carbon-Carbon Composites by Co-Carbonization of Phenolic Resin and Oxidized PAN Fibers," Carbon, 34 (7), 841-849, 1996.

12. V. Liedtke and K. J. Huttinger, "Mesophase Pitches as Matrix Precursor of Carbon Fiber Reinforced Carbon: III. Mechanical Properties of Composites," Carbon, 34 (9), 1081-86, 1996.

13. A. A. Ogale, "Characterization of Microstructure Evolution in Pitch-Based Carbon Fibers During Heat Treatment", Technical Report, AFOSR Summer Faculty Research Program, Contract Number F49620-93-C-0063, August 1998.

14. F. Tuinstra and J. L. Koenig, *J. of Chem. Phys.*, **53**, 1126 (1970).

15. R. Vidano and D. B. Fischnach, *J. Am. Ceram. Soc.*, **61**, 13 (1978).

16. S.-C. Lui, Z. Iqbal, N. S. Murthy, K. Zero and N Murdie, *Extended Abstracts of 24th Biennial Conference on Carbon*, pp. 182, 11-16 July, Charleston, South Carolina (1999).

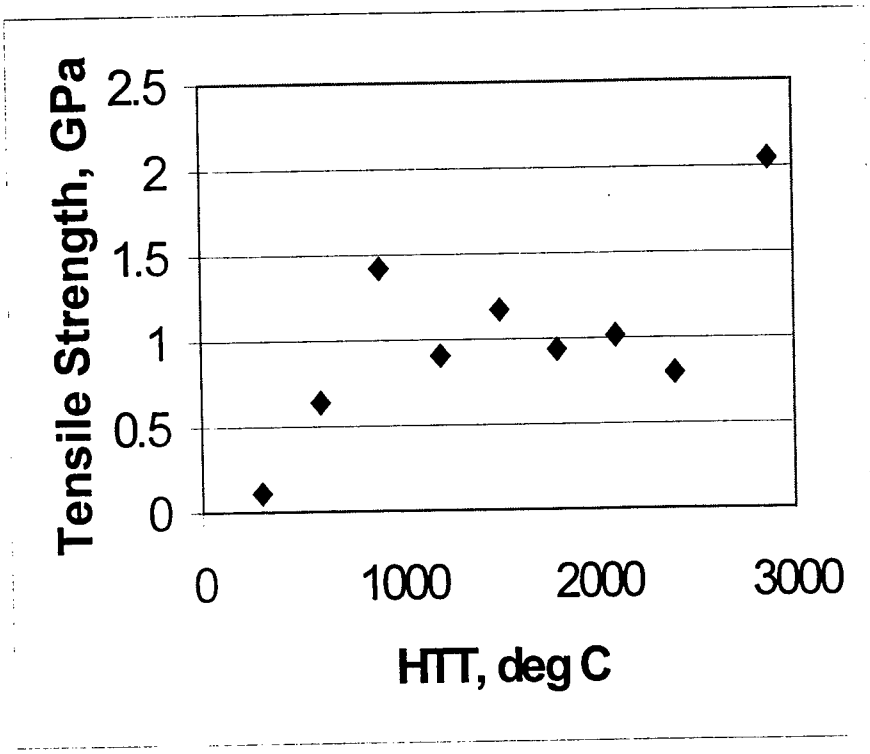

Figure 1. Tensile strength of AR mesophase fibers heat treated to various temperatures.

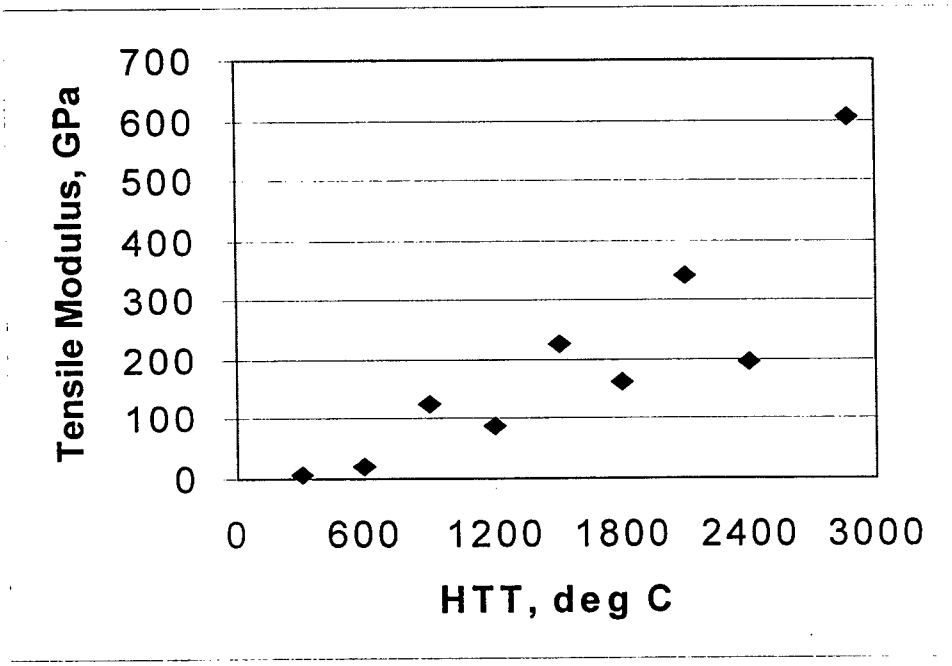

Figure 2. Tensile modulus of AR mesophase fibers heat treated to various temperatures.

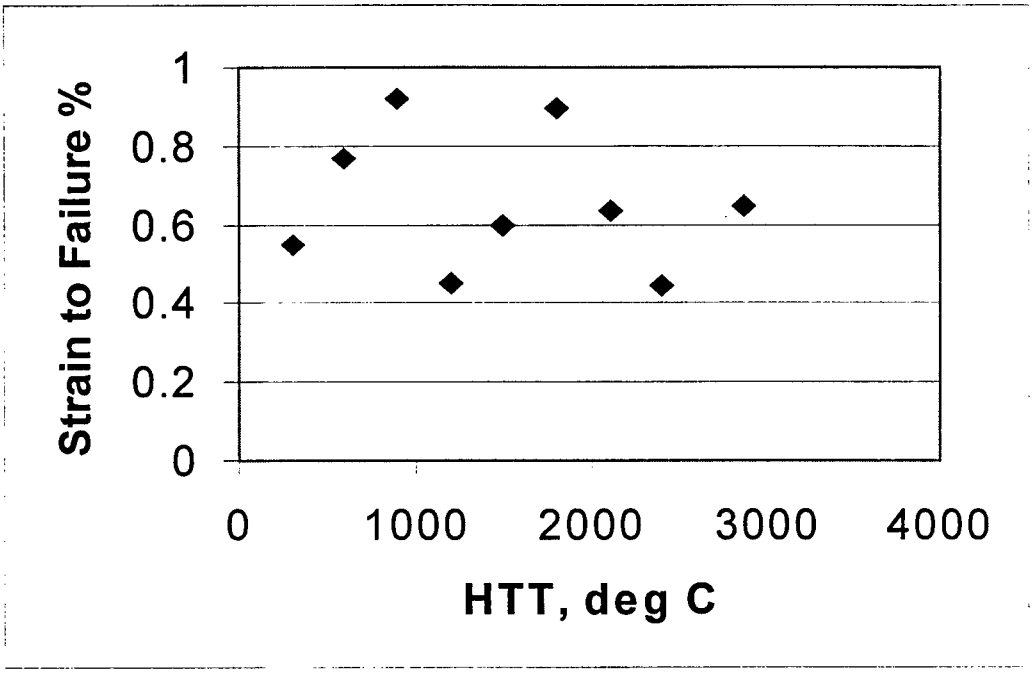

Figure 3. Strain-to-failure of AR fibers heat treated to various temperatures.

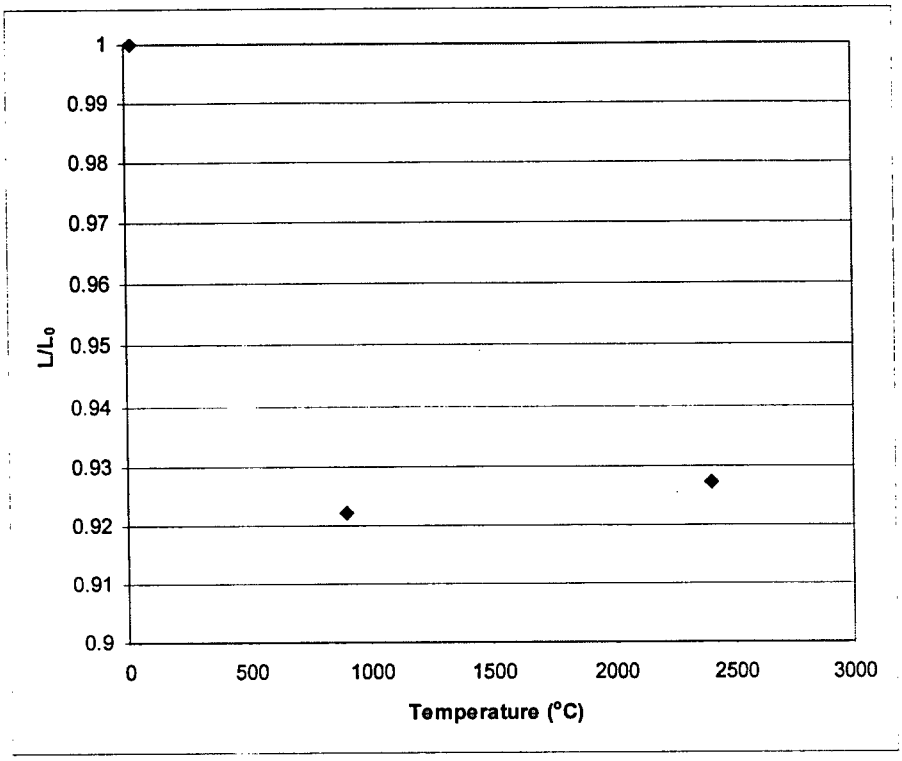

Figure 4. Length ratio of AR fibers as a function of the heat treatment temperature.

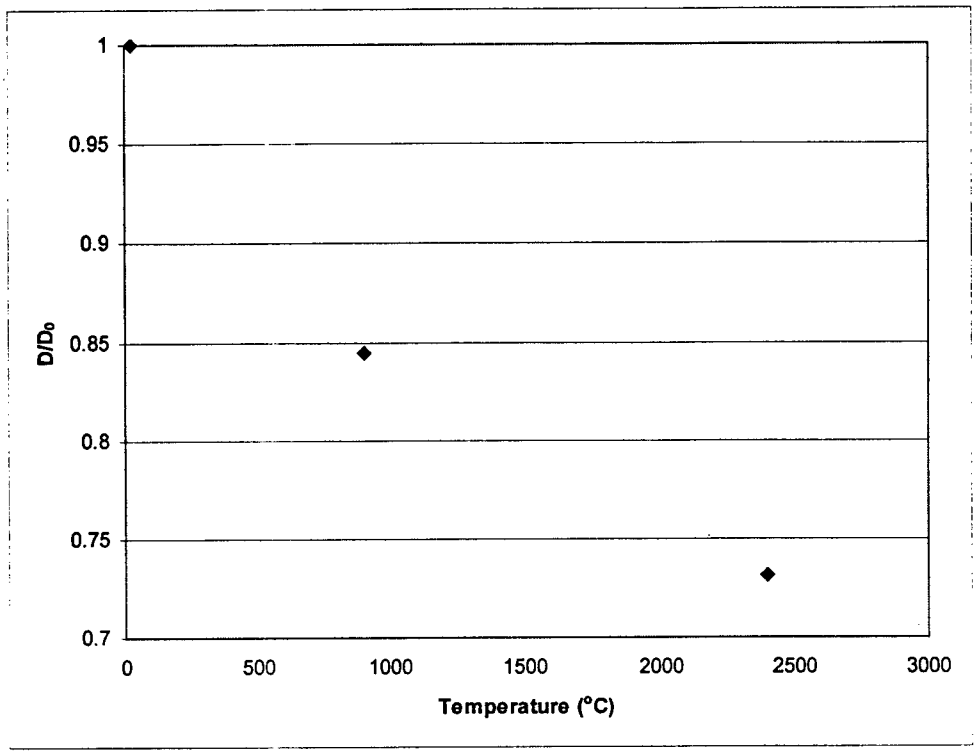

Figure 5. Fiber diameter ratio of AR fibersas a function of heat treatment temperatures.

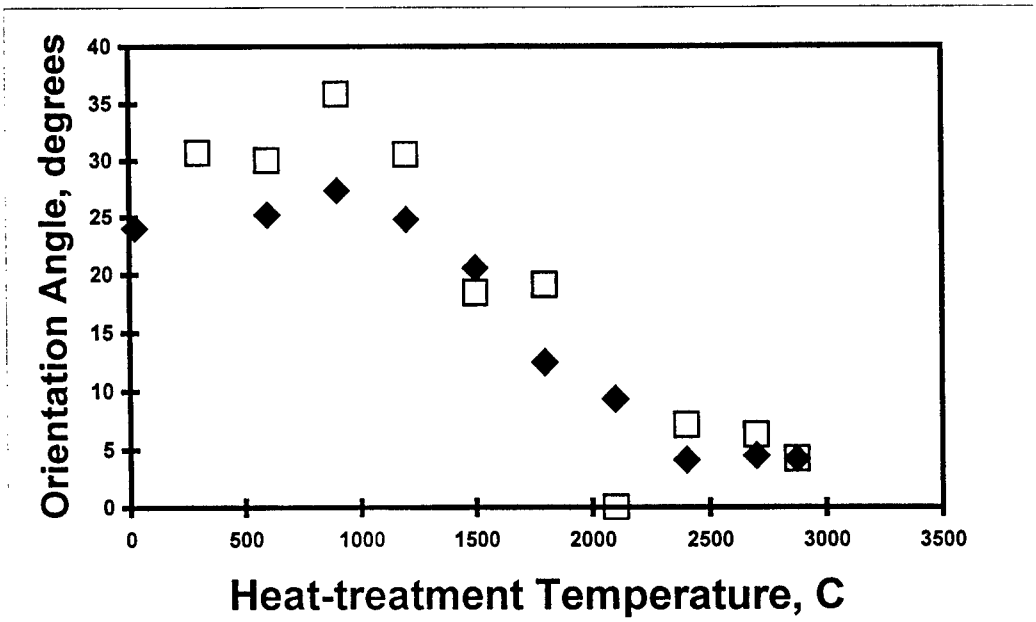

Figure 6. Orientation angle of AR mesophase pitch fibers heat treated to various temperatures.

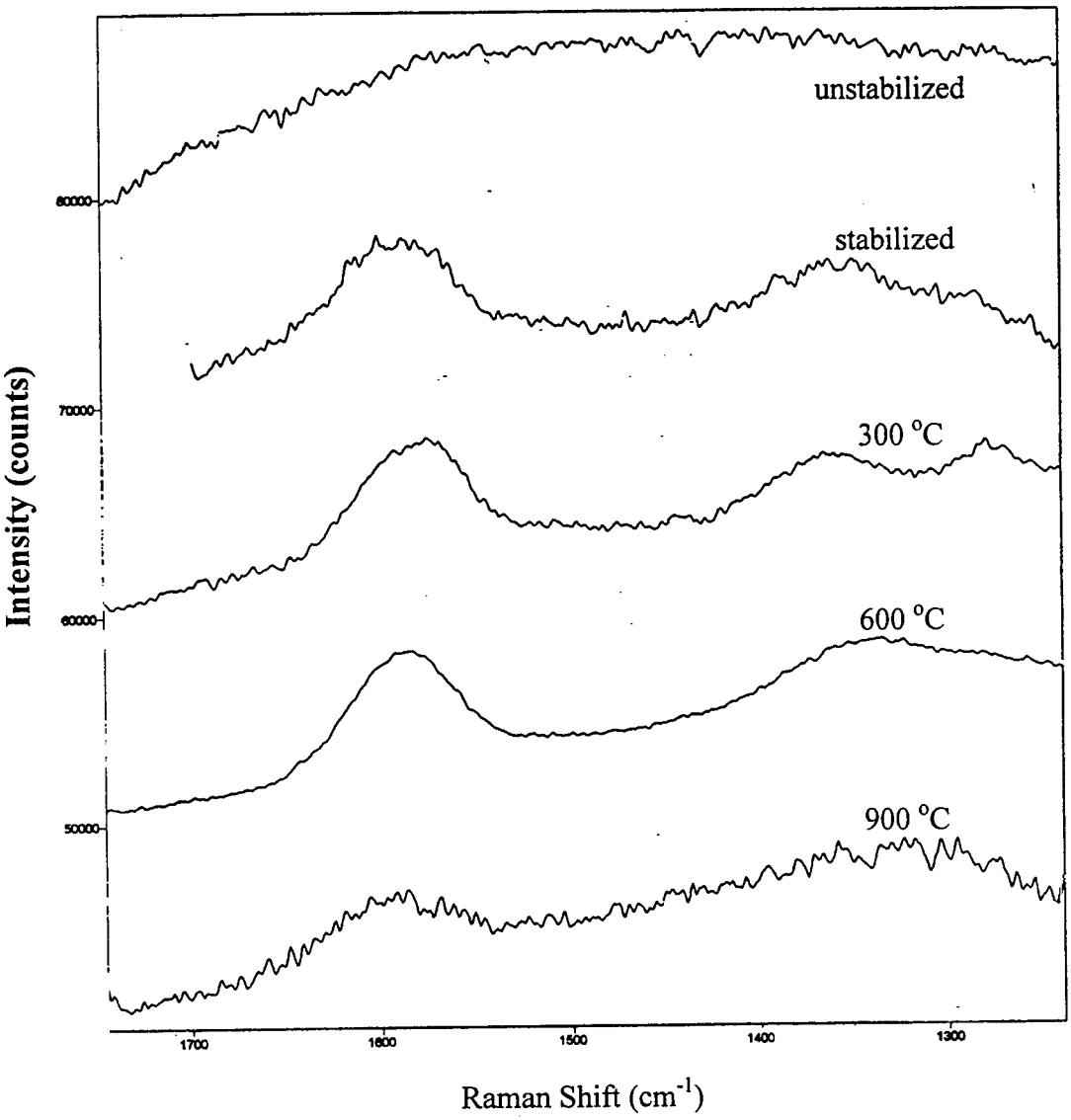

Figure 7. Micro-Raman spectra of AR pitch fibers heat-treated at different temperatures.

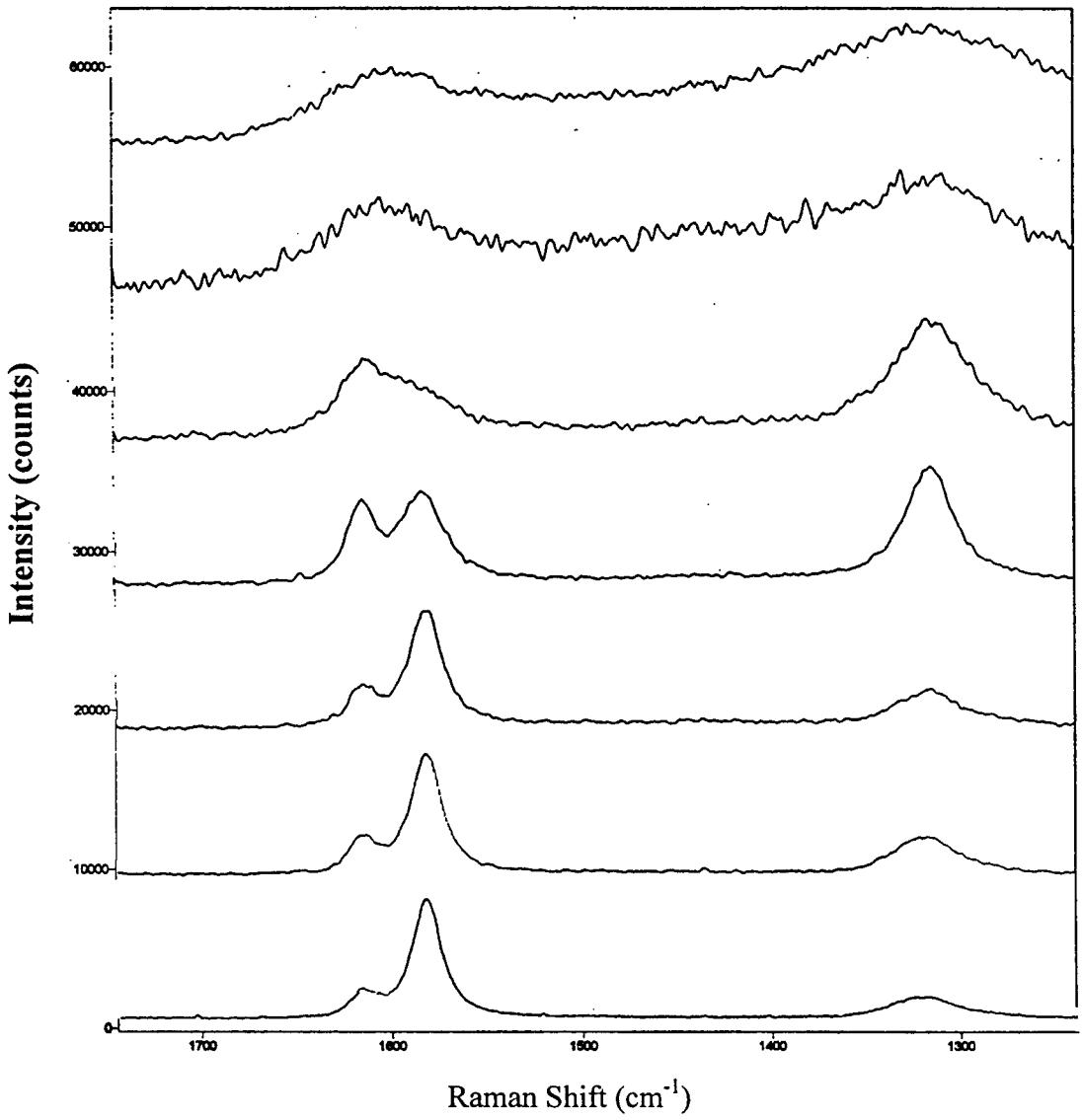

Figure 8. Micro-Raman spectra of AR pitch fibers heat-treated at different temperatures.

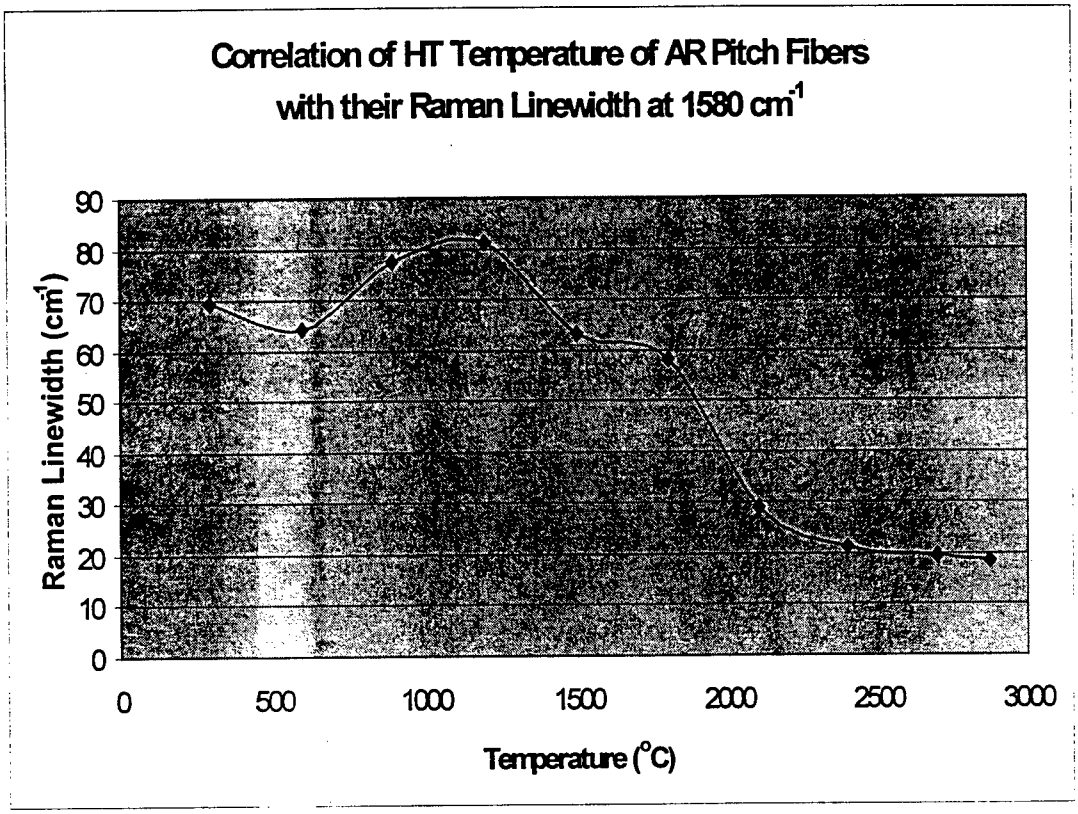

Figure 9. Peak width of G band from micro-Raman spectra of AR mesophase pitch fibers heat treated to various temperatures.

Table 1. Length and diameter measurements for AR mesophase pitch fibers heat treated to 900 °C and 2400 °C

Sample #	L0 (mm) (stabilized)	L900 (mm) (900 °C)	L2400 (mm) (2400 °C)	D0A (micron) (stabilized)	D0B (micron) (stabilized)	D900A (micron) (900 °C)	D900B (micron) (900 °C)	D2400A (micron) (2400 °C)	D2400B (micron) (2400 °C)
1	13.202	12.161	12.338	81	93	70	70	62	63
3	11.273	10.424	10.538	92	119	78	93	60	76
4	12.126	10.995	10.527	95	98	76	79	63	67
5	12.749	11.512	11.177	93	94	76	76	59	60
6	15.15	14.061	14.256	107	108	92	92	80	83
8	15.207	14.037	14.048	99	100	85	89	78	80
10	12.442	11.222	11.017	84	87	68	71	56	58
11	11.518	10.13	10.679	85	89	70	73	63	64
13	11.811	10.956	11.035	92	95	79	80	69	78
15	12.663	11.825	11.963	101	107	87	98	80	87
18	12.438	11.541	11.599	97	118	82	103	73	89
19	13.843	12.922	13.073	85	86	73	73	64	65
23	11.412	10.622	10.73	84	94	74	83	63	65
24	10.774	10.059	10.196	92	93	80	80	64	71
25	10.981	10.263	10.363	98	108	82	90	70	83
26	14.438	13.441	13.577	91	115	85	95	70	89
27	12.598	11.75	11.912	107	121	94	97	85	86

Table 2. Summary of length and diameter ratios for AR mesophase pitch fibers heat treated to 900 °C and 2400 °C

Sample #	L900/L0	L2400/L0	D900/D0	D2400/D0
1	0.921	0.935	0.808	0.721
3	0.925	0.935	0.815	0.645
4	0.907	0.868	0.803	0.673
5	0.903	0.877	0.813	0.636
6	0.928	0.941	0.856	0.758
8	0.923	0.924	0.874	0.794
10	0.902	0.885	0.813	0.667
11	0.879	0.927	0.822	0.730
13	0.928	0.934	0.850	0.786
15	0.934	0.945	0.889	0.803
18	0.928	0.933	0.859	0.753
19	0.933	0.944	0.854	0.754
23	0.931	0.940	0.882	0.721
24	0.934	0.946	0.865	0.730
25	0.935	0.944	0.835	0.741
26	0.931	0.940	0.880	0.772
27	0.933	0.946	0.840	0.753

BENCHMARKING AERODYNAMIC PANEL METHODS FOR FLIGHT LOADS IN MULTIDISCIPLINARY OPTIMIZATION

Ramana M. Pidaparti
Professor
Department of Mechanical Engineering

Purdue School of Engineering and Technology, IUPUI
723 W. Michigan Street
Indianapolis, IN 46202-5132

Final Report for:
Summer Research Extension Program (SREP: 99-0822)
Wright Research Site

Sponsored by:
Air Force Office of Scientific Research
Bolling Air Force Base, DC

February 2000

BENCHMARKING AERODYNAMIC PANEL METHODS FOR FLIGHT LOADS IN MULTIDISCIPLINARY OPTIMIZATION

Ramana M. Pidaparti
Professor
Department of Mechanical Engineering
Purdue School of Engineering & Technology
IUPUI, Indianapolis, IN 46202

Abstract

In the design of flight vehicles, flight load estimations need to be carried out in various design phases. The aerodynamic data (loads and pressure coefficients) generally comes from different theories and sources. Due to the numerically intensive nature of design optimization, accurate and efficient method of flight loads estimation is needed. The objective of this report is to compare the results of pressure distributions produced by two fluid dynamics codes for different flight regimes and mach numbers. Examples studied include a fighter wing, and wing-body configuration to illustrate how different components of flight vehicles affect the load distributions. The results obtained demonstrate the capabilities and limitations of the two fluid dynamics codes used in this study. The comparisons may serve as a benchmark for predicting the pressure distributions for use in aero-structure interaction studies in multidisciplinary design optimization.

BENCHMARKING AERODYNAMIC PANEL METHODS FOR FLIGHT LOADS IN MULTIDISCIPLINARY OPTIMIZATION

Ramana M. Pidaparti

Introduction

Design of modern flight vehicles that meets certain performance criteria and constraints requires integration of structures, aerodynamics, control and propulsion disciplines (multidisciplinary design optimization, MDO). Aeroelastic instabilities such as divergence, control reversal and flutter are some of the critical parameters that need to be considered in the preliminary and conceptual design phases. A large number of parameters including flight conditions (maneuvers) and type of aircraft affect the load distributions. Due to the numerically intensive nature of design optimization, accurate and reliable calculations of flight loads are needed for use in aeroelastic design applications. Hence, there is a need to investigate the capabilities and limitations of various aerodynamic panel methods for flight loads calculations in multidisciplinary design.

The aerodynamic data (loads and pressure coefficients) generally comes from different theories and sources. These include flat panel linear theory, 3D linear and non-linear theories and wind tunnel tests. Three-dimensional methods provide upper and lower surface pressure distributions as compared to flat panel methods, which give only the difference in the lower and upper surface pressure distributions. Also, various flight regimes (subsonic, transonic, supersonic and hypersonic) may have different effects (wakes, vortices, flow separation, shocks, viscosity, etc.), which greatly affect the flight loads.

Several aeroelastic optimization codes are being used for preliminary design of aircraft and spacecraft structures subjected to multidisciplinary constraints. Some examples are the Automated Structural Optimization System (ASTROS) [1], and MSC-NASTRAN [2]. Most of the design optimization software use lower order aerodynamic theories which can accurately predict the aeroelastic instabilities under a limited range of flow and flight conditions. These include low angles

of attack where boundary layer and separation effects are minimal. To study realistic load distributions in non-linear conditions, advanced aerodynamic methods such as Computational Fluid Dynamics (CFD) can be used. However, CFD based analyses are too expensive computationally for use in preliminary design studies of flight vehicles. A study benchmarking the capabilities and limitations of aerodynamic panel methods is therefore needed to evaluate the impact on aero-structure interactions in MDO.

The objective of this report is to compare the results of pressure distributions produced by two fluid dynamics codes for different flight regimes and mach numbers. Examples studied will include a fighter wing, and wing-body configuration to illustrate how different components of flight vehicles affect the load distributions. The results obtained demonstrate the capabilities and limitations of the two fluid dynamics codes used in this study. The comparisons may serve as a benchmark for predicting the pressure distributions for use in aero-structure interaction studies in multidisciplinary design optimization.

Software Tools

Several aerodynamic codes are available for investigating the flight loads. Three aerodynamic codes USSAERO/VSAERO/USM3D which are available are used for benchmarking the flight loads for aeroelastic design optimization. Both the USSAERO and VSAERO are an integral part of the ASTROS software which in turn can be used for the design optimization studies in the future for a variety of flight vehicles as well as other mechanical components. The USM3D code was developed by NASA Langley in the early1990's. A brief summary of the salient features of the aerodynamic codes used in this study for the flight loads estimation is described below.

USSAERO: This is a flat plate vortex lattice method aerodynamic code used for subsonic and supersonic flight conditions and is part of the ASTROS software. The code is capable of modeling multiple lifting surfaces, fuselages, and pods. The flight conditions include symmetric and antisymmetric maneuvers as well as steady subsonic and supersonic conditions. The flat-plate vortex lattice method uses a constant source distribution on body panels, and a combination of vortex and source distributions on wing and tail panels. For each wing panel, a linear variation of strength in the

streamwise direction and constant strength in chordwise direction is allowed. The strengths of these singularities are determined by satisfying Neumann boundary conditions. The code also accounts for thickness and camber effects in addition to compressibility at high subsonic flow conditions. More details about the method can be found in Ref. [3].

VSAERO: This aerodynamic code is based on constant source strength and doublet panels in 3D, and includes non-linear effects such as boundary layer thickness, wake roll-up and separated wakes. Subsonic flow conditions are treated. The code capabilities include both external and internal flows, skin-friction and boundary layer displacements and quasi-steady rotations. To account for viscous effects, an integral boundary layer calculation via viscous/potential flow coupling is provided in the VSAERO code. Specifically, VSAERO solves the Neumann problem of potential flow. Compressible flow can be analyzed by Prandtl-Glauert linearization. More details about the software capabilities can be found in Ref. [4]. Currently, VSAERO is being integrated in the design optimization code "ASTROS".

SPIN(g) is the geometry pre-processor to use with VSAERO. SPIN(g) can be used to create the geometry and can also be used to modify the geometry created previously by paneling. The wakes for the geometry are created through the use of SPIN(w) pre-processor. Only wakes and wake grid planes can be defined by SPIN(w). However, SPIN(w) can also be used to view the paneling. Both SPIN(g) and SPIN(w) can write input files for VSAERO. OMNI3D is the post-processor to view the VSAERO results. VSAERO allows a 3D surface to be defined and outputs Cp values on both the upper and lower surfaces of a lifting surface. All the standard plots of pressure distributions can be viewed using OMNI3D post-processor.

USM3D: This aerodynamic code is based on cell-centered, finite-volume upwind flow solver for solving the Euler equations on tetrahedral grids [5, 6]. Spatial discretization is accomplished based on an analytical formulation and by a novel cell reconstruction process. Across each cell face, the inviscid flux quantities are computed using the Roe flux-difference splitting approach or the Van Leer flux-vector splitting technique [7]. Solutions are advanced in time by a 3-stage Runga-Kutta explicit time-stepping scheme with implicit residual smoothing. This software is well developed and

can be applied to a broad spectrum of engineering needs with capabilities such as rapid grid generation, and inviscid flow analysis, inverse design, interactive boundary layers, and propulsion effects. Results are documented for complex aerodynamic problems including wing/pylon intersection of a transport wing with under-wing nacelles, etc. [7].

GRIDTOOL and VGRID are used to create the grid. GRIDTOOL is a graphical user interface (GUI) utility to serve as a window into the unstructured-grid generator, VGRID. The user provides a surface definition in IGES or GRIDGEN or simple networks, which are converted into NRUBS surface for manipulation within GRIDTOOL. This GUI provides easy access to many functions, which are useful in setting up an input file for VGRID. Unstructured triangular/tetrahedral grids are generated by forming cells starting from the domain boundaries marching towards the interior of the computational domain using VGRID, which is an interactive program [8]. For a 3D configuration, the geometry is divided into subdomains on which 3-or 4- sided parametric surface patches are defined. The VGRID code outputs a coordinate file of the vertex locations, cell-to-node connectivity file, and a triangle-to-patch correlation file. Boundary conditions are applied at the time of USM3D execution through a B.C. map file output by GRIDTOOL.

Post processing of the results is accomplished through the use of VPLOT3D interactive menu driven program [8]. VPLOT3D has the ability to display grids and flow quantities on either boundary surfaces or user defined arbitrary planes in the field. Flow quantities are displayed using line or filled contours, velocity vectors and particles traces.

Examples Studied

Two examples were run using the software described in the previous section to demonstrate the capabilities and limitations. As a first example, a generic fighter type of aircraft wing is considered. As a second example, wing-body configuration is considered. This example is carefully selected to illustrate the body-wing interactions and how they affect the load distributions and pressure coefficients under different flight conditions. The results of pressure distributions obtained are compared between the two codes VSAERO and USM3D.

Example 1: Fighter Aircraft Wing

A generic fighter type of aircraft wing with flap was considered as the first example. A NACA 0004 airfoil is used for the wing. The airflow around the F-16 wing geometry has been analyzed using the unstructured Euler solver USM3D and the panel code VSAERO. The unstructured grid that the USM3D code works on consists of 1,269,192 cells and 221,457 nodes. Figures 1 and 2 show the unstructured surface grid on the upper and lower wing surfaces, respectively. The VSAERO code, on the other hand, works on a structured grid. The structured surface grids on the upper and lower wing surfaces are shown in Figures 3 and 4, respectively.

The unstructured computational grid was partitioned into 32 blocks for parallel computing with USM3D. The parallel computations were done on a Linux cluster located at the NASA Glenn Research Center in Cleveland, Ohio. The VASERO code is a serial program, hence the computations obtained with VSAERO were done using a single processor at the Wright Paterson Air Force Research Lab in Dayton, Ohio.

For this problem, three test cases were considered. In the first test case, the free stream Mach number and the angle of attack are 0.8 and 1.0 degree, respectively. In the second test case, they are 0.8 and 5.0 degrees, respectively. And in the third test case, the Mach number is 0.4 and the angle of attack is 5.0 degrees.

Test Case 1: Free stream Mach number = 0.8, angle of attack = 1 degree

Pressure coefficient contours on the upper wing surface obtained by USM3D and VSAERO softwares are given in Figures 5 and 6, respectively. The pressure coefficient contours on the lower wing surface are similar to those given in Figures 5 and 6.

The surface pressure coefficient distributions at three wing span stations are plotted in Figures 7 through 12. In general, USM3D and VSAERO results are in good agreement but there are

some differences in the pressure coefficient distributions taken at the span station $\eta = 0.94$. This station is close to the wing tip.

Test Case 2: Free stream Mach number = 0.8, angle of attack = 5 degrees

The surface pressure coefficient distributions at three wing span stations are plotted in Figures 13 through 18. Again, USM3D and VSAERO results are in good agreement but there are some differences in the pressure coefficient distributions taken at the wing span station $\eta = 0.94$ and on the upper wing surface at the wing span station $\eta = 0.05$. These differences need to be examined carefully in future studies.

Test Case 3: Free stream Mach number = 0.4, angle of attack = 5 degrees

The surface pressure coefficient distributions at three wing span stations are plotted in Figures 19 through 24. USM3D and VSAERO results are in good agreement but this time the only significant difference between the pressure coefficient distributions occurs on the lower wing surface at the span station $\eta = 0.94$.

Example 2: Wing-body Configuration

The airflow around a wing-body geometry has been analyzed using the unstructured Euler solver USM3D and the panel code VSAERO. The unstructured grid that the USM3D code works on consists of 1,470,733 cells and 259,207 nodes. Figures 25 and 26 show the unstructured surface grid on the upper and wing-body geometry surfaces, respectively. The VSAERO code works on a structured grid. The structured surface grids on the upper and lower wing surfaces are shown in Figures 27 and 28, respectively.

The unstructured computational grid was partitioned into 32 blocks for parallel computing with USM3D. The parallel computations were done on a Linux cluster located at the NASA Glenn Research Center. The VASERO code is a serial program, hence the computations obtained with VSAERO were done using a single processor at the WPAFB, Dayton, Ohio.

Three test cases were considered in this example. In the first test case, the free stream Mach number and the angle of attack are 0.8 and 1.0 degree, respectively. In the second and third test cases, the Mach number and angle of attack are 0.8 and 5.0 deg., and, 0.4 and 5.0 deg., respectively.

Test Case 1: Freestream Mach number = 0.8, angle of attack = 1 degree

Pressure coefficient contours on the upper wing-body surface are given in Figures 29 and 30 while pressure coefficient contours on the lower wing-body surface are given in Figures 31 and 32. The surface pressure coefficient distributions at the centerline and three wing span stations are plotted in Figures 33 through 40. As can be seen from these comparisons, there are discrepancies observed between USM3D and VSAERO results on the upper wing-body surface. The results on the lower wing-body surface are in better agreement.

Test Case 2: Free stream Mach number = 0.8, angle of attack = 5 degrees

The surface pressure coefficient distributions at the centerline and three wing span stations are plotted in Figures 41 through 48. Again big discrepancies are observed between USM3D and VSAERO results on the upper wing-body surface. The results on the lower wing-body surface are in better agreement.

Test Case 3: Free stream Mach number = 0.4, angle of attack = 5 degrees

The surface pressure coefficient distributions at the centerline and three wing span stations are plotted in Figures 49 through 56. This time USM3D and VSAERO results are in good agreement on both the upper and lower wing-body surfaces.

Conclusions

The pressure distributions are obtained using two fluid dynamics codes VSAERO and USM3D. The examples studied include a fighter wing and a wing-body configuration. Different Mach numbers and angles of attack are considered. The results obtained are summarized below. For

the fighter wing considered, both VSAERO and USM3D gave similar pressure distributions for high Mach numbers (M=0.8) and high angles of attack (5 degrees). However, there are some differences in the magnitudes of pressure coefficients close to the wing tip and on the lower and upper wing surfaces. For the wing-body configuration considered, both VSAERO and USM3D gave results that are in good agreement for both the upper and lower wing-body surfaces for low Mach number (M=0.4) and high angle of attack (5 degrees). However, at high Mach numbers (M=0.8) and low and high angles of attack, both VSAERO and USM3D gave good results which are comparable for the lower wing-body surface. There are some discrepancies between VSAERO and USM3D for the pressure distributions on the upper wing-body surface. Overall, the limited results of pressure distributions obtained illustrate the capabilities of the VSAERO and USM3D codes investigated in this study. More cases should be studied in order to benchmark the codes for further capabilities and limitations. These results obtained from the proposed research can be also used in aircraft/space industries for design optimization studies.

Acknowledgements

The author thanks Ali Uzun (graduate student), Tyson Strutzenberg (undergraduate student at Purdue), Lt. Shad Reed, Capt. G. Anderson, Vicky Tischler, for help with VSAERO and USM3D softwares/runs. Thanks also to Dr. Hasan Akay (IUPUI), and Dr. Venkayya (AFRL) for their guidance and support. Finally, the support from the AFOSR is acknowledged.

References

1. Rodden W.P. and E.H. Johnson. (ed.) "MSC/NASTRAN Handbook for Aeroelastic Analysis, Version 68,", MacNeal-Schwendler Corp., 1994.

2. Johnson, E.H. and Venkayya, V.B., "Automated STRuctural Optimization System (ASTROS), Volume I, Theoretical Manual, Air Force Wright Patterson AFB, AFWAL-TR-88-3028, Wright Patterson Air Force Base, Ohio, 1988.

3. Woodward, F.A., "USSAERO Computer Program Development, Ver. B and C," NASA CR-3227, 1980.

4. Nathman, J.K., "VSAERO User's Manual, Version 6, Analytical Methods Inc., Redmond, Washington, November 1997.

5. Frink, N.T., "Upwind Scheme for Solving the Euler Equations on Unstructured Tetrahedral Meshes," AIAA Journal, Vol. 30, No. 1, pp 70-77, January 1992.

6. Frink, N. T., Parikh, P., and Pirzadeh, S., "A Fast Upwind Solver for the Euler Equations on Three-dimensional Unstructured Meshes," AIAA 91-0102, January 1991.

7. Frink, N. T., Pirzadeh, S. and Parikh, P., "An Unstructured-Grid Software System for Solving Complex Aerodynamic Problems," NASA CP-3291, May 9-11, 1995.

8. Parikh, P., Pirzadeh, S. and Lohner, R. "A Package for 3-D Unstructured Grid Generation, Finite Element Flow Solutions, and Flow-Field Visualization," NASA CR-182090, September 1990.

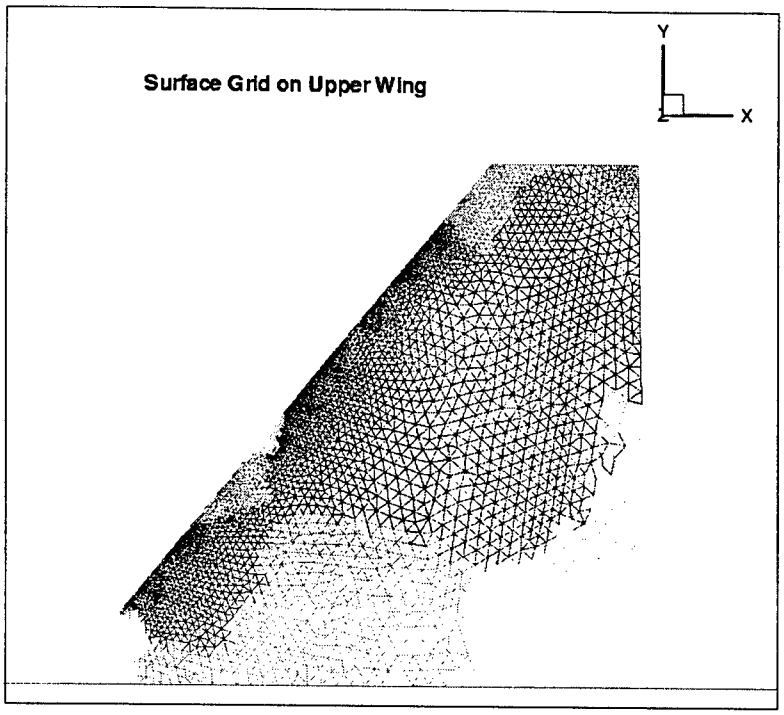

Figure 1. Surface triangulation on the upper wing surface

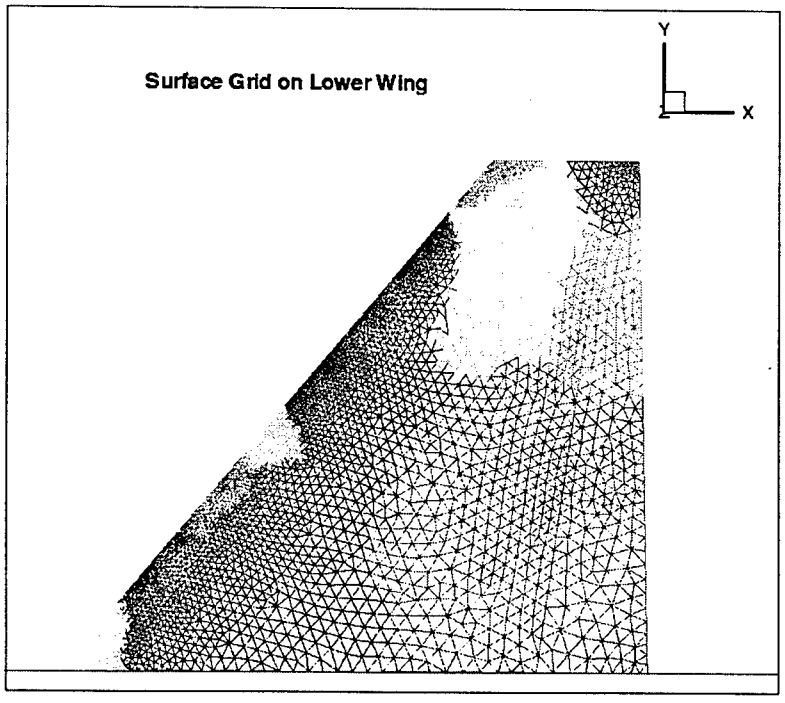

Figure 2. Surface triangulation on the lower wing surface

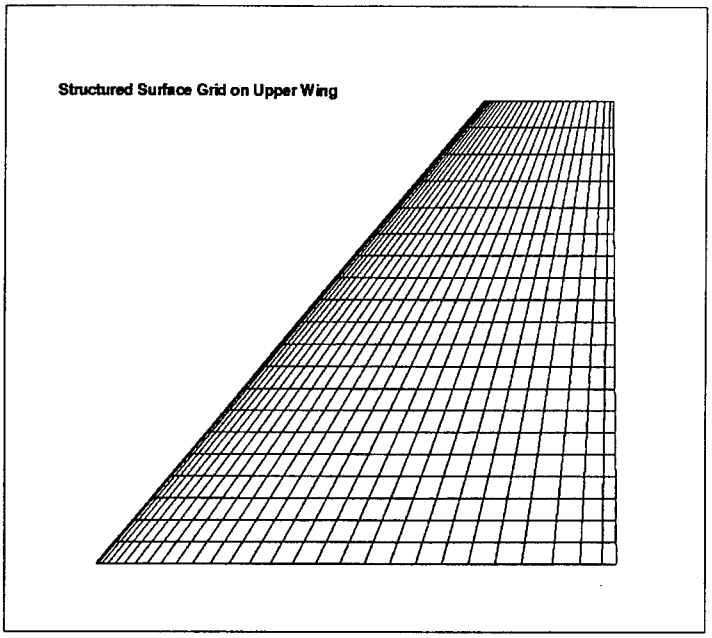

Figure 3. Structured VSAERO grid on the upper wing surface

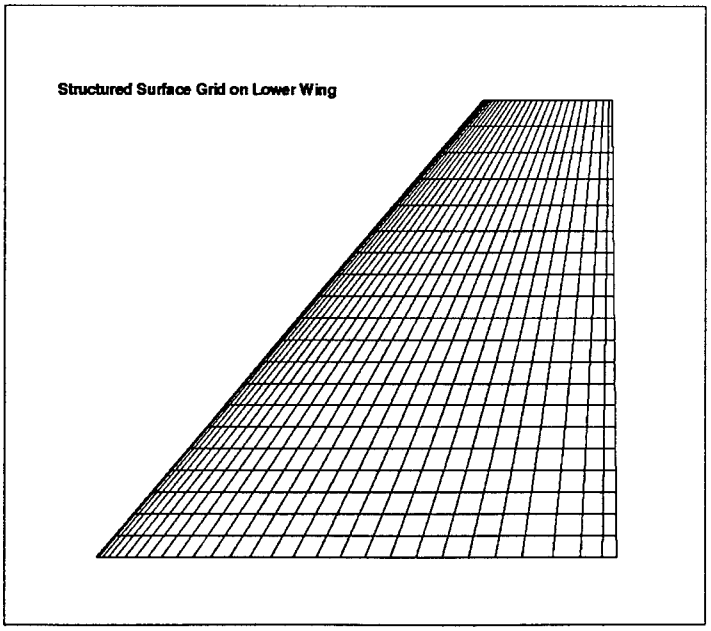

Figure 4. Structured VSAERO grid on the lower wing surface

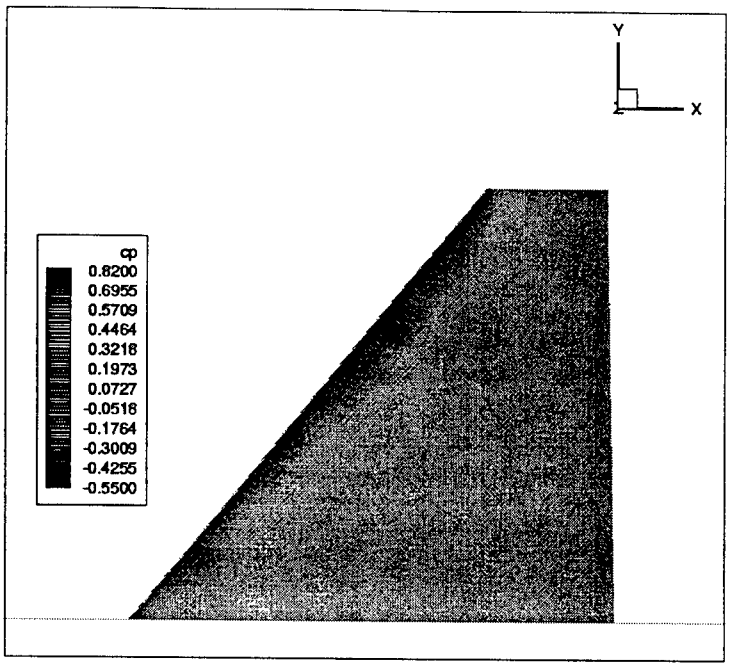

Figure 5. Cp contours on the upper wing - USM3D solution (M=0.8, AOA=1 deg.)

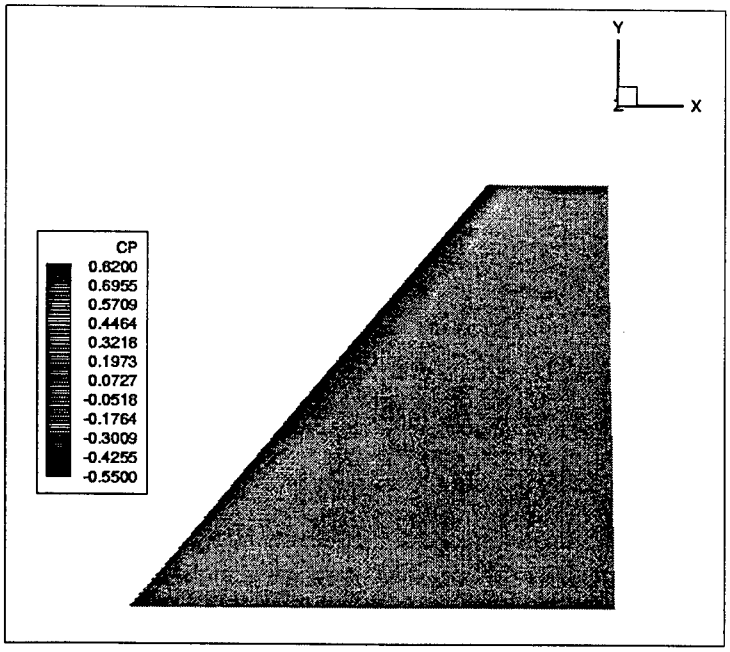

Figure 6. Cp contours on the upper wing - VSAERO solution (M=0.8, AOA=1 deg.)

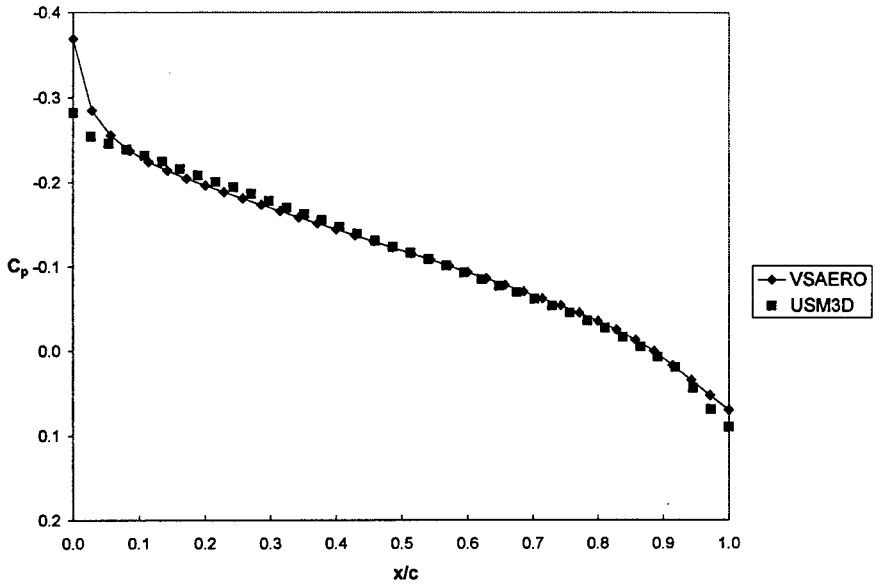

Figure 7. Pressure coefficient distribution on the upper wing surface at $\eta = 0.50$

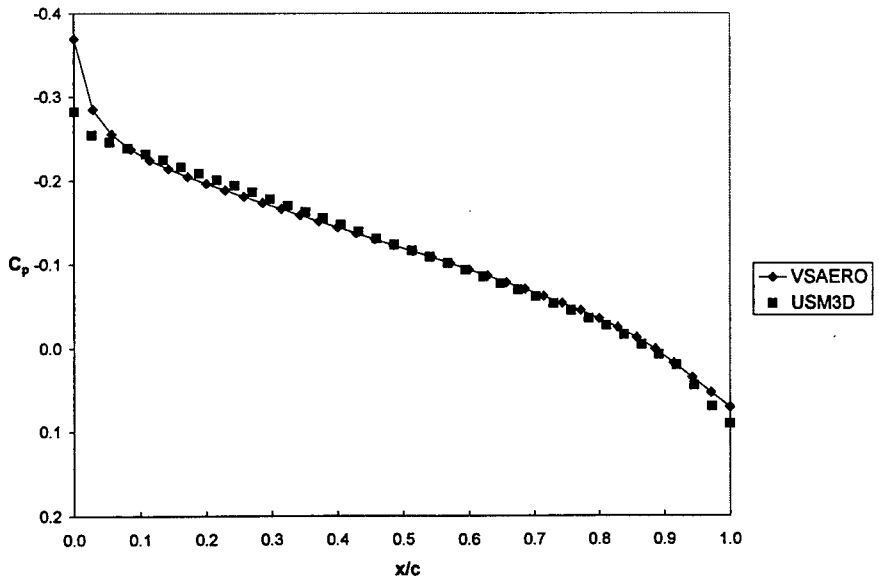

Figure 8. Pressure coefficient distribution on the lower wing surface at $\eta = 0.50$

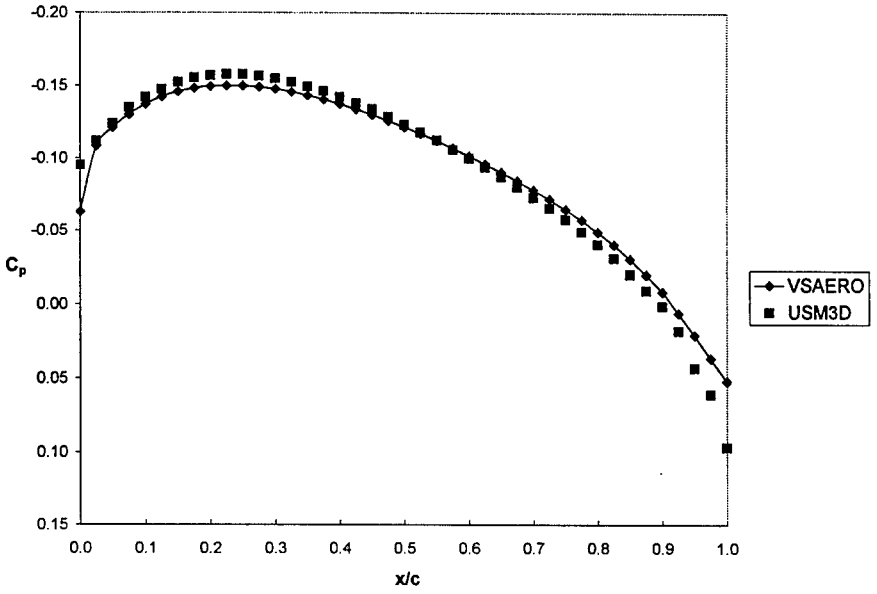

Figure 9. Pressure coefficient distribution on the upper wing surface at $\eta = 0.05$

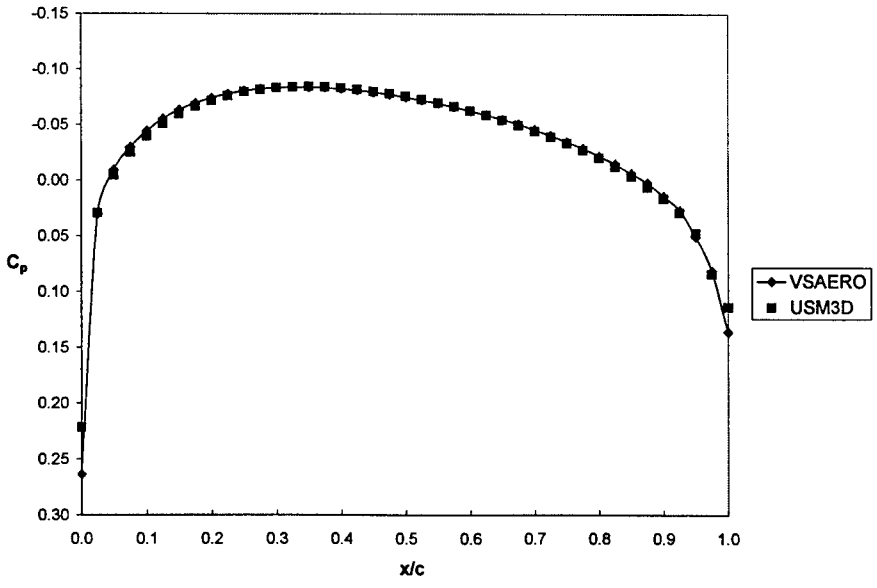

Figure 10. Pressure coefficient distribution on the lower wing surface at $\eta = 0.05$

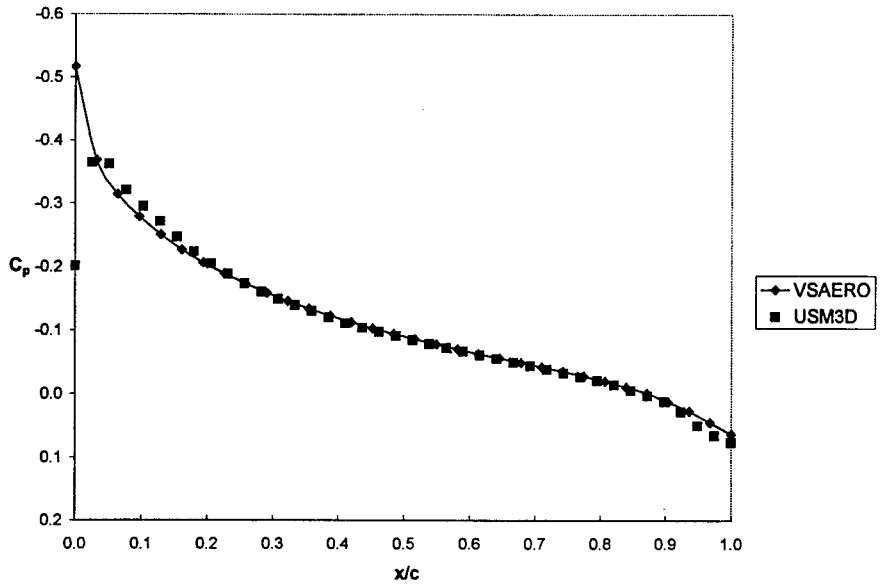

Figure 11. Pressure coefficient distribution on the upper wing surface at $\eta = 0.94$

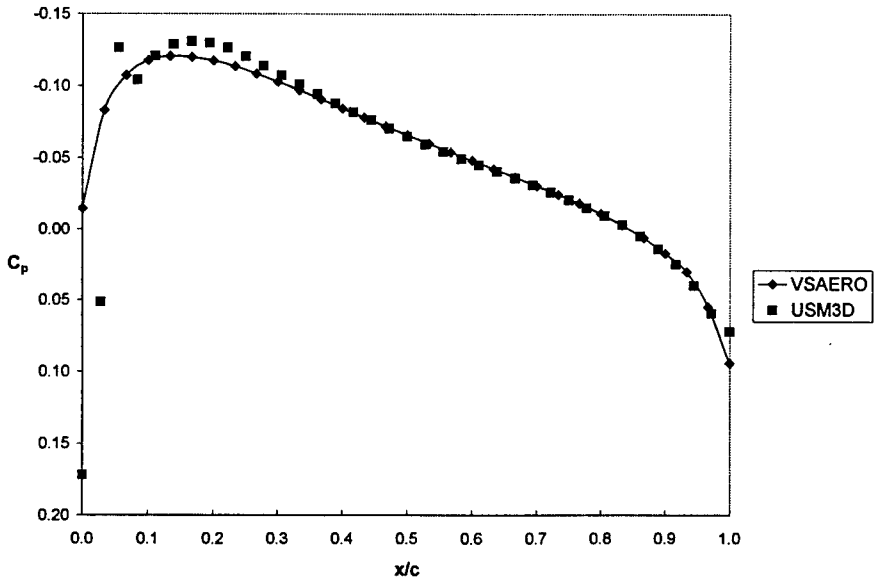

Figure 12. Pressure coefficient distribution on the lower wing surface at $\eta = 0.94$

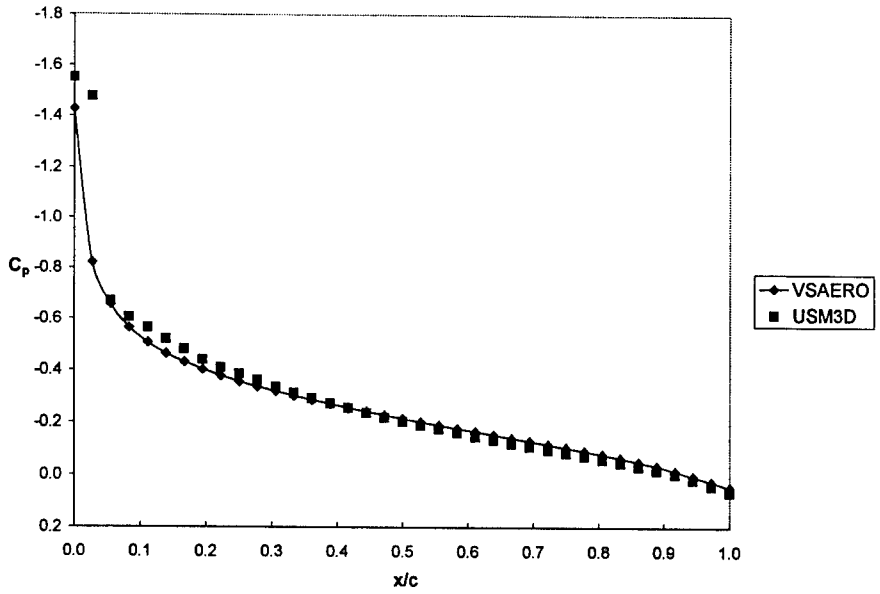

Figure 13. Pressure coefficient distribution on the upper wing surface at $\eta = 0.50$

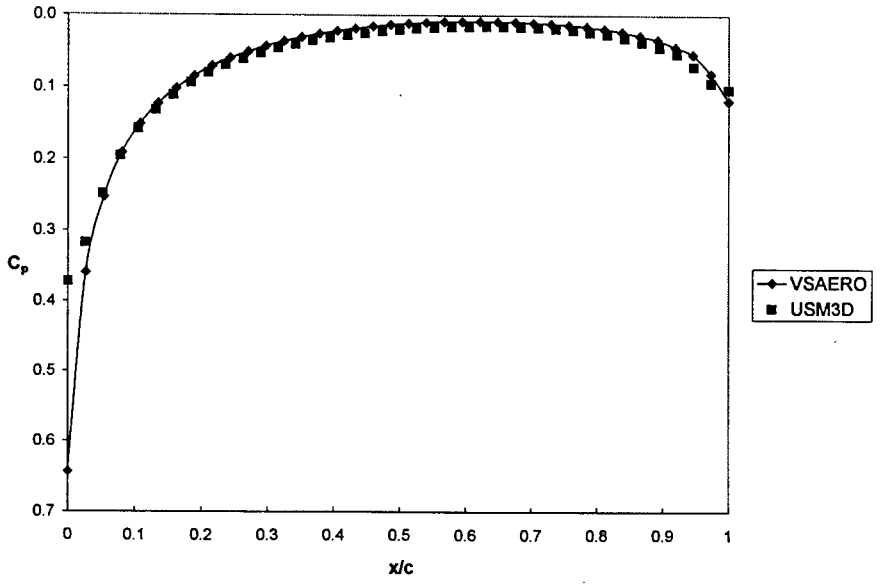

Figure 14. Pressure coefficient distribution on the lower wing surface at $\eta = 0.50$

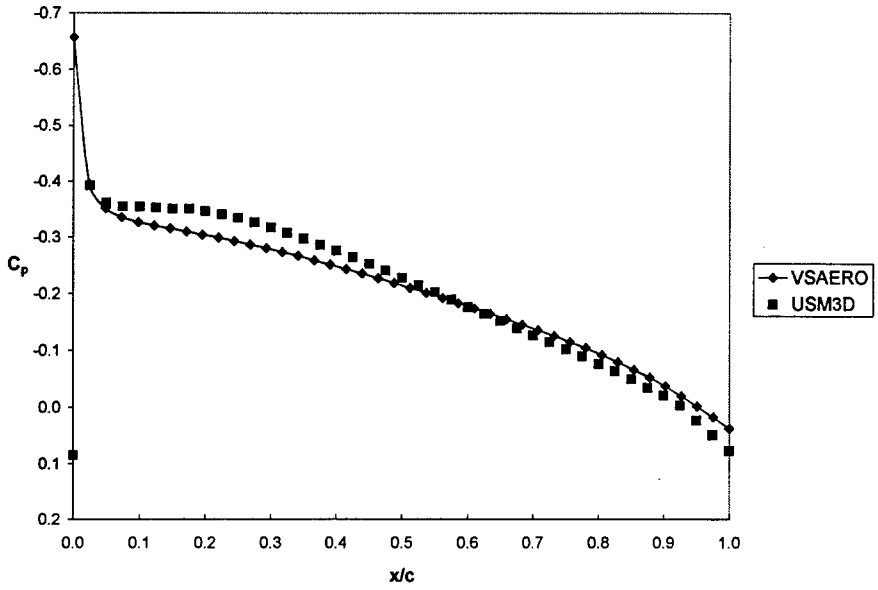

Figure 15. Pressure coefficient distribution on the upper wing surface at $\eta = 0.05$

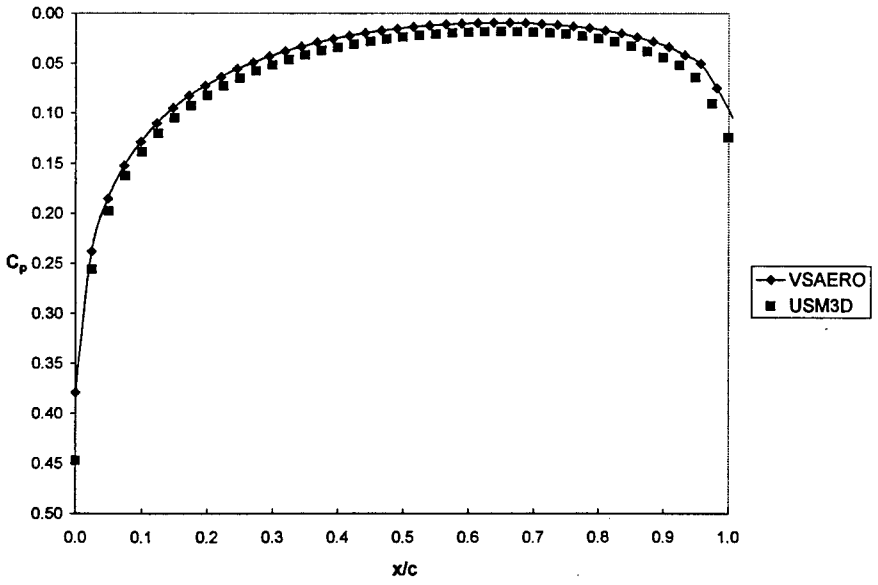

Figure 16. Pressure coefficient distribution on the lower wing surface at $\eta = 0.05$

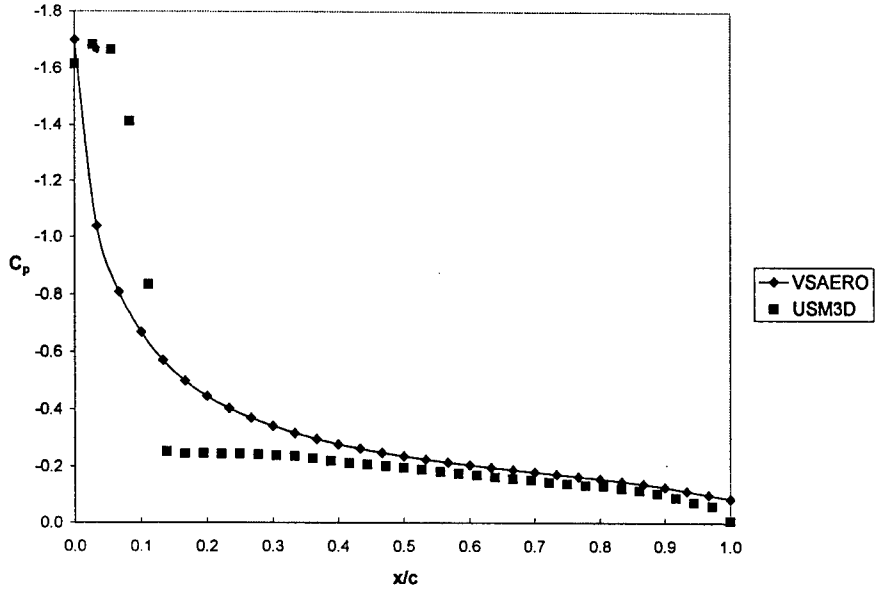

Figure 17. Pressure coefficient distribution on the upper wing surface at $\eta = 0.94$

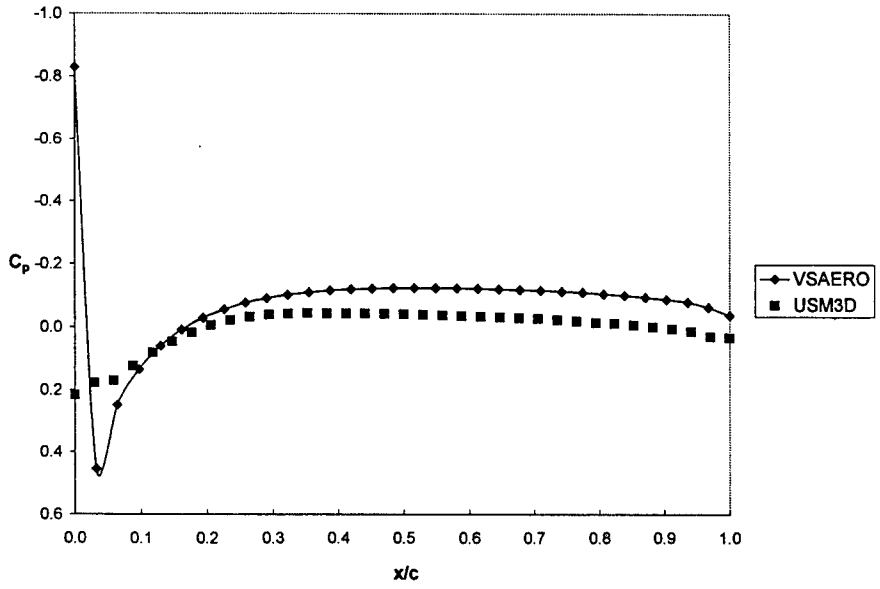

Figure 18. Pressure coefficient distribution on the lower wing surface at $\eta = 0.94$

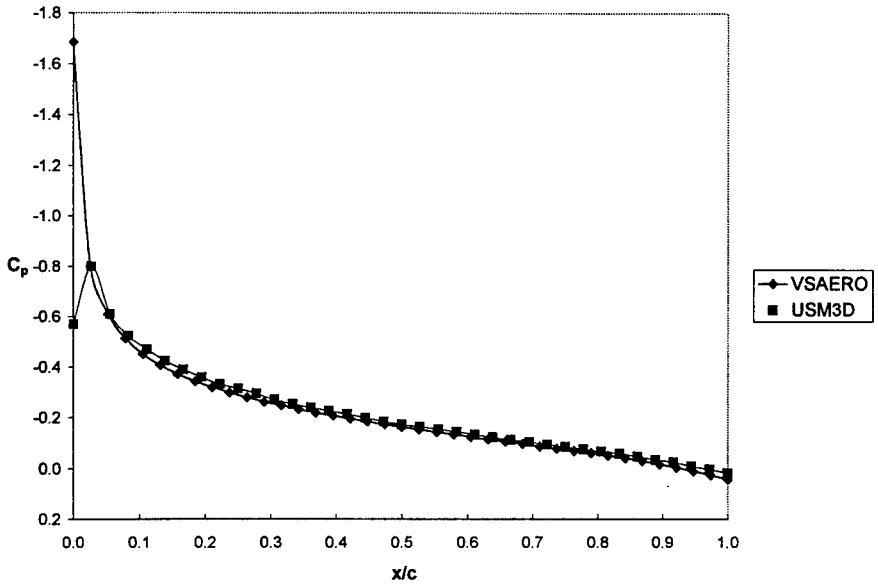

Figure 19. Pressure coefficient distribution on the upper wing surface at $\eta = 0.50$ (M=0.4, AOA=5 deg.)

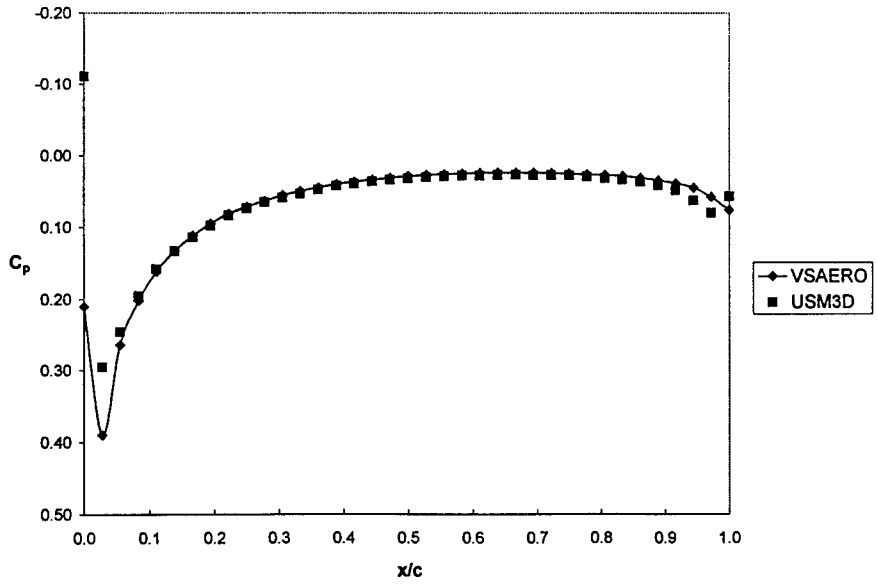

Figure 20. Pressure coefficient distribution on the lower wing surface at $\eta = 0.50$

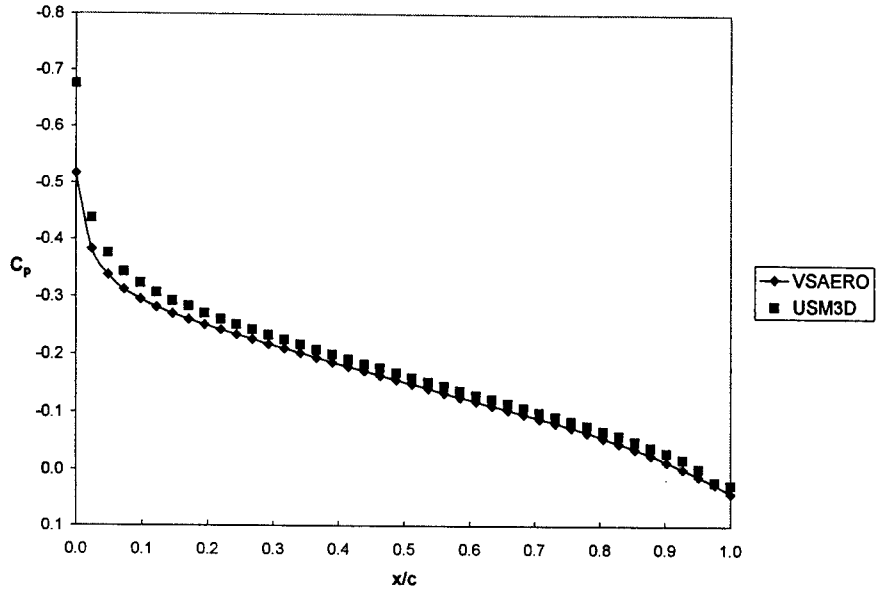

Figure 21. Pressure coefficient distribution on the upper wing surface at $\eta = 0.05$

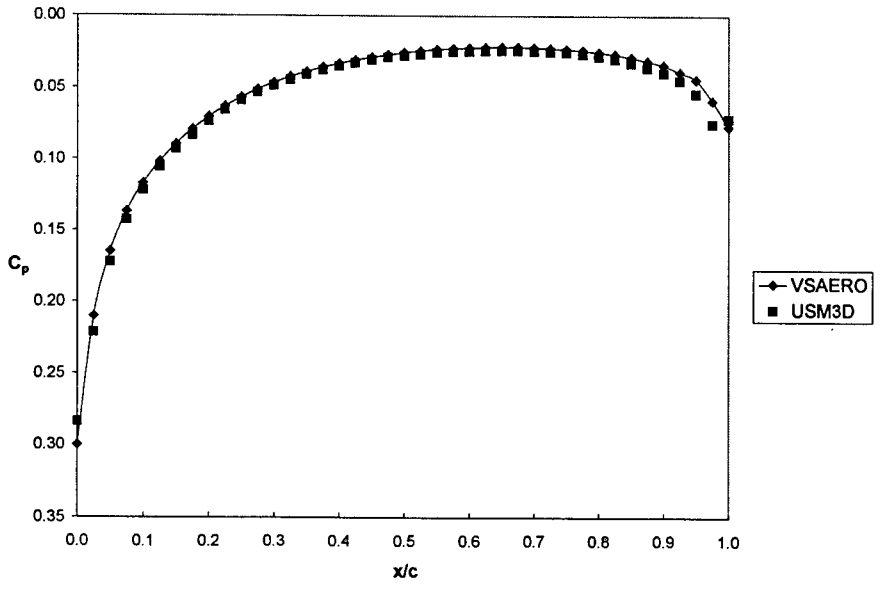

Figure 22. Pressure coefficient distribution on the lower wing surface at $\eta = 0.05$

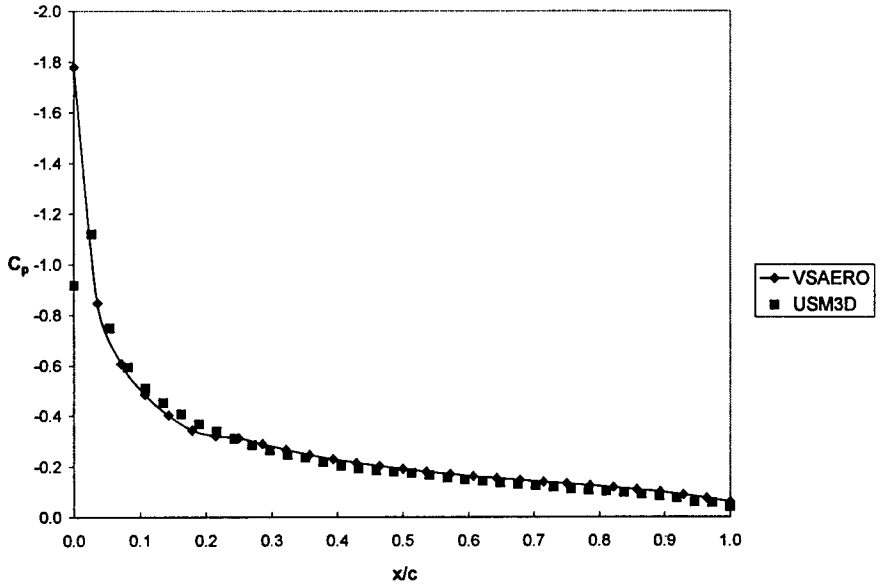

Figure 23. Pressure coefficient distribution on the upper wing surface at $\eta = 0.94$

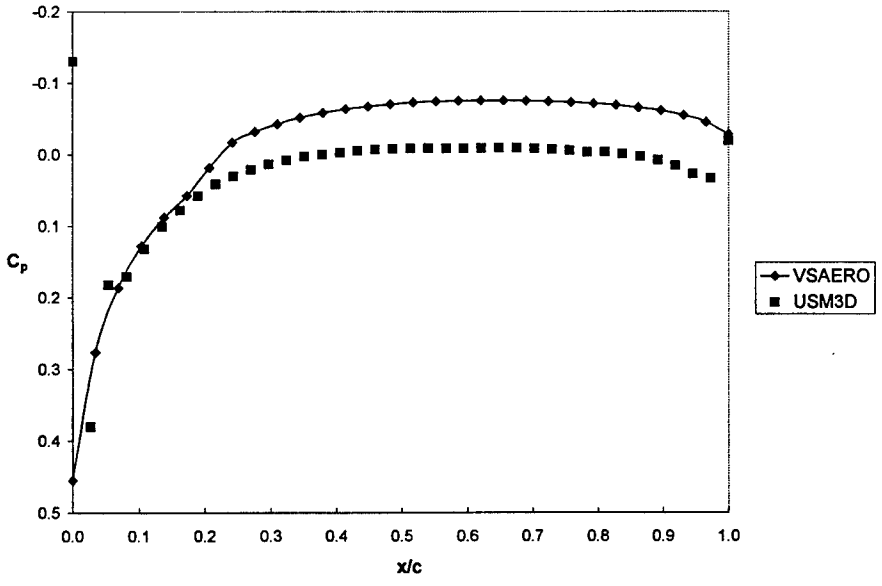

Figure 24. Pressure coefficient distribution on the lower wing surface at $\eta = 0.94$

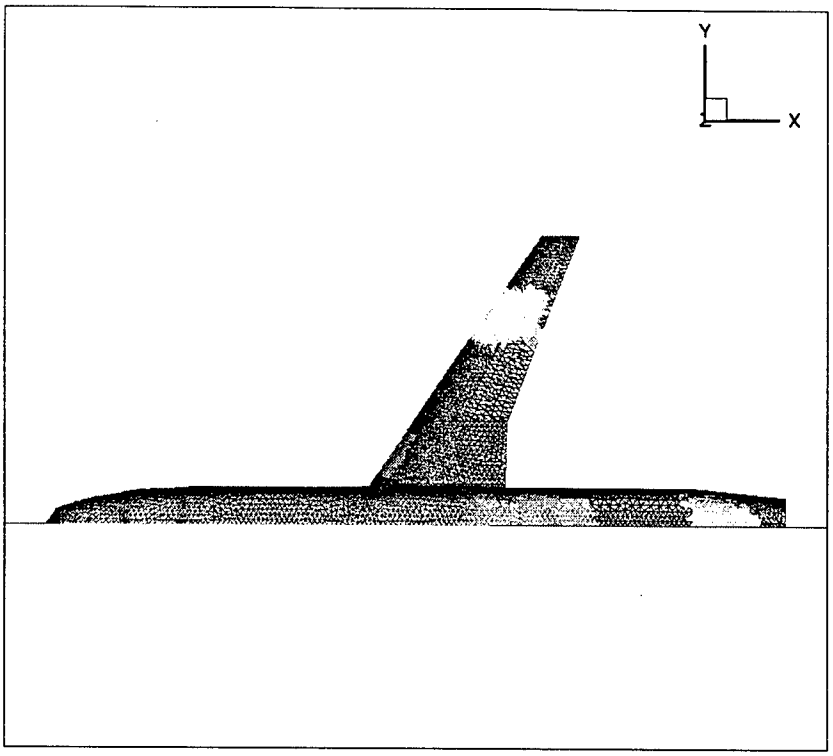

Figure 25. Surface triangulation on the upper wing-body geometry

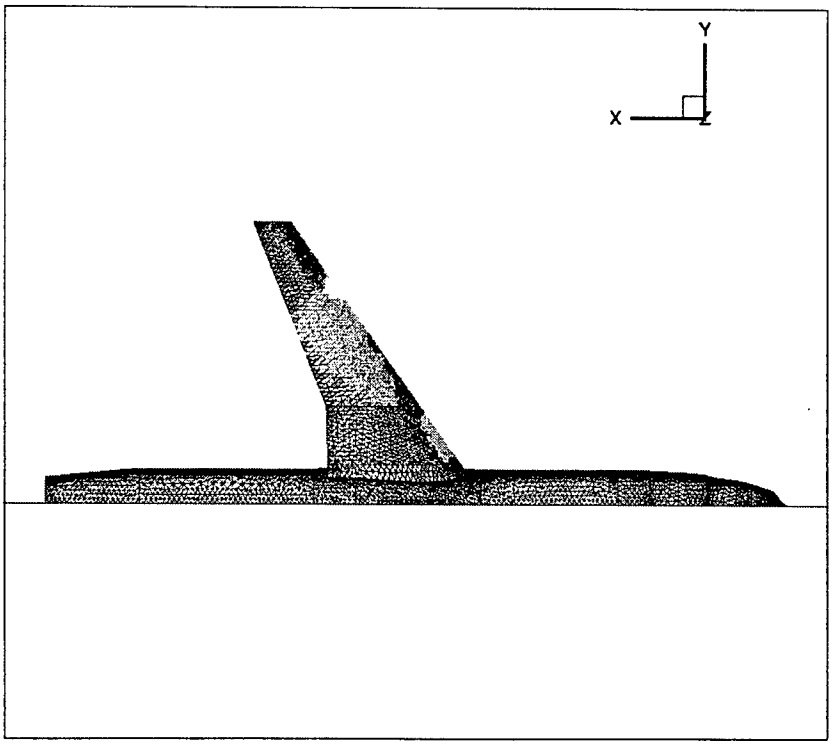

Figure 26. Surface triangulation on the lower wing-body geometry

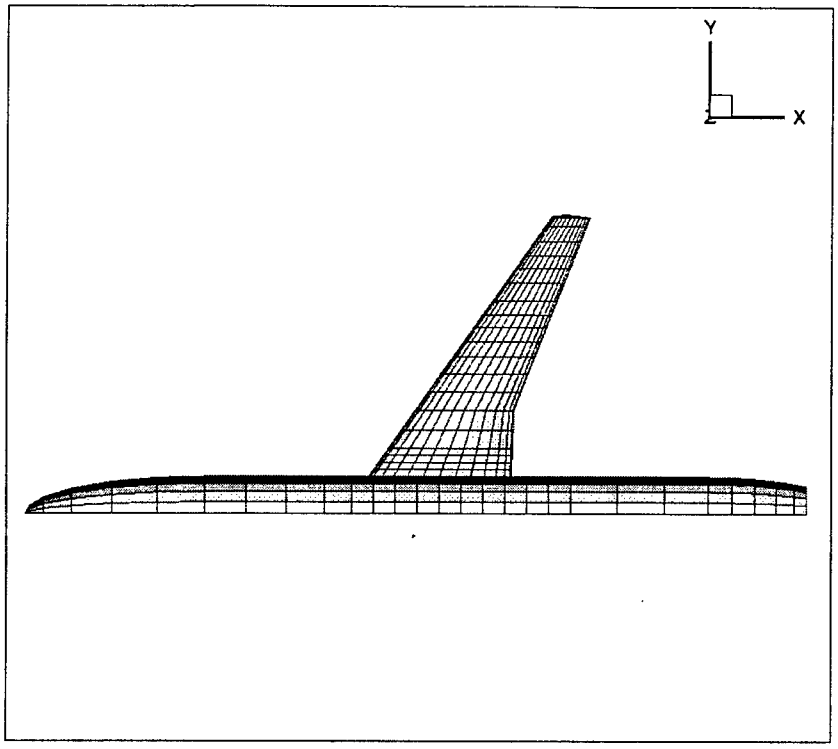

Figure 27. Structured VSAERO grid on the upper wing-body geometry

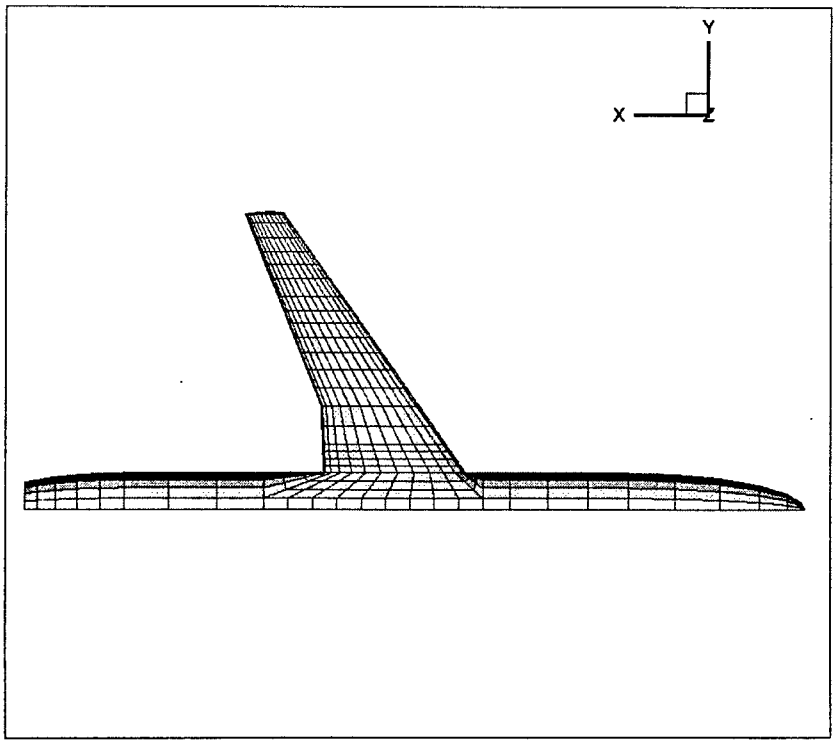

Figure 28. Structured VSAERO grid on the lower wing-body geometry

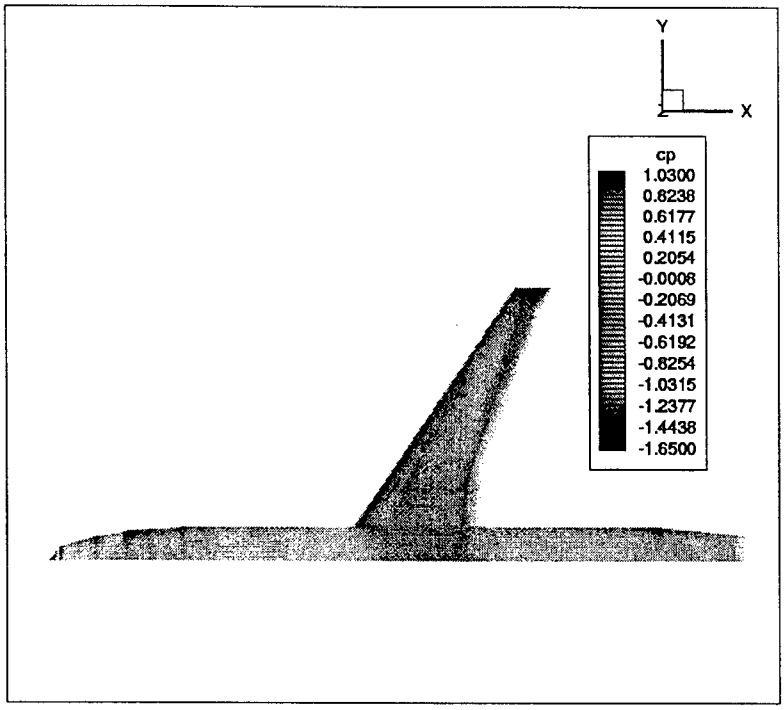

Figure 29. Cp contours on the upper wing-body geometry - USM3D solution

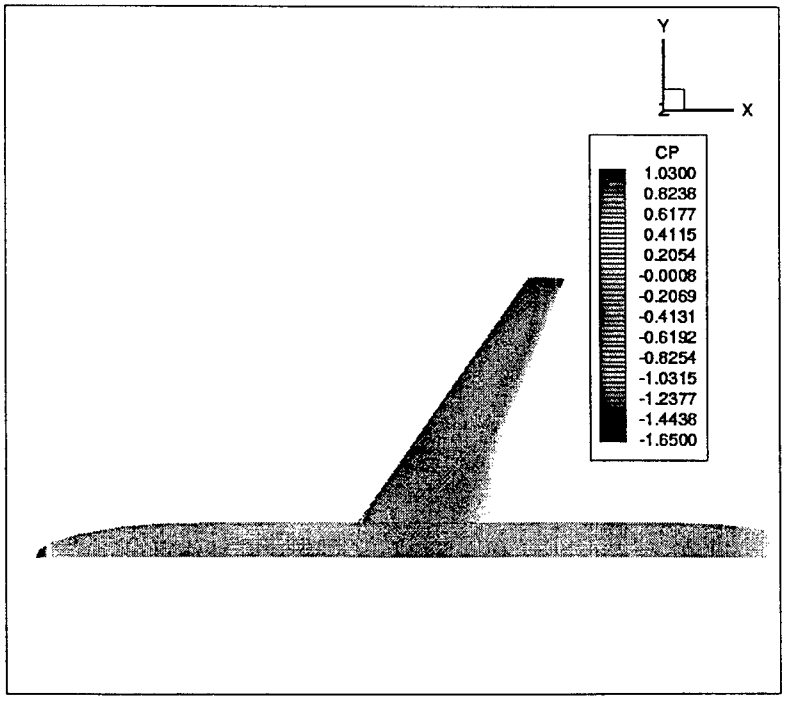

Figure 30. Cp contours on the upper wing-body geometry - VSAERO solution

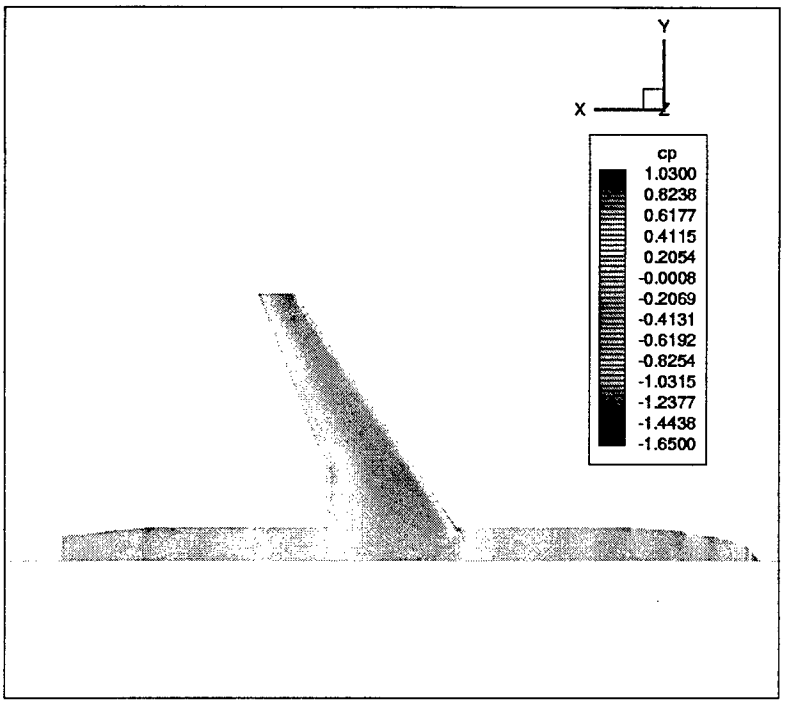

Figure 31. Cp contours on the lower wing-body geometry - USM3D solution

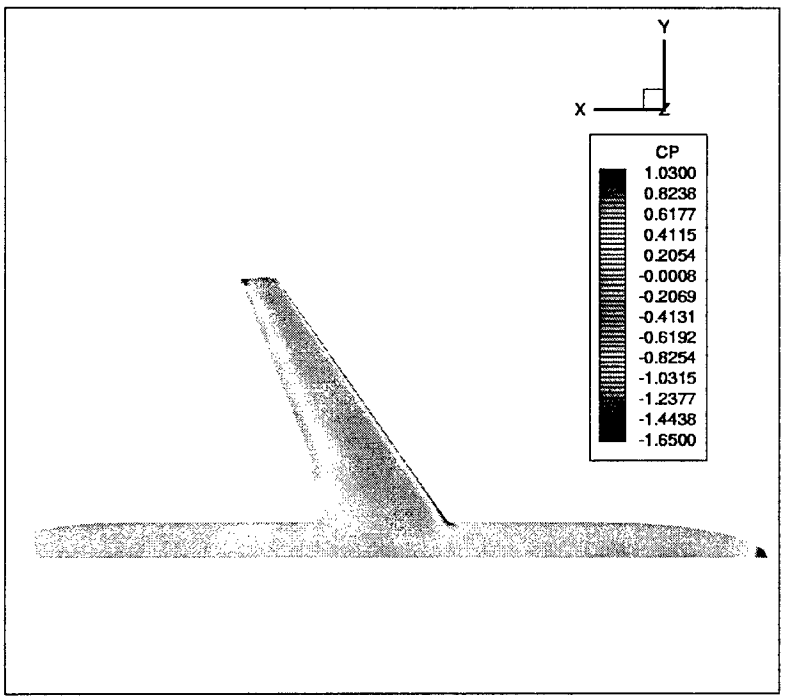

Figure 32. Cp contours on the lower wing-body geometry – VSAERO solution

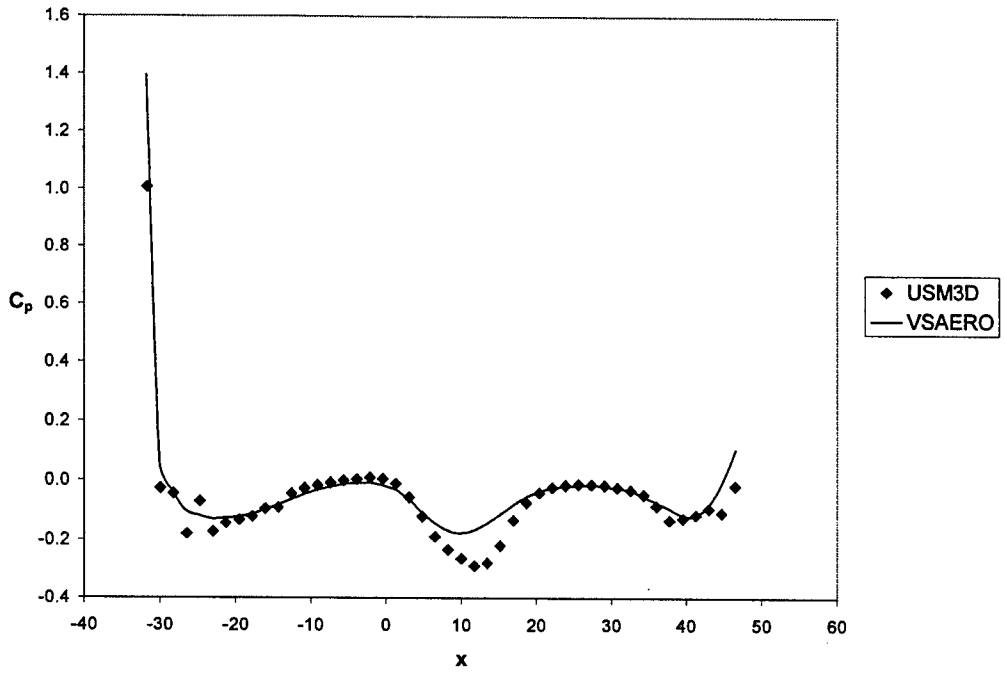

Figure 33. Pressure coefficient distribution on the upper wing-body surface at $\eta = 0.0$

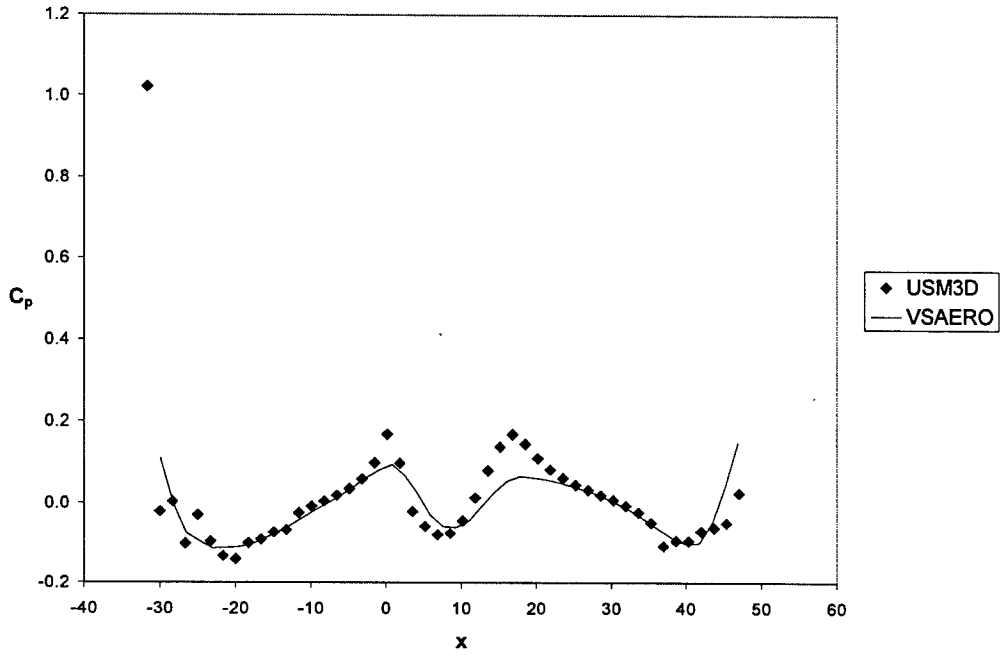

Figure 34. Pressure coefficient distribution on the lower wing-body surface at $\eta = 0.0$

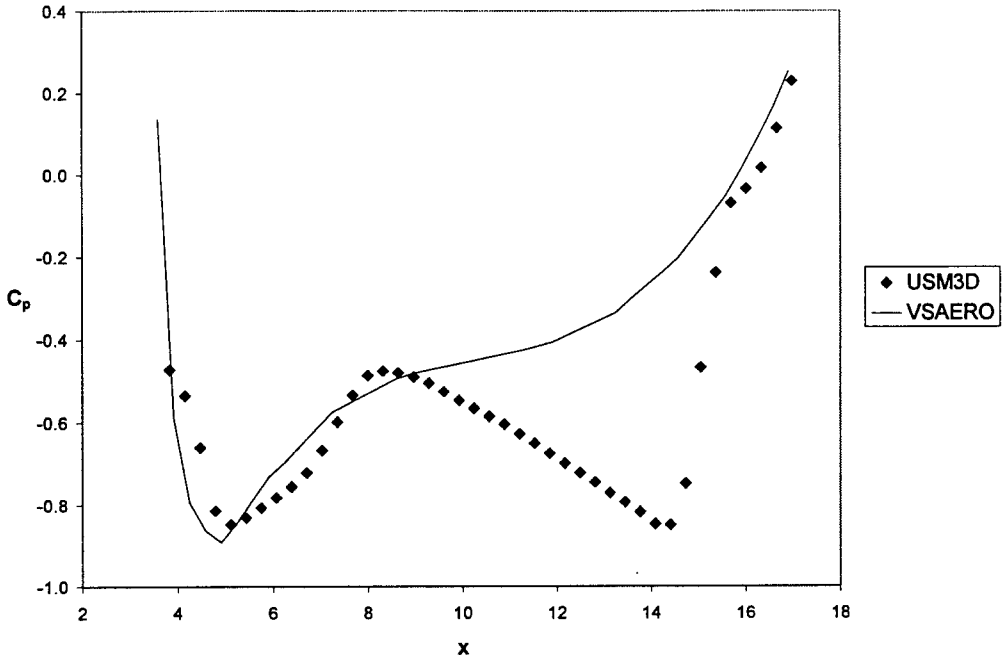

Figure 35. Pressure coefficient distribution on the upper wing-body surface at $\eta = 0.167$

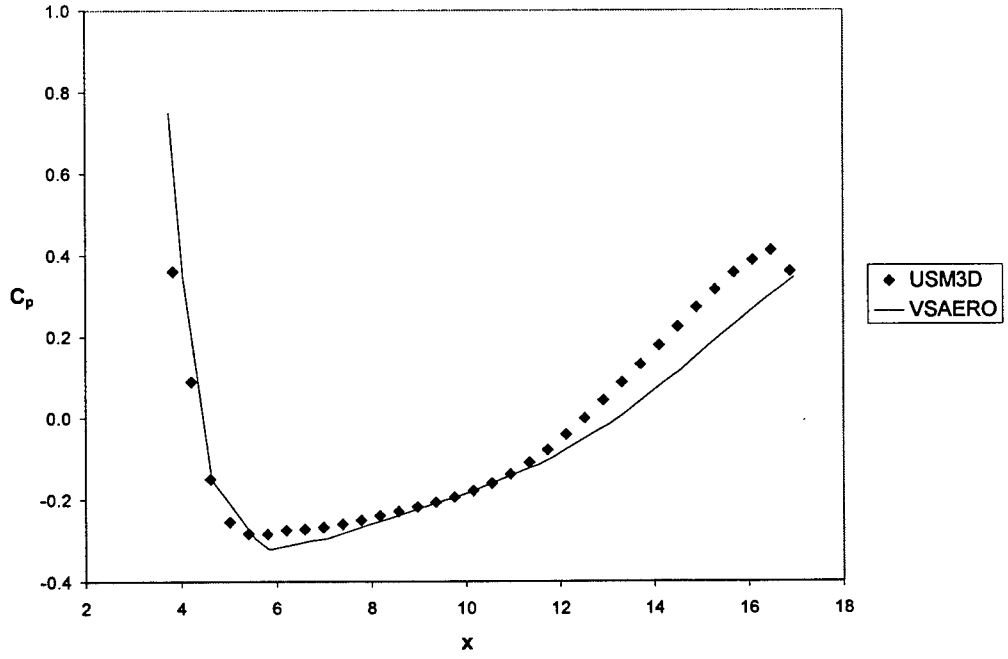

Figure 36. Pressure coefficient distribution on the lower wing-body surface at $\eta = 0.167$

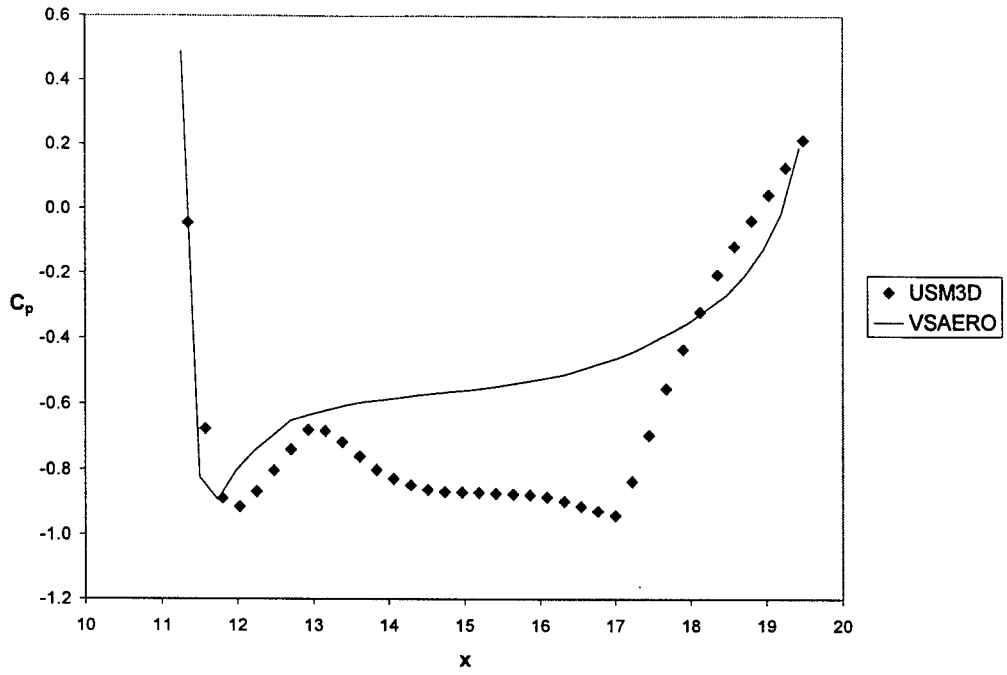

Figure 37. Pressure coefficient distribution on the upper wing-body surface at $\eta = 0.533$

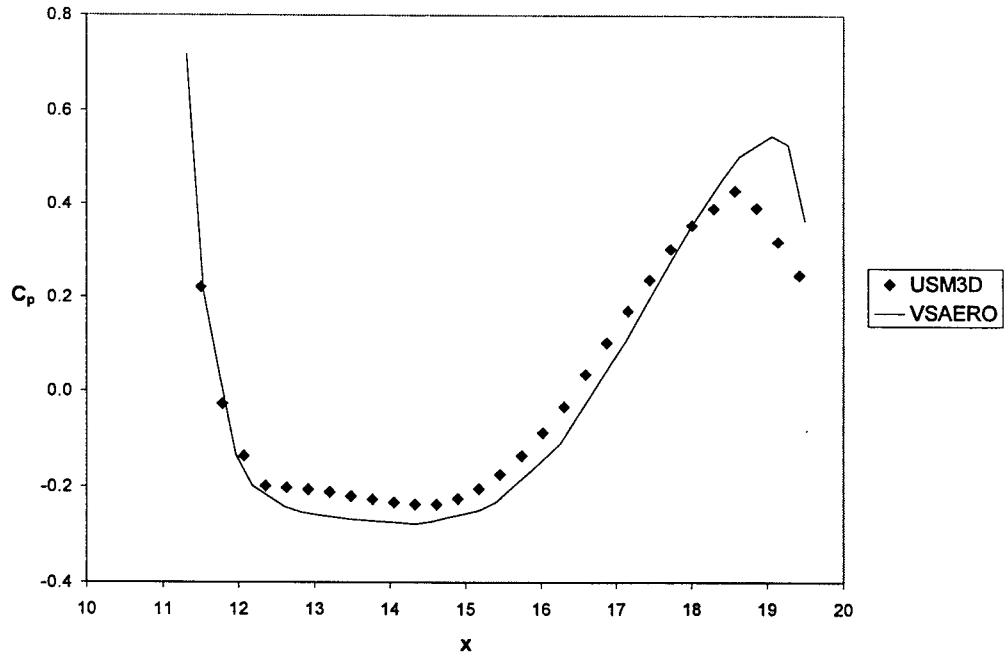

Figure 38. Pressure coefficient distribution on the lower wing-body surface at $\eta = 0.533$

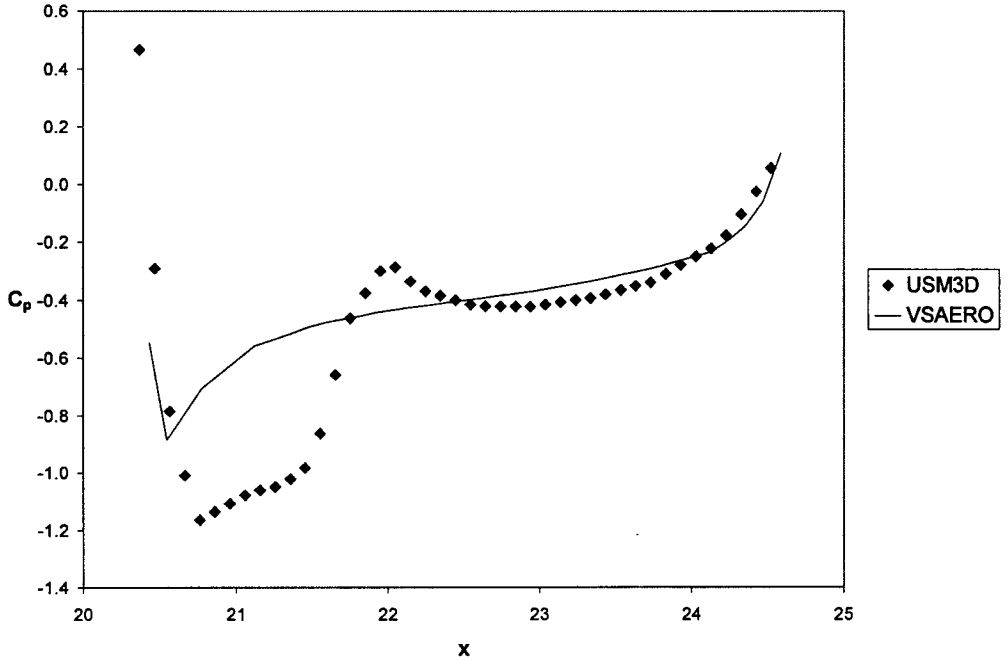

Figure 39. Pressure coefficient distribution on the upper wing-body surface at $\eta = 0.967$

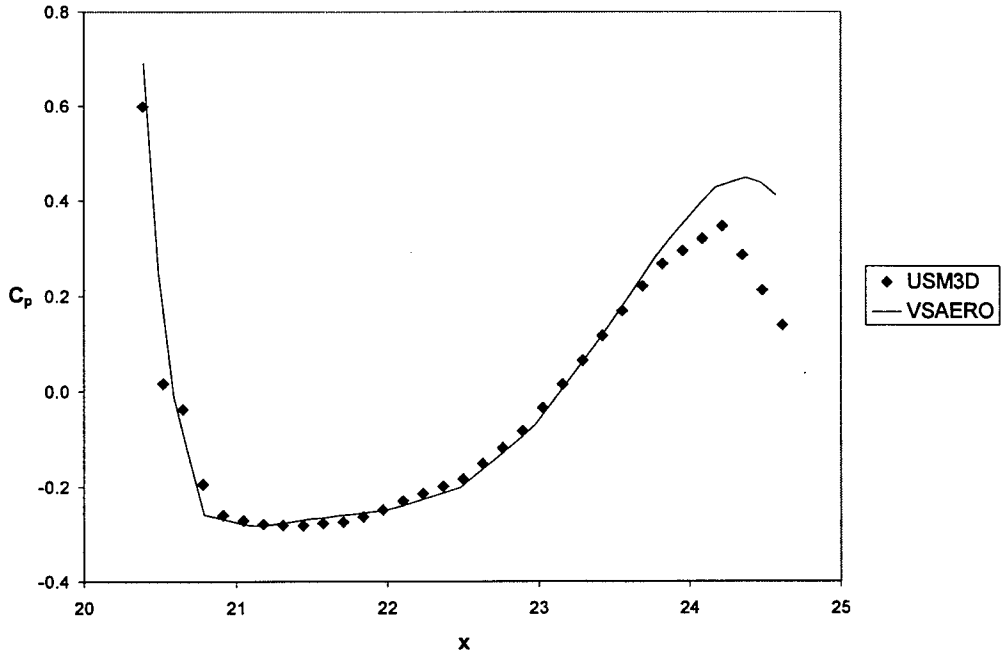

Figure 40. Pressure coefficient distribution on the lower wing-body surface at $\eta = 0.967$

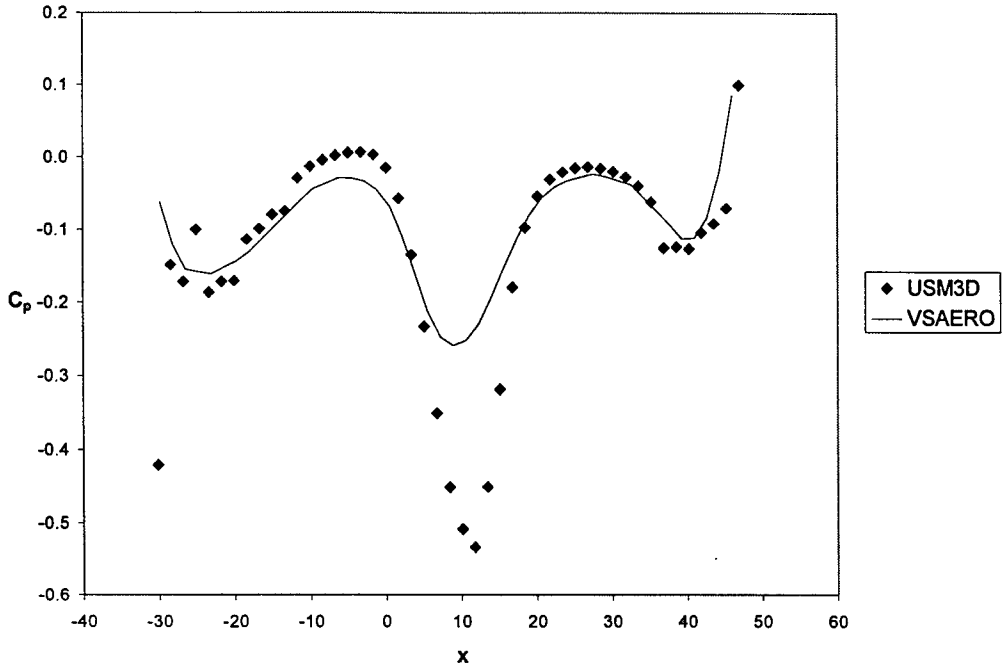

Figure 41. Pressure coefficient distribution on the upper wing-body surface at $\eta = 0.0$

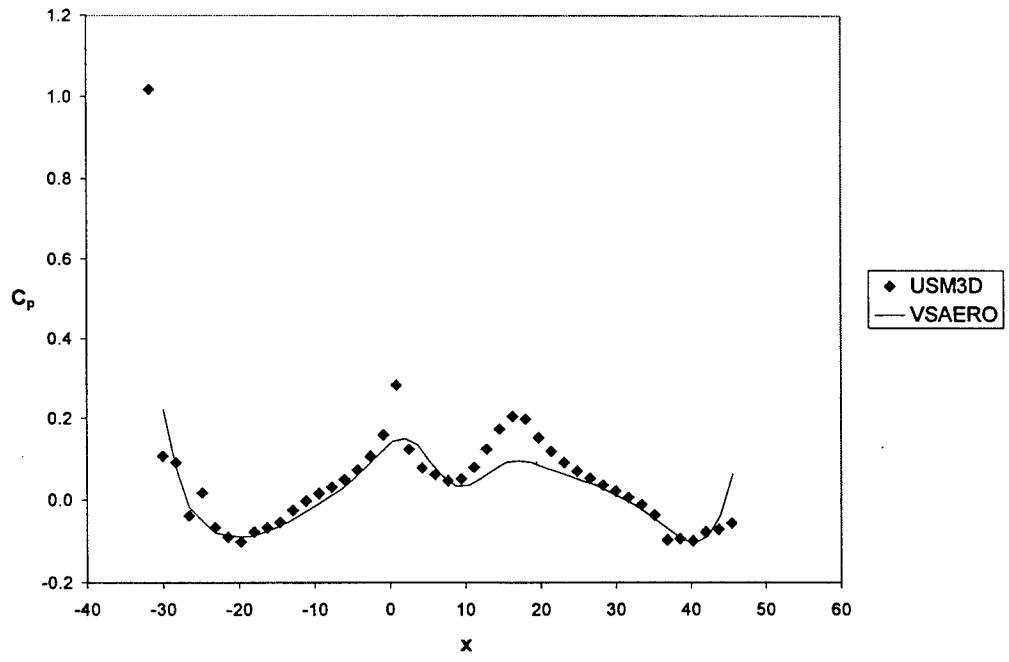

Figure 42. Pressure coefficient distribution on the lower wing-body surface at $\eta = 0.0$

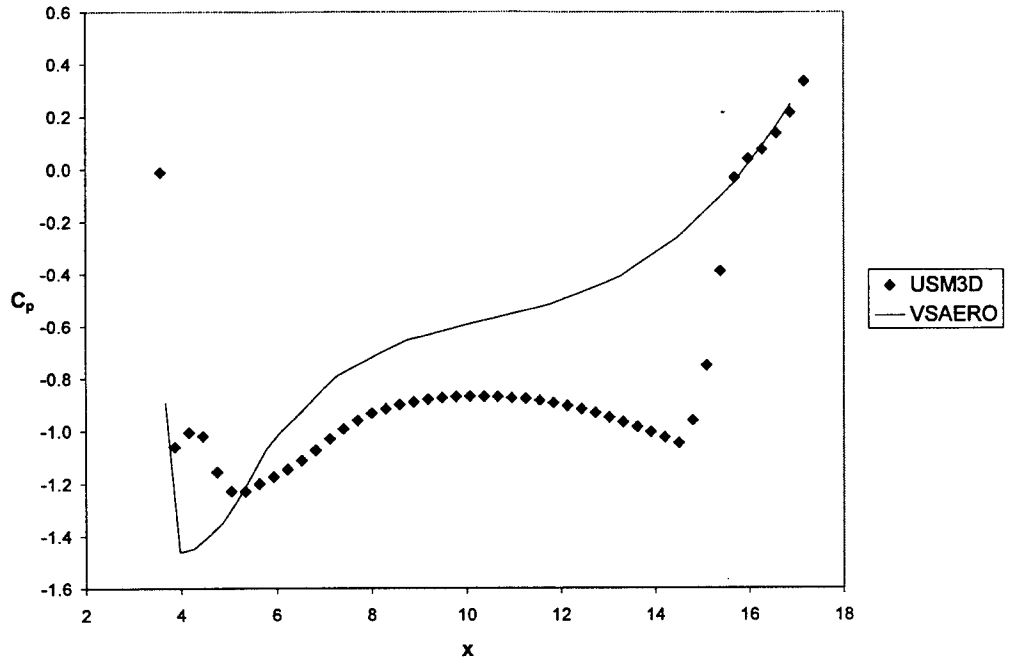

Figure 43. Pressure coefficient distribution on the upper wing-body surface at $\eta = 0.167$

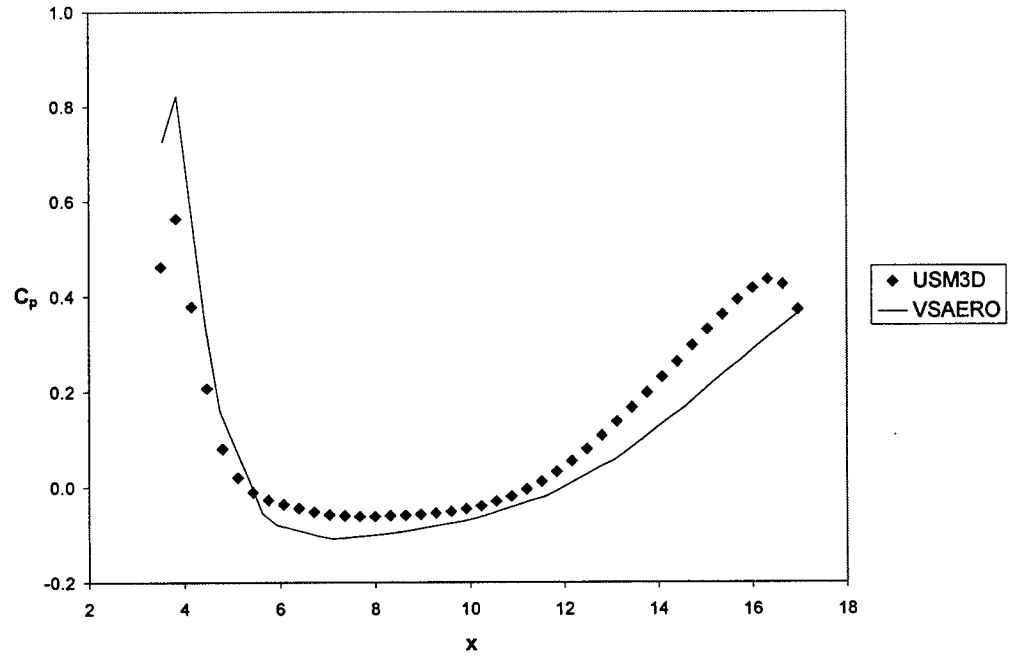

Figure 44. Pressure coefficient distribution on the lower wing-body surface at $\eta = 0.167$

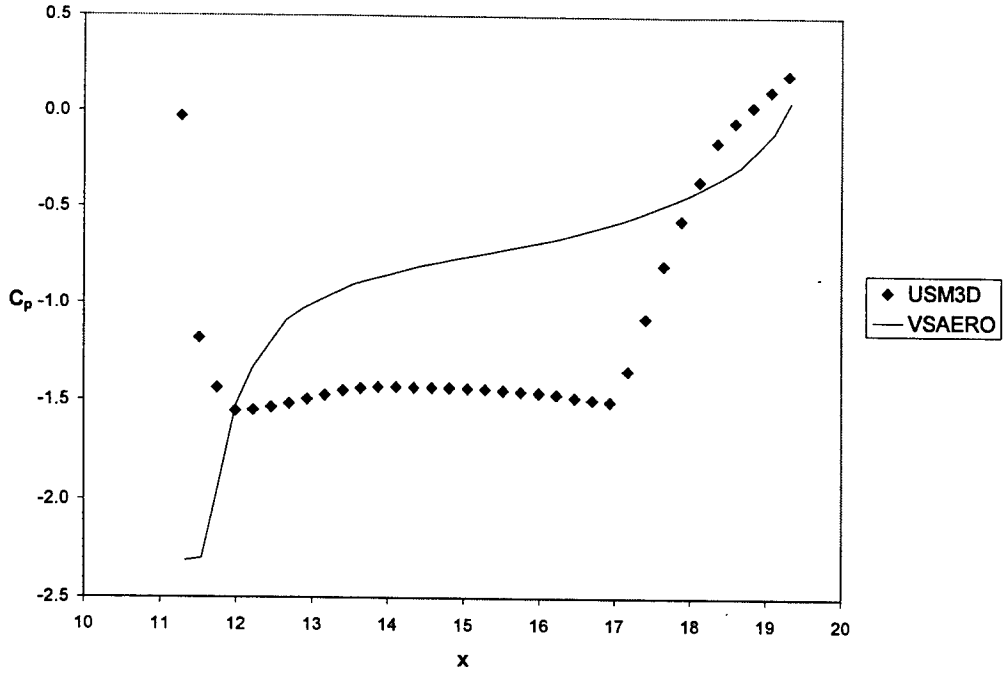

Figure 45. Pressure coefficient distribution on the upper wing-body surface at $\eta = 0.533$

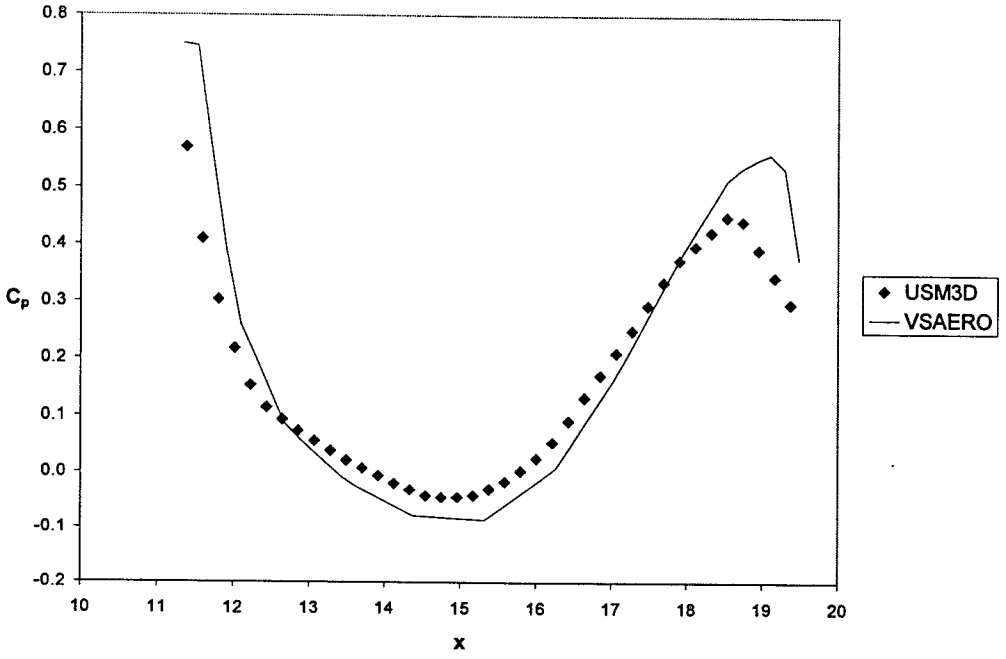

Figure 46. Pressure coefficient distribution on the lower wing-body surface at $\eta = 0.533$

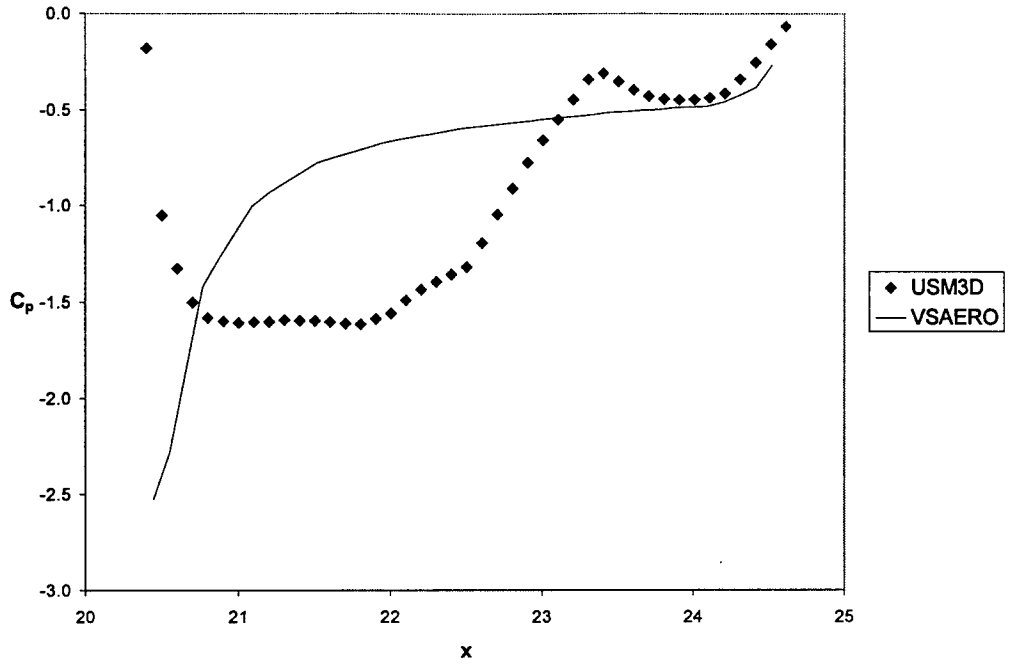

Figure 47. Pressure coefficient distribution on the upper wing-body surface at $\eta = 0.967$

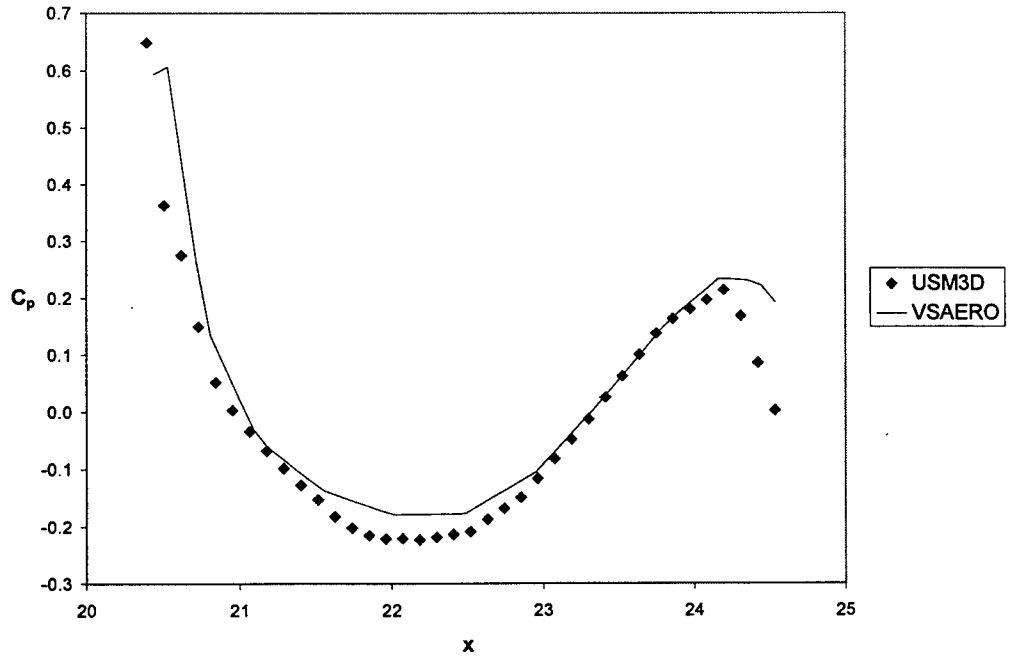

Figure 48. Pressure coefficient distribution on the lower wing-body surface at $\eta = 0.967$

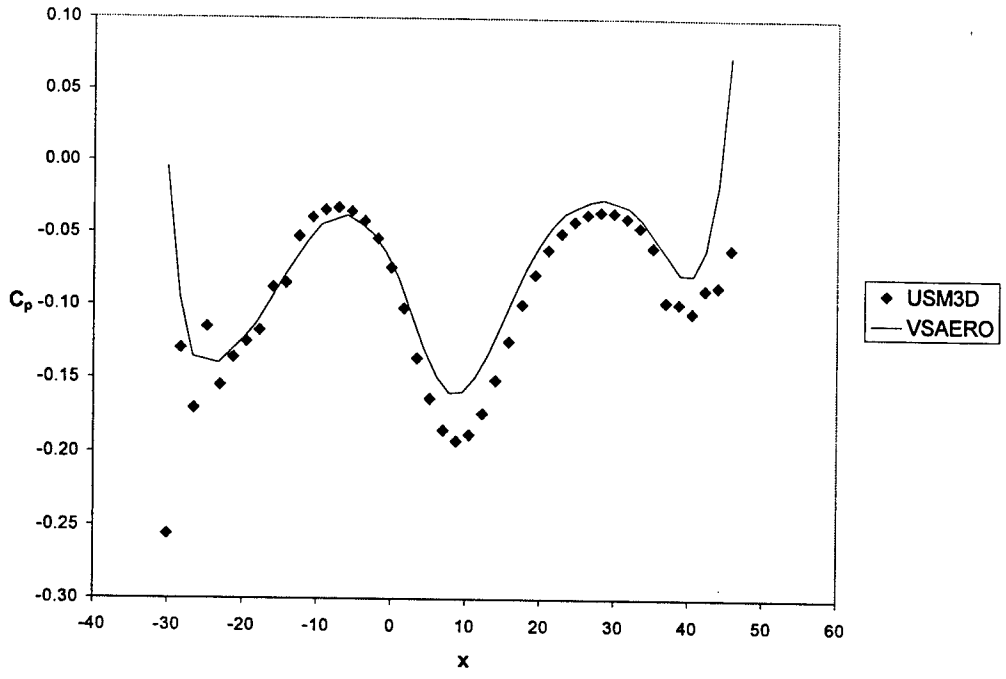

Figure 49. Pressure coefficient distribution on the upper wing-body surface at $\eta = 0.0$

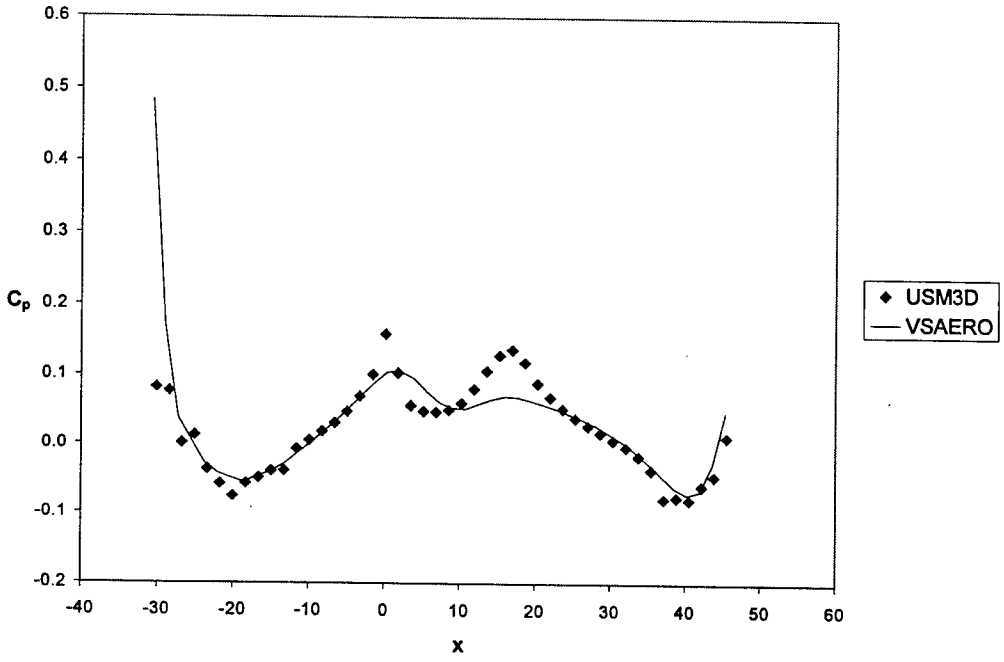

Figure 50. Pressure coefficient distribution on the lower wing-body surface at $\eta = 0.0$

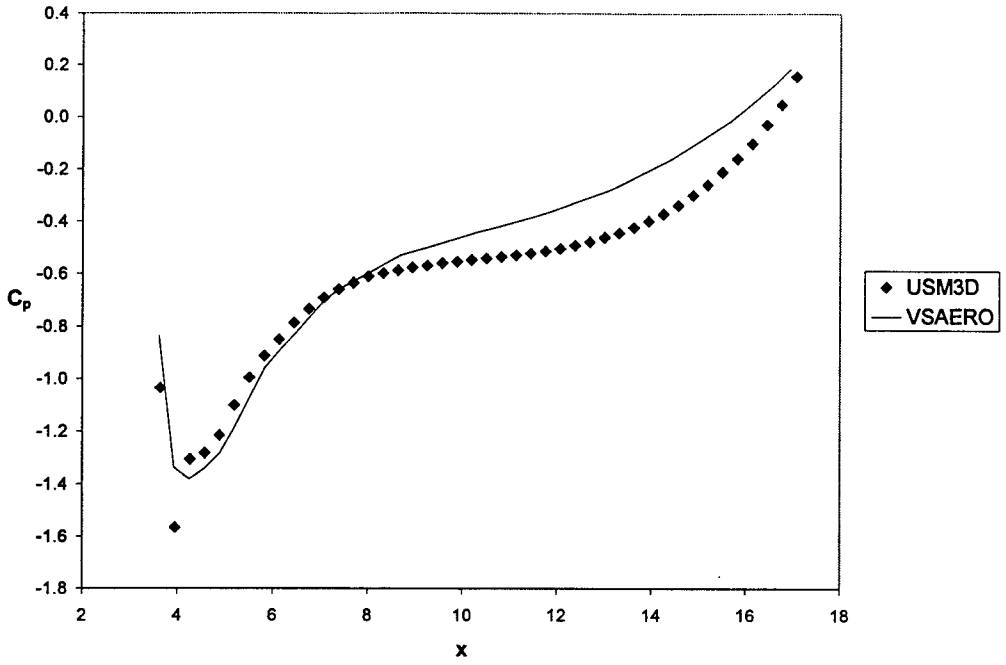

Figure 51. Pressure coefficient distribution on the upper wing-body surface at $\eta = 0.167$

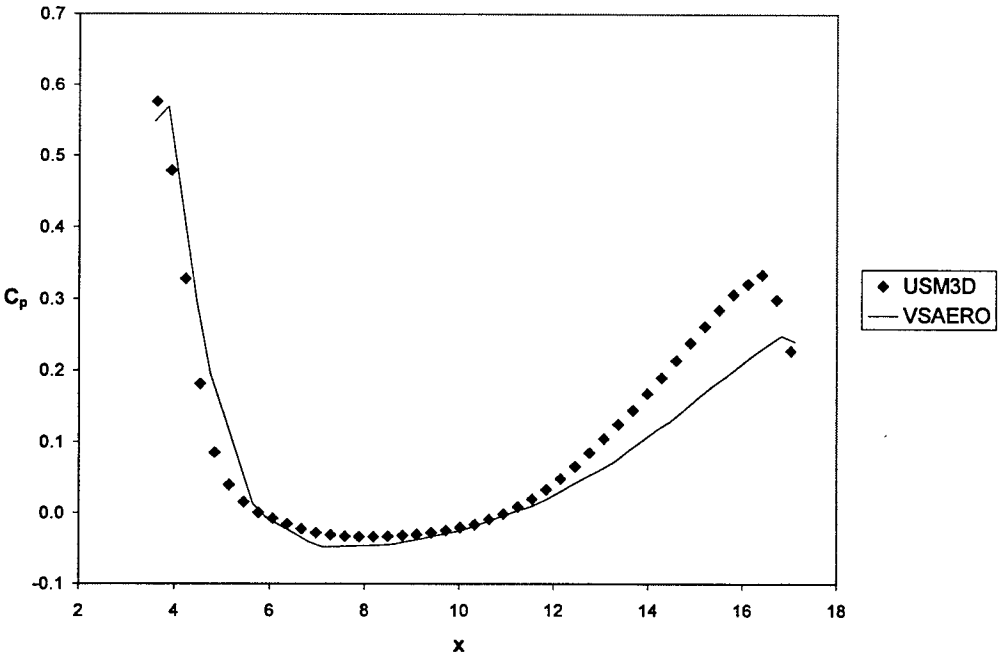

Figure 52. Pressure coefficient distribution on the lower wing-body surface at $\eta = 0.167$

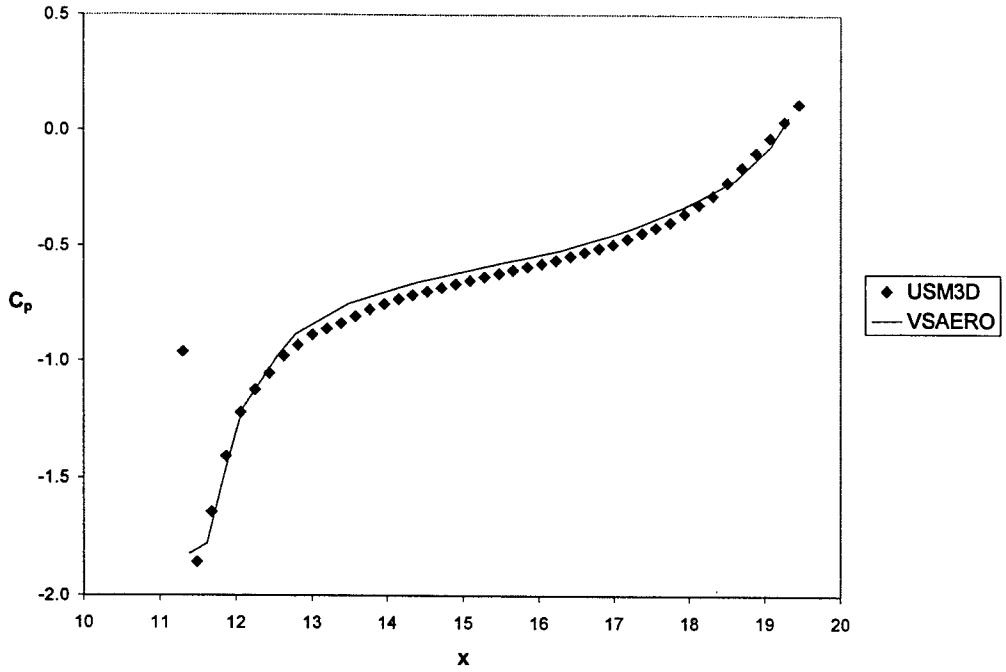

Figure 53. Pressure coefficient distribution on the upper wing-body surface at $\eta = 0.533$

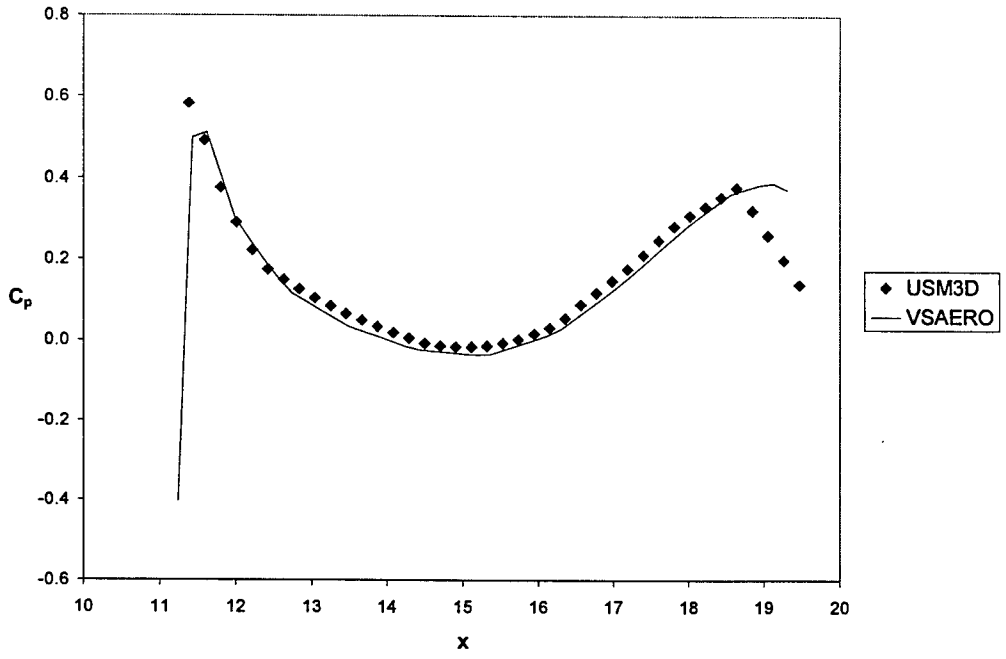

Figure 54. Pressure coefficient distribution on the lower wing-body surface at $\eta = 0.533$

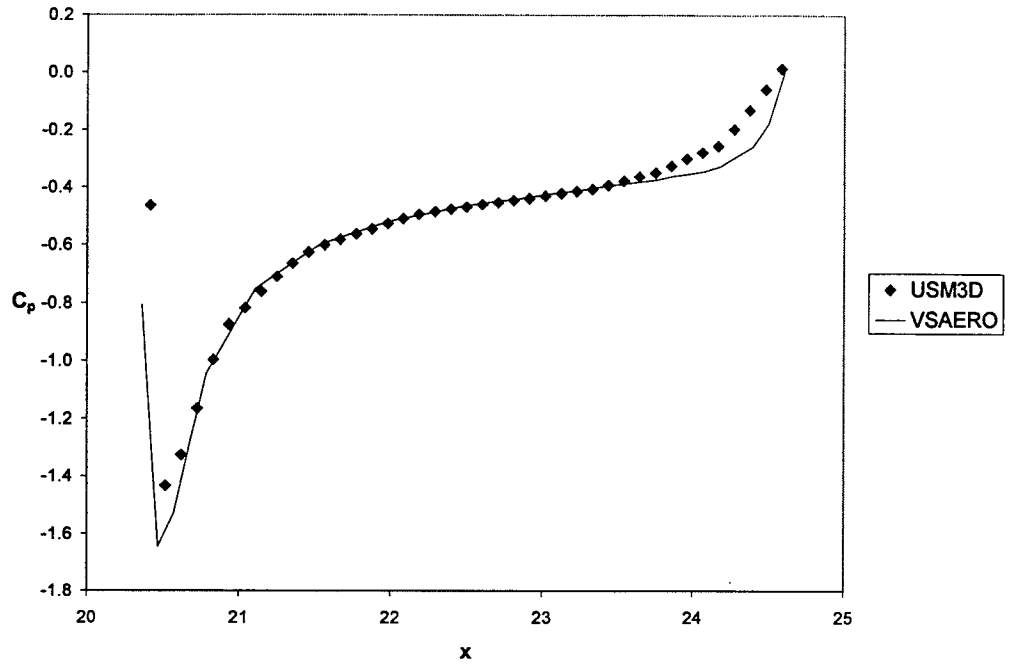

Figure 55. Pressure coefficient distribution on the upper wing-body surface at $\eta = 0.967$

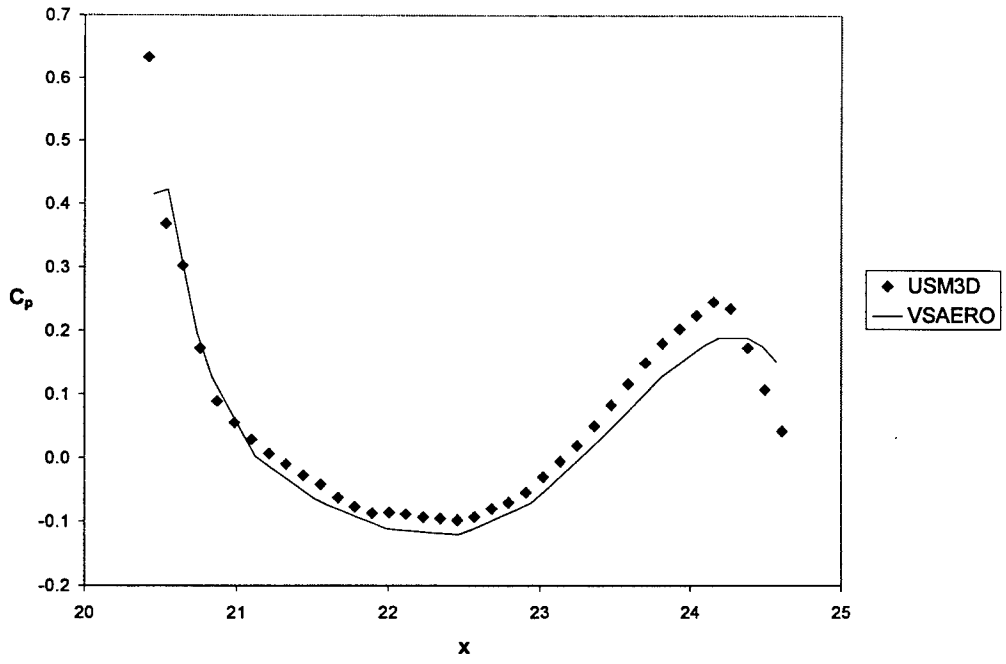

Figure 56. Pressure coefficient distribution on the lower wing-body surface at $\eta = 0.967$

Silicon Carbide Implant Activation and Surface Preparation Investigation

Stephen E. Saddow
Assistant Professor
Emerging Materials Research Laboratory
Department of Electrical & Computer Engineering

Mississippi State University
Box 9571
Mississippi State, MS 39762

Final Report for:
Summer Research Extension Program
Air Force Research Laboratories
Wright Patterson AFB

Sponsored by:
Air Force Office of Scientific Research
Bolling Green Air Force base, DC

And

Air Force Research Laboratories
Wright Patterson AFB

January 2000

Silicon Carbide Implant Activation and Surface Preparation Investigation

Stephen E. Saddow
Assistant Professor
Emerging Materials Research Laboratory
Department of Electrical & Computer Engineering
Mississippi State University

Abstract

Silicon Carbide is one of the hardest materials in nature, second only to boron nitride and diamond. This high degree of mechanical strength gives the material its desirable electronic properties – low leakage currents and high electric breakdown fields. The downside to silicon carbide from a device technology perspective is the material is thus difficult to process. In this investigation, two key device processing techniques for silicon carbide were studied, namely the activation of ion implanted silicon carbide and the quality of epitaxial layers grown on substrates polished using novel chemical-mechanical polishing (CMP) methods developed at AFRL.

The mechanical strength of silicon carbide does not permit the use of diffusion as a means to achieve selective doping as required by most electronic devices. While epitaxial layers may be doped during growth, ion implantation is needed to define such regions as drain and source wells, junction isolation regions, etc. While ion implantation has been studied in all of the silicon carbide polytypes, ion activation has resulted in serious crystal damage as these activation processes must be carried out at temperatures on the order of 1600°C. Ion implanted silicon carbide that is annealed in either a vacuum or hydrogen environment usually results in a surface morphology that is highly irregular due to the out diffusion of Si atoms. We have developed and report a successful process of using silicon overpressure, provided by silane in a CVD reactor during the anneal, to prevent the destruction of the silicon carbide surface. This process has proved to be robust and has resulted in complete ion activation at a annealing temperature of 1600°C.

The high mechanical integrity of silicon carbide substrates makes the realization of 'epi-ready' substrates challenging. In the narrow band gap semiconductors, such as Si and GaAs, the high degree of surface reactivity with the environment makes the development of substrate chemical-mechanical polishing (CMP) relatively straight forward. Silicon carbide, while substrate polishes do exist, is a technology that is far from 'epi-ready.' In this investigation, epitaxial layers of silicon carbide were grown on various substrates to assess the epi film quality as a function of surface finish. Simultaneous growth runs were conducted on as-received, CMP processed, oxidized and CMP plus oxidized substrates. The best epi film quality was achieved for the substrate that was only treated with CMP. Results of this investigation are disclosed and future work in this area proposed.

Acknowledgements

The author would like to thank the staff of the Emerging Materials Research Laboratory (EMRL) at Mississippi State University for their support during this project. In particular, Galyna Melnychuk and Thomas Schattner for their assistance in growing the epitaxial layers used in this study. Prof. John Williams and Tami Isaacs-Smith of Auburn University are gratefully acknowledged for their steady supply of ion-implanted samples used throughout this study. Dr. Alex Hsieh of the Army Research Laboratory is acknowledged for his timely support in performing AFM on the ion implanted samples.

I would like to thank the technical staff at the Air Force Research Laboratory (AFRL) for all of their kind assistance and for hosting my summer visit in 1998. In particular, Dr. Adam Saxler for his assistance with Hall Effect measurements, Dr. Jim Scofield for his overall technical support and Dr. Bill Mitchell for supplying the wafer pieces for CMP study and his technical support throughout the project. Without the assistance of the AFRL team this project would not have progressed as far as it did.

Characterization of BN-Doped SiC Epitaxial Layers

Stephen E. Saddow

1. Introduction

Silicon carbide is an ideal semiconductor for high-power and high-temperature applications due to the high level of material stability at elevated temperatures. This high degree of mechanical stability, while it lends itself well to these applications, makes the formation of device structures that require selective area doping difficult. Indeed, SiC is primarily an epitaxial technology where ion implantation is used to selectively dope regions in the epitaxial layer to implement a specific device structure. Although dopant diffusion is the preferred process in silicon technology to achieve selective doping, diffusion rates in SiC are simply too low to permit this approach.

Ion implantation in SiC has been demonstrated to be a suitable means for achieving degenerate doping densities for both p and n-type material with reasonable ion flux [1]. Unfortunately, the high bonding strength of the SiC lattice requires not only that the implant be carried out at elevated temperatures [1] but that the implant anneal be performed in excess of 1600 °C if full doping activation is to be achieved. It is widely believed that the degradation of the silicon carbide material surface after implant annealing is one reason responsible for MOSFET inversion layer carrier mobilities of less than 10 cm^2/V-s in 4H-SiC, a serious problem leading to unacceptable on-state resistances in these power devices [2]. As a consequence, the highest mobility MOSFET devices reported in SiC are either buried channel devices [3] or devices with a low thermal implant activation temperature [4] which also increases the series resistance in the drain and source regions. While the SiC lattice is inherently stable at lower temperatures, Si can out diffuse at elevated temperatures leading to a severe degradation in the surface morphology known as step bunching [5]. Numerous researchers have reported work on annealing SiC with various encapsulants which suppress the out diffusion of Si during the annealing process **[6,7]** but require that the encapsulating material be removed prior to continuing device fabrication.

A second key impact of SiC material that is directly related to its strong mechanical properties is the difficulty is preparing substrate surfaces for subsequent device epitaxial layer growth. Common methods such as CMP (chemical-mechanical polishing) are normally carried out using SiC grit in concert with diamond grit, appropriate solutions to suspend the particles in what is called a slurry, and then a chemical step that completes the process. The completed CMP'd wafer for such traditional narrow-bandgap semiconductors such as Si and GaAs has a mirror finish with no discernable surface or sub-surface damage. This is due to the relatively soft mechanical properties of these materials (in comparison with SiC!). The author, for instance, has significant experience in polishing both Si and GaAs wafers with the resulting surface finish being of excellent quality. Similar procedures for SiC are difficult at best, and thus an area of prime technological development. It was with this in mind that the collaboration between EMRL and AFRL was expanded to include CMP process evaluation as part of this study.

In this report both implant anneal and CMP research activities will be discussed with the main features/outcomes reported. In addition, future research is suggested for consideration so

that AFRL can continue to improve the state-of-the-art of SiC technology in both of these areas. First the Implant Anneal (IA) research is discussed followed by the CMP work.

2. Implant Annealing Research

Numerous groups have reported implantation results in SiC [1-3]. In particular, ion implantation is normally carried out in SiC at elevated temperatures (typically 700 °C) in order to make the annealing of the crystal after implantation possible. Anneals have been carried out by all major SiC device and materials groups, with the group at ABB using silane overpressure to anneal the crystal (and thus activate the implant) without degradation of the surface. This surface degradation, which occurs at temperatures above 1400 °C, is believed to be the result of out-diffusion of Si caused by the lack of Si over pressure during the anneal [1]. Annealing in Ar has been carried out by most groups with only the result of Prof. Williams at Auburn University showing any promise [8]. The goal of this phase of the research project was to establish a US capability to anneal ion implanted crystals using silane overpressure. This has been achieved and the results reported by the author and colleagues at the recent International Conference on SiC and Related Materials (ICSCRM) [10]. The results of this investigation are now described.

2.1 Ion Implanted 4H-SiC samples

Two sets of samples were investigated during the course of this experimental study. The first was provided by Purdue University and contained an n-type epitaxial layer with a doping density in the mid 10^{15} cm^{-3} range. Samples provided for implant annealing were implanted with both Al and B and were of the 4H and 6H polytype. The second set of samples, the majority of which is discussed here, were composed of a 6 μm n-type epitaxial layer grown by the Emerging Materials Research Lab with a doping density in the mid 10^{15} cm^{-3} range. A single epitaxial layer was grown on 4H-SiC (8° off-axis) and the sample diced into 5 mm squares to permit numerous implant studies to be conducted on epitxial layers of the same doping and thickness. A typical implant Al profile is shown in Fig. 1. Implants were carried out at 700°C through a 110nm Mo mask layer in order to implant the near surface regions of the SiC epilayers. Molybdenum does not react with SiC at the implant temperature, and following implantation, the mask layer was etched away prior to further processing. The AFM photograph in Fig. 2 shows that the surface of the epilayer is somewhat degrade by the implant process. However, bulk crystalline quality is well preserved, as indicated by the ion channeling spectra. These spectra were generated using standard Rutherford backscattering techniques and 2MeV He^{+} ions scattered at 170° to the direction of the incident beam.

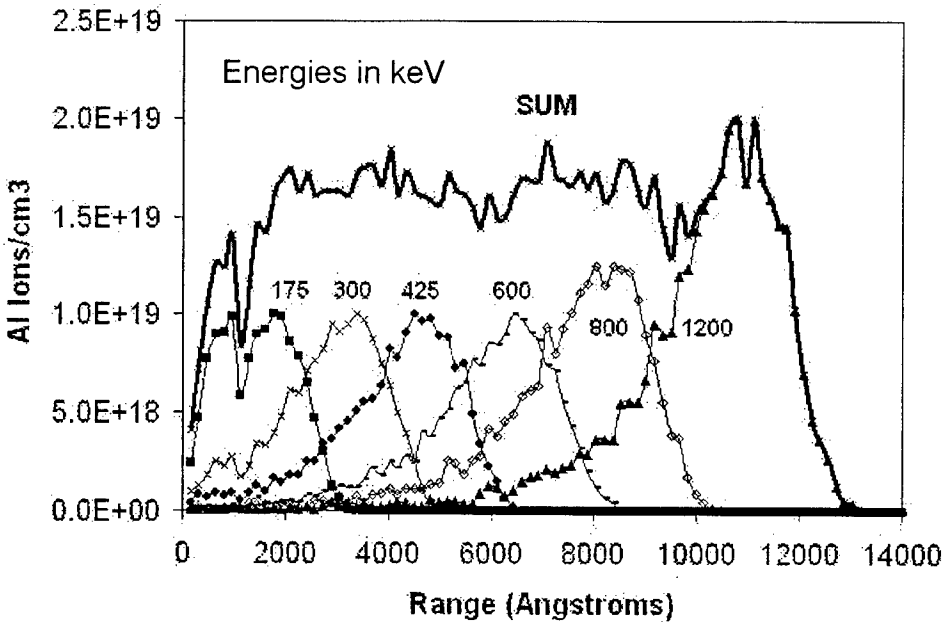

Figure 2.1 Implant schedule used for the implant anneal studies. Al was implanted at 700°C. Multiple implants starting at 175 keV used to achieve the box profile shown (SUM in fig.).

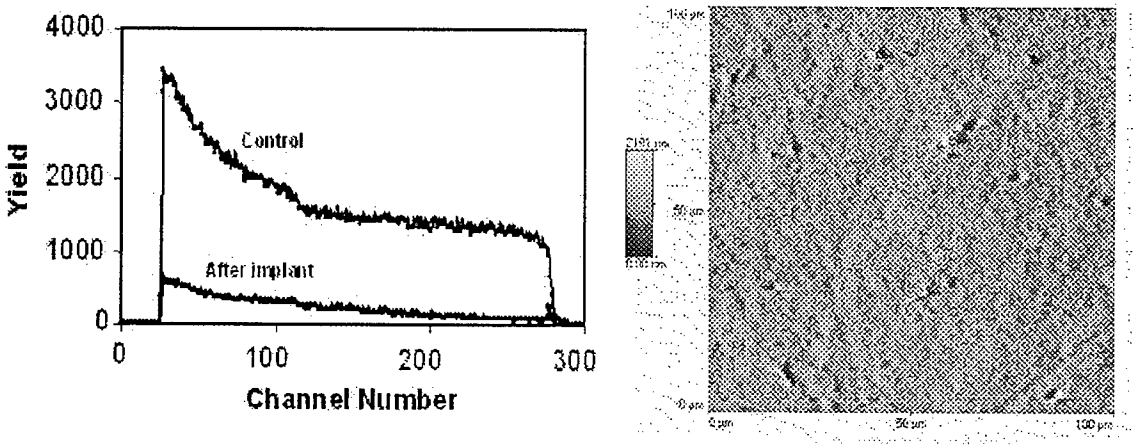

Figure 2.2 Channeling RBS and AFM data of 4H-SiC implanted with Al at 700°C. Note the crystal quality is degraded due to implant damage, as expected.

2.2 Silane Overpressure Annealing Experiments

A silane-based CVD reactor suitable for performing high-temperature anneals in a silicon rich ambient was used for these experiments. Annealing temperatures in excess of 1700 °C are possible by placing the sample to be annealed on a SiC coated graphite susceptor and heating the graphite using an RF induction coil, as has been discussed elsewhere for CVD growth of SiC epitaxial layers [9]. Preliminary experiments were conducted on Al and P implanted samples at 1600 °C at atmospheric pressure and under various silane flow conditions. Both a 3% silane in UHP hydrogen gas flow of 5 to 20 sccm were used to characterize the surface morphology as a function of silane flow. Prior to annealing the material was n-type with a doping density of 4-

5E15 cm^{-3}. After annealing the doping density was observed to be in excess of 1E19 cm^{-3} at the surface and was observed to be p-type. Unfortunately the method, using UHP hydrogen, did not result in a repeatable process.

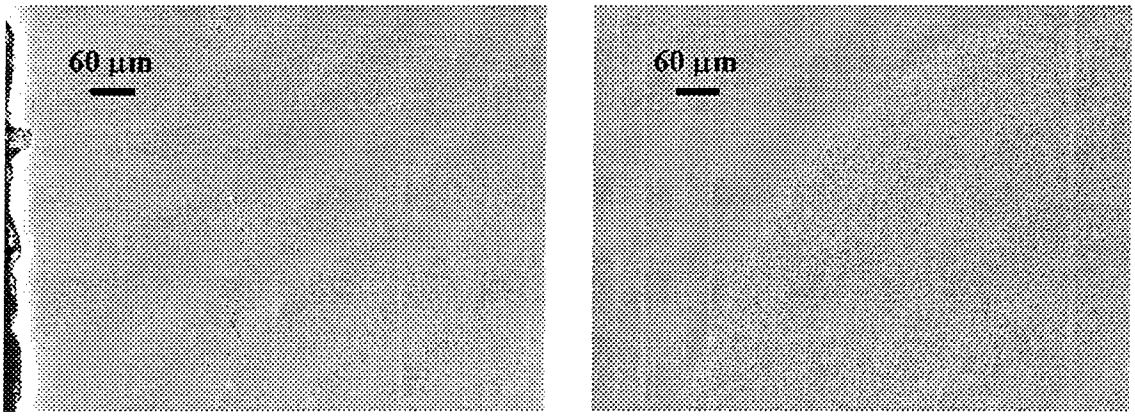

Figure 2.3 Optical micrographs showing the surface morphology after silane overpressure annealing in SiH_4/H_2. Step bunching was observed to occur on numerous occasions motivating the development of a SIH_4/Ar process.

Since H_2 is known to etch SiC at the temperatures required to anneal the implant, experiments using silane in argon (3% silane in 97% UHP Ar) were conducted and a process schedule established using this process chemistry. Since Ar does not etch SiC the concentration of Si in the reactor during annealing can be varied such that an optimum process is achieved. Figure 4 shows the surface morphology of Al implanted n-type 4H-SiC after annealing. Note that the surface morphology was not affected during the annealing process, indicating that a sufficient overpressure of Si was present during the anneal.

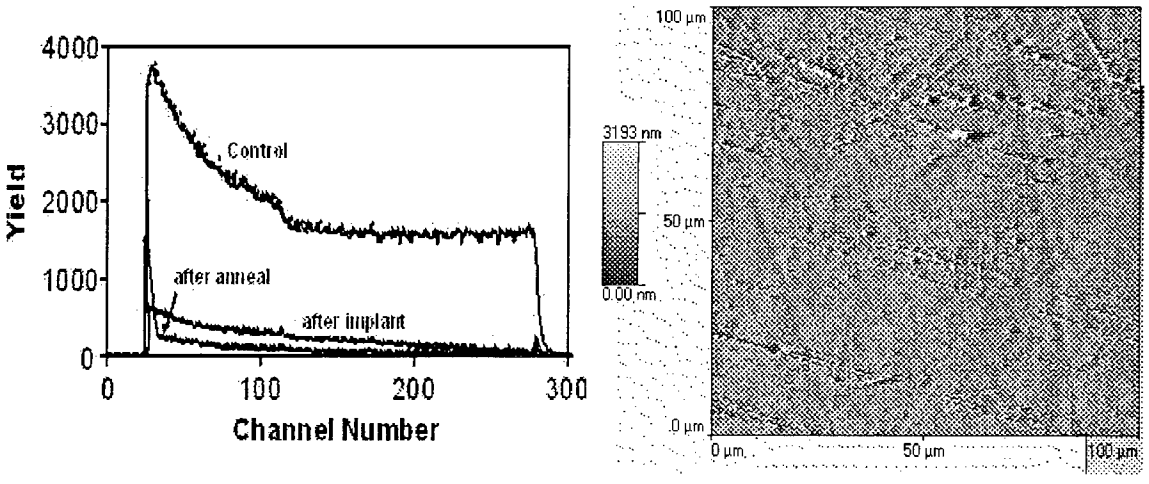

Figure 2.4 Channeling RBS and AFM data of 4H-SiC annealed using the Silane/Ar process. Note crystal damage from implant has been repaired.

The final process schedule developed during this research is as follows. After a 1 slm UHP Ar flow is established in the reactor, the RF generator is turned on and the susceptor heated to the annealing temperature. The silane in Ar gas flow of 20 sccm is not initiated until a

substrate temperature of 1490°C is reached to suppress Si droplet formation. After the annealing temperature of 1600°C is reached the 30 minute anneal is conducted. At this point the reactor is purged of silane by simultaneously turning off the silane in Ar flow (3 slm UHP Ar flow remains on) and the setpoint temperature is reduced to 1400°C. After one minute, the RF generator is turned off and the sample cooled to room temperature under Ar flow.

2.3 Summary

Implant anneal experiments were performed to develop a process schedule for silane overpressure annealing of ion implanted SiC [10]. In an effort to develop an optimum process with the smallest number of experiments, the same annealing temperature was used for all the studies conducted (1600 °C). The initial process used available silane in UHP H_2 of varying flow rates. While some success was achieved with this approach, the process proved to be sensitive to annealing conditions and step bunching was observed on most samples after annealing. Since H_2 is known to etch SiC at the temperatures needed to activate the implant, a silane in UHP Ar process was established with the process schedule shown to be robust and provide fully activated implants with no loss of crystal structure. Measurement of the free carrier mobility is now being conducted as well as selective ion implantation which is critical to advanced devices in SiC technology.

3. Surface Preparation Investigation

The objective of this phase of the research project was to assist AFRL (Dr. Mitchell) with the evaluation of chemical-mechanical polishing (CMP) processes on SiC substrates. One of the best methods to evaluate CMP methods is to grow epitaxial layers of semiconductor material on the prepared substrates and evaluate the resulting film. This evaluation normally consists of both morphological (SEM, AFM, etc.) and also electrical (IV, CV, breakdown voltage, leakage current, etc.). In this study we grew several epitaxial layers for morphological characterization at AFRL. The results of this study are now described.

3.1 CVD Growth Experiments:

The epi process used in this study was to grow approximately 1 μm of homoepi on four (4) substrates provided by AFRL, each with differing surface preparation methods. The homo-epi interface was then to be characterized by TEM at AFRL to attempt to quantify interfacial defects as a function of surface preparation. 30 minute CVD growth experiments were carried out on the following samples in the EMRL cold-wall (30 mm) reaction tube with an estimated epi thickness of 1 μm (this was chosen to make TEM evaluation easier as sample prep with materials containing thick epi layers is very time consuming):

Table 3.1 SiC CVD epi sample summary

Sample No.	Growth Run No.	Si/C[1)]	$N_D \times 10^{16}$ [cm^{-3}][2)]	Substrate process	Remarks
U036-09A	99-4H-199	0.2	5-6	CMP	Excellent morphology
X0127-11A	99-4H-199	0.2	6.5-8	No processing	Excellent morphology
U036-09B	99-4H-200	0.2	–	CMP + oxidation	Fine scratches on surface
X0127-11B	99-4H-200	0.2	5-6	Oxidation	Excellent morphology

[1)] Growth temp = 1535 °C
[2)] CV measurement w/Hg probe.

Figure 3.1 shows the resulting epi surface as measured using an optical microscope with the Nomarski technique. For all cases except substrate U036-09B, the surface morphology, as determined with Nomarski micrographs, was excellent. The doping density of the films were measured in EMRL using a Hg-probe CV technique. The average doping density in the film is included in Table 3.1 for reference.

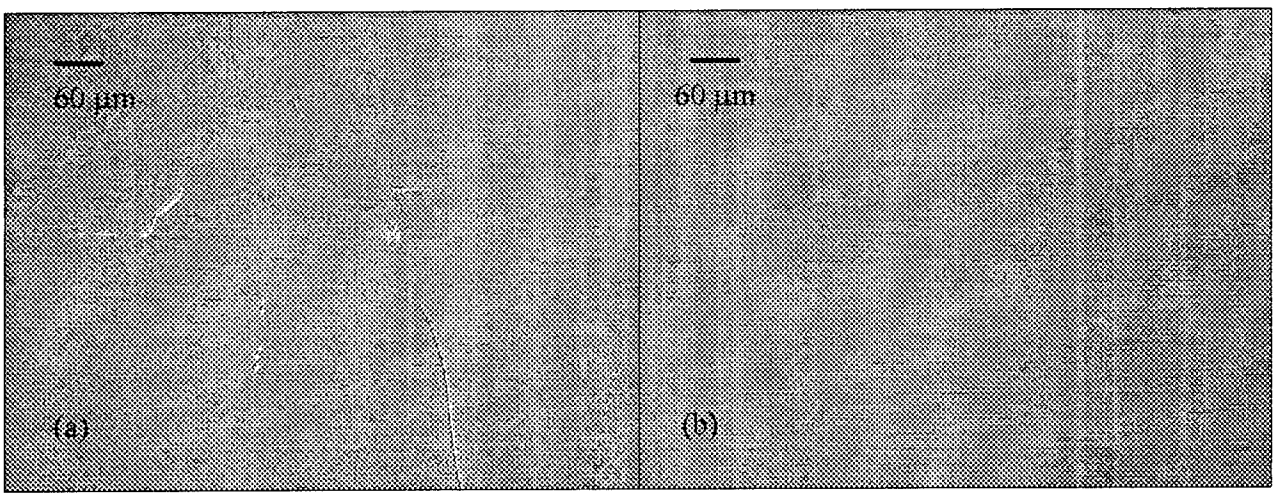

Fig 3.1 Nomarski micrograph of surface morphology from growth run 99-4H-200. (a) sample U036-09B showing fine scratch defects and (b) sample X0127-11B showing excellent surface quality.

All of the epi, except sample U036-09B, turned out to have good surface morphology and doping density. Due to the cracks present in the film grown on U036-09B, we did not attempt to measure CV. As U036-09B was grown simultaneously with sample X0127-11B we conclude that the cause of the film cracks must be related to surface preparation used. Of course, there may be some other explanation but this seems to be the only logical conclusion. Perhaps a more detailed understanding of the surface preparation conducted at AFRL prior to epi growth would

lend insight into the mechanism for these defects, which have never been observed in the EMRL reactor.

After growth the samples were shipped to Dr. Bill Mitchell of AFRL for evaluation. Dr. Jeff Brown of AFRL performed AFM measurements on these same samples, as shown in Figure 3.2 below. In all cases except one defects were observed to be present in the film. The one case where morphological defects were not observed was the case for CMP without an oxidation.

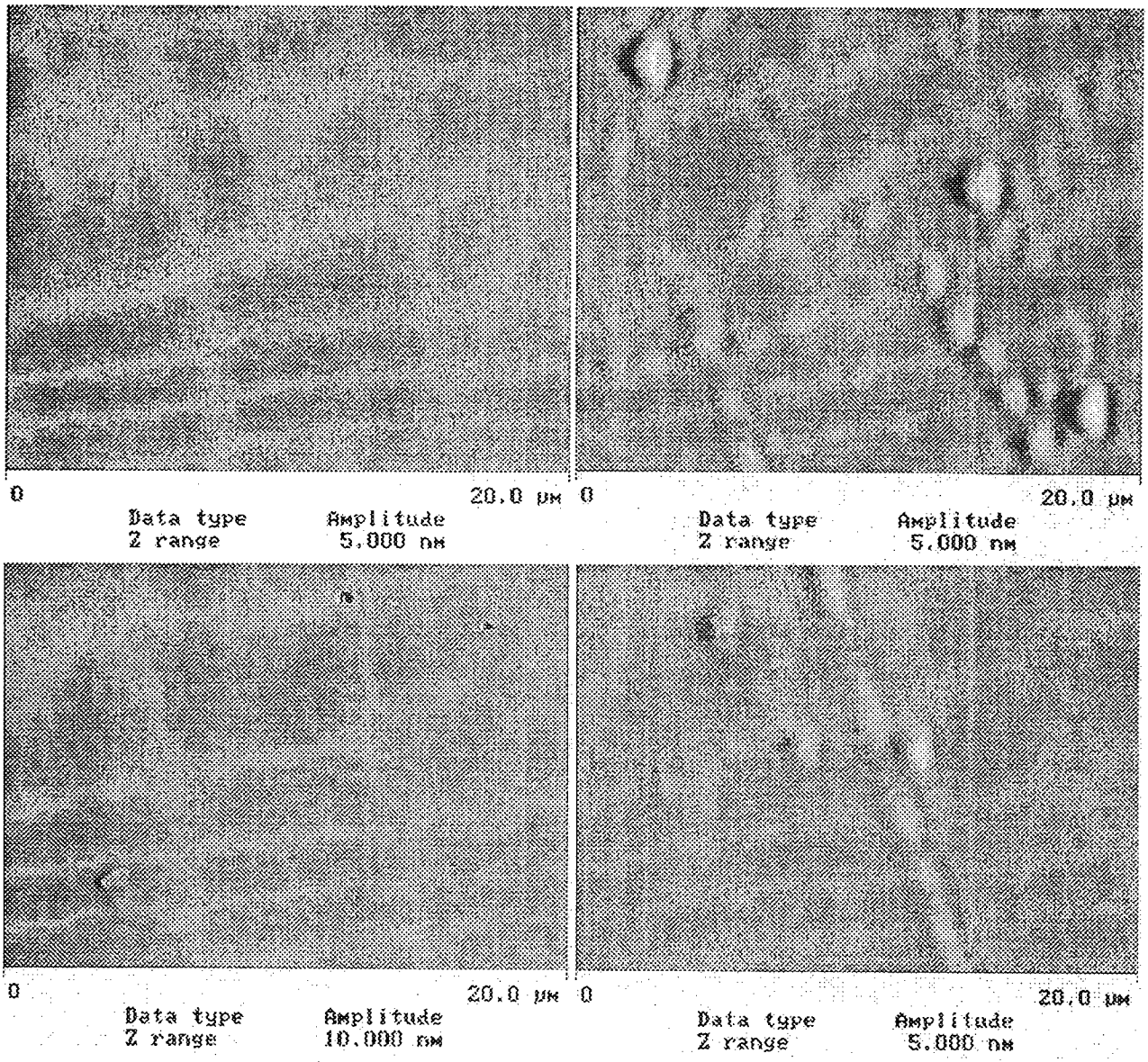

Fig 3.2 Atomic Force Microscopy data taken a AFRL on MSU epi samples listed in Table 3.1. (a) U0326-09A, (b) U0326-09B, (c) X0127-11A and (d) X0127-11B. Note that the epi layer with the best surface was case (a) which was for the substrate processed with CMP only (no oxidation).

4. Future Work

The implant annealing process developed by the author at EMRL was established in the smaller 35 mm CVD reaction tube with excellent results. EMRL now has a 75 mm CVD reactor on-line and work is on-going to transition these results to the larger tube. When successful EMRL will be in the unique position to anneal whole wafers (of up to 3" diameter) using the silane overpressure process. It is anticipated that this research will be completed during the next few months (spring semester 2000) and thus available to AFRL and other DoD researchers for use in their device research programs. The one piece of information, namely the resulting channel mobility for power MOSFET's processed with this technique also needs to be studied. In anticipation of this need, ONR is currently funding EMRL to fabricate power MOSFET's in collaboration with GE-CRD. Once this work has been completed, the results will be forwarded to AFRL for dissemination to the SiC community.

The CMP work studied as part of this grant clearly has lent some insight into how the surface properties of the substrate affect subsequent epi morphology. Clearly a more detailed investigation of the epi quality and the substrate-epi / interface is needed to quantify the impact of surface treatment on epi morphology and subsequent device performance. Indeed, samples have been delivered to AFRL for TEM investigation of the substrate/epi interface in an attempt to look at the defect structure emanating from interface. This should provide more insight to the problem and aide AFRL in the continuing improvement of their CMP methods.

5. References

[1] M. Capano, S. Ryu, M. R. Melloch, J. A. Cooper, and M. R. Buss, *J. of Elec. Mater.*, Vol 27, No.4, 1998.

[2] J. Tan, J.A. Cooper, Jr., and M.R. Melloch, IEEE Elect. Dev. Letters, Vol. 19, No. 12, Dec. 1998.

[3] S.T. Sheppard, M.R. Melloch, and J.A. Cooper, Jr., IEEE TED, Vol. 41, No. 7, p. 1257, July 1994.

[4] D. M. Brown, E. Downey, M. Ghezzo, J. Kretchmer, *et al*, *Phys. Stat. Sol. (a)*, Vol. 162,. No. 459, 1997.

[5] M. A. Capano, S. Ryu, J. A. Cooper, M. R. Melloch, K. Rottner, S. Karlsson, N. Nordell, A. Powell, and D. E. Walker, *J. Electronic Materials*, Vol. 28, No. 3, 1999.

[6] K. Jones, K. Xie, D. W. Eckart, M. C. Wood, *et al*, *J. Appl. Phys.*, Vol. 83, No. 12, 1998

[7] M. Spencer WOCSEMMAD 1999, New Orleans, LA, Feb 1999.

[8] J. Williams, private communication at ICSCRM'99, RTP, NC Oct 1999.

[9] S.E. Saddow, M.S. Mazzola, S.V. Rendakova, V.A. Dmitriev, *Matr. Science &. Engr. B*, B61-62, (1999).

[10] S. E. Saddow, M. Capano, J. A. Cooper, M. S. Mazzola, J. Williams and J. B. Casady, "High Temperature Implant Activation in 4H and 6H-SiC in a Silane Ambient to Reduce Step Bunching, " International Conference on SiC andRelated Materials (ICSCRM), Raleigh, NC, Oct 1999.

COMPUTATIONAL STUDY OF UNSTEADY FLOW INTERACTIONS BETWEEN CYLINDER WAKES, TURBINE BLADES, AND COOLANT INJECTION

Paavo Sepri
Associate Professor
Aerospace Engineering Program
Division of Engineering Sciences

Florida Institute of Technology
150 West University Boulevard
Melbourne, FL 32901-6988

Final Report for:
Summer Research Extension Program
Wright Patterson Research Site
Turbines Branch

Sponsored by:
Air Force Office of Scientific Research
Bolling Air Force Base
Washington, DC

and

Florida Institute of Technology
Melbourne, FL

February 2000

COMPUTATIONAL STUDY OF UNSTEADY FLOW INTERACTIONS BETWEEN CYLINDER WAKES, TURBINE BLADES, AND COOLANT INJECTION

Paavo Sepri
Associate Professor
Aerospace Engineering Program
Florida Institute of Technology

ABSTRACT

In the decreased Reynolds number regime associated with high altitude flight, the low-pressure turbine stages of modern aircraft suffer losses of efficiency as the suction side boundary layer becomes prone to flow separation. Computational results are presented utilizing the code VBI2D to demonstrate flow interactions between wakes generated by an upstream cylinder stage, a stage of Langston turbine blades, and coolant injection from within the turbine blades at a mid-chord station. It is shown that minor coolant pulsations at a frequency commensurate with the otherwise occurring bluff-body vortex shedding from the turbine blade can have the beneficial effect of retarding flow separation. Higher frequency pulsations do not seem to promote this desired effect. The computations also reveal that the blade lift is decreased periodically by the upstream passage of the cylinder wakes, and that minor pulsations in lift are discerned from the passage of cylinder vortices past the turbine blade. In an effort to explain a computed insensitivity of the total pressure loss coefficient, Y_p, to flow separation, a limiting analytical model is formulated for flow past a turbine stage. The model does indeed demonstrate that a loss in turbine power may not be well correlated with an increase in Y_p. It is shown that the loss in flow deflection associated with flow separation is compensated by a decrease in turbine blade drag, thereby tending to maintain a constant level of the total pressure loss coefficient. The model also demonstrates that an isentropic flow process has a character that is similar, although not identical, to processes which preserve Y_p. The model provides thermodynamic boundaries in the parametric space of flow deflection and imposed drag, to which a real flow should adhere.

COMPUTATIONAL STUDY OF UNSTEADY FLOW INTERACTIONS BETWEEN CYLINDER WAKES, TURBINE BLADES, AND COOLANT INJECTION

Paavo Sepri

INTRODUCTION

Context

This research report contains results obtained during the AFOSR 1999 Summer Research Extension Program (SREP) in supplement to the results obtained during the 1998 Summer Faculty Research Program (SFRP) by the author at the Wright-Patterson Research Site. The status and results of the SFRP research period have been reported previously by Sepri [1]. The main subject of the research has been comprised of computational simulations of unsteady flow interactions between a specific turbine blade configuration and wakes generated by upstream engine components, here simulated by a stage of cylinders. A specific topic of recent concern has been the loss of efficiency of low-pressure turbines operating at higher altitudes, at which the suction side boundary layer separates as the corresponding Reynolds number decreases. During the SFRP research, upstream wakes were computationally generated by a stage of moving cylinders, from which both periodic wake deficits and disturbances due to vortex shedding introduced flow effects on the downstream turbine blade stage. During the SREP research period, surface blowing has been added to the configuration in order to simulate a possible mechanism for alleviating the effects of flow separation.

The VBI2D [2,3] code was utilized earlier to compute a sequence of unsteady flows in which the Reynolds number (based on turbine blade chord) was decreased from 660K to 16.5K in six increments. In the SREP period, three additional Reynolds number cases have provided intermediate results to aid in identifying conditions of flow separation. The computational simulations have corresponded to typical laboratory conditions at the high Reynolds number end, and to higher altitude conditions (through stagnation pressure reductions that correspond to decreasing density) at the low Reynolds number end. In each run, after iterations had reached an approximately periodic condition, output was generated at twenty equal time intervals (reduced to ten during the SREP period) during one cycle of wake passages from the cylinders to the turbine blades.

The main issues which were identified from VBI2D computations during the SFRP period, and which provided focus for the present study have been as follows:

(1) Unsteady flow separation was demonstrated to occur on the suction side of the turbine blades at the lower Reynolds numbers, whereas negligible separation occurred at the higher Reynolds numbers, as expected.

(2) The passage of upstream wake defects caused significant swings (+/- 20 deg.) in the effective angle of attack of the flow approaching the turbine blade nose-tip.

(3) Surface skin friction plots demonstrated oscillating separations to occur on the turbine blade, that were assumed to be associated with vortex generation from the blade suction side itself.

(4) Plots of the turbulent viscosity coefficient, as produced within the limitations of the Baldwin-Lomax model, indicated that the main transition to turbulence occurs near the suction side mid-chord at higher R_e, but that the boundary layers are laminar at the lower values of R_e.

(5) Typical surface pressure plots indicated that separation causes decreases in both turbine blade lift (associated with turbine power output) and its stream-wise drag, which was somewhat unanticipated, but further considerations provided a plausible provisional explanation for the effect.

(6) At a Reynolds number of approximately 33K, a remarkable excitation of downstream oscillations in the turbine blade flow-field occurred. While the turbine blade exhibited mild oscillations in lift at higher R_e, which were at the same frequency as the vortices shed from the cylinders, at the lower R_e the oscillations were at a lower frequency. This event was initially assumed to correspond to a state of resonance at a sub-harmonic of the cylinder vortex shedding. Results from the SREP research period now indicate that these oscillations are consistent with vortices normally shed from a bluff body of larger size.

(7) The strong oscillations at lower R_e also produced large swings in the stagnation pressure loss coefficient (Y_p), so that Y_p even became negative at times. Such an occurrence was not initially anticipated, since negative excursions are associated with power production, rather than extraction. The graphs demonstrated that the swings in Y_p also coincided with the oscillations in the turbine blade lift.

(8) Cycle averaged pressure loss coefficients were graphed as a function of R_e. Contrary to initial expectations, Y_p did not exhibit a rapid rise at the lower Reynolds numbers. It was thought that an increase in Y_p would be an indication of loss in turbine efficiency due to flow separation. Although the trend in Y_p did not exhibit such a loss, it was clear from the decrease in lift that the turbine does indeed suffer a loss in extracted power.

(9) A simplified analytical model was created and presented to aid in the interpretation of the numerical results. The model does indeed show that Y_p need not vary significantly, provided both flow deflection and drag decrease simultaneously as flow separation occurs.

Objectives of the Present Research

The overall objective of the continuing research has been to study the effects of unsteady forcing on the flow-field environment of the turbine blade computationally. A major part of the present work has been to modify the VBI2D code so as to incorporate coolant mass injection (film cooling) from the interior of the turbine blade in order to influence boundary layer development on the suction side of the turbine blade. This has added a new feature to the code, which had not been implemented earlier. The mass injection component could also be used to analyze a mechanism for thermal protection of the turbine blade, although the present work has not focussed on this aspect. Rather, steady and unsteady blowing have been used to study the influence of transpiration on suction side boundary layer separation. As VBI3D (the three-dimensional version of the code) is developed further in the future, the two-dimensional mass injection may be extended to the more realistic cases of film cooling from an array of surface holes, although the 3-D extension is not part of the present SREP study.

The specific objectives of the research during the SREP period have fallen into three categories. First, of the seven Reynolds number runs yielding detailed data from the SFRP period, only three cases (16.5K, 33K, and 660K) had been scrutinized at an intermediate level of depth. Within the data-base that had been established, it has been of interest to explore the transition from high R_e behavior to low R_e behavior more fully, and to supply further runs at carefully selected intermediate conditions. Of particular interest, and of practical importance, is the question of possible resonance of turbine boundary layer flow with periodic oscillations generated by upstream engine components. A tantalizing indication of this phenomenon was observed earlier in the computations at a Reynolds number of 33K. In the present study, additional runs have been compiled at Reynolds numbers of 82.5K, 49.5K, and 24.75K. From these cases, and from information gathered from other published research, it now appears that the violent oscillations are not attributable to a resonance phenomenon per se, but rather they arise as the turbine blade enters into a flow regime that is consistent with vortex shedding from a bluff-body.

The second objective of the research deals with the modification of VBI2D to include mass injection from the interior of the turbine blade. This has been accomplished by utilizing the existing Langston blade geometry, and by creating surface blowing at a prescribed location. Initially, it had been desired to create an interior cavity meshing that would merge the interior flow with the exterior meshing via extensions of the interpolation schemes already used in the code for the exterior meshes. However, this procedure has not yet been implemented owing to time constraints imposed as a result of delays in transmitting an operational version of the VBI2D code to Florida Tech. Nevertheless, the simpler modeled surface transpiration presented herein has lead to computational results that shed more light on the flow separation phenomenon. As noted by Abhari [4], the mass flow rate of the coolant is influenced by fluctuations of pressure in the external flow, which may cause choking and unchoking of the injected flow if the pressure differentials are large. This complication is circumvented in the present computations, since a velocity distribution is prescribed on the blade surface. The effects of injection can be investigated by varying the mass flow rate, the injection angle, the flow distribution, and the time variation of the injection. In this study, different cases have been run to simulate the effects of periodic coolant flow pulsations as well as steady injection and suction on the suction side boundary layer of the turbine blade. Three different frequencies of pulsation have been investigated, and the results demonstrate that flow separation can be mitigated through this mechanism.

The third objective of the research involves continuation of the development of a simplified analytical model to describe the effects of flow separation on turbine performance. In the SFRP report by Sepri [1], the model was first presented in terms of parametric variations of flow deflection angle and a dimensionless expression for drag. The model has provided valuable insight to the interpretation of pressure loss coefficient, as calculated in the VBI2D cases. Here, a more complete extension of this model has been recorded. The model demonstrates that flow separation can indeed cause a loss in turbine power, while the pressure loss coefficient need not be an accurate indicator of this loss in efficiency.

Background

Recent articles contain descriptions of both experimental and computational investigations of vane/blade flow-field interactions. Dorney et al. [5] compare the development of a computed suction side boundary layer with experimental results. They comment that unsteady wakes from upstream vanes can have the effect of increasing the boundary layer displacement thickness on the blades. This effect, along with possible flow separation in the low Reynolds number regime, can cause a loss of efficiency, such that measured low-pressure turbine efficiencies at cruise conditions can be two points lower [5] than those at take-off. Three-dimensional computations of coolant ejection from leading-edge slots and shower-heads have recently been published, among which are those of Bohn et al. [6]. It is pointed out that accurate aerodynamic results depend on detailed meshing and flow-field computations of the interior plenum and passageways, since the surface exit conditions can be quite complicated. In their investigation, only a steady-state flow is computed. Among their conclusions is the observation that the passage vortex can have a strong displacement effect on the coolant flow away from the corner region towards the blade mid-span. Another recent investigation involving turbine blade blowing is the one by Brookfield and Waitz [7]. Here, a reduced-scale experiment was conducted for the purpose of reducing turbomachinery fan noise through mild blowing from the trailing edge of a turbine blade. The blowing reduces the wake deficit, which impinges on downstream stator components, thereby reducing the magnitude of acoustic pulsations. Thus, these articles describe cases of flow interactions that have relevance to the present investigation, in which the coolant injection has been imposed mid-way from leading edge to trailing edge on the suction surface.

Another category of relevance deals with oscillatory disturbances introduced into the flow around a turbine blade. These fall into three categories: (1) periodic excitation by either flaps, wires, or ribbons within the boundary layer, (2) an external acoustic excitation, and (3) periodic blowing from the interior of the turbine blade. Nishri and Wygnanski [8] have introduced periodic excitations by placing a small flaperon upstream of a highly deflected flap downstream of a plate boundary layer. Experiments demonstrate that the degree of separation on the flap can be significantly reduced through disturbances from the flaperon. This effect is shown to be sensitive to the frequency of excitation, and it appears to be most effective for a frequency corresponding to that of displacement of flow along the length of the body. In an earlier experiment, Katz et al. [9] have demonstrated a similar delay of separation on a flap in which the excitation was introduced by an oscillating flap placed considerably outside of the boundary layer. Nishri and Wygnanski also make the observation that periodic forcing is much more effective than steady blowing for the purpose of boundary layer control. This observation is in agreement with results of the computations presented herein. In an earlier work, Bar-Sever [10] introduced disturbances by oscillating a wire within a boundary layer, with the main conclusion that flow separation over an airfoil can be significantly delayed as the angle of attack is increased. In the subject of acoustic excitation, Zaman et al. [11] performed wind tunnel experiments in which a boundary layer over an airfoil (chord Reynolds number in the range 40K – 140K) was influenced by externally generated acoustic signals within the tunnel. The response was found to be frequency dependent, with significant improvement in delaying separation in some cases. However, it has become apparent that acoustic

resonances within the wind tunnel also have a significant influence on these results. An earlier work by Collins and Zelenevitz [12] also demonstrated that acoustic signals may trip a laminar boundary layer at an earlier stage than otherwise, producing a turbulent boundary layer that tends to remain attached. In all of these techniques, it appears that the oscillating transverse velocity component, v', near the surface, increases the tendency for mixing with the external stream, thereby acting to delay separation.

Experiments dealing with oscillatory blowing from interior cavities within an airfoil configuration have been performed by Seifert and Pack [13] and Seifert et al. [14]. The former experiment was conducted in a pressurized, cryogenic wind tunnel, so that results of earlier experiments could be extended to a higher chord Reynolds number regime, namely, 38 million. In accord with the lower Reynolds number results, oscillations that produced one to three vortices over the controlled surface delayed stall when the blowing was introduced near the leading edge region of the airfoil, and over the flap surface when introduced at the flap shoulder. It is remarkable that oscillatory blowing with essentially no net mass transfer seems to be considerably more effective at a lower amplitude of mass transfer than steady blowing at a larger rate of mass transfer. Seifert et al. [14], in an earlier experiment, introduced oscillations both near the leading edge of an airfoil and oscillatory blowing from a chamber near the shoulder of a deflected flap. The overall result is that oscillatory blowing increases lift and decreases form drag in a wide range of Reynolds numbers.

During the SFRP research period, computations with the VBI2D code seemed to indicate that a resonance might possibly occur within a Reynolds number range near 33K, as large oscillations in lift were observed for the turbine blade, which appeared to diminish somewhat at lower Reynolds numbers. In the present investigation, flows at several other neighboring Reynolds numbers have been computed with the aim of seeking out the possible resonance. However, it has become apparent that these lift oscillations may be attributed to vortex shedding from the turbine blade itself, which acts like a bluff-body owing to its large camber when the Reynolds number is reduced below a critical level. In two articles [15,16], Griffin reviews the nature of vortex streets generated behind bluff-bodies, and discusses a universal similarity rule for shedding frequencies based on characteristic lengths and velocities in the vicinity of the body. From the VBI2D computations, it is consistent that the lift oscillations fall into the frequency range of a bluff-body with an effective wake width displayed by the cambered airfoil.

The Vane-Blade Interaction (VBI) code has been developed by several investigators [2,3,17,18] at the Allison Engine Company under contract to the United States Air Force. The earlier two-dimensional version (VBI2D) has recently been extended to include 3-D unsteady computational capability, although this latter version is still under evaluation. In a previous study, Rivir et al. [19] utilized the VBI2D code to calculate flow fields for Langston [20,21] turbine blade cascades in the steady state mode and without wake effects for a variety of Reynolds numbers and cascade solidities. The code incorporates the Baldwin-Lomax [22] two-layer algebraic turbulence model. Among other results, it was observed that the Langston cascade (at the original pitch to chord spacing of

0.93) demonstrated separation at Re=50K, oscillating transition at 100K, and attached flow for higher Reynolds numbers.

Experimental investigations of flow in turbine passages have recently been reported by Blair [23], Baughn et al. [24], and Murawski et al. [25]. Blair has noted the several regions of high heat transfer produced by three-dimensional flow effects within the rotor passage, and has measured the effects of wall roughness on heat transfer. Furthermore, he discusses the sensitivity to changes in Reynolds number and inlet flow angle. Baughn et al. present comparisons of linear cascade experiments performed at UC Davis and the USAF Academy. The cascade geometries are similar to those of earlier tests performed by Langston et al. [20] and Graziani et al. [26] in linear cascades, and also to those of Dring et al. [27] and Blair et al. [28] in rotating tests. In the Reynolds number range of 67K to 144K, Baughn et al. note that an elevated level of free-stream turbulence influences the flow in augmenting heat transfer, advancing the location of transition, and removing observed flow striations from the blade pressure side (presumably caused by Görtler vortices). Furthermore, at the lower Reynolds numbers, evidence is presented of boundary layer separation on the blade suction side. Murawski et al. performed experiments in the linear, 2-D airfoil cascade at AFIT at Wright Patterson Air Force Base. The Reynolds number (based on exit velocity and suction surface length) was varied in the range of 50K to 300K, and the level of free-stream turbulence (FST) was varied in the range of 1.1% to 8.1 %. Separation on the suction surface was observed for all Reynolds numbers, with a shrinkage of the separation zone with increasing Reynolds number and increasing turbulence level. Wake surveys with a hot film have indicated that the width of the wake decreases with an increase of FST, and that it also decreases slightly with increasing Reynolds number. These trends are demonstrated to correlate well with the measured decreases in pressure loss coefficient as Reynolds number is increased. Calculations using the VBI2D code also indicate this trend of decreasing loss coefficient, although the effect of elevated FST is not included in the calculations, and the numerical results appear to underpredict the experimental values in some cases.

Among the many other studies of flow in turbine blade passages are those of Hodson [29], and Zaccaria and Lakshminarayana [30]. At Cambridge University, Hodson has measured velocities and surface pressure distributions by means of instrumentation fixed to the rotor system, so that time-resolved influences of stator wake passages could be directly observed. It is concluded that the main effects of unsteadiness can be associated with the periodic convection of the wakes through the blade passage. An interpretation of the origin of blade surface velocity fluctuations is offered, although it is also stated that the phase variations of the pressure distributions along the blade surfaces are not understood. At the Axial Flow Turbine Research Facility at Pennsylvania State University, Zaccaria and Lakshminarayana have utilized a two-dimensional LDV system to measure both time-resolved and cycle-averaged wake flow properties in a rotor passage. Among other observations, it is noted that wake interactions with the rotor leading edge cause considerable downstream influences as the wake introduces significant swings in the effective angle of attack.

Discussions of several other pertinent references have been included in the earlier report by Sepri [1], and these will not be repeated herein.

RESEARCH DESCRIPTION

Computational Methodology

The computer code used for the present study has been developed earlier by several investigators [2,3,17,18] at the Allison Engine Company under contract to the United States Air Force. The version that is applied to this continued study is designated VBI2D, as it calculates vane-blade flow interactions in a two-dimensional unsteady manner, utilizing a Reynolds-averaged compressible viscous flow model. Specifics of the computational methodology and operating procedures are described by Rao et al. [2,3]. Briefly, an O-grid system surrounds each vane or blade element, and the O-grid is embedded into an outer H-grid, which is contoured to conform to the main passages between the elements constituting each row of vanes or blades.

The overall geometry is taken to be that of an axisymmetric body of revolution, along which the fluid flows tangent to stream-surfaces. Specific vane and blade geometries are defined through further transformations, while the flow is restricted to lie within the stream-surfaces, thereby eliminating the possibility of 3-D flow. The vane and blade grid systems may be stationary, or may be in relative rotation. Interpolation procedures are used to transfer data between the overlapping O- and H- grids, as well as the overlapping vane and blade H-grids. The numerical method utilizes a five-stage Runge-Kutta scheme with implicit residual smoothing. Turbulence is modeled with the Baldwin-Lomax [22] two-layer algebraic eddy viscosity model. The computational procedure has consisted of an initial run in the steady state mode to set up an approximate flow condition (typically 2000 iterations were used), followed by runs in unsteady mode to set up the time dependent flow. The unsteady runs have been performed in sections of 40,140 iterations, each of which comprises a complete cylinder passage cycle. During this time period, output has been generated at ten equal time intervals for each R_e case, in order to resolve flow variations within each cycle. At the end of each cycle, a RESTART file is written, which provides input for the next cycle, so that a continuous time evolution can be obtained without starting from the beginning each time.

Code Modifications

A section of the turbine blade surface was chosen to be the source of transpiration from the blade interior. Initially, it had been desired to model a complete interior cavity with a passage to the blade surface. However, owing to time considerations, it has been expedient to take the simpler route of prescribing a surface boundary condition for the velocity field that would simulate a flow from the interior. Although this approach does not model an accurate entry condition, it does introduce an unsteady perturbation to the exterior flow that can be controlled in frequency, amplitude, and direction. The slot location on the blade surface was chosen to be approximately at mid-chord and of a length that is approximately 15% of the chord ($21 \leq I \leq 30$). The location of the transpiration may be observed in Fig. 20. The injection velocity profile was modeled to have a sine-squared distribution in space, so

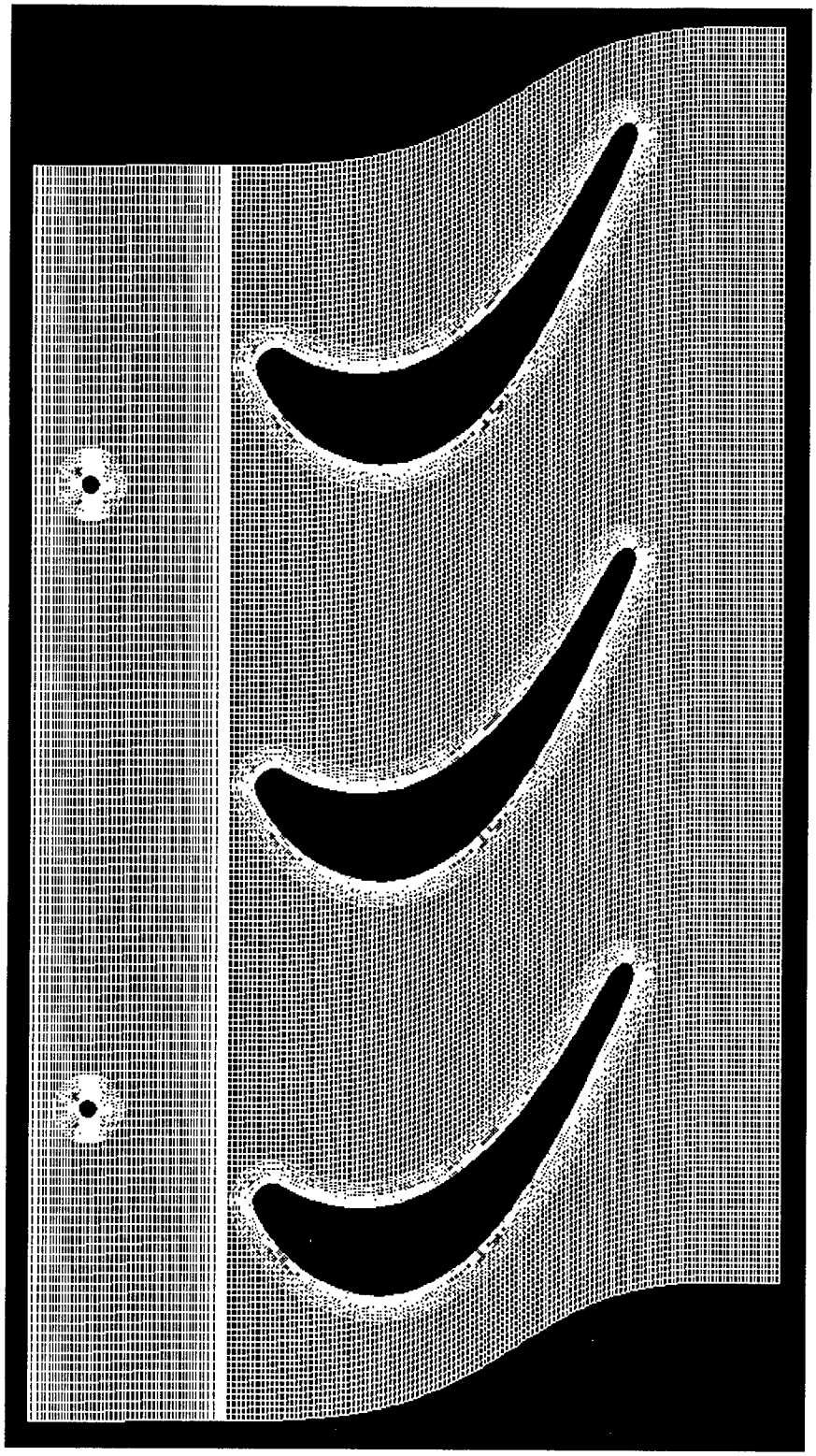

Figure 1: Cylinder/Langston Blade Geometry and Computational Grids.

as to vanish at the edges of the slot, producing a boundary layer type effect for the flow from the interior. The flow direction with respect to the local surface could be altered, and the amplitude and frequency of the transpiration could also be prescribed. The computational grid used for both the SFRP and SREP studies is shown in Fig. 1.

Computational Cases

During both research periods, the geometry has consisted of an upstream row of circular cylinders (R = 0.1 in) and a downstream row of Langston turbine blades (axial chord 4.0 in). The solidity (ratio of pitch to axial chord) was chosen to be 1.075 to conform with a recent experiment [24] at the Air Force Academy. Each spatial period has consisted of two cylinders upstream of three turbine blades, as may be deduced from Fig. 1. In all cases, the blade row was held stationary, while the upstream cylinders were set in motion, in order to produce the passage of wakes. The upstream flow incidence, with respect to the horizontal, was chosen to be 45°, close to the conditions of previous experiments. The axial and circumferential inlet Mach number components were taken to be 0.2, producing a total Mach number of 0.2828. The circumferential Mach number of the cylinders was taken to be 0.1, while for the last series of the SFRP period it was set at -0.1. The upstream stagnation temperature was specified to be 520 °R. In order to simulate the change in Reynolds number that occurs with increasing altitude, the upstream total pressure was varied in several increments from a maximum of 14.7 psia to a minimum of 0.3675 psia. The corresponding change in density results in a variation of axial chord R_e from 660K to 16.5K. During the SFRP period, computed output was extracted at twenty time intervals during one passage cycle of cylinder motion for seven Reynolds number cases (16.5K, 33K, 66K, 99K, 132K, 264K, 660K), and these were assigned case numbers as indicated in Table 1 of Reference 1. The VBI2D code has indicated 40,140 iterations to comprise one cycle in the present configuration.

During the SREP period, additional cases were run at Reynolds numbers of 24.75K, 49.5K, and 82.5K, as these were judged to provide further information at intermediate conditions that might demonstrate resonance instabilities triggered by upstream vortex shedding, and also to help determine the onset condition for severe flow separation on the turbine blade. Time evolutions for these three cases have been carried out for several cycles in order to assess the degree of cyclic repeatability and also to provide detailed evidence of flow differences due to changes in R_e. The case of R_e = 49.5K has appeared to provide a condition that is close to the boundary that divides separated from unseparated flows on the turbine blade. This case has been used for more extensive study, by continuing the computations after an Iteration Number of 240,840 with computations of altered boundary conditions in order to illustrate the effects of surface transpiration on the flow.

SIMPLIFIED ANALYTICAL MODEL

Basic Formulation

A simplified analytical model of flow through a turbine stage had been initiated during the SFRP period by the author. Here, that modeling effort is continued, and additional physical insight is offered to aid in the interpretation of the numerical results obtained from the VBI2D computations. In particular, total pressure generation and its connection to entropy is discussed. It is convenient to consider the following idealized model of steady 2-D flow across a turbine stage. The model is derived from considerations presented by Hawthorne [31] and private communications with Dr. Robert Gray [32].

Steady flow across an axisymmetric stator/rotor stage may be represented by the usual equations of mass conservation, momentum, energy, and fluid properties. Here, the geometry is taken to have the possibility of stream-surface flaring, as represented by the inlet radial thickness, b_1, and the exit radial thickness, b_2. The vanes and blades may either be stationary or in rotation, but it is assumed that the inlet and exit flows are circumferentially uniform and steady in an averaged sense. It is assumed that radial flow components are negligible. In a volume-averaged sense, in a stationary coordinate frame, the basic equations may be listed as follows in the commonly used notation for an arbitrary segment of the stage.

$$\rho_1 V_1 A_1 \cos(\beta_1) = \rho_2 V_2 A_2 \cos(\beta_2) = \dot{m}, \tag{1}$$

$$\dot{m}\left[V_2 \sin(\beta_2) - V_1 \sin(\beta_1)\right] = -F_y \tag{2}$$

$$\dot{m}\left[V_2 \cos(\beta_2) - V_1 \cos(\beta_1)\right] = p_1 A_1 - p_2 A_2 + F_x, \tag{3}$$

$$\dot{m}\left[C_p(T_2 - T_1) + \frac{1}{2}\left(V_2^2 - V_1^2\right)\right] = \dot{Q} - \dot{W}, \tag{4}$$

$$p = \rho R T. \tag{5}$$

Here, the cross-sectional area, A, may vary with stream-surface height, denoted by b. F_y and F_x represent net forces acting on the fluid in vertical and horizontal directions, respectively, as exerted by vanes and blades within the volume. The angle, β, represents the local flow angle relative to the axial direction, and it is taken to be positive in the downward direction relative to the horizontal. It is assumed that hub and end-wall effects are not included. The rotational rate of the turbine blades is represented by: $\overline{\Omega} = \Omega \bar{e}_x$. Accordingly, turbine power extracted from the flow is given by: $\dot{W} = \Omega R F_y$, and a possible heat transfer rate into the flow is represented by $\dot{Q}$.

For any stage, the basic equations may be transformed into a frame moving with the rotating system according to the usual vector decomposition, as follows:

$$V\cos(\beta) = U\cos(\alpha) \tag{6}$$

$$V\sin(\beta) = U\sin(\alpha) + \Omega R \tag{7}$$

With appropriate subscripts, these equations may be applied at either the inlet or the exit. Here, U and α represent the flow speed and relative flow angle as seen in the rotating frame. Upon squaring these expressions, combining at each station, and subtracting the totals at the two stations, one obtains:

$$U_1^2 - U_2^2 = V_1^2 - V_2^2 - 2\Omega R\left[V_1\sin(\beta_1) - V_2\sin(\beta_2)\right], \tag{8}$$

which may be combined with Eq. (2) to yield the following:

$$U_1^2 - U_2^2 = V_1^2 - V_2^2 - 2\Omega\frac{RF_y}{\dot{m}}. \tag{9}$$

Further substitution into Eq. (4) results in the energy equation as viewed in the rotor frame:

$$\dot{m}\left[C_p(T_2 - T_1) + \frac{1}{2}(U_2^2 - U_1^2)\right] = \dot{Q}. \tag{10}$$

The benefit of this procedure is that the turbine power term disappears in the rotor frame, in accord with the fact that the blades are stationary in this frame.

One may continue with this procedure to obtain an explicit parametric solution for the flow properties in the rotor frame. Substitution of Eq. (6) into Eq. (1) leads to the conservation of mass statement in the rotor frame of reference as follows:

$$\rho_1 U_1 A_1\cos(\alpha_1) = \rho_2 U_2 A_2\cos(\alpha_2) = \dot{m}. \tag{11}$$

The stream-wise momentum equation transforms to:

$$\dot{m}\left[U_2\cos(\alpha_2) - U_1\cos(\alpha_1)\right] = p_1 A_1 - p_2 A_2 + F_x. \tag{12}$$

Division by $\dot{m}u_1$ in Eq. (12) leads to the dimensionless representation:

$$\overline{U}\cos(\alpha_2) - \cos(\alpha_1) = \frac{1}{\gamma M_1^2 \cos(\alpha_1)}\left[1 - \frac{\overline{T}\cos(\alpha_1)}{\overline{U}\cos(\alpha_2)}\right] - \frac{d}{\cos(\alpha_1)}. \tag{13}$$

Here, the following notation has been introduced:

$$\overline{U} \equiv \frac{U_2}{U_1}; \qquad \gamma \equiv \frac{C_p}{C_v}; \qquad M_1^2 \equiv \frac{U_1^2}{\gamma R T_1}; \qquad \overline{T} \equiv \frac{T_2}{T_1}; \qquad d \equiv -\frac{F_X}{\rho_1 U_1^2 A_1}.$$

Similarly, the energy equation may be expressed in dimensionless form, as follows:

$$\overline{T} = 1 + q + \frac{\gamma - 1}{2} M_1^2 \left(1 - \overline{U}^2\right), \text{ where: } q \equiv \frac{\dot{Q}}{\dot{m} C_p T_1}. \tag{14}$$

Combination of Eqs. (13) and (14) leads to a single quadratic equation for the velocity ratio across the turbine stage:

$$A\overline{U}^2 - B\overline{U} + C = 0 \tag{15}$$

where: $A = \gamma M_1^2 \cos^2(\alpha_2) - \frac{\gamma - 1}{2} M_1^2$; $B = \frac{\cos(\alpha_2)}{\cos(\alpha_1)} + \gamma M_1^2 \cos(\alpha_2)\left[\cos(\alpha_1) - d\right]$; $C = 1 + \frac{\gamma - 1}{2} M_1^2 + q$.

The explicit relation for velocity ratio is then:

$$\overline{U} \equiv \frac{U_2}{U_1} = \frac{B - \left(B^2 - 4AC\right)^{1/2}}{2A}. \tag{16}$$

Here, d and q represent dimensionless drag and heating applied to the stage, respectively. Therefore, it is evident that the mean flow across the turbine stage depends on blade geometry (which influences flow deflection), drag (d), and heating (q), in addition to γ and M_1. Other flow properties may be explicitly obtained from the above representation in combination with the earlier equations, with the following results:

$$\overline{\rho} = \frac{\cos(\alpha_1)}{\cos(\alpha_2)}\left(\overline{UA}\right)^{-1}, \tag{17}$$

$$\overline{T} = 1 + q + \frac{\gamma - 1}{2} M_1^2 \left(1 - \overline{U}^2\right), \tag{18}$$

$$\overline{p} = \overline{\rho T} \tag{19}$$

$$M_2^2 = \frac{U_2^2}{\gamma R T_2} = M_1^2 \frac{\overline{U}^2}{\overline{T}}, \tag{20}$$

$$\overline{S} = \ell n\left(\overline{p}\right) - \gamma \ell n\left(\overline{\rho}\right), \text{ where: } \overline{S} \equiv \left(S_2 - S_1\right)/C_V. \tag{21}$$

It is perhaps more convenient to express the parametric solution in the stationary frame, since this corresponds to viewing a test engine for which the rotor speed can be varied. Furthermore, it is of interest to obtain an expression for the turbine power extracted in the process. Given inlet conditions for the turbine stage, β_1 and V_1, Eqs. (6) and (7) lead to the following relations:

$$U_1 = V_1 \left(1 - 2V_r \sin^2(\beta_1) + V_r^2 \sin^2(\beta_1)\right)^{1/2}, \tag{22}$$

$$\tan(\alpha_1) = \tan(\beta_1)\left[1 - V_r\right], \tag{23}$$

where :

$$V_r \equiv \frac{\Omega R}{V_1 \sin(\beta_1)} .$$

Here, V_r represents the ratio of turbine rotational speed to the vertical speed of the incoming flow. For a parametric variation of α_2 and d, Eq.(16) provides a solution for $\overline{U}$, from which flow properties in the stationary frame are obtained by the following relations:

$$\tan(\beta_2) = \tan(\alpha_2) + \frac{V_r}{\overline{U}} \frac{\cos(\alpha_1)}{\cos(\alpha_2)} \tan(\beta_1), \tag{24}$$

$$\overline{V} = \frac{V_2}{V_1} = \overline{U} \frac{\cos(\alpha_2)}{\cos(\alpha_1)} \frac{\cos(\beta_1)}{\cos(\beta_2)}, \tag{25}$$

$$C_L = 2\lambda\cos(\beta_1)\left[\sin(\beta_1) - \overline{V}\sin(\beta_2)\right], \tag{26}$$

$$\omega = 2V_r\sin(\beta_1)\left[\sin(\beta_1) - \overline{V}\sin(\beta_2)\right]. \tag{27}$$

Here,

$$\lambda = \frac{\text{pitch}}{\text{chord}} = \text{solidity}$$

$$C_L = \frac{F_y}{\frac{1}{2}\rho_1 V_1^2 S},$$

$$\omega = \frac{\dot{W}}{\frac{1}{2}\dot{m}V_1}.$$

The last of these terms, namely ω, represents the ratio of extracted turbine power to incoming kinetic energy flux. The pressure loss coefficient is expressed as follows as viewed in the stationary frame of reference:

$$Y_P \equiv \frac{P_{T_1} - P_{T_2}}{P_{T_1} - P_2} = \frac{\frac{p_1}{p_2}\left[1 + \frac{\gamma-1}{2}M_{V_1}{}^2\right]^{\frac{\gamma}{\gamma-1}} - \left[1 + \frac{\gamma-1}{2}M_{V_2}{}^2\right]^{\frac{\gamma}{\gamma-1}}}{\left[1 + \frac{\gamma-1}{2}M_{V_2}{}^2\right]^{\frac{\gamma}{\gamma-1}} - 1} \tag{28}$$

where,

$$M_{V_2}{}^2 = \frac{V_2{}^2}{\gamma R T_2} = M_{V_1}{}^2\frac{\overline{V}^2}{\overline{T}}$$

It is noted that the static pressure ratio is frame independent, whereas the Mach numbers depend on which frame of reference is utilized. Therefore, the pressure loss coefficient expressed in a stationary frame varies with the rotational speed of the rotor. Typical numerical cases are presented in the next section.

Analytical Results

The purpose of providing numerical results based on the simplified analytical model is to present guidelines to help interpret the output from VBI2D. In particular, during the SFRP research period, it was somewhat surprising that the total pressure loss coefficient did not exhibit a large increase upon flow separation at low Reynolds numbers, as had been anticipated. In this section, the model provides interpretations for: (1) total pressure and entropy, (2) lift coefficient and turbine power, (3) temperature and velocity, and (4) static pressure and density.

A series of computations has been performed in both stationary and rotating frames, in order to simulate a turbine stage operating at various speeds of rotation. The inlet conditions to the stage have been kept fixed at: M_{V_1} = 0.3, β_1 = 45 deg., in order to be representative of the VBI2D computations. Relative rates of rotation have been chosen to be: V_r = 0.0, 0.1, and 0.5, in order to simulate several conditions of turbine power. Conditions of flow separation, total drag, and surface heating are simulated by parametric variations of α_2 (exit flow angle in the rotating frame), d (dimensionless drag), and q (dimensionless heat input).

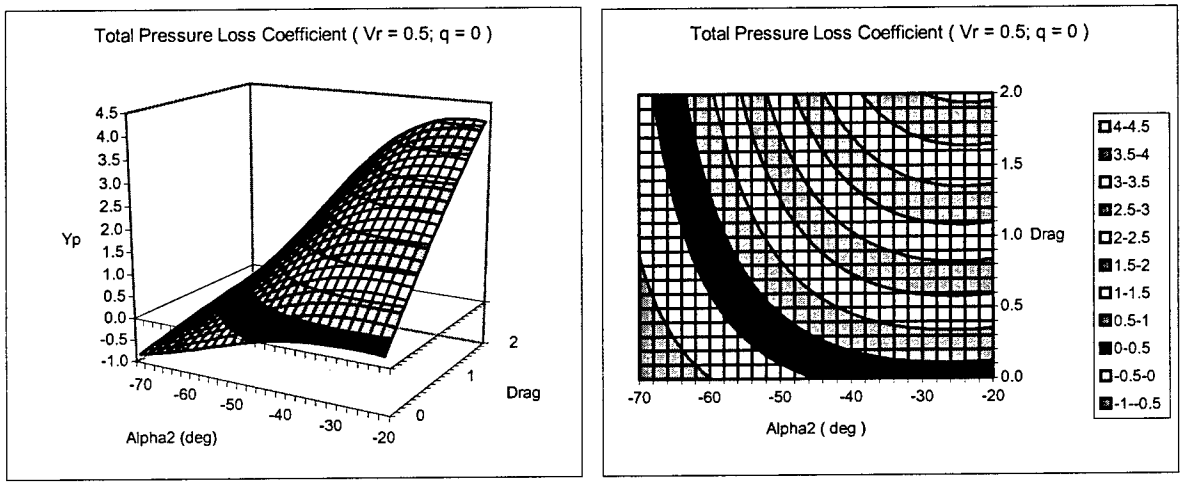

Figures 2a and 2b: Y_p Surface and Contours of Constant Y_p

The total pressure loss coefficient, Y_p (as computed from Eq. (28)), is shown in Figs. 2a and 2b for the case: V_r = 0.5 and q = 0.0. The first figure represents $Y_p(\alpha_2,d)$ as a curved surface depending on the exit angle and the degree of drag imposed on the flow by the blades, whereas the second figure represents the same case as a contour plot, displaying curves of constant Y_p. Of particular note is the curve Y_p = 0 (represented by the black-white interface), which separates the regions of positive and negative Y_p. Generally, as α_2 corresponds to a smaller flow deflection, the value of Y_p increases, and this is consistent with a flow undergoing separation on the blade suction side. Similarly, as the blade drag increases, there is an increase in the loss coefficient. However, owing to the large curvature of the turbine blade, it is reasonable that a separating flow will correlate with a decrease in blade drag, since the pressure differential suffers in both horizontal and vertical directions in this case. As a consequence,

Y_p may remain substantially unchanged in value as the flow transitions from an unseparated to a separated condition. This may be seen as a curve of constant Y_p in Fig. 2b. A similar plot of Y_p for the case $V_r = 0$ is shown in Fig. 3, and it is observed that the $Y_p = 0$ curve is relatively unchanged in location, although the rest of the Y_p values differ from those on Fig. 2b.

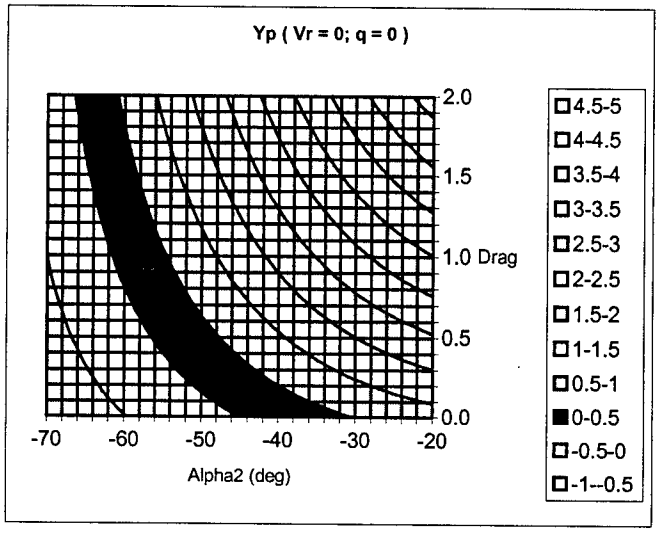

Figure 3: Y_p for a Stationary Turbine

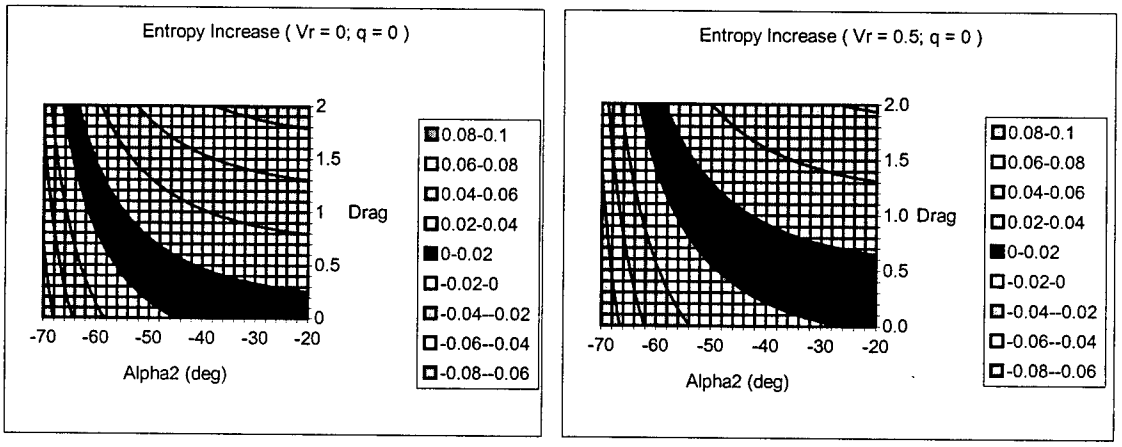

Figures 4a and 4b: Contours of Constant Entropy Increase

Corresponding plots for the change in entropy from inlet to exit are shown in Figs. 4a and 4b. It is remarkable that the curves for constant entropy and constant Y_p are quite similar to each other, although not identical. The curves corresponding to the cases of $\bar{S} = 0$ (refer to Eq. (21)) provide boundaries for flow conditions that are in accord with the Second Law of Thermodynamics for cases of no heating. Although it is possible for entropy to

decrease *locally* for a fluid element (especially in an unsteady context), a *global* increase would be in violation of this principle. Now, it is of interest to recall a result from the SFRP period [1], which is also presented in Fig. 28 herein. During one passage cycle of cylinders, the variation in Y_p is plotted for a case of severely separating flow at R_e = 33K. The oscillations in Y_p presumably correspond to flow separation and vortex shedding from the turbine blade itself, as correlated with the lift oscillations shown in Reference 1. It is remarkable that values of Y_p become negative occasionally, although the overall averaged value remains significantly positive. These local negative excursions for Y_p are likely to correspond to local decreases in entropy in the flow, although the overall result remains a net increase in entropy. One would expect the physically probable flow excursions to lie in the positive regions of $\bar{S}$. Another interesting effect involving entropy may be observed by comparing Figs. 4a and 4b. It is seen that as the rotor speed is increased (V_r = 0.0, 0.5), the $\bar{S}$ = 0 curve shifts towards smaller magnitudes of α_2, whereas there is a much smaller shift in the corresponding Y_p curve. The inference to be drawn is that the turbine stage operates at a higher total pressure loss as the rotor speed is increased in this range. Such an observation is in accord with the notion that the turbine extracts energy from the flow. Although figures are not presented herein, the model also shows that entropy levels are increased with heat addition, and decreased with heat extraction from the flow, as is to be expected from thermodynamic considerations.

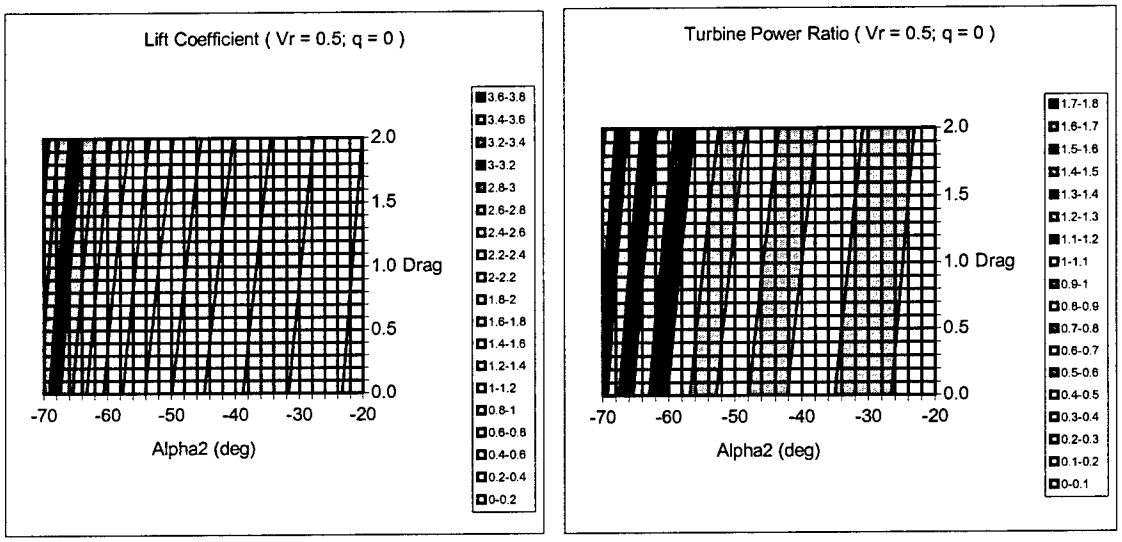

Figures 5a and 5b: Lift Coefficient on Turbine Blades and Turbine Power Ratio.

New plots concerning lift coefficient and power extraction are shown in Figs. 5a and 5b. These computations correspond to Eqs. 26 and 27, respectively. Since these two functions are seen to be proportional to each other, it is to be expected that the figures display similarity for a fixed rotor speed. However, the trends are somewhat opposite to those of Y_p and $\bar{S}$. Here, C_L increases as drag increases and it also increases with increasing flow deflection. In comparison with the Y_p graphs, it is seen that as the flow separates (decreasing both α_2 and d), the values of Y_p may remain nearly constant, but that power extracted by the turbine decreases rapidly, signifying a large loss of turbine efficiency. Clearly, this is associated with the loss in lift suffered by blades undergoing flow

separation. These results also seem to indicate that the use of Y_p as a measure of turbine efficiency may not be reliable in some circumstances.

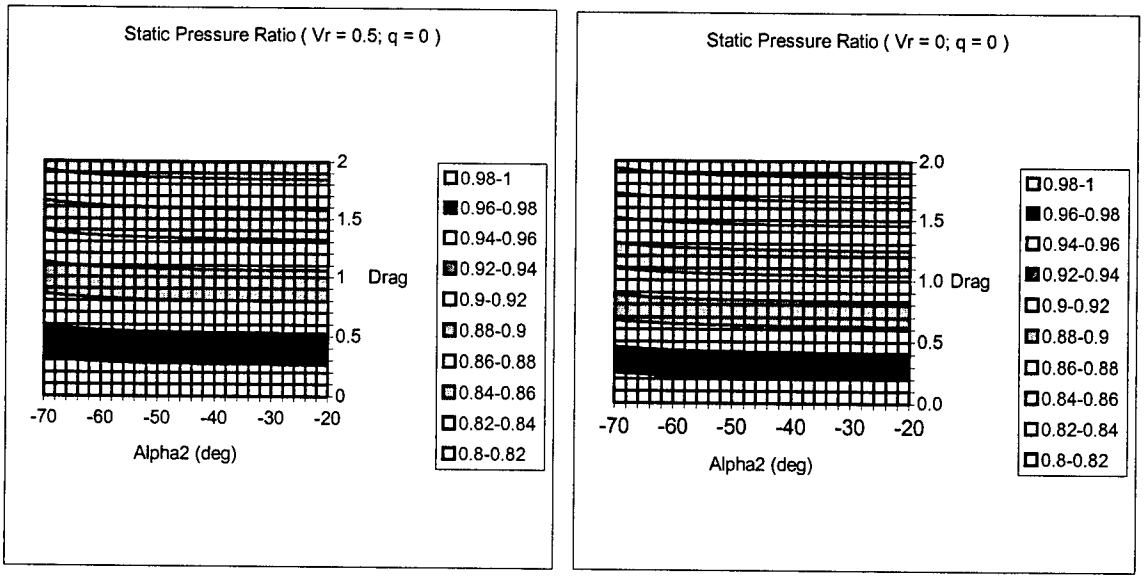

Figures 6a and 6b: Static Pressure Ratios for Turbines in Motion and Stationary.

In contrast to the plots of stagnation pressure, it is seen in Figs. 6a and 6b that the static pressure variation across the turbine stage depends primarily on drag, and that it is relatively insensitive to flow deflection. The temperature behaviors shown in Figs. 7a and 7b indicate isotherms that are relatively aligned with curves of constant lift.

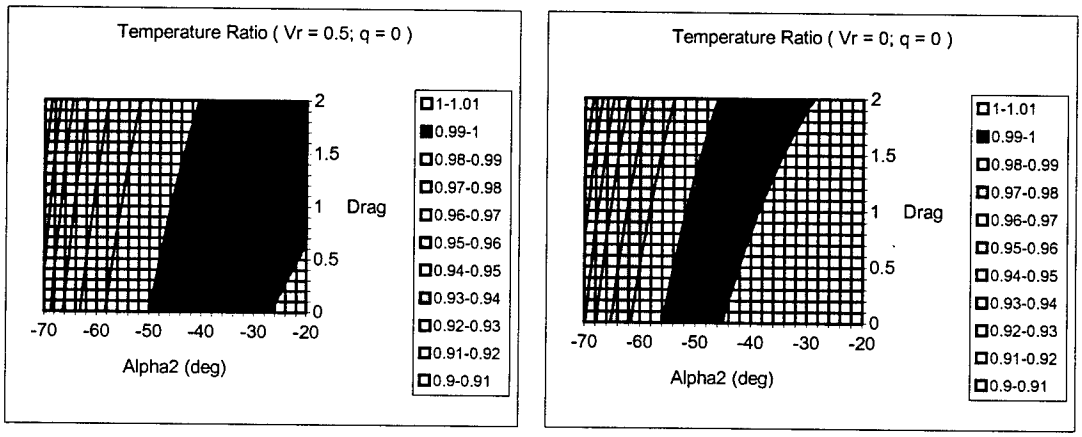

Figures 7a and 7b: Static Temperature Ratios for Turbines in Motion and Stationary.

Curves of constant density ratio (shown in Figs. 8a and 8b) are seen to be intermediate to those of static pressure and temperature. The plot corresponding to velocity ratio across the turbine stage (Fig. 9) contains a curve

of $\overline{V} = 1$, which divides the possible flow regimes into regions of relative deceleration and acceleration. Evidently, for cases of high drag and low flow deflection, the flow can decelerate while undergoing a decrease in density.

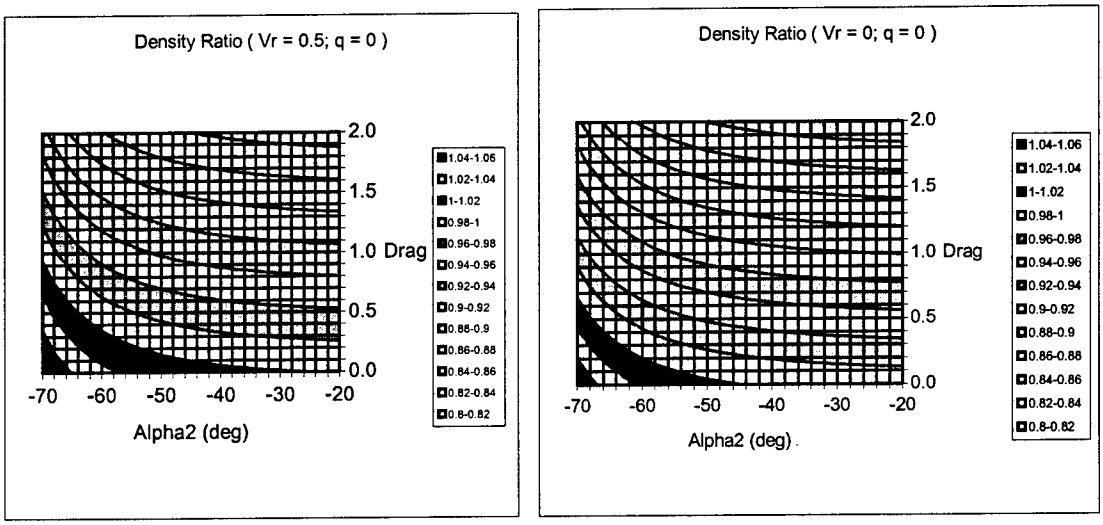

Figures 8a and 8b: Density Ratios for Turbines in Motion and Stationary.

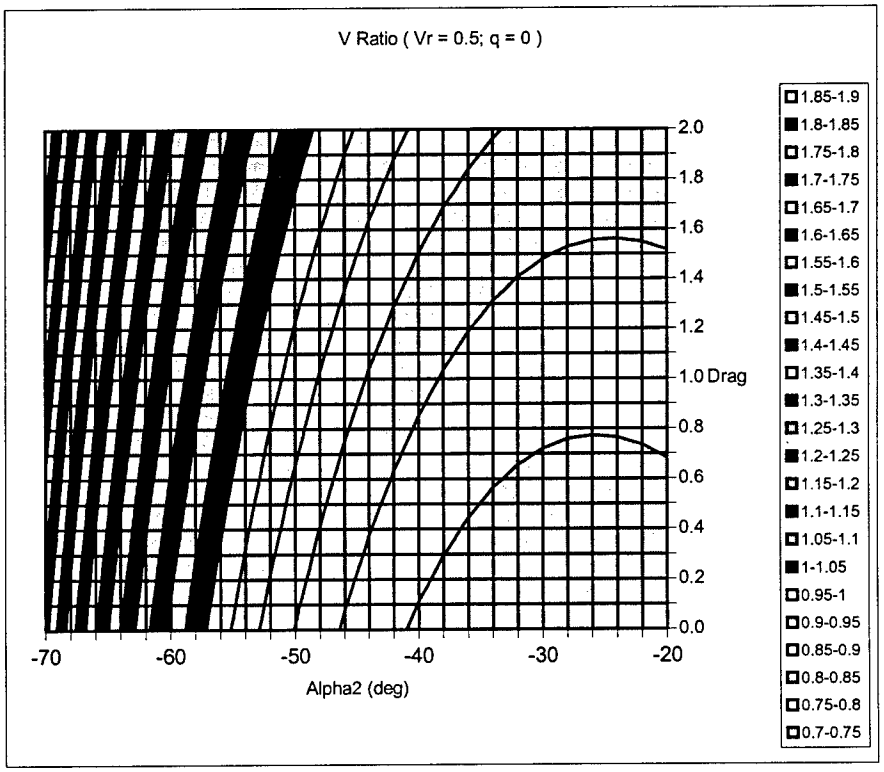

Figure 9: Velocity Ratio in Stationary Frame of Reference.

COMPUTATIONAL RESULTS

Flow Description

In the report by Sepri [1] for the SFRP research period, typical velocity flow-field figures were presented for high (660K) and low (16.5K) Reynolds numbers as computed using VBI2D (cases 713 and 113 in Table 1). These cases represented the extreme conditions for Reynolds number considered at that time, and it was evident that the suction side boundary layer remains largely attached for the high R_e case, while it separates approximately midway along the axial chord for the other case. During the SREP period, it has been of interest to refine the Reynolds number range at which significant flow separation commences. Earlier computations had indicated that the flow remains largely attached at R_e = 66K, while a strong oscillation occurs at R_e = 33K. . Here, the flow-field at R_e = 82.5K is shown in Fig. 10, and it is clear that this case is representative of the higher Reynolds number regime. The wake of the cylinder has just passed the nose-tip of the turbine blade

Figure 10: Constant Velocity Contours for R_e = 82.5K.

The velocity flow-field at the intermediate Reynolds number of 49.5K is shown in Fig. 11, and it is evident that a significant flow separation occurs at this condition. Apparently, separation becomes serious in the Reynolds number range of 50K – 60K.

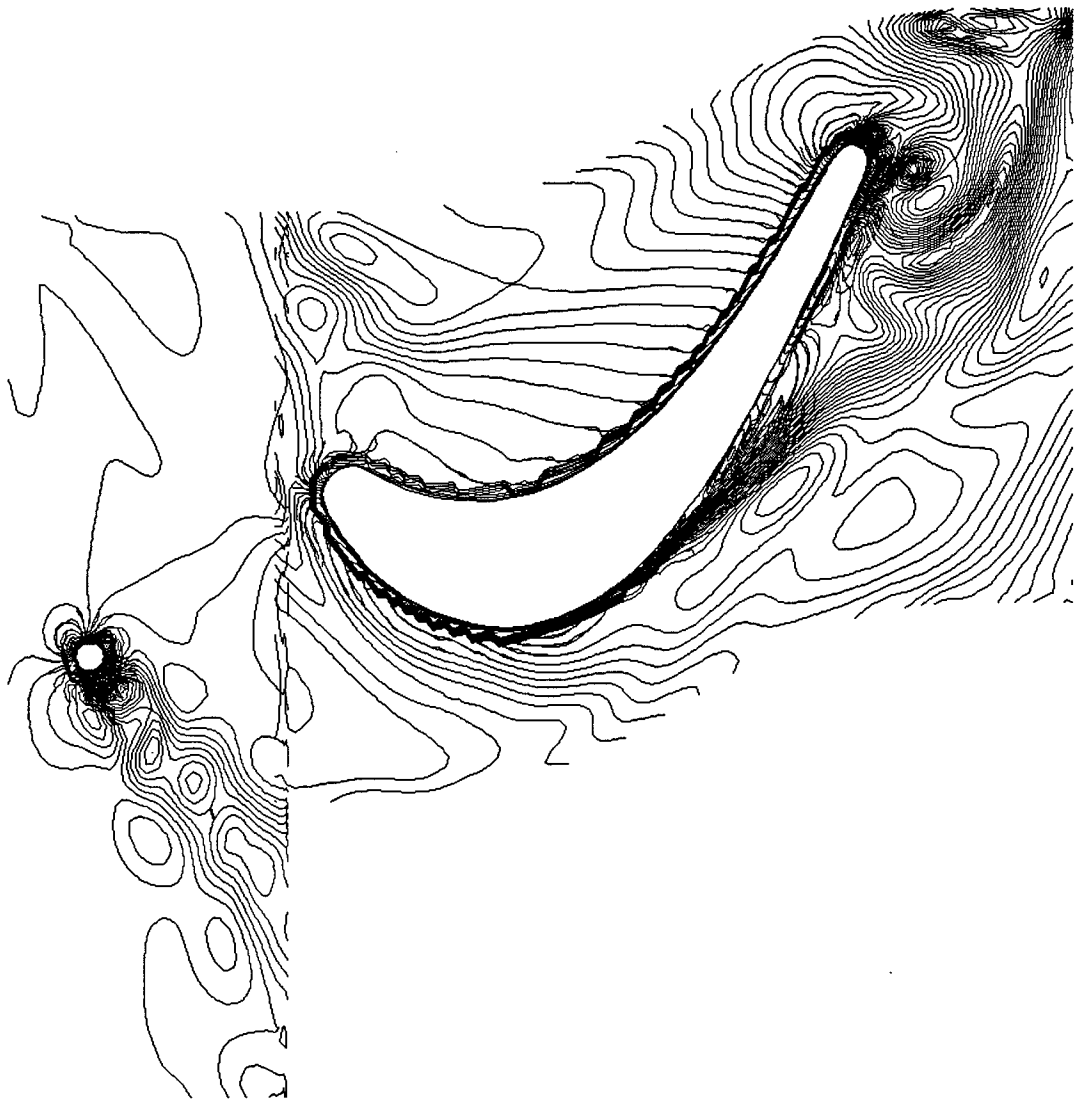

Figure 11: Constant Velocity Contours for R_e = 49.5K.

Representative skin friction distributions are shown for Cases 713 and 113 in Figs. 12a and 12b (note the different scales used for increased clarity). In the present convention, reverse flow on the suction side is indicated by positive values of skin friction, while for stream-wise flow it is indicated by negative values. These indications are reversed in sign on the pressure side. Some of the oscillations occurring on the suction side are perhaps attributable to the influence of cylinder induced vortices, while the aft flow reversals at low R_e (Case 113) are connected with separations originating from the turbine blade itself.

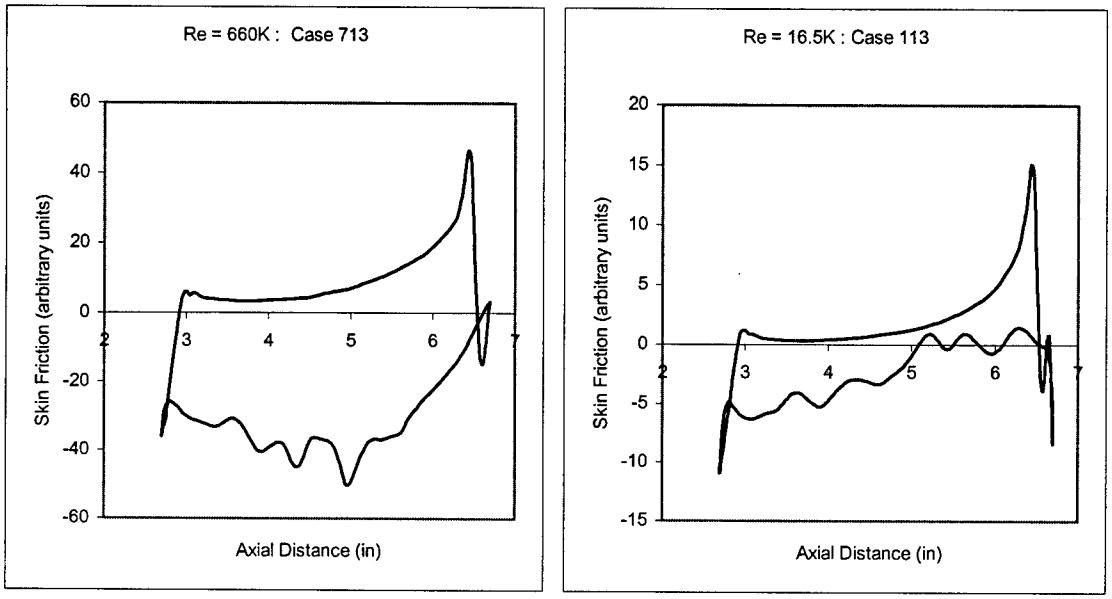

Figures 12a and 12b: Turbine Blade Skin Friction Profiles for R_e = 660K and 16.5K.

The locations of transition to turbulence, as set by the Baldwin-Lomax model, may be observed in Fig. 4 of Reference 1, in which the turbulent coefficient of viscosity is plotted at one grid point away from the surface along the periphery of the turbine blade. It is somewhat curious that the model is triggered at two isolated locations near the leading edge of the blade and briefly along the aft pressure side. The low R_e cases remain totally laminar, whereas for Case 713, the main transition occurs at two locations on the suction side near mid-chord. For the present computations at R_e = 49.5K, it is presumed that the separation occurring in Fig. 11 is a laminar one. A further illustration of flow separation on the suction side boundary layer is shown in Fig. 13, in which velocity vector plots demonstrate the onset of flow reversal near the surface.

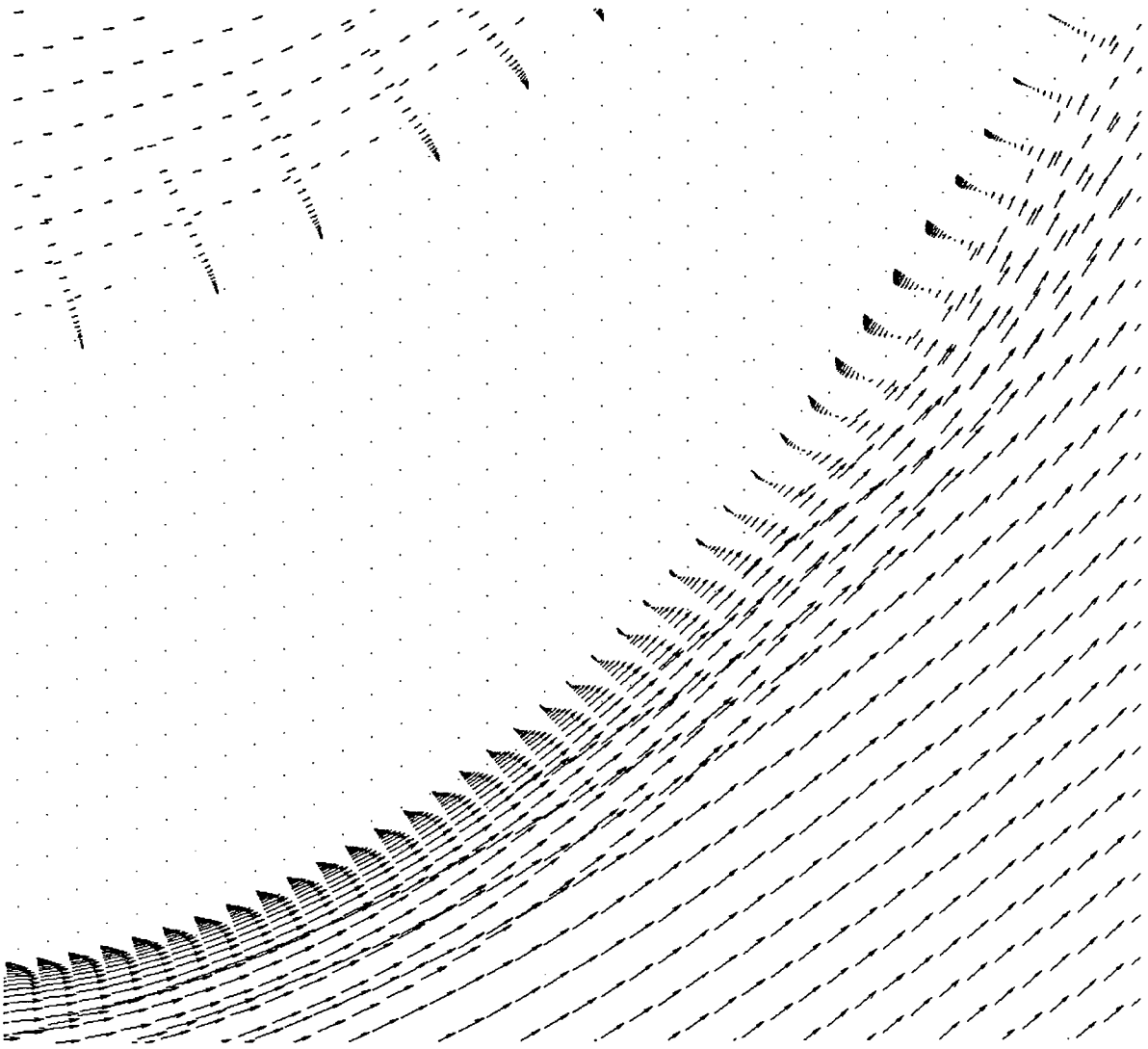

Figure 13: Velocity Profiles over Turbine Blade Showing Flow Separation.

Lift Histories

Some appreciation for the unsteady patterns that develop in the flow may be observed in the lift histories that are computed by VBI2D. Initial lift histories for Reynolds number cases of 24.75K, 49.5K, and 82.5K are shown in Figs. 14, 15, and 16, respectively, for the case of an impermeable surface. Lift on the cylinder is shown in the lighter shade, while lift on the turbine blade is shown as the darker line. Here, it is seen that after a transient period the lift histories become periodic on the whole.

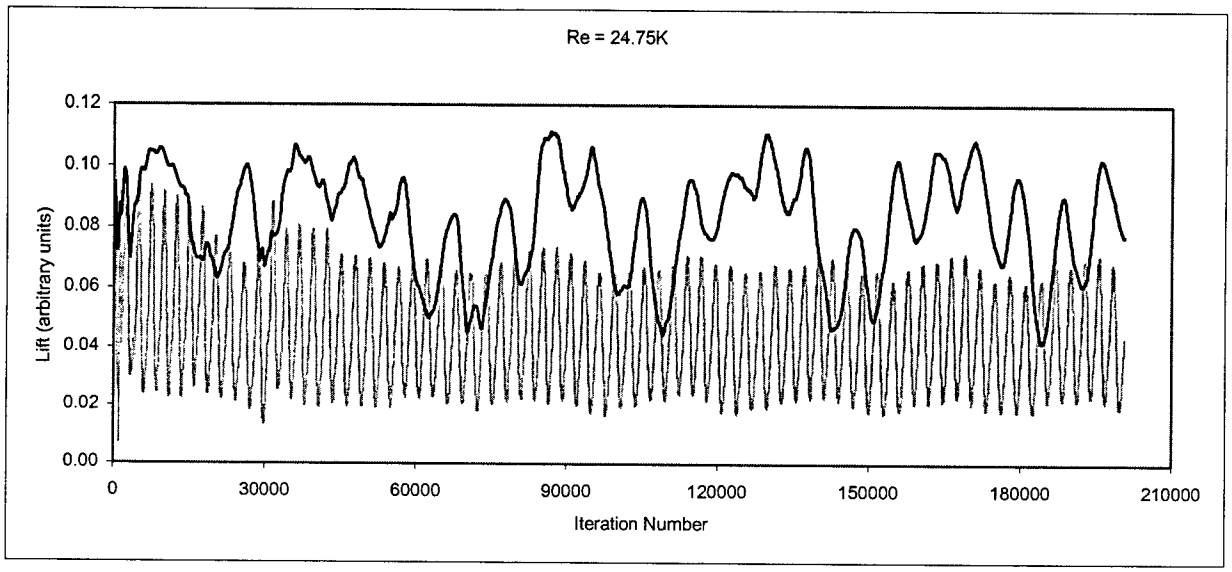

Figure 14: Lift History for R_e = 24.75K for Five Cycles.

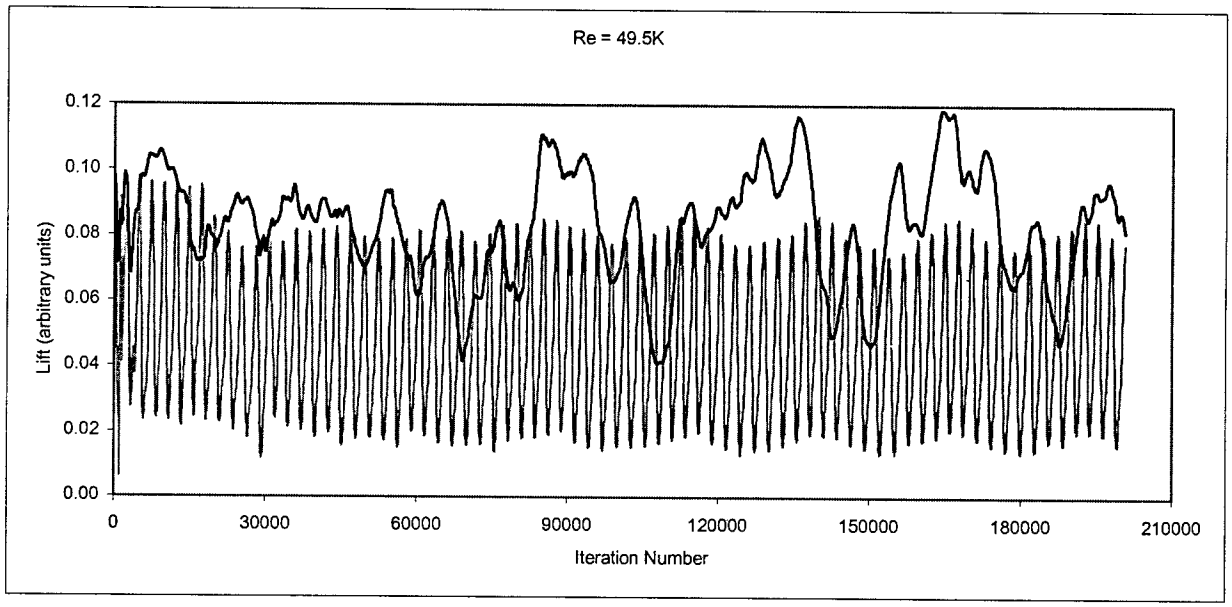

Figure 15: Lift History for R_e = 49.5K for Five Cycles.

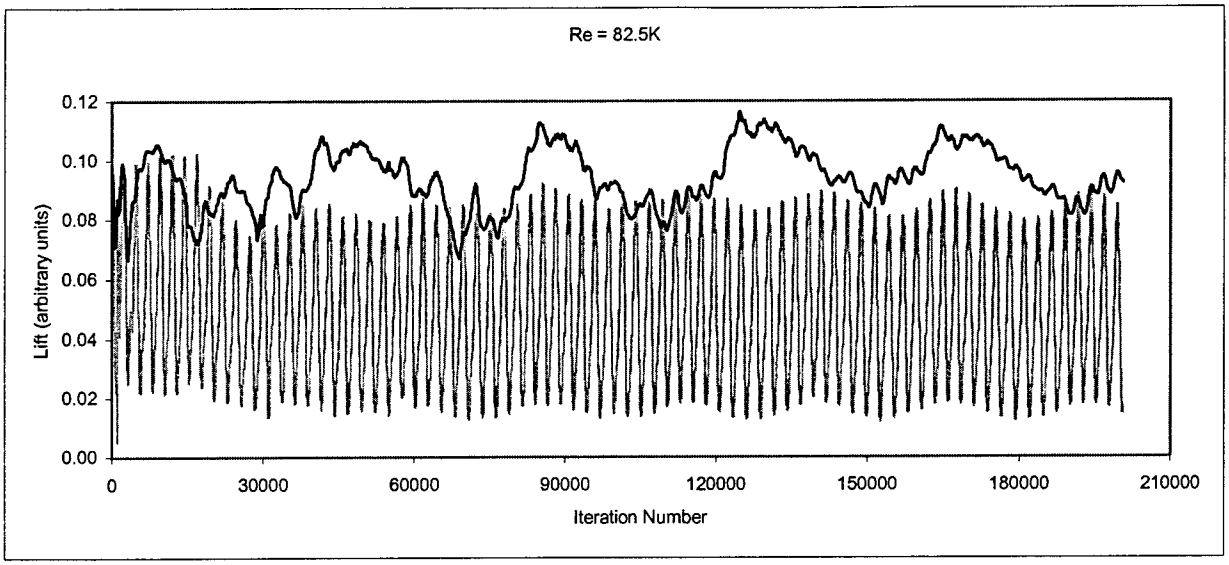

Figure 16: Lift History for R_e = 82.5K for Five Cycles.

One passage cycle of adjacent cylinder wakes with respect to the turbine blade configuration is computed in 40,140 iterations in time, and ten complete flow-field solutions are written for possible evaluation within each cycle. After a cyclic condition is achieved, the blade experiences a diminished lift during each cycle when the cylinder wake passes the nose-tip region of the blade, as may be seen most clearly in Fig.16. Smaller scale oscillations in blade lift are observed in Fig. 16, which are of nearly the same frequency as that of the vortices shed from the upstream cylinder. The slight shift in frequency might be attributed to the relative acceleration of the flow through the passageway between neighboring blades. It is also noteworthy that the envelope of cylinder lift oscillations exhibits an undulation that has a ratio of 3-to-2 as compared with the lift cycle frequency of the turbine blades. Evidently, the downstream passage of turbine blades has an upstream influence on the cylinder wakes, as should be the case for the subsonic flow considered herein.

In Figs. 14 and 15, the lift oscillations are seen to be of a much larger amplitude than those in Fig. 16, and they are at a significantly lower frequency. In these two cases, the flow is no longer attached, and vortex shedding characteristic of bluff-bodies [15] accompanies the unsteady flow separations from the suction surface. The decreased frequency of the shedding is consistent with the larger wake diameter of the blade as compared to that of the cylinder, so as to maintain a constant value for the Strouhal number [15]. Further evidence is not presented here for other Reynolds number cases, because these are quite similar to Fig. 16 for higher Reynolds numbers and to Fig. 14 for lower Reynolds numbers. It should be noted that in Fig. 15 are seen both high and low frequency oscillations, as the R_e = 49.5K case appears to represent elements of both high and low R_e flows. The next sections deal with modifications to the flow for cases of surface transpiration, both steady and unsteady.

Steady Transpiration

The flow condition existing at Iteration Number 240,840 (after five cycles) was utilized as the beginning condition for several subsequent computations in order to obtain a comparison for flow modifications caused by surface transpiration effects. The first of these cases involve steady transpiration, for which both blowing and suction were computed. As a baseline, the case of no transpiration is shown in Fig. 17 for a continuation of three cycles.

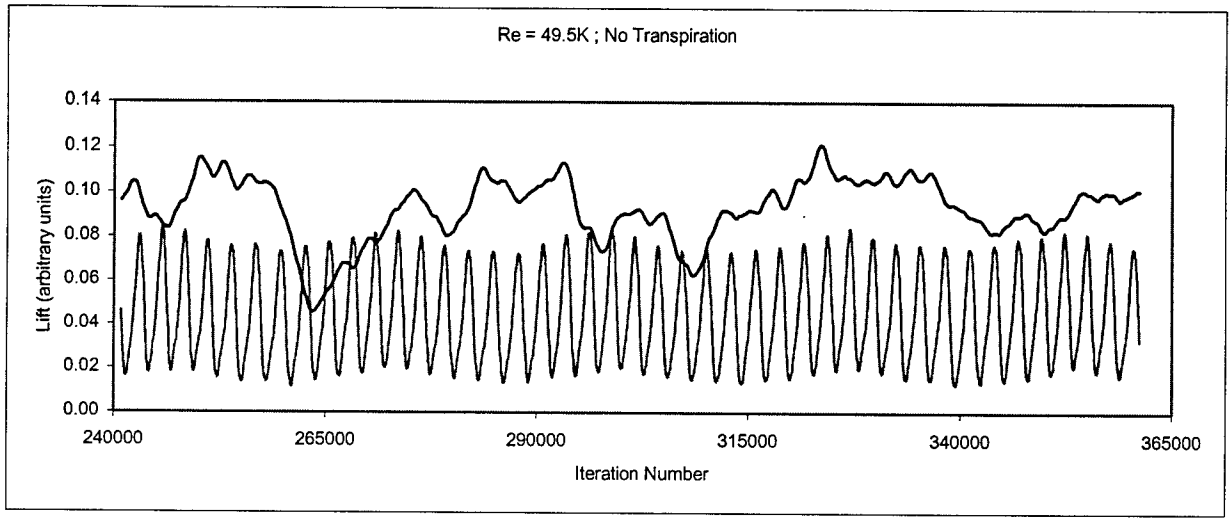

Figure 17: Lift History for R_e = 49.5K with No Transpiration for Three Cycles.

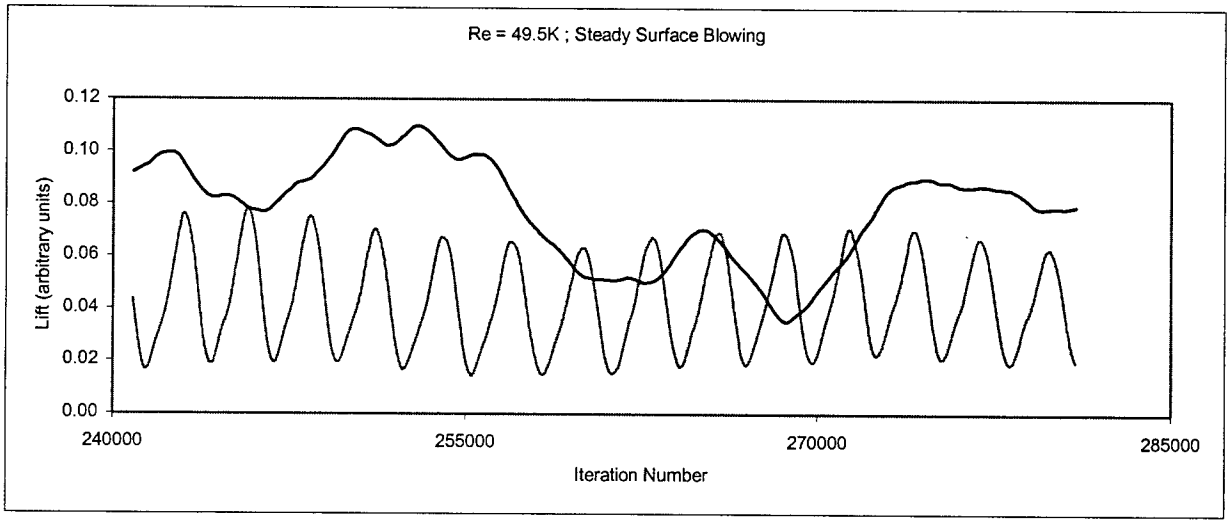

Figure 18: Lift History for R_e = 49.5K with Steady Surface Blowing for One Cycle.

It is interesting in Fig. 17 that the effect of flow separation (as indicated by the degree of lift loss) appears to diminish with increasing time. In fact, since this case represents a boundary between high and low Reynolds number regimes, the flow disturbances may be vanishing slowly, with the consequence that an unseparated flow condition may be the long-term asymptote. A continuation of the lift history is shown in Fig. 18 for the case of steady surface blowing. As might be expected for the case of steady blowing, the lift history is consistent with continued bluff-body separation, perhaps with even an unfavorable decrease in the blade lift. It is apparent that the start of transpiration introduces a flow transient that lasts for approximately one passage cycle, beyond which the flow approaches a new cyclic pattern. For the case of surface suction shown in Fig.19, after the transient period, it appears that the flow approaches an attached condition. Although a suction mechanism is not desirable in a practical application owing to blade heating consequences, it is of interest to observe the effect on flow separation as a limiting case of the computations. The same time period for computations is shown in Fig. 17 for the case of an impermeable blade surface. This figure represents the reference condition of a no-slip and no transpiration case for comparison with the cases involving transpiration.

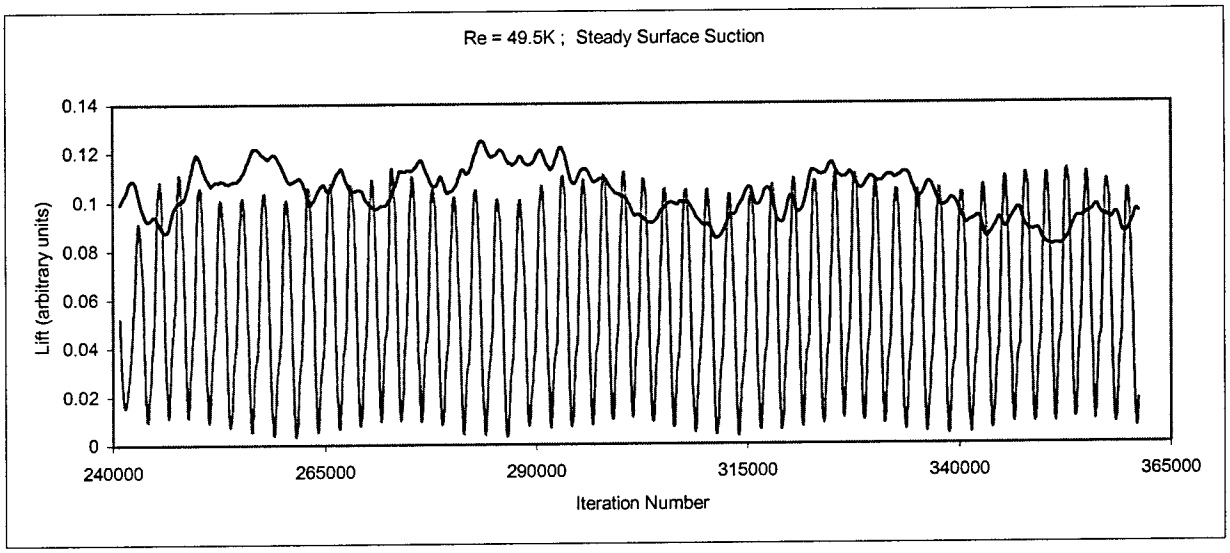

Figure 19: Lift History for R_e = 49.5K for Steady Surface Suction for Three Cycles.

Oscillatory Transpiration

Motivated by the experimental evidence given in References 8-13 supporting the beneficial effects of introducing periodic flow disturbances, three cases of oscillatory transpiration have been computed. These correspond to frequencies that are high, medium, and low compared to the shedding frequency of vortices from the upstream cylinders. These frequencies were also chosen in order to investigate whether a resonance with cylinder vortices could be detected in the downstream flow.

Figure 20: Contours of Constant Static Pressure for R_e = 49.5K and High Frequency Transpiration

In Fig. 20 are shown isobars for a case of high frequency surface transpiration, and these serve to illustrate two aspects: (1) the concentric rings of static pressure indicate the location and extent chosen for the surface transpiration, and (2) in this subsonic flow the high frequency disturbance emanates in the manner of a sound wave from the surface. The nominal case of oscillatory transpiration with frequency similar to that of the upstream vortex shedding is shown in Fig. 21. It is evident that the lift characteristics of the blade have been somewhat improved over the case of no transpiration shown in Fig. 17. As mentioned by Bar-Sever [10], it is possible that the excitation of vertical velocity components in the boundary layer cause increased mixing similar to that of a transitioning flow, which tends to keep the flow attached to the surface. Here, the surface perturbation is seen as a supplementary oscillation superimposed on the larger scale lift cycle. The frequency is seen to be slightly higher than that of the cylinder vortices.

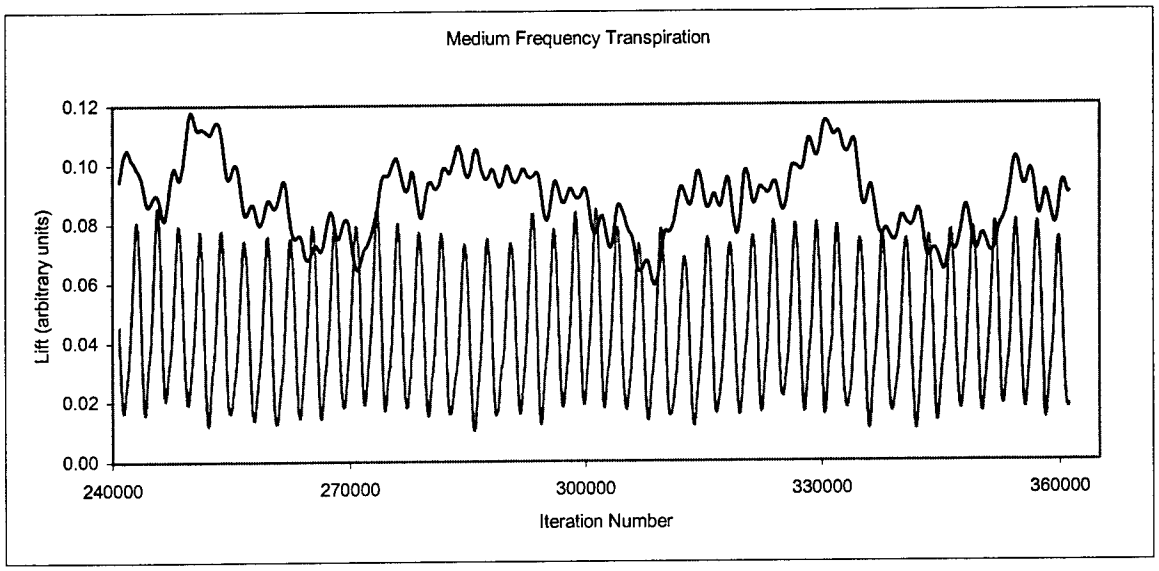

Figure 21: Lift History for R_e = 49.5K with Medium Frequency Transpiration.

In Fig. 22 is shown the case of a high frequency pulsation (two-and-one-half times the nominal frequency), and the overall effect is that the boundary layer remains separated. In this case, the bluff-body vortex shedding continues as the frequency of pulsed transpiration is too high to influence the larger scale motions.

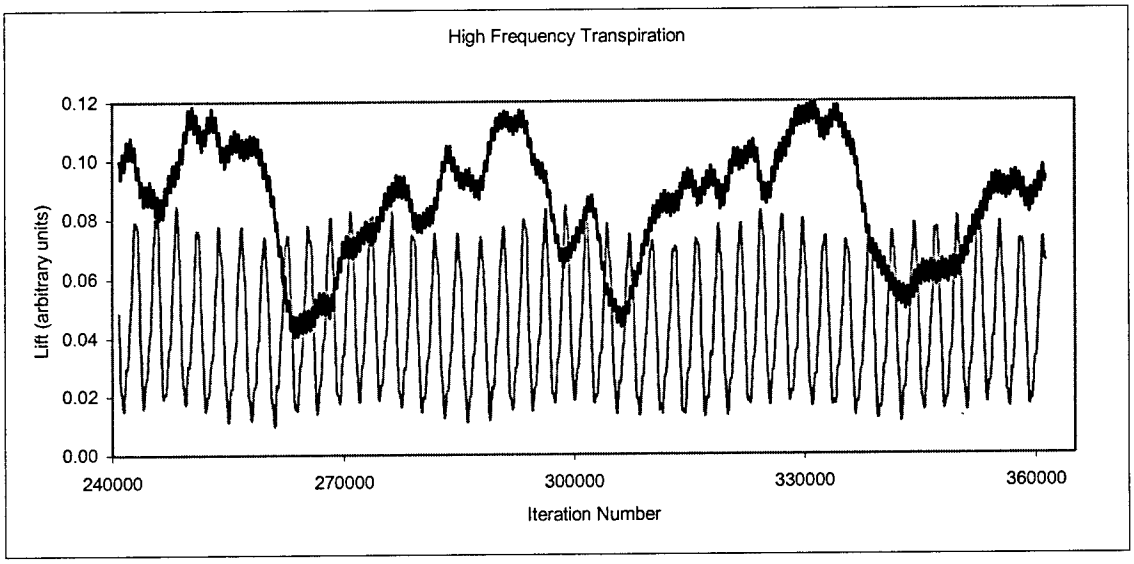

Figure 22: Lift History for R_e = 49.5K with High Frequency Transpiration.

In Fig. 23 is shown the case of a low frequency pulsation (one-fourth of the nominal frequency), and the effect is a favorable one so as to diminish the amount of separation. The pulsation of transpiration is approximately

of the same frequency as that of the bluff-body separation. It is concluded that a low frequency pulsation has the beneficial effect of retarding boundary layer separation in this Reynolds number range.

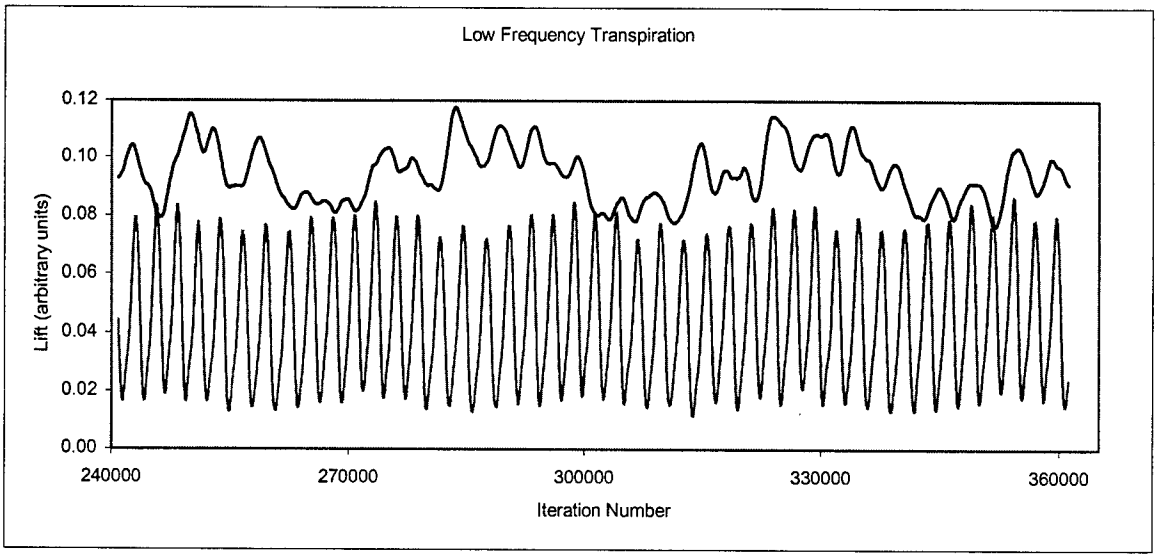

Figure 23: Lift History for R_e = 49.5K with Low Frequency Transpiration.

Pressure Coefficient

Typical pressure coefficient distributions on the turbine blade surface are shown in Figs. 24a and 24b as measured in the axial direction for R_e = 660K and 16.5K, respectively. These provide an indication of lift obtainable from the turbine blade. In Figs. 25a and 25b the same distributions are shown plotted in the vertical direction to show that there is also a decrease in turbine blade drag as flow separation occurs. Here, the reference pressure is taken to be the constant static pressure imposed upstream of the cylinders at the *start* of each R_e case. As each run progresses, the ambient static pressure level changes with time as power is either added or removed through the rotation of the cylinder stage. Presumably, the pressure level adjusts itself according to the emanation of acoustic waves through upstream and downstream boundaries. The choice of a constant reference pressure for each R_e case proves useful in comparing pressure distributions at different times, although the C_p distributions shown in the figures exhibit uncharacteristically high or low levels owing to the shift in actual ambient pressure with time. Pressure differentials, both vertical and axial, decrease significantly at lower R_e, as the degree of effective suction is reduced. Normally, one associates with separated flow an increase of airfoil drag. However, since the turbine blade tail section is highly inclined to the axial direction, a loss of relative suction corresponds to a decrease in both drag and lift.

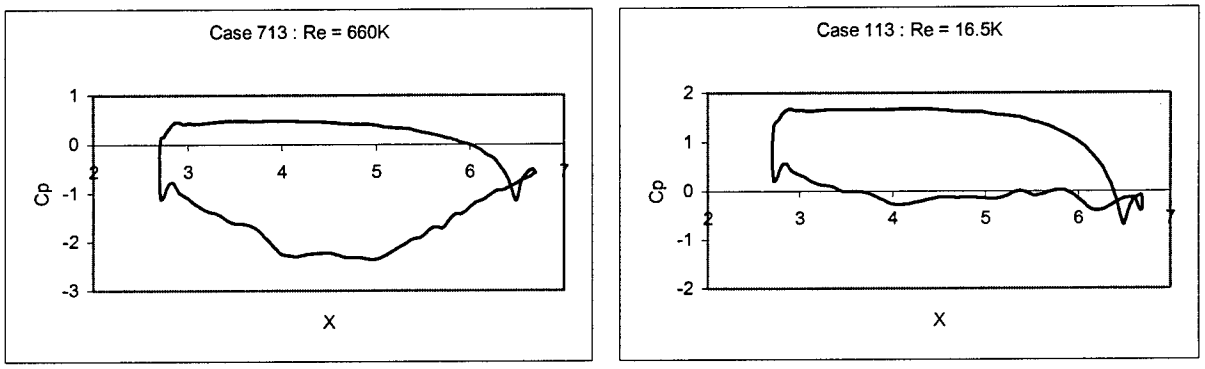

Figures 24a and 24b: Axial C_p Distributions for R_e = 660K and R_e = 16.5K, Respectively.

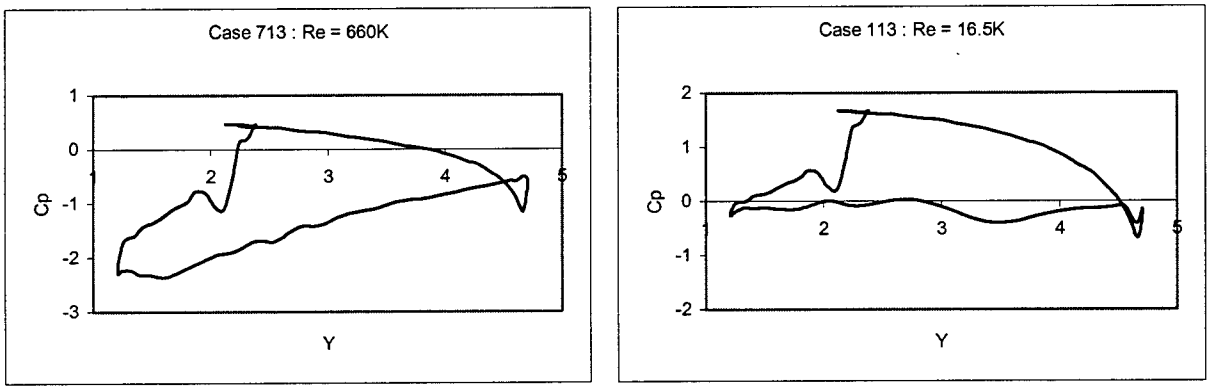

Figures 25a and 25b: Vertical C_p Distributions for R_e = 660K and R_e = 16.5K, Respectively.

Pressure Profiles

The stagnation pressure loss coefficient, as defined by Eq. (28), is computed for the VBI2D cases by performing a numerical quadrature in respective vertical cuts in order to find averaged values for the pressures. The inlet location was chosen to be the first column of the blade H-grid, and the exit location was the last column. Sample vertical distributions of the pressures are shown in Fig. 26. Here, fluctuations are seen both upstream and downstream of the turbine blade. Presumably, some of these variations may be due to influences of vortices swept downstream from the cylinders, and by the modification of total pressure in the unsteady flow around the blades. In particular, it is interesting to note the distribution of total pressure downstream of the turbine blade. In some locations, the total pressure rises significantly above its upstream value, whereas in other regions of the wake, the level is markedly lower. The reduction of total pressure by viscous losses is to be expected, but its generation may be somewhat surprising.

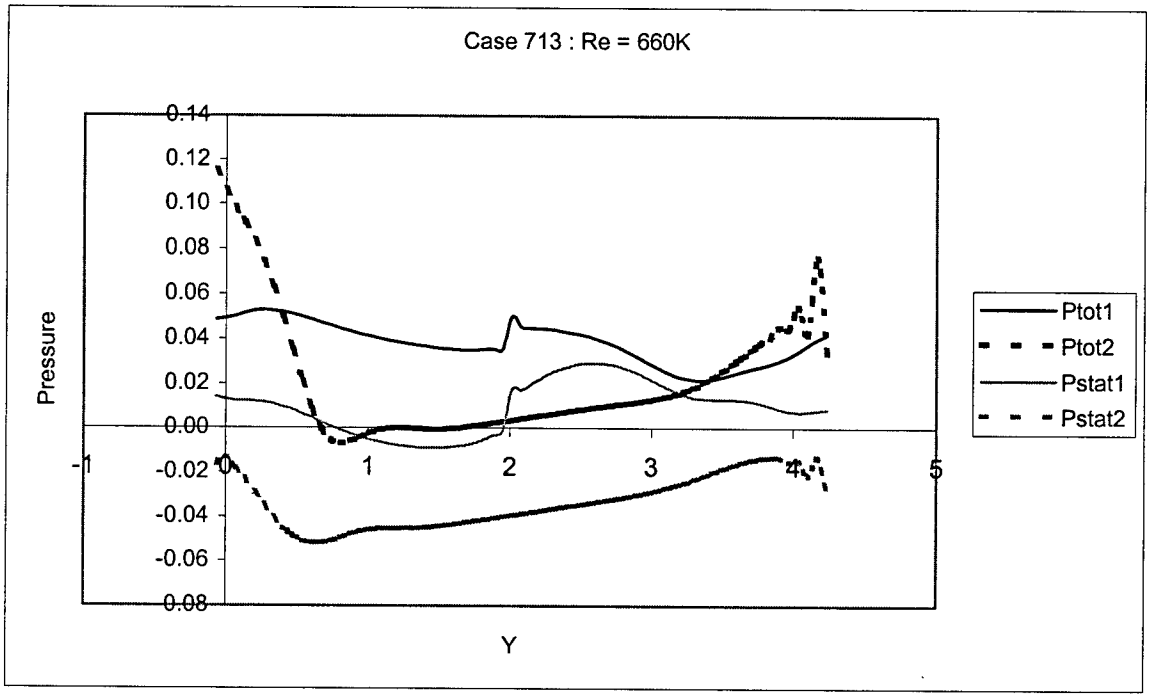

Figure 26: Vertical Pressure Profiles for Case 713 ; R_e = 660K.

Alternating regions of high and low stagnation pressure also occur in the wakes of the cylinders, as seen in Fig. 9 of Reference 1. Near peak locations in the wake, the stagnation pressure exceeds its level attained upstream of the cylinder. While such a circumstance is not to be expected for steady flows around stationary objects, it apparently can occur for unsteady flow about stationary objects, and certainly for flow about moving objects, which impart mechanical energy to the flow. A further indication of this phenomenon is shown in Fig. 27 in which

contours of constant total pressure, P_T, are shown at an instant of time for the case of high frequency transpiration at R_e = 49.5K. Although it is not clearly discernible in the black-and-white rendition, on the outside of the main gathering of contour lines there are islands of high P_T, which are significantly higher in magnitude than the P_T entering the system.

Figure 27: Contours of Constant Total Pressure for R_e = 49.5 with High Frequency Transpiration.

Evidently, the unsteady compressive nature of the surface transpiration causes an oscillatory generation and degeneration of total pressure. It is of interest to monitor whether this effect also causes islands of entropy decrease locally, as has been discussed in the section dealing with analytical modeling. Such decreases could occur through local conductive heat extraction from relatively compressed regions. A scrutiny of entropy plots from VBI2D has shown a few such regions to occur, but these are rare and of minor magnitude.

Stagnation Pressure Loss Coefficient

Variations in total pressure loss coefficient within one cycle are shown in Figs. 28 and 29 for two cases. Large oscillations occur within the cycle for the low R_e case, so that Y_p is even negative at times. It should be noted that flow structures, which are convected streamwise through the blade passages, would involve a phase lag between exit and inlet locations, whereas Y_p provides an instantaneous comparison between these locations. The higher R_e case exhibits no negative excursions.

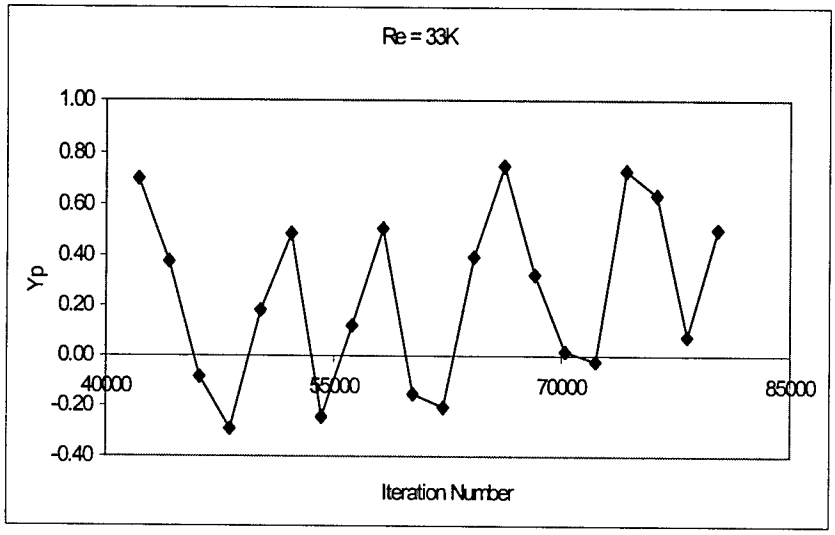

Figure 28: Total Pressure Loss Coefficient for R_e = 33K for One Cycle.

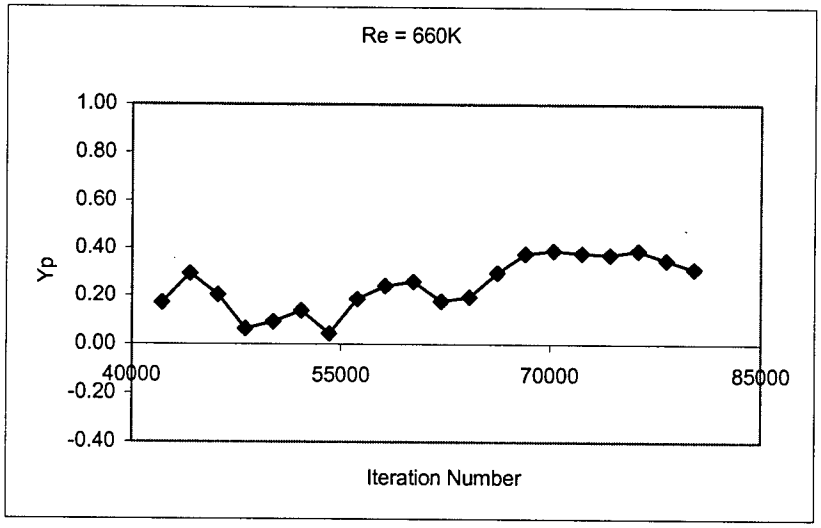

Figure 29: Total Pressure Loss Coefficient for R_e = 660K for One Cycle.

The results of averaging Y_p over ten equally spaced time intervals during each cycle are shown in Fig. 30 as R_e is varied. These results had been somewhat contrary to earlier expectations, but they are now considered to be satisfactorily explained. From previous studies [24,25], it was anticipated that Y_p would have small values at higher R_e; that there would be a marked break in the trend near 100K; and that Y_p would increase dramatically at lower R_e owing to the large losses associated with suction side separation. The present results do not support this view in that the calculated values for Y_p remain fairly constant (range of 0.2 – 0.3), with a peak occurring in the distribution near R_e = 132K.

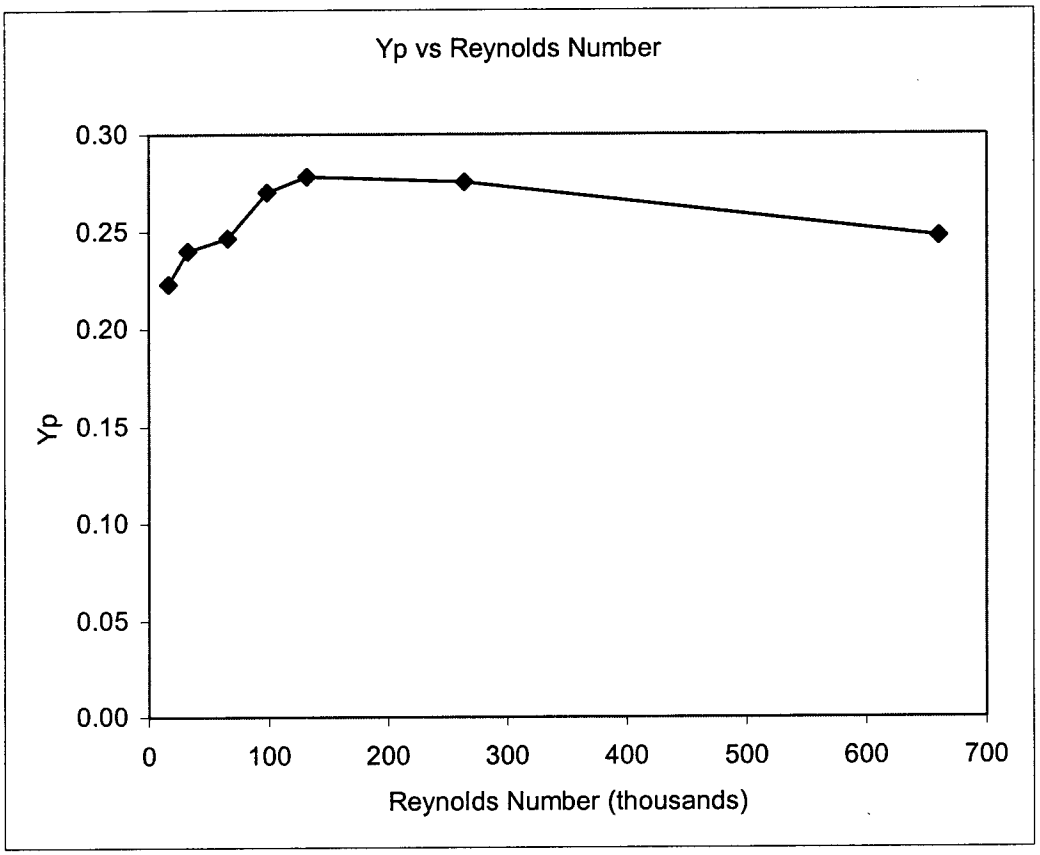

Figure 30: Total Pressure Loss Coefficient (averaged over one cycle) vs Reynolds Number.

CONCLUSIONS

In extension to the earlier research reported by Sepri [1], the unsteady VBI2D code has been applied to a sequence of additional Reynolds number cases for flow around a stationary cascade of Langston turbine blades influenced by the wakes of moving upstream cylinders. Furthermore, the code has been modified to include the effects of surface transpiration on the separating boundary layers in the low Reynolds number regime. Vortex shedding and wake deficits cause significant shifts (+/- 20 deg.) in the effective flow incidence at the blade nose-tip. At the lower Reynolds numbers (less than 50K), extensive suction side separations have been computed and quantified, whereas in the higher R_e range (higher than 60K), flow separation is non-existent or of minimal extent. In the intermediate range, the flow appears to exhibit influences from the upstream cylinder vortex shedding as well as the downstream flow separation on the turbine blade. It is shown that oscillatory transpiration on the suction side of the turbine blade can have the beneficial effect of promoting attached flow, provided the frequency of oscillation is less than that of the vortex shedding from the upstream cylinders, while being comparable to that of the otherwise occurring bluff-body shedding from the turbine blade configuration. Computations of the total pressure loss coefficient are presented at twenty equal time steps within a flow interaction cycle for two representative R_e cases, and cycle averaged results are presented as a function of R_e. A simplified analytical model is formulated to aid in the interpretation of the computed results. Averaged flow quantities are shown to vary in a parametric fashion with respect to flow deflection and drag as influenced by internal blade or vane configurations. Flows described by constant entropy processes and constant total pressure loss processes are shown to have similar, although not identical, characteristics. The oscillatory nature of the computed separating flow may have local regions of decreased entropy, while the overall flow conforms to the Second Law of Thermodynamics. One major conclusion is that while flow separation causes a dramatic loss of turbine power, the competing effects of decreased flow deflection and decreased drag combine so that Y_p is not altered as much as had been anticipated initially.

ACKNOWLEDGEMENTS

The author gratefully acknowledges the support received from the AFOSR Summer Research Extension Program through RDL under Contract Number F49620-93-C-0063 and Subcontract 99-0836. The work was made possible through the guidance of, and collaboration with, Dr. Richard B. Rivir, who served as the Laboratory Focal Point at Wright-Patterson AFB in the Turbines Branch. The author also wishes to thank Dr. Robert Gray for his many insightful discussions during the previous SFRP period, and Dr. Rolf Sondergaard for his invaluable assistance with VBI2D and its implementation.

REFERENCES

[1] Sepri, P., "A Computational Study of Turbine Blade Interactions with Cylinder Wakes at Various Reynolds Numbers", Final Report for AFOSR Summer Faculty Research Program, 1998, pp. 9-1 - 9-20.

[2] Rao, K.V., R.A. Delaney, and D.A. Topp, "Turbine Vane-Blade Interaction: Vol. I, 2-D Euler/Navier-Stokes Aerodynamic and Grid Generation Developments," Wright Patterson AFB, WL-TR-94-2073, 1994.

[3] Rao, K.V., J.W. Griffin, and R.A. Delaney, "Turbine Vane-Blade Interaction: Vol. II, 2-D Computer Program User's Manual," Wright Patterson AFB, WL-TR-94-2074, 1994.

[4] Abhari, R.S., "Impact of Rotor-Stator Interaction on Turbine Blade Film Cooling", *ASME Journal of Turbomachinery*, Vol. 118, 1996, pp. 123-133.

[5] Dorney, D.J., D.E. Ashpis, D.E. Halstead, and D.C. Wisler, "Study of Boundary-Layer Development in a Two-Stage Low-Pressure Turbine," *Journal of Propulsion and Power*, Vol. 16, No. 1, 2000, pp. 160-163.

[6] Bohn, D., V. Becker, K. Kusterer, L. Fottner, and S. Ardey, "Three-Dimensional Flow Analysis of Turbine Blade Cascades with Leading Edge Ejection," *Journal of Propulsion and Power*, Vol. 16, No. 1, 2000 pp. 49-56.

[7] Brookfield, J. M., and I.A. Waitz, "Trailing-Edge Blowing for Reduction of Turbomachinery Fan Noise," *Journal of Propulsion and Power*, Vol. 16, No. 1, 2000, pp. 57-64.

[8] Nishri, B., and I. Wygnanski, "Effects of Periodic Excitation on Turbulent Flow Separation from a Flap," *AIAA Journal*, Vol. 36, No. 4, 1998, pp. 547-556.

[9] Katz, Y., B. Nishri, and I. Wygnanski, "The Delay of Turbulent Boundary Layer Separation by Oscillatory Active Control," *Physics of Fluids A*, Vol. 1, No. 2, 1989, pp. 179-181.

[10] Bar-Sever, A., "Separation Control on an Airfoil by Periodic Blowing," *AIAA Journal*, Vol. 27, No. 6, 1989, pp. 820-821.

[11] Zaman, K.B.M.Q., A. Bar-Sever, and S.M. Mangalam, "Effect of Acoustic Excitation on the Flow over a Low-Re Airfoil," *Journal of Fluid Mechanics*, Vol. 182, 1987, pp. 127-148.

[12] Collins,F.G., and J. Zelenevitz, "Influence of Sound upon Separated Flow over Wings," *AIAA Journal*, Vol. 13, No. 3, 1975, pp. 408-410.

[13] Seifert, A., and L.G. Pack, "Oscillatory Control of Separation at High Reynolds Numbers," *AIAA Journal*, Vol. 37, No. 9, 1999, pp. 1062-1071.

[14] Seifert, A., T. Bachar, D. Koss, M. Shepshelovich, and I. Wygnanski, "Oscillatory Blowing: A Tool to Delay Boundary-Layer Separation," *AIAA Journal*, Vol. 31, No. 11, 1993, pp. 2052-2060.

[15] Griffin, O.M, "Universal Similarity in the Wakes of Stationary and Vibrating Bluff Structures," *ASME Journal of Fluids Engineering*, Vol. 103, 1981, pp. 52-58.

[16] Griffin, O.M., "Vortex Shedding from Bluff Bodies in a Shear Flow: A Review," *ASME Journal of Fluids Engineering*, Vol. 107, 1985, pp. 298-306.

[17] Lewis, J.P., R.A. Delaney, and E.J. Hall, "Numerical Prediction of Turbine Vane-Blade Aerodynamic Interaction," *ASME Journal of Turbomachinery*, Vol. 111, 1989, pp. 387-393.

[18] Rao, K.V., R.A. Delaney, and M.G. Dunn, "Vane-Blade Interaction in a Transonic Turbine, Part I: Aerodynamics," *Journal of Propulsion and Power*, Vol. 10, No. 3, 1994, pp. 305-317.

[19] Rivir, R., R. Sondergaard, M. Dahlstrom, and E. Ervin, "Low Reynolds Number Turbine Blade Cascade Calculations," ISROMAC-6 The 6th International Symposium on Transport Phenomena and Dynamics of Rotating Machinery, Honolulu, HI., 1996.

[20] Langston, L.S., M.L. Nice, and. R.M. Hooper, "Three-Dimensional Flow Within a Turbine Cascade Passage," *ASME Journal of Engineering for Power*, Vol. 99, 1977, pp. 21-28.

[21] Langston, L.S., "Research on Cascade Secondary and Tip-Leakage Flows – Periodicity and Surface Flow Visualization," AGARD Conference Proceedings No. 469, 1989, pp. 1-19.

[22] Baldwin, B.S., and H. Lomax, "Thin Layer Approximation and Algebraic Model for Separated Turbulent Flows," AIAA Paper 78-257, 1978, pp. 1-8.

[23] Blair, M.F., "An Experimental Study of Heat Transfer in a Large-Scale Turbine Rotor Passage," *ASME Journal of Turbomachinery*, Vol. 116, 1994, pp. 1-13.

[24] Baughn, J.W., R.J. Butler, A.R. Byerley, and R.B. Rivir, "An Experimental Investigation of Heat Transfer, Transition, and Separation on Turbine Blades at Low Reynolds Number and High Turbulence Intensity," ASME International Mechanical Engineering Congress and Exposition, 1995.

[25] Murawski, C.S., R. Sondergaard, R.B. Rivir, V. Kambiz, T.W. Simon, and R.J. Volino, "Experimental Study of the Unsteady Aerodynamics in a Linear Cascade with Low Reynolds Number Low Pressure Turbine Blades," ASME Paper 97-GT-95, 1997.

[26] Graziani, R.A., M.F. Blair, J.R. Taylor, and R.E. Mayle, "An Experimental Study of Endwall and Airfoil Surface Heat Transfer in a Large Scale Turbine Blade Cascade," *Journal of Engineering for Power*, Vol. 102, 1980, pp. 257-267.

[27] Dring, R.P., H.D. Joslyn, and L.W. Hardin, "An Investigation of Axial Compressor Rotor Aerodynamics," *ASME Journal of Engineering for Power*, Vol. 104, 1982, pp. 84-96.

[28] Blair, M.F., R.P. Dring, and H.D. Joslyn, "The Effects of Turbulence and Stator/Rotor Interactions on Turbine Heat Transfer: Part 2 - Effects of Reynolds Number and Incidence," *ASME Journal of Turbomachinery*, Vol. 111, 1989, pp. 91-103.

[29] Hodson, H.P., "Measurements of Wake-Generated Unsteadiness in the Rotor Passages of Axial Flow Turbines," *Journal of Engineering for Gas Turbines and Power*, Vol. 107, 1984, pp. 467-476.

[30] Zaccaria, M.A., and B. Lakshminarayana, "Unsteady Flow Field Due to Nozzle Wake Interaction With the Rotor in an Axial Flow Turbine: Part I – Rotor Passage Flow Field," *ASME Journal of Turbomachinery*, Vol. 119, 1997, pp. 201-213.

[31] Hawthorne, W.R., *Aerodynamics of Turbines and Compressors*, Princeton University Press, 1964.

[32] Gray, R.E., Private Communication, 1998.

Dr. Hongchi Shi's report was unavailable at the time of publication.

Final Report for:

CONTRACT F49620-93-C-0063 (SREP 99-0807)

SIGNAL AND IMAGE PROCESSING FOR FOPEN/GPEN SAR

Project Director:

Mehrdad Soumekh
Department of Electrical Engineering
State University of New York at Buffalo
Amherst, New York 14260
Phone: (716) 645-2422, extension 2138
Fax: (716) 645-3656
Email: msoum@eng.buffalo.edu

Final Report:

SIGNAL AND IMAGE PROCESSING FOR FOPEN/GPEN SAR

Mehrdad Soumekh
Department of Electrical & Computer Engineering
State University of New York at Buffalo
Amherst, New York 14260

In this effort, we examined practical issues that are associated with implementing the high-resolution stripmap/spotlight SAR imaging algorithm, known as the SAR wavefront reconstruction method [1], [2], on a Distributed-Memory (DM) High Performance Computer (HPC). The SAR wavefront imaging method is an approximation-free algorithm that provides high-resolution and accurate coherent target information that is useful for advanced SAR information post-processing, e.g., automatic target recognition. However, the highly-accurate information base of the wavefront reconstruction algorithm is formed via the Fourier (FFT) processing of relatively large databases. For real-time processing in an operational SAR system, this requirement puts restrictions on the minimum size of the Random Access Memory (RAM) of the computer used for the SAR wavefront image formation.

Meanwhile, due to the limited area and cooling restrictions on a radar-carrying aircraft, the DM-HPCs are the practical choice for on board processing of SAR data. Unfortunately, in a DM-HPC, unlike a shared memory HPC, the RAM associated with each processor cannot be addressed by the other processors. In this case, the RAM available to each DM processor (currently around 64 to 128 MBytes) is not sufficient for, e.g, processing some of the recently-acquired high-resolution X band or UHF band (FOPEN) SAR data via the wavefront reconstruction algorithm.

A practical solution for the above-mentioned problem is to form lower-resolution images of subpatches of the target area from subsets of the synthetic aperture or synthetic *subapertures* [3]; this reduces the size of the data that are processed and the FFTs used for wavefront reconstruction. Moreover, the sizes of the subpatch and subapertures can be determined a priori by the user based on the available RAM. Provided that the subaperture imaging algorithm preserves the coherent information among the lower-resolution images, the user could coherently add the lower-resolution images to form the desired high-resolution SAR image.

The challenges for this processing are

i. To extract the SAR signature (or phase history data) of a given subpatch from the measured SAR data, a process that we refer to as *digital-spotlighting;* and

ii. Appropriate digital signal processing of subaperture SAR data that yields *calibrated* lower-resolution SAR images that can be combined coherently. We have addressed these issues via exploiting spectral (Doppler) properties of the SAR signal that is based on Gabor's wavefront reconstruction theory.

The reconstructions that follow exhibit the application of this method in processing the wide-bandwidth and wide-beamwidth FOPEN SAR P-3 data. The recosntructions show the spectral and spatial domain images that are formed with 6 subapertures; each subaperture that contain 2048 slow-time samples. (The total number of the slow-time samples is 12228.) The image formed by coherently combining these subapertures (lower-resolution) images and its spectrum are also shown. The result is identical to processing the entire 12228 slow-time samples simultaneously. The dashed lines in the spectral domain image shows the filter that was used by the MIT-LL processor to avoid slow-time Doppler aliasing. For compoarison purposes, the image formed by the MIT-LL processor with 16384 slow-time samples is also provided.

We also implemented and tested a proposed signal subspace processing for Moving Target Detection (MTD) with uncalibrated monopulse SAR images [1] using realistic Displaced Phase Center Array (DPCA) SAR data. The SAR data were part of a four-channel DPCA database at X band (spotlight mode); the data were provided by the Air Force Research Laboratory at Wright Patterson Base, Ohio [4]. The DPCA-SAR data were collected over a scene that contained various moving and stationary targets on a clear land; there were also moving and stationary targets near an area with man-made structures and dense trees. The data were originally collected for processing through conventional Ground Moving Target Indicator (GMTI) methods. However, Our processing was the first attempt to coherently combine the entire slow-time domain data (approximately 4800 pulses taken over 5 degrees of look angle) for GMTI.

A non-overlapping block-based implementation of the signal subspace algorithm was used for processing of the DPCA. Our preliminary results indicate that the proposed signal subspace method can overcome the miscalibration between the two channels of the DPCA over the entire slow-time period, and provide a reliable statistic for GMTI on both a clear land and a foliage region. The measured SAR data were originally collected for processing via the polar format reconstruction. This document also provides the description of a method used for converting polar format (motion compensated phase history) data into a database that is suitable for error-free wavefront reconstruction; the resultant wavefront reconstruction SAR images are superior to those obtained via polar format processing.

References

1. M. Soumekh, *Synthetic Aperture Radar Signal Processing with MATLAB Algorithms,* New York: Wiley, 1999.

2. M. Soumekh, *Fourier Array Imaging,* Englewood Cliffs, NJ: Prentice Hall, 1994.

3. M. Soumekh, G. Guenther, M. Linderman and R. Kohler, "Digitally-Spotlighted Sub-aperture SAR Image Formation Using High Performance Computing," *Proceedings of SPIE's Annual International Symposium on Aerospace/Defense Sensing, Simulation, and Controls,* Orlando, April 2000.

4. M. Soumekh, S. Sworrell, E. Zelnio and B. Keaffaber, "SAR Wavefront Reconstruction Using Motion Compensated Phase History (Polar Format) Data and DPCA-Based GMTI," *Proc. of SPIE's Annual International Symposium on Aerospace/Defense Sensing, Simulation, and Controls,* Orlando, April 2000.

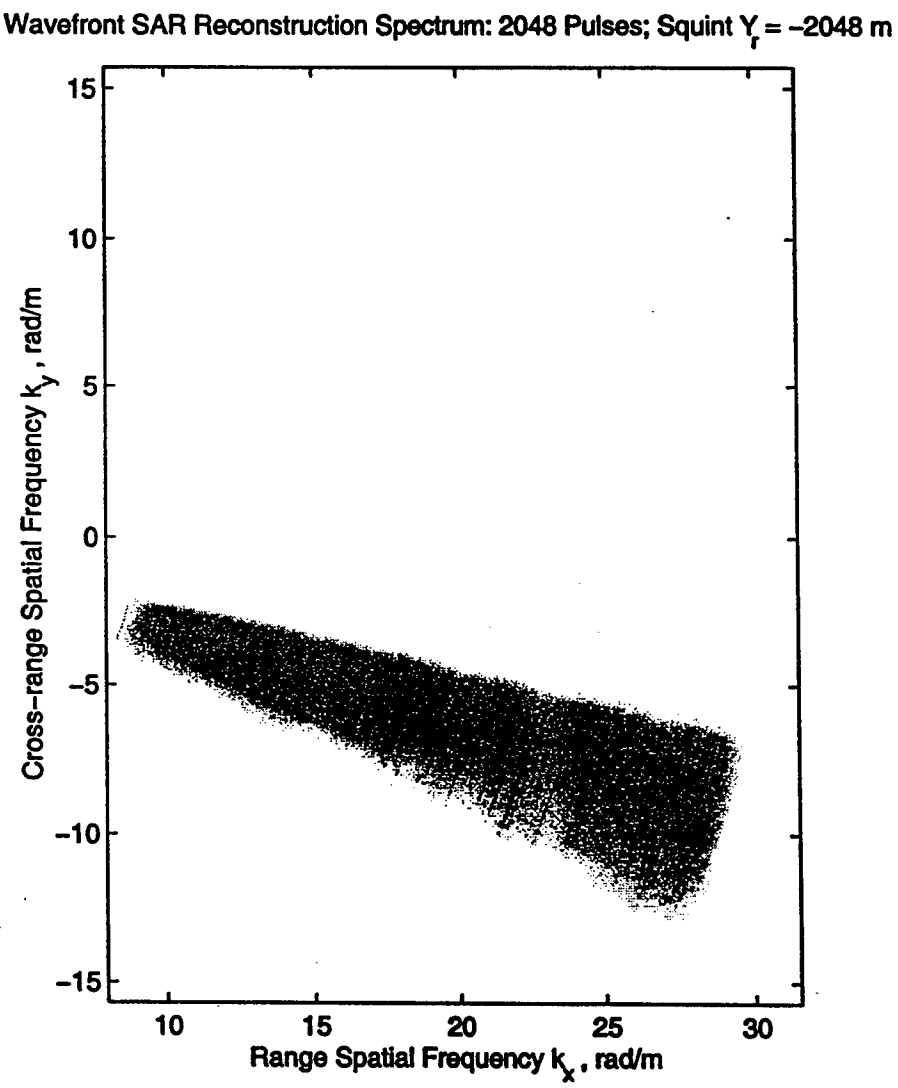
Wavefront SAR Reconstruction Spectrum: 2048 Pulses; Squint Y_r = -2048 m
15
10
5
0
-5
-10
-15
10
15
20
25
30
Cross-range Spatial Frequency k_y , rad/m
Range Spatial Frequency k_x , rad/m

Wavefront SAR Reconstruction: P–3 Data; 2048 Pulses; Squint Y_r = –2048 r

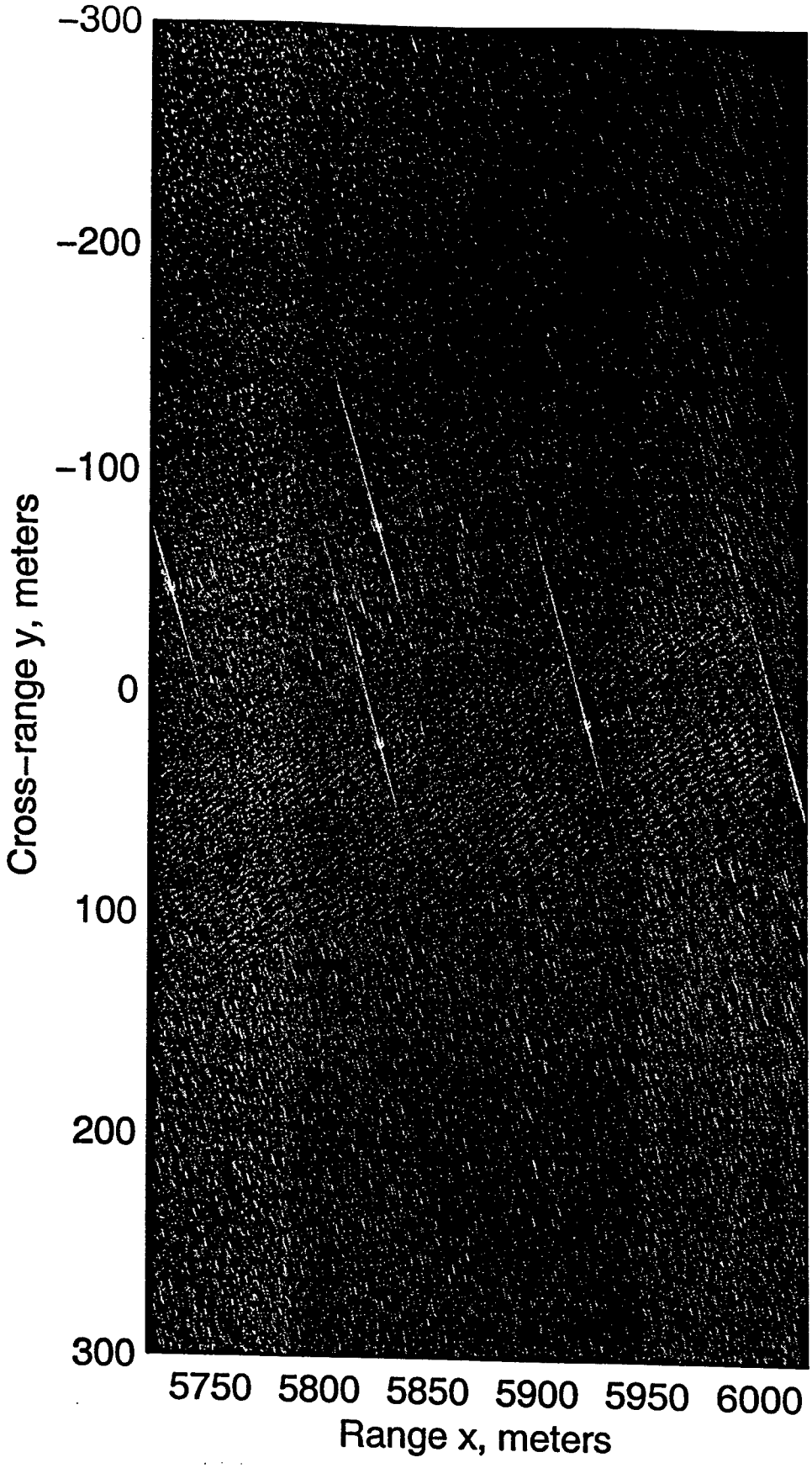

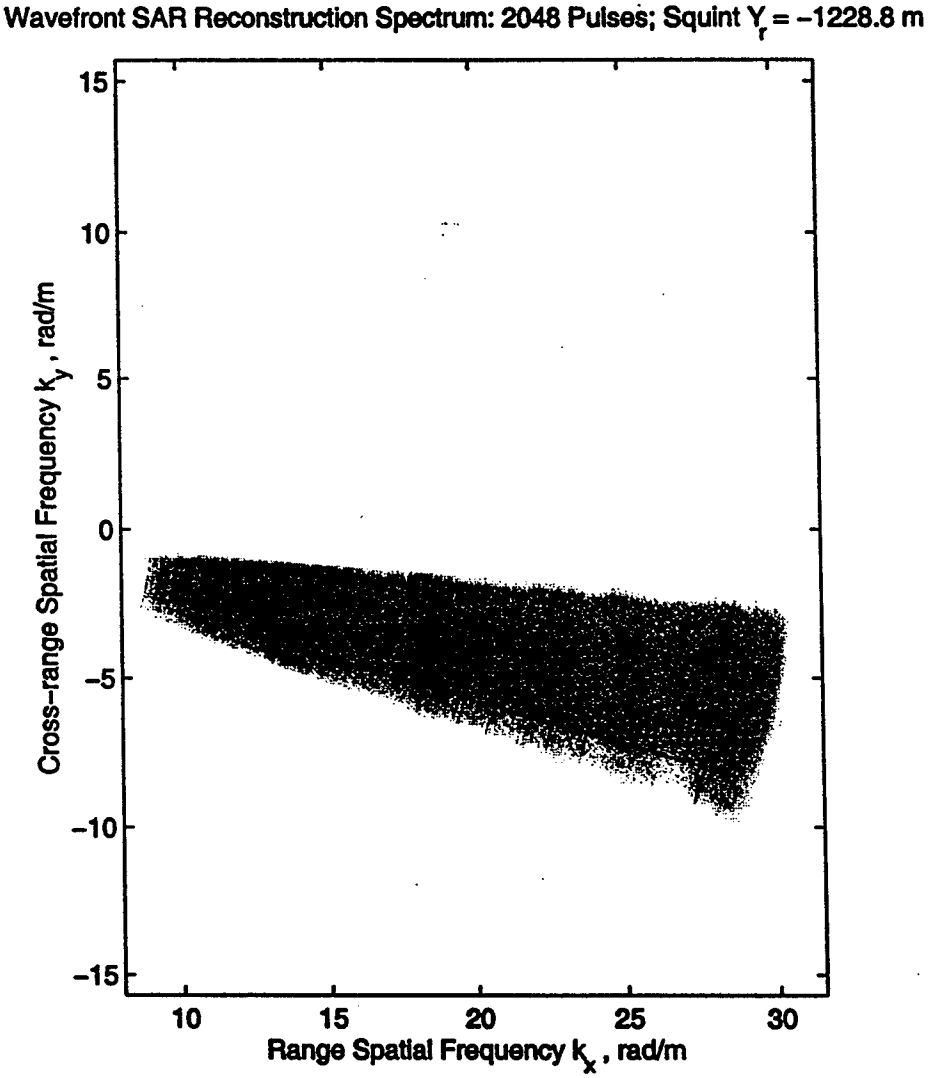
Wavefront SAR Reconstruction Spectrum: 2048 Pulses; Squint Y_r = −1228.8 m
15
10
5
0
−5
−10
−15
Cross−range Spatial Frequency k_y , rad/m
10
15
20
25
30
Range Spatial Frequency k_x , rad/m

Wavefront SAR Reconstruction: P–3 Data; 2048 Pulses; Squint $Y_r = -1228.8$

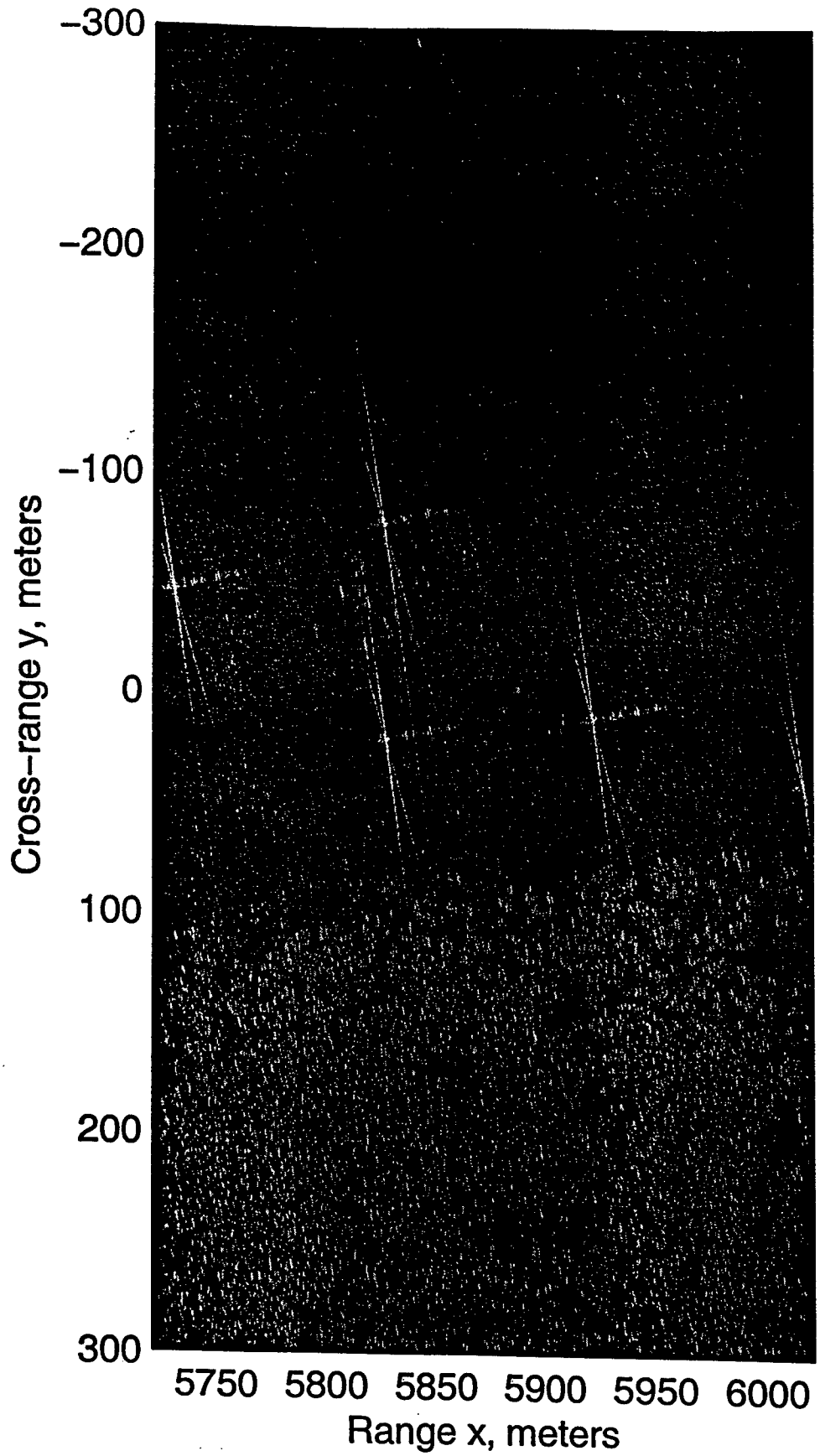

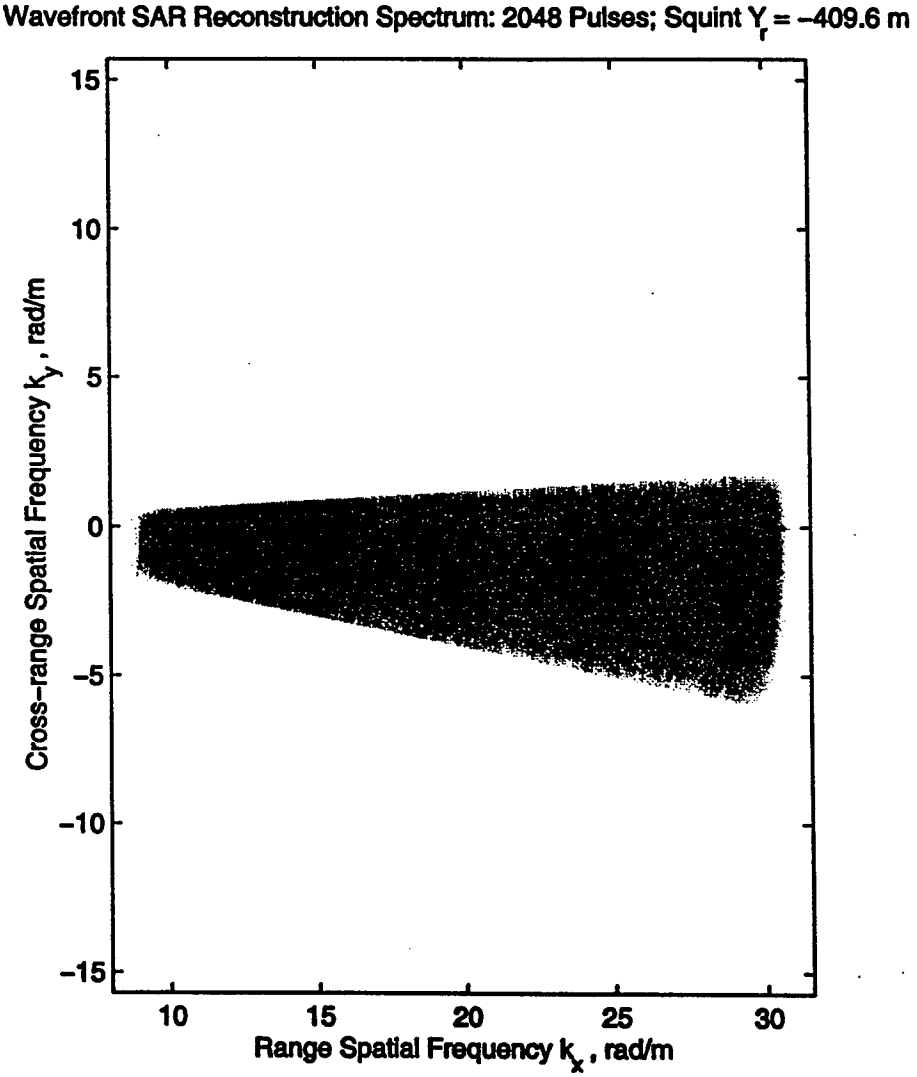
Wavefront SAR Reconstruction Spectrum: 2048 Pulses; Squint Y_r = -409.6 m
15
10
5
0
-5
-10
-15
Cross-range Spatial Frequency k_y , rad/m
10
15
20
25
30
Range Spatial Frequency k_x , rad/m

Wavefront SAR Reconstruction: P–3 Data; 2048 Pulses; Squint $Y_r = -409.6$

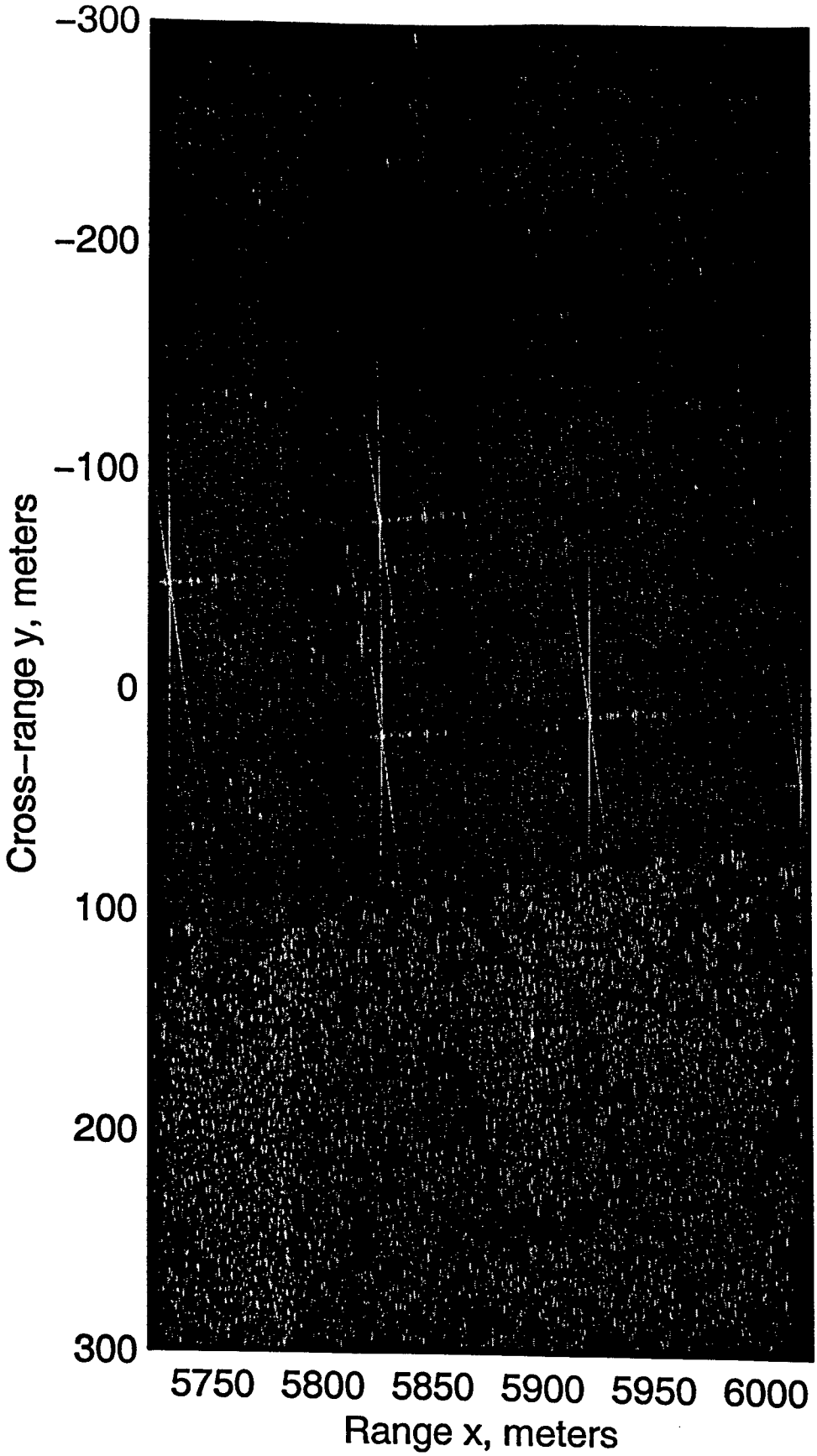

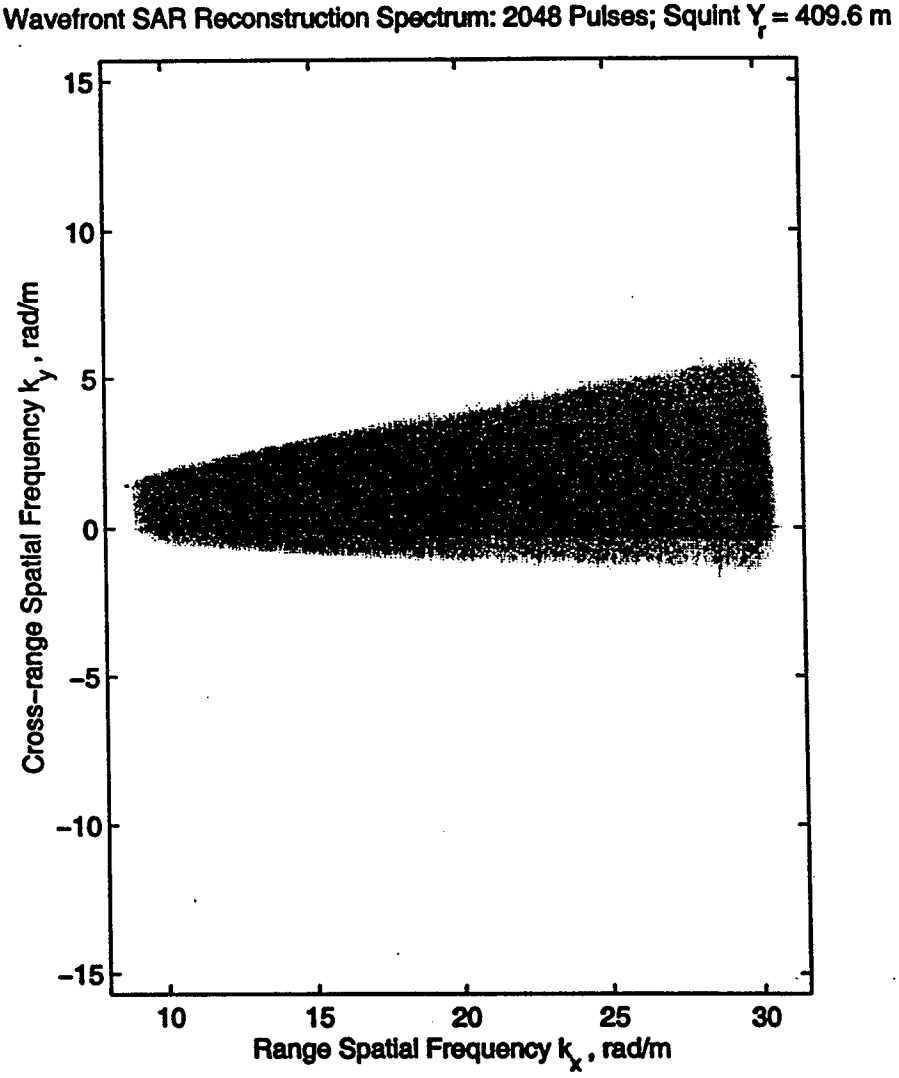
Wavefront SAR Reconstruction Spectrum: 2048 Pulses; Squint Y_r = 409.6 m
15
10
5
0
-5
-10
-15
Cross-range Spatial Frequency k_y , rad/m
10
15
20
25
30
Range Spatial Frequency k_x , rad/m

Wavefront SAR Reconstruction: P–3 Data; 2048 Pulses; Squint Y_r = 409.6 m

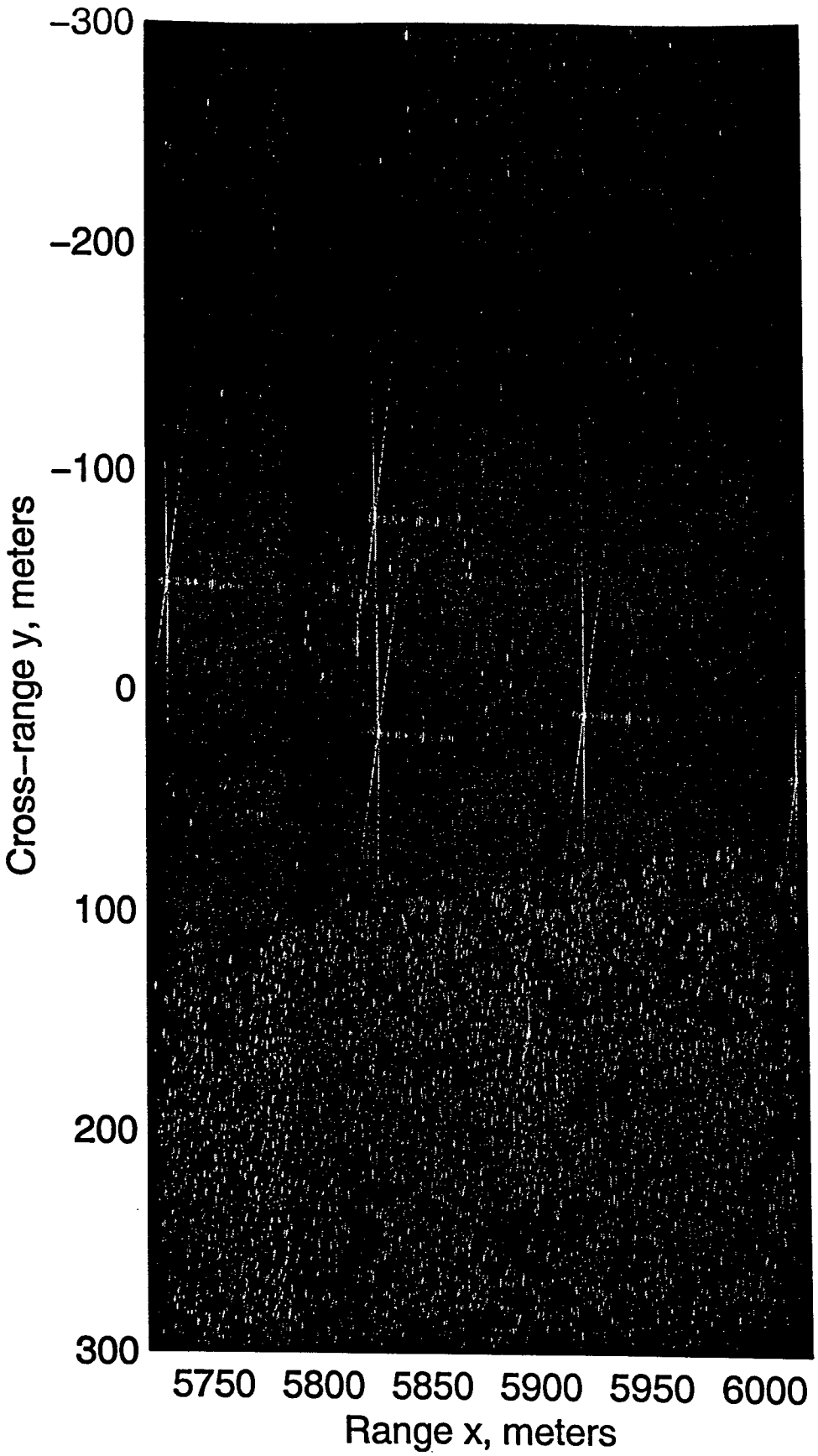

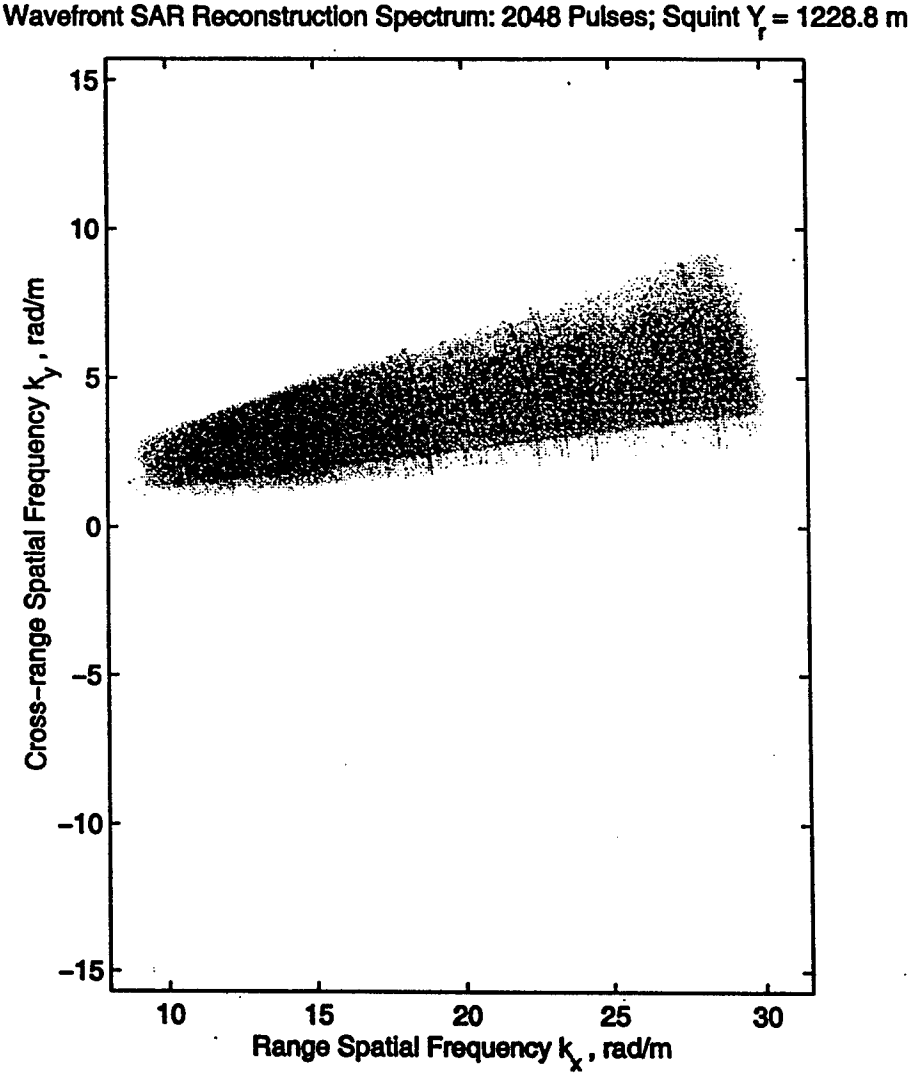
Wavefront SAR Reconstruction Spectrum: 2048 Pulses; Squint Y_f = 1228.8 m
15
10
5
0
-5
-10
-15
10
15
20
25
30
Cross-range Spatial Frequency k_y , rad/m
Range Spatial Frequency k_x , rad/m

Wavefront SAR Reconstruction: P–3 Data; 2048 Pulses; Squint Y_r = 1228.8 r

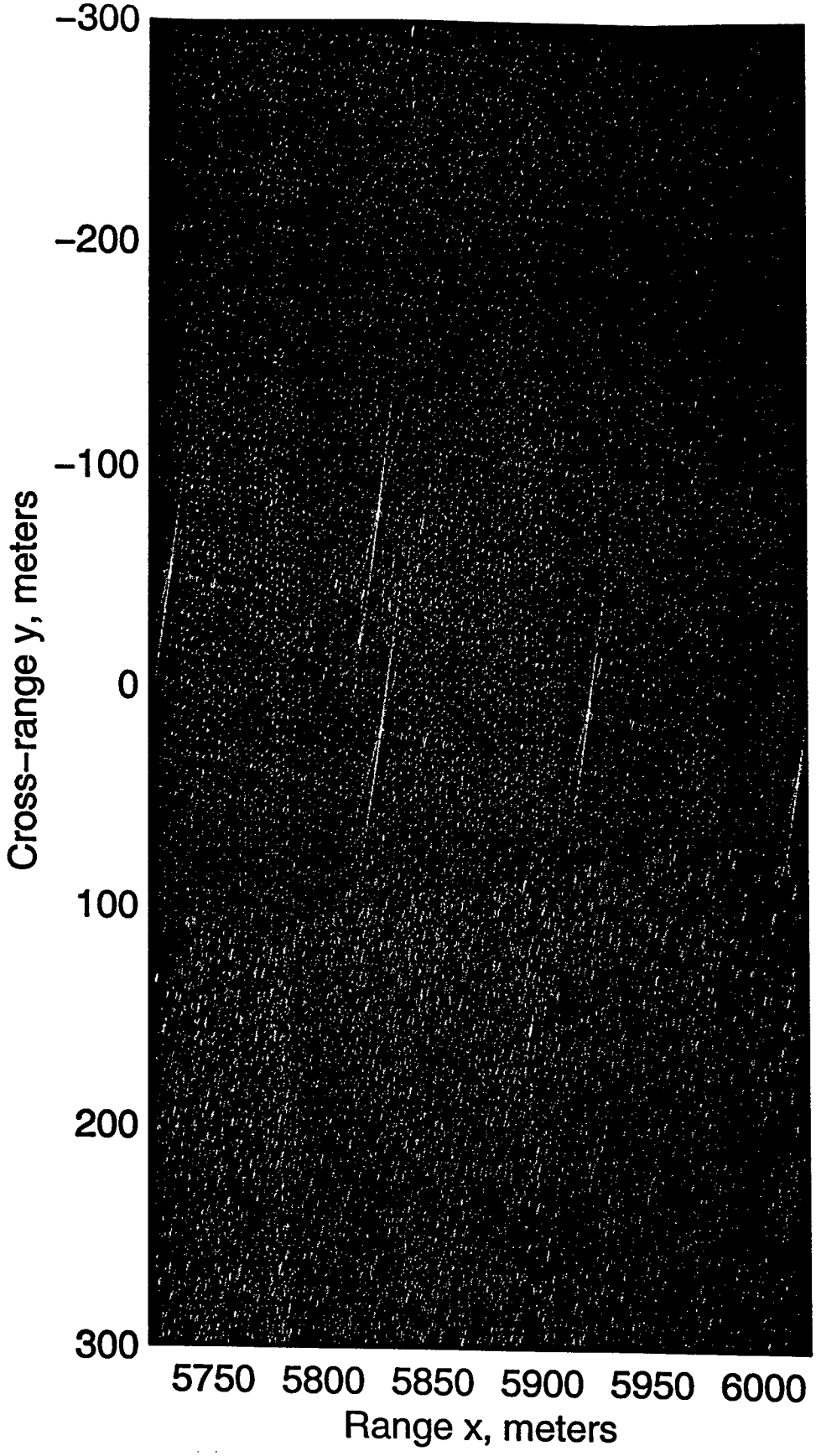

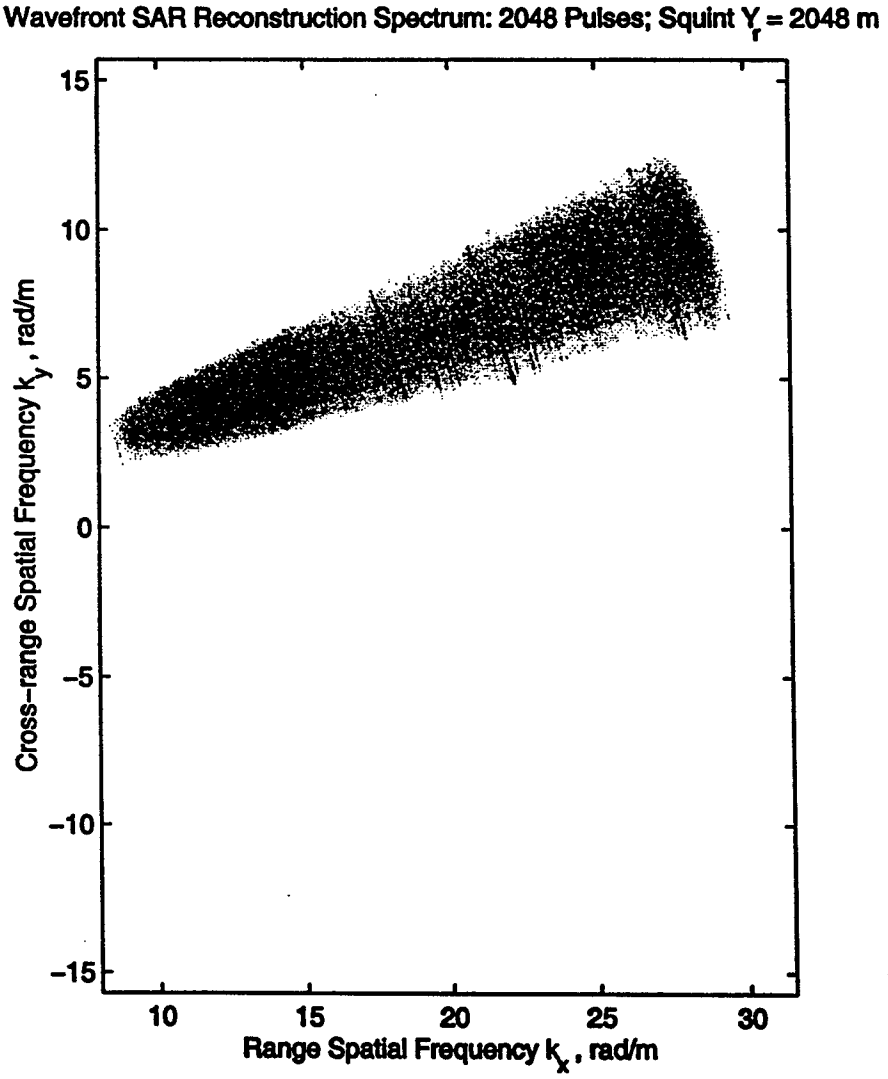
Wavefront SAR Reconstruction Spectrum: 2048 Pulses; Squint Y_r = 2048 m
15
10
5
0
-5
-10
-15
Cross-range Spatial Frequency k_y , rad/m
10
15
20
25
30
Range Spatial Frequency k_x , rad/m

Wavefront SAR Reconstruction: P–3 Data; 2048 Pulses; Squint Y_r = 2048 m

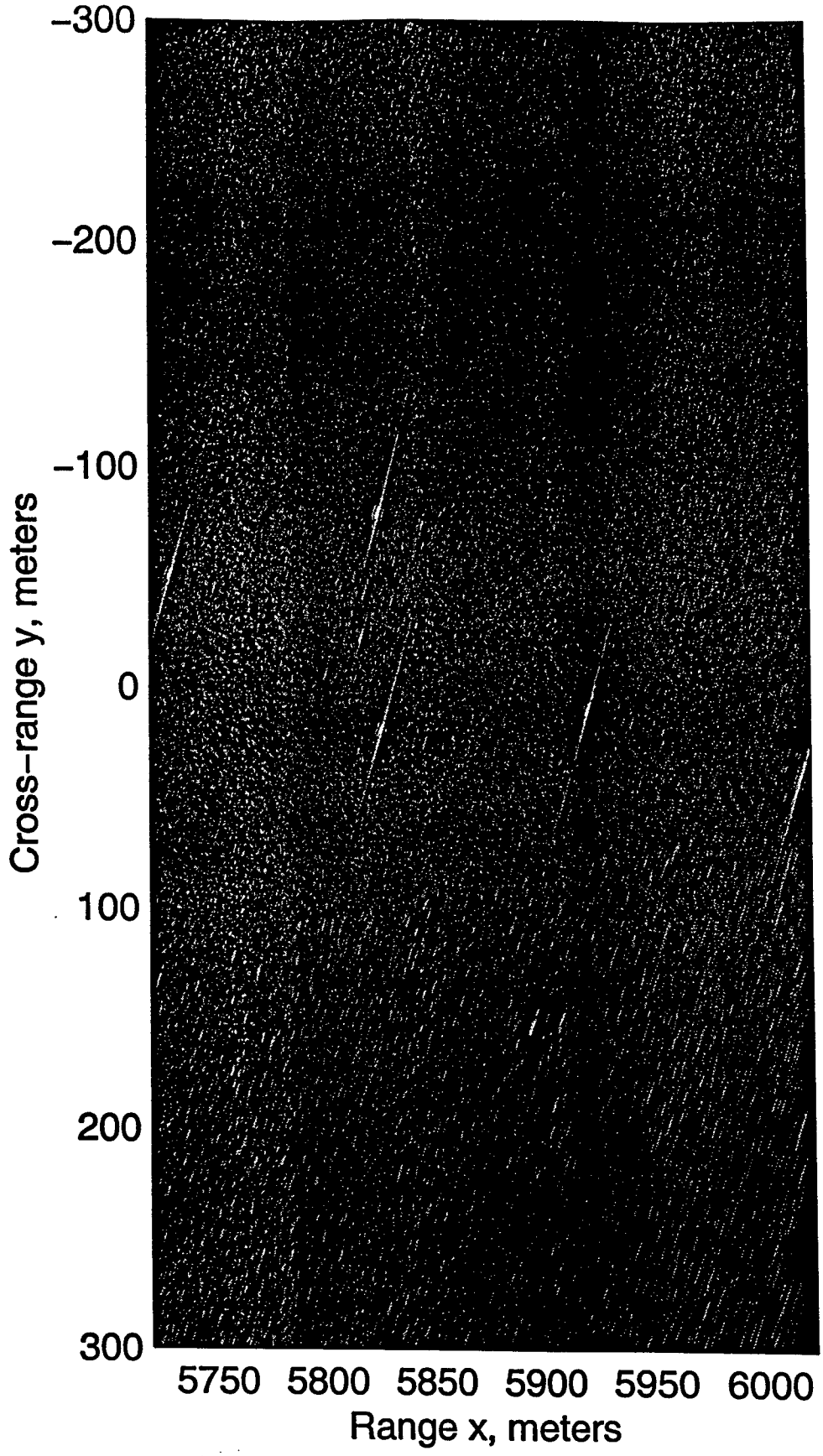

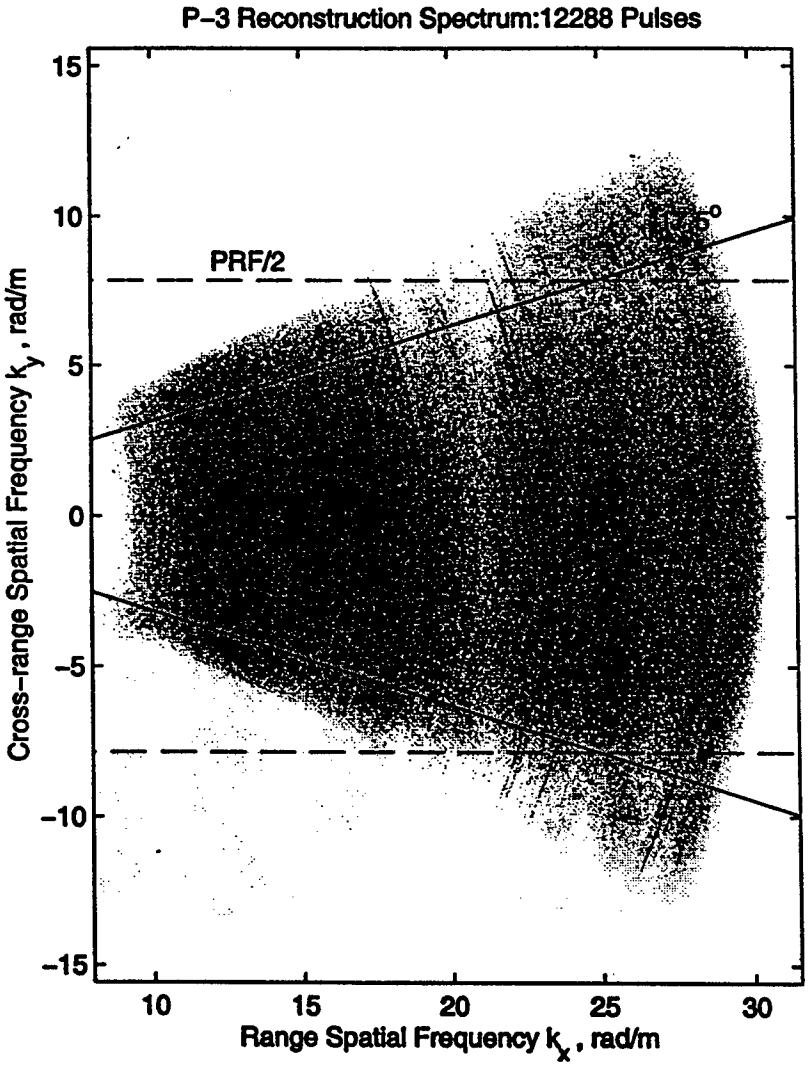
P–3 Reconstruction Spectrum:12288 Pulses
15
10
5
0
–5
–10
–15
PRF/2
10
15
20
25
30
Cross–range Spatial Frequency k_y, rad/m
Range Spatial Frequency k_x, rad/m

P–3 Subaperture Reconstruction: 12288 Pulses; Calibrated

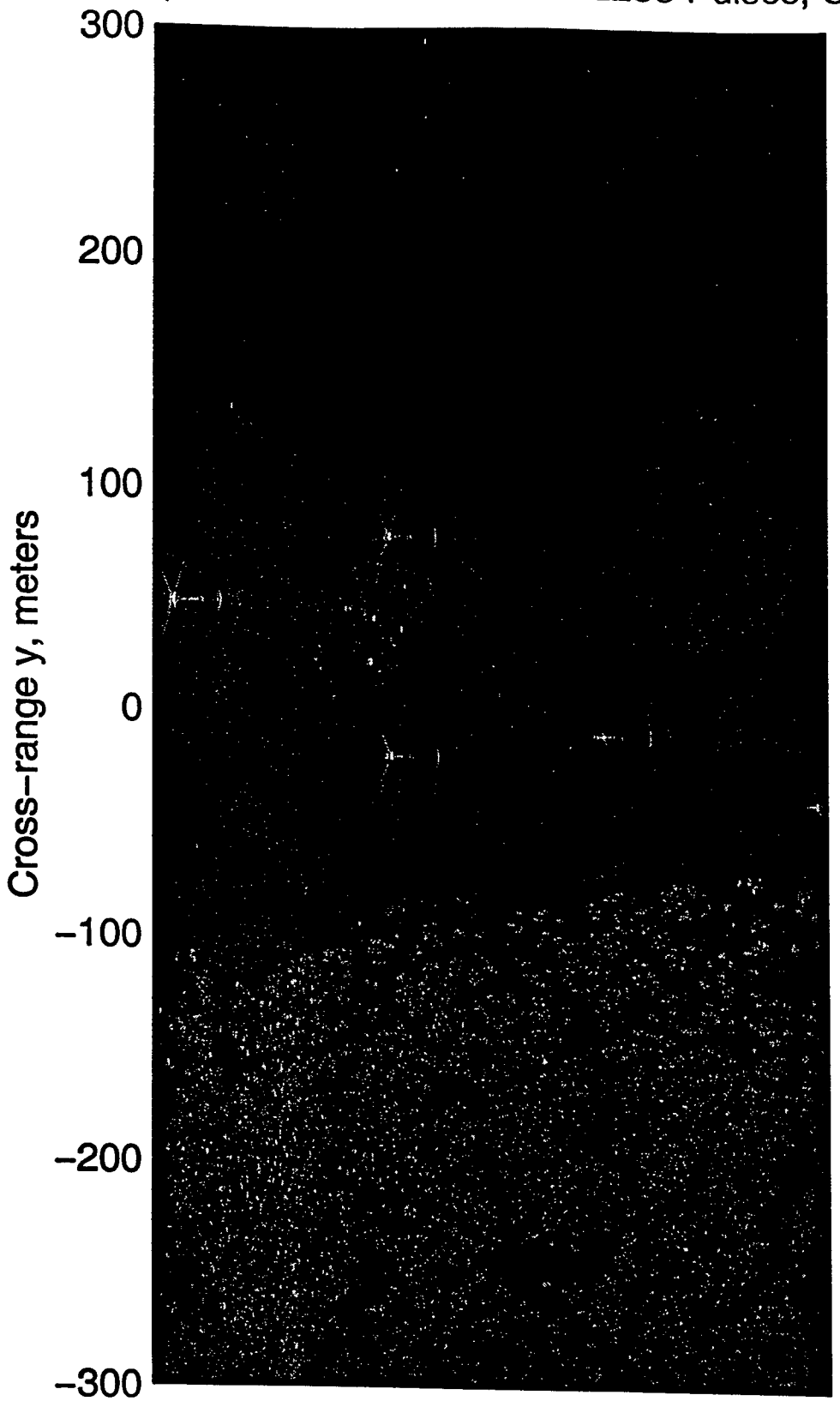

MIT–LL Reconstruction: P–3 Data; 16384 Pulses; Level 4

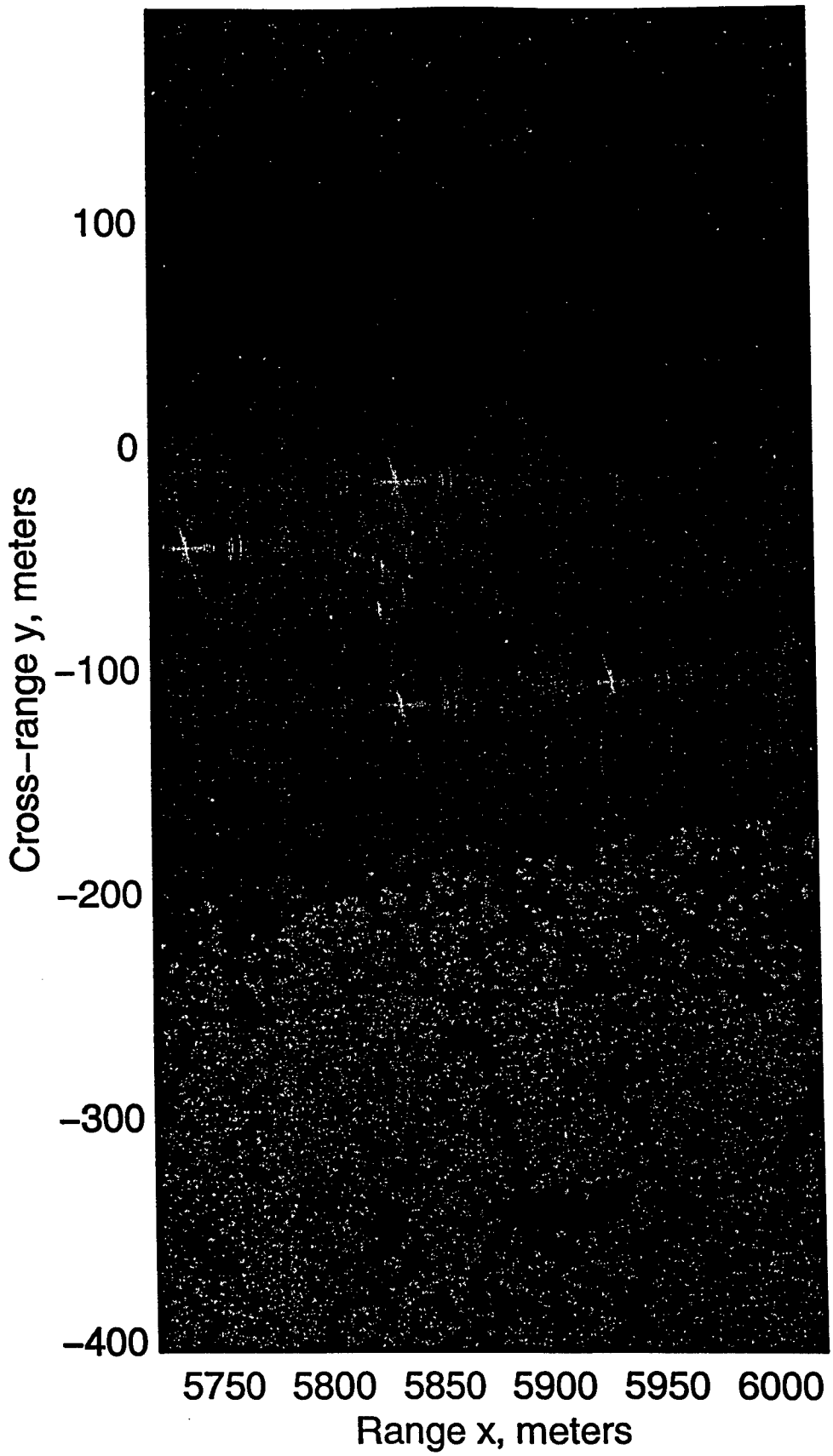

IN SITU SYNTHESIS OF DISCONTINUOUSLY REINFORCED TITANIUM ALLOY COMPOSITES VIA BLENDED ELEMENTAL POWDER METALLURGY PROCESSING

Craig A. Riviello
Ph. D. Candidate
Department of Mechanical and Materials Engineering
Wright State University

Wright State University
Department of Mechanical and Materials Engineering
204 Russ Center
3640 Colonel Glenn Highway
Dayton OH 45435-0001

Final Report for:
Summer Research Extension Program

Sponsored by:
Air Force Office of Scientific Research
Bolling Air Force Base, DC

and

Air Force Research Laboratory
Materials and Manufacturing Directorate
Wright-Patterson Air Force Base, Ohio

February 2000

IN SITU SYNTHESIS OF DISCONTINUOUSLY REINFORCED TITANIUM ALLOY COMPOSITES VIA BLENDED ELEMENTAL POWDER METALLURGY PROCESSING

Craig A. Riviello
Ph. D. Candidate
Department of Mechanical and Materials Engineering
Wright State University

Abstract

Discontinuously reinforced titanium (DRTi) matrix composites offer higher specific modulus, specific strength, wear resistance and thermal stability as compared to their unreinforced titanium alloy counterparts. These materials also offer the significant advantages of nearly isotropic properties when compared to continuously reinforced composites and the ability to be processed using conventional metal working techniques making them cost competitive for aerospace applications. In this study two alloys were selected for investigation; DRTi-6Al-4V and DRTi-10V-2Fe-3Al, both reinforced with 15 volume percent titanium boride (TiB). The composites were fabricated by the blended elemental powder metallurgy technique by *in situ* synthesis of the TiB from titanium diboride (TiB_2). The blended elemental powder metallurgy approach allows more control of alloy microstructure and a wider range of reinforcement volume percentage than conventional casting techniques or prealloyed powder techniques. Typically, morphology, not volume percentage, of the reinforcement phase is limited by the phase diagram for casting approaches. Hypereutectic compositions with primary TiB particles are likely to have poor fatigue properties. Needle morphology, better for strength and fatigue, can be obtained for hypereutectic compositions only by *in situ* reaction with TiB_2. Observations are made of an intermediate phase with a feathery morphology identified as TiB that eventually transforms with extended time at temperature to the more recognized needle morphology. The kinetics and diffusion mechanisms of the TiB_2 transformation to TiB in the temperature range of 1100°C to 1400°C (2012°F to 2552°F) are discussed.

IN SITU SYNTHESIS OF DISCONTINUOUSLY REINFORCED TITANIUM ALLOY COMPOSITES VIA BLENDED ELEMENTAL POWDER METALLURGY PROCESSING

Craig A. Riviello

INTRODUCTION

There is a broad range of Air Force requirements for discontinuously reinforced metals (DRX) with improved properties, where 'X' can be Al, Mg, Ti, etc. The successful development and implementation of discontinuously reinforced aluminum (DRA) alloys under the Air Force's Title III Program has paved the way for other DRX alloys.

Highly loaded structures require DRX with improved strength and stiffness. Discontinuously reinforced titanium (DRTi) alloy composites offer higher specific modulus, specific strength, wear resistance and thermal stability as compared to their unreinforced titanium alloy counterparts. These materials also offer the significant advantages of nearly isotropic properties when compared to continuously reinforced composites and the ability to be processed using conventional metal working techniques making them cost competitive for aerospace applications.

The use of conventional ingot metallurgy titanium products has lead to higher costs at almost every production stage when compared to powder metallurgy techniques. A major incentive is to reduce the cost of the processing steps or to eliminate them altogether, while maintaining superior properties over conventional ingot metallurgy products.[1,2,3] The blended elemental (BE) powder metallurgy process has been identified as a promising approach to overcome the high production cost of titanium alloy parts for the following reasons:[1]

- An inexpensive by-product of the production of sponge titanium, sponge fines, can be used directly as the raw material (cost savings);
- The melting and hot production processes which contribute to the high cost can be eliminated (cost savings);
- Near net shape capability achieves extremely high material yields (exceeding 90% for the BE method compared to just 20% to 50% for normal ingot forging methods) allowing a considerable reduction in post-processing costs for machining and grinding operations (cost savings); and

- Powder metallurgy methods can produce compositions difficult to achieve by conventional ingot metallurgy, resulting in a dramatic increase in freedom of control of the microstructure (performance improvement)

The improved properties of DRX alloys are achieved through the introduction of a high strength and high modulus reinforcement phase in the discontinuous form of whiskers, platelets, and/or particles.[1,4,5] The ideal reinforcement should meet the following conditions:[1,2,3]

- High strength and stiffness, as well as the capability to maintain high strength at high temperatures;
- Thermodynamic stability with titanium alloys from room to sintering temperatures;
- Insolubility of the elements comprising the reinforcing compound in the titanium matrix and the titanium atoms in the reinforcing compound; i.e., mutual insolubility;
- A coherent boundary between the matrix and reinforcing compound;
- Minimal difference in thermal expansion between the matrix and reinforcing compound.

Previous studies have shown that titanium (mono) boride (TiB) is a superior reinforcement compound in titanium alloys for the reasons outlined above.[1,4,5] However, TiB is a line compound formed by a peritectic reaction and cannot be obtained in powder form; therefore, an *in situ* synthesis of TiB is required by the transformation of titanium diboride (TiB_2). The advantages of *in situ* processing when compared with conventional powder metallurgy and casting particulate approaches include cost-effectiveness, homogeneous distribution of reinforcement, finer particles, improved wettability between the reinforcement and matrix and elimination of the deleterious interface reaction.[5]

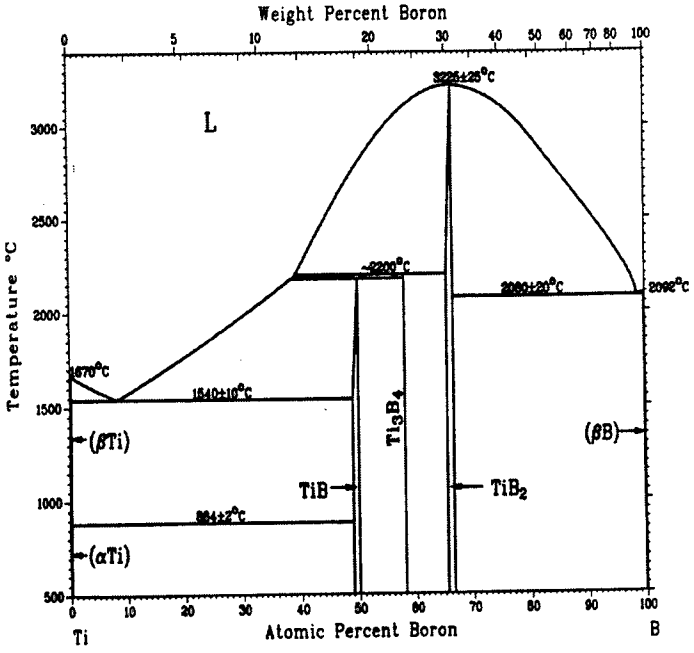

Figure 1

Titanium-Boron Phase Diagram

The BE powder metallurgy approach allows more control of alloy microstructure and a wider range of reinforcement volume percentage than conventional casting techniques or prealloyed powder techniques. Typically, morphology, not volume percentage, of the reinforcement phase is limited by the phase diagram for casting approaches. Hypereutectic compositions with primary TiB particles are likely to have poor fatigue properties. Needle morphology, better for strength and fatigue, can be obtained for hypereutectic compositions only by *in situ* reaction with TiB_2.

PROBLEM DISCUSSION

The transformation of TiB_2 to TiB occurs by the decomposition of the TiB_2 and the subsequent diffusion of boron, and possibly titanium, to form TiB needles. As seen from the phase diagram, TiB_2 is thermodynamically unstable in titanium and will decompose according to the governing reaction equation:

$$Ti + TiB_2 \rightarrow 2TiB$$

The theoretical thermodynamic calculations also support the reaction occurring as the system undergoes a decrease in free energy as evidenced in Figure 2.

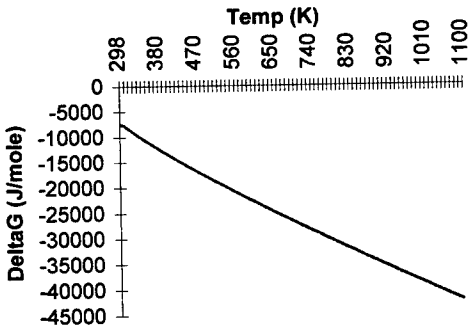

Figure 2 ΔG vs. Temp. for the Reaction
$Ti + TiB_2 \rightarrow 2TiB$

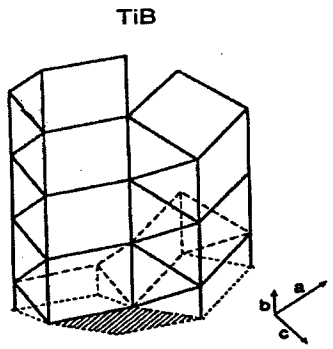

Figure 3 TiB Crystal Structure

The atomic radii difference between titanium and boron, 0.147 nm for titanium and 0.092 nm for boron, would support interstitial diffusion, but is also indicative of limited solubility of boron in titanium. The crystal structure of TiB also supports the interstitial diffusion

mechanism although a short circuit diffusion path could be argued. Boron atoms could diffuse along the zigzag chains within the TiB structure, but the lattice arrangement also presents what are referred to as "boron-free pipes", as identified by the cross-hatched parallelogram in Figure 3, that may serve as a short circuit path for boron atoms to reach the tip of the needle to sustain continued growth.

Numerous authors have experimented and analyzed the diffusion of boron in titanium through the use of various types of diffusion couples over a wide range of temperatures.[6-13] As such, each has reported different diffusion coefficients and pre-exponentials, none of which provides a clear picture of whether the diffusion mechanism is interstitial or substitutional. It is evident that there are different growth rates of the diffusion couple reaction layer and the TiB needles, with the needles growing much faster than the reaction layer. Fan *et. al.* stated that the growth of the needles was approximately six times that of the reaction layer.[13] It is not made clear how this figure was arrived at, but references are made to scanning electron microscope (SEM) micrographs with no mention of any type of method to isolate the resultant needles. If this is indeed how needle lengths were determined, then again, a significant amount of error could be introduced by not accurately portraying the needle lengths in the two-dimensional realm of the SEM. It is sufficient to state at this point in time that the needles do indeed grow faster than the reaction layer as evidenced from the diffusion couple micrographs, but to arrive at accurate diffusion parameters would be a rigorous procedure.

Saito, whose work was a great influence on this research, used the blended elemental powder metallurgy approach to fabricate his composites.[1,2,3] He concentrated in the temperature range of 1300°C (2372°F) to obtain the *in situ* transformation of his composites, but does not provide any diffusion data. Because the formation of the TiB reinforcement phase is via the *in situ* method, it was not only important in this research to identify the diffusion mechanism, but also to understand the times over the selected temperature range of 1100°C to 1400°C (2012°F to 2552°F) for which TiB_2 was completely transformed to TiB. This information could assist future researchers in expanding their efforts to larger size powders to fabricate DRTi composites, with the associated cost savings that are inherent with larger size powders. Different size powders will lead to different times to effectively

transform the TiB_2, however an accurate pre-exponential and activation energy will assist researchers in pinpointing the transformation time without the rigors of diffusion couples and trial and error experiments.

EXPERIMENTAL PROCEDURE

Material

Two discontinuously reinforced titanium alloy composites were selected for investigation in this study: DRTi-6Al-4V and DRTi-10V-2Fe-3Al, both reinforced with 15 volume percent TiB obtained from the *in situ* reaction of TiB_2 (referred to hereafter as DRTi-6Al-4V/TiB/15p or DRTi-10V-2Fe-3Al/TiB/15p). The blended elemental powder metallurgy approach was used to fabricate these composites. Elemental powders of titanium, aluminum, vanadium, iron, titanium diboride and aluminum/vanadium master (35Al/65V wt%) alloy were procured. The titanium powder was obtained from Crucible Research Corporation as gas atomized, -100 mesh (≤ 150 microns) with an oxygen content of approximately 800 ppm. The other powders, except for the master alloy, were obtained as -325 mesh (≤ 45 microns). The master alloy ranged in size from -30 mesh (≤ 600 microns) to +200 mesh (≥ 75 microns). The as-received morphology of the powders is documented in Figures 4 through 9. The chemical analysis of the powders is presented in Table 1.

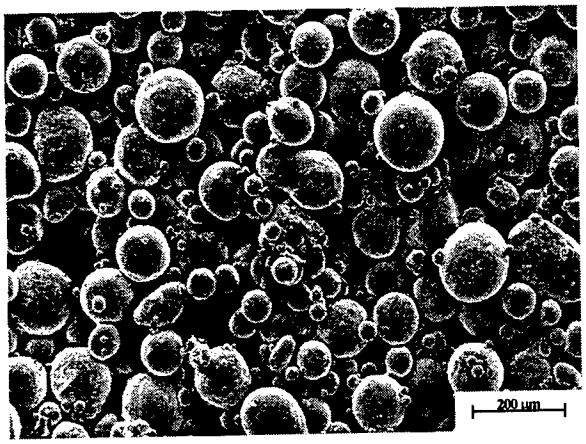

Figure 4

-100 mesh Titanium

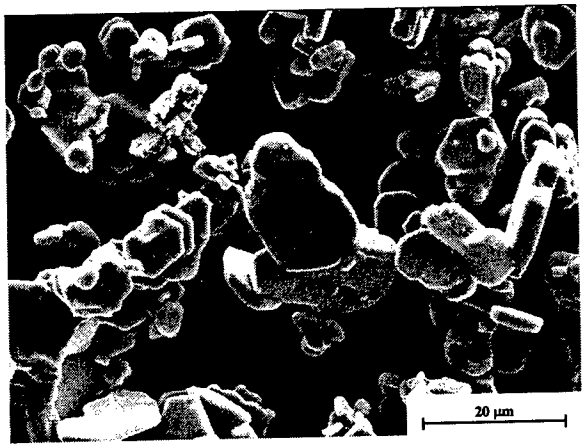

Figure 5

-325 mesh Titanium Diboride

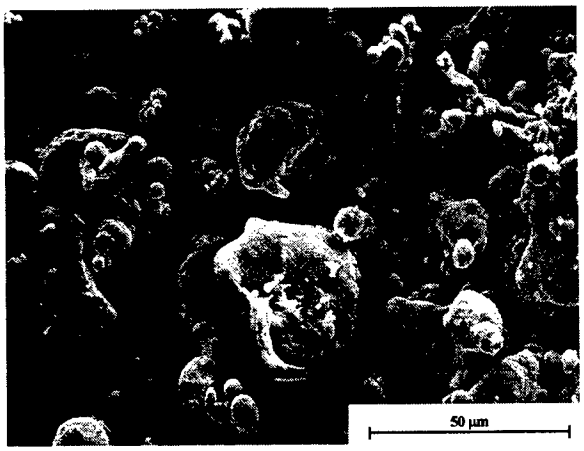

Figure 6

-325 mesh Aluminum

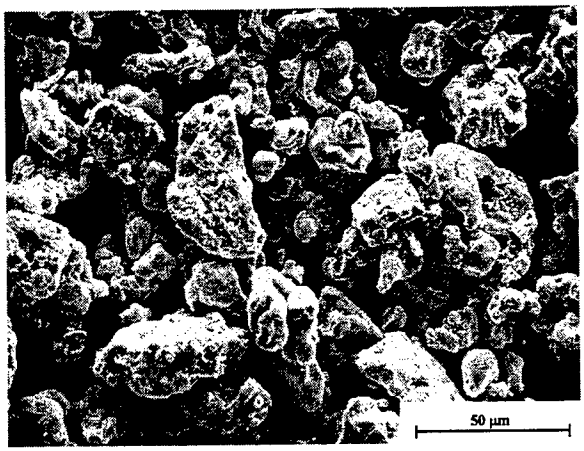

Figure 7

-325 mesh Iron

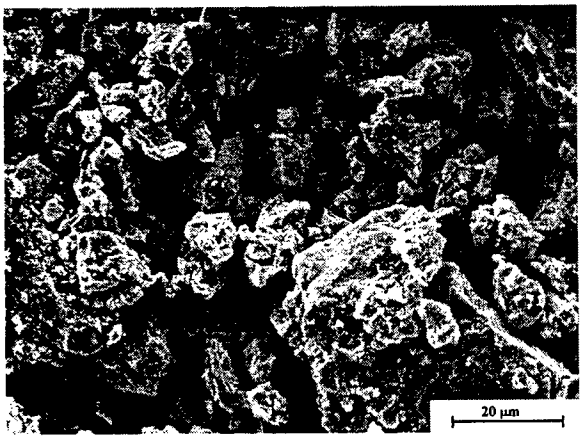

Figure 8

-325 mesh Vanadium

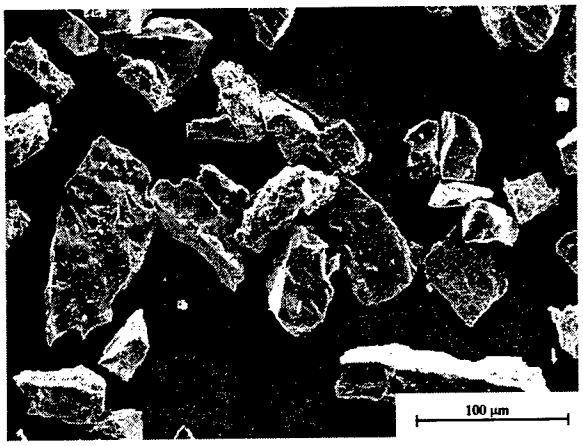

Figure 9

-30/+200 mesh Aluminum/Vanadium

Powder Blending

The powders were weighed based on calculations for the required reinforcement volume percentage and initially dry blended for 24 hours at 176 RPM on a U.S. Stoneware model 784AVM jar mill. Sundrica developed the following formula for finding the optimal rate of rotation that balances gravitational and centrifugal forces acting on the powder:[14]

$$N_o = 32/d^{1/2}$$

where d is the container diameter in inches and N_o is the optimal rate of rotation in RPM. Stainless steel spheres were added to the mix and the powder was dry blended for an additional 24 hours.

	Al (-325 mesh)	Al-V Master	Fe (-325 mesh)	V (-325 mesh)	Ti (-100 mesh)	TiB_2 (-325 mesh)
O	0.371	0.076	1.65	4.26	0.098	0.421
N	<0.003	0.010	0.005	0.050	0.008	0.021
C	0.0044	0.0326	0.0268	0.0556	0.0164	0.4326
Fe	0.12	0.12	Base	0.030	0.028	
B						29.54
Cr			0.060			
Cu			0.034			
Ni			0.021			
Ti					Base	Base
V		Base		Base		
Zr						0.015
Al	Base	31.91	0.45	0.097		
Ca			0.22			
Mn			0.40			
Cl						
H					0.0093	

Table 1 Constituent Weight Percentages of As-Received Powder

Figures 10 and 11 document the powder distribution after mixing. Preliminary assessment indicated the powder was evenly distributed with the smaller particles filling the voids between the larger titanium particles.

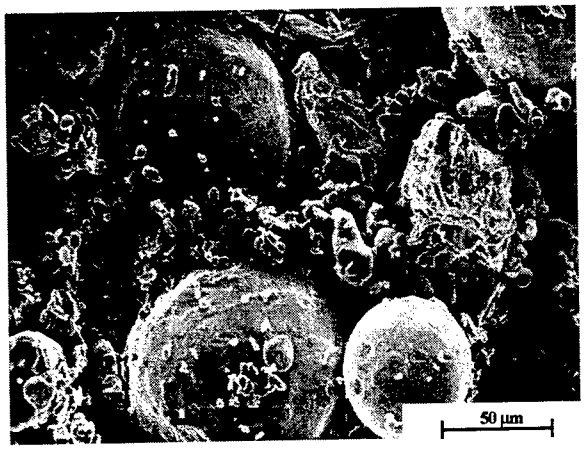

Figure 10

Blended DRTi-6Al-4V/TiB_2

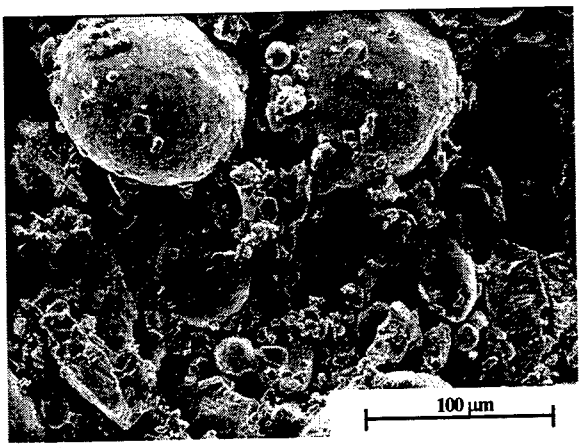

Figure 11

Blended DRTi-10V-2Fe-3Al/TiB_2

Cold compacts of approximately 0.5-inch diameter by 0.25-inch thick were fabricated from the blended powders using a Carver Laboratory Press and applying a force of 12,000 pounds. Compacts of each alloy were vacuum heat treated for one hour at temperatures of 900, 1000, 1100, 1200, 1300 and 1400°C (1652°F to 2552°F) and furnace cooled at a rate of 25°C/min. Additional compacts of each alloy were vacuum heat treated for 4 hours at 1100, 1200, 1300 and 1400°C (2012°F to 2552°F). X-ray diffraction was accomplished on a Rigaku "Rotaflex" Series RU-200B diffractometer

Extrusion

Two extrusion cans, 7.6 cm (3-inch) in diameter fabricated from commercially available Ti-6Al-4V round stock, were filled with the blended powders in an argon atmosphere glove box, vacuum outgassed and sealed. Each can contained approximately 1.1 kg (2.5 pounds) of blended powder. The vacuum outgassing occurred in a two step sequence; the blended powder was back filled twice with argon, then heated to 300°C (572°F) for 24 hours while back filling twice again with argon.[15,16] The cans were heated to 1065°C (1950°F) for 1.5 hours, blind die compacted and turned on a lathe to return to their cylindrical form, reheated to 1065°C (1950°F) for 1 hour and extruded through a 20 mm (0.8 inch) square die at a reduction ratio of 10.2:1. The temperature of 1065°C (1950°F) was chosen to compare with previous published extrusion results done at this temperature.[4,17]

Hot Isostatic Pressing

Hot isostatic pressing (HIPing) of the blended powders was used as an alternative approach to fabricate the composites. Two HIP cans, 2.5 cm (1-inch) in diameter fabricated from commercially available Ti-6Al-4V round stock, were filled with the blended powders in an argon atmosphere glove box, vacuum outgassed and sealed. Each can contained approximately 160 grams (0.35 pounds) of powder. The outgassing sequence was the same as for the extrusion process. The cans were hot isostatically pressed (HIPed) at 1065°C (1950°F) for 3 hours at 103.4 MPa (15 ksi).

Microstructural Evaluation

Specimens, approximately 5 mm in thickness were cut from the extruded and HIPed products, sectioned to smaller sizes to remove the can material on a Buehler diamond saw and mounted in Konductomet. The samples where wet ground using diamond abrasive wheels in the following sequence: fine grind, rough polish and medium polish, using water as a lubricant. The samples were then hand ground using 9 μm diamond paste, placed in a Buehler Vibromet containing 1 μm diamond polishing medium for eight hours and finally, 2 to 4 hours in a Buehler Vibromet containing 0.06 μm colloidal silica polishing medium. Microstructural features were examined using a LEICA Stereoscan 360FE SEM. Electron probe microanalysis (EPMA) was conducted on a JEOL Superprobe 733 microanalyzer. Electrolytic deep etching in a solution of methanol and 7% hydrochloric acid, utilizing a Struers Polipower power supply set at 0-30 volts and 0-10 milliamps, accomplished extraction of the TiB needles.

Diffusion Couples

Diffusion couples where fabricated by filling four commercially pure titanium HIP cans with pure TiB_2 powder. Each can was evacuated and then HIPed at either 1100°C (2012°F) for 6 hours, 1200°C (2192°F) for 9 hours, 1300°C (2372°F) for 6 hours or 1400°C (2552°) for 6 hours, all at a pressure of 103.4 MPa (15 ksi). Each can was sectioned into approximately 5 mm specimens which were then heat treated to a balance of 16, 32 or 64 hours at their respective temperatures. Measurements of the reaction layer thickness were conducted via backscatter using a LEICA Stereoscan 360FE SEM. Anywhere from 12 to 20 individual measurements were taken on each specimen to obtain a statistical average of the reaction layer thickness.

RESULTS/DISCUSSION

Heat Treatment Mapping

Because the formation of the TiB reinforcement phase is via the *in situ* method, it was important in this research to understand the times over the selected temperature range of 1100°C to 1400°C (2012°F to 2552°F) for which TiB_2 completely transformed to TiB. A heat treatment mapping study was undertaken utilizing a combination of cold compacts of the blended powders and extruded specimens to determine the transformation times at temperatures of TiB_2 particles to TiB needles for the starting size of powders outlined in the previous section.

As supported by the X-ray diffraction (XRD) patterns on pages 13 and 14, the transformation of TiB_2 to TiB is easily discerned. The circled times in Figure 12 indicate no further presence of TiB_2 and the results show that the transformation is a thermally activated process. The additional heat treatments for both alloys beyond the transformation times assisted in the analysis of TiB needle growth during extended time at temperature.

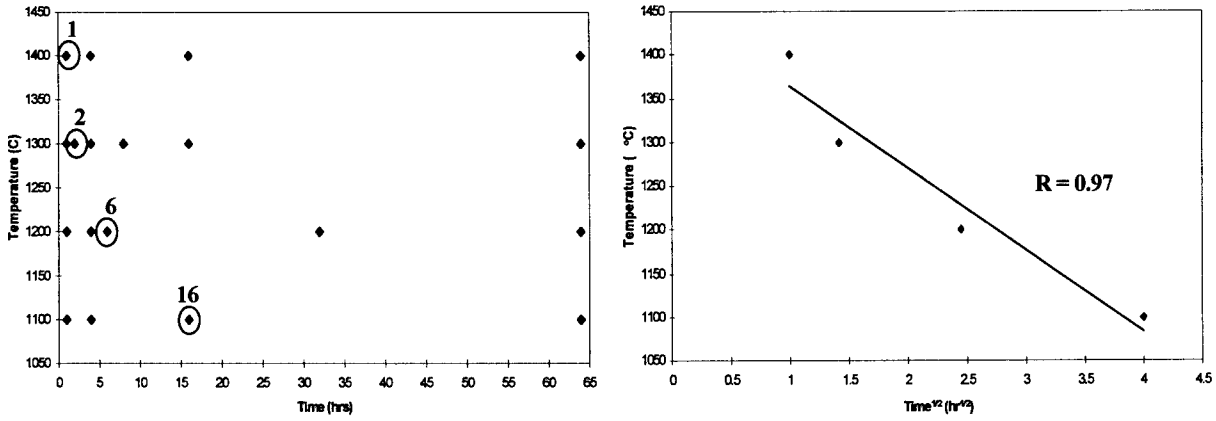

Figure 12 Transformation Times at Temperature

The as-extruded and as-HIPed chemical compositions are shown in Tables 2 and 3 and the as-extruded and as-HIPed microstructures are shown in Figures 13 through 16 (ED denotes extrusion direction). Both processing techniques were utilized such that a direct comparison of the microstructures could be performed. Given that the two microstructures display the same features, HIPing would be utilized for further processing requirements, as it is more effective from time and cost standpoints. The micrographs reveal reinforcement clusters that were originally TiB_2 particles filling the voids between the titanium powder particles. The original

DRTi-6Al-4V/TiB/15p X-Ray Diffraction Patterns
1 hr Heat Treatment Interval

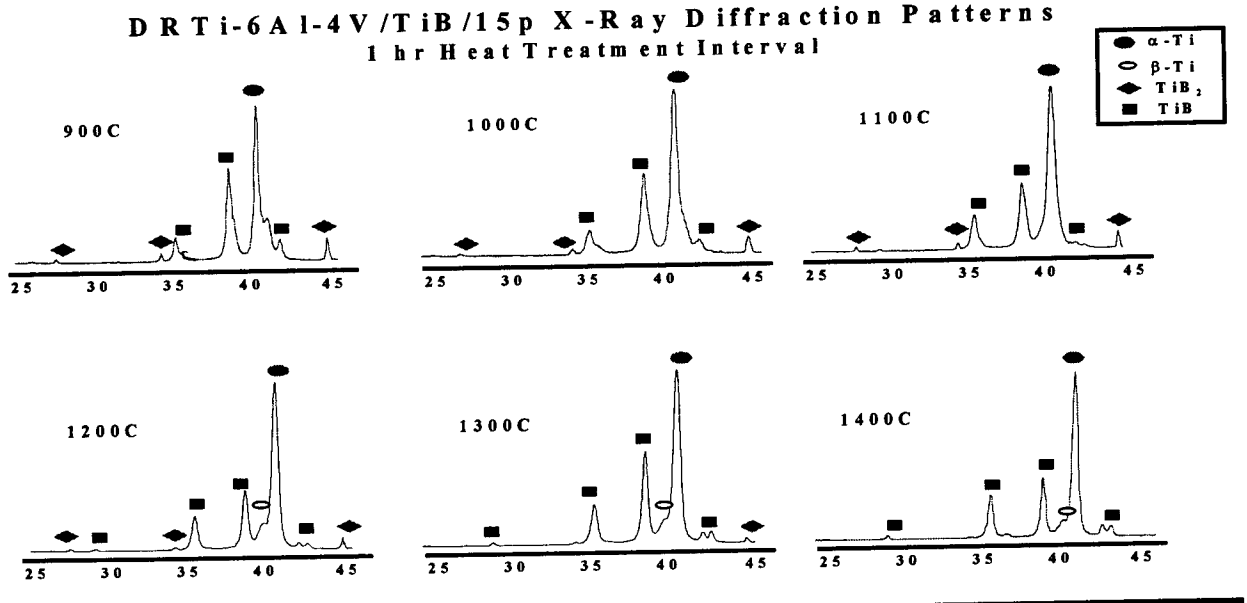

DRTi-6Al-4V/TiB/15p X-Ray Diffraction Patterns
4 hr Heat Treatment Interval

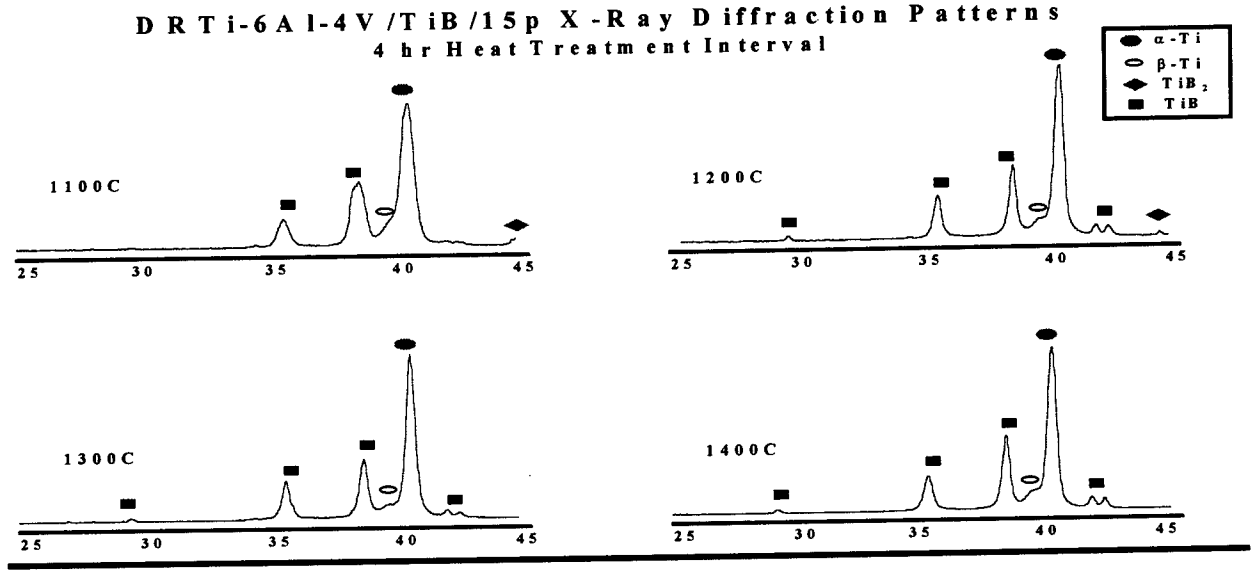

DRTi-6Al-4V/TiB/15p X-Ray Diffraction Patterns
1300C Heat Treatment

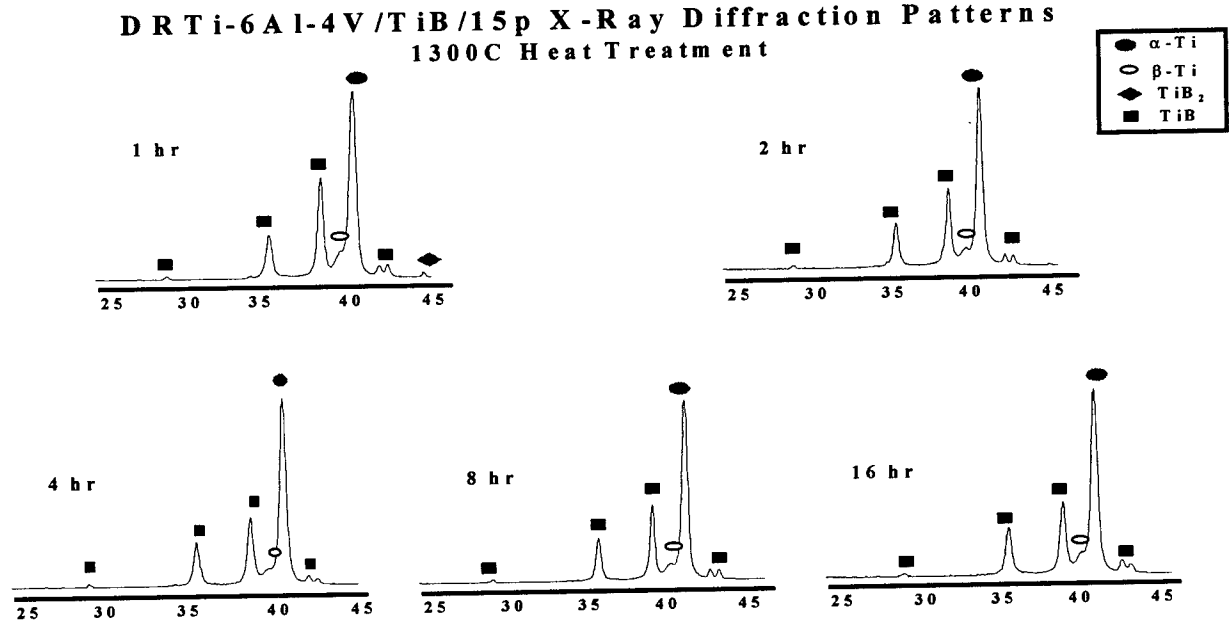

DRTi-10V-2Fe-3Al/TiB/15p X-Ray Diffraction Patterns

1 hr Heat Treatment Interval

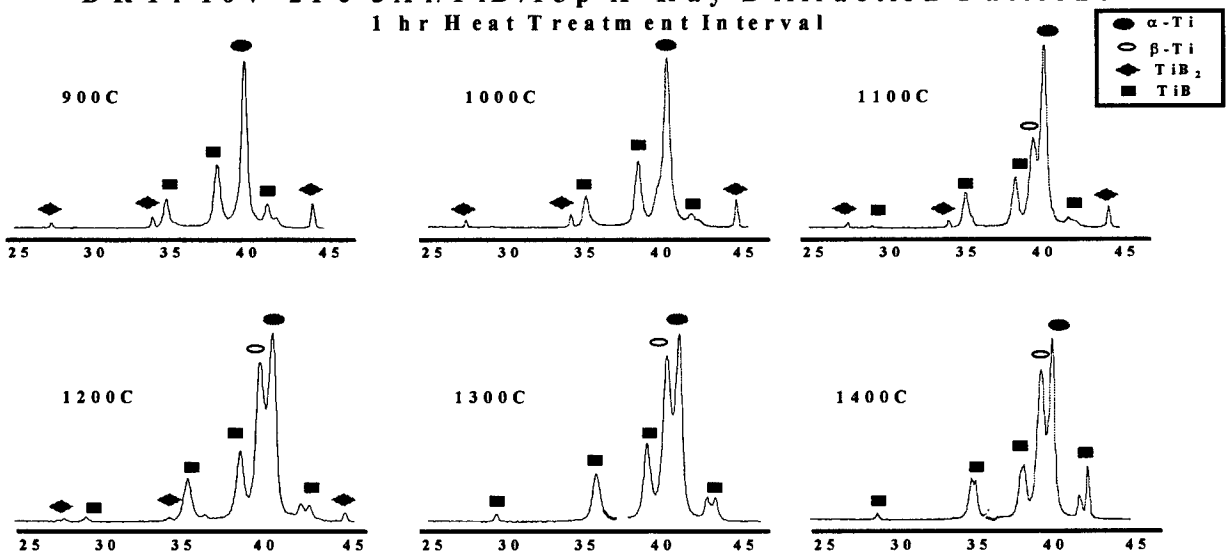

DRTi-10V-2Fe-3Al/TiB/15p X-Ray Diffraction Patterns

4 hr Heat Treatment Interval

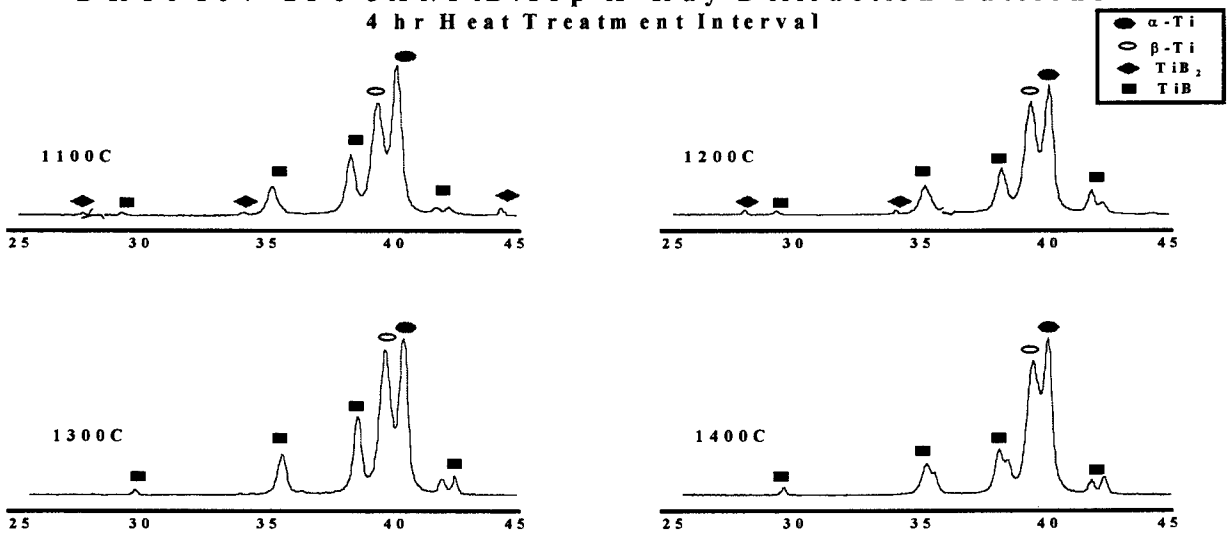

DRTi-10V-2Fe-3Al/TiB/15p X-Ray Diffraction Patterns

1300C Heat Treatment

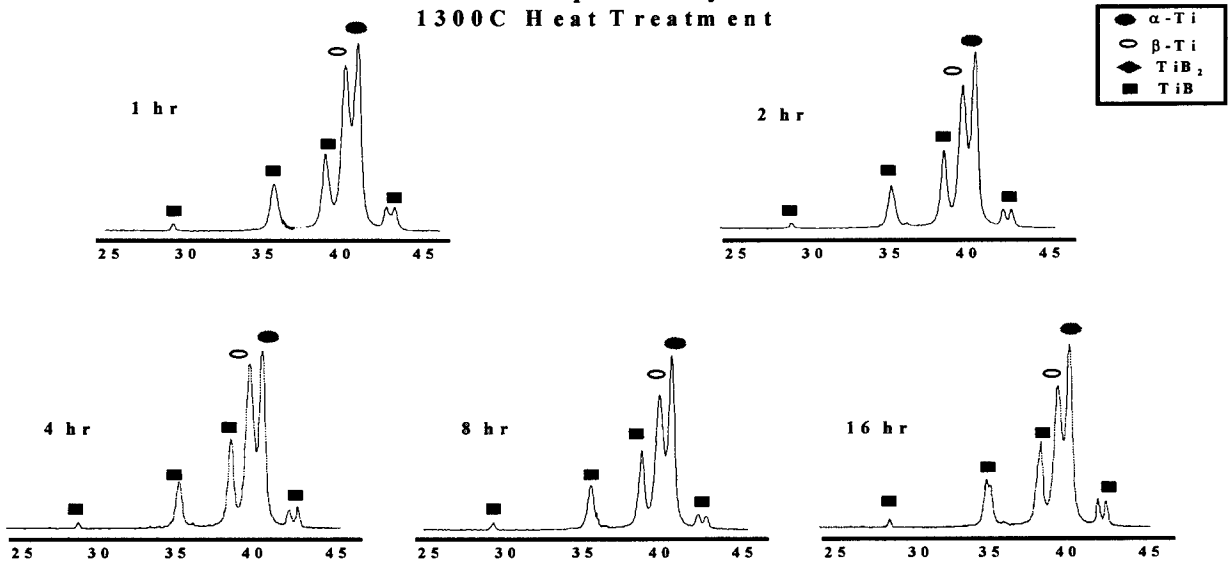

	Al	V	Fe	O	C	N	B
DRTi-6Al-4V	5.29	3.37	0.049	0.159	0.0548	0.013	2.72
Spec	5.5-6.75	3.5-4.5	0.3	0.08-0.2	0.05-0.1	0.05	---
DRTi-10V-2Fe-3Al	2.49	8.14	1.55	0.173	0.0522	0.008	2.52
Spec	2.6-3.4	9-11	1.6-2.2	0.13	0.05	0.05	---

Table 2

Constituent Weight Percentages of As-Extruded Composites

	Al	V	Fe	O	C	N	B
DRTi-6Al-4V	4.95	3.11	0.068	0.131	0.07	0.008	4.02
Spec	5.5-6.75	3.5-4.5	0.3	0.08-0.2	0.05-0.1	0.05	---
-325 Mesh DRTi-6Al-4V	5.36	2.66	0.069	0.438	0.058	0.019	2.71
Spec	5.5-6.75	3.5-4.5	0.3	0.08-0.2	0.05-0.1	0.05	---
DRTi-10V-2Fe-3Al	2.62	8.91	1.83	0.215	0.0625	0.01	3.34
Spec	2.6-3.4	9-11	1.6-2.2	0.13	0.05	0.05	---

Table 3

Constituent Weight Percentages of As-HIPed Composites

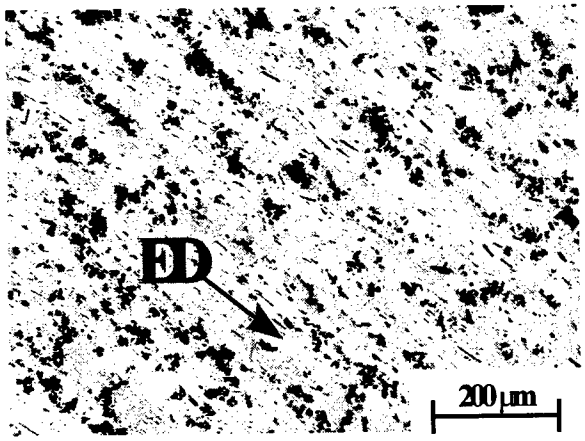

Figure 13

DRTi-6Al-4V/TiB/15p As-Extruded

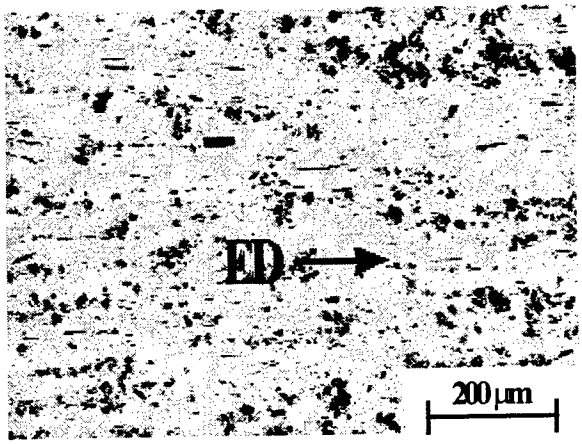

Figure 14

DRTi-10V-2Fe-3Al/TiB/15p As-Extruded

titanium powder boundaries are visible in the as-HIPed microstructure. X-ray diffraction of these samples confirmed the presence of TiB_2 and TiB as would be expected since the processing time at the extrusion temperature of 1065°C was well below the time required to obtain complete transformation at this temperature. Additionally, it appears that there are very few TiB needles in what was formerly a titanium particle indicating the limited solubility of boron in titanium of 0.001 a/o[3] to <0.003 a/o[18] and a sluggish diffusion rate.

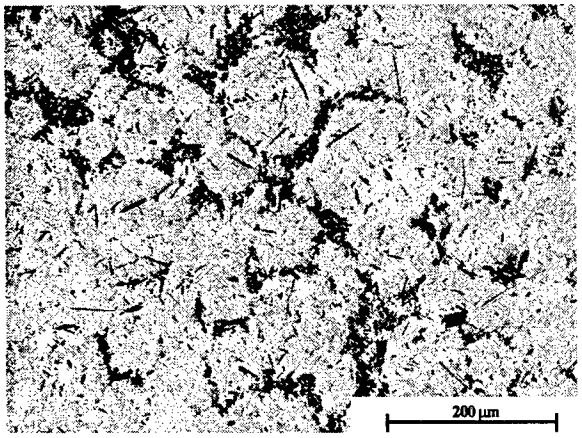

Figure 15

DRTi-6Al-4V/TiB/15p As-HIPed

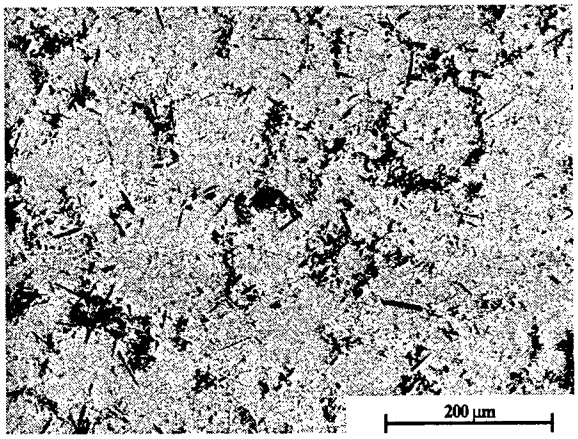

Figure 16

DRTi-10V-2Fe-3Al/TiB/15p As-HIPed

Closer examination of the clusters revealed a center consisting of untransformed TiB_2 surrounded by a layer with a feathery-like morphology. Identification of this feathery morphology was undertaken through the use of XRD analysis, energy dispersive spectroscopy (EDS) and electron probe microanalysis (EPMA). As might be expected from the phase diagram, Ti_3B_4 should be present as an intermediate compound with the decomposition of TiB_2; however, XRD analysis, EDS via the SEM, or EPMA did not detect Ti_3B_4. This suggests that Ti_3B_4 is not present, at least, in bulk quantities. Further analysis using EDS in conjunction with the transmission electron microscope will confirm or deny the presence of Ti_3B_4, but only if the small amount which may be present is happened upon.

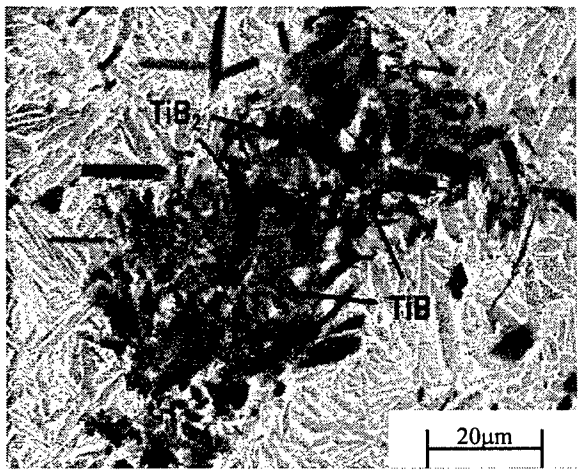

Figure 17

DRTi-6Al-4V/TiB/15p Clusters

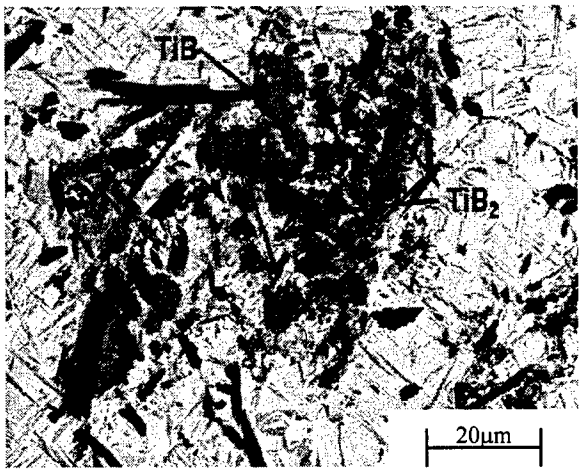

Figure 18

DRTi-10V-2Fe-3Al/TiB/15p Clusters

A series of clusters were characterized using EPMA and the feathery morphology identified as TiB, a phase quite distinct from the expected needle morphology. Figure 19 is a representative example of the EPMA with the TiB and TiB_2 regions pointed out in Figures 17 and 18.

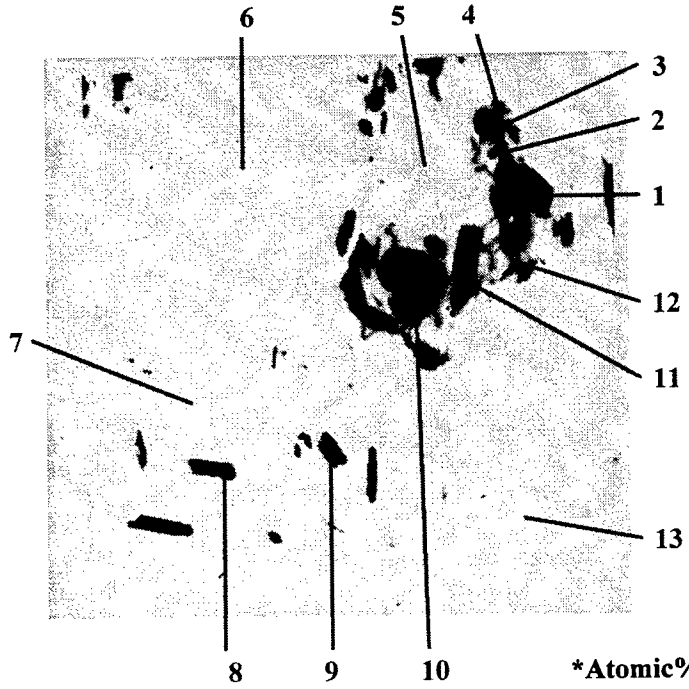

	*Atomic%				
Spot	Ti	Al	V	B	Phase
1	35.0	0	0.2	64.8	TiB_2
2	51.7	0.1	0.6	47.6	TiB
3	35.1	0	0.2	64.7	TiB_2
4	54.0	0.8	0.6	44.6	TiB
5	80.0	8.6	3.2	8.3	Matrix
6	77.6	8.6	5.3	8.6	Matrix
7	80.6	8.5	1.3	9.6	Matrix
8	52.5	0.1	0.2	47.2	TiB
9	53.3	0	0.2	46.5	TiB
10	34.6	0	0.2	65.3	TiB_2
11	35.6	0	0.2	64.2	TiB_2
12	51.6	0.3	0.5	47.6	TiB
13	84.8	8.9	0.6	5.8	Matrix

***Atomic% of Ti-6Al-4V: 86.2% Ti, 10.2% Al, 3.6%V**

Figure 19 DRTI-6Al-4V/TiB/15p As-Extruded EPMA

At this point attention was given to understanding how the transformation of TiB_2 to TiB takes place rather than evaluating the mechanical properties of the composites would be poor, as the clustered reinforcement particles would promote crack initiation and propagation. Specimens from the extruded product were heat treated in a sequence that mirrored the original mapping study. X-ray diffraction duplicated the results of the previous mapping study suggesting a good correlation between the cold compacts and the extruded specimens. Representative samples of completely transformed microstructures are shown in Figures 20 and 21. Clustering is still present in these microstructures with large areas of matrix present, lending further credence to the low solubility of boron in titanium.

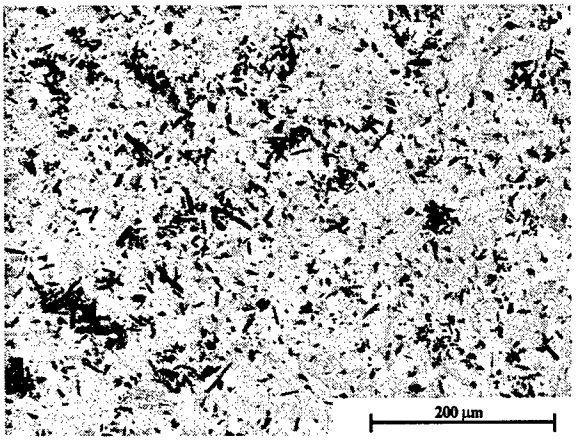

Figure 20

Completely transformed microstructure of DRTi-6Al-4V/TiB/15p at 1300℃/2 hrs

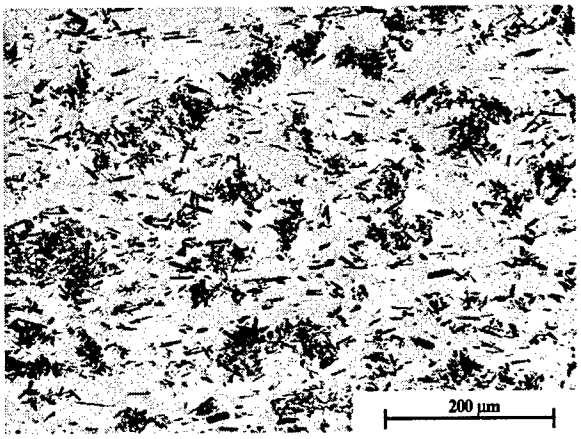

Figure 21

Completely transformed microstructure of DRTi-10V-2Fe-3Al/TiB/15p at 1300℃/1hr

Electrolytic deep etching was undertaken to expose the clusters for further analysis and characterization. Figures 22 and 23 reveal that the feathery morphology is actually a large conglomeration of very fine needles. Figures 24 through 27 document the TiB needle morphology at various heat treatment temperatures for the two alloys. It appears that at the lower temperatures there is a mixture of coarse and very fine TiB needles. These fine needles appear to decrease significantly and eventually disappear with extended time at temperature. At the higher temperatures evidence of the fine needles is not seen. This suggests that these fine needles form first with the decomposition of the TiB_2, then with extended time at temperature either coarsen to

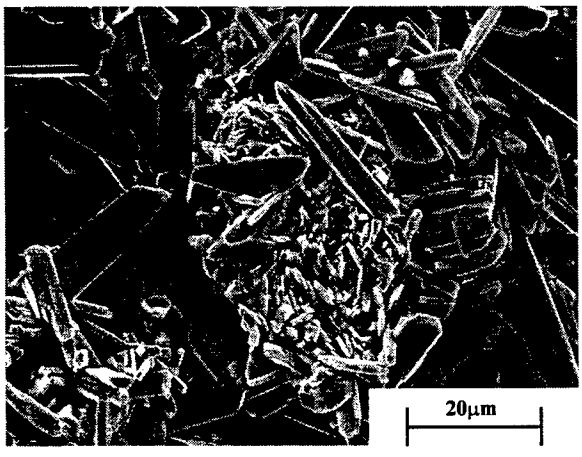

Figure 22

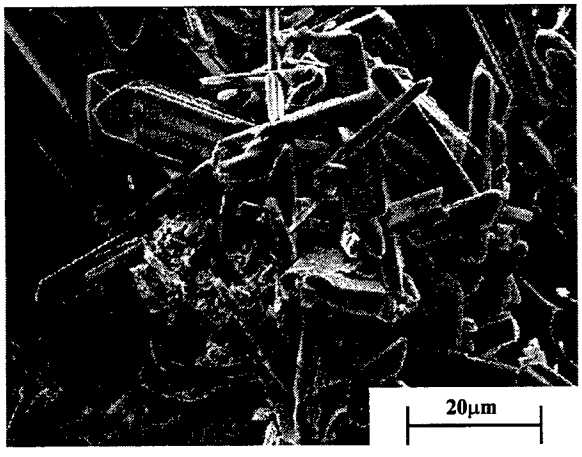

Figure 23

1300℃/1hr heat treated specimen revealing small needles comprising feathery phase morphology

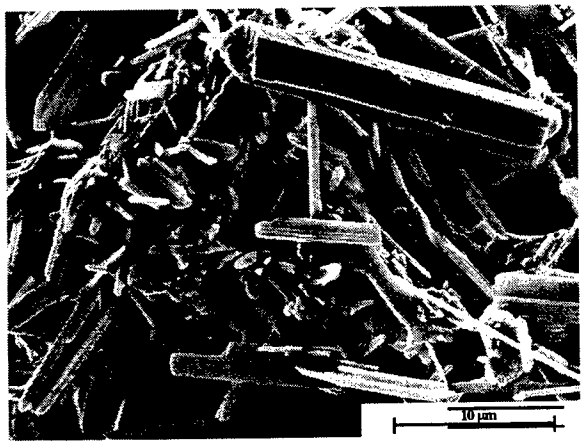

Figure 24

TiB Needles in DRTi-6Al-4V/TiB/15p at 1100C/1hr

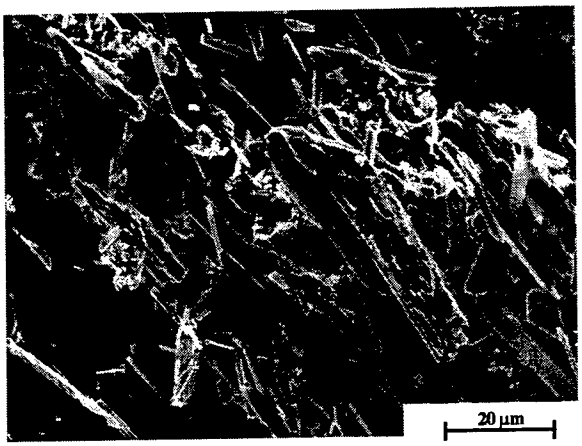

Figure 25

TiB Needles in DRTi-10V-2Fe-3Al/TiB/15p at 1100C/1hr

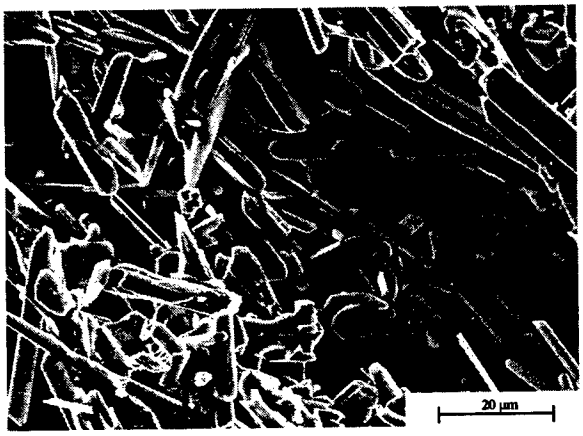

Figure 26

TiB Needles in DRTi-6Al-4V/TiB/15p at 1400C/1hr

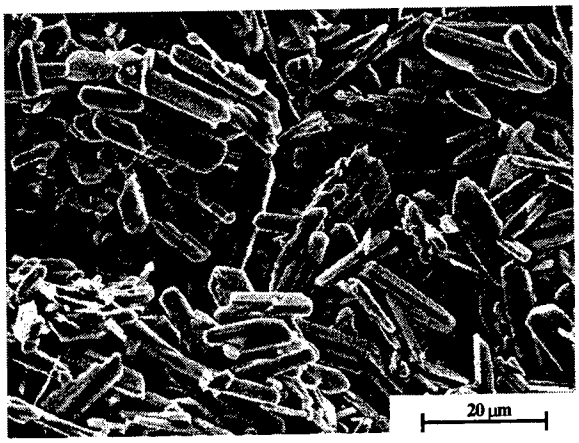

Figure 27

TiB Needles in DRTi-10V-2Fe-3Al/TiB/15p at 1300C/1hr

form larger needles or become sacrificial, supplying boron for the continued coarsening of surrounding needles. This is also suggested by Gorsse *et. al.*[19] who argue that the total population of needles decreases with increasing annealing time and the aspect ratio (L/D) of all needles grows to approximately ten before leveling out. The population and length of needles at an annealing temperature of 1100°C (2012°F) are shown schematically in Figures 28 and 29 and enhances the argument that the initial fine needles either continue to coarsen forming larger needles or become sacrificial, supplying boron to surrounding needles.

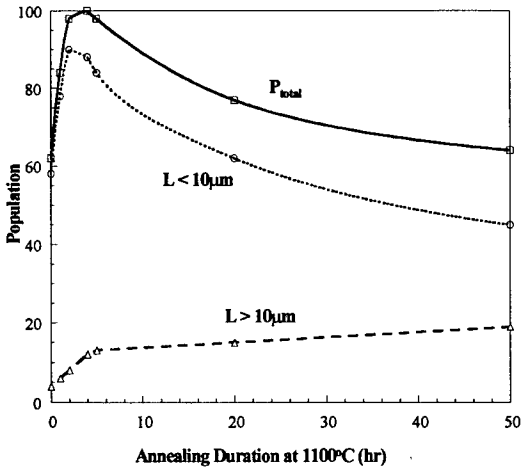

Figure 28 Population, Length and Shape Factor as a Function of Annealing Time

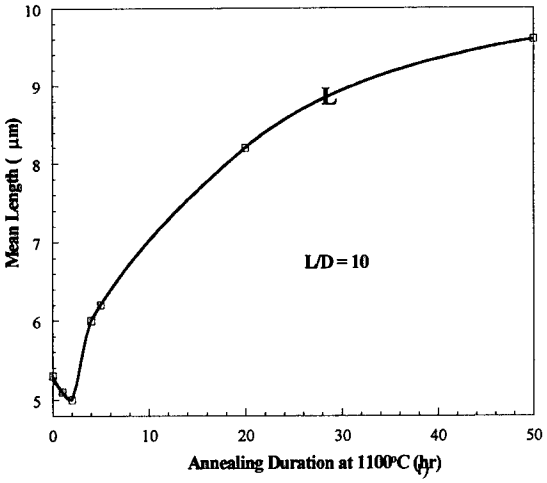

Figure 29 Mean Length of Needles vs. Annealing Time

To further test the results of the transformation times at temperature a second extrusion was accomplished. Additionally, the hypothesis of obtaining a uniform distribution via the alignment of the needles during extrusion was to be tested. Enough blended powder remained from the initial batch to accomplish a small extrusion. Filling, vacuum outgassing and blind die compaction of the extrusion cans proceeded as outlined previously, however, each can was heated at 1300°C (2372°F) for 3 hours prior to extruding; a time period long enough to obtain complete transformation of the TiB_2. The billets were then extruded at 1065°C (1950°F) at a 10.2:1 reduction ratio.

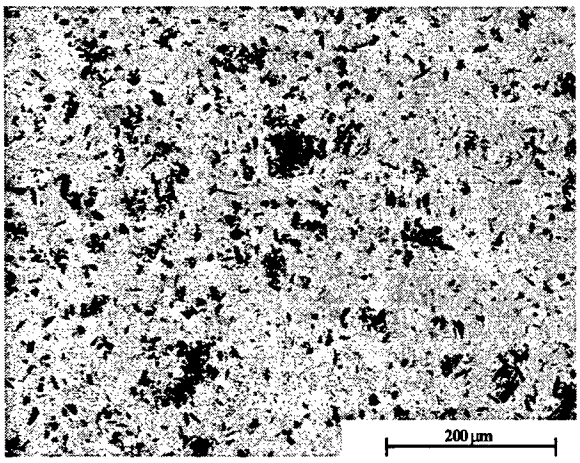

Figure 30

DRTi-6Al-4V/TiB/15p heat treated at 1300℃ then extruded

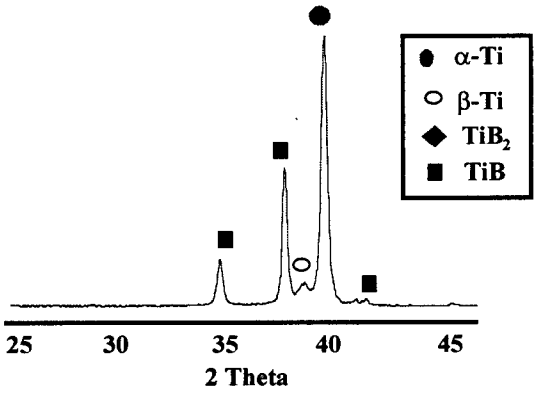

Figure 31

DRTi-6Al-4V/TiB/15p Diffraction Pattern

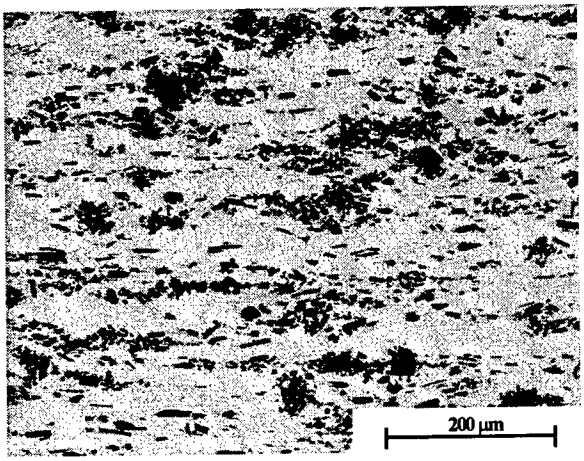

Figure 32

DRTi-10V-2Fe-3Al/TiB/15p heat treated at 1300℃ then extruded

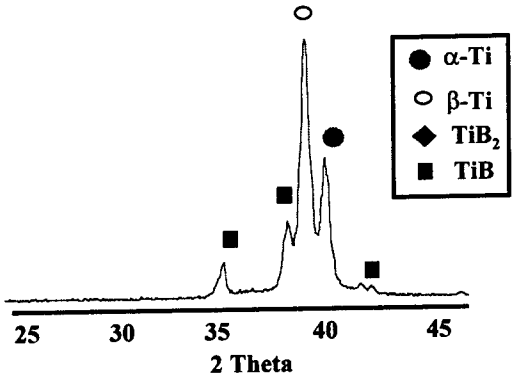

Figure 33

DRTi-10V-2Fe-3Al/TiB/15p Diffraction Pattern

Figures 30 and 32 show the observed microstructure for the DRTi-6Al-4V/TiB/15p alloy and DRTi-10V-2Fe-3Al/TiB/15p alloy, respectively. It can readily be seen that the clustering is still present, but cracking within the clusters was now evident. Figures 31 and 33 are the x-ray diffraction patterns for this extruded material confirming complete transformation of the TiB_2 to TiB.

One final test was attempted to prove that a uniform distribution of TiB needles could be obtained with the powders at hand. The –100 mesh (≤ 150 microns) titanium powder was sieved to extract all remaining –325 mesh (≤ 45 microns) powder. Processing of the powder was the same as already outlined. The powder was consolidated via HIPing at 1300°C (2372°F) for 4 hours at 103.4 MPa (15 ksi); the time chosen to obtain complete transformation. The as-HIPed microstructure is shown in Figure 34 revealing a uniform distribution of TiB needles and proving, that a discontinuously reinforced titanium alloy composite can be produced as long as the starting size of powders is the same.

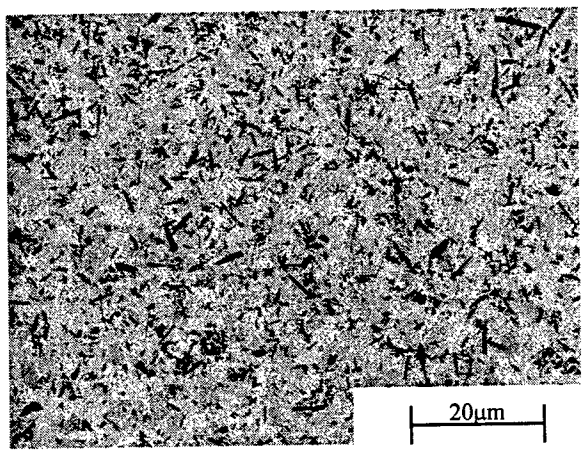

Figure 34

DRTi-6Al-4V/TiB/15p As-HIPed

Analysis of the reaction layer thickness of the Ti-TiB_2 diffusion couples enabled a plot of thickness (x) versus time ($t^{1/2}$) to be developed. From this the various diffusion coefficients for the temperature range of 1100°C to 1400°C (2012°F to 2552°F) were determined, which in turn lead to the evaluation of the activation energy and the pre-exponential. Comparison of the work of others[6-13] with the current research identifies an activation energy (Q) of approximately 194 kJ/mol and is represented in Figure 35. The pre-exponential (D_o) of 9.58E-08 m^2/s is in the range suggesting substitutional diffusion is occurring, however, determination of the various constants that comprise D_o must still be accomplished to support the suggested mechanism.

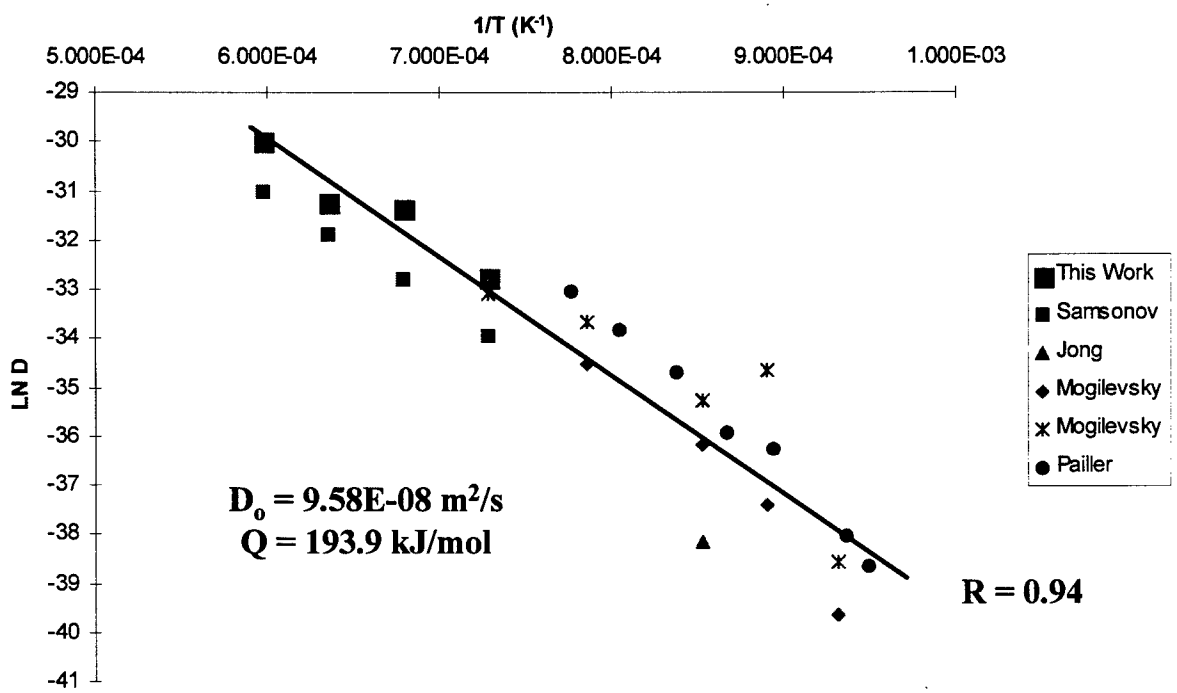

Figure 35 Comparison of experimental work with that of published work

During the analysis of the diffusion couples it was noticed that the reaction layer had some rather distinct morphological features as evidenced by the micrographs in Figure 36. A fine grain structure is apparent near the TiB_2, whereas columnar grains begin to appear near the center of the reaction layer. At approximately three-quarters of the way across the reaction layer

there exists some of the titanium matrix trapped within the layer as supported by EPMA (Spots 14 and 15 in Figure 37).

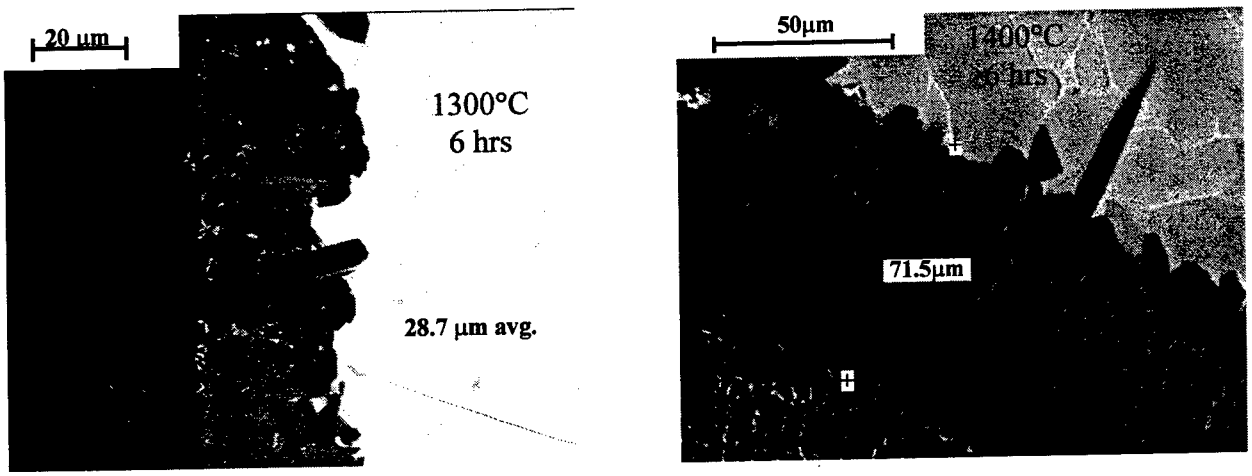

Figure 36 Ti/TiB_2 diffusion couples showing needles extending beyond reaction layer

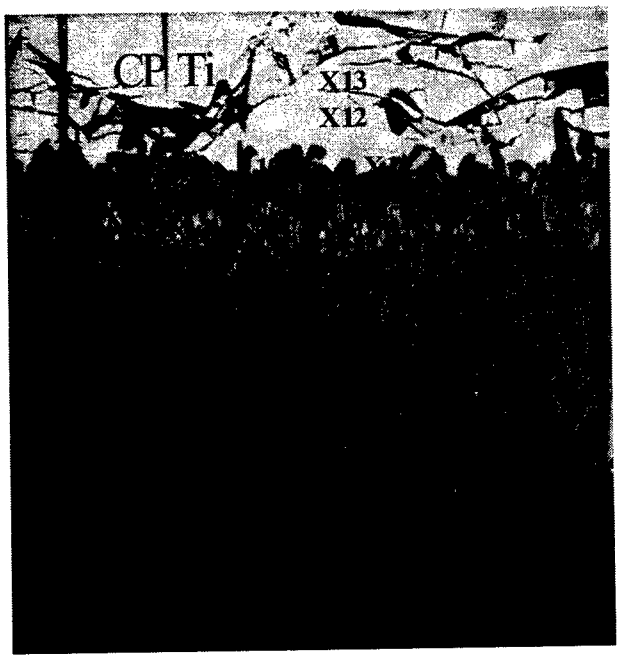

	Atomic%		
Spot	Ti	B	Phase
1	36.0	64.0	TiB_2
2	34.0	66.0	TiB_2
3	36.7	63.3	TiB_2
4	34.5	65.5	TiB_2
5	54.0	46.0	TiB
6	54.5	45.5	TiB
7	54.8	45.2	TiB
8	53.8	46.2	TiB
9	54.9	45.1	TiB
10	55.1	44.9	TiB
11	84.3	15.7	Matrix
12	83.7	16.3	Matrix
13	83.3	16.7	Matrix
14	70.1	29.9	Matrix
15	79.3	20.7	Matrix
16	55.5	44.5	TiB
17	54.8	45.2	TiB
18	54.5	45.5	TiB
19	54.9	45.1	TiB
20	54.1	45.9	TiB
21	55.7	44.3	TiB
22	55.4	44.6	TiB

Figure 37 EPMA of Reaction Layer

The reaction layer was exposed by etching and is represented in Figure 38. The morphology is comprised of very fine needles with larger needles protruding through. The columnar grain features of the reaction layer may indicate that the larger needles are engulfed by the growing front even as it continues to form new large needles ahead of it. This lends further support that some of the smaller needles coarsen to become new larger needles as the front grows and the remaining smaller needles become sacrificial to supply the necessary boron for continued growth of the surrounding larger needles. Additionally, the fine grain structure near the TiB_2 may actually be transformed TiB_2 suggesting that the reaction layer is actually growing in both directions. This argument suggests two diffusion mechanisms are occurring simultaneously, interstitial diffusion of boron through TiB and substitutional diffusion of titanium through TiB in the opposite direction. The value of D_o would support this hypothesis in that the diffusion couples would be measuring the rate limiting step, that is, substitutional diffusion over interstitial diffusion. If this is truly the case, then the measurements of the reaction layer thickness in the diffusion couples and hence the determination of D_o is incorrect because it assumes only one type of mechanism and does not account for the different flux rates of boron and titanium. The original Ti/TiB_2 interface is unknown, however, a diffusion couple with inert markers has been devised to determine this.

Figure 38
Reaction Front Morphology

Determination of the diffusion parameters for the needles is a much more complicated procedure than those of the reaction layer. In the two-dimensional realm of the SEM, which was sufficient for measuring the thickness of the reaction layer, the true orientation of the needles is unknown, therefore the true length of the needles would be unknown. Needles need to be collected by etching away the matrix, however, not all the needles are the same length so a

statistical average length would have to be utilized and the assumption made that the needles begin to form immediately. It is sufficient to state at this point in time that the needles do indeed grow faster than the reaction layer as evidenced from the diffusion couple micrographs (Figures 36 and 38), but to arrive at accurate diffusion parameters will be a rigorous procedure.

CONCLUSIONS

Discontinuously reinforced titanium alloy composites can be fabricated successfully via the blended elemental powder metallurgy processing technique provided the starting powder sizes are the same; in this case, -325 mesh ($\leq$ 45 microns). Initial trials proved unsuccessful in that using larger titanium powder enabled the smaller TiB_2 powder to fill the voids between the titanium particles resulting in a clustered microstructure. Further research is required to resolve if larger size powders can be used to fabricate these composites as the limited solubility of boron in titanium and the sluggish diffusion rate will be major factors in achieving a uniform distribution of reinforcement. A heat treatment mapping study identified the time at temperature at which TiB_2 completely transformed to TiB in the temperature range of 1100°C to 1400°C (2012°F to 2552°F). In particular, at 1100°C (2012°F) the transformation took up to 16 hours, at 1200°C (2192°F) it took up to six hours, two hours at 1300°C (2372°F) and finally, the transformation took one hour or less at 1400°C (2552°F). Smaller size powders would take less time, but with the trade-off of the more expensive cost that is concomitant with smaller size powders.

During the transformation of TiB_2 to TiB an intermediate phase with a feathery morphology was observed. The phase was shown to be TiB, but in a morphology quite distinct from the expected needle morphology. This phase eventually disappeared with extended time at temperature forming a coarse needle morphology with an aspect ratio of approximately ten. Further analysis of this feathery phase through the use of electrolytic deep etching revealed it to be a large conglomeration of very fine needles. Given the sheer number of these fine needles it became evident that the total population of needles decreased with extended time at temperature suggesting that some of these needles continue to coarsen to form larger needles while the remainder become sacrificial, supplying boron to surrounding needles enabling them to coarsen.

Numerous authors have experimented and analyzed the diffusion of boron in titanium through the use of various types of diffusion couples over a wide range of temperatures.[6-13] As such, each has reported different diffusion coefficients and pre-exponentials, none of which provides a clear picture of whether the diffusion mechanism is interstitial or substitutional. It is evident that there are different growth rates of the diffusion couple reaction layer and the TiB needles, with the needles growing much faster than the reaction layer. Comparison of the work of these authors with the current research identified an activation energy (Q) of approximately 194 kJ/mol and a pre-exponential (D_o) of 9.58E-08 m^2/s. This is in the range indicating substitutional diffusion is occurring. The atomic radii difference between titanium and boron, 0.147 nm for titanium and 0.092 nm for boron, would support interstitial diffusion, but is also indicative of limited solubility of boron in titanium. The crystal structure of TiB also supports the interstitial diffusion mechanism although a short circuit diffusion path could be argued. Boron atoms could diffuse along the zigzag chains within the TiB structure, but the lattice arrangement also presents what are referred to as "boron-free pipes" that may serve as a short circuit path for boron atoms to reach the tip of the needle to sustain continued growth.

This argument is suggesting that two diffusion mechanisms are occurring simultaneously, interstitial diffusion of boron through TiB and substitutional diffusion of titanium through TiB in the opposite direction. The value of D_o would support this hypothesis in that the diffusion couples would be measuring the rate limiting step, that is, substitutional diffusion over interstitial diffusion. The original Ti/TiB_2 interface is unknown, however, work is progressing to devise a diffusion couple with inert markers to determine this.

Acknowledgments

Many thanks to Dr. Daniel Miracle, Dr. Awadh Pandey, and Dr. Jonathan Spowart at the Air Force Research Laboratory, Wright-Patterson Air Force Base, Ohio for their guidance, support and continued encouragement in the pursuit of this research. I also wish to thank Dr. Ragahavan Srinivasan and the late Dr. Isaac Weiss of the Department of Mechanical and Materials Engineering, Wright State University, Dayton, Ohio whose guidance and support have been extremely beneficial as I move through my Ph.D. program. Finally, thank you to the Air

Force Office of Scientific Research for allowing me the opportunity to participate in their Summer Research Extension Program.

REFERENCES

1. Saito, T. *A Cost Effective P/M Titanium Matrix Composite for Automobile Use.* Advanced Performance Materials **2**, 121-144, 1995.
2. Saito, T., Furuta, T., Yamaguchi, T., and Ogino, K. *A New Low Cost MMC of TiB Particle Dispersed in Titanium Alloy.* Proc. Conf. 1993 Powder Met. World Congress, Y. Bando and L. Kosuge, Eds., JPMA-JSPM, , 642-645, 1993.
3. Saito, T., Furuta, T., and Yamaguchi, T. *Development of a Low Cost Titanium Matrix Composite.* Recent Advances in Titanium Matrix Composites, TMS, Warrendale, PA, F.H. Froes and J. Storer, Eds., 1995.
4. Srivatsan, T.S., Soboyejo, W.O. and Lederich, R.J. *Tensile Deformation and Fracture Behavior of a Titanium Alloy Metal Matrix Composite.* Composites Part A **28A**, 365-376, 1997.
5. Fan, Z., Miodownik, A.P., Chandrasekaran, L., and Ward-Close, M. *The Young's Moduli of In Situ Ti/TiB Composites Obtained by Rapid Solidification Processing.* Journal of Materials Science **29**, 1127-1134, 1994.
6. Samsonov, G.V. and Zhunkovskii, G.L. *Mechanism of the Reaction of Refractory Metals With Boron in Vacuum Boriding.* Poroshkovaya Metallurgiya **6**, 44-52, 1970.
7. Jong, E.N.T., Flower, H.M. and West, D.R.F. *Interfacial Reaction Kinetics in α- and β-Titanium Based Metal Matrix Composites.* Titanium '92: Science and Technology, TMS, Warrendale, PA, F.H. Froes and I. Caplan, Eds., 2561-2568, 1993.
8. Mogilevsky, P., Werner, A. and Dudek, H.J. *Application of Diffusion Barriers in Composite Materials.* Materials Science and Engineering **A242**, 235-247, 1998.
9. Mogilevsky, P., Werner, A. and Dudek, A.J. *Reactive Formation of TiB at the TiB_2-Ti Interface.* Defect and Diffusion Forum **143-147**, 585-590, 1997.

10. Pailler, R., Lahave, M., Thebault, J. and Naslain, R. *Chemical Interaction Phenomena at High Temperature Between Boron Fibers and Titanium Metal (or TA6V Alloy).* Failure Modes in Composites **4**, 265-284, 1979.

11. Reeves, A.J., Stobbs, W.M. and Clyne, T.W. *The Effect of Interfacial Reaction on the Mechanical Behaviour of Ti Reinforced With SiC and TiB_2 Particles.* Metal Matrix Composites Processing, Microstructure and Properties, 12th Risø Int. Symp., N. Hansen, D.J. Jensen, T. Leffers, H. Lilholt, T. Lorentzen, A.S. Pedersen, O.B. Pedersen and B. Ralph, Eds., Risø Natl. Lab., Roskilde, Denmark, 631-636, 1991.

12. Mogilevsky, P., Gutmanas, E.Y., Gotman, I. and Telle, R. *Reactive Formation of Coatings at Boron Carbide Interface With Ti and Cr Powders.* Journal of the European Ceramics Society **15**, 527-535, 1995.

13. Fan, Z., Guo, Z.X. and Cantor, B. *The Kinetics and Mechanism of Interfacial Reaction in Sigma Fiber-Reinforced Ti MMCs.* Composites Part A **28A**, 131-140, 1997.

14. Sundrica, J. *Determination of the Optimal Rotational Speed for Powder Mixing.* Intl. J. Powder Met. Tech., **17**, 291-294, 1981.

15. Kirchoff, S.D., Adkins, J.Y., Griffith, W.M. and Martorelli, I.A. *Effective Method for Degassing Evaluation of Aluminum P/M Alloys.* Rapidly Solidified Powder Aluminum Alloys, ASTM STP 890, ASTM, Philadelphia, PA, M.E. Fine and E.A. Starke, Jr., Eds., 354-366, 1986.

16. Zimmer, W.H., Director of Engineering, Dynamet Technology, Inc., private communication.

17. Soboyejo, W.O., Lederich, R.J. and Sastry, S.M.L. *Mechanical Behavior of Damage Tolerant TiB Whisker Reinforced In-Situ Titanium Matrix Composites.* Acta Met. **42**, 8, 2579-2591, 1994.

18. Larson, D.J., Liu, T. and Miller, M.K. *Boron Solubility and Boride Compositions in $\alpha_2 + \gamma$ Titanium Aluminides.* Intermetallics **5**, 411-414, 1997.

19. Gorsse, S., Chaminade, J.P. and Le Petitcorps, Y. *In Situ Preparation of Titanium Base Composites Reinforced by TiB Single Crystals Using a Powder Metallurgy Technique.* Composites Part A **29A**, 1229-1234, 1998.